METAL COMPOUND ELECTROCATALYSTS FOR HYDROGEN PEROXIDE SYNTHESIS, ELECTRO-FENTON PROCESS, AND BIOMASS VALORIZATION

by

HONGYUAN SHENG

A dissertation submitted in partial fulfillment of
the requirements for the degree of

DOCTOR OF PHILOSOPHY
(CHEMISTRY)

at the
UNIVERSITY OF WISCONSIN–MADISON
2022

Date of final oral examination: February 3rd, 2022

The dissertation is approved by the following members of the Final Oral Committee:

Song Jin, Professor, Chemistry (Analytical, Chemical Biology, Inorganic, Materials, Physical)
J. R. Schmidt, Professor, Chemistry (Materials, Physical)
Shannon S. Stahl, Professor, Chemistry (Inorganic, Organic)
Kyoung-Shin Choi, Professor, Chemistry (Analytical, Inorganic, Materials)

PREFACE

METAL COMPOUND ELECTROCATALYSTS FOR HYDROGEN PEROXIDE SYNTHESIS, ELECTRO-FENTON PROCESS, AND BIOMASS VALORIZATION

HONGYUAN SHENG, PH.D.

UNIVERSITY OF WISCONSIN-MADISON

2022

Electrochemical synthesis of high-value chemicals using renewable electricity offers a sustainable alternative to conventional chemical manufacturing. Hydrogen peroxide (H_2O_2) is a useful and green oxidant, but its centralized chemical production is energy-intensive and unsafe. Decentralized electrosynthesis of H_2O_2 directly at the point of use via the selective two-electron oxygen reduction reaction ($2e^-$ ORR) is attractive, yet robust and cost-effective electrocatalysts that are active and selective in acidic (or neutral) solutions where H_2O_2 is stable are lacking. My graduate research with Prof. Song Jin at the University of Wisconsin-Madison has focused on the experimental developments of new, stable, and selective acidic (and neutral) $2e^-$ ORR catalysts based on earth-abundant metal compounds.

Chapter 1 gives an overview of this dissertation, in which I provide a focused summary and outlook of metal compound-based $2e^-$ ORR catalysts for acidic (and neutral) H_2O_2 electrosynthesis and the electro-Fenton process. I first introduce the computational frameworks for predictive identification of stable metal compounds that are selective and active toward $2e^-$ ORR.

I then overview the experimental practices for rigorously evaluating metal compound-based 2e$^-$ ORR catalysts, from basic electrochemical techniques to catalyst leaching and side reaction monitoring to scaled-up H_2O_2 bulk electrosynthesis. I further discuss the uses of metal compound-based cathodes in the electro-Fenton process for various applications from environmental treatment to valuable chemical transformations. Finally, future challenges and opportunities in search of new better-performing metal compound-based 2e$^-$ ORR catalysts are proposed.

Chapters 2 through 4 present the main body of my graduate research resulting from the close collaboration with computational chemists in Prof. J. R. Schmidt's group at the University of Wisconsin-Madison, in which we achieved new mechanistic understanding and established rational catalyst design rules that led to the new discovery of a series of earth-abundant metal dichalcogenide compound catalysts (CoS_2, $CoSe_2$, and $NiSe_2$) for acidic 2e$^-$ ORR with significant improvements in both catalyst stability and H_2O_2 electrosynthesis performance.

In Chapter 2, I present our first joint computational-experimental demonstration of pyrite-type cobalt disulfide (CoS_2), an earth-abundant transition metal compound, catalyzes 2e$^-$ ORR in acidic solution with high selectivity and activity. Computations successfully predict the high activity and selectivity of CoS_2 towards 2e$^-$ ORR due to the modest binding of OOH* adsorbate on the single Co site of CoS_2 and the kinetically disfavored O-O bond scission resulting from the lack of active site ensembles. Both rotating ring-disk electrode (RRDE) measurements of drop-casted CoS_2 nanomaterials and H_2O_2 bulk electrosynthesis experiments using CoS_2 nanowires directly grown on carbon fiber paper electrodes followed by chemical quantification of the H_2O_2 product show efficient H_2O_2 electrosynthesis in acidic solution with high H_2O_2 selectivity and good operational stability. CoS_2 also catalyzes 2e$^-$ ORR in neutral solution with less activity and selectivity.

In Chapter 3, earth-abundant cobalt diselenide ($CoSe_2$) pyrite and marcasite polymorphs are established as the new benchmark $2e^-$ ORR catalysts that show significant improvements in both catalyst stability and selectivity for H_2O_2 electrosynthesis in acidic solution. New mechanistic understanding is achieved from calculated bulk and surface Pourbaix diagrams that predict the high stability of $CoSe_2$ polymorphs against surface oxidation and catalyst leaching due to the weak O* binding to Se sites, fully supported by experiments. RRDE measurements show that $CoSe_2$ polymorphs are highly active, selective, and stable for $2e^-$ ORR, consistent with computations, and deliver higher kinetic current densities for H_2O_2 production in acidic solution than the state-of-the-art noble metal or single-atom catalysts. $CoSe_2$ marcasite nanowires directly grown on carbon paper electrodes allow for the steady bulk electrosynthesis of H_2O_2 in acidic solution with a high accumulated concentration of 547 ppm achieved. Such efficient and stable H_2O_2 electrosynthesis by $CoSe_2$ marcasite in acidic solution further enables the effective electro-Fenton process, which converts the produced H_2O_2 to the more oxidizing hydroxyl radical (·OH), for model organic pollutant degradation.

Chapter 4 is centered around utilizing the electro-Fenton process for enabling valuable chemical transformations. Electrochemical valorization of surplus biomass-derived feedstocks such as glycerol into high-value chemicals offers a sustainable route for utilizing biomass resources and decarbonizing chemical manufacturing; however, glycerol is typically valorized solely via anodic oxidation, with lower-value products such as hydrogen gas generated at cathode. In this chapter, I demonstrate that the ·OH-generating electro-Fenton process enables the efficient electrochemical valorization of glycerol to value-added oxidation products in the cathodic half-cell. This is made possible by the computational-guided discovery of a new nickel diselenide ($NiSe_2$) $2e^-$ ORR catalyst for stable and selective H_2O_2 electrosynthesis in acidic solution. A new

proof-of-concept linear paired electrochemical process is demonstrated for concurrently valorizing glycerol into the same oxidation products at both $NiSe_2$ cathode and Pt anode, and achieves high glycerol conversion and high selectivity for valuable C_3 products with little external energy input needed. This novel use of the electro-Fenton process and this conceptual strategy of linear pairing opens up new opportunities for enabling electrochemical valorization of diverse biomass-derived feedstocks with high atom efficiency and low energy cost.

Chapter 5 presents the collaborative systematic study, within Prof. Song Jin's group and with Prof. George Huber's group at the University of Wisconsin-Madison, of a series of earth-abundant cobalt-based spinel oxide (MCo_2O_4, M = Mn, Fe, Co, Ni, Cu, and Zn) nanostructures as anode electrocatalysts for electrochemical oxidation of glycerol. Among this spinel oxide series, $CuCo_2O_4$ is identified as the intrinsically most active catalyst for glycerol oxidation in alkaline solution, and is efficient and stable for the selective glycerol oxidation to formic acid with high glycerol conversion and high overall Faradaic efficiency toward all value-added products achieved, as demonstrated using $CuCo_2O_4$ nanostructures directly grown on carbon fiber paper electrodes for the bulk electrolysis reactions of glycerol oxidation.

Chapter 6 switches gear and presents the collaborative study, with Prof. Shannon Stahl's group at the University of Wisconsin-Madison, on exploring electrochemical energy conversion applications of redox-active water-soluble organic molecules, which can be used to decouple the two half-reactions of water electrolysis and enable spatial and temporal separation of the hydrogen and oxygen evolution to mitigate the gas crossover issue. In this chapter, a tetrasubstituted quinone molecule is demonstrated to exhibit significantly enhanced stability than the previously reported benchmarking anthraquinone derivatives. This enhanced stability, confirmed by symmetric flow battery experiments under relevant conditions, enables stable decoupled hydrogen and oxygen evolution in a continuous flow electrolysis cell.

The following appendices provide complementary information to the works presented in the main chapters. Specifically, Appendices 1, 2, 3, 4, 5, and 6 provide additional figures and tables pertaining to Chapters 1, 2, 3, 4, 5, and 6, respectively.

This dissertation constitutes significant advances in developing stable, selective, and active metal compound-based electrocatalysts for H_2O_2 electrosynthesis, the electro-Fenton process, and biomass valorization. The integrated computational-experimental studies presented here reveal new general mechanistic insights and rational design rules that provide guidance for future developments of high-performance metal compound-based electrocatalysts for electrochemical synthesis of high-value chemicals.

ACKNOWLEDGMENTS

Time flies by so fast that I am now right in front of the finishing line of my graduate school degree dash. This dissertation would not have been possible without the support, guidance, and advice from many people.

I must dedicate my earnest gratitude to my parents, Xiaozhong Sheng and Hong Tong. Thank you for your endless love and unconditional support throughout the journey of my life. You are my role models in life, and I love you from the bottom of my heart.

I must extend my sincere appreciation to my Ph.D. advisor, Professor Song Jin. Your breadth and depth of knowledge, and fearless dedication to ground-breaking scientific discovery have always been my inspiration in graduate school. I feel so fortunate to have worked with and learnt from you throughout the years. Thank you for your mentorship that plays an irreplaceable role in my intellectual growth as a scientific researcher, and will keep influencing me in the future.

I also acknowledge my committee members, Professor J. R. Schmidt, Professor Shannon Stahl, and Professor Kyoung-Shin Choi. Thank you for serving on my committee and providing invaluable suggestions since my second year in graduate school. I learnt electrochemistry basics from the course Prof. Choi taught during my first semester in graduate school, and had the fortune to collaborate with Prof. Schmidt and Prof. Stahl during my graduate research that broadened my interdisciplinary research interests.

I am thankful for my fellow labmates in the Jin group, who made great impacts on my life in graduate school. Senior members of the Jin group have helped me in so many ways from day one since I joined the Jin group. I thank Dr. Lianna Dang for mentoring me during my first research

project and offering me trainings on a variety of lab techniques. I thank Dr. Wenjie Li for discussing electrochemistry and sharing his knowledge and expertise with me. I appreciate the generous help from Dr. Yuzhou Zhao, Dr. Nitish Mathur, Dr. (now Prof.) Yongping Fu, Dr. Matthew Stolt, Dr. Melinda Schearer, Dr. Lichen Xiu, Dr. Leith Samad, and Kyle Czech, and Matthew Haveman. My cohort of Fall 2016 entering class in the Jin group, Dr. Matthew Hautzinger, (soon-to-be Dr.) Dongxu Pan, Dr. Tim Tiambeng, Dr. Natalia Spitha, Brandon Lamb, Stephanie Lamb, and Kayla Lloyd, have been special to me as we go through many things together during graduate school, and I treasure the connections between us and appreciate your help in and out the lab. My life in graduate school would not have been the same without junior members of the Jin group. Dominic Ross is my graduate mentee working on electrocatalysis research. I am grateful for a lot of insightful scientific discussions and feel lucky to have you as an amazing comrade, especially for those sleepless nights we spent at the beamlines at the Advanced Photon Source. I am sure you will be a great mentor for Gerardo Quintana Cintron. Dave Kaiman and Jarryd Featherman are my former undergraduate mentees, I am grateful for these mentoring opportunities as learning experiences for me, and I appreciate your contributions to my research. Rui Wang, Katelyn Michael, and Dr. Chih-Jung Chen are other major players of the current electrochemistry research in the Jin group, and I appreciate you help and encouragement. I thank David Roberts, Chris Roy, Willa Mihalyi-Koch, Emily Reasoner, Erika Jackson, Kristel Forlano, and Dr. Jaeyong Park for being great and fun officemates and labmates to talk with, thank you for making my life in graduate school better. I also thank the first-year students who just joined the Jin group, Yueai Lin, Chris Triggs, Gerardo Quintana Cintron, Ethan Auleciems, and Jaan Andrews, and I wish you have fun in the Jin group. My appreciation also goes to other former members of the Jin group. I thank Dr. (now Prof.) Jie Chen, Dr. Liang Cai, Dr. (now Prof.) Yang

Yang, Prof. Bo Song, Prof. Ying Yang, and Dr. (now Prof.) Yifan Dong for your help and encouragement during my early years in graduate school. I thank Dr. Xiaotong Han, Dr. Jinzhen Huang, Prof. Fengmei Wang, and Dr. Hui-Chun Fu, who I had pleasure to work with on electrochemistry research. I thank Dr. Ming-Yu Kuo for being a kind and fun officemate. I thank Prof. Xiaohua Yang and Prof. Diwen Ying who worked on preliminary electrocatalysis research related to my graduate research before I joined the Jin group. I also thank other visiting scholars in the Jin group, Dr. Poulomi Roy, Dr. Jun Dai, Dr. Meiying Leng, Dr. Jing Li, Dr. Huawei Liu, Dr. Tianqi Guo, and Dr. Yuliang Yuan.

I am grateful for my collaborators, who made important contributions to my graduate research. My special gratitude goes to Prof. J. R. Schmidt, Dr. Aurora Janes, and Dr. Eric Hermes who conducted all the computational electrocatalysis research presented in Chapters 1 through 4 of this dissertation. This dissertation would not have been possible without your hard work. I will miss this productive long-term collaboration, and the numerous enlightening discussions with J. R., Aurora, Song, Dominic, and Kwan Lee during our project meetings. I am also grateful for another collaboration with Prof. Shannon Stahl, Dr. (now Prof.) Fei Wang, and Dr. James Gerken, which led to the work presented in Chapter 6 of this dissertation. Thank you for this experience that got me involved with electrochemistry of organic molecules and flow devices, which will be helpful for my research in the future. I also thank Prof. George Huber and Dr. Theodore Walker for their help with the work presented in Chapter 5 of this dissertation. I also thank Prof. Carlo Segre, Dr. Yujia Ding, Dr. Joshua Wright, and John Katsoudas for their help with the beamline experiments conducted at the Advanced Photon Source.

I would also thank academic and administrative staff in the chemistry department and on the UW-Madison campus, including but not limited to Dr. Rob McClain, Dr. Heike Hofstetter,

James Lazarcik, Tracy Drier, Steve Myers, Dr. Pamela Doolittle, Susan Martin-Zernicke, Liv West, Dr. Arrietta Clauss, Taylor Mathewson, Dr. Matthew Sanders, and Jeff Nielsen. My graduate research and education would not have been the same without your help and support.

Finally, I would thank my friends who made my life in graduate school colorful. I want to thank Dr. Xianyuan Zhao, Dr. Hanming Yang, Dr. Erdong Lu, (soon-to-be Dr.) Dongxu Pan, Dr. Zihui Li, Dr. Si-Jie Chen, Dr. Yusi Cui, Dr. Lei Liu, (soon-to-be Dr.) Feng Pan, Shao-Chun Wang, Xingyang Fu, Chuanhong Liu, Ruosen Xie, Dr. Qinrui Liu, Xiaoyu Jiang, and many others for those joyful and memorable moments.

Hongyuan Sheng

02/02/2022

TABLE OF CONTENTS

LIST OF FIGURES

LIST OF SCHEMES

LIST OF TABLES

CHAPTER 1

Metal Compound-Based Electrocatalysts for Electrochemical Synthesis of Hydrogen Peroxide and the Electro-Fenton Process[*]

1.1 Introduction

Hydrogen peroxide (H_2O_2) is a useful and green oxidant with diverse applications in pulp and paper industry, chemical manufacturing, wastewater treatment, and healthcare disinfection.[1] The COVID-19 pandemic also contributes to the recent rapid growth of the global H_2O_2 market.[2] The prevalent chemical production of H_2O_2 via the anthraquinone process is energy-intensive and unsafe as it produces up to 70 wt% concentrated H_2O_2 at centralized plants and requires hazardous transportation to end-users.[1] Decentralized electrosynthesis of H_2O_2 via two-electron oxygen reduction reaction ($2e^-$ ORR)[3-6] offers a more sustainable route because it can be driven by increasingly affordable renewable electricity,[7] eliminate the need for H_2 gas, and produce dilute H_2O_2 directly at the point of use, which is advantageous for distributed applications such as water treatment that requires <0.1 wt% H_2O_2.[3] The key challenge is to develop robust electrocatalysts with high activity, selectivity, and stability for the desired $2e^-$ (vs. the competing $4e^-$) ORR pathway. H_2O_2 can also be electrogenerated by two-electron water oxidation reaction,[8] but this Account focuses only on the $2e^-$ ORR approach.

---

[*] This chapter will be submitted for future publication, in collaboration with R. Dominic Ross, J. R. Schmidt, and Song Jin.

Various classes of selective 2e$^-$ ORR catalysts, including noble metal alloys,[9,10] carbon materials,[11-13] single-atom catalysts,[14-17] and metal compounds,[18-23] have been studied for H_2O_2 electrosynthesis under different pH conditions.[3,6] Compared to alkaline condition where H_2O_2 is unstable,[24] acidic and neutral conditions are attractive for several reasons besides the chemical stability of H_2O_2. Acidic H_2O_2 electrosynthesis can proceed in the technologically mature proton exchange membrane (PEM) devices.[3] On-site water disinfection and environmental treatment can benefit from acidic H_2O_2 electrosynthesis because the electro-Fenton process operates at the optimum pH of ~3 to convert the produced H_2O_2 into the more oxidizing hydroxyl radical (·OH) for the removal of persistent bacteria and organic pollutants.[25] Neutral solutions are noncorrosive and can avoid the need for neutralization for practical applications.[13,15,22] Nevertheless, high-performance yet cost-effective 2e$^-$ ORR catalysts in acidic (and neutral) solutions are still under development.

Metal compounds, an emerging class of 2e$^-$ ORR catalysts, are generally less summarized in the recent reviews of H_2O_2 electrosynthesis, probably due to fewer existing examples and less explored structure-property relationships. By integrating computation and experiment, our recent research established rational catalyst design rules that led to the discovery of a series of binary (CoS_2,[18] $CoSe_2$,[19] $NiSe_2$[20]) and ternary ($CuCo_{2-x}Ni_xS_4$, $0 \le x \le 1.2$[21]) earth-abundant metal chalcogenide compounds as new and robust 2e$^-$ ORR catalysts in acidic (and neutral) solutions, and achieved mechanistic insights into the catalyst stability, selectivity, and activity. We realized significant improvements in both catalyst stability and H_2O_2 bulk electrosynthesis performance from the systematic studies of these metal chalcogenide-based acidic 2e$^-$ ORR catalysts, and utilized the more stable $CoSe_2$[19] and $NiSe_2$[20] catalysts for the electro-Fenton process[25] that is more demanding for catalyst stability. In addition to demonstrating electro-Fenton degradation of an organic pollutant using a $CoSe_2$ cathode,[19] we further established a novel approach of enabling electrochemical valorization of glycerol, a surplus and low-cost biomass-derived feedstock, into value-added oxidation products via the electro-Fenton process at a $NiSe_2$ cathode.[20]

This Account is aimed to provide a focused summary and outlook of metal compound-based $2e^-$ ORR catalysts for acidic (and neutral) H_2O_2 electrosynthesis and the electro-Fenton process. We first introduce our developed computational frameworks for predictive identification of stable metal compounds that are selective and active toward $2e^-$ ORR. We then overview the experimental practices for rigorously evaluating metal compound-based $2e^-$ ORR catalysts, from basic electrochemical techniques to catalyst leaching and side reaction monitoring to scaled-up H_2O_2 bulk electrosynthesis. We further discuss the uses of metal compound-based cathodes in the electro-Fenton process for various applications from environmental treatment to valuable chemical transformations. Finally, future challenges and opportunities in search of new better-performing metal compound-based $2e^-$ ORR catalysts are proposed.

1.2 Fundamentals of Selective $2e^-$ ORR on Metal Compound-Based Catalysts

1.2.1 Thermodynamic Considerations

The thermodynamics of $2e^-$ ORR ($O_2 + 2\ H^+ + 2\ e^- \rightarrow H_2O_2$, $E^o = 0.69$ V vs. reversible hydrogen electrode, RHE) and $4e^-$ ORR ($O_2 + 4\ H^+ + 4\ e^- \rightarrow 2\ H_2O$, $E^o = 1.23$ V vs. RHE) are often described by the volcano relations between the thermodynamic limiting potential (U_L) and the energetics of key reaction intermediates.[26] $2e^-$ ORR proceeds via the adsorption of OOH* ($O_2 + * + H^+ + e^- \rightarrow OOH^*$, where * is an unoccupied surface binding site) followed by its desorption to form H_2O_2 ($OOH^* + H^+ + e^- \rightarrow H_2O_2 + *$); $4e^-$ ORR occurs via the O-O bond cleavage processes (thermal cleavage: $O_2 + 2\ * \rightarrow 2\ O^*$, and $OOH^* + * \rightarrow O^* + OH^*$; electrochemical reductive elimination: $OOH^* + H^+ + e^- \rightarrow O^* + H_2O$).[18] The key intermediates of $2e^-$ ORR (OOH*) and $4e^-$

ORR (OH*) follow the linear scaling relationship ($\Delta G_{OOH*} = \Delta G_{OH*} + 3.2$ eV[26]), resulting in the $2e^-$ and $4e^-$ ORR volcanos (Figure 1.1a).[6] The $2e^-$ ORR activity, determined by the OOH* adsorption energy (ΔG_{OOH*}), is maximized at the peak of $2e^-$ ORR volcano. Moving leftwards from $2e^-$ ORR volcano peak, the catalyst surface binds OOH* (and OH*) more strongly, and U_L of $4e^-$ ORR is always more positive than that of $2e^-$ ORR, indicating the $4e^-$ pathway will dominate because there is a greater driving force to form H_2O than H_2O_2 (Figure 1.1a, blue region). To the right of $2e^-$ ORR volcano peak, U_L of the $2e^-$ and $4e^-$ pathways overlap, and moving rightwards will increase the selectivity (but lowering the activity) for $2e^-$ ORR because the formation of OH* (and OOH*) becomes more difficult (Figure 1.1a, green region). Besides electronic effects described above, the $2e^-$ ORR selectivity can also be improved by controlling geometric (or ensemble) effects by rearranging catalyst surface atoms to change adsorption sites of reaction intermediates, so that O* can be destabilized relative to OOH*, deviating from the conventional scaling relationship.[9,27]

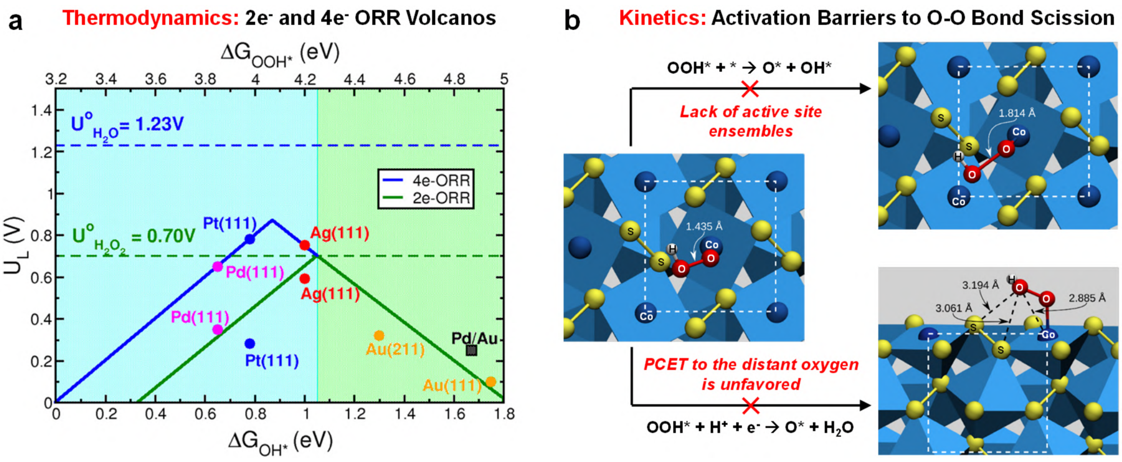

Figure 1.1. Thermodynamic and kinetic considerations of ORR pathways.

(**a**) $2e^-$ ORR (green trace) and $4e^-$ ORR (blue trace) volcano plots. Shaded green (weak OOH* binding) and blue (strong OOH* binding) areas represent the regions with high selectivity for $2e^-$

and 4e$^-$ pathway, respectively. Reprinted from ref [6]. Copyright 2020 American Chemical Society. (**b**) 2e$^-$ ORR selectivity can be kinetically controlled by increasing the activation barriers to the O-O bond cleavage processes, as illustrated on the CoS_2 (100) surface that lacks active site ensembles. Pictures in (b) are adapted from ref [18]. Copyright 2019 American Chemical Society.

1.2.2 Kinetic Considerations

The recent developments of 2e$^-$ ORR catalysts often only consider the thermodynamics of the ORR pathways based on the volcano relations (Section 1.2.1). However, we would highlight that kinetic considerations of suppressing the undesired O-O bond cleavage are also important (Figure 1.1b), which laid the foundation for our recent discovery of a series of metal compound-based new 2e$^-$ ORR catalysts.[18-20] OOH* is possible be cleaved thermally by two adjacent active sites or electrochemically via reductive elimination, which can be thermodynamically suppressed by destabilizing O* and/or OH* on the catalyst surface (Section 1.2.1). These O-O bond cleavage processes can also be kinetically suppressed by increasing their activation barriers, and one effective strategy is to increase the interatomic distances between neighboring active sites on the catalyst surface. Take our recently established CoS_2 catalyst[18] as an example, the Co active sites are spatially separated by disulfide anions in the lattice, and the Co-Co interatomic distance is much longer than the O-O bond length in OOH* (Figure 1.1b, left). To thermally cleave OOH* onto neighboring Co active sites, the transition state requires not only substantial elongation of the O-O bond by ~0.4 Å but also significant lattice distortion of CoS_2 to shorten the Co-Co distance, resulting in a high activation barrier (Figure 1.1b, top path). Due to the lack of active site ensembles, only one of the oxygens in OOH* interacts closely with the CoS_2 surface. Unlike the more facile proton-coupled electron transfer (PCET) to the surface-bound oxygen (forming H_2O_2), reductive elimination of OOH* is unfavored because PCET to the distant oxygen requires through-space transfer (~3 Å) or tunneling through the O-O bond (Figure 1.1b, bottom path). We envision the kinetic suppression of O-O bond cleavage could serve as one of the general design principles in search of more selective 2e$^-$ ORR catalysts based on metal compounds.

1.2.3 Merits of Metal Compounds as 2e$^-$ ORR Catalysts

Metal compounds offers many exciting attributes for tailoring catalytic properties for 2e$^-$ ORR. The presence of several distinct (metal and nonmetal) binding sites on metal compound surfaces allow for independently tunable binding energies of surface adsorbates (OOH* vs. OH* vs. O*). The dispersed metal sites, separated by nonmetal sites in lattices, suppress the undesired O-O bond cleavage. Well-defined crystalline and multi-elemental motifs provide diverse yet controllable structural and electronic tunability (composition and phase control,[18-21] doping and vacancy engineering[28,29]) for achieving optimized selectivity, stability, and activity toward 2e$^-$ ORR. Therefore, there remain underexplored opportunities for developing high-performance 2e$^-$ ORR catalysts based on metal compounds.

1.3 Computational Design of Metal Compound-Based 2e$^-$ ORR Catalysts

1.3.1 Stability Pre-Screening by Bulk Pourbaix Diagrams and Surface Adsorbate Analyses

The electrochemical stability is one of the most important factors for metal compound-based electrocatalysts, which can be predicted by density functional theory (DFT) calculations. The bulk phase stability of a metal compound in aqueous environment is described by its bulk Pourbaix diagram, which maps the Gibbs free energy difference with respect to its Pourbaix stable domain (ΔG_{pbx}) as a function of potential and pH, and is available from the Materials Project database.[30] Depending on the energy barriers for bulk decomposition reactions and the nature of decomposition products, the bulk of metal compounds can remain stable with ΔG_{pbx} up to 0.5 eV/atom.[31] The surface stability of a metal compound against corrosion and reconstruction can be examined by the Gibbs free energy change associated with the adsorption of O* and/or OH* on the surface when in equilibrium with water.[32] Although bulk Pourbaix diagrams and surface oxygen adsorbate energetics are often employed for elucidating the (in)stability of metal compound-based catalysts for hydrogen evolution reaction (HER)[33] or oxygen evolution reaction (OER)[34] in corrosive acidic solutions, such stability assessments are scarcely performed in the recent studies of 2e$^-$ ORR catalysts.

Our recent work of binary metal dichalcogenide-based acidic 2e$^-$ ORR catalysts[18-20] has routinely examined bulk Pourbaix diagrams and surface oxygen adsorbate energetics, allowing us to achieve significantly improved catalyst stability and develop mechanistic understanding and rational design rules for stable metal compound-based 2e$^-$ ORR catalysts. We computationally pre-screened the stability of a series of metal compounds: cubic pyrite-type *c*-CoS_2, *c*-$CoSe_2$, *c*-$NiSe_2$, and orthorhombic marcasite-type *o*-$CoSe_2$ (Figure 1.2a). The O* and OH* binding strengths on the most stable facets of these compounds display general trends depending on the nature of chalcogen and metal (Figure 1.2b). For CoS_2 and both $CoSe_2$ polymorphs, the chalcogen is the preferential binding site for O*, but O* binds substantially more strongly to S than to Se by 0.59 eV at the calculated standard equilibrium potential of 2e$^-$ ORR (U^o_{RHE}). Such difference suggests that CoS_2 is more prone to surface oxidation, occurring at the S site and forming highly soluble SO_4^{2-}, followed by Co^{2+} leaching and catalyst degradation. Switching from $CoSe_2$ to $NiSe_2$ resulted in a change in the O* preferential binding site from Se to Ni, suggesting that $NiSe_2$ is even more resistant to surface oxidation than both $CoSe_2$ polymorphs because of the low affinity of O* to its Se site. In addition, the OH* binding strength to Ni is much weaker that to Co, which helps stabilizing the adsorbate-free clean surface of $NiSe_2$, relative to the surfaces adsorbed with OH* (and/or O*), over a wide potential range (yellow region in Figure 1.2c). Overall, the DFT-predicted surface stability follows the order of *c*-$NiSe_2$ > (*c*-$CoSe_2$ ≈ *o*-$CoSe_2$) > *c*-CoS_2, in agreement with the bulk phase stability indicated by the Materials Project database.[18-20] Note that O* and OH* can also form during ORR if the O-O bond cleavage takes place (Figure 1.1b). Therefore, we consider these surface oxygen adsorbate analyses are readily generalizable for stability pre-screening of various metal compounds under aqueous environments and ORR operating conditions.

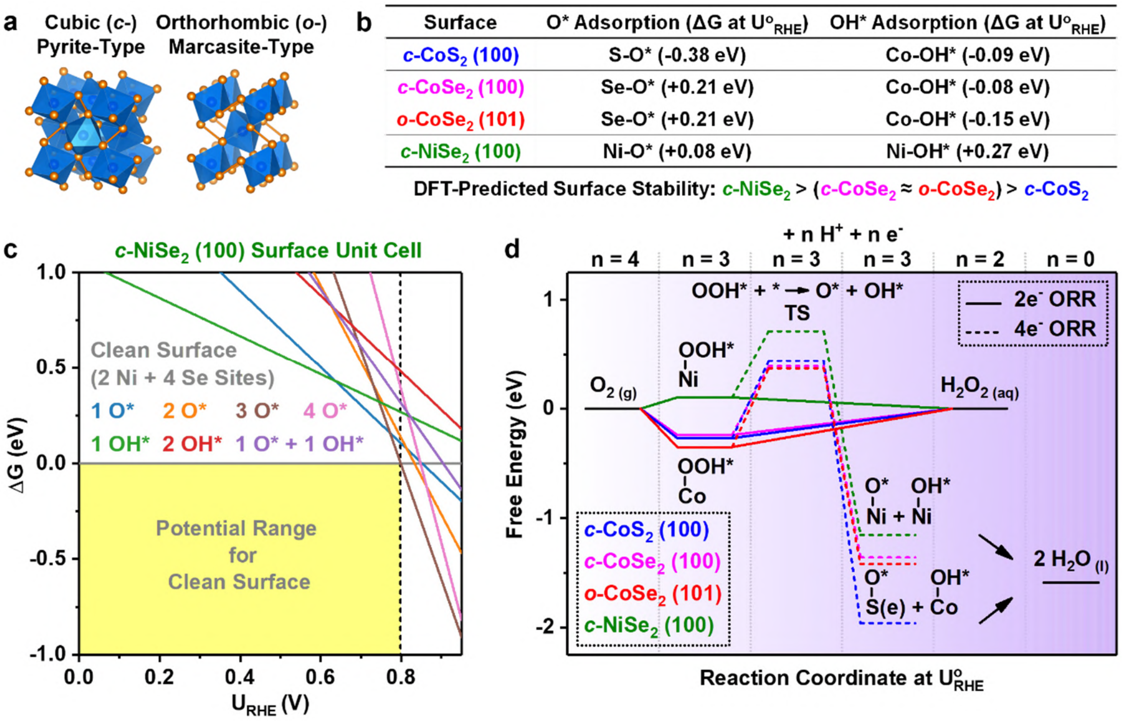

Surface	O* Adsorption (ΔG at U^o_{RHE})	OH* Adsorption (ΔG at U^o_{RHE})
c-CoS_2 (100)	S-O* (-0.38 eV)	Co-OH* (-0.09 eV)
c-$CoSe_2$ (100)	Se-O* (+0.21 eV)	Co-OH* (-0.08 eV)
o-$CoSe_2$ (101)	Se-O* (+0.21 eV)	Co-OH* (-0.15 eV)
c-$NiSe_2$ (100)	Ni-O* (+0.08 eV)	Ni-OH* (+0.27 eV)

DFT-Predicted Surface Stability: *c*-$NiSe_2$ > (*c*-$CoSe_2$ ≈ *o*-$CoSe_2$) > *c*-CoS_2

Figure 1.2. Computational pre-screening of stability, selectivity, and activity of metal compound-based 2e$^-$ ORR catalysts.

(**a**) Crystal structures of pyrite- and marcasite-type metal chalcogenides. (**b**) Energetics of O* and OH* adsorption to their preferential binding sites on the most stable facets of *c*-CoS_2, *c*-$CoSe_2$, *o*-$CoSe_2$, and *c*-$NiSe_2$. (**c**) Comparisons of free energies of different O* and/or OH* coverages on *c*-$NiSe_2$ (100) surface unit cell comprising of two Ni and four Se sites. For 3 O* and 4 O* coverages, two O* bind to Ni, and the rest of O* bind to Se. For the other O* and/or OH* coverages, all adsorbates bind to Ni. (**d**) Free energy diagrams of the 2e$^-$ and 4e$^-$ ORR pathways. Pictures in panel (a), and source data for *c*-CoS_2, *c*-$CoSe_2$, and *o*-$CoSe_2$ in panels (b) and (d) are adapted from ref [19]. Copyright 2020 Royal Society of Chemistry. Source data for *c*-$NiSe_2$ in panels (b) to (d) are adapted from ref [20].

1.3.2 Selectivity and Activity Assessments by Free Energy Diagrams

The 2e$^-$ ORR selectivity and activity can be computationally assessed by free energy diagrams of the desired 2e$^-$ and competing 4e$^-$ ORR pathways (Figure 1.2d).[18-20] Our recent work showed that all four binary metal dichalcogenides (*c*-CoS_2, *c*-$CoSe_2$, *o*-$CoSe_2$, and *c*-$NiSe_2$) are expected to be selective and active for 2e$^-$ ORR because they exhibit similarly high activation barriers to the undesired OOH* cleavage (0.61 to 0.72 eV at U_{RHE}^{o}, top dashed traces in Figure 1.2d), and nearly thermoneutral OOH* adsorption at U_{RHE}^{o} (solid traces in Figure 1.2d). The differences among these metal dichalcogenides lie in the adsorption energetics of the reaction intermediate(s) of 2e$^-$ ORR (OOH*) and 4e$^-$ ORR (O* and OH*). Changing the metal from Co to Ni weakens the OOH* adsorption, making *c*-$NiSe_2$ situated on the weak OOH* binding leg of the 2e$^-$ ORR volcano. In contrast, *c*-CoS_2, *c*-$CoSe_2$, and *o*-$CoSe_2$ are all situated on the strong OOH* binding leg. As the 2e$^-$ ORR selectivity can be influenced by the OOH* adsorption energy (Figure 1.1a), *c*-$NiSe_2$ could be even more selective for 2e$^-$ ORR than Co-based chalcogenides. Changing the chalcogen from S to Se and the metal from Co to Ni collectively weaken the O* and OH* adsorption and destabilize the 4e$^-$ ORR intermediates (bottom dashed traces in Figure 1.2d), which also promotes the 2e$^-$ ORR pathway. By combining thermodynamic analysis of ORR pathways and microkinetic modeling of O-O bond cleavage processes (the latter is a more unique contribution from our recent work[18-20] compared to other 2e$^-$ ORR studies), our computational frameworks serve as predictive tools for unveiling general trends in the 2e$^-$ ORR selectivity and activity of metal compound-based catalysts.

1.4 Experimental Development of Metal Compound-Based 2e$^-$ ORR Catalysts

1.4.1 Rotating Ring-Disk Electrode Evaluation

Rotating ring-disk electrode (RRDE) comprising of a glassy carbon disk and a Pt ring offers facile assessments of the 2e$^-$ ORR catalytic properties of solid catalysts. The drop-casting method is typically used to coat a uniform catalyst film on the disk. We caution the use of carbon additives in catalyst film since carbon materials exhibit nontrivial 2e$^-$ ORR activities especially under alkaline and neutral pH.[11] Similar attention should be paid to the glassy carbon disk as it also catalyzes 2e$^-$ ORR under alkaline pH.[3] In an undivided three-electrode cell (with a reference electrode and a graphite counter electrode), the 2e$^-$ ORR activity and selectivity can be evaluated at a certain rotation rate in O_2-saturated electrolyte solution, where linear sweep voltammetry (LSV) is applied to the disk for catalyzing ORR, meanwhile the ring is held at a constant potential (1.2 to 1.3 V vs. RHE) for selective and diffusion-limited oxidation of the produced H_2O_2. When evaluating 2e$^-$ ORR at neutral pH, it is critical to use buffered electrolyte solution to avoid the alkaline shift in the near-electrode local pH since ORR consumes protons. The potential range for LSV on the disk should not exceed the electrochemical stability window of the catalyst, which is indicated by bulk Pourbaix diagrams and surface oxygen adsorbate energetics for the case of metal compounds (Section 1.3.1). After subtracting background current (recorded under Ar-saturated condition) from disk current (i_{disk}) and ring current (i_{ring}), the H_2O_2 selectivity (p_{RRDE}) is calculated as: $p_{\text{RRDE}} = \frac{\frac{i_{\text{ring}}}{N}}{i_{\text{disk}} + \frac{i_{\text{ring}}}{N}} \times 100\%$, where N is the collection efficiency (calibrated using a ferri-/ferrocyanide redox couple). This method of determining H_2O_2 selectivity is more accurate than the Koutechy-Levich method.[35] We note that the measured H_2O_2 selectivity by RRDE can depend on the areal catalyst loading,[18-21] therefore measuring the double-layer capacitance (C_{dl}) of catalyst film, which correlates to the electrochemically active surface area (ECSA) and can be measured by cyclic voltammetry (CV) in non-Faradaic potential region under Ar-saturated condition for most cases, is critical for fair comparisons of the $2e^-$ ORR selectivity and activity. Figure 1.3a summarizes the representative RRDE assessments of our recently established binary metal dichalcogenide[18-20] and ternary thiospinel[21] $2e^-$ ORR catalysts in 0.05 M H_2SO_4 solution.

Each binary metal chalcogenide catalyst (*c*-CoS_2,[18] *c*-$CoSe_2$,[19] *o*-$CoSe_2$,[19] *c*-$NiSe_2$[20]) was tested at various catalyst loadings, and their optimum overall electrode performances for H_2O_2 production (i.e., high partial current density at small overpotential) were achieved at high catalyst loadings (shown in Figure 1.3a$_1$). All three Co-based chalcogenides exhibit similarly high $2e^-$ ORR activity as they require nearly zero overpotential for the catalytic onset. They show high H_2O_2 selectivity (up to 86%) in the small overpotential region, but the H_2O_2 selectivity obviously decreases with increasing overpotential at high catalyst loadings. This potential-dependent H_2O_2 selectivity indicates the undesired O-O bond cleavage processes dominate at large overpotentials on these Co-based catalysts.[18,19] In comparison, the $2e^-$ ORR catalytic onset potential on $NiSe_2$ is less positive, but its H_2O_2 selectivity shows relatively little dependence on overpotential and remains high (up to 90%) over a wide potential range.[20] Such differences in the H_2O_2 selectivity profiles of $NiSe_2$ vs. Co-based chalcogenides could result from several possible causes: (1) the weaker OOH* binding to Ni than to Co (by 0.34 to 0.45 eV[18-20]) makes $NiSe_2$ and Co-based chalcogenides situated on the different legs of $2e^-$ ORR volcano (Figure 1.2a), which could affect the $2e^-$ ORR selectivity (Section 1.2.1); (2) the weaker OH* binding to Ni than to Co (by 0.35 to 0.42 eV, see Figure 1.2b) relatively destabilizes this $4e^-$ ORR intermediate on $NiSe_2$, which could promote 2e$^-$ ORR. Co-based chalcogenides tested at low catalyst loadings show less dramatic decrease in H_2O_2 selectivity with increasing overpotential, and their H_2O_2 selectivity profiles became more similar to that of $NiSe_2$ (Figure 1.3b). Future theoretical and experimental studies are needed to examine the various competing catalytic processes in greater details and elucidate the causes for the dependence of H_2O_2 selectivity on overpotential and catalyst loading, which will accelerate the discovery of more selective metal compound-based 2e$^-$ ORR catalysts.

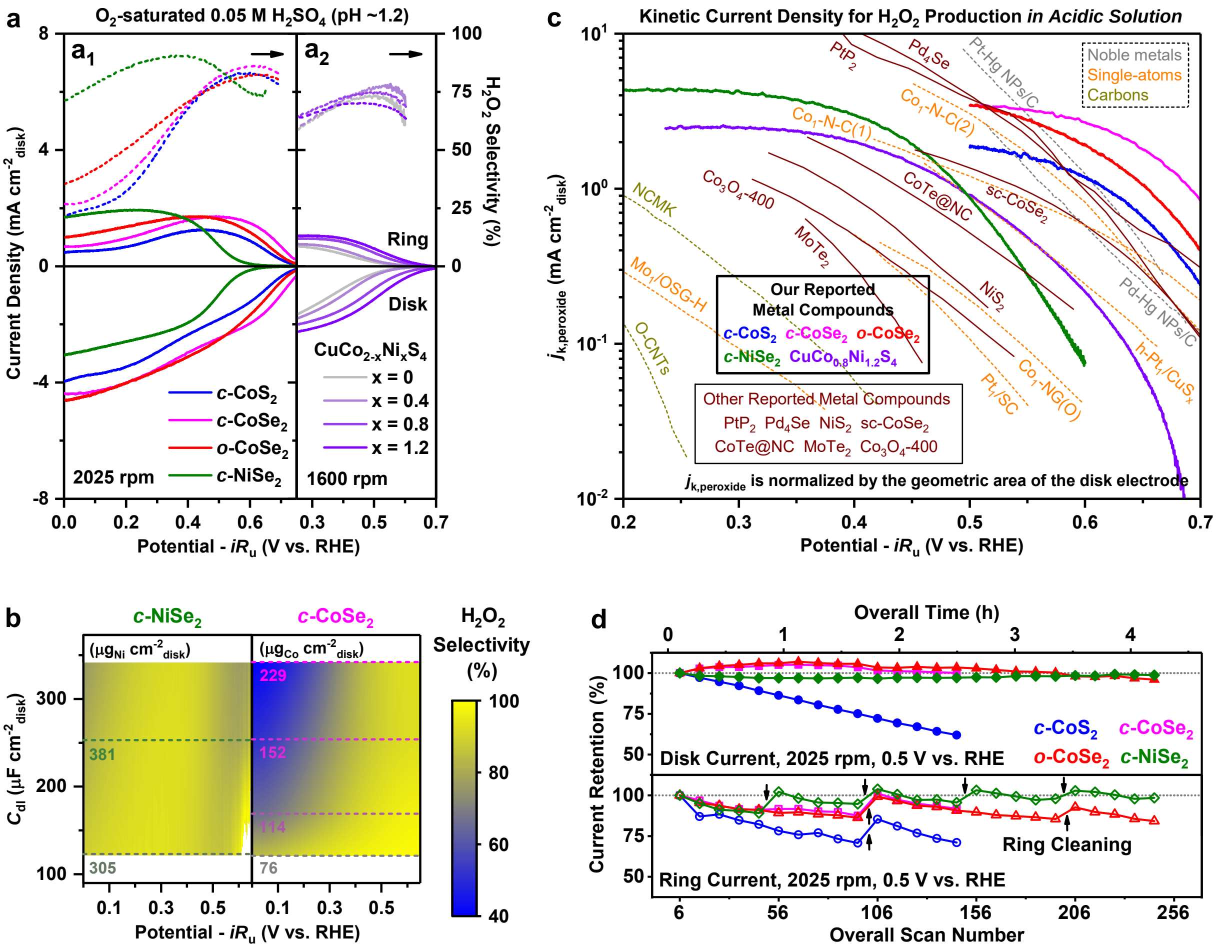

Figure 1.3. RRDE assessments of metal compound-based 2e$^-$ ORR catalysts.

(**a**) Representative RRDE voltammograms and the corresponding H_2O_2 selectivity of (**a$_1$**) binary metal chalcogenide (*c*-CoS_2,[18] *c*-$CoSe_2$,[19] *o*-$CoSe_2$,[19] *c*-$NiSe_2$[20]) and (**a$_2$**) ternary thiospinel ($CuCo_{2-x}Ni_xS_4$, $0 \le x \le 1.2$[21]) catalysts in O_2-saturated 0.05 M H_2SO_4. (**b**) The H_2O_2 selectivity plotted against potential and double-layer capacitance (C_{dl}) for *c*-$NiSe_2$ vs *c*-$CoSe_2$ from RRDE experiments in 0.05 M H_2SO_4. (**c**) Comparisons of kinetic current densities for H_2O_2 production ($j_{k,peroxide}$) on metal compound-based $2e^-$ ORR catalysts (vs. other classes of $2e^-$ ORR catalysts) based on RRDE experiments at 1600 rpm in acidic solution. (**d**) RRDE stability test of *c*-CoS_2 vs. *c*-$CoSe_2$ vs. *o*-$CoSe_2$ vs. *c*-$NiSe_2$ in 0.05 M H_2SO_4. Source data for *c*-CoS_2, *c*-$CoSe_2$, and *o*-$CoSe_2$ in panels (a), (c), and (d) are adapted from ref [19]. Copyright 2020 Royal Society of Chemistry. Source data for *c*-$CoSe_2$ in panel (b), and source data for *c*-$NiSe_2$ in panels (a)–(d) are adapted from ref [20]. Source data for $CuCo_{2-x}Ni_xS_4$ in panels (a) and (c) are adapted from ref [21]. Copyright 2021 American Chemical Society. Detailed catalyst and electrode information are described in Table A1.1.

The series of ternary thiospinel ($CuCo_{2-x}Ni_xS_4$, $0 \leq x \leq 1.2$) catalysts serve as examples to show the $2e^-$ ORR catalytic properties of metal compounds can be systematically modified by compositional tuning (Figure 1.3a2).[21] These catalysts were tested at a constant catalyst loading with similar C_{dl} values across all samples. Incorporating greater amounts of Ni in the thiospinel catalyst systematically increases $2e^-$ ORR activity without compromising high H_2O_2 selectivity (up to 78%), and the bulk crystal structure of thiospinel remains the same when the Ni content increases (up to $x = 1.2$). Similar to $NiSe_2$, the most Ni-rich phase among this thiospinel series ($CuCo_{0.8}Ni_{1.2}S_4$) shows the least decrease in H_2O_2 selectivity with increasing overpotential. These examples reveal the power of unveiling catalyst design principles via modifying the compositions of well-defined crystal structures.

1.4.2 Kinetic Current Density for H_2O_2 Production

To quantitatively compare the $2e^-$ ORR catalyst performances from RRDE experiments, kinetic current density for H_2O_2 production ($j_{k,peroxide}$) can be derived by correcting the partial current density for H_2O_2 production ($j_{\mathrm{peroxide}} = \frac{i_{\mathrm{ring}}}{N \times A_{\mathrm{disk}}}$, where A_{disk} is the geometric area of the disk) for mass-transport loss: $j_{\mathrm{k,peroxide}} = (\frac{1}{j_{\mathrm{peroxide}}} - \frac{1}{j_{\mathrm{L,peroxide}}})^{-1}$, where $j_{\mathrm{L,peroxide}}$ is the diffusion-limited current density for H_2O_2 production (~3 mA $\mathrm{cm^{-2}}_{\mathrm{disk}}$ at 1600 rpm in O_2-saturated dilute aqueous solutions[18,19]). We note that $j_{\mathrm{k,peroxide}}$ is normalized by A_{disk} (mA $\mathrm{cm^{-2}}_{\mathrm{disk}}$) and reflects overall electrode performance rather than intrinsic catalytic property. An alternative term is mass activity for H_2O_2 production normalized by catalyst mass (mA $\mathrm{g^{-1}}_{\mathrm{catalyst}}$), but mass activity can vary with the specific surface area of a sample for different catalysts or even for different morphologies of the same catalyst. Additionally, the H_2O_2 selectivity can also be influenced by catalyst mass (Section 1.4.1). Therefore, $j_{\mathrm{k,peroxide}}$ normalized by A_{disk} has its practical merit from the point of view of end applications.

Figure 1.3c summarizes $j_{\mathrm{k,peroxide}}$ achieved by the reported $2e^-$ ORR catalysts from RRDE experiments at 1600 rpm under O_2-saturated condition, with a specific focus on acidic solution and metal compound-based catalysts from our reports of metal dichalcogenide[18-20] and thiospinel[21] catalysts and other reports.[22,23,36-40] In the small overpotential region, Co-based dichalcogenides[18,19] show clearly more efficient H_2O_2 production than single-atom[16,17,41-43] or carbon[11,12] catalysts, and display comparable or even better overall electrode performances than the state-of-the-art noble metal alloys.[9,10] Noble metal compounds such as PtP_2[22] and Pd_4Se[23] eliminate the use of toxic Hg, yet can deliver comparable or higher $j_{\mathrm{k,peroxide}}$ than Pt-Hg[11] and Pd-Hg[12] alloys. These encouraging results show the promise of metal compounds as high-performance acidic $2e^-$ ORR catalysts. However, many metal compounds exhibit decreasing H_2O_2 selectivity with increasing overpotential (Section 1.4.1), which prevents them from achieving high $j_{\mathrm{k,peroxide}}$ at large overpotentials (see curvatures in Figure 1.3c) and restrict their efficient H_2O_2 production to the small overpotential region with limited current density. Therefore, future studies should focus on developing metal compound-based 2e$^-$ ORR catalysts that are not only highly active but also highly selective up to large overpotentials to achieve high $j_{\mathrm{k,peroxide}}$ for high-rate H_2O_2 production at large current densities (in synergy with the future perspectives in Section 1.4.1).

Comparisons of $j_{\mathrm{k,peroxide}}$ also make it clear that there is more need for developing high-performance 2e$^-$ ORR catalysts in acidic and neutral solutions (as opposed to alkaline solution). Figure A1.1 and A1.2 summarize $j_{\mathrm{k,peroxide}}$ achieved by the reported neutral and alkaline 2e$^-$ ORR catalysts, respectively. There exist much fewer examples of neutral 2e$^-$ ORR catalysts (Figure A1.1), and many of them were tested in unbuffered neutral solutions where the alkaline shift in the near-electrode local pH during ORR operation could give an inaccurate depiction of neutral 2e$^-$ ORR catalytic properties (see Section 1.4.1). Our established $CoSe_2$ polymorph catalysts[19] (tested in neutral phosphate buffer) and other reported noble metal compounds (PtP_2,[22] Pd_4Se[23]) also show clearly higher $j_{\mathrm{k,peroxide}}$ than single-atom[14,15] and carbon[11,12] catalysts under neutral conditions (Figure A1.1). On the other hand, the cost-effective carbon materials show very efficient H_2O_2 production at alkaline pH compared to other classes of catalysts (Figure A1.2), which poses less urgent need for developing new alkaline 2e$^-$ ORR catalysts.

1.4.3 Catalyst Stability and Leaching Monitoring

It is crucial to use quantitative metrics to rigorously characterize the stability of acidic (and neutral) 2e$^-$ ORR catalysts because of the corrosive acidic solution and the oxidizing environment involving the O_2 reactant and H_2O_2 product. We performed long-term RRDE stability tests of binary metal dichalcogenide catalysts by continuously applying LSV scans on the disk,[18-20] similar to the typical accelerated degradation tests for 4e$^-$ ORR catalysts.[44] By monitoring the disk current and ring current at a fixed potential of 0.5 V vs. RHE, the catalyst stability follows the trend of *c*-

$NiSe_2$ > (c-$CoSe_2$ ≈ o-$CoSe_2$) > c-CoS_2 in O_2-saturated 0.05 M H_2SO_4 (Figure 1.3d), in agreement with our computational stability pre-screening based on surface adsorbate analyses (see Section 1.3.1). We also routinely recovered the spent catalysts from RRDE to verify their surface and bulk structural stability by X-ray photoelectron spectroscopy (XPS) and Raman spectroscopy.[18-20]

The leaching of catalytic active elements is a major cause of electrocatalyst instability, which can be quantified by elemental analyses of spent electrolytes using inductively coupled plasma mass spectrometry (ICP-MS). Catalyst leaching-based metrics have been introduced for evaluating the stability of acidic OER catalysts in terms of stability number;[45] however, catalyst leaching monitoring has been scarcely practiced in the recent $2e^-$ ORR catalyst studies. Pt-Hg alloy was found to experience severe leaching of toxic Hg, three orders of magnitude higher than the leaching of Pt, under potentiostatic operation at 0.5 V vs. RHE in O_2-saturated 0.1 M $HClO_4$ (Figure 1.4a, left), hindering its practical application. In comparison, PtP_2 showed greatly reduced leaching of heavy metals under the same conditions (Figure 1.4a, right), but it still experienced substantial loss in activity over time due to catalyst leaching and nanoparticle aggregation, and required an Al_2O_3 overcoat for stabilization (Figure 1.4b).[22]

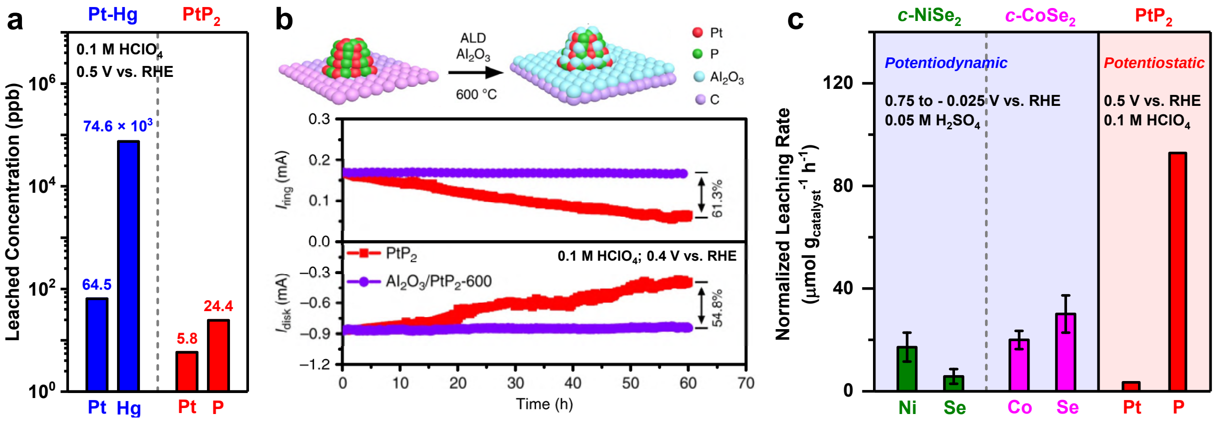

Figure 1.4. Catalyst leaching monitoring of metal compound-based $2e^-$ ORR catalysts.

(**a**) The concentrations of leached elements from PtP_2 (vs. Pt-Hg, catalyst loading is 0.2 $mg_{catalyst}$ cm^{-2}_{disk} for both) after operating at 0.5 V vs. RHE in O_2-saturated 0.1 M $HClO_4$ (40 mL) for 6 hours. Source data are adapted from ref [22]. (**b**) The activity loss of PtP_2 during RRDE testing, and its stabilization by an Al_2O_3 overcoat. Reprinted from ref [22]. Copyright 2020 Nature Publishing Group. (**c**) The normalized leaching rates of metal and nonmetal elements (μmol $g_{catalyst}^{-1}$ h^{-1}) of *c*-$NiSe_2$ and *c*-$CoSe_2$ after long-term RRDE stability tests in acidic solution. Reprinted from ref [20]. For comparison, source data for PtP_2 in panel (c) are adapted from ref [22].

Our recent work has routinely monitored catalyst leaching to benchmark the stability of metal chalcogenide-based acidic $2e^-$ ORR catalysts.[18-21] Figure 1.4c shows the direct comparisons of the metal and selenium leaching rates, normalized by the catalyst masses (μmol $g_{catalyst}^{-1}$ h^{-1}), of *c*-$NiSe_2$ and *c*-$CoSe_2$ catalysts during long-term RRDE stability tests in O_2-saturated 0.05 M H_2SO_4 (vide supra). The ratio between the Co and Se leaching rates of $CoSe_2$ is close to the 1:2 stoichiometry (Figure 1.4c, middle). This suggests the leaching of $CoSe_2$ could be initiated by the surface oxidation of Se_2^{2-} to the readily soluble SeO_x due to the preferential affinity of O* to its Se site (Figure 1.2b), followed by the near-stoichiometric dissolution of Co^{2+} from the surface. In contrast, the Se leaching from the more stable $NiSe_2$ is not only much more suppressed compared to $CoSe_2$, but also slower than the Ni leaching (Figure 1.4c, left). These suggest the leaching of $NiSe_2$ could mainly result from the preferential adsorption of O* and OH* to its Ni site (Figure 1.2b) and the subsequent acid-base reaction with the electrolyte to dissolve Ni^{2+}. Future studies (see below) will be helpful for confirming the catalyst leaching mechanisms of $NiSe_2$ vs. $CoSe_2$. We note that PtP_2 exhibits a much faster anion leaching (Figure 1.4c, right) than $NiSe_2$ and $CoSe_2$, yet the slower metal leaching may be a potential advantage of noble metal compounds compared to earth-abundant metal compounds.

Since electrocatalyst leaching can closely depend on operating conditions such as applied potential,[45] future studies of $2e^-$ ORR catalysts may utilize in situ or operando techniques for real-time detection of dissolved species. In situ ICP-MS technique using a stationary probe near rotating disk electrode (SPRDE-ICPMS)[46] has been implemented for real-time elucidation of the potential-dependent dissolutions of OER[47] and $4e^-$ ORR[48] catalysts. Besides, electrochemical quartz crystal microbalance (EQCM)[49] can also probe the dissolutions of electrocatalysts in real time by monitoring their mass changes as a function of potential. These techniques will provide in-depth understanding and future guidance for developing more stable metal compound-based $2e^-$ ORR catalysts.

1.4.4 Faradaic Side Reaction of H_2O_2 Electroreduction

RRDE only provides instantaneous detection of H_2O_2 transiently produced by $2e^-$ ORR catalysts, with negligible H_2O_2 concentration in the bulk solution. H_2O_2 can be electrochemically reduced to water ($H_2O_2 + 2\ H^+ + 2\ e^- \rightarrow 2\ H_2O$, $E^o = 1.76$ V vs. RHE) that is thermodynamically more favorable than $2e^-$ ORR. To ensure that the produced H_2O_2 can accumulate in the bulk solution and reach practically useful concentrations, it is critical to evaluate peroxide reduction reaction (PRR) as a possible Faradaic side reaction, which has seldomly been investigated in the recent $2e^-$ ORR studies.[20,43,50]

PRR can be studied in Ar-saturated H_2O_2-containing solution using the catalyst-coated RRDE by only connecting the disk to the three-electrode cell. The same RRDE tested for $2e^-$ ORR in O_2-saturated H_2O_2-free solution (Section 1.4.1) can be reused to ensure the same catalyst loading and head-to-head comparisons of PRR vs. $2e^-$ ORR. We recently presented systematic RRDE studies of PRR on *c*-$NiSe_2$ and *c*-$CoSe_2$ catalysts in acidic solutions.[20] PRR and $2e^-$ ORR on *c*-$NiSe_2$ exhibit similar catalytic onset potentials, and the rate of PRR increases with higher overpotential and H_2O_2 concentration (Figure 1.5a). The rates of PRR and 2e$^-$ ORR are described by current densities: $j_{\text{PRR}} = \frac{i_{\text{PRR}}}{A_{\text{disk}}}$, and $j_{\text{peroxide}} = \frac{i_{\text{ring}}}{N \times A_{\text{disk}}}$ (see Section 1.4.2). At nontrivial H_2O_2 concentration, the net rate of H_2O_2 production should correlate to $j_{\text{peroxide}} - j_{\text{PRR}}$, which remains positive only in a certain potential range and displays a parabolic trend peaking at an optimum potential (Figure 1.5b). Comparatively, the net rate of H_2O_2 production on *c*-$CoSe_2$ is less affected by PRR at low overpotentials as it exhibits a more positive catalytic onset potential for 2e$^-$ ORR (Figure 1.5a and 1.3a$_1$). Understanding PRR is informative for identifying the optimum operating conditions for bulk electrosynthesis of H_2O_2 (see Section 1.4.5 below), but it is more important to investigate the mechanism of PRR[51] and the ways to suppress it, which would lead to better-performing metal compound-based 2e$^-$ ORR catalysts for practical H_2O_2 electrosynthesis.

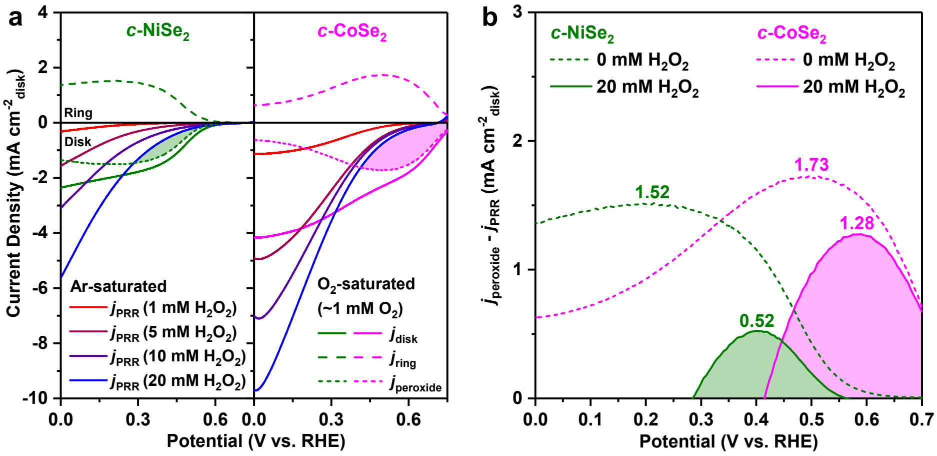

Figure 1.5. RRDE studies of peroxide reduction reaction (PRR) on metal compound-based 2e$^-$ ORR catalysts.

(**a**) Disk current densities (j_{disk}), ring current densities (j_{ring}), and partial current densities for H_2O_2 production (j_{peroxide}) of *c*-$NiSe_2$ and *c*-$CoSe_2$ catalysts at 1600 rpm in O_2-saturated 0.05 M H_2SO_4, in comparison with PRR current densities (j_{PRR}) at 1600 rpm in Ar-saturated 0.05 M H_2SO_4

containing 1, 5, 10, or 20 mM H_2O_2. (**b**) Net rates of H_2O_2 production on *c*-$NiSe_2$ and *c*-$CoSe_2$ catalysts are expected to correlate to $j_{peroxide} - j_{PRR}$. Reprinted from ref [20].

1.4.5 Bulk Electrosynthesis and Accumulation of H_2O_2

Bulk electrosynthesis of H_2O_2 on metal compound-based $2e^-$ ORR catalysts can typically be evaluated in a conventional H-cell where the produced H_2O_2 accumulates in the catholyte that is separated from the anolyte by a proton exchange membrane to avoid the oxidation of H_2O_2 at the anode (Figure 1.6a). The produced H_2O_2 can be chemically quantified by spectrophotometric and titration methods.[52] We usually directly grew nanostructured metal chalcogenide catalysts on carbon fiber paper (CFP) as the cathode with high mechanical stability, and carried out H_2O_2 electrosynthesis in a small volume (3–5 mL) of catholyte based on our two-fold considerations: (1) The rapid accumulation of H_2O_2 in a small solution volume allows evaluating the maximum achievable H_2O_2 concentrations by metal compound-based $2e^-$ ORR catalysts and whether they catalyze the undesired H_2O_2 electroreduction; (2) Higher concentrations of H_2O_2 pose more stringent requirements for the stability of metal compound-based $2e^-$ ORR catalysts during H_2O_2 bulk electrosynthesis.

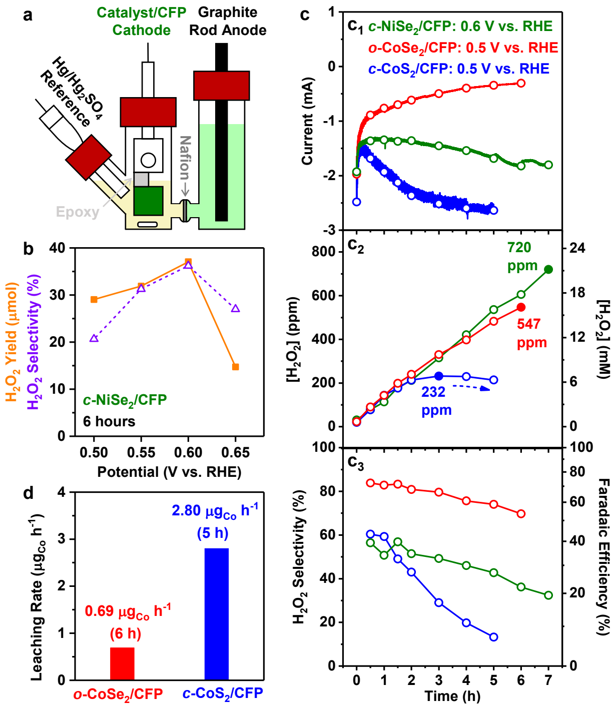

Figure 1.6. Bulk electrosynthesis of H_2O_2 on metal compound-based 2e$^-$ ORR catalysts in the H-cell setup.

(**a**) Schematic of three-electrode H-cell. (**b**) H_2O_2 yield and selectivity of *c*-$NiSe_2$/CFP (~1.06 μg$_{Ni}$ cm$^{-2}_{geo}$, ~1 cm$^{2}_{geo}$) operated at different fixed applied potentials (0.50, 0.55, 0.60, or 0.65 V vs. RHE) for 6 hours in O_2-saturated 0.05 M H_2SO_4 (4 mL, stirred at 1200 rpm). (**c**) H_2O_2 bulk electrosynthesis on *c*-CoS_2/CFP vs. *o*-$CoSe_2$/CFP vs. *c*-$NiSe_2$/CFP in 0.05 M H_2SO_4. (d) Metal leaching of *o*-$CoSe_2$/CFP vs. *c*-CoS_2/CFP (~0.37 mg$_{Co}$ cm$^{-2}_{geo}$ and ~1 cm$^{2}_{geo}$ for both) in (c). Source data for *c*-CoS_2/CFP and *o*-$CoSe_2$/CFP in panels (c) and (d) are adapted from ref [19]. Copyright 2020 Royal Society of Chemistry. Panel (a) and source data for *c*-$NiSe_2$/CFP in panels (b) and (c) are adapted from ref [20].

We found both the cumulative H_2O_2 yield and selectivity from H_2O_2 bulk electrosynthesis on *c*-$NiSe_2$/CFP in O_2-saturated 0.05 M H_2SO_4 were potential-dependent, and peaked at the optimum potential of 0.60 V vs. RHE (Figure 1.6b).[20] These observations were in agreement with

RRDE studies of PRR (Section 1.4.4) where the net rate of H_2O_2 production on *c*-$NiSe_2$ displayed a parabolic trend as a function of potential in H_2O_2-containing solution (Figure 1.5b). Therefore, it is critical to operate H_2O_2 bulk electrosynthesis at the optimum potential to maximize H_2O_2 production and minimize the undesired H_2O_2 electroreduction. We also observed distinct H_2O_2 bulk electrosynthesis performances among binary metal dichalcogenide catalysts (*c*-CoS_2 vs. *o*-$CoSe_2$ vs *c*-$NiSe_2$) in 0.05 M H_2SO_4 (Figure 1.6c).[19,20] *c*-CoS_2 showed the most severe PRR side reaction, as evidenced by the increasing cathodic current over time (Figure 1.6c$_1$), and the H_2O_2 concentration only reached a maximum of 232 ppm and started decreasing afterwards (Figure 1.6c$_2$). In contrast, *o*-$CoSe_2$ was the least affected by PRR, achieving the steadily increasing H_2O_2 concentration up to 547 ppm (Figure 1.6c$_2$) with the highest H_2O_2 selectivity among these three catalysts (Figure 1.6c$_3$). *c*-$NiSe_2$ exhibited a moderate H_2O_2 selectivity for bulk electrosynthesis (Figure 1.6c$_3$) likely due to it was more affected by PRR than $CoSe_2$ (Figure 1.5b), but *c*-$NiSe_2$ still showed steady accumulation of H_2O_2 up to a higher concentration of 720 ppm (Figure 1.6c$_2$).

Metal leaching monitoring and suppression is crucial for H_2O_2 bulk electrosynthesis on metal compound-based $2e^-$ ORR catalysts not only because the accumulated H_2O_2 is more demanding for catalyst stability than RRDE conditions (Section 1.4.3), but also because certain metal cations (Co^{3+}/Co^{2+}, Cu^{2+}/Cu^+, etc.) may chemically decompose the produced H_2O_2 (similar to the Fe^{2+}-mediated Fenton reaction, see Section 1.4.5 below).[25] We showed that the leaching of Co^{2+} from *o*-$CoSe_2$ during H_2O_2 bulk electrosynthesis was clearly much slower than that from *c*-CoS_2 (Figure 1.6d),[19] which may also account for *o*-$CoSe_2$'s high H_2O_2 selectivity (Figure 1.6c$_3$). Another relevant example is that as-synthesized $CuCo_{2-x}Ni_xS_4$ thiospinel catalysts exhibit an easily leached copper species that prevents H_2O_2 accumulation, therefore catalyst pre-treatment in acid is essential to guarantee H_2O_2 accumulation.[21]

While an H-cell offers a simple setup for small-scale H_2O_2 electrosynthesis by submerging supported catalysts in electrolytes, it suffers from several drawbacks including low solubility of O_2 in the liquid phase, limited diffusion of O_2 to the catalyst surface, and high local concentration of H_2O_2 near the cathode, all of which hinder the production rate, concentration, and selectivity but can be overcome by device engineering.[53-55] The O_2 solubility and diffusion limitations can primarily be addressed by the use of gas diffusion electrodes (GDEs, comprising a hydrophobic gas diffusion layer loaded with catalysts) and flow cells that maintain the direct delivery of a constant flow of gaseous O_2 to the catalyst surface at the three-phase boundary. A recent work of a layer-templated $CoSe_2$ (sc-$CoSe_2$) catalyst coated on GDE cathode used a flow cell (Figure 1.7a) to achieve a large H_2O_2 partial current density up to 60 mA cm^{-2} at 0 V vs. RHE (Figure 1.7b) for high-rate and selective H_2O_2 production in recirculated 0.5 M H_2SO_4.[37] The sc-$CoSe_2$ GDE cathode showed over 100 hours of stable continuous operation at a total current density of 63 mA cm^{-2} with >90% Faradaic efficiency toward H_2O_2 (Figure 1.7c), but the electrolyte was replaced every hour with fresh electrolyte (with ~1900 ppm H_2O_2 produced every hour), so the maximum achievable H_2O_2 concentration by the sc-$CoSe_2$ GDE was not approached. Another recent work operated the PtP_2 GDE in a PEM fuel cell (Figure 1.7d) and reached a high concentration plateau of ~40,000 ppm H_2O_2 (~4 wt%) in a large volume (600 mL) of neutral water by continuously recycling the water flow (Figure 1.7e), whereas only ~500 ppm was accumulated in steady state without recycling the water flow (Figure 1.7e inset).[22] Optimizing other conditions, such as the hydrophobicity of GDE to avoid cathode flooding, and the catalyst loading, water flow rate, and temperature to minimize thermochemical and/or electrochemical degradation of H_2O_2, were necessary to maximize H_2O_2 accumulation. These results show the promise of scaling up H_2O_2 electrosynthesis on metal compound-based $2e^-$ ORR catalysts in well-engineered devices with high practical performances. Importantly, the cell configurations and operating conditions must be accurately reported for benchmarking the performances of GDEs.[56] Comparing the H_2O_2 electrosynthesis performances under significantly different cell conditions can obfuscate atomic-level insights into the structural design of metal compound-based $2e^-$ ORR catalysts.

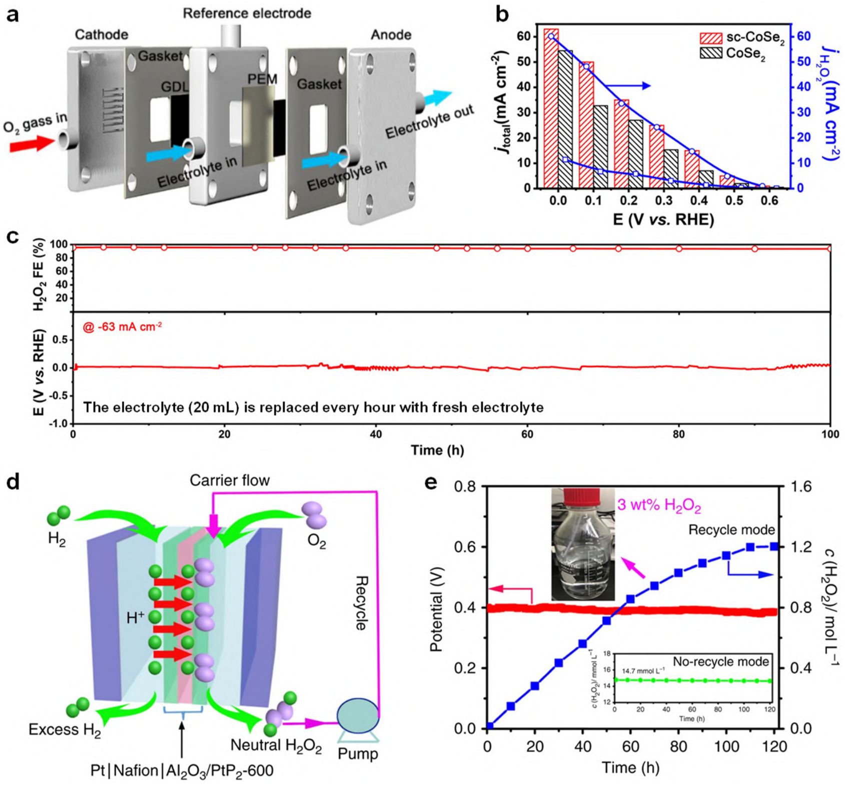

Figure 1.7. Bulk electrosynthesis of H_2O_2 on metal compound-based $2e^-$ ORR catalysts in flow cells.

(**a**) Schematic of a flow electrolyzer using a GDE cathode coated with a layer-templated sc-$CoSe_2$ catalyst. (**b**) Total current density and H_2O_2 partial current density of the sc-$CoSe_2$ GDE (in comparison to the GDE coated with a bulk $CoSe_2$ catalyst). (**c**) Continuous operation of the sc-$CoSe_2$ GDE. Panels (a)–(c) are reprinted from ref [37]. Copyright 2021 Wiley-VCH GmbH. (**d**) Schematic of a PEM fuel cell using a GDE cathode coated with a PtP_2 catalyst. (**e**) H_2O_2 accumulation to a high concentration plateau in neutral water by recycling the water flow (vs. the much lower steady-state concentration without recycling the water flow as shown in the inset). Panels (d) and (e) are reprinted from ref [22]. Copyright 2020 Nature Publishing Group.

1.5 Use of Metal Compound-Based 2e$^-$ ORR Catalysts in the Electro-Fenton Process

1.5.1 Environmental Applications

The electro-Fenton process is useful for environmental applications as it converts the electrogenerated H_2O_2 (E^o = 1.76 V vs. RHE) to the more oxidizing ·OH (E^o = 2.80 V vs. RHE). This process occurs via Fe^{2+} mediation at the optimum pH of ~3 ($Fe^{2+} + H_2O_2 + H^+ \rightarrow Fe^{3+} + H_2O + \cdot OH$), where Fe^{2+} is regenerated at the 2e$^-$ ORR cathode ($Fe^{3+} + e^- \rightarrow Fe^{2+}$) to accelerate the ·OH production.[25] The electro-Fenton process is more demanding for cathode stability than 2e$^-$ ORR because ·OH is more oxidizing than H_2O_2. Considering the significantly enhanced catalyst stability and acidic H_2O_2 bulk electrosynthesis performance of $CoSe_2$ (vs. CoS_2, see Figure 1.3d and 1.6c), we showed the effective electro-Fenton degradation of rhodamine B (RhB), a model organic pollutant, at a $CoSe_2$ cathode (Figure 1.8a).[19] Other reports also used metal compounds such as CoS_2[57] and CoSP[58] for similar electro-Fenton applications of organic pollutant removal. Future studies should not only carefully examine the stability of metal compound-based 2e$^-$ ORR catalysts during electro-Fenton operations, but also expand their electro-Fenton applications to other environmental challenges such as isolating microplastics from wastewater[59,60] and separating plastic mixtures.[61]

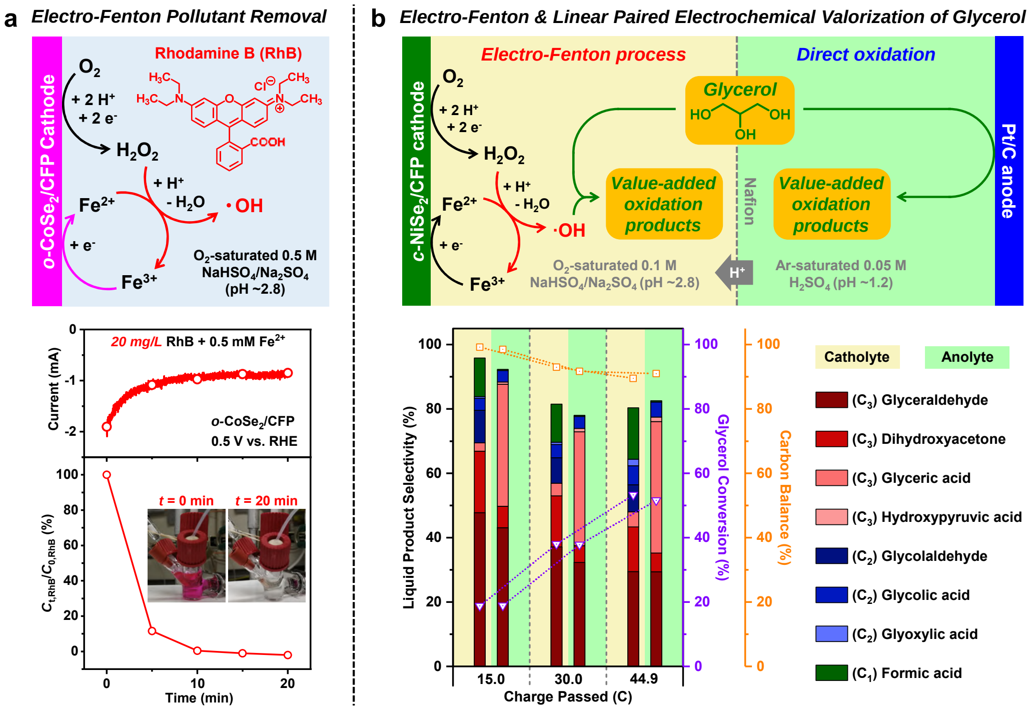

Figure 1.8. Uses of metal compound-based 2e$^-$ ORR catalysts in the electro-Fenton process for both environmental and biomass valorization applications.

(**a**) Scheme of the electro-Fenton process, and the effective electro-Fenton degradation of rhodamine B (RhB) at *o*-$CoSe_2$ cathode. Reprinted from ref [19]. Copyright 2020 Royal Society of Chemistry. (**b**) Scheme of linear paired electrochemical valorization of glycerol into the same oxidation products via the electro-Fenton process at the stable $NiSe_2$ cathode and via anodic oxidation at Pt anode simultaneously, with high glycerol conversion and high selectivity for value-added C_3 products achieved. Reprinted from ref [20].

1.5.2 Biomass Valorization into Value-Added Chemicals

The deployment of the electro-Fenton process has been largely limited to environmental applications,[25] which motivated us to explore different approaches of utilizing the electro-Fenton process for enabling valuable chemical transformations. For example, oxidative upgrading of biomass-derived feedstocks typically occurs solely via anodic oxidation,[62] but the electro-Fenton process may uniquely enable such oxidation reactions in the cathodic half-cell due to the strong oxidizing power of ·OH. In fact, chemically generated ·OH from H_2O_2 has found use in biomass-to-chemical conversion[63] such as carbohydrate oxidation[64,65] and lignin depolymerization,[66] but the electro-Fenton process is comparatively less developed for making high-value chemicals[67-69] than these as mentioned chemical processes.

Our recent work[20] utilized the electro-Fenton process at the stable $NiSe_2$ cathode to enable the novel and efficient cathodic valorization of glycerol to the desired C_3 oxidation products (glyceraldehyde, dihydroxyacetone, and glyceric acid) with less C_2 and C_1 products formed. More importantly, cathodic valorization of glycerol can be linear paired with anodic oxidation to produce the same oxidation products at both $NiSe_2$ cathode and Pt anode simultaneously, and achieve high glycerol conversion and high selectivity for value-added C_3 products (Figure 1.8b). It is noteworthy that, after adjusting the supporting electrolyte condition, this linear paired system for concurrent valorization of glycerol (~50 mM) can operate at a very small cell voltage (<0.2 V) with little external energy input needed, which can theoretically be made into an unbiased system upon further optimization in the future. This novel use of the electro-Fenton process and this conceptual strategy of linear pairing the electro-Fenton process with anodic oxidation opens up new opportunities for enabling electrochemical valorization of biomass-derived feedstocks (5-hydroxymethylfurfural, glucose, etc.)[62] with high atom efficiency and low energy cost.

1.6 Conclusions and Outlook

Overall, we summarized our developed computational frameworks and experimental practices that led to the new discovery of a series of binary (CoS_2,[18] $CoSe_2$,[19] $NiSe_2$[20]) and ternary ($CuCo_{2-x}Ni_xS_4$, $0 \leq x \leq 1.2$[21]) metal chalcogenide compound catalysts for selective $2e^-$ ORR in acidic (and neutral) solutions. Our new theoretical understanding provided guidance for rationally tailoring the crystal structures of metal compounds to enhance the 2e$^-$ ORR selectivity and stability by suppressing the undesired O-O bond cleavage and surface oxidative degradation, respectively. Rigorous experimental monitoring of catalyst leaching and H_2O_2 electroreduction side reaction allowed us to achieve significant improvements in both catalyst stability and H_2O_2 bulk electrosynthesis performance of metal chalcogenide-based 2e$^-$ ORR catalysts. The electro-Fenton process on these robust and stable metal chalcogenide catalysts not only found use in environmental treatment, but also enabled the novel cathodic valorization and proof-of-concept linear paired electrochemical valorization of biomass-derived glycerol feedstock.

Future developments of new metal compound-based 2e$^-$ ORR catalysts should focus more on acidic and neutral conditions (see Section 1.4.2). Given that 2e$^-$ ORR catalysts may exhibit pH-dependent catalytic properties, computational models can be insightful for elucidating such pH-dependence[70,71] and identifying promising catalyst candidates for active and selective acidic and neutral 2e$^-$ ORR. Moreover, the emerging computational approach of active motif screening[27] has led to high-throughput prediction of several promising binary phases (Pd_7Se_4, PdSe, Rh_3Se_8, $CuSe_2$, etc.) with expected high activity, selectivity, and stability for acidic or neutral 2e$^-$ ORR. These exciting predictions are waiting to be experimentally realized, and this approach of active motif screening may be further developed for more complicated element combinations. In addition, the recently demonstrated computational approach of combining the bulk Pourbaix stability from the Materials Project and the oxygen adsorbate energetics from the Catalysis Hub for OER catalyst discovery[72] could also be a high-throughput method for screening metal compounds as 2e$^-$ ORR catalysts. Besides binary metal dichalcogenides and ternary thiospinels that we demonstrated in our recent work,[18-21] there remain many metal compounds unexplored or underexplored for 2e$^-$ ORR. For example, the Chevrel phases possess high degrees of compositional flexibility for catalytic applications,[73] but they have only been briefly explored for 2e$^-$ ORR in alkaline solution.[74] In fact, a majority of 2e$^-$ ORR studies of metal compound-based catalysts were performed in alkaline solution, which is probably less productive given the efficient alkaline 2e$^-$ ORR on carbon materials (see Section 1.4.2 and Figure A1.2). Therefore, future experimental developments of metal compound-based 2e$^-$ ORR catalysts are recommended to prioritize the acidic and neutral conditions, and utilize in situ or operando techniques, such as X-ray absorption spectroscopy (XAS) and Raman spectroscopy for probing the structural and electronic evolutions of the working catalysts,[37] and attenuated total reflectance infrared spectroscopy (ATR-IR)[75] and ambient pressure XPS (APXPS)[76] for capturing key ORR adsorbates, to complement the computational modeling and achieve atomic-level mechanistic insights into catalyst design.

1.7 References

1. Campos-Martin, J. M.; Blanco-Brieva, G.; Fierro, J. L. G. Hydrogen Peroxide Synthesis: An Outlook beyond the Anthraquinone Process. *Angew. Chem. Int. Ed.* ***45***, 6962-6984 (2006).

2. Hydrogen Peroxide Market Share, Size, Trends, Industry Analysis Report, By Function (Disinfectant, Bleaching, Oxidant, Others); By Application; By Region; Segment Forecast, 2021 - 2028. https://www.researchandmarkets.com/reports/5459592/hydrogen-peroxide-market-share-size-trends (accessed January 18, 2022).

3. Yang, S.; Verdaguer-Casadevall, A.; Arnarson, L.; Silvioli, L.; Čolić, V.; Frydendal, R.; Rossmeisl, J.; Chorkendorff, I.; Stephens, I. E. L. Toward the Decentralized Electrochemical Production of H2O2: A Focus on the Catalysis. *ACS Catal.* ***8***, 4064-4081 (2018).

4. Jiang, Y.; Ni, P.; Chen, C.; Lu, Y.; Yang, P.; Kong, B.; Fisher, A.; Wang, X. Selective Electrochemical H2O2 Production through Two-Electron Oxygen Electrochemistry. *Adv. Energy Mater.* ***8***, 1801909 (2018).

5. Perry, S. C.; Pangotra, D.; Vieira, L.; Csepei, L.-I.; Sieber, V.; Wang, L.; Ponce de León, C.; Walsh, F. C. Electrochemical synthesis of hydrogen peroxide from water and oxygen. *Nat. Rev. Chem.* ***3***, 442-458 (2019).

6. Siahrostami, S.; Villegas, S. J.; Bagherzadeh Mostaghimi, A. H.; Back, S.; Farimani, A. B.; Wang, H.; Persson, K. A.; Montoya, J. A Review on Challenges and Successes in Atomic-Scale Design of Catalysts for Electrochemical Synthesis of Hydrogen Peroxide. *ACS Catal.* ***10***, 7495-7511 (2020).

7. Seh, Z. W.; Kibsgaard, J.; Dickens, C. F.; Chorkendorff, I.; Nørskov, J. K.; Jaramillo, T. F. Combining theory and experiment in electrocatalysis: Insights into materials design. *Science* ***355***, eaad4998 (2017).

8. Shi, X.; Back, S.; Gill, T. M.; Siahrostami, S.; Zheng, X. Electrochemical Synthesis of H2O2 by Two-Electron Water Oxidation Reaction. *Chem* ***7***, 38-63 (2021).

9. Siahrostami, S.; Verdaguer-Casadevall, A.; Karamad, M.; Deiana, D.; Malacrida, P.; Wickman, B.; Escudero-Escribano, M.; Paoli, E. A.; Frydendal, R.; Hansen, T. W.; Chorkendorff, I.; Stephens, I. E. L.; Rossmeisl, J. Enabling direct H2O2 production through rational electrocatalyst design. *Nat. Mater.* ***12***, 1137-1143 (2013).

10. Verdaguer-Casadevall, A.; Deiana, D.; Karamad, M.; Siahrostami, S.; Malacrida, P.; Hansen, T. W.; Rossmeisl, J.; Chorkendorff, I.; Stephens, I. E. L. Trends in the Electrochemical Synthesis of H2O2: Enhancing Activity and Selectivity by Electrocatalytic Site Engineering. *Nano Lett.* ***14***, 1603-1608 (2014).

11. Lu, Z.; Chen, G.; Siahrostami, S.; Chen, Z.; Liu, K.; Xie, J.; Liao, L.; Wu, T.; Lin, D.; Liu, Y.; Jaramillo, T. F.; Nørskov, J. K.; Cui, Y. High-efficiency oxygen reduction to hydrogen peroxide catalysed by oxidized carbon materials. *Nat. Catal.* ***1***, 156-162 (2018).

12. Sun, Y.; Sinev, I.; Ju, W.; Bergmann, A.; Dresp, S.; Kühl, S.; Spöri, C.; Schmies, H.; Wang, H.; Bernsmeier, D.; Paul, B.; Schmack, R.; Kraehnert, R.; Roldan Cuenya, B.; Strasser, P. Efficient Electrochemical Hydrogen Peroxide Production from Molecular Oxygen on Nitrogen-Doped Mesoporous Carbon Catalysts. *ACS Catal.* ***8***, 2844-2856 (2018).

13. Xia, C.; Xia, Y.; Zhu, P.; Fan, L.; Wang, H. Direct electrosynthesis of pure aqueous H2O2 solutions up to 20% by weight using a solid electrolyte. *Science* ***366***, 226-231 (2019).

14. Sun, Y.; Silvioli, L.; Sahraie, N. R.; Ju, W.; Li, J.; Zitolo, A.; Li, S.; Bagger, A.; Arnarson, L.; Wang, X.; Moeller, T.; Bernsmeier, D.; Rossmeisl, J.; Jaouen, F.; Strasser, P. Activity–Selectivity Trends in the Electrochemical Production of Hydrogen Peroxide over Single-Site Metal–Nitrogen–Carbon Catalysts. *J. Am. Chem. Soc.* ***141***, 12372-12381 (2019).

15. Jiang, K.; Back, S.; Akey, A. J.; Xia, C.; Hu, Y.; Liang, W.; Schaak, D.; Stavitski, E.; Nørskov, J. K.; Siahrostami, S.; Wang, H. Highly selective oxygen reduction to hydrogen peroxide on transition metal single atom coordination. *Nat. Commun.* ***10***, 3997 (2019).

16. Gao, J.; Yang, H. b.; Huang, X.; Hung, S.-F.; Cai, W.; Jia, C.; Miao, S.; Chen, H. M.; Yang, X.; Huang, Y.; Zhang, T.; Liu, B. Enabling Direct H2O2 Production in Acidic Media through Rational Design of Transition Metal Single Atom Catalyst. *Chem* ***6***, 658-674 (2020).

17. Shen, R.; Chen, W.; Peng, Q.; Lu, S.; Zheng, L.; Cao, X.; Wang, Y.; Zhu, W.; Zhang, J.; Zhuang, Z.; Chen, C.; Wang, D.; Li, Y. High-Concentration Single Atomic Pt Sites on Hollow CuSx for Selective O2 Reduction to H2O2 in Acid Solution. *Chem* **5**, 2099-2110 (2019).

18. Sheng, H.; Hermes, E. D.; Yang, X.; Ying, D.; Janes, A. N.; Li, W.; Schmidt, J. R.; Jin, S. Electrocatalytic Production of H2O2 by Selective Oxygen Reduction Using Earth-Abundant Cobalt Pyrite (CoS2). *ACS Catal.* ***9***, 8433-8442 (2019).

19. Sheng, H.; Janes, A. N.; Ross, R. D.; Kaiman, D.; Huang, J.; Song, B.; Schmidt, J. R.; Jin, S. Stable and selective electrosynthesis of hydrogen peroxide and the electro-Fenton process on CoSe2 polymorph catalysts. *Energy Environ. Sci.* ***13***, 4189-4203 (2020).

20. Sheng, H.; Janes, A. N.; Ross, R. D.; Hofstetter, H.; Schmidt, J. R.; Jin, S. Linear Paired Electrochemical Valorization of Glycerol Enabled by the Electro-Fenton Process Using a Stable NiSe2 Cathode. *To be submitted for future publication (see Chapter 4)* (2022).

21. Ross, R. D.; Sheng, H.; Parihar, A.; Huang, J.; Jin, S. Compositionally Tuned Trimetallic Thiospinel Catalysts for Enhanced Electrosynthesis of Hydrogen Peroxide and Built-In Hydroxyl Radical Generation. *ACS Catal.* ***11***, 12643-12650 (2021).

22. Li, H.; Wen, P.; Itanze, D. S.; Hood, Z. D.; Adhikari, S.; Lu, C.; Ma, X.; Dun, C.; Jiang, L.; Carroll, D. L.; Qiu, Y.; Geyer, S. M. Scalable neutral H2O2 electrosynthesis by platinum diphosphide nanocrystals by regulating oxygen reduction reaction pathways. *Nat. Commun.* ***11***, 3928 (2020).

23. Yang, C.; Bai, S.; Yu, Z.; Feng, Y.; Huang, B.; Lu, Q.; Wu, T.; Sun, M.; Zhu, T.; Cheng, C.; Zhang, L.; Shao, Q.; Huang, X. A newly-explored Pd-based nanocrystal for the pH-universal electrosynthesis of H2O2. *Nano Energy* ***89***, 106480 (2021).

24. Qiang, Z.; Chang, J.-H.; Huang, C.-P. Electrochemical generation of hydrogen peroxide from dissolved oxygen in acidic solutions. *Water Res.* ***36***, 85-94 (2002).

25. Brillas, E.; Sirés, I.; Oturan, M. A. Electro-Fenton Process and Related Electrochemical Technologies Based on Fenton's Reaction Chemistry. *Chem. Rev.* ***109***, 6570-6631 (2009).

26. Kulkarni, A.; Siahrostami, S.; Patel, A.; Nørskov, J. K. Understanding Catalytic Activity Trends in the Oxygen Reduction Reaction. *Chem. Rev.* ***118***, 2302-2312 (2018).

27. Back, S.; Na, J.; Ulissi, Z. W. Efficient Discovery of Active, Selective, and Stable Catalysts for Electrochemical H2O2 Synthesis through Active Motif Screening. *ACS Catal.* ***11***, 2483-2491 (2021).

28. Chen, Q.; Ma, C.; Yan, S.; Liang, J.; Dong, K.; Luo, Y.; Liu, Q.; Li, T.; Wang, Y.; Yue, L.; Zheng, B.; Liu, Y.; Gao, S.; Jiang, Z.; Li, W.; Sun, X. Greatly Facilitated Two-Electron Electroreduction of Oxygen into Hydrogen Peroxide over TiO2 by Mn Doping. *ACS Appl. Mater. Interfaces* ***13***, 46659-46664 (2021).

29. Dong, K.; Liang, J.; Wang, Y.; Ren, Y.; Xu, Z.; Zhou, H.; Li, L.; Liu, Q.; Luo, Y.; Li, T.; Asiri, A. M.; Li, Q.; Ma, D.; Sun, X. Plasma-induced defective TiO2-x with oxygen vacancies: A high-active and robust bifunctional catalyst toward H2O2 electrosynthesis. *Chem Catal.* ***1***, 1437-1448 (2021).

30. The Materials Project. https://materialsproject.org/ (accessed January 18, 2022).

31. Singh, A. K.; Zhou, L.; Shinde, A.; Suram, S. K.; Montoya, J. H.; Winston, D.; Gregoire, J. M.; Persson, K. A. Electrochemical Stability of Metastable Materials. *Chem. Mater.* ***29***, 10159-10167 (2017).

32. Hansen, H. A.; Rossmeisl, J.; Nørskov, J. K. Surface Pourbaix diagrams and oxygen reduction activity of Pt, Ag and Ni(111) surfaces studied by DFT. *Phys. Chem. Chem. Phys.* ***10***, 3722-3730 (2008).

33. Wang, Z.; Zheng, Y.-R.; Montoya, J.; Hochfilzer, D.; Cao, A.; Kibsgaard, J.; Chorkendorff, I.; Nørskov, J. K. Origins of the Instability of Nonprecious Hydrogen Evolution Reaction Catalysts at Open-Circuit Potential. *ACS Energy Lett.* ***6***, 2268-2274 (2021).

34. Wang, Z.; Zheng, Y.-R.; Chorkendorff, I.; Nørskov, J. K. Acid-Stable Oxides for Oxygen Electrocatalysis. *ACS Energy Lett.* **5**, 2905-2908 (2020).

35. Zhou, R.; Zheng, Y.; Jaroniec, M.; Qiao, S.-Z. Determination of the Electron Transfer Number for the Oxygen Reduction Reaction: From Theory to Experiment. *ACS Catal.* ***6***, 4720-4728 (2016).

36. Liang, J.; Wang, Y.; Liu, Q.; Luo, Y.; Li, T.; Zhao, H.; Lu, S.; Zhang, F.; Asiri, A. M.; Liu, F.; Ma, D.; Sun, X. Electrocatalytic hydrogen peroxide production in acidic media enabled by NiS2 nanosheets. *J. Mater. Chem. A* **9**, 6117-6122 (2021).

37. Zhang, X.-L.; Su, X.; Zheng, Y.-R.; Hu, S.-J.; Shi, L.; Gao, F.-Y.; Yang, P.-P.; Niu, Z.-Z.; Wu, Z.-Z.; Qin, S.; Wu, R.; Duan, Y.; Gu, C.; Zheng, X.-S.; Zhu, J.-F.; Gao, M.-R. Strongly Coupled Cobalt Diselenide Monolayers for Selective Electrocatalytic Oxygen Reduction to H2O2 under Acidic Conditions. *Angew. Chem. Int. Ed.* ***60***, 26922-26931 (2021).

38. Zhang, L.; Liang, J.; Yue, L.; Dong, K.; Xu, Z.; Li, T.; Liu, Q.; Luo, Y.; Liu, Y.; Gao, S.; Asiri, A. M.; Kong, Q.; Guo, X.; Sun, X. CoTe nanoparticle-embedded N-doped hollow carbon polyhedron: an efficient catalyst for H2O2 electrosynthesis in acidic media. *J. Mater. Chem. A* **9**, 21703-21707 (2021).

39. Zhao, X.; Wang, Y.; Da, Y.; Wang, X.; Wang, T.; Xu, M.; He, X.; Zhou, W.; Li, Y.; Coleman, J. N.; Li, Y. Selective electrochemical production of hydrogen peroxide at zigzag edges of exfoliated molybdenum telluride nanoflakes. *Natl. Sci. Rev.* ***7***, 1360-1366 (2020).

40. Yan, L.; Cheng, X.; Wang, Y.; Wang, Z.; Zheng, L.; Yan, Y.; Lu, Y.; Sun, S.; Qiu, W.; Chen, G. Exsolved Co3O4 with tunable oxygen vacancies for electrocatalytic H2O2 production. *Mater. Today Energy* ***24***, 100931 (2022).

41. Jung, E.; Shin, H.; Lee, B.-H.; Efremov, V.; Lee, S.; Lee, H. S.; Kim, J.; Hooch Antink, W.; Park, S.; Lee, K.-S.; Cho, S.-P.; Yoo, J. S.; Sung, Y.-E.; Hyeon, T. Atomic-level tuning of Co–N–C catalyst for high-performance electrochemical H2O2 production. *Nat. Mater.* ***19***, 436-442 (2020).

42. Choi, C. H.; Kim, M.; Kwon, H. C.; Cho, S. J.; Yun, S.; Kim, H.-T.; Mayrhofer, K. J. J.; Kim, H.; Choi, M. Tuning selectivity of electrochemical reactions by atomically dispersed platinum catalyst. *Nat. Commun.* ***7***, 10922 (2016).

43. Tang, C.; Jiao, Y.; Shi, B.; Liu, J.-N.; Xie, Z.; Chen, X.; Zhang, Q.; Qiao, S.-Z. Coordination Tunes Selectivity: Two-Electron Oxygen Reduction on High-Loading Molybdenum Single-Atom Catalysts. *Angew. Chem. Int. Ed.* ***59***, 9171-9176 (2020).

44. Zhang, J.; Sasaki, K.; Sutter, E.; Adzic, R. R. Stabilization of Platinum Oxygen-Reduction Electrocatalysts Using Gold Clusters. *Science* ***315***, 220-222 (2007).

45. Geiger, S.; Kasian, O.; Ledendecker, M.; Pizzutilo, E.; Mingers, A. M.; Fu, W. T.; Diaz-Morales, O.; Li, Z.; Oellers, T.; Fruchter, L.; Ludwig, A.; Mayrhofer, K. J. J.; Koper, M. T. M.; Cherevko, S. The stability number as a metric for electrocatalyst stability benchmarking. *Nat. Catal.* ***1***, 508-515 (2018).

46. Lopes, P. P.; Strmcnik, D.; Tripkovic, D.; Connell, J. G.; Stamenkovic, V.; Markovic, N. M. Relationships between Atomic Level Surface Structure and Stability/Activity of Platinum Surface Atoms in Aqueous Environments. *ACS Catal.* ***6***, 2536-2544 (2016).

47. Chung, D. Y.; Lopes, P. P.; Farinazzo Bergamo Dias Martins, P.; He, H.; Kawaguchi, T.; Zapol, P.; You, H.; Tripkovic, D.; Strmcnik, D.; Zhu, Y.; Seifert, S.; Lee, S.; Stamenkovic, V. R.; Markovic, N. M. Dynamic stability of active sites in hydr(oxy)oxides for the oxygen evolution reaction. *Nat. Energy* ***5***, 222-230 (2020).

48. Lopes, P. P.; Li, D.; Lv, H.; Wang, C.; Tripkovic, D.; Zhu, Y.; Schimmenti, R.; Daimon, H.; Kang, Y.; Snyder, J.; Becknell, N.; More, K. L.; Strmcnik, D.; Markovic, N. M.; Mavrikakis, M.; Stamenkovic, V. R. Eliminating dissolution of platinum-based electrocatalysts at the atomic scale. *Nat. Mater.* ***19***, 1207-1214 (2020).

49. Dam, V. A. T.; de Bruijn, F. A. The Stability of PEMFC Electrodes: Platinum Dissolution vs Potential and Temperature Investigated by Quartz Crystal Microbalance. *J. Electrochem. Soc.* ***154***, B494 (2007).

50. Tang, C.; Chen, L.; Li, H.; Li, L.; Jiao, Y.; Zheng, Y.; Xu, H.; Davey, K.; Qiao, S.-Z. Tailoring Acidic Oxygen Reduction Selectivity on Single-Atom Catalysts via Modification of First and Second Coordination Spheres. *J. Am. Chem. Soc.* ***143***, 7819-7827 (2021).

51. Stewart, K. L.; Gewirth, A. A. Mechanism of Electrochemical Reduction of Hydrogen Peroxide on Copper in Acidic Sulfate Solutions. *Langmuir* ***23***, 9911-9918 (2007).

52. Gill, T. M.; Zheng, X. Comparing Methods for Quantifying Electrochemically Accumulated H2O2. *Chem. Mater.* ***32***, 6285-6294 (2020).

53. Jung, E.; Shin, H.; Hooch Antink, W.; Sung, Y.-E.; Hyeon, T. Recent Advances in Electrochemical Oxygen Reduction to H2O2: Catalyst and Cell Design. *ACS Energy Lett.* ***5***, 1881-1892 (2020).

54. Tang, J.; Zhao, T.; Solanki, D.; Miao, X.; Zhou, W.; Hu, S. Selective hydrogen peroxide conversion tailored by surface, interface, and device engineering. *Joule* (2021).

55. Zhang, X.; Xia, Y.; Xia, C.; Wang, H. Insights into practical-scale electrochemical H2O2 synthesis. *Trends Chem.* (2020).

56. Ehelebe, K.; Schmitt, N.; Sievers, G.; Jensen, A. W.; Hrnjić, A.; Collantes Jiménez, P.; Kaiser, P.; Geuß, M.; Ku, Y.-P.; Jovanovič, P.; Mayrhofer, K. J. J.; Etzold, B.; Hodnik, N.; Escudero-Escribano, M.; Arenz, M.; Cherevko, S. Benchmarking Fuel Cell Electrocatalysts Using Gas Diffusion Electrodes: Inter-lab Comparison and Best Practices. *ACS Energy Lett.*, 816-826 (2022).

57. Ridruejo, C.; Alcaide, F.; Álvarez, G.; Brillas, E.; Sirés, I. On-site H2O2 electrogeneration at a CoS2-based air-diffusion cathode for the electrochemical degradation of organic pollutants. *J. Electroanal. Chem.* ***808***, 364-371 (2018).

58. Alcaide, F.; Álvarez, G.; Guelfi, D. R. V.; Brillas, E.; Sirés, I. A stable CoSP/MWCNTs air-diffusion cathode for the photoelectro-Fenton degradation of organic pollutants at pre-pilot scale. *Chem. Eng. J.* ***379***, 122417 (2020).

59. Sun, J.; Dai, X.; Wang, Q.; van Loosdrecht, M. C. M.; Ni, B.-J. Microplastics in wastewater treatment plants: Detection, occurrence and removal. *Water Res.* ***152***, 21-37 (2019).

60. Tagg, A. S.; Harrison, J. P.; Ju-Nam, Y.; Sapp, M.; Bradley, E. L.; Sinclair, C. J.; Ojeda, J. J. Fenton's reagent for the rapid and efficient isolation of microplastics from wastewater. *Chem. Commun.* ***53***, 372-375 (2017).

61. Wang, J.-c.; Wang, H. Fenton treatment for flotation separation of polyvinyl chloride from plastic mixtures. *Sep. Purif. Technol.* ***187***, 415-425 (2017).

62. Lucas, F. W. S.; Grim, R. G.; Tacey, S. A.; Downes, C. A.; Hasse, J.; Roman, A. M.; Farberow, C. A.; Schaidle, J. A.; Holewinski, A. Electrochemical Routes for the Valorization of Biomass-Derived Feedstocks: From Chemistry to Application. *ACS Energy Lett.* ***6***, 1205-1270 (2021).

63. Teong, S. P.; Li, X.; Zhang, Y. Hydrogen peroxide as an oxidant in biomass-to-chemical processes of industrial interest. *Green Chem.* ***21***, 5753-5780 (2019).

64. Moody, G. J. The action of fenton's reagent on carbohydrates. *Tetrahedron* ***19***, 1705-1710 (1963).

65. Vitale, A. A.; Bernatene, E. A.; Vitale, M. G.; Pomilio, A. B. New Insights of the Fenton Reaction Using Glycerol as the Experimental Model. Effect of O2, Inhibition by Mg2+, and Oxidation State of Fe. *J. Phys. Chem. A* ***120***, 5435-5445 (2016).

66. Zeng, J.; Yoo, C. G.; Wang, F.; Pan, X.; Vermerris, W.; Tong, Z. Biomimetic Fenton-Catalyzed Lignin Depolymerization to High-Value Aromatics and Dicarboxylic Acids. *ChemSusChem* ***8***, 861-871 (2015).

67. Chou, C. F.; Chou, T. C. Paired electrooxidation IV. Decarboxylation of sodium gluconate to D-arabinose. *J. Appl. Electrochem.* ***33***, 741-745 (2003).

68. Wang, Z.-X.; Li, G.; Yang, F.; Chen, Y.-L.; Gao, P. Electro-Fenton degradation of cellulose using graphite/PTFE electrodes modified by 2-ethylanthraquinone. *Carbohydr. Polym.* ***86***, 1807-1813 (2011).

69. Keller, R. G.; Weyand, J.; Vennekoetter, J. B.; Kamp, J.; Wessling, M. An electro-Fenton process coupled with nanofiltration for enhanced conversion of cellobiose to glucose. *Catal. Today* ***364***, 230-241 (2021).

70. Kelly, S. R.; Kirk, C.; Chan, K.; Nørskov, J. K. Electric Field Effects in Oxygen Reduction Kinetics: Rationalizing pH Dependence at the Pt(111), Au(111), and Au(100) Electrodes. *J. Phys. Chem. C* ***124***, 14581-14591 (2020).

71. Kim, H. W.; Bukas, V. J.; Park, H.; Park, S.; Diederichsen, K. M.; Lim, J.; Cho, Y. H.; Kim, J.; Kim, W.; Han, T. H.; Voss, J.; Luntz, A. C.; McCloskey, B. D. Mechanisms of Two-Electron and Four-Electron Electrochemical Oxygen Reduction Reactions at Nitrogen-Doped Reduced Graphene Oxide. *ACS Catal.* ***10***, 852-863 (2020).

72. Rao, K. K.; Lai, Y.; Zhou, L.; Haber, J. A.; Bajdich, M.; Gregoire, J. M. Overcoming Hurdles in Oxygen Evolution Catalyst Discovery via Codesign. *Chem. Mater.* ***34***, 899-910 (2022).

73. Perryman, J. T.; Velázquez, J. M. Design Principles for Multinary Metal Chalcogenides: Toward Programmable Reactivity in Energy Conversion. *Chem. Mater.* ***33***, 7133-7147 (2021).

74. Xia, F.; Li, B.; Liu, Y.; Liu, Y.; Gao, S.; Lu, K.; Kaelin, J.; Wang, R.; Marks, T. J.; Cheng, Y. Carbon Free and Noble Metal Free Ni2Mo6S8 Electrocatalyst for Selective Electrosynthesis of H2O2. *Adv. Funct. Mater.* ***31***, 2104716 (2021).

75. Nayak, S.; McPherson, I. J.; Vincent, K. A. Adsorbed Intermediates in Oxygen Reduction on Platinum Nanoparticles Observed by In Situ IR Spectroscopy. *Angew. Chem. Int. Ed.* ***57***, 12855-12858 (2018).

76. Casalongue, H. S.; Kaya, S.; Viswanathan, V.; Miller, D. J.; Friebel, D.; Hansen, H. A.; Nørskov, J. K.; Nilsson, A.; Ogasawara, H. Direct observation of the oxygenated species during oxygen reduction on a platinum fuel cell cathode. *Nat. Commun.* ***4***, 2817 (2013).

CHAPTER 2

Electrocatalytic Production of H_2O_2 by Selective Oxygen Reduction Using Earth-Abundant Cobalt Pyrite (CoS_2)*

2.1 Abstract

Decentralized on-site production of hydrogen peroxide (H_2O_2) relies on efficient, robust and inexpensive electrocatalysts for the selective two-electron ($2e^-$) oxygen reduction reaction (ORR). Here we combine computations and experiments to demonstrate cobalt pyrite (CoS_2), an earth-abundant transition metal compound, is both active and selective towards $2e^-$ ORR in acidic solution. CoS_2 nanomaterials drop-casted on rotating ring-disk electrode (RRDE) showed selective and efficient H_2O_2 formation in 0.05 M H_2SO_4 at high catalyst loadings, with their operational stability evaluated by structural and surface analyses. CoS_2 nanowires directly grown on high-surface-area carbon fiber paper electrode boosted the overall performance of bulk ORR electrolysis and the H_2O_2 product was chemically quantified to yield a ~70% H_2O_2 selectivity at 0.5 V vs. RHE, in good agreement with the RRDE results. Computations suggested the modest binding of OOH* adsorbate on the single Co site of CoS_2 and the kinetically disfavored O-O bond scission due to the lack of active site ensembles in the crystal structure, consistent with the experimentally observed activity and selectivity. CoS_2 also catalyzes $2e^-$ ORR with less activity and selectivity in non-corrosive neutral solution. This work opens up the exploration of diverse

---

* This chapter was originally published in *ACS Catal.* **9**, 8433-8442 (2019), in collaboration with Eric D. Hermes, Xiaohua Yang, Diwen Ying, Aurora N. Janes, Wenjie Li, J. R. Schmidt, and Song Jin.

earth-abundant transition metal compounds in search of highly active and selective electrocatalysts for efficient H_2O_2 production.

2.2 Introduction

Hydrogen peroxide (H_2O_2) is an efficient and environmentally benign oxidant with diverse industrial applications including pulp- and paper-bleaching, chemical synthesis, and wastewater treatment.[1,2] Commercial production of H_2O_2 (5.5 million tons per year in 2015) has been almost exclusively through an indirect anthraquinone process that involves sequential hydrogenation (under H_2 gas) and autoxidation (in air) of anthraquinone.[1,2] Direct chemical synthesis of H_2O_2 from H_2 and O_2 gases has also been explored, yet a very few noble metal alloy catalysts show satisfactory selectivity towards H_2O_2.[3-5] Both chemical approaches of H_2O_2 synthesis use large quantities of H_2 gas, which is both costly and energy intensive to obtain. Moreover, these centralized production methods require long-distance transportation of concentrated H_2O_2 to end-users with significant expenses and safety concerns. In fact, low concentrations of H_2O_2 are usually sufficient for most applications, which motivates sustainable on-site production and utilization of H_2O_2 in a decentralized manner.

In this context, direct H_2O_2 production via electrochemical, rather than chemical, reduction of O_2 eliminates the need for H_2 gas, allowing for not only reduction in both costs and energy consumption but also safer deployment in a modular and decentralized fashion. The electricity needed in electrochemical oxygen reduction reaction (ORR) can come from renewable solar and wind energy,[6] which are also decentralized and becoming more affordable. The major challenge here is to selectively reduce O_2 to H_2O_2 (vs. H_2O) via two-electron (vs. four-electron) pathway. Recent developments of selective two-electron ($2e^-$) ORR catalysts have been mostly focused on carbon materials[7-12] and noble metals.[13-18] In carbon materials, carbon defects[7-10] and heteroatom dopants[9,11] were exploited as the active sites for selective 2e$^-$ ORR; however, they are sufficiently active only in alkaline solution[8,11] where H_2O_2 is unstable,[1] and significant challenges remain in rational synthesis of defects and dopants with atomic precision. Selective 2e$^-$ ORR over noble metals necessitates isolation of active sites to suppress O-O bond scission by adjacent active sites (and thus 4e$^-$ ORR), which was realized by either dispersing active metals within inert matrices (e.g., Pd-Au,[13,14] Pt-Hg,[15] Pd-Hg[16]) or anchoring single metal atoms onto supports;[17-19] however, they involve expensive or sometimes toxic metals. Compared to noble metals, earth-abundant transition metal compounds not only enable better isolation of active (metal) sites but also offer unique surface structural motifs with more diverse and controllable tunability, allowing for optimized adsorbate binding and therefore potentially enhanced activity and selectivity towards H_2O_2 production. In addition, as both acidic and alkaline solutions are corrosive, on-site production of H_2O_2 in non-corrosive neutral solution is advantageous for practical wastewater treatment applications by avoiding the need for neutralization.

Here we present a joint computational/experimental study to demonstrate that earth-abundant cobalt pyrite (CoS_2) is both active and selective towards 2e$^-$ ORR in acidic and neutral solutions, with its catalytic performance in acidic solution comparable to those of the state-of-the-art catalysts containing noble and/or toxic metals. Chemical quantification of the H_2O_2 product electrogenerated on the CoS_2 catalyst from the bulk ORR electrolysis in acidic solution further demonstrates the promise of this catalyst for practical applications. Computations reveal general mechanistic insights into the activity and selectivity of earth-abundant transition metal compounds towards 2e$^-$ ORR. This study opens up new directions in search of more active and selective electrocatalysts for efficient decentralized production of H_2O_2.

2.3 Results and Discussion

2.3.1 Computational Assessments of ORR Pathways on CoS_2

Metallic pyrites have been known as versatile earth-abundant electrocatalysts towards hydrogen evolution, triiodide- and polysulfide-reduction,[20,21] which led us consider metallic pyrites as possible 2e$^-$ ORR electrocatalysts. Computational modeling of ORR was performed on the CoS_2 (100) surface using density functional theory (DFT) and the computational hydrogen electrode (CHE) approach.[22-26] Surface energy of the (100) facet (0.032 eV/Å^2) is considerably lower than those of the (110) or (111) facets (0.060 and 0.057 eV/Å^2, respectively) since the (100) surface preserves the disulfide (S_2^{2-}) dumbbells. As such, our initial computational work focuses on the thermodynamically most stable (100) facet, which is the most probable facet present in our experimental samples (see below) and also the simplest one to start with to generate mechanistic insights. The activity of CoS_2 towards 2e$^-$ ORR is governed by the following proton-coupled electron transfer (PCET) steps,[23-25]

$$O_2 + * + (H^+ + e^-) \rightarrow OOH* \qquad (1)$$

$$OOH* + (H^+ + e^-) \rightarrow H_2O_2 + * \qquad (2)$$

where * is the unoccupied active site (Co site in CoS_2), and OOH* is the sole adsorbate for 2e$^-$ ORR. The first PCET step, forming OOH*, is modestly exergonic (ΔG = -0.14 eV) at the thermodynamic potential of 2e$^-$ ORR (Figure 2.1a). The overpotential of 2e$^-$ ORR on CoS_2 is therefore determined by the reduction of OOH* to H_2O_2 (only 0.14 eV uphill in free energy), making CoS_2 very active towards H_2O_2 formation. On the other hand, the selectivity of 2e$^-$ vs. 4e$^-$ ORR is determined by the resistance to O-O bond scission,[23-25] forming O* and/or OH* as adsorbates for 4e$^-$ ORR,

$$O_2 + 2 * \rightarrow 2 O* \qquad (3)$$

$$OOH* + * \rightarrow O* + OH* \qquad (4)$$

$$OOH* + (H^+ + e^-) \rightarrow O* + H_2O \qquad (5)$$

The O-O bonds in adsorbed O_2 and OOH* can potentially be thermally cleaved onto adjacent active sites (Equation 3 and 4), but these processes exhibit substantial activation energy barriers on CoS_2 (0.59 and 0.78 eV, respectively). We find that the crucial O-O bond cleave process in OOH* happens preferentially via a binuclear pathway across two neighboring Co sites (barrier of 0.78 eV) rather than neighboring Co and S sites (0.84 eV), most likely due to the strong binding preference of O* to S and OH* to Co, respectively. Another possible pathway is the migration of OOH* onto S prior to dissociation; however, we can disregard this pathway because the energetics of this migration is less favorable than the binuclear dissociation barrier across neighboring Co sites. This is consistent with the established understandings on molecular ORR catalyst cobalt porphyrins that (1) monomeric cobalt porphyrins usually catalyze $2e^-$ ORR and (2) cofacial dicobalt porphyrins catalyze $4e^-$ ORR.[27]

Focusing specifically on the key potential-determining step, OOH* cleavage is unlikely to compete with the rapid reduction of OOH* to H_2O_2 (Equation 2). This observation lies in sharp contrast to close-packed metal surfaces, which in turn display minimal activation barriers for rapid OOH* scission (0.06, 0.16, and 0.06 eV on (111) facet of Pd, Pt, and Cu).[26] We hypothesize that such difference is associated with the absence of active ensemble sites in the crystal structure of CoS_2. The neighboring Co sites in CoS_2 are separated by 3.941 Å, while the minimum-energy configuration of OOH* has an O-O bond length of only 1.435 Å (Figure 2.1b). To reach the transition state for OOH* scission, the O-O bond in OOH* elongates considerably to 1.814 Å and becomes highly strained (Figure 2.1c), the CoS_2 also experiences significant lattice distortion with a shorter distance between neighboring Co sites (3.645 Å). In contrast, the transition state for OOH* scission on close-packed metal surfaces is much less distorted from the reactant geometry. In addition, O-O bond cleavage through reductive elimination of OOH* (Equation 5) is also kinetically disfavored on CoS_2. Compared to most metal surfaces that interact closely with both oxygens in OOH*, only one of the oxygens in OOH* is in the immediate vicinity of the CoS_2 surface due to its isolated active sites (Figure 2.1d). As a result, PCET to the surface-bound oxygen on CoS_2 (leading to H_2O_2) likely dominates over that to the distant oxygen (yielding H_2O and O*) which requires through-space transfer (approximately 3 Å, see Figure 2.1d) or tunneling through the O-O bond. Addition of an empirical dispersion-correction to these density functional results does not qualitatively alter this picture (Figure A2.1 in the Appendix 2).[28]

Our experimental results (see below) suggest that the operating catalyst surface appears to be unoxidized, and thus we do not expect a high surface coverage of O*. Nonetheless, we find that the binding energy of OOH* is fairly insensitive to the coverage of O* on S (its preferred binding site), with an adjacent O* altering the OOH* binding energy by only ~0.07 eV. We discount the buildup of OH* due to its presumed rapid reduction to water. Overall, our computational results suggest that $2e^-$ ORR is selectively initiated at low overpotential on the single Co site of CoS_2, while $4e^-$ ORR on CoS_2 is kinetically suppressed by the large spacing between neighboring Co sites.

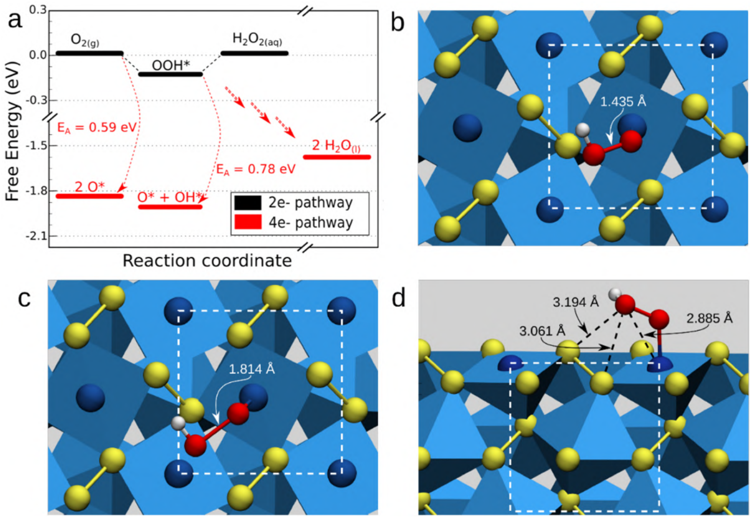

Figure 2.1. Computational modeling of ORR on the CoS_2 (100) surface.

(**a**) Free energy diagram for both $2e^-$ and $4e^-$ ORR at the calculated standard equilibrium reduction potential of $2e^-$ ORR. Top view of (**b**) the CoS_2 surface with adsorbed OOH* and (**c**) the transition state for OOH* scission. (**d**) Side view of the CoS_2 surface with adsorbed OOH*.

2.3.2 Experimental Verification of Selective $2e^-$ ORR on CoS_2 in Acidic and Neutral Solutions

To experimentally verify our computational predictions, we prepared CoS_2 nanomaterials via thermal sulfidation of hydrothermally synthesized cobalt hydroxide carbonate hydrate nanomaterials (Figure A2.2a).[21] Scanning electron microscopy (SEM) images of CoS_2 showed the nanowire morphology with surface roughness (Figure A2.2b), while powder X-ray diffraction (PXRD) (Figure A2.2c) and energy dispersive X-ray spectroscopy (EDS) (Figure A2.3) confirmed the phase purity and elemental compositions of CoS_2. We systematically studied the catalytic activity and selectivity of the CoS_2 nanomaterials towards $2e^-$ ORR in both acidic (0.05 M H_2SO_4) and neutral (0.05 M Na_2SO_4) solutions using a rotating ring-disk electrode (RRDE) that consists of a glassy carbon (GC) disk surrounded by a Pt ring. The collection efficiency of the bare RRDE, calibrated with a reversible and fast ferri-/ferrocyanide redox couple when both ferricyanide reduction on the GC disk and ferrocyanide oxidation on the Pt ring are diffusion-limited, is 0.43 and is independent of the RRDE rotation rate (Figure A2.4). To determine ORR selectivity using this collection efficiency value, the Pt ring needs to drive fast H_2O_2 oxidation without triggering water oxidation.[29,30] This ring potential is usually set between 1.2 V and 1.3 V vs. RHE regardless of the pH of electrolyte.[31,32] We experimentally verified that 1.3 V vs. RHE is an appropriate ring potential for both 0.05 M H_2SO_4 and 0.05 M Na_2SO_4 by performing ORR measurements and analyzing H_2O_2 selectivity of commercial Pt/C (a known $4e^-$ ORR catalyst[31]) and Vulcan carbon black (moderately selective towards $2e^-$ ORR but has a poor activity[11]), as shown in Figure A2.5 and A2.6.

We then drop-casted CoS_2 nanomaterials on RRDE (cobalt loading = 305 $\mu g/cm^2_{disk}$) without carbon support and measured their intrinsic activity and selectivity towards $2e^-$ ORR in both acidic and neutral solutions without interference from carbon (Figure 2.2). The disk potential was set not to exceed 0.80 V vs. RHE to prevent anodic dissolution of CoS_2 via oxidation of sulfide to sulfate.[33,34] We note that, for the ease of directly visualizing the H_2O_2 selectivity from the RRDE voltammograms (Figure 2.2a and 2.2c), both the disk and the ring current densities are presented based on the geometric area of the disk electrode (0.126 cm^2), and the ring current density was further adjusted by collection efficiency. In 0.05 M H_2SO_4 (pH 1.26), the catalytic onset on CoS_2 was close to the thermodynamic potential of $2e^-$ ORR (0.69 V vs. RHE). As the disk potential was swept negatively, the disk current density kept increasing, while the ring current density reached its maximum and then declined (Figure 2.2a), indicating the optimal H_2O_2 production on CoS_2 in acidic solution takes place at the low overpotential region. Nevertheless, the H_2O_2 selectivity peaked at 70~80% and remained above 50% over a wide potential range (above 0.35 V vs. RHE,

Figure 2.2b), suggesting H_2O_2 is the primary ORR product on CoS_2 in acidic solution before $4e^-$ ORR takes over at high overpotentials. We further performed the same RRDE measurement in 0.1 M $HClO_4$ (pH 1.02) to show that the ORR activity and selectivity of CoS_2 in acidic solution are unaffected by the electrolyte anions (Figure A2.7a to A2.7d). The H_2O_2 selectivity of CoS_2 in 0.05 M H_2SO_4 (determined by the RRDE method) exhibits a slight dependence on the rotation rate (Figure 2.2b); such dependence, as documented in the RRDE theory and reported on other ORR catalysts, is characteristic of the ORR that has multiple parallel pathways.[29] To further confirm this, we examined the ORR on CoS_2 under a higher concentration of acid (0.5 M H_2SO_4, pH 0.35) and still observed such dependence (Figure A2.7e and A2.7f), suggesting the local pH variation at the catalyst surface (which might be more severe in more diluted acidic solution) is unlikely to be the cause of such dependence. Electrochemically active surface areas (ECSAs) of drop-casted CoS_2 in different acidic solutions were estimated by double-layer capacitance (C_{dl}) measurements (Figure A2.8). In the neutral solution of 0.05 M Na_2SO_4 (pH 6.14), the catalytic onset on CoS_2 took place around 0.54 V vs. RHE (150 mV overpotential for $2e^-$ ORR), both the ring current density (Figure 2.2c) and the H_2O_2 selectivity (below 50%, Figure 2.2d) were lower than those achieved in 0.05 M H_2SO_4. To explain the observed pH dependence of the H_2O_2 selectivity, we suggest that, in neutral solution where proton concentration is sufficiently low, H_2O instead of H^+ becomes the major proton source involved in the ORR elementary steps (Equation 1 to 5) and therefore alters the catalytic mechanism and selectivity. Note that using unbuffered 0.05 M Na_2SO_4 as the neutral electrolyte, even though closer to the practical applications, has some limitations because the local pH at the catalyst surface could become more alkaline under ORR conditions and may vary across the potential sweep. We do not present experimental results of the ORR on CoS_2 in alkaline solution because (1) H_2O_2 is known to be chemically less stable in alkaline solution,[1] which we experimentally verified by observing a higher decomposition rate of nonstabilized H_2O_2 in alkaline solution compared with that in acidic solution which is negligible over the time period of one week (Figure A2.9); (2) CoS_2 is not chemically stable in alkaline solution under oxidative environments.[35] Overall, these results show that electrocatalytic production of H_2O_2 on CoS_2 is quite efficient in acidic solution and is feasible in non-corrosive neutral solution.

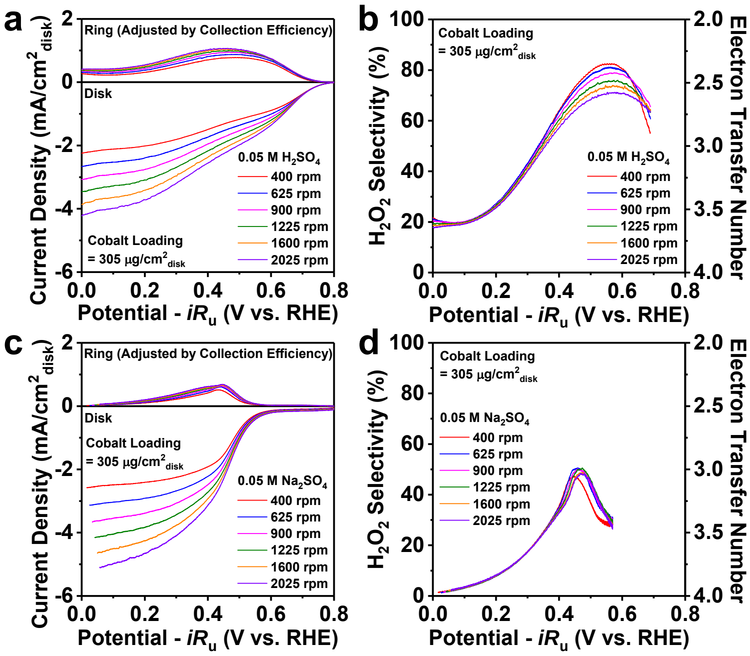

Figure 2.2. RRDE experiments of CoS_2 catalyst in acidic and neutral solutions. (**a,c**) RRDE measurements of drop-casted CoS_2 (cobalt loading = 305 μg/cm$^2_{disk}$) at different rotation rates and (**b,d**) the corresponding H_2O_2 selectivity in O_2-saturated (**a,b**) 0.05 M H_2SO_4 and (**c,d**) 0.05 M Na_2SO_4.

To explore the optimal operating conditions of electrocatalytic H_2O_2 production on CoS_2 in acidic solution, we investigated the influence of catalyst loadings on the ORR activity and selectivity of drop-casted CoS_2 in 0.05 M H_2SO_4 at 2025 rpm (Figure 2.3, A2.10, and Table A2.1).

As the cobalt loading was gradually reduced from 305 to 76 μg/cm$^2_{disk}$, the disk current density became smaller (Figure 2.3a) due to the lower amount of catalytic active sites, however the H_2O_2 selectivity at high overpotentials clearly improved (Figure 2.3b). Interestingly, the two lowest cobalt loadings (76 and 152 ug/cm$^2_{disk}$) exhibited essentially the same H_2O_2 selectivity over the entire potential range. We hypothesize that (1) when the catalyst loading is below a certain critical value, the catalytic active sites are likely to be completely saturated by the steady-state O_2 flux at the RRDE surface, yielding the nearly identical H_2O_2 selectivity profiles; (2) as the catalyst loadings go beyond this critical value, the excess catalytic active sites that are not saturated by the O_2 flux might trigger side reactions (4e$^-$ ORR, H_2O_2 reduction and/or decomposition) at high overpotentials that reduces the H_2O_2 selectivity. Nevertheless, at the more important low overpotential region, the high selectivity of H_2O_2 formation on CoS_2 is less affected by catalyst loadings (Figure 2.3b) and the ring current density still increases with higher catalyst loadings (Figure 2.3c). This is particularly the case at 0.46 V vs. RHE where the maximum ring current density was achieved at the highest cobalt loading (Figure 2.3d). Since the practical focus of electrocatalytic H_2O_2 production is to boost the overall H_2O_2 yield at small overpotentials, these results suggest a high catalyst loading of CoS_2 should be used for the best overall performance of electrocatalytic H_2O_2 production in acidic solution. The catalyst loading effects of drop-casted CoS_2 were also studied in 0.05 M Na_2SO_4 (Figure A2.11). ECSAs of drop-casted CoS_2 in both 0.05 M H_2SO_4 and 0.05 M Na_2SO_4 systematically increased at higher catalyst loadings (Figure A2.12).

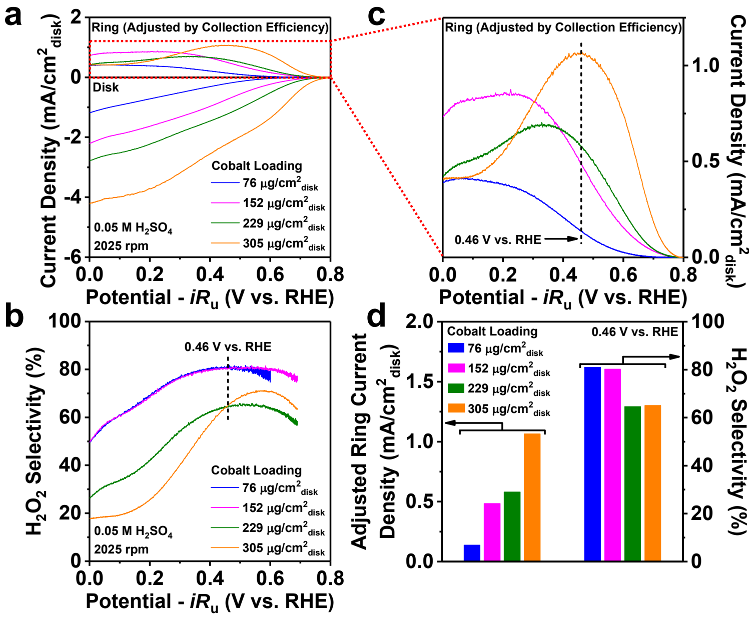

Figure 2.3. Dependence of RRDE experiments on catalyst loading of CoS_2.

(**a**) RRDE measurements of drop-casted CoS_2 with various cobalt loadings at 2025 rpm in O_2-saturated 0.05 M H_2SO_4 (adapted from Figure 2.2a and A2.10). Comparisons of (**b**) the H_2O_2 selectivity and (**c**) the ring current density . Comparisons of the ring current density and the H_2O_2 selectivity at 0.46 V vs. RHE are highlighted in (**d**).

2.3.3 Comparisons of Kinetic Current Densities for H_2O_2 Production in Acidic Solution

To compare the catalytic performance of CoS_2 with other reported ORR electrocatalysts for H_2O_2 production in acidic solution based on RRDE measurements, we extracted the kinetic current density for H_2O_2 production ($j_{\text{k peroxide}}$, see definition in the Appendix 2) from the RRDE voltammograms of CoS_2 (cobalt loading = 305 $\mu g/cm^2_{\text{disk}}$) in 0.05 M H_2SO_4 (shown in Figure 2.2a) by correcting the ring current density (i.e., the hydrogen peroxide current density, j_{peroxide}, see definition in the Appendix 2) for mass-transport loss (see Figure A2.13 and Table A2.2 for details). From the point of view of end applications, $j_{\text{k peroxide}}$ is the most relevant parameter to reflect how much H_2O_2 product can be generated on the catalyst electrode (i.e., the actual yield of H_2O_2

product) at a given potential without mass-transport limitation. We note that $j_{\mathrm{k\ peroxide}}$ can be affected by the catalyst loading and the catalyst surface area; therefore, we normalized $j_{\mathrm{k\ peroxide}}$ to the geometric area of disk electrode for the ease of directly comparing the overall electrode performances of CoS_2 and other reported ORR catalysts (with their RRDE electrode information summarized in Table A2.3). Comparison of the mass-transport corrected Tafel plots of $j_{\mathrm{k\ peroxide}}$ in acidic solution (Figure 2.4) clearly show that, at the most important low overpotential region, the overall electrode performance of H_2O_2 production on the CoS_2 catalyst is competitive with those on the state-of-the-art catalysts based on noble and/or toxic metals.

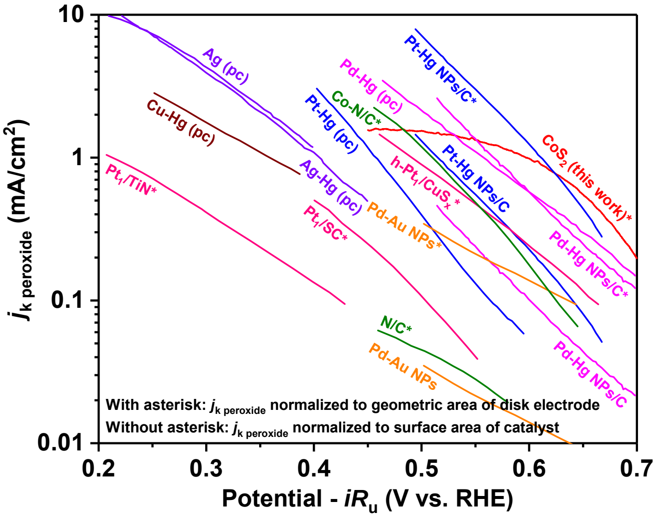

Figure 2.4. Comparisons of kinetic current densities for H_2O_2 production in acidic solution for CoS_2 and other reported 2e$^-$ ORR electrocatalysts based on RRDE measurements. Mass-transport corrected Tafel plots are constructed to extract kinetic current densities for H_2O_2 production ($j_{\mathrm{k\ peroxide}}$, see definition in the Appendix 2) in acidic solution for CoS_2 and other reported ORR electrocatalysts based on RRDE measurements. Data for CoS_2 (red trace) is from this work based on the RRDE voltammogram of drop-casted CoS_2 (cobalt loading = 305 µg/cm$^2_{\mathrm{disk}}$) in 0.05 M H_2SO_4 at the rotation rate of 1600 rpm (shown in Figure 2.2a), and is cut-off at 0.45 V vs. RHE where the ring current density (i.e., the hydrogen peroxide current density,

j_{peroxide}, see definition in the Appendix 2) at 1600 rpm reaches its maximum. The curvature in data for CoS_2 is due to the decrease in the H_2O_2 selectivity of CoS_2 at higher overpotentials. Other data are adapted from previous literature (as summarized in Table A2.3 in the Appendix 2): ref. 14 for Pt-Au NPs; ref. 15 for Pt-Hg NPs/C and Pt-Hg (pc); ref. 16 for Pd-Hg NPs/C, Pd-Hg (pc), Ag (pc), Ag-Hg (pc), Cu-Hg (pc); ref. 17 for Pt_1/SC; ref. 18 for Pt_1/TiN; ref. 19 for h-Pt_1/CuS_x; ref. 36 for N/C; ref. 37 for Co-N/C. The data with asterisk (*) is normalized with the geometric area of disk electrode. The data without asterisk is normalized to the surface area of catalyst (when available).

2.3.4 Operational Stability and Characterization of Tested CoS_2 Catalyst

We further examined the operational stability of drop-casted CoS_2 by running successive RRDE scans in 0.05 M H_2SO_4 and 0.05 M Na_2SO_4 while sequentially changing the rotation rate back and forth between 400 and 2025 rpm (Figure A2.14, A2.15). In both acidic and neutral solutions, the disk current density for the highest cobalt loading (305 $\mu g/cm^2_{\text{disk}}$) stayed almost unchanged over the scans (Figure A2.14d and A2.15d), suggesting CoS_2 is reasonably stable under ORR conditions; on the other hand, the ring current density slightly decreased during operational stability tests (Figure A2.14e and A2.15e), which is likely due to the gradual poisoning of the Pt ring by the strongly absorbing sulfate anions from the electrolytes rather than the degradation of H_2O_2 selectivity (similar observations were also reported in a recent RRDE study of $2e^-$ ORR on carbon materials in strongly absorbing phosphate buffer solution[8]). At lower cobalt loadings, however, the decrease in the disk current density was more significant in both solutions (Figure A2.16). We further assessed the phase purity and surface chemical states of CoS_2 before and after operational stability tests with Raman spectroscopy and X-ray photoelectron spectroscopy (XPS). Raman spectra confirmed that the crystal structure of CoS_2 was well-preserved without the appearance of impurity phases after operational stability tests (Figure 2.5a). The binding energies of the predominant Co 2p (778.9 and 794.0 eV) and S 2p (163.0 and 164.0 eV) XPS signals, in good agreement with the literature values of pristine surface-unoxidized CoS_2,[21] remained the same after operational stability tests in both solutions (Figure 2.5b and 2.5c). We observed sulfate XPS signals (169.3 eV) after operational stability tests albeit their weak intensities. Although the sulfate peak might arise from sulfonate groups in the Nafion ionomer (we ruled out the possibility of residual H_2SO_4 electrolyte in the tested catalyst by examining the catalysts tested in $HClO_4$ electrolyte, see Figure A2.17), we suspect the CoS_2 surface could be slowly oxidized into sulfate species by the dissolved O_2 or the electrogenerated H_2O_2 under ORR conditions and then be quickly refreshed to expose unoxidized CoS_2 upon the subsequent dissolution of sulfate species in both acidic and neutral solutions.

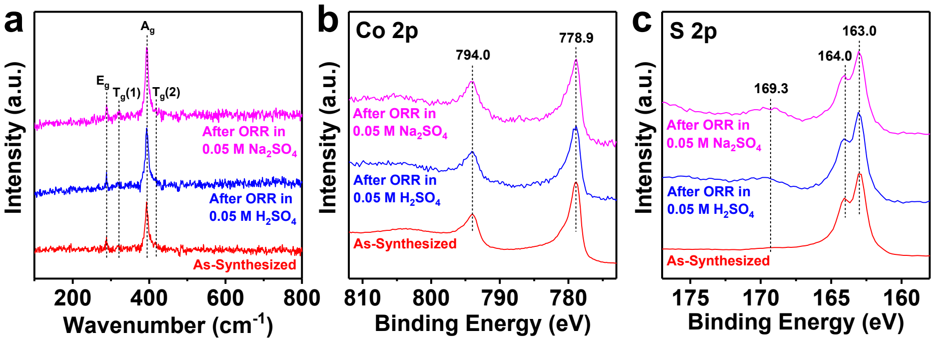

Figure 2.5. Structural and compositional characterizations of CoS_2 catalyst before and after RRDE stability tests in acidic and neutral solutions.

(**a**) Raman spectra, (**b**) Co 2p and (**c**) S 2p XPS spectra.

We also carried out the Koutecky-Levich (K-L) analysis as an alternative to determine the H_2O_2 selectivity (or the electron transfer number of the ORR). Since the K-L method requires a sufficient catalyst loading to completely react with the steady-state O_2 flux at the electrode surface and reach the limiting current,[30] we performed the K-L analysis on the highest catalyst loading of drop-casted CoS_2 in 0.05 M H_2SO_4. We used commercial Pt/C as an internal standard of the $4e^-$ ORR in acidic solution for the K-L analysis to deduce the electron transfer number of the ORR on drop-casted CoS_2 by comparing the slope of the K-L plots (Figure A2.18 and Table A2.4) to minimize the impact by the uncertainties in the diffusion constant of O_2 in the ionomer film and the kinematic parameters of the electrolyte. The K-L analysis (Figure A2.18c) yields similar (or slightly higher) H_2O_2 selectivity values of drop-casted CoS_2 and a similar trend up to about 0.46 V vs. RHE compared with the RRDE method (Figure 2.2b); however, the H_2O_2 selectivity from the K-L method is clearly higher at the low overpotential region. We think the RRDE method is better for drop-casted CoS_2 electrode than the K-L method because the K-L method is only applicable to single-step and one-way reactions with a first-order dependence on the gas phase reactant, while the ORR is a multistep process with parallel pathways.[29,30] Therefore, we prefer to report the H_2O_2 selectivity determined by the RRDE method.

2.3.5 Bulk Accumulation and Chemical Detection of the Produced H_2O_2 on Integrated Electrode of CoS_2 Nanowires Grown on Carbon Fiber Paper (CoS_2/CFP)

Finally, since RRDE only enables instantaneous detection of H_2O_2 intermediate, to ensure H_2O_2 is indeed electrochemically produced on CoS_2 and can accumulate in the solution (which is critical for practical on-site production of H_2O_2), we carried out chemical, rather than electrochemical (RRDE), detection of H_2O_2 using a ceric sulfate titration method ($2\ Ce^{4+} + H_2O_2 \rightarrow 2\ Ce^{3+} + 2\ H^+ + O_2$).[8] To achieve a larger catalytic current and therefore a higher H_2O_2 yield, we directly grew CoS_2 nanowires onto high-surface-area three-dimensional carbon fiber paper substrate as the working electrode (CoS_2/CFP, Figure 2.6a). A three-electrode H-cell setup (Figure A2.19) was used to avoid the oxidation of H_2O_2 product on the counter electrode, and a minimal volume (3 mL) of electrolyte was filled into the working electrode compartment to obtain higher concentrations of H_2O_2. In 0.05 M H_2SO_4, the catalytic onset on CoS_2/CFP was similar to that on drop-casted CoS_2, while the plain CFP was inert towards the ORR (Figure A2.20). To perform the bulk ORR electrolysis on CoS_2/CFP in acidic solution, we set the working electrode potential at 0.5 V vs. RHE (around the optimal operating potential identified earlier from the RRDE results) and applied vigorous stirring (1200 rpm) to facilitate the mass transport of O_2 (Figure A2.20b). Two working electrodes with similar geometric areas (0.907 and 0.875 cm^2_{CFP}) fabricated from one synthesis of CoS_2/CFP (cobalt loading = ~374 $\mu g/cm^2_{CFP}$) were tested, showing highly reproducible results (Figure 2.6b, A2.21). During the 60-min bulk electrolysis, multiple aliquots of electrolyte were sampled out of the working electrode compartment at specific time intervals for chemical detection of H_2O_2 (Figure A2.22). Soon after the bulk electrolysis started, the overall catalytic current quickly reached steady state, the cumulative H_2O_2 yield displayed an almost linear increase for about 30 min (Figure 2.6c) with the cumulative H_2O_2 selectivity and Faradaic efficiency staying above 70% and 54% (Figure 2.6d, matched well with the RRDE results). As the bulk electrolysis further progressed, the overall catalytic current started to slowly increase, while the cumulative H_2O_2 yield experienced a less steady growth. We speculate that the accumulation of H_2O_2 in the electrolyte might speed up side reactions such as H_2O_2 reduction (generating additional current without increasing H_2O_2 yield) and/or decomposition (by Nafion membrane or other impurities[15]). Nevertheless, at the end of the 60-min electrolysis, the cumulative H_2O_2 selectivity and Faradaic efficiency remained nearly 60% and 43%, and the cumulative H_2O_2 yield and concentration could eventually reach around 13 μmol and 148 mg/L. PXRD confirmed the crystalline phase of CoS_2 in the post-electrolysis CoS_2/CFP electrode (Figure A2.23). It is worth noting that there have been very few ORR catalysts reported with chemically quantified H_2O_2 production in acidic solutions, and most are based on noble metals.[15] The overall H_2O_2 production performance of CoS_2/CFP is comparable to that of the benchmark Pt-Hg alloy catalyst[15] under similar acidic conditions (see details in Table A2.5), making CoS_2 a more inexpensive and practical catalyst candidate for applications.

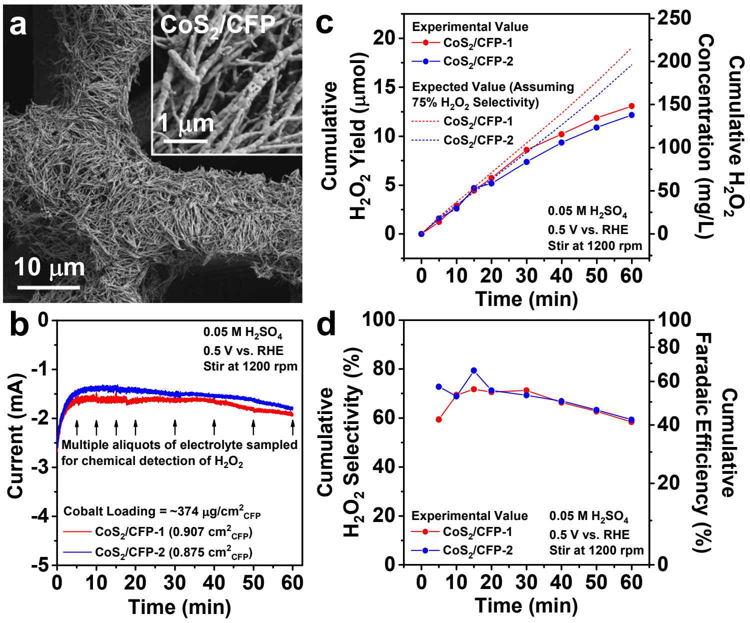

Figure 2.6. Electrocatalytic production of H_2O_2 on CoS_2/CFP in a three-electrode H-cell setup and chemical quantification of H_2O_2 product.

(**a**) SEM image of CoS_2/CFP. (**b**) Bulk ORR electrolysis of two CoS_2/CFP electrodes at 0.5 V vs. RHE in O_2-saturated 0.05 M H_2SO_4 and the corresponding (**c**) cumulative H_2O_2 yield, (**d**) cumulative H_2O_2 selectivity and Faradaic efficiency.

2.4 Conclusions

In conclusion, our combined computational/experimental study demonstrates CoS_2 as an earth-abundant transition metal compound showing great promise for electrocatalytic production of H_2O_2 in acidic and neutral solutions. Computations successfully predict the high activity and selectivity of CoS_2 towards $2e^-$ ORR due to the modest binding of OOH* adsorbate and the kinetically disfavored O-O bond scission resulting from its structural features. Both RRDE measurements of drop-casted CoS_2 nanomaterials and bulk ORR electrolysis using CoS_2 nanowires directly grown on high-surface-area carbon fiber paper electrode followed by chemical quantification of H_2O_2 product show highly efficient electrocatalytic production of H_2O_2 on CoS_2 in acidic solution (0.05 M H_2SO_4) with a ~70% H_2O_2 selectivity at ~0.5 V vs. RHE and good operational stability. CoS_2 also catalyzes $2e^-$ ORR with less activity and selectivity in non-corrosive neutral solution (0.05 M Na_2SO_4) that has practical implications. This integrated study, guided by computations, not only establishes an efficient and new earth-abundant electrocatalyst (CoS_2) for H_2O_2 production in acidic and neutral solutions, but also reveals general mechanistic insights into the activity and selectivity of earth-abundant transition metal compounds towards $2e^-$ ORR with unprecedented details, creating new opportunities in search of more active and selective electrocatalysts for highly efficient decentralized on-site production of H_2O_2.

2.5 Methods and Materials

2.5.1 Computational Methods

All calculations were performed using the Vienna Ab-initio Simulation Package (VASP)[38-41] version 5.4.1 via the ASE interface.[42] Core electrons were treated using the projector augmented wave (PAW) method[43,44] (valence electrons were expanded in plane waves up to 400 eV) in conjunction with the PBE exchange-correlation functional.[45,46] Single point calculations were performed with the continuum solvent method VASPsol to account for solvation effects for surface bound species.[47,48] The lattice constant of CoS_2 was determined by fitting to an equation of state,[49,50] with all atoms allowed to relax at a series of fixed lattice constants. The (100) surface of CoS_2 was modeled as a 1×1 slab with two repeats of the optimized primitive bulk unit cell in the direction perpendicular to the surface, yielding a thickness of 0.95 nm (a total of 8 Co atoms and 16 S atoms). Bulk calculations were performed using a Γ-centered 10×10×10 Monkhorst-Pack mesh,[51] while slab calculations used a 10×10×1 mesh. The bottom half of the slab was fixed to the bulk geometry while the upper half was allowed to relax. Transition states were determined using the nudged elastic band (NEB) and dimer routines and were confirmed to have one imaginary frequency corresponding to the reaction coordinate.[52-56] Vibrational frequencies for all calculations were determined by diagonalization of the mass-weighted partial Hessian (most earth-abundant isotopic masses) comprising all relaxed atoms.[57]

Binding free energies were calculated relative to $O_{2(g)}$ and $H^+_{(aq)} + e^-_{(aq)}$. The free energy of $H^+_{(aq)} + e^-_{(aq)}$ was determined at a given voltage relative to the standard hydrogen electrode (SHE) via its equilibrium with $H_{2(g)}$ (the so-called computational hydrogen electrode).[22] To circumvent well-known issues with the DFT treatment of $O_{2(g)}$, its free energy was chosen to match the experimental reduction potential of $1/2\ O_2 + 2\ H^+ + 2\ e^- \rightarrow H_2O$ ($E^o = 1.229$ V). The free energies of all other species were determined by $G = H - T{\cdot}S^o$, where H is the enthalpy, including both zero-point and thermal enthalpy corrections, and S^o is the total experimental entropy at 298K and 1 bar (for gas-phase species) or calculated under the harmonic approximation (for surface-bound species). The free energy of liquid $H_2O_{(l)}$ was determined using the free energy of formation of liquid $H_2O_{(l)}$ and gas phase $H_2O_{(g)}$. The solvation free energy of $H_2O_{2(aq)}$ was determined using the experimental Henry's law constant.[58] The calculated standard equilibrium reduction potential of the 2e$^-$ ORR reaction $O_{2(g)} + 2\ H^+ + 2\ e^- \rightarrow H_2O_{2(aq)}$ is 0.81 V (as compared to the experimental value of 0.69 V).

In addition, energetics were also calculated with the PBE-D3(ABC) dispersion-corrected density functional method (Figure A2.1).[28] While adding a dispersion correction caused adsorbed intermediates to bind more strongly to the CoS_2 surface, it led to an overall very small change in the energetics (compare Figures 2.1 and A2.1), and therefore did not affect the qualitative results.

2.5.2 Chemicals

All chemicals were used as received without any purification. Deionized nanopure water (Thermo Scientific, Barnstead Nanopure, 18.2 MΩ·cm) was used for all experiments.

2.5.3 Materials Synthesis

The synthesis of CoS_2 nanomaterials and the direct growth of CoS_2 nanowires onto carbon fiber paper substrate (CoS_2/CFP) follow a published procedure[21] with minor modifications (see the Appendix 2 for details).

2.5.4 Materials Characterization

Powder X-ray diffraction (PXRD) patterns were collected on a Bruker D8 ADVANCE powder X-ray diffractometer using Cu Kα radiation. Scanning electron microscopy (SEM) and the corresponding energy dispersive X-ray spectroscopy (EDS) were performed on a Zeiss SUPRA 55VP field emission SEM equipped with a Thermo Fisher Scientific UltraDry EDS detector. The accelerating voltages for SEM and the corresponding EDS analyses were 1 and 17 kV, respectively. X-ray photoelectron spectroscopy (XPS) was performed on a Thermo Scientific K-Alpha XPS system with an Al Kα X-ray source. Raman spectroscopy was collected on a Horiba Labram Aramis Raman Spectrometer using a 532-nm laser source with attenuated laser intensity to avoid sample degradation. Detailed sample preparations for SEM, XPS, and Raman spectroscopy are described in the Appendix 2.

2.5.5 Electrode Preparation

All working electrodes for electrochemical measurements were prepared on a rotating ring-disk electrode (RRDE-3A, ALS Co., Ltd) comprised of a glassy carbon (GC) disk (O.D. 4 mm) surrounded by a Pt ring (I.D. 5 mm, O.D. 7 mm). The RRDE was polished successively with de-agglomerated 1, 0.3, and 0.05 micron alumina suspensions (Allied High Tech Products, Inc.) on a polishing cloth (Buehler, MicroCloth, PSA) pre-wet with nanopure water, followed by rinsing thoroughly with nanopure water and methanol, sonicating in methanol for less than 20 s, and drying under ambient condition before use. To prepare working electrodes of drop-casted CoS_2 with the same Nafion loading but different cobalt loadings (Table A2.1), the same amount (~5 mg) of CoS_2 powders were suspended in different volumes of the 1:9 (V/V) mixture of Nafion solution (Sigma-Aldrich, 5 wt% in lower aliphatic alcohols and water) and nanopure water by sonicating for 1 h, then a fixed volume (10 μL) of the suspension was drop-casted onto the disk of RRDE and dried under ambient condition at a rotation rate of 700 rpm to achieve a uniform catalyst film.[59]

2.5.6 Electrode Measurements

RRDE measurements were performed in a single-compartment three-electrode cell connected to two synchronized Bio-Logic SP-200 potentiostats. A graphite rod and a Hg/Hg_2SO_4 (saturated K_2SO_4) electrode were used as the counter and reference electrodes. Solutions of 0.05 M H_2SO_4, 0.5 M H_2SO_4 (diluted from concentrated H_2SO_4, Sigma-Aldrich, 95.0-98.0%), and 0.1 M $HClO_4$ (diluted from concentrated $HClO_4$, Sigma-Aldrich, 70%, trace metal basis) were used as the acidic electrolyte; solution of 0.05 M Na_2SO_4 (prepared from Na_2SO_4, Sigma-Aldrich, ≥99.0%, anhydrous) was used as the neutral electrolyte. The pH values of as-prepared and O_2-saturated electrolytes (purged with O_2 gas for at least 15 min) were measured as following:

pH = 1.26 for as-prepared 0.05 M H_2SO_4; pH = 1.26 for O_2-saturated 0.05 M H_2SO_4

pH = 5.71 for as-prepared 0.05 M Na_2SO_4; pH = 6.14 for O_2-saturated 0.05 M Na_2SO_4

pH = 1.02 for as-prepared 0.1 M $HClO_4$; pH = 0.35 for as-prepared 0.5 M H_2SO_4

The increase in pH value after purging the electrolyte with O_2 gas was due to the elimination of dissolved CO_2 gas, which has a more pronounced effect on neutral electrolyte compared with acidic electrolyte. The Hg/Hg_2SO_4 (saturated K_2SO_4) reference electrode was calibrated against the standard saturated calomel electrode (SCE, $E_{SCE} = 0.241$ V vs. NHE). Since the ORR measurements were performed in O_2-saturated electrolytes, all potentials were reported versus the reversible hydrogen electrode (RHE) according to pH values of O_2-saturated electrolytes:

$$E_{Hg/Hg2SO4} = E_{SCE} + 0.404\text{ V} = 0.645\text{ V vs. NHE (in 0.05 M } H_2SO_4)$$

$$E\text{ vs. RHE} = E\text{ vs. NHE} + 0.059 \times 1.26\text{ V} = E\text{ vs. } Hg/Hg_2SO_4 + 0.719\text{ V (in 0.05 M } H_2SO_4)$$

$$E_{Hg/Hg2SO4} = E_{SCE} + 0.409\text{ V} = 0.650\text{ V vs. NHE (in 0.1 M } HClO_4)$$

$$E\text{ vs. RHE} = E\text{ vs. NHE} + 0.059 \times 1.02\text{ V} = E\text{ vs. } Hg/Hg_2SO_4 + 0.710\text{ V (in 0.1 M } HClO_4)$$

$$E_{Hg/Hg2SO4} = E_{SCE} + 0.434\text{ V} = 0.675\text{ V vs. NHE (in 0.5 M } H_2SO_4)$$

$$E\text{ vs. RHE} = E\text{ vs. NHE} + 0.059 \times 0.35\text{ V} = E\text{ vs. } Hg/Hg_2SO_4 + 0.696\text{ V (in 0.5 M } H_2SO_4)$$

$$E_{Hg/Hg2SO4} = E_{SCE} + 0.383\text{ V} = 0.624\text{ V vs. NHE (in 0.05 M } Na_2SO_4)$$

$$E\text{ vs. RHE} = E\text{ vs. NHE} + 0.059 \times 6.14\text{ V} = E\text{ vs. } Hg/Hg_2SO_4 + 0.986\text{ V (in 0.05 M } Na_2SO_4)$$

Detailed protocols for RRDE measurements are described in the Appendix 2.

2.5.7 Bulk ORR Electrolysis on Integrated CoS_2/CFP Electrode and Chemical Quantification of H_2O_2 Product

For bulk ORR electrolysis, CoS_2 nanowires directly grown on carbon fiber paper (CoS_2/CFP) was used as the working electrode to achieve a larger catalytic current and therefore a higher H_2O_2 yield. To prepare working electrodes of CoS_2/CFP, 5-minute epoxy (Devcon) was used to define the geometric area of the working electrodes to about 1 cm × 1 cm (Figure A2.19a). A three-electrode H-cell setup was used to avoid the oxidation of H_2O_2 product on the counter electrode, and a minimal volume (3 mL) of electrolyte was filled into the working electrode compartment to obtain higher concentrations of H_2O_2 (Figure A2.19b). Detailed protocols for bulk ORR electrolysis and chemical quantification of H_2O_2 product are described in the Appendix 2.

2.6 References

1. Campos-Martin, J. M.; Blanco-Brieva, G.; Fierro, J. L. G. Hydrogen Peroxide Synthesis: An Outlook beyond the Anthraquinone Process. *Angew. Chem. Int. Ed.* ***45***, 6962-6984 (2006).

2. Yang, S.; Verdaguer-Casadevall, A.; Arnarson, L.; Silvioli, L.; Čolić, V.; Frydendal, R.; Rossmeisl, J.; Chorkendorff, I.; Stephens, I. E. L. Toward the decentralized electrochemical production of H2O2: A focus on the catalysis. *ACS Catal.* ***8***, 4064-4081 (2018).

3. Edwards, J. K.; Freakley, S. J.; Lewis, R. J.; Pritchard, J. C.; Hutchings, G. J. Advances in the direct synthesis of hydrogen peroxide from hydrogen and oxygen. *Catal. Today* ***248***, 3-9 (2015).

4. Freakley, S. J.; He, Q.; Harrhy, J. H.; Lu, L.; Crole, D. A.; Morgan, D. J.; Ntainjua, E. N.; Edwards, J. K.; Carley, A. F.; Borisevich, A. Y.; Kiely, C. J.; Hutchings, G. J. Palladium-tin catalysts for the direct synthesis of H_2O_2 with high selectivity. *Science* ***351***, 965-968 (2016).

5. Wilson, N. M.; Pan, Y.-T.; Shao, Y.-T.; Zuo, J.-M.; Yang, H.; Flaherty, D. W. Direct Synthesis of H_2O_2 on AgPt Octahedra: The Importance of Ag–Pt Coordination for High H_2O_2 Selectivity. *ACS Catal.* ***8***, 2880-2889 (2018).

6. Chu, S.; Cui, Y.; Liu, N. The path towards sustainable energy. *Nat. Mater.* ***16***, 16-22 (2016).

7. Liu, Y.; Quan, X.; Fan, X.; Wang, H.; Chen, S. High-Yield Electrosynthesis of Hydrogen Peroxide from Oxygen Reduction by Hierarchically Porous Carbon. *Angew. Chem. Int. Ed.* ***54***, 6837-6841 (2015).

8. Lu, Z.; Chen, G.; Siahrostami, S.; Chen, Z.; Liu, K.; Xie, J.; Liao, L.; Wu, T.; Lin, D.; Liu, Y.; Jaramillo, T. F.; Nørskov, J. K.; Cui, Y. High-efficiency oxygen reduction to hydrogen peroxide catalysed by oxidized carbon materials. *Nat. Catal.* ***1***, 156-162 (2018).

9. Chen, S.; Chen, Z.; Siahrostami, S.; Higgins, D.; Nordlund, D.; Sokaras, D.; Kim, T. R.; Liu, Y.; Yan, X.; Nilsson, E.; Sinclair, R.; Nørskov, J. K.; Jaramillo, T. F.; Bao, Z. Designing Boron Nitride Islands in Carbon Materials for Efficient Electrochemical Synthesis of Hydrogen Peroxide. *J. Am. Chem. Soc.* ***140***, 7851-7859 (2018).

10. Sa, Y. J.; Kim, J. H.; Joo, S. H. Active Edge-Site-Rich Carbon Nanocatalysts with Enhanced Electron Transfer for Efficient Electrochemical Hydrogen Peroxide Production. *Angew. Chem. Int. Ed.* ***58***, 1100-1105 (2019).

11. Sun, Y.; Sinev, I.; Ju, W.; Bergmann, A.; Dresp, S.; Kühl, S.; Spöri, C.; Schmies, H.; Wang, H.; Bernsmeier, D.; Paul, B.; Schmack, R.; Kraehnert, R.; Roldan Cuenya, B.; Strasser, P. Efficient electrochemical hydrogen peroxide production from molecular oxygen on nitrogen-doped mesoporous carbon catalysts. *ACS Catal.* ***8***, 2844-2856 (2018).

12. Shi, X.; Zhang, Y.; Siahrostami, S.; Zheng, X. Light-Driven $BiVO_4$–C Fuel Cell with Simultaneous Production of H_2O_2. *Adv. Energy Mater.* ***8***, 1801158 (2018).

13. Jirkovský, J. S.; Panas, I.; Ahlberg, E.; Halasa, M.; Romani, S.; Schiffrin, D. J. Single Atom Hot-Spots at Au–Pd Nanoalloys for Electrocatalytic H_2O_2 Production. *J. Am. Chem. Soc.* ***133***, 19432-19441 (2011).

14. Pizzutilo, E.; Kasian, O.; Choi, C. H.; Cherevko, S.; Hutchings, G. J.; Mayrhofer, K. J. J.; Freakley, S. J. Electrocatalytic synthesis of hydrogen peroxide on Au-Pd nanoparticles: From fundamentals to continuous production. *Chem. Phys. Lett.* ***683***, 436-442 (2017).

15. Siahrostami, S.; Verdaguer-Casadevall, A.; Karamad, M.; Deiana, D.; Malacrida, P.; Wickman, B.; Escudero-Escribano, M.; Paoli, E. A.; Frydendal, R.; Hansen, T. W.; Chorkendorff, I.; Stephens, I. E. L.; Rossmeisl, J. Enabling direct H_2O_2 production through rational electrocatalyst design. *Nat. Mater.* ***12***, 1137-1143 (2013).

16. Verdaguer-Casadevall, A.; Deiana, D.; Karamad, M.; Siahrostami, S.; Malacrida, P.; Hansen, T. W.; Rossmeisl, J.; Chorkendorff, I.; Stephens, I. E. L. Trends in the electrochemical synthesis of H2O2: Enhancing activity and selectivity by electrocatalytic site engineering. *Nano Lett.* ***14***, 1603-1608 (2014).

17. Choi, C. H.; Kim, M.; Kwon, H. C.; Cho, S. J.; Yun, S.; Kim, H.-T.; Mayrhofer, K. J. J.; Kim, H.; Choi, M. Tuning selectivity of electrochemical reactions by atomically dispersed platinum catalyst. *Nat. Commun.* ***7***, 10922 (2016).

18. Yang, S.; Kim, J.; Tak, Y. J.; Soon, A.; Lee, H. Single-atom catalyst of platinum supported on titanium nitride for selective electrochemical reactions. *Angew. Chem. Int. Ed.* ***55***, 2058-2062 (2016).

19. Shen, R.; Chen, W.; Peng, Q.; Lu, S.; Zheng, L.; Cao, X.; Wang, Y.; Zhu, W.; Zhang, J.; Zhuang, Z.; Chen, C.; Wang, D.; Li, Y. High-Concentration Single Atomic Pt Sites on Hollow CuS_x for Selective O_2 Reduction to H_2O_2 in Acid Solution. *Chem* (2019).

20. Faber, M. S.; Park, K.; Cabán-Acevedo, M.; Santra, P. K.; Jin, S. Earth-Abundant Cobalt Pyrite (CoS_2) Thin Film on Glass as a Robust, High-Performance Counter Electrode for Quantum Dot-Sensitized Solar Cells. *J. Phys. Chem. Lett.* ***4***, 1843-1849 (2013).

21. Faber, M. S.; Dziedzic, R.; Lukowski, M. A.; Kaiser, N. S.; Ding, Q.; Jin, S. High-Performance Electrocatalysis Using Metallic Cobalt Pyrite (CoS_2) Micro- and Nanostructures. *J. Am. Chem. Soc.* ***136***, 10053-10061 (2014).

22. Nørskov, J. K.; Rossmeisl, J.; Logadottir, A.; Lindqvist, L.; Kitchin, J. R.; Bligaard, T.; Jónsson, H. Origin of the Overpotential for Oxygen Reduction at a Fuel-Cell Cathode. *J. Phys. Chem. B* ***108***, 17886-17892 (2004).

23. Viswanathan, V.; Hansen, H. A.; Rossmeisl, J.; Nørskov, J. K. Unifying the $2e^-$ and $4e^-$ Reduction of Oxygen on Metal Surfaces. *J. Phys. Chem. Lett.* ***3***, 2948-2951 (2012).

24. Hansen, H. A.; Viswanathan, V.; Nørskov, J. K. Unifying Kinetic and Thermodynamic Analysis of 2 e^- and 4 e^- Reduction of Oxygen on Metal Surfaces. *J. Phys. Chem. C* ***118***, 6706-6718 (2014).

25. Kulkarni, A.; Siahrostami, S.; Patel, A.; Nørskov, J. K. Understanding Catalytic Activity Trends in the Oxygen Reduction Reaction. *Chem. Rev.* ***118***, 2302-2312 (2018).

26. Ford, D. C.; Nilekar, A. U.; Xu, Y.; Mavrikakis, M. Partial and complete reduction of O_2 by hydrogen on transition metal surfaces. *Surf. Sci.* ***604***, 1565-1575 (2010).

27. Zhang, W.; Lai, W.; Cao, R. Energy-Related Small Molecule Activation Reactions: Oxygen Reduction and Hydrogen and Oxygen Evolution Reactions Catalyzed by Porphyrin- and Corrole-Based Systems. *Chem. Rev.* ***117***, 3717-3797 (2017).

28. Grimme, S.; Antony, J.; Ehrlich, S.; Krieg, H. A consistent and accurate ab initio parametrization of density functional dispersion correction (DFT-D) for the 94 elements H-Pu. *J. Chem. Phys.* ***132***, 154104 (2010).

29. Zhou, R.; Zheng, Y.; Jaroniec, M.; Qiao, S.-Z. Determination of the Electron Transfer Number for the Oxygen Reduction Reaction: From Theory to Experiment. *ACS Catal.* ***6***, 4720-4728 (2016).

30. Wei, C.; Rao, R. R.; Peng, J.; Huang, B.; Stephens, I. E. L.; Risch, M.; Xu, Z. J.; Shao-Horn, Y. Recommended Practices and Benchmark Activity for Hydrogen and Oxygen Electrocatalysis in Water Splitting and Fuel Cells. *Adv. Mater.* ***0***, 1806296 (2019).

31. Falkowski, J. M.; Concannon, N. M.; Yan, B.; Surendranath, Y. Heazlewoodite, Ni3S2: A Potent Catalyst for Oxygen Reduction to Water under Benign Conditions. *J. Am. Chem. Soc.* ***137***, 7978-7981 (2015).

32. You, B.; Jiang, N.; Sheng, M.; Drisdell, W. S.; Yano, J.; Sun, Y. Bimetal–Organic Framework Self-Adjusted Synthesis of Support-Free Nonprecious Electrocatalysts for Efficient Oxygen Reduction. *ACS Catal.* ***5***, 7068-7076 (2015).

33. Zhu, L.; Susac, D.; Teo, M.; Wong, K. C.; Wong, P. C.; Parsons, R. R.; Bizzotto, D.; Mitchell, K. A. R.; Campbell, S. A. Investigation of CoS_2-based thin films as model catalysts for the oxygen reduction reaction. *J. Catal.* ***258***, 235-242 (2008).

34. Jirkovský, J. S.; Björling, A.; Ahlberg, E. Reduction of Oxygen on Dispersed Nanocrystalline CoS_2. *J. Phys. Chem. C* ***116***, 24436-24444 (2012).

35. Jin, S. Are Metal Chalcogenides, Nitrides, and Phosphides Oxygen Evolution Catalysts or Bifunctional Catalysts? *ACS Energy Lett.* ***2***, 1937-1938 (2017).

36. Hasché, F.; Oezaslan, M.; Strasser, P.; Fellinger, T.-P. Electrocatalytic hydrogen peroxide formation on mesoporous non-metal nitrogen-doped carbon catalyst. *J. Energy Chem.* ***25***, 251-257 (2016).

37. Yamanaka, I.; Ichihashi, R.; Iwasaki, T.; Nishimura, N.; Murayama, T.; Ueda, W.; Takenaka, S. Electrocatalysis of heat-treated cobalt-porphyrin/carbon for hydrogen peroxide formation. *Electrochim. Acta* ***108***, 321-329 (2013).

38. Kresse, G.; Hafner, J. Ab initio molecular dynamics for liquid metals. *Phys. Rev. B* ***47***, 558-561 (1993).

39. Kresse, G.; Hafner, J. Ab initio molecular-dynamics simulation of the liquid-metal--amorphous-semiconductor transition in germanium. *Phys. Rev. B* ***49***, 14251-14269 (1994).

40. Kresse, G.; Furthmüller, J. Efficient iterative schemes for ab initio total-energy calculations using a plane-wave basis set. *Phys. Rev. B* ***54***, 11169-11186 (1996).

41. Kresse, G.; Furthmüller, J. Efficiency of ab-initio total energy calculations for metals and semiconductors using a plane-wave basis set. *Comp. Mater. Sci.* ***6***, 15-50 (1996).

42. Bahn, S. R.; Jacobsen, K. W. An object-oriented scripting interface to a legacy electronic structure code. *Comput. Sci. Eng.* ***4***, 56-66 (2002).

43. Blöchl, P. E. Projector augmented-wave method. *Phys. Rev. B* ***50***, 17953-17979 (1994).

44. Kresse, G.; Joubert, D. From ultrasoft pseudopotentials to the projector augmented-wave method. *Phys. Rev. B* ***59***, 1758-1775 (1999).

45. Perdew, J. P.; Burke, K.; Ernzerhof, M. Generalized Gradient Approximation Made Simple. *Phys. Rev. Lett.* ***77***, 3865-3868 (1996).

46. Perdew, J. P.; Burke, K.; Ernzerhof, M. Generalized Gradient Approximation Made Simple [Phys. Rev. Lett. 77, 3865 (1996)]. *Phys. Rev. Lett.* ***78***, 1396-1396 (1997).

47. Mathew, K.; Sundararaman, R.; Letchworth-Weaver, K.; Arias, T. A.; Hennig, R. G. Implicit solvation model for density-functional study of nanocrystal surfaces and reaction pathways. *J. Chem. Phys.* ***140***, 084106 (2014).

48. Mathew, K.; Hennig, R. G. Implicit self-consistent description of electrolyte in plane-wave density-functional theory. *arXiv e-prints* (2016). https://arxiv.org/abs/1601.03346 (accessed Jun 12, 2019).

49. Alchagirov, A. B.; Perdew, J. P.; Boettger, J. C.; Albers, R. C.; Fiolhais, C. Energy and pressure versus volume: Equations of state motivated by the stabilized jellium model. *Phys. Rev. B* ***63***, 224115 (2001).

50. Alchagirov, A. B.; Perdew, J. P.; Boettger, J. C.; Albers, R. C.; Fiolhais, C. Reply to "Comment on 'Energy and pressure versus volume: Equations of state motivated by the stabilized jellium model' ". *Phys. Rev. B* ***67***, 026103 (2003).

51. Monkhorst, H. J.; Pack, J. D. Special points for Brillouin-zone integrations. *Phys. Rev. B* ***13***, 5188-5192 (1976).

52. Henkelman, G.; Jónsson, H. Improved tangent estimate in the nudged elastic band method for finding minimum energy paths and saddle points. *J. Chem. Phys.* ***113***, 9978-9985 (2000).

53. Jónsson, H.; Mills, G.; Jacobsen, K. W.: Nudged Elastic Band Method for Finding Minimum Energy Paths of Transitions. In *Classical and Quantum Dynamics in Condensed Phase Simulations*; Berne, B. J., Ciccotti, G., Coker, D. F., Eds.; World Scientific, 1998; pp 385–404.

54. Henkelman, G.; Jónsson, H. A dimer method for finding saddle points on high dimensional potential surfaces using only first derivatives. *J. Chem. Phys.* ***111***, 7010-7022 (1999).

55. Heyden, A.; Bell, A. T.; Keil, F. J. Efficient methods for finding transition states in chemical reactions: Comparison of improved dimer method and partitioned rational function optimization method. *J. Chem. Phys.* ***123***, 224101 (2005).

56. Kästner, J.; Sherwood, P. Superlinearly converging dimer method for transition state search. *J. Chem. Phys.* ***128***, 014106 (2008).

57. Cohen, E. R.; Cvitas, T.; Frey, J. G.; Holström, B.; Kuchitsu, K.; Marquardt, R.; Mills, I.; Pavese, F.; Quack, M.; Stohner, J.; Strauss, H. L.; Takami, M.; Thor, A. J.: *Quantities, Units and Symbols in Physical Chemistry: Edition 3*; IUPAC & RSC Publishing, 2007.

58. NIST Chemistry WebBook. https://webbook.nist.gov/cgi/cbook.cgi?ID=C7722841&Mask=10#Solubility (accessed Jun 12, 2019).

59. Garsany, Y.; Singer, I. L.; Swider-Lyons, K. E. Impact of film drying procedures on RDE characterization of Pt/VC electrocatalysts. *J. Electroanal. Chem.* ***662***, 396-406 (2011).

CHAPTER 3

Stable and Selective Electrosynthesis of Hydrogen Peroxide and the Electro-Fenton Process on $CoSe_2$ Polymorph Catalysts[*]

3.1 Abstract

Electrochemical synthesis of hydrogen peroxide (H_2O_2) in acidic solution can enable the electro-Fenton process for decentralized environmental remediation, but robust and inexpensive electrocatalysts for the selective two-electron oxygen reduction reaction ($2e^-$ ORR) are lacking. Here, we present a joint computational/experimental study that shows both structural polymorphs of earth-abundant cobalt diselenide (orthorhombic *o*-$CoSe_2$ and cubic *c*-$CoSe_2$) are stable against surface oxidation and catalyst leaching due to the weak O* binding to Se sites, highly active and selective for $2e^-$ ORR, and deliver higher kinetic current densities for H_2O_2 production than the state-of-the-art noble metal or single-atom catalysts in acidic solution. *o*-$CoSe_2$ nanowires directly grown on carbon paper electrodes allow for the steady bulk electrosynthesis of H_2O_2 in 0.05 M H_2SO_4 with a practically useful accumulated concentration of 547 ppm, the highest among the reported $2e^-$ ORR catalysts in acidic solution. Such efficient and stable H_2O_2 electrogeneration further enables the effective electro-Fenton process for model organic pollutant degradation.

---

[*] This chapter was originally published in *Energy Environ. Sci.* ***13***, 4189-4203 (2020), in collaboration with Aurora N. Janes, R. Dominic Ross, Dave Kaiman, Jinzhen Huang, Bo Song, J. R. Schmidt, and Song Jin.

3.2 Introduction

Hydrogen peroxide (H_2O_2) is a versatile and green oxidant with a myriad of applications in industrial, environmental, healthcare, and household settings. It is among the list of disinfectants for use against SARS-CoV-2, a novel coronavirus that causes the COVID-19 pandemic.[1] The annual global production of H_2O_2 reached over 5 million tons in 2015 and has been steadily growing,[2] the majority of which is produced via the indirect anthraquinone process.[3] This energy- and waste-intensive multistep process relies on centralized chemical plants and produces up to 70 wt% concentrated solutions of H_2O_2 that are both hazardous and expensive to store and transport to end-users.[3] Although such centralized H_2O_2 production may benefit large-scale industrial applications,[2] many distributed applications including water treatment, medical disinfection, and household sanitation require only very low concentrations of H_2O_2. For example, a concentration less than 1000 ppm (29 mM) is sufficient for water treatment.[4] This motivates alternative approaches to the direct and decentralized production of dilute H_2O_2 at the point of use.[4-7] While direct chemical synthesis of H_2O_2 from H_2 and O_2 gases could be a potential alternative production method, it still needs H_2 gas and must operate under large quantities of inert carrier gas and solvent due to flammability concerns, and very few noble metal alloy catalysts show satisfactory selectivity toward H_2O_2 production as opposed to decomposition and/or further reduction to H_2O.[8,9]

Direct electrochemical synthesis of H_2O_2 from the two-electron oxygen reduction reaction ($2e^-$ ORR) offers a more sustainable solution to decentralized manufacturing.[4-7] It can be driven by the increasingly affordable renewable electricity[10,11] and eliminates the need for H_2 gas (which requires significant energy to produce from steam methane reforming and has a large carbon footprint[12]). The key challenge here is to develop robust electrocatalysts featuring high activity and selectivity toward the 2e$^-$ (vs. the competing 4e$^-$) ORR pathway. Defective[13-15] and heteroatom-doped[16-18] carbon materials have shown promise for the selective 2e$^-$ ORR in *alkaline* solution ($O_2 + H_2O + 2\ e^- \rightarrow HO_2^- + OH^-$, $E^o = 0.76$ V vs. RHE); however, H_2O_2 is unstable in base especially at pH >9,[7] and the 2e$^-$ ORR *activities* of carbon materials under acidic and neutral conditions are inferior to those under alkaline conditions, which is still the case after introducing transition metal single-atom coordination motifs into the carbon matrices.[19-23]

The electrosynthesis of H_2O_2 in *acidic* solution ($O_2 + 2\ H^+ + 2\ e^- \rightarrow H_2O_2$, $E^o = 0.69$ V vs. RHE) would also be advantageous for on-site water disinfection and environmental treatment applications.[7] For example, the electro-Fenton process operates at an optimal pH of ~3, where the electrogenerated H_2O_2 at the cathode reacts with Fe^{2+} and produces hydroxyl radical (·OH) as an even more potent oxidant for the removal of a wide variety of persistent organic pollutants from wastewater streams. Compared to the conventional *chemical* Fenton process, the *electro*-Fenton process not only avoids the transportation and storage of hazardous H_2O_2 but also features significantly enhanced ·OH production rates and organics mineralization capabilities because of the rapid regeneration of Fe^{2+} at the cathode.[24] However, the cathode used for the electro-Fenton process has been almost exclusively carbon materials to date,[25] which suffer from insufficient catalytic activity for H_2O_2 production in acidic solution. The state-of-the-art 2e$^-$ ORR electrocatalysts under acidic conditions are based on noble metal alloys,[26,27] which are not commercially viable as they involve expensive and/or toxic metals (such as Hg). Therefore, developing efficient and cost-effective 2e$^-$ ORR catalysts for the electrosynthesis of H_2O_2 in acidic solution remains an important but relatively underexplored target.

Our recent work has demonstrated the promise of earth-abundant transition metal compound electrocatalysts for the selective 2e$^-$ ORR in acidic solution.[28] The unique structural motifs of metal compounds, such as cobalt disulfide (CoS_2), enable the intrinsic separation of active metal sites by the lattice anions, which could potentially suppress O-O bond scission by adjacent active sites and resist the undesired 4e$^-$ ORR that yields the H_2O byproduct. This motivates us to look into cobalt diselenide ($CoSe_2$), which has larger anions increasing the separation between the neighboring Co active sites, in order to achieve enhanced 2e$^-$ ORR selectivity. Selenium is also less electronegative than sulfur, which can impact the electronic structures and therefore the adsorbate binding energies and activation barriers. However, $CoSe_2$ can exist in two structural polymorphs with different crystal structures, the *cubic* pyrite-type (*c*-$CoSe_2$) and the *orthorhombic* marcasite-type (*o*-$CoSe_2$), whereas CoS_2 always exists as the *cubic* pyrite-type (*c*-CoS_2). These distinct structures of $CoSe_2$ polymorphs vs. CoS_2 can influence not only the catalyst activity and selectivity but also the catalyst stability under acidic electrochemical operations, which is critical from a practical perspective. For example, $CoSe_2$[29,30] appears to be more electrochemically stable than CoS_2[31-33] for hydrogen evolution reaction (HER) in acidic solution.

Here, we report the stable and selective electrosynthesis of H_2O_2 and the effective electro-Fenton process on $CoSe_2$ polymorph catalysts in the more practically relevant acidic solution, due to the new understandings from both theory and experiment that lead to significantly improved catalyst stability. Theoretical calculations of bulk and surface Pourbaix diagrams reveal general mechanistic insights into the enhanced electrochemical stability of $CoSe_2$ polymorphs against surface oxidation. Computational modelling of 2e$^-$ ORR energetics also predicts them to be active and selective electrocatalysts for H_2O_2 production. Electrochemical measurements and rigorous monitoring of catalyst dissolution show that $CoSe_2$ polymorphs are the best-performing $2e^-$ ORR catalysts reported so far in *acidic* solution and are more resistant to catalyst leaching. Remarkably, bulk electrosynthesis of H_2O_2 using *o*-$CoSe_2$ nanostructures grown on carbon paper electrode successfully accumulates a practically useful H_2O_2 concentration of 547 ppm (16 mM) in *acidic* solution, significantly higher than those achieved by previously reported catalysts in similar H-cells. The *o*-$CoSe_2$ electrode further enables the effective electro-Fenton process and the efficient degradation of recalcitrant organic pollutant, showing great promise for on-site water treatment applications.

3.3 Results and Discussion

3.3.1 Bulk Pourbaix Diagrams and Electrochemical Stability of $CoSe_2$ Polymorphs

Practical electrochemical H_2O_2 production necessitates stable electrocatalysts for the selective $2e^-$ ORR. The crystal structures of both $CoSe_2$ polymorphs in comparison with *c*-CoS_2 are shown in Figure 3.1a–c. According to the calculated bulk Pourbaix diagrams available from the Materials Project,[34,35] the electrochemical stability window of *c*-CoS_2 is limited (Figure A3.1a in the Appendix 3), in agreement with a recent report.[36] In contrast, both $CoSe_2$ polymorphs exhibit much wider electrochemical stability windows that cover the entire potential range of interest for *acidic* $2e^-$ ORR (Figure A3.1b,c in the Appendix 3). As such, $CoSe_2$ polymorphs are anticipated to better retain their structural integrity under acidic electrochemical operations, whereas *c*-CoS_2 is more prone to catalyst degradation due to surface oxidation and Co^{2+} dissolution. Therefore, the enhanced electrochemical stability of $CoSe_2$ polymorphs could make them more practical $2e^-$ ORR catalysts in acidic solution for on-site water treatment applications.

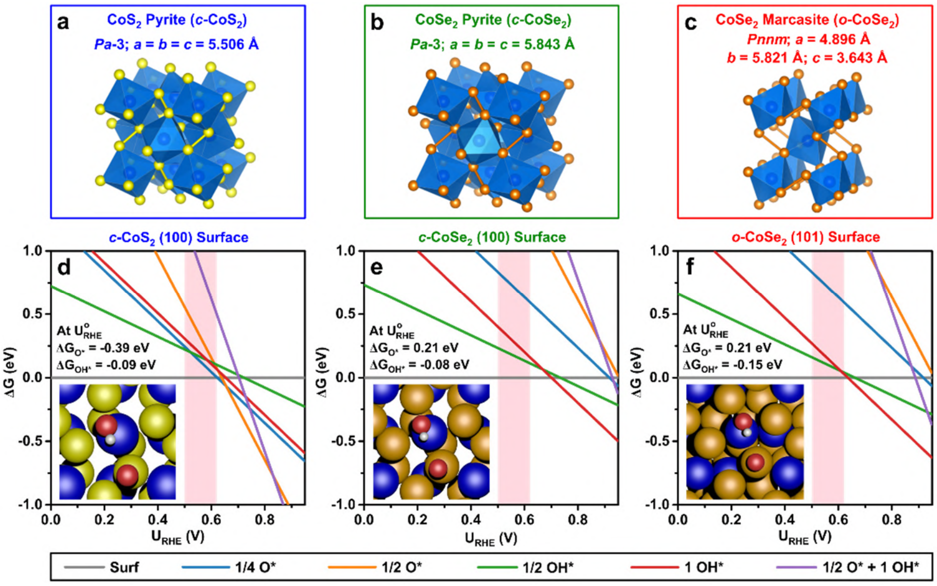

Figure 3.1. Crystal structures and surface Pourbaix diagrams of pyrite-type (*c*-) and marcasite-type (*o*-) CoSe$_2$ polymorphs in comparison with pyrite-type CoS$_2$.

(**a–c**) Crystal structures, space groups, and lattice constants of (**a**) *c*-CoS$_2$, (**b**) *c*-CoSe$_2$, and (**c**) *o*-CoSe$_2$. The Co, S, and Se atoms are displayed in blue, yellow, and orange, respectively. (**d–f**) Calculated surface Pourbaix diagrams (ΔG vs. U_{RHE}) of (**d**) *c*-CoS$_2$ (100), (**e**) *c*-CoSe$_2$ (100), and (**f**) *o*-CoSe$_2$ (101) surfaces. Co and S/Se sites are the preferential binding sites for OH* and O*, respectively. A wide variety of surface coverages (from clean surface to ¾ ML O* + 1 ML OH*) are examined. For the sake of clarity, only the most stable surface coverages in the potential range of 0 to 1 V are shown here, and all the modelled surface coverages are shown in Figure A3.3 (Appendix 3). Surface free energies are assumed to be in equilibrium with $H_2O_{(l)}$. The unit cell has two Co binding sites and four S/Se binding sites. Binding energies of O* and OH* (ΔG_{O^*} and ΔG_{OH^*}) at the calculated standard equilibrium potential of 2e$^-$ ORR (U^o_{RHE}) and top views of the catalyst surfaces with O* and OH* bound to their preferential binding sites are shown as insets. The Co, S, Se, O, and H atoms are displayed in blue, yellow, orange, red, and white, respectively.

The highlighted regions in light red represent the experimentally relevant potential range where the optimal H_2O_2 production performances are achieved.

3.3.2 Mechanistic Insights from Surface Pourbaix Diagrams of $CoSe_2$ Polymorphs

To understand these differences in the electrochemical stability of $CoSe_2$ polymorphs vs. *c*-CoS_2 and to gain general mechanistic insights, we constructed calculated surface Pourbaix diagrams to predict the most thermodynamically stable surface termination of each catalyst for a given set of potential and pH conditions under the assumption that the surfaces can be approximated in equilibrium with $H_2O_{(l)}$.[37,38] The equilibrated proton-coupled electron transfer (PCET) reaction for a general surface intermediate can then be written as:

$$\text{X-O}_m\text{H}_n{*} + (2m - n)\,(\text{H}^+ + \text{e}^-) \rightleftharpoons \text{X}{*} + m\text{H}_2\text{O} \quad (1)$$

where X is the surface binding site, *m* is the number of oxygen atoms, and *n* is the number of hydrogen atoms. The free energy of this reaction can be written as:

$$\Delta G(U,pH) = G_{S*} + mG_{H_2O} - G_{X\text{-}O_mH_n*} - (2m - n)(G_{e^-} + G_{H^+}) \quad (2)$$

Using the computational hydrogen electrode (CHE) method[39-42] ($G_{e^-} + G_{H^+} = \frac{1}{2}G_{H_2} - U_{SHE} - 2.303k_B\,T\,pH$) and converting standard hydrogen electrode to reversible hydrogen electrode ($U_{RHE} = U_{SHE} + 2.303k_B\,T\,pH$), the free energy can be rewritten as a function of U_{RHE}:

$$\Delta G(U_{RHE}) = G_{S*} + mG_{H_2O} - G_{X\text{-}O_mH_n*} - (2m - n)(\tfrac{1}{2}G_{H_2} - U_{RHE}) \quad (3)$$

We used density functional theory (DFT) and the CHE method[39-42] to construct calculated surface Pourbaix diagrams of all three catalysts on their most thermodynamically stable facets. We found that the (100) facet of cubic *c*-$CoSe_2$ has the lowest surface energy (Table A3.1a in the

Appendix 3), in agreement with cubic *c*-CoS_2.[28] For orthorhombic *o*-$CoSe_2$, we investigate the (101) facet because it is not only the facet with the lowest surface energy (Table A3.1b in the Appendix 3) but also keeps the Se_2^{2-} dumbbells intact and is structurally similar to the (100) facets of cubic *c*-CoS_2 and *c*-$CoSe_2$ (see Figure A3.2 in the Appendix 3). We utilized a 1×1 unit cell slab of the catalyst surface that has 2 Co binding sites and 4 S/Se binding sites to model surface intermediate coverages as a function of potential (Figure 3.1d–f). The preferential binding sites for O* and OH* are Co and S/Se sites, respectively (see insets of Figure 3.1d–f). Therefore, we investigated ¼, ½, ¾, and 1 monolayer (ML) O* coverages, ½ and 1 ML OH* coverages, and any combinations thereof. For example, the co-adsorption of ¼ ML O* and ½ ML OH* on $CoSe_2$ polymorphs and *c*-CoS_2 in equilibrium with their clean surfaces can be written respectively as:

$$\text{Co-OH}^* + \text{Se-O}^* + 3(\text{H}^+ + \text{e}^-) \rightleftharpoons \text{Co}^* + \text{Se}^* + \text{H}_2\text{O} \quad (4)$$

$$\text{Co-OH}^* + \text{S-O}^* + 3(\text{H}^+ + \text{e}^-) \rightleftharpoons \text{Co}^* + \text{S}^* + \text{H}_2\text{O} \quad (5)$$

where OH* and O* are bound to their preferential binding site of Co and S/Se, respectively (see Equation 1 for the general form of these equations). For the sake of clarity, Figure 3.1d–f only show the most thermodynamically stable surface coverages in the potential (U_{RHE}) range of 0 to 1 V, while all the modelled surface coverages are shown in Figure A3.3 (Appendix 3). We note that the calculated standard equilibrium potential of $2e^-$ ORR (U^o_{RHE}) is 0.81 V, slightly higher than the experimental value (E^o) of 0.69 V. Since our experimental results show that the optimal H_2O_2 production performances are achieved at 0.5 V vs. RHE (vide infra), the experimentally relevant potential range between 0.5 and 0.62 V is highlighted in Figure 3.1d–f. At 0.5 V, all surfaces are predicted to be mostly free of adsorbates. However, at the most important 0.62 V, we predict ¼

ML O* coverage on *c*-CoS_2 (Figure 3.1d), a clean *c*-$CoSe_2$ surface (Figure 3.1e), and 1 ML OH* coverage on *o*-$CoSe_2$ (Figure 3.1f).

The differences in the surface terminations of all three catalysts under equilibrium conditions with $H_2O_{(l)}$ can be explained by the relative differences in the O* and OH* binding strengths. O* binds 0.59 eV more strongly to S sites of *c*-CoS_2 than to Se sites of $CoSe_2$ polymorphs (see ΔG_{O*} values in Figure 3.1d–f). Therefore, we predict a moderate O* coverage on *c*-CoS_2 at low overpotentials (Figure 3.1d), which will likely lead to surface oxidation, the formation of SO_4^{2-}, and the subsequent leaching of Co^{2+}. In contrast, O* coverage is not the most stable surface termination on $CoSe_2$ polymorphs at low overpotentials (Figure 3.1e,f) because of the weak O* binding to Se sites, suggesting that $CoSe_2$ polymorphs should be more resistant to surface oxidation and catalyst degradation, consistent with their wide electrochemical stability windows in the bulk Pourbaix diagrams (Figure A3.1b,c in the Appendix 3).

While changing the nature of the anion in the catalyst modifies the binding strength of O* and leads to increased stability of $CoSe_2$ polymorphs, switching from the *cubic* to *orthorhombic* crystal structure affects the binding strength of OH* to the preferential Co binding sites. The (101) surface of orthorhombic *o*-$CoSe_2$, which has a longer Co-Co interatomic distance than the (100) surfaces of both cubic structures (Figure A3.2d–f in the Appendix 3), exhibits a slight increase in the OH* binding strength by 0.06 and 0.07 eV compared to the (100) surface of cubic *c*-CoS_2 and *c*-$CoSe_2$, respectively (see ΔG_{OH*} values in Figure 3.1d–f). At low overpotentials, we predict a moderate to high OH* coverage on both $CoSe_2$ polymorphs, which will slowly decrease as the overpotential increases. As OH* binds to Co sites, a higher OH* coverage decreases the number of Co site ensembles available to break the O-O bond in OOH*. Thus, OH* coverage on Co sites may increase the $2e^-$ ORR selectivity, suggesting orthorhombic *o*-$CoSe_2$ could be more selective than cubic *c*-$CoSe_2$ and *c*-CoS_2. Overall, the surface and bulk Pourbaix diagrams predict that both $CoSe_2$ polymorphs are more electrochemically stable than *c*-CoS_2, while *o*-$CoSe_2$ could be the most intrinsically selective toward 2e$^-$ ORR among all three catalysts.

3.3.3 Computational Prediction of Selective 2e$^-$ ORR Energetics on $CoSe_2$ Polymorphs

We further calculated free energy diagrams of 2e$^-$ ORR vs. the competing 4e$^-$ ORR pathway to elucidate the catalytic activity and selectivity of $CoSe_2$ polymorphs. The catalytic activity toward 2e$^-$ ORR is governed by the following PCET reactions:

$$O_{2(g)} + * + (H^+ + e^-) \rightarrow OOH^* \quad (6)$$

$$OOH^* + (H^+ + e^-) \rightarrow H_2O_{2(aq)} + * \quad (7)$$

where the preferential binding sites for OOH* are Co sites on all three catalysts. At the calculated standard equilibrium potential of 2e$^-$ ORR (U^o_{RHE}), the first PCET step (Equation 6) is moderately downhill by 0.27, 0.24, and 0.35 eV on *c*-CoS_2 (100), *c*-$CoSe_2$ (100), and *o*-$CoSe_2$ (101) surfaces, respectively (Figure 3.2), indicating that all three catalysts should be active toward 2e$^-$ ORR, and *c*-$CoSe_2$ could be the most intrinsically active among all three catalysts.

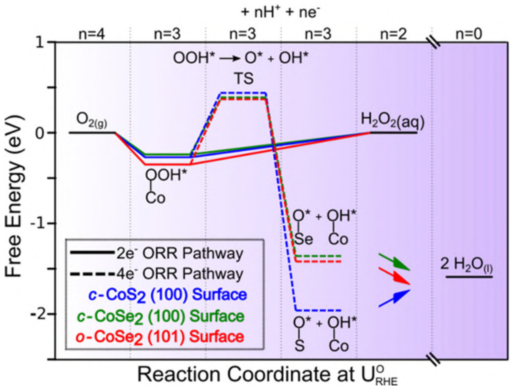

Figure 3.2. Calculate free energy diagrams of 2e$^-$ and 4e$^-$ ORR pathways on *c*-$CoSe_2$ and *o*-$CoSe_2$ polymorphs in comparison with *c*-CoS_2.

Calculated free energy diagrams were performed on *c*-CoS_2 (100), *c*-$CoSe_2$ (100), and *o*-$CoSe_2$ (101) surfaces at the calculated standard equilibrium potential of 2e^- ORR (U^{o}_{RHE}). Possible 2e^- and 4e^- ORR pathways are depicted in solid and dashed lines, respectively. The traces for *c*-CoS_2 (100), *c*-$CoSe_2$ (100), and *o*-$CoSe_2$ (101) surfaces are displayed in blue, green, and red, respectively. These calculations are performed on clean surfaces as the binding energies of OOH* are insensitive to other surface adsorbates present on *c*-CoS_2[28] and both $CoSe_2$ polymorphs at low overpotentials (see surface Pourbaix diagrams in Figure 3.1).

While the catalytic activity of 2e^- ORR is determined by Equations 6 and 7, the catalytic selectivity of 2e^- vs. 4e^- ORR is set by the resistance to O-O bond scission in OOH* adsorbate:

$$OOH^* + {}^* \rightarrow O^* + OH^* \quad (8)$$

$$OOH^* + (H^+ + e^-) \rightarrow O^* + H_2O_{(l)} \quad (9)$$

The cleavage of the O-O bond in OOH* will result in a buildup of O* and OH* on the catalyst surface (Equation 8). These species can either lead to oxidation/dissolution of the catalyst or be further reduced to $H_2O_{(l)}$. Breaking the O-O bond in OOH* requires an ensemble of neighboring Co sites to move toward each other, after which OOH* will dissociate into O* and OH* that are initially bound to Co sites.[28] O* can then easily migrate to S/Se sites, which are the preferential binding sites for O* on all three catalysts. Alternatively, the O-O bond in OOH* could be cleaved through reductive elimination (Equation 9) to form O* and $H_2O_{(l)}$. However, this is unlikely as only the proximal oxygen in OOH* interacts strongly with the catalyst surface. Therefore, PCET to the surface-bound oxygen to form H_2O_2 (Equation 7) will likely dominate over PCET to the distant oxygen to form $H_2O_{(l)}$ and O* (Equation 9).[28] The OOH* dissociation barriers on all three catalysts are fairly similar (Figure 3.2), in agreement with the similarity of their OOH* binding energies and surface structures. The (101) surface of *o*-$CoSe_2$ exhibits a slightly higher OOH* dissociation barrier of 0.72 eV than the (100) surface of *c*-CoS_2 and *c*-$CoSe_2$ where the barrier is 0.71 and 0.63 eV, respectively (Figure 3.2). These barriers to O-O bond scission on $CoSe_2$ polymorphs and CoS_2 are significantly higher than those on close-packed metals such as Pd (0.06 eV), Pt (0.16 eV), and Cu (0.06 eV),[42] indicating that spatial separation of neighboring Co sites by S/Se anions (Figure A3.2 in the Appendix 3) is critical to the selective $2e^-$ ORR pathway. Overall, the calculated free energy diagrams suggest that both $CoSe_2$ polymorphs are active and selective $2e^-$ ORR catalysts and that *c*-$CoSe_2$ could be more intrinsically active while *o*-$CoSe_2$ could be more intrinsically selective.

3.3.4 Synthesis and Characterization of Nanostructured $CoSe_2$ Polymorph Catalysts

We synthesized nanostructured $CoSe_2$ polymorph catalysts via hydrothermal selenization of cobalt hydroxide carbonate hydrate (CHCH) precursor at 220 °C,[43] followed by thermal annealing at higher temperatures to remove excess elemental Se impurity and to control the polymorphism of *o*-$CoSe_2$ and *c*-$CoSe_2$ at 300 and 500 °C, respectively (Figure 3.3a). We also synthesized *c*-CoS_2 catalyst via vapor-phase sulfidation of CHCH precursor at 500 °C as a comparison sample.[31] The low-temperature hydrothermal selenization at 220 °C enables access to the metastable marcasite-type $CoSe_2$ that undergoes structural transformation into the pyrite-type polymorph at temperatures higher than 300 °C. Powder X-ray diffraction (PXRD) pattern confirmed the marcasite structure of as-converted $CoSe_2$ sample; however, there was *crystalline* elemental Se impurity (Figure A3.4a in the Appendix 3). After thermal annealing in Ar atmosphere (790 torr) at 300 °C, the crystalline Se impurity was eliminated while the marcasite structure was retained (Figure 3.3b). The complete polymorphic transformation of marcasite- to pyrite-type $CoSe_2$ took place at a higher annealing temperature of 500 °C (Figure 3.3b, and Figure A3.4b in the Appendix 3). Raman spectra further confirmed the polymorphic purity of the $CoSe_2$ samples annealed at 300 and 500 °C, respectively, given their distinct Se-Se stretching mode signals at 179 vs. 189 cm^{-1} (Figure 3c, and Figure A3.5a in the Appendix 3). Additional Raman (Figure A3.5b in the Appendix 3) and X-ray photoelectron spectroscopy (XPS) characterization (Figure A3.6 in the Appendix 3) also showed that, for the *o*-$CoSe_2$ sample annealed at 300 °C, an extended annealing time was necessary to completely remove residual *amorphous* elemental Se impurity without affecting the marcasite structure. Scanning electron microscopy (SEM) images showed that the 300 °C annealing retained the nanoscale morphology and surface roughness of the *o*-$CoSe_2$ sample, whereas the 500 °C annealing enlarged the grain sizes of the *c*-$CoSe_2$ sample (Figure 3.3a, and Figure A3.7 in the Appendix 3). These structural characterization results confirmed that both $CoSe_2$ polymorph catalysts studied in this work, the *c*-$CoSe_2$ sample annealed at 500 °C for 1 h and the *o*-$CoSe_2$ sample annealed at 300 °C for 3 h, are polymorphic pure and free of elemental Se impurity (Figure 3.3a–c).

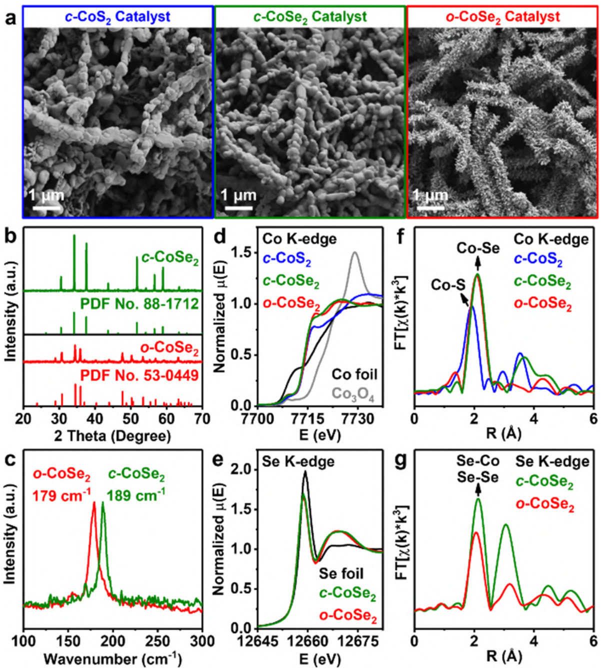

Figure 3.3. Structural characterization of nanostructured *c*-$CoSe_2$ and *o*-$CoSe_2$ catalysts in comparison with *c*-CoS_2 catalyst.

(**a**) SEM images, (**b**) PXRD patterns, (**c**) Raman spectra, (**d**) Co K-edge and (**e**) Se K-edge XANES spectra, Fourier transforms of (**f**) Co K-edge and (g) Se K-edge EXAFS spectra of as-synthesized *c*-$CoSe_2$, *o*-$CoSe_2$, and *c*-CoS_2 catalysts. Standard PXRD patterns of *c*-$CoSe_2$ (PDF No. 88-1712) and o-CoSe2 (PDF No. 53-0449) are from the International Centre for Diffraction Data (ICDD) database. The Co K-edge XANES spectra of Co foil and Co_3O_4 are shown in (**d**) and the Se K-edge XANES spectra of Se foil are shown in (**e**) for comparison.

We further carried out X-ray absorption spectroscopy (XAS) measurements on *c*-$CoSe_2$ and *o*-$CoSe_2$ catalysts in comparison with *c*-CoS_2 catalyst (Figure 3.3d–g). The X-ray absorption near-edge structure (XANES) spectra at Co K-edge (Figure 3.3d) matched with previous reports[44,45] and suggested the identical +2 oxidation state of Co in all three catalysts (whose edge positions coincide and lie in between the Co foil and Co_3O_4 references), and the Se K-edge spectra (Figure 3.3e) showed that both $CoSe_2$ polymorphs exhibited the same oxidation state of Se. Extended X-ray absorption fine structure (EXAFS) spectra (Figure 3.3f,g) showed that the Co-Se distances in both $CoSe_2$ polymorphs were greater than the Co-S distance in *c*-CoS_2 by ~0.1 Å (see the first shell fitting results in Figure A3.8 and Table A3.2 in the Appendix 3), consistent with their lattice constants (Figure 3.1a).

3.3.5 Experimental Studies of $CoSe_2$ Polymorphs as Selective $2e^-$ ORR Electrocatalysts

We first used the rotating ring-disk electrode (RRDE) to examine the catalytic activity and selectivity toward electrochemical H_2O_2 production: the catalyst samples were drop-casted on the glassy carbon disk electrode catalyzing ORR; meanwhile, the surrounding Pt ring electrode was held at a constant potential to selectively oxidize H_2O_2 (the $2e^-$ ORR product) under diffusion-limited conditions without triggering the oxidation of water (the $4e^-$ ORR product). Since ORR depletes protons in the vicinity of the catalyst surface, we checked the local pH near the operating RRDE in O_2-saturated 0.05 M H_2SO_4 solution (pH 1.20) using commercial Pt/C, which catalyzes almost only $4e^-$ ORR, and carbon black, which is moderately selective but poorly active toward $2e^-$ ORR, as benchmark catalysts (Figure A3.9 in the Appendix 3). We found the local pH was unaffected during electrochemical operations (see Figure A3.9 and additional discussion in the Appendix 3).

We systematically investigated the $2e^-$ ORR activity and selectivity of *c*-$CoSe_2$ and *o*-$CoSe_2$ catalysts to experimentally validate and further elaborate the mechanistic insights predicted by our calculated free energy diagrams and surface Pourbaix diagrams. As these catalyst samples may exhibit different specific surface areas, we performed RRDE measurements of each catalyst with various catalyst loadings for fair comparisons (see Table A3.3 in the Appendix 3). In 0.05 M H_2SO_4 solution (pH 1.20), both $CoSe_2$ polymorph catalysts showed efficient and selective H_2O_2 production at low overpotentials (Figure 3.4a), consistent with the calculated free energy diagrams (Figure 3.2). The ORR catalytic onset on both $CoSe_2$ polymorphs took place at potentials slightly more positive than the standard equilibrium potential of $2e^-$ ORR ($E^o = 0.69$ V vs. RHE), which is due to the Nernstian shift in the $2e^-$ ORR equilibrium potential when the bulk concentration of H_2O_2 is very low.[21] We investigated the H_2O_2 selectivity of both $CoSe_2$ polymorphs as a function of overpotential and catalyst loading (Figure 3.4a). In the low overpotential region, the overall ORR current density (delivered on the disk electrode) and the partial current density for H_2O_2 production (j_{peroxide}, detected on the ring electrode and further adjusted by the collection efficiency) steadily increased with higher catalyst loadings, while the H_2O_2 selectivity appeared to be very high (>80%) and fairly insensitive to the catalyst loading. In the high overpotential region, however, the H_2O_2 production was less selective as the catalyst loading increased. These observations can be rationalized by our calculated surface Pourbaix diagrams (Figure 3.1e,f). At low overpotentials, both $CoSe_2$ polymorphs feature high OH* coverages on surface Co sites and fewer unsaturated Co active sites for the undesired OOH* scission, explaining their *intrinsic* high selectivity toward 2e$^-$ ORR across various catalyst loadings. As the overpotential increases, both $CoSe_2$ polymorphs form clean surfaces with many unsaturated Co sites, which may allow for the competing 4e$^-$ ORR pathway via OOH* scission. As the catalyst loading increases, the total amount of unsaturated Co sites and the catalyst film thickness also increase, which may trigger more side reactions of H_2O_2 reduction and/or decomposition, and lower the H_2O_2 selectivity.[19] These RRDE results suggest that $CoSe_2$ polymorphs should operate at low overpotentials, where they are *intrinsically* selective toward 2e$^-$ ORR, and with high catalyst loadings to achieve the optimal overall electrode performances for H_2O_2 production in acidic solution.

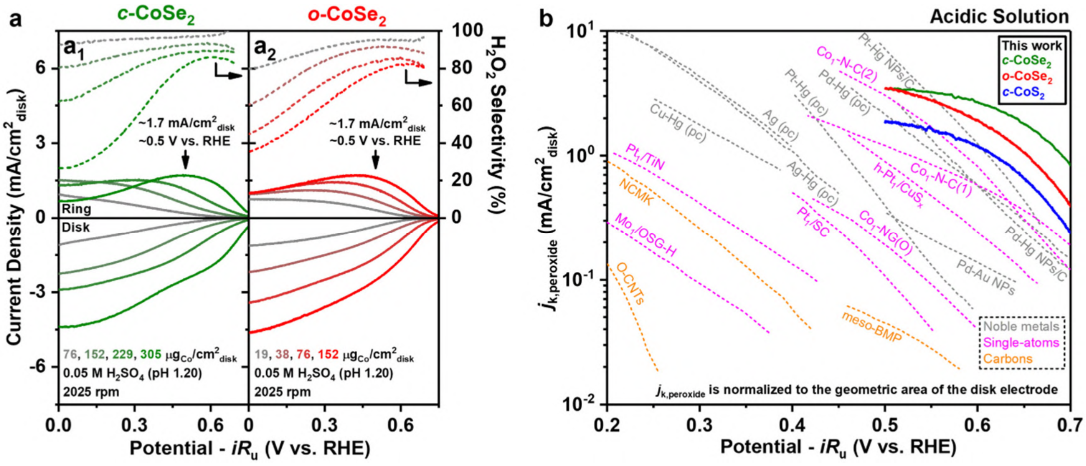

Figure 3.4. Electrochemical characterization of selective 2e$^-$ ORR on *c*-$CoSe_2$ and *o*-$CoSe_2$ catalysts.

(**a**) RRDE voltammograms recorded at 2025 rpm and the corresponding H_2O_2 selectivity of (**a$_1$**) *c*-$CoSe_2$ and (**a$_2$**) *o*-$CoSe_2$ catalyst with various catalyst loadings in O_2-saturated 0.05 M H_2SO_4 solution (pH 1.20). (**b**) Kinetic current densities for H_2O_2 production normalized to the geometric area of the disk electrode ($j_{k,peroxide}$) on *c*-$CoSe_2$ (305 $\mu g_{Co}/cm^2_{disk}$) and *o*-$CoSe_2$ (152 $\mu g_{Co}/cm^2_{disk}$) catalysts, in comparison with *c*-CoS_2 (305 $\mu g_{Co}/cm^2_{disk}$) and previously reported $2e^-$ ORR catalysts (noble metals, single-atom catalysts, and carbon materials) based on RRDE measurements in acidic solution. The traces for *c*-$CoSe_2$, *o*-$CoSe_2$, and *c*-CoS_2 catalysts are from this work, which are recorded at 1600 rpm and cut off at 0.5 V vs. RHE where $j_{peroxide}$ reaches its approximate maximum. Other traces are from previous reports (as summarized in Table A3.6 in the Appendix 3): ref. 26 for Pt-Hg NPs/C and Pt-Hg (pc); ref. 27 for Pd-Hg NPs/C, Pd-Hg (pc), Ag (pc), Ag-Hg (pc), Cu-Hg (pc); ref. 46 for Pd-Au NPs; ref. 47 for Pt_1/SC; ref. 48 for Pt_1/TiN; ref. 49 for h-Pt_1/CuS_x; ref. 19 for Co_1-N-C(1); ref. 21 for Co_1-NG(O); ref. 22 for Co_1-N-C(2); ref. 23 for Mo_1-OSG-H; ref. 13 for O-CNTs; ref. 16 for meso-BMP; ref. 18 for NCMK.

We further carried out head-to-head comparisons between both $CoSe_2$ polymorph and CoS_2 catalysts based on RRDE measurements in acidic solution. The catalytic properties of *c*-CoS_2 and *c*-$CoSe_2$ were directly compared at the same catalyst loading (76, 152, 229, or 305 $\mu g_{Co}/cm^2_{disk}$) because they delivered similar overall current densities (Figure A3.10a in the Appendix 3). *c*-$CoSe_2$ was clearly more selective toward $2e^-$ ORR than *c*-CoS_2 in the low overpotential region (Figure A3.10a$_1$–a$_4$ in the Appendix 3), consistent with the calculated surface Pourbaix diagrams which predict that the undesired OOH* scission can be effectively suppressed on $CoSe_2$ due to high OH* coverages on surface Co sites. On the other hand, it was not straightforward to directly compare the catalytic properties of *c*-CoS_2 and *o*-$CoSe_2$ at the same catalyst loading because *o*-$CoSe_2$ delivered a much higher overall ORR current density than *c*-CoS_2 (Figure A3.10b$_1$ in the

Appendix 3); this is perhaps not surprising given their very different nanoscale morphologies (Figure 3.3a). Therefore, we performed fair comparisons between *c*-CoS_2 (76, 152, 229, or 305 $\mu g_{Co}/cm^2_{disk}$) and *o*-$CoSe_2$ (19, 38, 76, or 152 $\mu g_{Co}/cm^2_{disk}$) when they delivered similar overall ORR current densities at different catalyst loadings (Figure A3.10b_2–b_5 in the Appendix 3). Similar to the *c*-$CoSe_2$ polymorph and as expected from surface Pourbaix diagrams, *o*-$CoSe_2$ was also more selective toward $2e^-$ ORR than *c*-CoS_2 at low overpotentials. Moreover, compared to *c*-CoS_2 and *c*-$CoSe_2$, the H_2O_2 selectivity of *o*-$CoSe_2$ in the high overpotential region was slightly better retained as the catalyst loading increased (Figure A3.10 in the Appendix 3). Since the binding strength of OH* to *o*-$CoSe_2$ is greater than that to *c*-CoS_2 and *c*-$CoSe_2$, it is less favorable to completely reduce OH* via PCET and form a clean surface of *o*-$CoSe_2$ at high overpotentials, which may result in its enhanced H_2O_2 selectivity in the high overpotential region.

These RRDE experiments confirm that both $CoSe_2$ polymorphs are highly active and selective $2e^-$ ORR electrocatalysts in acidic solution. The optimal overall electrode performances for H_2O_2 production can be achieved at the highest catalyst loadings when $j_{peroxide}$ reached the maximum of ~1.7 mA/cm^2_{disk} at ~0.5 V vs. RHE on both catalysts (Figure 3.4a), but *o*-$CoSe_2$ required a much lower catalyst loading (152 $\mu g_{Co}/cm^2_{disk}$) than *c*-$CoSe_2$ (305 $\mu g_{Co}/cm^2_{disk}$) to achieve a similar overall electrode performance, because the *o*-$CoSe_2$ sample exhibited a much higher double layer capacitance (C_{dl}) value and thus a larger electrochemically active surface area (ECSA) than the *c*-$CoSe_2$ sample (Figure A3.11 and Table A3.4 in the Appendix 3). Therefore, the high-surface-area *o*-$CoSe_2$ catalyst is more advantageous for practical electrochemical H_2O_2 production because of the lower catalyst loadings and reduced catalyst cost.

To quantitatively compare the H_2O_2 production performances of both $CoSe_2$ catalysts with previously reported $2e^-$ ORR catalysts in acidic solution, we extracted *kinetic* current density for

H_2O_2 production ($j_{k,peroxide}$) by correcting as-measured $j_{peroxide}$ for mass-transport loss using Koutecky-Levich (K-L) analysis based on RRDE voltammograms recorded at various rotation rates. An example of the K-L analysis on *c*-$CoSe_2$ catalyst is shown in Figure A3.12 and Table A3.5 (Appendix 3). $j_{k,peroxide}$ is normalized the geometric area of the disk electrode to reflect *the overall yield* of H_2O_2 product without mass-transport limitation, which clearly increased with higher catalyst loadings (Figure A3.12c in the Appendix 3). Although this $j_{k,peroxide}$ normalized to the disk area can be affected by the catalyst loading and the catalyst surface area and thus does not reflect the intrinsic catalyst property, it is important for practical applications. Therefore, we chose the highest catalyst loadings of *c*-$CoSe_2$ (305 $\mu g_{Co}/cm^2_{disk}$) and *o*-$CoSe_2$ (152 $\mu g_{Co}/cm^2_{disk}$) for comparisons with previously reported $2e^-$ ORR catalysts in acidic solution (Figure 3.4b). Both *c*-$CoSe_2$ and *o*-$CoSe_2$ catalysts show clearly more efficient H_2O_2 production than *c*-CoS_2 and other reported single-atom[22] or carbon[18] catalysts, and display even better overall electrode performances than the state-of-the-art noble metal catalysts[26,27] in the more important low overpotential region. This comparison of $j_{k,peroxide}$ reveals that $CoSe_2$ polymorph catalysts are the best-performing $2e^-$ ORR electrocatalysts reported so far in *acidic* solution (as summarized in Table A3.6 in the Appendix 3).

3.3.6 Enhanced Catalyst Stability of $CoSe_2$ Polymorphs from RRDE Measurements

We examined the catalyst stability of both $CoSe_2$ polymorphs for electrochemical H_2O_2 production in 0.05 M H_2SO_4 solution by continuously applying RRDE scans while sequentially changing the rotation rate (Figure A3.13a in the Appendix 3), analogous to the accelerated degradation tests typically applied to conventional $4e^-$ ORR catalysts.[50,51] These RRDE scans recorded at the highest rotation rate of 2025 rpm clearly revealed the enhanced catalyst stability of *c*-$CoSe_2$ (305 $\mu g_{Co}/cm^2_{disk}$) and *o*-$CoSe_2$ (152 $\mu g_{Co}/cm^2_{disk}$) (Figure 3.5a). The disk currents and the ring currents of both $CoSe_2$ polymorphs were relatively stable during catalyst stability tests (Figure 3.5a$_2$,a$_3$), whereas those of *c*-CoS_2 (305 $\mu g_{Co}/cm^2_{disk}$) evidently decreased over time (Figure 3.5a$_1$). We further quantitatively compared the disk current and ring current retentions of all three catalysts at 0.5 V vs. RHE where $j_{peroxide}$ reached its approximate maximum (Figure 3.5b). Over the same time period of 2.5 h, the disk current of *c*-$CoSe_2$ was almost completely retained (~100%), whereas *c*-CoS_2 only retained 62% of its initial disk current (Figure 3.5b$_1$). Notably, the high-surface-area *o*-$CoSe_2$ displayed a near-unity disk current retention over a longer time period of 4.2 h (Figure 3.5b$_1$). Note that the slight decrease in the ring currents of both $CoSe_2$ polymorphs (Figure 3.5b$_2$) was mainly due to the formation of surface PtO_x on the ring electrode after its continuous operation at the high potential of 1.3 V vs. RHE.[13,20] After periodic electrochemical cleaning of the ring electrode (see Figure A3.13b in the Appendix 3 for details), the ring currents of both $CoSe_2$ polymorphs were immediately recovered (Figure 3.5b$_2$), indicating that the electrochemical H_2O_2 production was stable on both $CoSe_2$ polymorphs.

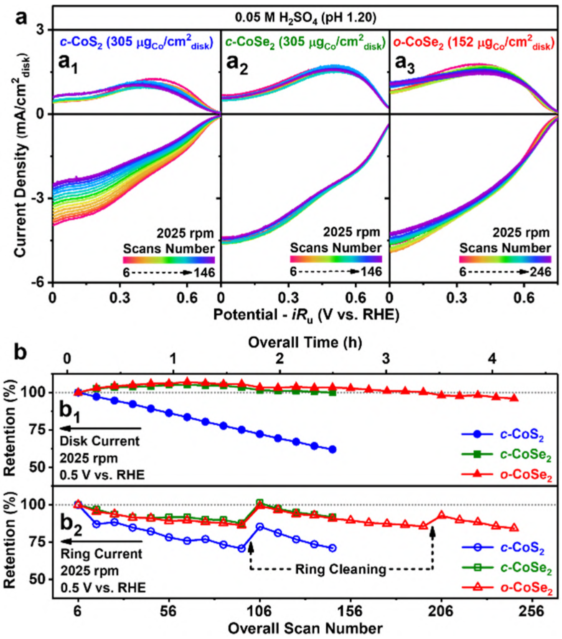

Figure 3.5. Enhanced stability of *c*-$CoSe_2$ and *o*-$CoSe_2$ catalysts from RRDE measurements.

(**a**) RRDE voltammograms of (**a$_1$**) *c*-CoS_2 (305 μg$_{Co}$/cm$^2_{disk}$), (**a$_2$**) *c*-$CoSe_2$ (305 μg$_{Co}$/cm$^2_{disk}$), and (**a$_3$**) *o*-$CoSe_2$ (152 μg$_{Co}$/cm$^2_{disk}$) recorded at 2025 rpm during catalyst stability tests in O_2-saturated 0.05 M H_2SO_4 solution (pH 1.20). (**b**) Retention rates of (**b$_1$**) disk current and (**b$_2$**) ring current at 2025 rpm and 0.5 V vs. RHE (where $j_{peroxide}$ reaches its approximate maximum) during catalyst stability tests. The rotation rate profile of catalyst stability tests and the protocol for electrochemical cleaning of the ring electrode are shown in Figure A3.13 (Appendix 3).

To better understand the origin of the enhanced catalyst stability of $CoSe_2$, we recovered all of the tested catalysts to examine their surface composition and structural integrity using Raman spectroscopy and XPS. Raman spectra suggested the crystal structures of all tested catalysts, including the apparently least stable *c*-CoS_2 catalyst, were well retained without the formation of crystalline or amorphous impurities (Figure A3.14 in the Appendix 3). XPS spectra suggested their surface chemical states remained the same as the pristine catalysts (Figure A3.15 in the Appendix 3). This is understandable because the bulk Pourbaix diagram (Figure A3.1a in the Appendix 3) suggests the degradation of *c*-CoS_2 via surface oxidation yields soluble species of Co^{2+} and SO_4^{2-} that can readily leach into electrolyte solutions without being detected by XPS. The leaching of *c*-CoS_2 was also implied by the slight change in its surface composition after the catalyst stability test, whereas both $CoSe_2$ polymorphs appeared to be more stable with minimal changes in their surface compositions (Table A3.7 in the Appendix 3). Therefore, it is essential to quantify the Co^{2+} leaching rate by using inductively coupled plasma mass spectrometry (ICP-MS) to analyze the tested electrolyte solutions, so that the stability of these three catalysts can be differentiated based on the total amount of Co^{2+} leached per hour (μg$_{Co}$/h). As summarized in Table 3.1 (also see details in Table A3.8 in the Appendix 3), the more stable *o*-$CoSe_2$ (152 μg$_{Co}$/cm$^2_{disk}$) and *c*-$CoSe_2$ (305 μg$_{Co}$/cm$^2_{disk}$) exhibited similar leaching rates of 0.31 and 0.39 μg$_{Co}$/h, respectively, whereas the least stable *c*-CoS_2 (305 $\mu g_{Co}/cm^2_{disk}$) leached almost twice as fast (0.66 $\mu g_{Co}/h$). In fact, this Co^{2+} leaching from $CoSe_2$ could potentially be transient and take place mostly at the initial stage of electrochemical operations (see later discussion). These leaching results are consistent with our theoretical prediction that both $CoSe_2$ polymorphs are better resistant to surface oxidation than *c*-CoS_2, because the binding strength of O* to Se sites is substantially weaker than that to S sites by 0.59 eV, and display significantly enhanced catalyst stability for the electrosynthesis of H_2O_2 in acidic solution.

Table 3.1. Average cobalt leaching rates of *c*-$CoSe_2$ and *o*-$CoSe_2$ in comparison with *c*-CoS_2 during catalyst stability tests in 0.05 M H_2SO_4 solution from RRDE measurements.

Catalyst	Catalyst Loading[a]	Stability Test Duration	[Co] in Tested Electrolyte[b]	Average Cobalt Leaching Rate
c-CoS_2	305 $\mu g_{Co}/cm^2_{disk}$	2.5 h (151 scans)	36.6 $\mu g_{Co}/L$	0.66 $\mu g_{Co}/h$
c-$CoSe_2$	305 $\mu g_{Co}/cm^2_{disk}$	2.5 h (151 scans)	21.8 $\mu g_{Co}/L$	0.39 $\mu g_{Co}/h$
o-$CoSe_2$	152 $\mu g_{Co}/cm^2_{disk}$	4.2 h (251 scans)	28.5 $\mu g_{Co}/L$	0.31 $\mu g_{Co}/h$

[a] Geometric area of the disk electrode is 0.126 cm^2_{disk}.

[b] [Co] in the tested electrolyte solution (45 mL) was determined by ICP-MS analysis (see details in Table A3.8 in the Appendix 3).

3.3.7 Bulk Electrosynthesis and Chemical Detection of H_2O_2 Produced on $CoSe_2$ Marcasite

From a practical perspective, it is critical to confirm that the electrogenerated H_2O_2 on $CoSe_2$ catalysts can indeed accumulate in solution and reach concentrations that are relevant to applications, for example, no more than 1000 ppm (29 mM) for water treatment.[4] RRDE measurements only allow instantaneous and *electrochemical* detection of H_2O_2. Therefore, we performed bulk electrolysis to produce H_2O_2 using integrated electrode of *o*-$CoSe_2$ nanowires directly grown on three-dimensional carbon fiber paper substrate (denoted as *o*-$CoSe_2$/CFP, see Figure A3.16 in the Appendix 3) and carried out *chemical* detection of the produced H_2O_2 via redox titration using cerium(IV) sulfate ($2\ Ce^{4+} + H_2O_2 \rightarrow 2\ Ce^{3+} + 2\ H^+ + O_2$) followed by UV-Vis spectrophotometry.[13] We chose *o*-$CoSe_2$ (marcasite) over *c*-$CoSe_2$ (pyrite) for bulk electrolysis experiments because our earlier RRDE results showed that *o*-$CoSe_2$ featured a higher C_{dl} value (which implies a larger ECSA) and delivered a higher catalytic current for H_2O_2 production than *c*-$CoSe_2$ at the same catalyst loading (Figure 3.4a). For comparison purposes, another working electrode of *c*-CoS_2 nanowires grown on carbon fiber paper (*c*-CoS_2/CFP, see Figure A3.17 in the Appendix 3) that had the same geometric area of ~1 cm^2_{geo} (Figure A3.19 in the Appendix 3) and same catalyst loading of ~370 $\mu g_{Co}/cm^2_{geo}$ (Table A3.9 in the Appendix 3) was studied. Bulk electrosynthesis of H_2O_2 was performed in a two-compartment three-electrode H-cell setup (Figure A3.18 in the Appendix 3, also see details in the Experimental Section).

We carried out the bulk electrosynthesis of H_2O_2 on *o*-$CoSe_2$/CFP and *c*-CoS_2/CFP in O_2-saturated 0.05 M H_2SO_4 solution (4 mL) at the constant potential of 0.5 V vs. RHE, near the optimal potential where the maximum $j_{peroxide}$ was achieved from RRDE measurements, over long periods of time (5–6 h, see Figure 3.6). As the H_2O_2 product was accumulated in the solution, the overall catalytic current of *o*-$CoSe_2$/CFP displayed a Nernstian response (Figure 3.6a red curve). In contrast, the overall catalytic current of *c*-CoS_2/CFP only exhibited an initial Nernstian response immediately after the bulk electrolysis started and then gradually *increased* as the bulk electrolysis proceeded (Figure 3.6a blue curve). The produced H_2O_2 was periodically quantified at various time points using the UV-vis spectrophotometric method described above (Figure A3.22 in the

Appendix 3, also see details in the Experimental Section). During the bulk electrolysis using *o*-$CoSe_2$/CFP, the cumulative H_2O_2 concentration kept increasing and reached a high concentration of 547 ppm after 6 h (Figure 3.6b red curve). As for *c*-CoS_2/CFP, despite delivering a larger overall catalytic current, the cumulative H_2O_2 concentration increased less steadily and only reached a maximum of 232 ppm over 3 h and then started decreasing afterwards (Figure 3.6b blue curve). We further calculated the cumulative H_2O_2 yield on both electrodes taking into account the evaporation of electrolyte solution during bulk electrolysis (see Table A3.10 in the Appendix for details): the cumulative H_2O_2 yield on *o*-$CoSe_2$/CFP consistently increased to 33.7 μmol over 6 h, whereas that on *c*-CoS_2/CFP peaked at the 3 h mark with only 19.6 μmol (Figure 3.6c). As a result, the cumulative H_2O_2 selectivity on *o*-$CoSe_2$/CFP reached ~83% during the first hour of bulk electrolysis and still remained ~70% over the long period of 6 h, whereas the selectivity on *c*-CoS_2/CFP started off with a lower value of ~60% and drastically decreased to ~13% over 5 h (see Figure 3.6d, and Table A3.11 in the Appendix 3). Moreover, ICP-MS analysis of the tested electrolyte solutions (see Table A3.12 in the Appendix 3, and inset of Figure 3.6a) showed that *o*-$CoSe_2$/CFP exhibited an average cobalt leaching rate of 0.69 μg_{Co}/h over 6 h, much lower than that of *c*-CoS_2/CFP (2.80 μg_{Co}/h over 5 h). In fact, since the Co^{2+} leaching from $CoSe_2$ took place mostly at the initial stage of electrochemical operations (see later discussion), this average leaching rate of 0.69 μg_{Co}/h could be a *lower bound* estimate of the operational stability of *o*-$CoSe_2$/CFP. These observations also led us to suspect that *electrochemical* side reactions of H_2O_2 reduction and/or decomposition were much more pronounced on *c*-CoS_2/CFP and eventually outcompeted the H_2O_2 production, which could account for the abnormal increase in the overall current (Figure 3.6a) and the significant decrease in the H_2O_2 selectivity (Figure 3.6d) during the bulk electrolysis using *c*-CoS_2/CFP.

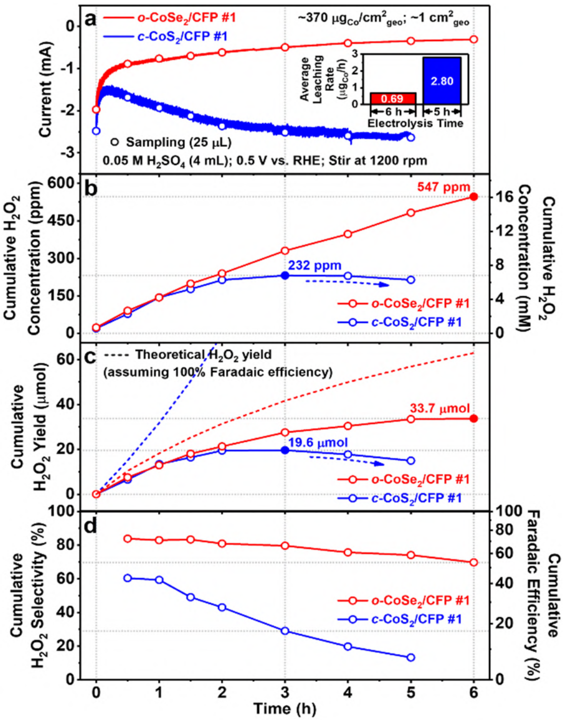

Figure 3.6. Bulk electrosynthesis and chemical detection of H_2O_2 produced on *o*-$CoSe_2$ nanowires grown on carbon fiber paper (*o*-$CoSe_2$/CFP) in comparison with *c*-CoS_2/CFP. (**a**) Chronoamperometry curves of *o*-$CoSe_2$/CFP and *c*-CoS_2/CFP (with the same catalyst loading of ~370 $\mu g_{Co}/cm^2_{geo}$ and the same geometric area of ~1 cm^2_{geo}) at 0.5 V vs. RHE in O_2-saturated 0.05 M H_2SO_4 solution (pH 1.20) under vigorous stirring (1200 rpm). The average cobalt leaching rates (μg_{Co}/h) of *o*-$CoSe_2$/CFP and *c*-CoS_2/CFP during bulk electrolysis is shown as an inset. (**b**) Cumulative H_2O_2 concentration, (**c**) cumulative H_2O_2 yield, and (**d**) cumulative H_2O_2 selectivity and Faradaic efficiency during bulk electrolysis.

We designed additional bulk electrolysis experiments to prove that the *electrochemical* side reactions of H_2O_2 reduction and/or decomposition are indeed much less prone on *o*-$CoSe_2$/CFP. We reason that the additional catalytic current triggered by those side reactions should correlate with the H_2O_2 concentration. Therefore, after accumulating an appreciable concentration of H_2O_2 from the bulk electrolysis using *o*-$CoSe_2$/CFP, we reintroduced fresh *H_2O_2-free* electrolyte solution and performed another bulk electrolysis reusing the same *o*-$CoSe_2$/CFP electrode (Figure A3.21a–d in the Appendix 3). The overall catalytic current of *o*-$CoSe_2$/CFP in the H_2O_2-free solution was identical to that in the H_2O_2-containing solution (Figure A3.21a in the Appendix 3), suggesting *o*-$CoSe_2$/CFP is highly resistant to those electrochemical side reactions that consume the H_2O_2 product. In contrast, *c*-CoS_2/CFP behaved very differently in the analogous experiments (Figure A3.21e–h in the Appendix 3). The overall catalytic current of *c*-CoS_2/CFP in the H_2O_2-containing solution was substantially greater than that in the fresh H_2O_2-free solution (Figure A3.21e in the Appendix 3), resulting in the significant loss of H_2O_2 product due to the prevalence of side reactions. Therefore, *o*-$CoSe_2$/CFP is much more effective than *c*-CoS_2/CFP for the bulk electrosynthesis of H_2O_2 that can reach practically useful concentrations.

We further utilized these bulk electrolysis experiments to investigate the catalyst leaching behaviors of *o*-$CoSe_2$/CFP vs. *c*-CoS_2/CFP in more details. We collected the tested electrolyte solutions at the end of each consecutive run of bulk electrolysis using each working electrode (Figure A3.21 in the Appendix 3) and performed ICP-MS analysis to examine the cobalt leaching rate during each run (Figure A3.22 and Table A3.12 and A3.13 in the Appendix 3). We observed *transient* leaching of *o*-$CoSe_2$/CFP taking place mostly at the initial stage of electrochemical operations, and the Co^{2+} leaching was negligible during the second run of bulk electrolysis (see Figure A3.22a,b in the Appendix 3 for two replicate experiments). This transient leaching could be due to the loss of loosely-bound *o*-$CoSe_2$ particles from CFP substrate at the beginning. In fact, if this initial transient leaching was excluded, the cobalt leaching rate of *o*-$CoSe_2$/CFP after reaching its steady state was less than 0.2 μg_{Co}/h (Figure A3.22a,b in the Appendix 3). In contrast, *c*-CoS_2/CFP displayed *continuous* leaching behavior during both runs of bulk electrolysis (Figure A3.22c in the Appendix 3) with a leaching rate greater than 2 μg_{Co}/h, an order of magnitude higher than *o*-$CoSe_2$/CFP. These *bulk* leaching results further confirmed the enhanced electrochemical stability of *o*-$CoSe_2$ under more stringent operating conditions for a much longer timescale. To our knowledge, there has been no rigorous analysis of metal leaching in the recently reported earth-abundant 2e$^-$ ORR catalysts for a direct comparison, but we found that the steady state cobalt leaching rate of *o*-$CoSe_2$ presented here is much lower than those of other cobalt-based electrocatalysts recently reported for water splitting reactions (Table A3.14 in the Appendix 3). Hopefully this careful study on the stability of earth-abundant 2e$^-$ ORR catalysts through quantitative metal leaching rate analysis will stimulate the research community to look into this important issue more in the future. Furthermore, Raman, XPS (Figure A3.23 and Table A3.7 in the Appendix 3), and XAS (Figure A3.24 and Table A3.15 in the Appendix 3) characterization confirmed the structural and compositional integrity of the tested *o*-$CoSe_2$/CFP electrodes after the bulk electrosynthesis of H_2O_2.

Significantly, the accumulated concentration of 547 ppm H_2O_2 using *o*-$CoSe_2$/CFP demonstrated here is the highest among the few previous reports of 2e$^-$ ORR electrocatalysts that showed the bulk electrosynthesis of H_2O_2 in *acidi*c solution in similar H-cells (see Table A3.16 and additional discussion in the Appendix 3).[22,26] In fact, the cumulative H_2O_2 concentrations previously demonstrated were one or two order(s) of magnitude lower because larger volumes of electrolyte solution was often used. The stable operation of *o*-$CoSe_2$/CFP for 6 h demonstrated here is among the longest trial of the bulk electrosynthesis of H_2O_2 in *acidic* solution and, more importantly, *no* other report ever examined the catalyst leaching under these practically relevant conditions (Table A3.16 in the Appendix 3). Given the insights discussed above on the possible electrochemical side reactions of H_2O_2 at higher H_2O_2 concentrations, the catalyst stability is less challenged when evaluated under much less stringent operating conditions without a significant buildup of H_2O_2 in the electrolyte solution. To accumulate a high concentration of H_2O_2 useful for practical applications, we not only need highly active and selective $2e^-$ ORR electrocatalysts, they also must be robust and highly resistant to electrochemical side reactions under stringent operating conditions.

3.3.8 Electro-Fenton Degradation of Model Organic Pollutant on $CoSe_2$ Marcasite

H_2O_2 is particularly useful for water treatment and environmental remediation, utilizing the Fenton's reaction between H_2O_2 and Fe^{2+} (Equation 10) to generate hydroxyl radical (·OH) as an even more powerful oxidant ($E^{\circ}_{\cdot OH/H_2O}$ = 2.80 V vs. SHE). This approach can be used to remove persistent organic pollutants[52-54] from wastewater through advanced oxidation processes. Furthermore, in the so-called *electro*-Fenton process, H_2O_2 is electrogenerated from $2e^-$ ORR at the cathode, while Fe^{2+} is rapidly regenerated from the reduction of Fe^{3+} (E° = 0.77 V vs. SHE, Equation 11) at the same cathode (Figure 3.7a).[24] This significantly enhances the ·OH production rates and the organics mineralization capabilities compared to the conventional *chemical* Fenton process.[25] It is noteworthy that the Fenton's reaction exhibits the highest rate at an optimal acidic pH of 2.8–3.0 when the speciation of Fe^{2+} reaches its maximum.[24] Therefore, the successful bulk electrosynthesis of H_2O_2 in *acidic* solution makes *o*-$CoSe_2$/CFP a promising cathode for the electro-Fenton process.

$$Fe^{2+} + H_2O_2 + H^+ \rightarrow Fe^{3+} + H_2O + \cdot OH \quad (10)$$

$$Fe^{3+} + e^- \rightarrow Fe^{2+} \quad (11)$$

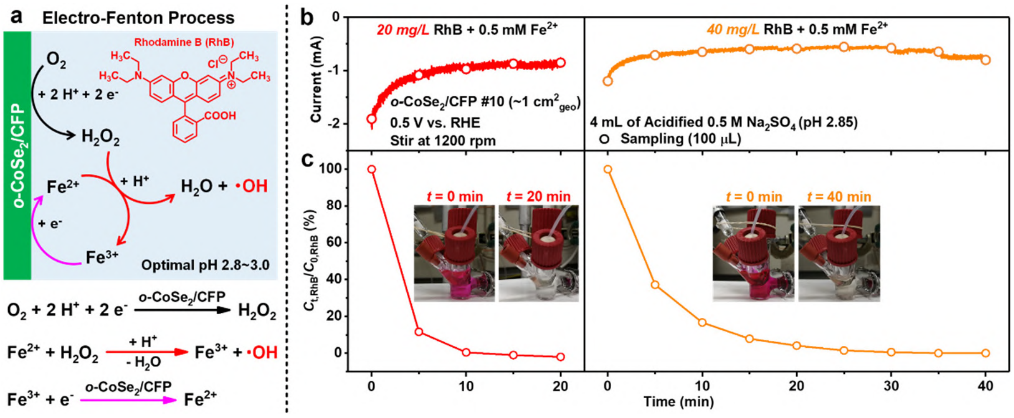

Figure 3.7. Electro-Fenton degradation of Rhodamine B (RhB) on *o*-$CoSe_2$/CFP.

(**a**) Schematic of the electro-Fenton process and the (electro)chemical reactions involved. (**b**) Chronoamperometry curves of *o*-$CoSe_2$/CFP at 0.5 V vs. RHE when both RhB and Fe^{2+} are present in O_2-saturated acidified 0.5 M Na_2SO_4 solution (pH 2.85) under vigorous stirring (1200 rpm) at room temperature. The same *o*-$CoSe_2$/CFP cathode is reused for two consecutive electro-Fenton degradation tests with different initial concentrations of RhB (20 or 40 mg/L) but the same concentration of Fe^{2+} (0.5 mM). (**c**) Decays of the RhB concentrations over time. The inset photographs show the color changes of the electrolyte solutions before and after each electro-Fenton degradation test.

We used Rhodamine B (RhB) as a model organic pollutant[55] to demonstrate the effective electro-Fenton process on *o*-$CoSe_2$/CFP (Figure 3.7a). Electro-Fenton degradation tests were performed at room temperature in O_2-saturated acidified 0.5 M Na_2SO_4 solution (pH 2.85) with the presence of both RhB (20 or 40 mg/L) and Fe^{2+} (0.5 mM) in a three-electrode H-cell setup using *o*-$CoSe_2$/CFP as the working cathode operated at 0.5 V vs. RHE (same as the earlier bulk electrolysis experiments) to enable efficient H_2O_2 production. We used UV-Vis spectrophotometry to monitor the organic dye concentration as a function of time during each test (Figure A3.25 in the Appendix 3). The overall catalytic current of the *o*-$CoSe_2$/CFP cathode displayed a Nernstian response, indicating the accumulation of the electrogenerated H_2O_2 in solution (Figure 3.7b). During the same time, the concentration of RhB decreased rapidly (Figure 3.7c) and the color of the solutions faded (insets of Figure 3.7c). Moreover, this current remained steady regardless of the decay of the RhB concentration over time (Figure 3.7b,c), suggesting that RhB was degraded via the electro-Fenton process rather than the direct electrochemical destruction on the cathode. Significantly, the *o*-$CoSe_2$/CFP cathode completely degraded and decolored 20 mg/L of RhB within a short period of 20 min, and remained highly efficient when it was reused for removing higher concentrations (40 mg/L) of RhB under similar operating conditions (Figure 3.7c). These results show that *o*-$CoSe_2$ is a very promising cathode for electro-Fenton process and water treatment applications, which is rooted in its enhanced selectivity and stability for the bulk electrosynthesis of H_2O_2 in *acidic* solution.

3.4 Conclusions

In conclusion, this joint computational/experimental study demonstrates stable and selective electrosynthesis of H_2O_2 and effective electro-Fenton process on $CoSe_2$ polymorph catalysts in acidic solution, establishing new understandings on catalyst stability for $2e^-$ ORR and significantly advancing the practical production and utilization of H_2O_2 in acidic solution. Calculated surface Pourbaix diagrams reveal the weak binding of O* to Se sites and predict better electrochemical stability for $CoSe_2$ than CoS_2. Additionally, both $CoSe_2$ polymorphs are computationally predicted to be active and selective $2e^-$ ORR electrocatalysts. RRDE experiments in 0.05 M H_2SO_4 show that $CoSe_2$ polymorphs are the best-performing $2e^-$ ORR electrocatalysts reported so far in *acidic* solution, delivering higher kinetic current densities for H_2O_2 production at low overpotentials than reported state-of-the-art noble metal or single-atom catalysts. Detailed structural characterization and ICP-MS analysis of tested $CoSe_2$ catalysts and electrolyte solutions confirm their enhanced catalyst stability and resistance to catalyst leaching during prolonged electrochemical operations. Using *o*-$CoSe_2$ nanostructures directly grown on carbon fiber paper electrode, bulk electrosynthesis of H_2O_2 in 0.05 M H_2SO_4 achieved a high accumulated H_2O_2 concentration of 547 ppm (16 mM) thanks to the effective suppression of electrochemical side reactions, surpassing other reported $2e^-$ ORR catalysts evaluated in *acidic* solution in similar H-cells. Such robust H_2O_2 production allows for the effective electro-Fenton process on the *o*-$CoSe_2$ electrode and the efficient degradation of a model organic pollutant, demonstrating its great promise for on-site water treatment applications. This integrated study not only establishes $CoSe_2$ polymorphs as the new benchmark $2e^-$ ORR electrocatalysts in *acidic* solution and demonstrates effective on-site electrosynthesis of H_2O_2, but also reveals new mechanistic insights and introduces new design rules for stable and efficient earth-abundant transition metal compound electrocatalysts for decentralized production and utilization of H_2O_2.

3.5 Experimental Section

3.5.1 Computational Method

Spin polarized electronic structure calculations were performed using the Vienna Ab initio Simulation package (VASP)[56-59] interfaced with the Atomic Simulation Environment (ASE).[60] Projector augmented wave (PAW) pseudopotentials[61,62] with a cutoff of 450 eV were used to treat core electrons, and the Perdew-Burke-Ernzerhof (PBE) functional[63,64] was used to treat exchange and correlation. Dispersion was treated using Grimme's D3(ABC) method.[65] To better describe the Co 3d electrons in *c*-$CoSe_2$, a Hubbard U parameter,[66] $U_{eff} = 2.0$ eV, was taken from a previous report.[67] A variety of Hubbard U parameters were tested for *c*-CoS_2 and *o*-$CoSe_2$, and were found to have little to no effect on geometries or energies; therefore, no Hubbard U parameter was used for these two catalysts. Solvation effects were treated using the continuum solvent method

VASPsol.[68,69] The Brillouin zone was sampled using a (10,10,10) and (10,10,1) Γ-centered Monkhorst-Pack mesh[70] for bulk and surface calculations, respectively. Lattice constants were determined by fitting to an equation of state (EOS).[71] The (100) surfaces of *c*-CoS_2 and *c*-$CoSe_2$ and (101) surface of *o*-$CoSe_2$ were modelled as a 1×1 unit cell slab with two repeats in the z-direction, leading to a total of 8 Co atoms and 16 S/Se atoms and a vacuum gap of at least 15 Å. The top half of the slabs were allowed to relax while the bottom half were frozen to simulate bulk. For each ionic configuration, the electronic energy was converged below 10^{-6} eV. Both the clean slab and adsorbates were allowed to relax until forces were converged below 0.005 eV/Å^2. Transition states were located using the nudged elastic band (NEB) method[72,73] and were refined using the dimer method.[74-76] All transition states were confirmed saddle points with one imaginary frequency corresponding to bond breaking. Binding energies were calculated with respect to $O_{2(g)}$ and $H^+_{(aq)}$ and e^-. The energy of $H^+_{(aq)}$ and e^- was calculated using the computational hydrogen electrode (CHE) method,[39] where $H^+_{(aq)}$ is assumed to be in thermodynamic equilibrium with $H_{2(g)}$. In order to avoid well-known errors in the DFT treatment of $O_{2(g)}$, the free energy of $O_{2(g)}$ was determined by matching the experimental standard equilibrium potential (1.229 V) of the reaction ½ $O_{2(g)} + 2\ H^+_{(aq)} + 2\ e^- \rightarrow H_2O_{(l)}$. The free energies of species were calculated using $G = H - T\ S$, where H is the enthalpy including zero-point energy (ZPE) and thermal corrections, and S is either the total experimental entropy at 298 K and 1 bar (for gas phase species) or calculated under the harmonic approximation (for surface bound species). The free energy of $H_2O_{(l)}$ was calculated using the experimental free energy of formation for $H_2O_{(l)}$ and $H_2O_{(g)}$. The solvation free energy of $H_2O_{2(aq)}$ was calculated using the experimental Henry's law constant.[77] The calculated standard equilibrium potential of 2e- ORR reaction $O_{2(g)} + 2\ H^+_{(aq)} + 2\ e^- \rightarrow H_2O_{2(aq)}$ is 0.81 V, while the experimental standard equilibrium potential is 0.69 V.

3.5.2 Chemicals

All chemicals were purchased from Sigma-Aldrich and used as received without further purification, unless noted otherwise. Deionized nanopure water (18.2 MΩ·cm) from Thermo Scientific Barnstead water purification systems was used for all experiments.

3.5.3 Materials Synthesis

The synthesis of nanostructured *c*-$CoSe_2$, *o*-$CoSe_2$, and *c*-CoS_2 catalysts as well as the direct growth of *o*-$CoSe_2$ and *c*-CoS_2 nanowires on carbon fiber paper substrates (*o*-$CoSe_2$/CFP and *c*-CoS_2/CFP) followed published procedures[31,43] with minor modifications. Detailed methods are described in the Appendix 3.

3.5.4 Materials Characterization

Powder X-ray diffraction (PXRD) patterns were collected on a Bruker D8 ADVANCE powder X-ray diffractometer using Cu Kα radiation. Scanning electron microscopy (SEM) was performed on a Zeiss SUPRA 55VP field emission scanning electron microscope at the accelerating voltage of 1 kV. X-ray photoelectron spectroscopy (XPS) was performed on a Thermo Scientific K-Alpha XPS system with an Al Kα X-ray source. Raman spectroscopy was collected on a Horiba LabRAM ARAMIS Raman spectrometer using a 532 nm laser source with an attenuated laser intensity to avoid sample degradation. X-ray absorption spectroscopy (XAS) was collected in the transmission mode at the Advanced Photon Source (APS) Beamline 10-BM-B, and was analyzed using ATHENA and ARTEMIS softwares.[78] Detailed sample preparation are described in the Appendix 3.

3.5.5 Electrode Preparation

Drop-casted catalyst powders were prepared on a rotating ring-disk electrode (RRDE-3A, ALS Co., Ltd) made of a glassy carbon disk (with a geometric area of 0.126 cm^2) surrounded by a

Pt ring. The collection efficiency of the bare RRDE was 0.43 based on experimental calibration using ferri-/ferrocyanide redox couple. The RRDE was polished with 1, 0.3, and 0.05 μm alumina suspensions (Allied High Tech Products) on a polishing cloth (Buehler, MicroCloth) successively, thoroughly rinsed with nanopure water and methanol, briefly sonicated in methanol for less than 20 s, and dried under ambient condition before use. Catalyst inks were prepared by suspending pre-weighed catalyst powders in desired volumes of the 9:1 (v/v) mixture of nanopure water and 5 wt% Nafion solution via sonication for 1 h. A fixed volume of catalyst ink was then drop-casted onto the glassy carbon disk and dried under ambient condition at the rotation rate of 700 rpm to form a uniform catalyst film with controlled catalyst loading (see Table A3.3 in the Appendix 3**)**.

3.5.6 Electrochemical Measurements

RRDE measurements were conducted in an undivided three-electrode cell using a Bio-Logic VMP-300 multichannel potentiostat. A graphite rod and a Hg/Hg_2SO_4 (saturated K_2SO_4) electrode was used as the counter electrode and the reference electrode, respectively. The acidic electrolyte solution of 0.05 M H_2SO_4 (pH 1.20) was prepared from concentrated H_2SO_4 (95.0–98.0%). The Hg/Hg_2SO_4 reference electrode was calibrated against a standard saturated calomel electrode (SCE, E_{SCE} = 0.241 V vs. SHE):

$$E_{Hg/Hg_2SO_4} = E_{SCE} + 0.403 \text{ V vs. SCE} = 0.644 \text{ V vs. SHE}$$

All potentials were reported versus reversible hydrogen electrode (RHE): E vs. RHE = E vs. SHE + 0.059 V × pH = E vs. Hg/Hg_2SO_4 + 0.715 V. Prior to RRDE measurements, the electrolyte solution was purged with O_2 gas for at least 15 min. During the measurements, a blanket of O_2 gas was maintained over the surface of the electrolyte solution. Under O_2-saturated condition, the Pt ring was first conditioned by running cyclic voltammetry (CV) between 0.05 and 1.20 V vs. RHE (without iR-correction) at 100 mV/s and 1600 rpm for 10 cycles, meanwhile holding the disk at 0.75 V vs. RHE; the catalyst-coated disk was then conditioned by running CV between -0.025 and 0.75 V vs. RHE (without iR-correction) at 100 mV/s and 1600 rpm for 10 cycles, meanwhile holding the Pt ring at 1.3 V vs. RHE. The catalytic properties were evaluated by performing linear sweep voltammetry (LSV) of the catalyst-coated disk from 0.75 to -0.025 V vs. RHE (without iR-correction) at 50 mV/s and various rotation rates, meanwhile holding the Pt ring at 1.3 V vs. RHE. The electrolyte solution was finally saturated with Ar gas for background current measurements. Uncompensated resistance (R_u) was measured by electrochemical impedance spectroscopy (EIS), iR-correction was manually performed after background current correction. The H_2O_2 selectivity (p) is calculated using the following equation:

$$p = \frac{2 \times \frac{i_{\text{ring}}}{N}}{i_{\text{disk}} + \frac{i_{\text{ring}}}{N}} \times 100\%$$

where i_{disk} and i_{ring} are the background-corrected disk and ring current, respectively, N is the collection efficiency (0.43). For the ease of directly visualizing the H_2O_2 selectivity from RRDE voltammograms, both the disk and the ring current densities (j_{disk} and j_{ring}) are normalized to the geometric area of the disk electrode (A_{disk}), and the ring current density is further adjusted by the collection efficiency:

$$j_{\text{disk}} = \frac{i_{\text{disk}}}{A_{\text{disk}}}$$

$$j_{\text{ring}} = \frac{i_{\text{ring}}}{A_{\text{disk}} \times N} = j_{\text{peroxide}}$$

where j_{peroxide} is the partial disk current density for H_2O_2 production. Detailed derivation of the kinetic current density for H_2O_2 production ($j_{\mathrm{k,peroxide}}$) from Koutecky-Levich analysis of j_{peroxide} is described in the Appendix 3. To estimate electrochemically active surface area (ECSA), double layer capacitance (C_{dl}) was determined under Ar-saturated condition by performing CV of the catalyst-coated disk between -0.025 V and 0.75 V vs. RHE (without *iR*-correction) at various scan rates. After RRDE measurements, the tested electrolyte solutions were collected and filtered with 0.22 μm syringe filters (Restek) three times, then the concentrations of the dissolved Co^{2+} were measured by inductively coupled plasma mass spectrometry (ICP-MS) using a Shimadzu ICPMS-2030 spectrometer. ICP-MS standard solutions were prepared by dissolving $CoSO_4 \cdot 7H_2O$ (≥99%) in a solution of 0.05 M H_2SO_4.

3.5.7 Bulk Electrosynthesis and Chemical Detection of the Produced H_2O_2

o-$CoSe_2$/CFP and *c*-CoS_2/CFP (both with the area of ~1 cm^2_{geo} and the catalyst loading of ~370 $\mu g_{\mathrm{Co}}/cm^2_{\mathrm{geo}}$) were used as the working electrodes for bulk electrolysis in O_2-saturated 0.05 M H_2SO_4 solution (pH 1.20). 5 min epoxy (Devcon) was used to define the geometric area of the working electrodes (~1 cm^2_{geo}). A graphite rod and a Hg/Hg_2SO_4 (saturated K_2SO_4) electrode was used as the counter electrode and the reference electrode, respectively. A two-compartment three-electrode H-cell setup was used to avoid the oxidation of H_2O_2 product on the counter electrode. A minimal volume (3–4 mL) of electrolyte solution was used and vigorously stirred at 1200 rpm in the working electrode compartment to achieve higher H_2O_2 concentrations under facilitated mass transfer of oxygen gas. The working electrodes were operated at the constant potential of 0.5 V vs. RHE. During each run of bulk electrolysis, a small aliquot of electrolyte solution was periodically sampled from the working electrode compartment and titrated with the stock solution of $Ce(SO_4)_2$ in 0.5 M H_2SO_4 for UV-vis spectrophotometric detection of the produced H_2O_2.

Detailed calculations of cumulative H_2O_2 concentration, H_2O_2 yield, Faradaic efficiency, and average catalyst leaching rate are described in the Appendix 3.

3.5.8 Electro-Fenton Degradation of Model Organic Pollutant

Electron-Fenton degradation tests were conducted in a two-compartment three-electrode H-cell (same as bulk electrolysis experiments) using Rhodamine B (RhB) (≥95%) as a model organic pollutant and *o*-$CoSe_2$/CFP (~370 $\mu g_{Co}/cm^2_{geo}$; ~1 cm^2_{geo}) as the working cathode which was operated at the constant potential of 0.5 V vs. RHE. O_2-saturated acidified 0.5 M Na_2SO_4 (pH 2.85) was used as the electrolyte solution to maintain the optimal acidic pH for the Fenton's reaction. Both RhB (20 or 40 mg/L) and Fe^{2+} (0.5 mM) were added only to the electrolyte solution in the working electrode compartment which was vigorous stirred (1200 rpm). During each electro-Fenton degradation test, a small aliquot of electrolyte solution was periodically sampled from the working electrode compartment and quantitatively diluted with the stock solution of acidified 0.5 M Na_2SO_4 (pH 2.85) for UV-vis spectrophotometric determination of the organic dye concentration.

3.6 References

1. List N: Disinfectants for Use Against SARS-CoV-2. U.S. Environmental Protection Agency. https://www.epa.gov/pesticide-registration/list-n-disinfectants-use-against-sars-cov-2 (accessed April 14, 2020).

2. Ciriminna, R.; Albanese, L.; Meneguzzo, F.; Pagliaro, M. Hydrogen peroxide: A key chemical for today's sustainable development. *ChemSusChem* **9**, 3374-3381 (2016).

3. Campos-Martin, J. M.; Blanco-Brieva, G.; Fierro, J. L. G. Hydrogen peroxide synthesis: An outlook beyond the anthraquinone process. *Angew. Chem. Int. Ed.* ***45***, 6962-6984 (2006).

4. Yang, S.; Verdaguer-Casadevall, A.; Arnarson, L.; Silvioli, L.; Čolić, V.; Frydendal, R.; Rossmeisl, J.; Chorkendorff, I.; Stephens, I. E. L. Toward the decentralized electrochemical production of H2O2: A focus on the catalysis. *ACS Catal.* ***8***, 4064-4081 (2018).

5. Jiang, Y.; Ni, P.; Chen, C.; Lu, Y.; Yang, P.; Kong, B.; Fisher, A.; Wang, X. Selective electrochemical H2O2 production through two-electron oxygen electrochemistry. *Adv. Energy Mater.* ***8***, 1801909 (2018).

6. Perry, S. C.; Pangotra, D.; Vieira, L.; Csepei, L.-I.; Sieber, V.; Wang, L.; Ponce de León, C.; Walsh, F. C. Electrochemical synthesis of hydrogen peroxide from water and oxygen. *Nat. Rev. Chem.* ***3***, 442-458 (2019).

7. Qiang, Z.; Chang, J.-H.; Huang, C.-P. Electrochemical generation of hydrogen peroxide from dissolved oxygen in acidic solutions. *Water Res.* ***36***, 85-94 (2002).

8. Edwards, J. K.; Freakley, S. J.; Lewis, R. J.; Pritchard, J. C.; Hutchings, G. J. Advances in the direct synthesis of hydrogen peroxide from hydrogen and oxygen. *Catal. Today* ***248***, 3-9 (2015).

9. Freakley, S. J.; He, Q.; Harrhy, J. H.; Lu, L.; Crole, D. A.; Morgan, D. J.; Ntainjua, E. N.; Edwards, J. K.; Carley, A. F.; Borisevich, A. Y.; Kiely, C. J.; Hutchings, G. J. Palladium-tin catalysts for the direct synthesis of H2O2 with high selectivity. *Science* ***351***, 965 (2016).

10. Chu, S.; Cui, Y.; Liu, N. The path towards sustainable energy. *Nat. Mater.* ***16***, 16-22 (2017).

11. Seh, Z. W.; Kibsgaard, J.; Dickens, C. F.; Chorkendorff, I.; Nørskov, J. K.; Jaramillo, T. F. Combining theory and experiment in electrocatalysis: Insights into materials design. *Science* ***355***, eaad4998 (2017).

12. Murray, A. T.; Voskian, S.; Schreier, M.; Hatton, T. A.; Surendranath, Y. Electrosynthesis of hydrogen peroxide by phase-transfer catalysis. *Joule* ***3***, 2942-2954 (2019).

13. Lu, Z.; Chen, G.; Siahrostami, S.; Chen, Z.; Liu, K.; Xie, J.; Liao, L.; Wu, T.; Lin, D.; Liu, Y.; Jaramillo, T. F.; Nørskov, J. K.; Cui, Y. High-efficiency oxygen reduction to hydrogen peroxide catalysed by oxidized carbon materials. *Nat. Catal.* ***1***, 156-162 (2018).

14. Kim, H. W.; Ross, M. B.; Kornienko, N.; Zhang, L.; Guo, J.; Yang, P.; McCloskey, B. D. Efficient hydrogen peroxide generation using reduced graphene oxide-based oxygen reduction electrocatalysts. *Nat. Catal.* ***1***, 282-290 (2018).

15. Xia, C.; Xia, Y.; Zhu, P.; Fan, L.; Wang, H. Direct electrosynthesis of pure aqueous H2O2 solutions up to 20% by weight using a solid electrolyte. *Science* ***366***, 226 (2019).

16. Hasché, F.; Oezaslan, M.; Strasser, P.; Fellinger, T.-P. Electrocatalytic hydrogen peroxide formation on mesoporous non-metal nitrogen-doped carbon catalyst. *J. Energy Chem.* ***25***, 251-257 (2016).

17. Iglesias, D.; Giuliani, A.; Melchionna, M.; Marchesan, S.; Criado, A.; Nasi, L.; Bevilacqua, M.; Tavagnacco, C.; Vizza, F.; Prato, M.; Fornasiero, P. N-doped graphitized carbon nanohorns as a forefront electrocatalyst in highly selective O2 reduction to H2O2. *Chem* ***4***, 106-123 (2018).

18. Sun, Y.; Sinev, I.; Ju, W.; Bergmann, A.; Dresp, S.; Kühl, S.; Spöri, C.; Schmies, H.; Wang, H.; Bernsmeier, D.; Paul, B.; Schmack, R.; Kraehnert, R.; Roldan Cuenya, B.; Strasser, P. Efficient electrochemical hydrogen peroxide production from molecular oxygen on nitrogen-doped mesoporous carbon catalysts. *ACS Catal.* ***8***, 2844-2856 (2018).

19. Sun, Y.; Silvioli, L.; Sahraie, N. R.; Ju, W.; Li, J.; Zitolo, A.; Li, S.; Bagger, A.; Arnarson, L.; Wang, X.; Moeller, T.; Bernsmeier, D.; Rossmeisl, J.; Jaouen, F.; Strasser, P. Activity–selectivity trends in the electrochemical production of hydrogen peroxide over single-site metal–nitrogen–carbon catalysts. *J. Am. Chem. Soc.* ***141***, 12372-12381 (2019).

20. Jiang, K.; Back, S.; Akey, A. J.; Xia, C.; Hu, Y.; Liang, W.; Schaak, D.; Stavitski, E.; Nørskov, J. K.; Siahrostami, S.; Wang, H. Highly selective oxygen reduction to hydrogen peroxide on transition metal single atom coordination. *Nat. Commun.* ***10***, 3997 (2019).

21. Jung, E.; Shin, H.; Lee, B.-H.; Efremov, V.; Lee, S.; Lee, H. S.; Kim, J.; Hooch Antink, W.; Park, S.; Lee, K.-S.; Cho, S.-P.; Yoo, J. S.; Sung, Y.-E.; Hyeon, T. Atomic-level tuning of Co–N–C catalyst for high-performance electrochemical H2O2 production. *Nat. Mater.* ***19***, 436-442 (2020).

22. Gao, J.; Yang, H. b.; Huang, X.; Hung, S.-F.; Cai, W.; Jia, C.; Miao, S.; Chen, H. M.; Yang, X.; Huang, Y.; Zhang, T.; Liu, B. Enabling direct H2O2 production in acidic media through rational design of transition metal single atom catalyst. *Chem* ***6***, 658-674 (2020).

23. Tang, C.; Jiao, Y.; Shi, B.; Liu, J.-N.; Xie, Z.; Chen, X.; Zhang, Q.; Qiao, S. Coordination tunes selectivity: Two-electron oxygen reduction on high-loading molybdenum single-atom catalysts. *Angew. Chem. Int. Ed.* ***59***, 2-8).

24. Brillas, E.; Sirés, I.; Oturan, M. A. Electro-Fenton process and related electrochemical technologies based on Fenton's reaction chemistry. *Chem. Rev.* ***109***, 6570-6631 (2009).

25. Brillas, E.; Garcia-Segura, S. Benchmarking recent advances and innovative technology approaches of Fenton, photo-Fenton, electro-Fenton, and related processes: A review on the relevance of phenol as model molecule. *Sep. Purif. Technol.* ***237***, 116337 (2020).

26. Siahrostami, S.; Verdaguer-Casadevall, A.; Karamad, M.; Deiana, D.; Malacrida, P.; Wickman, B.; Escudero-Escribano, M.; Paoli, E. A.; Frydendal, R.; Hansen, T. W.; Chorkendorff, I.; Stephens, I. E. L.; Rossmeisl, J. Enabling direct H2O2 production through rational electrocatalyst design. *Nat. Mater.* ***12***, 1137-1143 (2013).

27. Verdaguer-Casadevall, A.; Deiana, D.; Karamad, M.; Siahrostami, S.; Malacrida, P.; Hansen, T. W.; Rossmeisl, J.; Chorkendorff, I.; Stephens, I. E. L. Trends in the electrochemical synthesis of H2O2: Enhancing activity and selectivity by electrocatalytic site engineering. *Nano Lett.* ***14***, 1603-1608 (2014).

28. Sheng, H.; Hermes, E. D.; Yang, X.; Ying, D.; Janes, A. N.; Li, W.; Schmidt, J. R.; Jin, S. Electrocatalytic production of H2O2 by selective oxygen reduction using earth-abundant cobalt pyrite (CoS2). *ACS Catal.* ***9***, 8433-8442 (2019).

29. Kong, D.; Wang, H.; Lu, Z.; Cui, Y. CoSe2 nanoparticles grown on carbon fiber paper: An efficient and stable electrocatalyst for hydrogen evolution reaction. *J. Am. Chem. Soc.* ***136***, 4897-4900 (2014).

30. Zhang, X.-L.; Hu, S.-J.; Zheng, Y.-R.; Wu, R.; Gao, F.-Y.; Yang, P.-P.; Niu, Z.-Z.; Gu, C.; Yu, X.; Zheng, X.-S.; Ma, C.; Zheng, X.; Zhu, J.-F.; Gao, M.-R.; Yu, S.-H. Polymorphic cobalt diselenide as extremely stable electrocatalyst in acidic media via a phase-mixing strategy. *Nat. Commun.* ***10***, 5338 (2019).

31. Faber, M. S.; Dziedzic, R.; Lukowski, M. A.; Kaiser, N. S.; Ding, Q.; Jin, S. High-performance electrocatalysis using metallic cobalt pyrite (CoS2) micro- and nanostructures. *J. Am. Chem. Soc.* ***136***, 10053-10061 (2014).

32. Cabán-Acevedo, M.; Stone, M. L.; Schmidt, J. R.; Thomas, J. G.; Ding, Q.; Chang, H.-C.; Tsai, M.-L.; He, J.-H.; Jin, S. Efficient hydrogen evolution catalysis using ternary pyrite-type cobalt phosphosulphide. *Nat. Mater.* ***14***, 1245-1251 (2015).

33. Liu, W.; Hu, E.; Jiang, H.; Xiang, Y.; Weng, Z.; Li, M.; Fan, Q.; Yu, X.; Altman, E. I.; Wang, H. A highly active and stable hydrogen evolution catalyst based on pyrite-structured cobalt phosphosulfide. *Nat. Commun.* ***7***, 10771 (2016).

34. The Materials Project. https://materialsproject.org/ (accessed April 14, 2020).

35. Singh, A. K.; Zhou, L.; Shinde, A.; Suram, S. K.; Montoya, J. H.; Winston, D.; Gregoire, J. M.; Persson, K. A. Electrochemical stability of metastable materials. *Chem. Mater.* ***29***, 10159-10167 (2017).

36. Zhao, W.-W.; Bothra, P.; Lu, Z.; Li, Y.; Mei, L.-P.; Liu, K.; Zhao, Z.; Chen, G.; Back, S.; Siahrostami, S.; Kulkarni, A.; Nørskov, J. K.; Bajdich, M.; Cui, Y. Improved oxygen reduction reaction activity of nanostructured CoS2 through electrochemical tuning. *ACS Appl. Energy Mater.* ***2***, 8605-8614 (2019).

37. Vinogradova, O.; Krishnamurthy, D.; Pande, V.; Viswanathan, V. Quantifying confidence in DFT-predicted surface Pourbaix diagrams of transition-metal electrode–electrolyte interfaces. *Langmuir* ***34***, 12259-12269 (2018).

38. Hansen, H. A.; Rossmeisl, J.; Nørskov, J. K. Surface Pourbaix diagrams and oxygen reduction activity of Pt, Ag and Ni(111) surfaces studied by DFT. *Phys. Chem. Chem. Phys.* ***10***, 3722-3730 (2008).

39. Nørskov, J. K.; Rossmeisl, J.; Logadottir, A.; Lindqvist, L.; Kitchin, J. R.; Bligaard, T.; Jónsson, H. Origin of the overpotential for oxygen reduction at a fuel-cell cathode. *J. Phys. Chem. B* ***108***, 17886-17892 (2004).

40. Viswanathan, V.; Hansen, H. A.; Rossmeisl, J.; Nørskov, J. K. Unifying the 2e– and 4e– reduction of oxygen on metal surfaces. *J. Phys. Chem. Lett.* ***3***, 2948-2951 (2012).

41. Kulkarni, A.; Siahrostami, S.; Patel, A.; Nørskov, J. K. Understanding catalytic activity trends in the oxygen reduction reaction. *Chem. Rev.* ***118***, 2302-2312 (2018).

42. Ford, D. C.; Nilekar, A. U.; Xu, Y.; Mavrikakis, M. Partial and complete reduction of O2 by hydrogen on transition metal surfaces. *Surf. Sci.* ***604***, 1565-1575 (2010).

43. Chen, P.; Xu, K.; Tao, S.; Zhou, T.; Tong, Y.; Ding, H.; Zhang, L.; Chu, W.; Wu, C.; Xie, Y. Phase-transformation engineering in cobalt diselenide realizing enhanced catalytic activity for hydrogen evolution in an alkaline medium. *Adv. Mater.* ***28***, 7527-7532 (2016).

44. Butala, M. M.; Doan-Nguyen, V. V. T.; Lehner, A. J.; Göbel, C.; Lumley, M. A.; Arnon, S.; Wiaderek, K. M.; Borkiewicz, O. J.; Chapman, K. W.; Chupas, P. J.; Balasubramanian, M.; Seshadri, R. Operando Studies Reveal Structural Evolution with Electrochemical Cycling in Li–CoS2. *J. Phys. Chem. C* ***122***, 24559-24569 (2018).

45. Zhu, Y.; Chen, H.-C.; Hsu, C.-S.; Lin, T.-S.; Chang, C.-J.; Chang, S.-C.; Tsai, L.-D.; Chen, H. M. Operando Unraveling of the Structural and Chemical Stability of P-Substituted CoSe2 Electrocatalysts toward Hydrogen and Oxygen Evolution Reactions in Alkaline Electrolyte. *ACS Energy Lett.* ***4***, 987-994 (2019).

46. Pizzutilo, E.; Kasian, O.; Choi, C. H.; Cherevko, S.; Hutchings, G. J.; Mayrhofer, K. J. J.; Freakley, S. J. Electrocatalytic synthesis of hydrogen peroxide on Au-Pd nanoparticles: From fundamentals to continuous production. *Chem. Phys. Lett.* ***683***, 436-442 (2017).

47. Choi, C. H.; Kim, M.; Kwon, H. C.; Cho, S. J.; Yun, S.; Kim, H.-T.; Mayrhofer, K. J. J.; Kim, H.; Choi, M. Tuning selectivity of electrochemical reactions by atomically dispersed platinum catalyst. *Nat. Commun.* ***7***, 10922 (2016).

48. Yang, S.; Kim, J.; Tak, Y. J.; Soon, A.; Lee, H. Single-atom catalyst of platinum supported on titanium nitride for selective electrochemical reactions. *Angew. Chem. Int. Ed.* ***55***, 2058-2062 (2016).

49. Shen, R.; Chen, W.; Peng, Q.; Lu, S.; Zheng, L.; Cao, X.; Wang, Y.; Zhu, W.; Zhang, J.; Zhuang, Z.; Chen, C.; Wang, D.; Li, Y. High-concentration single atomic Pt sites on Hollow CuSx for selective O2 reduction to H2O2 in acid solution. *Chem* **5**, 2099-2110 (2019).

50. Zhang, J.; Sasaki, K.; Sutter, E.; Adzic, R. R. Stabilization of platinum oxygen-reduction electrocatalysts using gold clusters. *Science* ***315***, 220 (2007).

51. Kibsgaard, J.; Gorlin, Y.; Chen, Z.; Jaramillo, T. F. Meso-structured platinum thin films: Active and stable electrocatalysts for the oxygen reduction reaction. *J. Am. Chem. Soc.* ***134***, 7758-7765 (2012).

52. Brillas, E.; Calpe, J. C.; Casado, J. Mineralization of 2,4-D by advanced electrochemical oxidation processes. *Water Res.* ***34***, 2253-2262 (2000).

53. Brillas, E.; Mur, E.; Sauleda, R.; Sànchez, L.; Peral, J.; Domènech, X.; Casado, J. Aniline mineralization by AOP's: anodic oxidation, photocatalysis, electro-Fenton and photoelectro-Fenton processes. *Appl. Catal. B: Environ.* ***16***, 31-42 (1998).

54. Oturan, M. A.; Peiroten, J.; Chartrin, P.; Acher, A. J. Complete destruction of p-nitrophenol in aqueous medium by electro-Fenton method. *Environ. Sci. Technol.* ***34***, 3474-3479 (2000).

55. Yuan, S.; Fan, Y.; Zhang, Y.; Tong, M.; Liao, P. Pd-catalytic in situ generation of H2O2 from H2 and O2 produced by water electrolysis for the efficient electro-Fenton degradation of Rhodamine B. *Environ. Sci. Technol.* ***45***, 8514-8520 (2011).

56. Kresse, G.; Hafner, J. Ab initio molecular dynamics for liquid metals. *Phys. Rev. B* ***47***, 558-561 (1993).

57. Kresse, G.; Hafner, J. Ab initio molecular-dynamics simulation of the liquid-metal--amorphous-semiconductor transition in germanium. *Phys. Rev. B* ***49***, 14251-14269 (1994).

58. Kresse, G.; Furthmüller, J. Efficiency of ab-initio total energy calculations for metals and semiconductors using a plane-wave basis set. *Comput. Mater. Sci.* ***6***, 15-50 (1996).

59. Kresse, G.; Furthmüller, J. Efficient iterative schemes for ab initio total-energy calculations using a plane-wave basis set. *Phys. Rev. B* ***54***, 11169-11186 (1996).

60. Bahn, S. R.; Jacobsen, K. W. An object-oriented scripting interface to a legacy electronic structure code. *Comput. Sci. Eng.* ***4***, 56-66 (2002).

61. Blöchl, P. E. Projector augmented-wave method. *Phys. Rev. B* ***50***, 17953-17979 (1994).

62. Kresse, G.; Joubert, D. From ultrasoft pseudopotentials to the projector augmented-wave method. *Phys. Rev. B* ***59***, 1758-1775 (1999).

63. Perdew, J. P.; Burke, K.; Ernzerhof, M. Generalized gradient approximation made simple. *Phys. Rev. Lett.* ***77***, 3865-3868 (1996).

64. Perdew, J. P.; Burke, K.; Ernzerhof, M. Generalized gradient approximation made simple [Phys. Rev. Lett. 77, 3865 (1996)]. *Phys. Rev. Lett.* ***78***, 1396-1396 (1997).

65. Grimme, S.; Antony, J.; Ehrlich, S.; Krieg, H. A consistent and accurate ab initio parametrization of density functional dispersion correction (DFT-D) for the 94 elements H-Pu. *J. Chem. Phys.* ***132***, 154104 (2010).

66. Anisimov, V. I.; Zaanen, J.; Andersen, O. K. Band theory and Mott insulators: Hubbard U instead of Stoner I. *Phys. Rev. B* ***44***, 943-954 (1991).

67. Wu, X.; Han, S.; He, D.; Yu, C.; Lei, C.; Liu, W.; Zheng, G.; Zhang, X.; Lei, L. Metal organic framework derived Fe-doped CoSe2 incorporated in nitrogen-doped carbon hybrid for efficient hydrogen evolution. *ACS Sustain. Chem. Eng.* ***6***, 8672-8678 (2018).

68. Mathew, K.; Sundararaman, R.; Letchworth-Weaver, K.; Arias, T. A.; Hennig, R. G. Implicit solvation model for density-functional study of nanocrystal surfaces and reaction pathways. *J. Chem. Phys.* ***140***, 084106 (2014).

69. Mathew, K.; Hennig, R. G.; Bértoli, J.: henniggroup/VASPsol: VASPsol Solvation Module V1.0 (Version V1.0). Zenodo, 2019.

70. Monkhorst, H. J.; Pack, J. D. Special points for Brillouin-zone integrations. *Phys. Rev. B* ***13***, 5188-5192 (1976).

71. Alchagirov, A. B.; Perdew, J. P.; Boettger, J. C.; Albers, R. C.; Fiolhais, C. Energy and pressure versus volume: Equations of state motivated by the stabilized jellium model. *Phys. Rev. B* ***63***, 224115 (2001).

72. Henkelman, G.; Uberuaga, B. P.; Jónsson, H. A climbing image nudged elastic band method for finding saddle points and minimum energy paths. *J. Chem. Phys.* ***113***, 9901-9904 (2000).

73. Henkelman, G.; Jóhannesson, G.; Jónsson, H.: Methods for finding saddle points and minimum energy paths. In *Theoretical Methods in Condensed Phase Chemistry*; Schwartz, S. D., Ed.; Kluwer Academic Publishers, 2002; Vol. 5; pp 269-302.

74. Henkelman, G.; Jónsson, H. A dimer method for finding saddle points on high dimensional potential surfaces using only first derivatives. *J. Chem. Phys.* ***111***, 7010-7022 (1999).

75. Heyden, A.; Bell, A. T.; Keil, F. J. Efficient methods for finding transition states in chemical reactions: Comparison of improved dimer method and partitioned rational function optimization method. *J. Chem. Phys.* ***123***, 224101 (2005).

76. Kästner, J.; Sherwood, P. Superlinearly converging dimer method for transition state search. *J. Chem. Phys.* ***128***, 014106 (2008).

77. NIST Chemistry WebBook. https://webbook.nist.gov/cgi/cbook.cgi?ID=C7722841&Mask=10#Solubility (accessed April 14, 2020).

78. Ravel, B.; Newville, M. ATHENA, ARTEMIS, HEPHAESTUS: data analysis for X-ray absorption spectroscopy using IFEFFIT. *J. Synchrotron Radiat.* ***12***, 537-541 (2005).

CHAPTER 4

Linear Paired Electrochemical Valorization of Glycerol Enabled by the Electro-Fenton Process Using a Stable $NiSe_2$ Cathode*

4.1 Abstract

Electrochemical valorization of surplus biomass-derived feedstocks such as glycerol into high-value chemicals offers a sustainable route for utilizing biomass resources and decarbonizing chemical manufacturing; however, glycerol is typically valorized solely via anodic oxidation, with lower-value products such as hydrogen gas generated at cathode. Here, we establish the efficient cathodic valorization of glycerol to the desirable C_3 products via the electro-Fenton process at a stable $NiSe_2$ cathode, built upon the theoretical understanding of $NiSe_2$'s high selectivity and stability toward acidic H_2O_2 electrosynthesis fully supported by experiments. A proof-of-concept linear paired electrochemical process for concurrently valorizing glycerol into the same oxidation products at both $NiSe_2$ cathode and Pt anode achieves high selectivity for value-added C_3 products and high glycerol conversion with little external energy input needed, and an unbiased system can be anticipated upon future optimization. This conceptual strategy of linear pairing is generalizable for enabling atom-efficient electro-refinery of diverse biomass-derived feedstocks.

---

* This chapter will be submitted for future publication, in collaboration with Aurora N. Janes, R. Dominic Ross, Heike Hofstetter, J. R. Schmidt, and Song Jin.

4.2 Introduction

Harnessing solar and wind generated electricity for electrochemical synthesis of high-value chemicals from biomass feedstocks offers a sustainable alternative to conventional chemical manufacturing from fossil fuels[1-3]. Glycerol is a byproduct of the rapidly growing biodiesel production and has become a surplus biomass-derived chemical[4] with a low price of 0.17 $/kg[5]. Oxidative upgrading of glycerol is very attractive[6-8], because all C_3 and C_2 oxidation products have higher economic values than glycerol[7-9]. Compared to thermal oxidation that requires high temperature and oxygen pressure, electrochemical oxidation[9] poses several advantages including near-ambient operation, less reagent waste, and distributed small-scale production[3,8].

Electrochemical oxidation of glycerol typically occurs at catalytic anodes containing noble metals[10-13] or earth-abundant metals[14-16], which is paired with either four-electron oxygen reduction reaction ($4e^-$ ORR) in a fuel cell[9,17] or hydrogen evolution reaction (HER) in an electrolytic cell[9,18] (Scheme 4.1a). In either case, the chemicals generated at cathode have lower economic values (e.g., ~1 $/kg for H_2 from steam methane reforming[19]) than the glycerol-derived chemicals generated at anode [e.g., ~150 $/kg for dihydroxyacetone (DHA)[7,20]]. Recently, anodic glycerol oxidation has been paired with CO_2[21] or CO[22] reduction reaction (CO_2/CORR) that generates C_1 and/or C_{2+} products at cathode[23] (Scheme 4.1a), but the different cathode and anode feeds lead to different product portfolios between the two half-cells with additional system complexity and separation cost. Using glycerol as the sole feed in a linear paired electrochemical system[3,24-26] to produce the same value-added oxidation products at both cathode and anode simultaneously could be appealing.

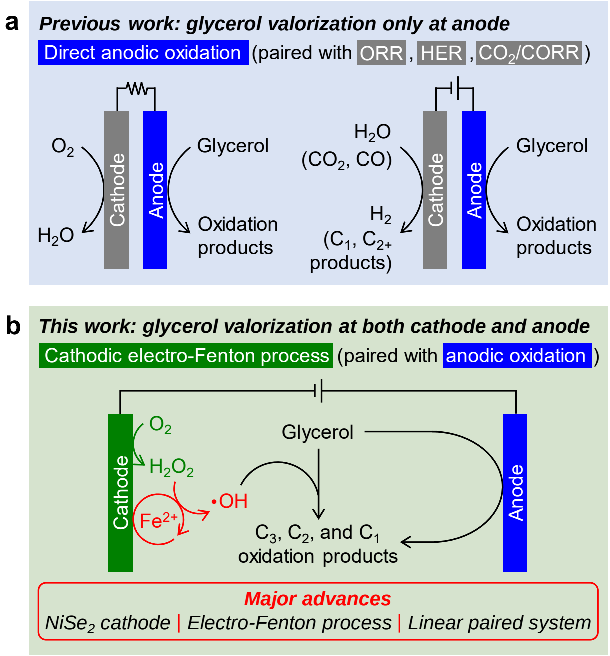

Scheme 4.1. Comparison of different pairing strategies for electrochemical valorization of glycerol.

(**a**) In previous work, anodic oxidation of glycerol is paired either with 4e$^-$ ORR in a fuel cell or with HER or CO_2/CORR in an electrolytic cell. (**b**) In this work, cathodic valorization of glycerol enabled by the electro-Fenton process at a stable $NiSe_2$ cathode is further linear paired with the anodic oxidation to concurrently produce the same glycerol-derived oxidation products at both cathode and anode.

Linear paired electrochemical valorization of glycerol requires a cathodic reaction that can generate oxidative species to oxidize glycerol. Hydrogen peroxide (H_2O_2) is an oxidant (E^o = 1.76 V vs. SHE) that can be cathodically generated via the selective 2e$^-$ ORR ($O_2 + 2\ H^+ + 2\ e^- \rightarrow H_2O_2$)[27,28], and be further converted into the even more oxidizing hydroxyl radical ($\cdot OH$, E^o = 2.80 V vs. SHE) by the Fe^{2+}-mediated electro-Fenton process in acidic solutions ($Fe^{2+} + H_2O_2 + H^+ \rightarrow Fe^{3+} + H_2O + \cdot OH$) where Fe^{2+} is regenerated at the H_2O_2-generating cathode ($Fe^{3+} + e^- \rightarrow Fe^{2+}$)[29]. The deployment of electro-Fenton process has been largely limited to environmental pollutant removal[29], but chemically generated ·OH from H_2O_2 has found use in biomass-to-chemical processes[30] such as carbohydrate oxidation[31,32] and lignin depolymerization[33]. These works suggest it might be possible to utilize electro-Fenton process for electrochemical oxidation of glycerol to value-added products. However, robust, inexpensive, and selective $2e^-$ ORR electrocatalysts to produce H_2O_2 under slightly acidic conditions are needed for enabling efficient electro-Fenton process.

Here, we present the first systematic investigation of cathodic valorization of glycerol via the electro-Fenton process, and the further linear pairing with the anodic oxidation to concurrently produce the same glycerol-derived oxidation products at both cathode and anode (Scheme 4.1b). This is made possible by the discovery of a stable and earth-abundant $NiSe_2$ electrocatalyst for the selective $2e^-$ ORR and electro-Fenton process in acidic solutions. Building on the recent developments of transition metal compounds[34,35] as selective $2e^-$ ORR catalysts that are more cost-effective than noble metals[36] and more catalytically active than carbon-based materials in acidic solution[37], we combine theory and experiment to elucidate the origins of $NiSe_2$'s high selectivity toward acidic $2e^-$ ORR and excellent stability against surface oxidative leaching. $NiSe_2$ cathode operated at the optimum potential for H_2O_2 bulk electrosynthesis enables the efficient glycerol valorization in the cathodic half-cell, with high glycerol conversion and high selectivity for valuable C_3 products achieved. Finally, a new linear paired electrochemical system comprising of $NiSe_2$ cathode and Pt anode for efficient concurrent glycerol valorization to C_3 products is demonstrated under a marginal external applied bias.

4.3 Results and Discussion

4.3.1 Identifying *c*-NiSe₂ Catalyst for the Electro-Fenton Process

The Fe^{2+}-mediated electro-Fenton process operates at an optimum pH of ~3[29] and poses more stringent requirements for catalyst stability than $2e^-$ ORR because ·OH is more oxidizing than H_2O_2. Therefore, an electrocatalyst that is not only selective for acidic $2e^-$ ORR but also stable in the presence of strong oxidants such as H_2O_2 and ·OH is needed. We utilized the calculated bulk Pourbaix diagrams available from the Materials Project[38] to identify promising earth-abundant catalyst candidates with high aqueous electrochemical stability in the pH and potential ranges of interest for acidic $2e^-$ ORR. Compared to cubic pyrite-type $CoSe_2$ (*c*-$CoSe_2$, Figure 4.1a, left), an acidic $2e^-$ ORR catalyst with demonstrated stability[35], cubic $NiSe_2$ (*c*-$NiSe_2$, Figure 4.1a, right) exhibits an even wider electrochemical stability window (Figure A4.1 in the Appendix 4). Therefore, $NiSe_2$ could be a promising cathode catalyst for the electro-Fenton process.

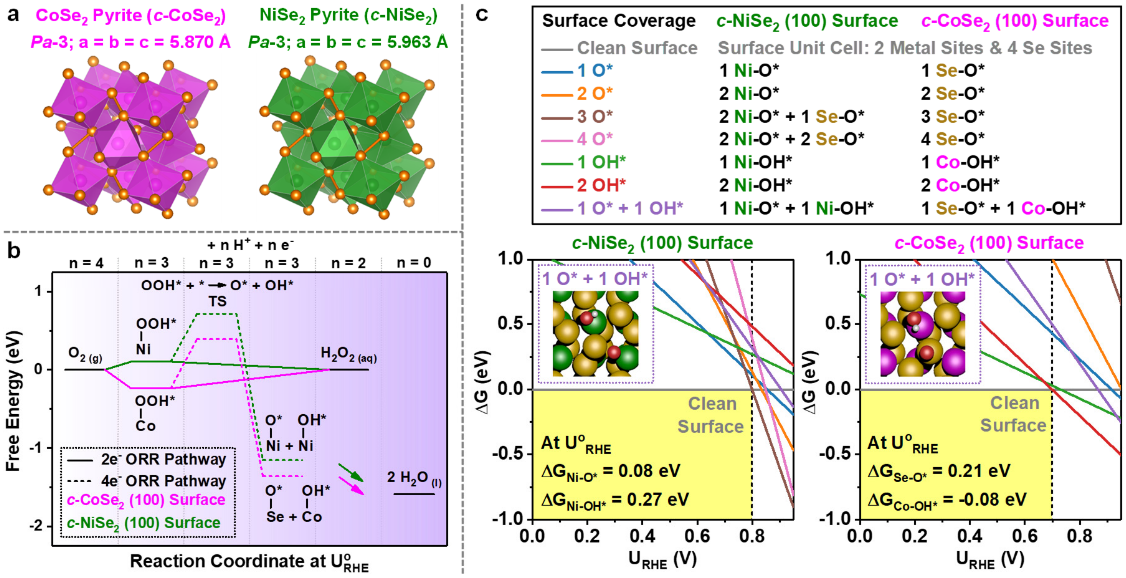

Figure 4.1. Computational assessments of the ORR energetics and the surface stability of *c*-$NiSe_2$ (in comparison with *c*-$CoSe_2$).

(**a**) Crystal structures of *c*-$NiSe_2$ and *c*-$CoSe_2$. (**b**) Calculated free energy diagrams of the $2e^-$ vs. $4e^-$ ORR pathway on the *c*-$NiSe_2$ vs. *c*-$CoSe_2$ (100) surface at U^o_{RHE}. (**c**) Different coverages of O* and/or OH* (top) and comparisons of their free energies (bottom) on the *c*-$NiSe_2$ vs. *c*-$CoSe_2$ (100) surface in equilibrium with water. For *c*-$NiSe_2$, Ni is the preferential binding site for both OH* and O*. For *c*-$CoSe_2$, Co is the preferential binding site for OH*, and Se is the preferential binding site for O*. The binding energies (ΔG) of O* and OH* on their preferential binding sites at U^o_{RHE} are shown as the bottom insets in panel c. The yellow shaded regions indicate the potential range where the adsorbate-free clean surface is lower in free energy compared to the O*- and/or OH*-adsorbed surfaces. The inset images show the co-adsorption of one O* and one OH* to their preferential binding sites on the surface unit cell comprising of two metal sites and four Se sites. The Ni, Co, Se, O, and H atoms are displayed in green, magenta, orange, red, and white, respectively.

The promise of *c*-$NiSe_2$ as an active and selective $2e^-$ ORR catalyst is revealed by the calculated free energy diagrams of the ORR energetics on the most thermodynamically stable (100) surface (Figure 4.1b). The $2e^-$ ORR (Figure 4.1b, solid traces) proceeds via the adsorption of OOH* ($O_{2(g)} + * + H^+ + e^- \rightarrow OOH*$, where * is the unoccupied surface binding site) followed by its desorption to form H_2O_2 ($OOH* + H^+ + e^- \rightarrow H_2O_{2(aq)} + *$). At the calculated standard equilibrium potential of $2e^-$ ORR (U^o_{RHE}), the preferential binding of OOH* to the Ni site on *c*-$NiSe_2$ is relatively weak (endothermic by 0.10 eV), whereas the Co site on *c*-$CoSe_2$ preferentially binds to OOH* more strongly (exothermic by 0.24 eV)[35]. Thus, *c*-$NiSe_2$ is expected to be not only active for $2e^-$ ORR as the OOH* adsorption is nearly thermoneutral at U^o_{RHE}, but also selective toward $2e^-$ (vs. $4e^-$) ORR because it is situated on the weak OOH* binding leg of the $2e^-$ ORR volcano[36]. In contrast, *c*-$CoSe_2$ is situated on the strong OOH* binding leg. Furthermore, the $2e^-$

ORR selectivity is also kinetically governed by the resistance to the O-O bond cleavage in OOH*, which leads to the competing 4e$^-$ ORR (Figure 4.1b, dashed traces). We reasoned that the OOH* dissociation on pyrite-type structures likely proceeds via a dinuclear pathway across two neighboring metal sites (OOH* + * → O* + OH*)[34]. But this pathway features a high activation barrier of 0.61 eV (0.63 eV) on *c*-$NiSe_2$ (*c*-$CoSe_2$) and is kinetically disfavored due to the large spacing between the neighboring metal sites separated by diselenide anions. Thus, computational assessments of ORR pathways suggest that *c*-$NiSe_2$ should be active and selective for 2e$^-$ ORR.

The surface stability of *c*-$NiSe_2$ under aqueous electrochemical environments is evaluated by considering O* and/or OH* adsorbate formation when the surface is in equilibrium with water. Unlike *c*-$CoSe_2$ where O* and OH* preferentially bind to Se (Se-O*) and Co (Co-OH*), respectively, Ni on *c*-$NiSe_2$ is the preferential binding site for both O* (Ni-O*) and OH* (Ni-OH*). On a surface unit cell comprising of two metal sites and four Se sites, should O* builds up on the *c*-$NiSe_2$ surface, a significant O* coverage would have to be reached (which is unlikely because O* binds to Ni endothermically by 0.08 eV at U^{o}_{RHE}) before any O* would bind to Se; however, any presence of O* on *c*-$CoSe_2$ would bind to Se immediately (Figure 4.1c, top). Since one possible degradation pathway of pyrite-type structures is the oxidation of dichalcogenide anions followed by the dissolution of metal cations (Figure A4.1), the low affinity of O* to Se on *c*-$NiSe_2$ could lead to an increased resistance to surface oxidation. In addition, OH* binds to Ni more strongly (endothermic by 0.27 eV) than to Co (exothermic by 0.08 eV) at U^{o}_{RHE}, which allows the *c*-$NiSe_2$ surface to stay clean and mostly free of adsorbate over a wider range of potentials compared to the *c*-$CoSe_2$ surface (Figure 4.1c, bottom). Note that O* and OH* can also form during ORR if the O-O bond cleavage occurs (Figure 4.1b). Therefore, these surface adsorbate analyses suggest *c*-$NiSe_2$ should be more resistant to surface oxidation and degradation under aqueous environments and ORR operating conditions.

4.3.2 Electrocatalytic Properties and Stability of *c*-$NiSe_2$ for Acidic $2e^-$ ORR

We synthesized nanostructured *c*-$NiSe_2$ (Figure A4.2) via a hydrothermal method, and examined the acidic $2e^-$ ORR catalytic properties of the powder sample by drop-casting on a rotating ring-disk electrode (RRDE) (see Methods and Materials for details). We also synthesized nanostructured *c*-$CoSe_2$ catalyst as a comparison (Figure A4.3). RRDE experiments were performed with various catalyst loadings that resulted in similar ranges of double-layer capacitances (C_{dl}) between these two catalysts (Figure A4.4) for fair comparisons. In O_2-saturated 0.05 M H_2SO_4 (pH ~1.2), *c*-$NiSe_2$ exhibits high H_2O_2 selectivity (up to 95%) and relatively little dependence on overpotential and catalyst loading (Figure 4.2a and 4.2b, left). In contrast, although *c*-$CoSe_2$ is more catalytically active toward $2e^-$ ORR, the H_2O_2 selectivity decreases more dramatically with increasing overpotential and catalyst loading (Figure 4.2a and 4.2b, right). Such differences between the H_2O_2 selectivity profiles of *c*-$NiSe_2$ and *c*-$CoSe_2$ are also observed at pH ~2.8 in O_2-saturated 0.1 M $NaHSO_4$/Na_2SO_4 buffer (Figure A4.5 and A4.6), further showing that *c*-$NiSe_2$ is more selective toward acidic $2e^-$ ORR than *c*-$CoSe_2$.

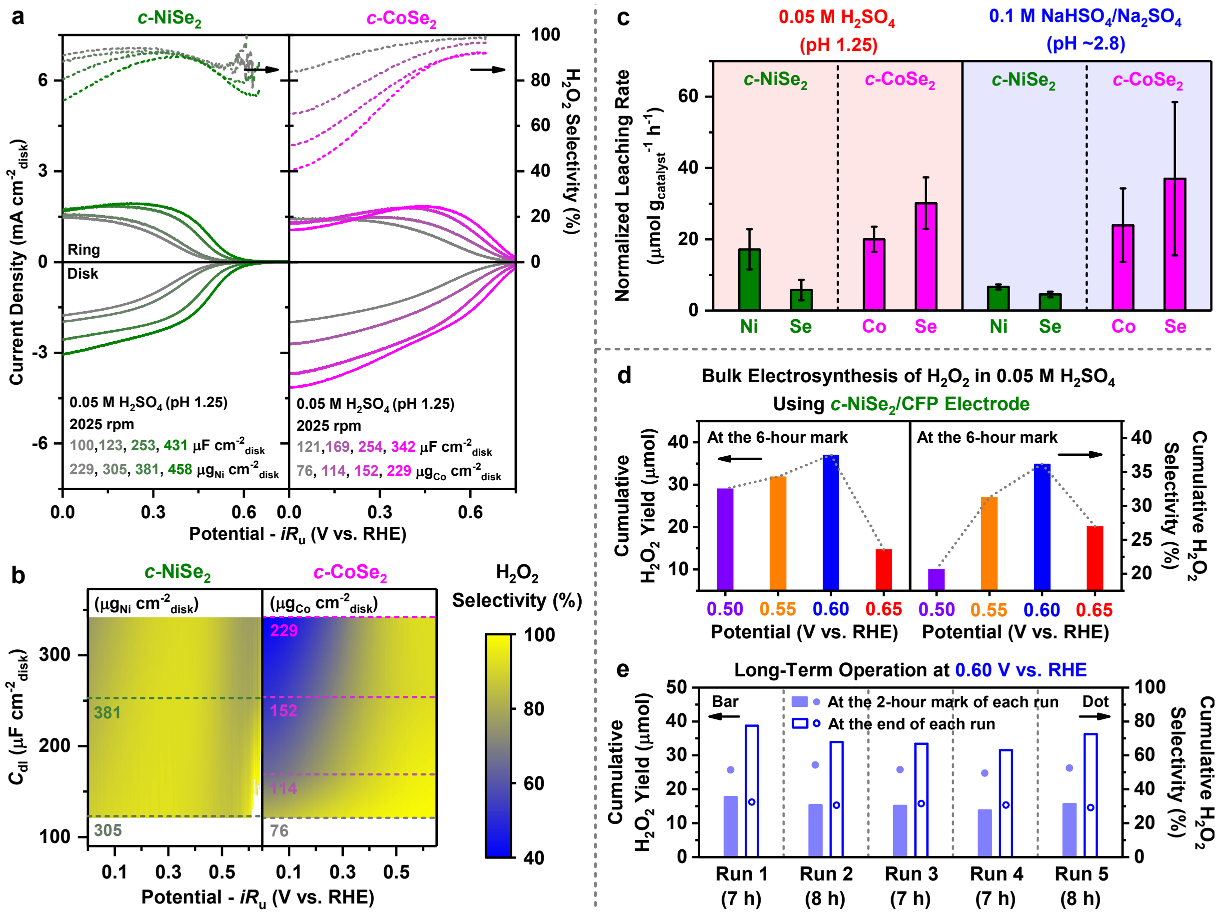

Figure 4.2. The electrocatalytic properties and stability of *c*-NiSe₂ (in comparison with *c*-CoSe₂) for acidic 2e⁻ ORR and the bulk electrosynthesis of H_2O_2.

(**a**) RRDE voltammograms recorded at 2025 rpm and (**b**) the H_2O_2 selectivity profile of drop-casted *c*-$NiSe_2$ (left) and *c*-$CoSe_2$ (right) catalysts with various catalyst loadings in O_2-saturated 0.05 M H_2SO_4 (pH ~1.2). (**c**) Normalized metal and selenium leaching rates of drop-casted *c*-$NiSe_2$ and *c*-$CoSe_2$ catalysts during RRDE stability tests in O_2-saturated 0.05 M H_2SO_4 (pH ~1.2, left) and 0.1 M $NaHSO_4/Na_2SO_4$ buffer (pH ~2.8, right). For each catalyst, the error bars result from four RRDE stability tests at different catalyst loadings (Table A4.1). (**d**) The cumulative H_2O_2 yield (left) and H_2O_2 selectivity (right) after 6 hours for four trials of H_2O_2 bulk electrosynthesis in O_2-saturated 0.05 M H_2SO_4 (4 mL, stirred at 1200 rpm) using four $NiSe_2$/CFP electrodes (~1.06

mg_{Ni} cm^{-2}_{geo}, ~1 cm^{2}_{geo}) operated at different fixed applied potentials (0.50, 0.55, 0.60, 0.65 V vs. RHE) (see details in Figure A4.13). (**e**) Long-term (37 hours) sustained bulk electrosynthesis of H_2O_2 in O_2-saturated 0.05 M H_2SO_4 at the optimum potential of 0.60 V vs. RHE using one $NiSe_2$/CFP electrode repeatedly for five consecutive runs (see details in Figure A4.16).

The stability of *c*-$NiSe_2$ (vs. *c*-$CoSe_2$) catalyst for acidic $2e^-$ ORR was evaluated by long-term RRDE stability tests at various catalyst loadings. The catalyst stability is monitored by tracking the disk potential at a certain disk current density (j_{disk}) or peroxide current density ($j_{peroxide}$) (Figure A4.7). The stable disk potential throughout the tests shows that *c*-$NiSe_2$ exhibits a higher catalyst stability than *c*-$CoSe_2$ at both pH ~1.2 (0.05 M H_2SO_4) and pH ~2.8 (0.1 M $NaHSO_4$/Na_2SO_4) (Figure A4.8 and A4.9). The spent catalysts show no obvious structural and compositional change (Figure A4.10). We further performed elemental analyses of the spent electrolytes to quantify the leaching rates of metal and selenium from the catalysts normalized by the catalyst masses (μmol $g_{catalyst}^{-1}$ h^{-1}). The ratio between the Co and Se leaching rates of the less stable *c*-$CoSe_2$ is close to the 1:2 stoichiometry (Figure 4.2c and Table A4.1). This suggests the leaching of *c*-$CoSe_2$ could be initiated by the surface oxidation of Se_2^{2-} to the readily soluble SeO_x due to the preferential affinity of O* to its Se site (Figure 4.1c), followed by the near-stoichiometric dissolution of Co^{2+} from the surface. In contrast, the Se leaching from the more stable *c*-$NiSe_2$ is not only much more suppressed compared to *c*-$CoSe_2$, but also slower than the Ni leaching (Figure 4.2c). These suggest the leaching of *c*-$NiSe_2$ could mainly result from the preferential adsorption of O* and OH* to its Ni site (Figure 4.1c) and the subsequent acid-base reaction with the electrolyte to dissolve Ni^{2+}. This hypothesis could be supported by the slower leaching of *c*-$NiSe_2$ under the less acidic pH of ~2.8 (Figure 4.2c), and future studies will be helpful for confirming the catalyst leaching mechanisms. These in-depth catalyst leaching studies demonstrate the enhanced stability of *c*-$NiSe_2$ for acidic $2e^-$ ORR.

4.3.3 Bulk Electrosynthesis of H_2O_2 in Acidic Solution Using *c*-$NiSe_2$ Cathode

We further performed constant-potential bulk electrosynthesis using integrated electrodes of *c*-$NiSe_2$ nanosheets directly grown on carbon fiber paper ($NiSe_2$/CFP, Figure A4.11) to accumulate H_2O_2 in O_2-saturated 0.05 M H_2SO_4 in a two-compartment three-electrode H-cell (Figure A4.12) at various applied potentials ranging from 0.50 to 0.65 V vs. RHE (Figure 4.2d and Figure A4.13). Both the cumulative H_2O_2 yield and selectivity after 6 hours of bulk electrosynthesis are potential-dependent, and peak at the optimum potential of 0.60 V vs. RHE (Figure 4.2d). Cyclic voltammograms recorded before and after each electrosynthesis trial suggest additional cathodic current is generated on $NiSe_2$/CFP after the accumulation of H_2O_2 in the bulk solution (Figure A4.13), likely due to the electroreduction of the produced H_2O_2 to water as the Faradaic side reaction.

To understand the potential-dependent bulk electrosynthesis of H_2O_2 on $NiSe_2$/CFP, we studied the side reaction of H_2O_2 electroreduction in competition with $2e^-$ ORR on *c*-$NiSe_2$ catalyst drop-casted on RRDE. In 0.05 M H_2SO_4, the catalytic onset potential of H_2O_2 electroreduction on *c*-$NiSe_2$ coincides with that of $2e^-$ ORR, and the rate of H_2O_2 electroreduction increases with higher overpotential and H_2O_2 concentration (Figure A4.14a). Therefore, as H_2O_2 concentration builds up, the net rate of H_2O_2 production (i.e., the production rate minus the electroreduction rate of H_2O_2) on *c*-$NiSe_2$ is positive only in a certain potential range and displays a parabolic trend peaking at an optimum potential (Figure A4.14b). Similarly, H_2O_2 electroreduction also occurs on *c*-$CoSe_2$ but it affects the net rate of H_2O_2 production less because *c*-$CoSe_2$ exhibits a more positive catalytic onset potential for $2e^-$ ORR (Figure A4.14 and Figure 4.2a). A similar parabolic trend in the net rate of H_2O_2 production on *c*-$NiSe_2$ is observed in 0.1 M $NaHSO_4/Na_2SO_4$ buffer at pH ~2.8 (Figure A4.15). These results show the importance of taking into account H_2O_2 electroreduction and operating $NiSe_2$/CFP at the optimum applied potential for H_2O_2 bulk electrosynthesis.

We demonstrated the sustained bulk electrosynthesis of H_2O_2 in O_2-saturated 0.05 M H_2SO_4 at the optimum 0.60 V vs. RHE using one $NiSe_2$/CFP electrode repeatedly for five consecutive runs over 37 hours (Figure 4.2e). Since the cathodic current on $NiSe_2$/CFP gradually increased over time because of the electroreduction of the accumulated H_2O_2, we replaced the catholyte with fresh H_2O_2-free electrolyte between runs to maintain the steady net production of H_2O_2 (Figure A4.16). Over the initial 2-hour period of each run, the $NiSe_2$/CFP electrode consistently accumulated 203 ± 10 ppm H_2O_2 and produced 15.4 ± 1.4 μmol H_2O_2 with a cumulative H_2O_2 selectivity of 51.8 ± 1.8% with no obvious decay (Figure 4.2e and A4.16). A higher H_2O_2 yield of 34.8 ± 2.8 μmol and a higher accumulated concentration of 661 ± 53 ppm were achieved over a longer period of 7.4 ± 0.5 hours at the end of each run, but with a lower H_2O_2 selectivity of 30.8 ± 1.2% (Figure 4.2e and A4.16). $NiSe_2$/CFP shows a similar H_2O_2 bulk electrosynthesis performance in O_2-saturated 0.1 M $NaHSO_4/Na_2SO_4$ buffer at pH ~2.8 (Figure A4.17). The spent $NiSe_2$/CFP electrode is structurally and compositionally stable after H_2O_2 bulk electrosynthesis (Figure A4.18). These experiments also suggest that the unavoidable electroreduction of H_2O_2 could limit the maximum accumulated concentration of H_2O_2 and the overall selectivity achievable using these new earth-abundant electrocatalysts, however, the electro-Fenton process of converting H_2O_2 to $\cdot OH$ may allow us to utilize the produced H_2O_2 as an oxidant more efficiently by circumventing the undesired H_2O_2 electroreduction to water.

4.3.4 Glycerol Valorization via the Electro-Fenton Process at *c*-$NiSe_2$ Cathode

To enable glycerol valorization by the electro-Fenton process, we operated $NiSe_2$/CFP cathode at the fixed potential of 0.60 V vs. RHE in O_2-saturated 0.1 M $NaHSO_4/Na_2SO_4$ buffer (pH ~2.8) containing glycerol and Fe^{2+}. The balanced equation shows that cathodic glycerol conversion consumes protons (Figure 4.3a). To maintain the proton balance and stabilize the acidic pH in the cathodic half-cell, it is critical to place 0.05 M H_2SO_4 in the anode compartment to solely transport protons through the Nafion membrane (Figure A4.19). We used proton and carbon-13 nuclear magnetic resonance (^1H and ^{13}C NMR) to identify and quantify the many possible C_3, C_2, and C_1 products that can be sequentially formed from the oxidation of glycerol (Figure 4.3b, details of NMR in Figure A4.20 and A4.21). Control experiments show that the electrogenerated H_2O_2 itself is not capable of oxidizing glycerol without the presence of Fe^{2+} (Figure A4.22), which confirms that the electro-Fenton process is indeed responsible for glycerol valorization at the cathode.

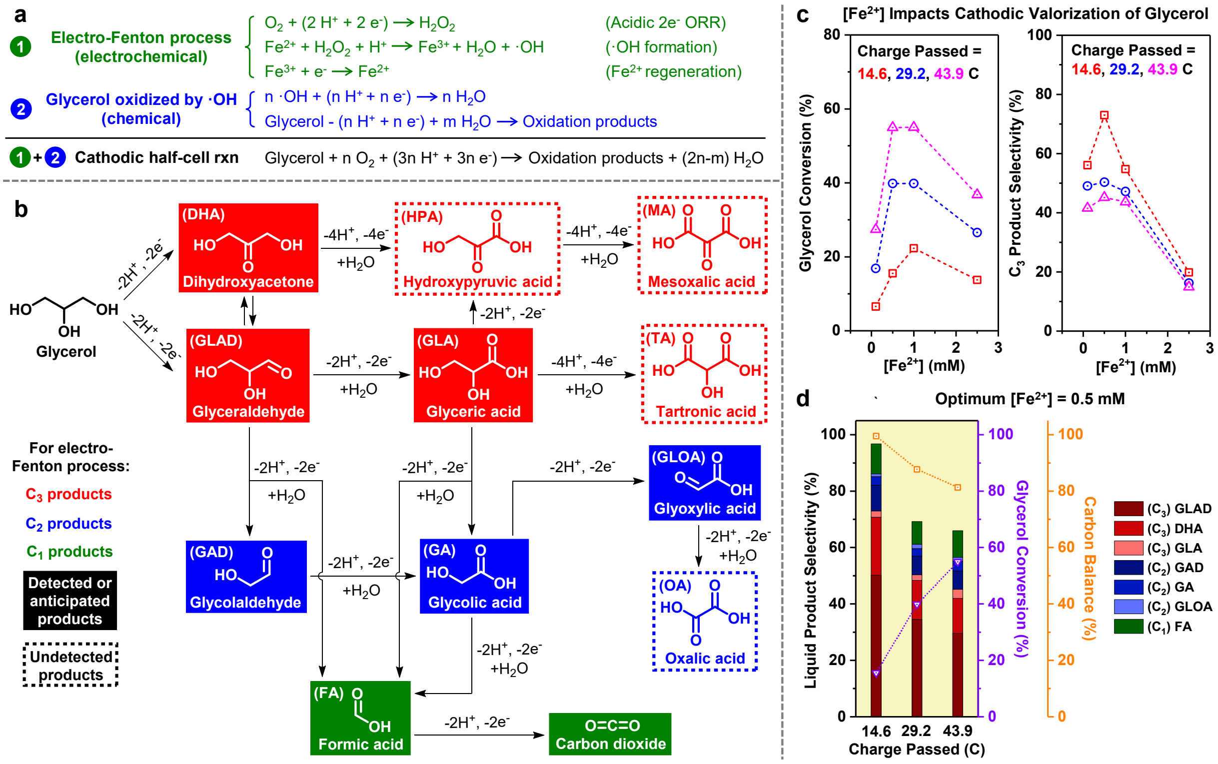

Figure 4.3. Glycerol valorization enabled by the electro-Fenton process on $NiSe_2$/CFP in the cathodic half-cell.

(**a**) Balanced equation of cathodic glycerol valorization, which suggests proton consumption. (**b**) Possible reaction pathways of glycerol oxidation into various C_3, C_2, and C_1 products by the electro-Fenton process at $NiSe_2$/CFP cathode. The detected (or anticipated) and undetected products are labeled based on NMR analyses. (**c**) Glycerol conversion (left) and the selectivity toward all detected C_3 products (right) as a function of $[Fe^{2+}]$ (0.1, 0.5, 1.0, or 2.5 mM) after passing a controlled amount of charge through $NiSe_2$/CFP cathode in O_2-saturated 0.1 M $NaHSO_4$/Na_2SO_4 buffer (pH ~2.8) starting with ~50 mM glycerol (see details in Figure A4.23 and A4.24). (**d**) Liquid product selectivity, glycerol conversion percentage, and carbon balance of all detected liquid products for cathodic valorization of glycerol (~50 mM) under the optimum $[Fe^{2+}]$ of 0.5 mM.

We further studied the impact of Fe^{2+} concentration ($[Fe^{2+}]$) on the glycerol valorization via the electro-Fenton process starting with ~50 mM glycerol in O_2-saturated 0.1 M $NaHSO_4/Na_2SO_4$ buffer (pH ~2.8). The rate of ·OH formation from the Fenton reaction should increase with higher $[Fe^{2+}]$ based on the rate law, but too much Fe^{2+} would consume the formed ·OH and decrease the oxidizing power ($Fe^{2+} + \cdot OH + H^+ \rightarrow Fe^{3+} + H_2O$).[29] After a controlled amount of charge is passed through $NiSe_2$/CFP cathode at 0.60 V vs. RHE (Figure A4.23), high glycerol conversion is achieved when $[Fe^{2+}]$ is 0.5 mM or 1.0 mM, while too little Fe^{2+} (0.1 mM) results in low glycerol conversion likely due to the slow ·OH formation (Figure 4.3c, left). On the other hand, the selectivity toward all detected C_3 products [glyceraldehyde (GLAD), dihydroxyacetone (DHA), glyceric acid (GLA)] remain relatively high when $[Fe^{2+}]$ is 1.0 mM or below but decreases substantially when $[Fe^{2+}]$ is increased to 2.5 mM (Figure 4.3c, right). One possible explanation is that at high $[Fe^{2+}]$, the high ·OH formation rate increases the relative concentration of ·OH to glycerol locally near the cathode, driving the glycerol oxidation further to primarily C_2 [glycolaldehyde (GAD), glycolic acid (GA), glyoxylic acid (GLOA)] and C_1 [formic acid (FA)] products (Figure A4.24). This could also explain the relatively low glycerol conversion when $[Fe^{2+}]$ is 2.5 mM despite the fast ·OH formation rate (Figure 4.3c, left). Overall, we identified 0.5 mM as the optimum $[Fe^{2+}]$ to concurrently achieve high glycerol conversion and high C_3 product selectivity for cathodic valorization of glycerol (Figure 4.3d and Table A4.2). As the glycerol conversion proceeds further with more charge passed, the C_3 product selectivity decreases due to the sequential oxidation of intermediate products, and the loss in the carbon balance of all detected liquid products likely results from the oxidation of FA to gaseous CO_2 undetectable by NMR (vide infra). The spent $NiSe_2$/CFP cathode was shown to be structurally and compositionally stable after the electro-Fenton process (Figure A4.25).

4.3.5 Pairing the Electro-Fenton Process with Anodic Oxidation for Glycerol Valorization

To valorize glycerol at both cathode and anode in a linear paired fashion, anodic glycerol oxidation needs to operate in acidic solution to match with the pH requirement of the electro-Fenton process. We prepared the anode by drop-casting commercial Pt/C catalyst[12,13] on carbon fiber paper. This paired electrochemical system needs to operate in a two-compartment H-cell (Figure 4.4a) rather than in an undivided cell because the O_2 needed for the electro-Fenton process can undergo the undesirable ORR on the Pt/C anode[39]. Therefore, anodic glycerol oxidation was performed in an Ar-saturated H_2SO_4 solution containing 50 mM glycerol, so that protons were solely transported through the Nafion membrane (Figure 4.4a) and stabilized the pH of the catholyte (O_2-saturated $NaHSO_4$/Na_2SO_4 buffer containing 50 mM glycerol and 0.5 mM Fe^{2+}, pH ~2.8) where the electro-Fenton process took place.

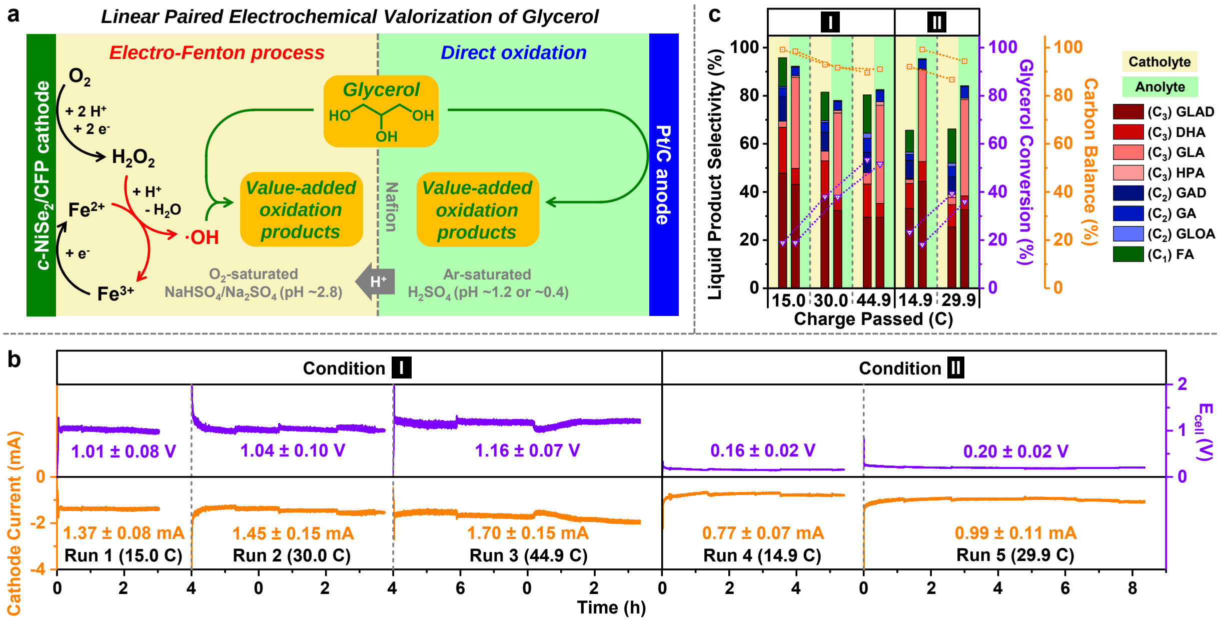

Figure 4.4. Linear paired electrochemical valorization of glycerol via the electro-Fenton process at $NiSe_2$/CFP cathode and oxidation at Pt/C anode.

(**a**) Schematic illustration and working principle of the linear paired system in a two-compartment H-cell (see details in Figure A4.27). (**b**) The cathode current and cell voltage (E_{cell}) over time, which shows the steady operation of the linear paired system comprising of a $NiSe_2$/CFP cathode (~1.24 mg_{Ni} $cm^{-2}{}_{geo}$, ~1 $cm^2{}_{geo}$) operated at 0.60 V vs. RHE in O_2-saturated $NaHSO_4$/Na_2SO_4 buffer (pH ~2.8, containing ~50 mM glycerol and 0.5 mM Fe^{2+}) and a Pt/C anode (~2 mg_{Pt} $cm^{-2}{}_{geo}$, ~1 $cm^2{}_{geo}$) operated in Ar-saturated H_2SO_4 solution (containing ~50 mM glycerol). The E_{cell} and current are influenced by different supporting electrolyte concentrations (Condition I: 0.1 M $NaHSO_4$/Na_2SO_4 for catholyte, and 0.05 M H_2SO_4 for anolyte; Condition II: 0.5 M $NaHSO_4$/Na_2SO_4 for catholyte, and 0.5 M H_2SO_4 for anolyte). (**c**) Liquid product selectivity, glycerol conversion, and carbon balance of glycerol valorization after paired electrolyses under different supporting electrolyte conditions (I and II, as described in panel b).

Anodic glycerol oxidation glycerol at Pt/C anode in 0.05 M H_2SO_4 (pH ~1.2) was first evaluated in the half-cell without linear pairing (Figure A4.26). To mimic the operation of the paired system, we applied a constant current of 1.7 mA (Figure A4.26c) to approximately match with the current on $NiSe_2$/CFP cathode in the electro-Fenton half-cell studies (Figure A4.23a). After a controlled amount of charge was passed, the applied potential of Pt/C anode was relatively stable around 0.55 V vs. RHE, and glycerol was selectively oxidized into C_3 products [GLAD, DHA, GLA, hydroxypyruvic acid (HPA)] with very small quantities of C_2 (GA) and C_1 (FA) products (Figure A4.26e and Table A4.2). The anodic half-cell studies show the viability of valorizing glycerol in a linear paired electrochemical system that theoretically could operate at a negligible cell voltage (<50 mV) with little external energy input needed if the internal resistance is negligible (Note A4.1).

We then demonstrated the proof-of-concept linear paired electrochemical valorization of glycerol by feeding glycerol in both cathode and anode compartments of the H-cell where $NiSe_2$/CFP cathode was operated at 0.60 V vs. RHE and Pt/C anode matched the current (Figure A4.27). With 0.1 M $NaHSO_4$/Na_2SO_4 (pH ~2.8) catholyte and 0.05 M H_2SO_4 (pH ~1.2) anolyte, the paired system operated steadily at a cell voltage around 1 V (Figure 4.4b, Condition I), and the product distributions in the catholyte and anolyte (Figure 4.4c, Condition I) resembled the respective half-cell studies under similar conditions closely (vide supra). This cell voltage is higher than the theoretical value due to the large solution IR drop between the anode and the reference electrode located on opposite sides of the membrane (Figure A4.28a and Note A4.2). When a higher supporting electrolyte concentration of 0.5 M was applied for both catholyte and anolyte, the paired system operated at a much lower cell voltage below 0.2 V (Figure 4.4b, Condition II) due to the greatly decreased solution IR drop at the anode (Figure A4.28b). After a controlled amount of charge was passed, the product distributions in the anolyte were mostly unaffected by this higher supporting electrolyte concentration (Figure 4.4c, Condition II), whereas the detected liquid products in the catholyte decreased in quantities (see possible explanations in Note A4.3). The C_3 product selectivity in both catholyte and anolyte of the paired system decreased with increasing glycerol conversion (Figure 4.4c) due to the sequential oxidation of intermediate products, similar to the respective half-cell studies (vide supra). Since FA was detected as a late-stage oxidation product in both catholyte and anolyte (Table A4.3), control experiments suggested that both the electro-Fenton process and the anodic oxidation could further oxidize FA into gaseous CO_2 (Figure A4.29), which may account for the loss in the carbon balance of all detected liquid products in both catholyte and anolyte (Note A4.4). Finally, we note that the residual redundant cell voltage of 0.2 V for this paired system appears to be mostly caused by the internal resistance.

By employing zero-gap cell designs involving membrane electrode assemblies to lower the ohmic overpotential and by designing more active cathode and anode electrocatalysts to lower the activation overpotentials further, we believe that paired electrochemical systems for glycerol valorization that need no external bias and no external energy input could be realized.

4.4 Conclusions

In summary, we demonstrated a new linear paired electrochemical process for concurrent glycerol valorization by the electro-Fenton process at a stable and earth-abundant $NiSe_2$ cathode and the direct oxidation at a Pt anode. This process is enabled by the development of $NiSe_2$ as a highly selective and stable $2e^-$ ORR catalyst for H_2O_2 production in acidic solution, which is elucidated by calculated free energy diagrams and surface adsorbate analyses and experimentally shown with RRDE and catalyst leaching studies together with sustained bulk electrosynthesis of H_2O_2 using integrated cathode of $NiSe_2$ catalyst grown on carbon fiber paper. At the optimum operating potential of 0.60 V vs. RHE, the electro-Fenton process at $NiSe_2$ cathode led to efficient cathodic glycerol valorization and achieved high selectivity toward valuable C_3 oxidation products and high glycerol conversion. The linear paired system resulted in similar glycerol conversion and product selectivity to the respective half-cell studies, and can operate at a very small cell voltage below 0.2 V after adjusting the supporting electrolyte condition, which could theoretically be made into an unbiased system after further optimization in the future. The design principles for stable and selective cathode catalysts for acidic H_2O_2 production and the electro-Fenton process, and the conceptual strategy of linear pairing the electro-Fenton process with anodic oxidation presented here can open up new opportunities for electrochemical valorization of a variety of biomass feedstocks with high atom efficiency and low energy cost.

4.5 Methods and Materials

4.5.1 Computational Method

Spin polarized electronic structure calculations were performed using the Vienna Ab initio Simulation package (VASP)[40-43] interfaced with the Atomic Simulation Environment (ASE)[44]. Projector augmented wave (PAW) pseudopotentials[45,46] with a cutoff of 450 eV were used to treat core electrons, and the Perdew–Burke–Ernzerhof (PBE) functional[47,48] was used to treat exchange and correlation. Dispersion was treated using Grimme's D3(ABC) method[49]. To better describe the Co 3d electrons in *c*-$CoSe_2$, a Hubbard U parameter[50], $U_{eff} = 2.0$ eV, was taken from a previous report[51]. A variety of Hubbard U parameters were tested for *c*-$NiSe_2$, and were found to have little to no effect on the geometries or energies; therefore, no Hubbard U parameter was used for this catalyst. Solvation effects were treated using the continuum solvent method VASPsol[52,53]. The Brillouin zone was sampled using a (10, 10, 10) and (10, 10, 1) Γ-centered Monkhorst–Pack mesh[54] for bulk and surface calculations, respectively. Lattice constants were determined by fitting to an equation of state (EOS)[55].

The (100) surfaces of *c*-$NiSe_2$ and *c*-$CoSe_2$ (with the respective lowest free energy) were modelled as a 1 × 1 unit cell slab with two repeats in the z-direction, leading to a total of 8 metal atoms and 16 Se atoms and a vacuum gap of at least 15 Å. The top half of the slabs was allowed to relax while the bottom half was frozen to simulate the bulk. For each ionic configuration, the electronic energy was converged below 10^{-6} eV. Both the clean slab and adsorbates were allowed to relax until the forces were converged below 0.005 eV $Å^{-2}$. Transition states were located using the nudged elastic band (NEB) method[56,57] and were refined using the dimer method[58-60]. All transition states were confirmed saddle points with one imaginary frequency corresponding to bond breaking.

Binding energies were calculated with respect to $O_{2(g)}$ and $H^+_{(aq)}$ and e^-. The energy of $H^+_{(aq)}$ and e^- was calculated using the computational hydrogen electrode (CHE) method[61], where $H^+_{(aq)}$ is assumed to be in thermodynamic equilibrium with $H_{2(g)}$. In order to avoid well-known errors in the DFT treatment of $O_{2(g)}$, the free energy of $O_{2(g)}$ was determined by matching the experimental standard equilibrium potential (1.229 V) of the reaction $1/2\ O_{2(g)} + 2\ H^+_{(aq)} + 2\ e^- \rightarrow H_2O_{(l)}$. The free energies of species were calculated using $G = H - T \cdot S$, where H is the enthalpy including zero-point energy (ZPE) and thermal corrections, and S is either the total experimental entropy at 298 K and 1 bar (for gas phase species) or calculated under the harmonic approximation (for surface bound species). The free energy of $H_2O_{(l)}$ was calculated using the experimental free energy of formation for $H_2O_{(l)}$ and $H_2O_{(g)}$. The solvation free energy of $H_2O_{2(aq)}$ was calculated using the experimental Henry's law constant[62]. The calculated standard equilibrium potential (U^{o}_{RHE}) of the 2e$^-$ ORR reaction $O_{2(g)} + 2\ H^+_{(aq)} + 2\ e^- \rightarrow H_2O_{2(aq)}$ is 0.81 V, slightly higher than the experimental standard equilibrium potential of 0.69 V.

Free energies of different surface adsorbate coverages were calculated to predict the most thermodynamically stable surface termination of each catalyst for a given set of potential and pH conditions under the assumption that the surfaces can be approximated in equilibrium with $H_2O_{(l)}$.[63,64] The equilibrated proton-coupled electron transfer reaction for a general surface intermediate can then be written as:

$$\text{X-O}_m\text{H}_n{}^* + (2m - n)\ (\text{H}^+ + \text{e}^-) \rightleftharpoons \text{X}^* + m\ \text{H}_2\text{O}$$

where X is the surface binding site, m is the number of oxygen atoms, and n is the number of hydrogen atoms. The free energy of this reaction can be written as:

$$\Delta G(\text{U,pH}) = G_{\text{S}^*} + m\ G_{\text{H}_2\text{O}} - G_{\text{X-O}_m\text{H}_n{}^*} - (2m - n)\ (G_{\text{e}^-} + G_{\text{H}^+})$$

Using the computational hydrogen electrode (CHE) method[61,65-67] ($G_{e^-} + G_{H^+} = ½G_{H_2} - U_{SHE} - 2.303k_B \cdot T \cdot pH$) and converting the standard hydrogen electrode (SHE) to the reversible hydrogen electrode (RHE) ($U_{RHE} = U_{SHE} + 2.303k_B \cdot T \cdot pH$), the free energy can be rewritten as a function of U_{RHE}:

$$\Delta G(U_{RHE}) = G_{S*} + m\, G_{H_2O} - G_{X\text{-}O_mH_n*} - (2m - n)\,(½G_{H_2} - U_{RHE})$$

A 1 × 1 unit cell slab of the (100) surface of each catalyst that has two metal binding sites and four Se binding sites was used to model intermediate surface coverages as a function of potential. For *c*-$NiSe_2$, the Ni site is the preferential binding site for both OH* and O*. For *c*-$CoSe_2$, the Co site is the preferential binding site for OH*, and the Se site is the preferential binding site for O*. A wide variety of surface coverages were examined on various combinations of binding sites. For the sake of clarity, only the most thermodynamically stable surface coverages (in the U_{RHE} range of 0 V to 0.95 V) on the most preferential combination of binding sites were shown in Figure 4.1c.

4.5.2 Chemicals

All chemicals were purchased from Sigma-Aldrich and used as received without further purification, unless noted otherwise. Deionized nanopure water (18.2 MΩ·cm) from Thermo Scientific Barnstead water purification systems was used for all experiments.

4.5.3 Materials Synthesis

c-$NiSe_2$ powder sample was prepared by a hydrothermal method. Following a procedure modified from a previous report[68], nickel hydroxide ($Ni(OH)_2$) precursor was first synthesized by dissolving 451.3 mg of $NiSO_4 \cdot 6H_2O$ (Acros Organics, 98+%) in 58.3 mL of water and 8.75 mL of 2 M ammonia aqueous solution (diluted from ammonium hydroxide solution, 28.0-30.0% NH_3 basis), and heating the solution at 180 °C for 24 h in a sealed 100-mL Teflon-lined stainless-steel autoclave. The resulting $Ni(OH)_2$ precursor was hydrothermally converted into *c*-$NiSe_2$ as follows: 4.29 g of NaOH (≥97.0%) and 571 mg of Se powder (≥99.5%) were suspended in 50 mL of water via sonication and heated at 220 °C for 24 h in a sealed 80-mL autoclave; upon cooling to room temperature, 35 mg of $Ni(OH)_2$ precursor was suspended in 10 mL of water and added dropwise into the Se-containing solution under vigorous stirring, and then heated at 180 °C for another 24 h in the same autoclave. The as-converted *c*-$NiSe_2$ product powder was successively washed with water, 1.25 M Na_2S (nonahydrate, ≥98.0%) aqueous solution (to dissolve the elemental Se impurity[69]), and water four times for each washing step, and dried under vacuum at 50 °C. To prepare $Ni(OH)_2$ precursor on carbon fiber paper ($Ni(OH)_2$/CFP), Teflon-coated carbon fiber paper (Fuel Cell Earth, TGP-H-060) was first treated with oxygen plasma at 150 W power for 5 min for each side and annealed in air at 700 °C for 5 min. A 3 cm × 6 cm piece of annealed CFP was placed in the solution made of 2.1 mmol of $Ni(NO_3)_2 \cdot 6H_2O$ (≥97.0%), 4.2 mmol of NH_4F (≥98.0%), and 10.5 mmol of urea (99.0-100.5%) in 80 mL of water, and heated at 110 °C for 5 h in a sealed 100-mL autoclave. $NiSe_2$/CFP was prepared by the same hydrothermal selenization method described above, except for using a 1.5 cm × 6 cm piece of $Ni(OH)_2$/CFP as the precursor. The as-converted $NiSe_2$/CFP was immersed in 1.25 M Na_2S aqueous solution for three times to remove any excess elemental Se, rinsed with water and ethanol, and dried under N_2 gas flow. The areal loading of *c*-$NiSe_2$ grown on CFP was determined by the mass change of CFP after the materials growth. The *c*-$CoSe_2$ powder sample was prepared from the published procedures[35]. All catalyst samples were stored in a glove box filled with Ar gas to minimize the exposure to air.

4.5.4 Materials Characterization

Powder X-ray diffraction (PXRD) patterns were collected on a Bruker D8 ADVANCE powder X-ray diffractometer using Cu Kα radiation. Scanning electron microscopy (SEM) was performed on a Zeiss SUPRA 55VP field emission scanning electron microscope at an accelerating voltage of 1 kV. For SEM imaging, powder samples were drop-casted onto silicon wafer substrates. X-ray photoelectron spectroscopy (XPS) was performed on a Thermo Scientific K-Alpha XPS system with an Al Kα X-ray source. Raman spectroscopy was performed on a Thermo Fisher Scientific DXR3xi Raman Imaging Microscope using a 50 μm confocal pinhole aperture and a 532 nm laser source and with a low laser power of 0.1 mW and an exposure time of 1.0 second to avoid sample degradation. For XPS and Raman experiments, powder samples were drop-casted onto graphite substrates, which were made by cutting thin slices of graphite rod (Graphite Store, low wear EDM rod), abrading with 600 grit silicon carbide paper (Allied High Tech Products), and sonicating in water and ethanol until clean. X-ray absorption spectroscopy (XAS) of $NiSe_2$/CFP before and after electrochemical testing was performed in transmission mode at the Advanced Photon Source (APS) Beamline 10-BM-B, and analyzed using ATHENA and ARTEMIS software[70].

4.5.5 Rotating Ring-Disk Electrode Measurement

RRDE measurements were conducted in an undivided three-electrode cell with a graphite rod counter electrode and a Hg/Hg_2SO_4 (saturated K_2SO_4) reference electrode (calibrated against a saturated calomel electrode) connected to a Bio-Logic VMP-300 multichannel potentiostat. The 0.05 M H_2SO_4 supporting electrolyte solution (pH ~1.2) was prepared from concentrated H_2SO_4 (95.0–98.0%); the 0.1 M $NaHSO_4/Na_2SO_4$ buffer solution (pH~2.8) was prepared by adjusting the pH of 0.1 M Na_2SO_4 (≥99.0%) using 0.1 M H_2SO_4. All potentials were reported versus RHE (E vs. RHE = E vs. SHE + 0.059 × pH). Prior to RRDE measurements, the electrolyte solution (40–45 mL) was purged with O_2 gas for >10 min and a blanket of O_2 gas was maintained above the electrolyte solution during the measurements. Under O_2-saturated condition, the catalyst-coated disk was first conditioned by running cyclic voltammetry (CV) between − 0.025 V and 0.75 V vs. RHE at 100 mV s^{-1} and 1600 rpm for 10 cycles, while holding the Pt ring at 1.3 V *vs.* RHE. The Pt ring was then conditioned by running CV between 0.05 V and 1.20 V vs. RHE at 100 mV s^{-1} and 1600 rpm for 10 cycles while holding the disk at 0.75 V vs. RHE to remove the surface PtO_x [71,72]. The $2e^-$ ORR catalytic properties were evaluated by performing linear sweep voltammetry of the catalyst-coated disk from 0.75 to − 0.025 V vs. RHE at 50 mV s^{-1} and various rotation rates, meanwhile holding the Pt ring at 1.3 V vs. RHE. Finally, the background current, double-layer capacitance (C_{dl}, determined by CV of the disk between − 0.025 V and 0.75 V vs. RHE at various scan rates and 0 rpm), and uncompensated resistance (R_u, determined by electrochemical impedance spectroscopy of the disk at 0.75 V vs. RHE) were measured under Ar-saturated conditions. By manually conducting background current and *iR* corrections, the H_2O_2 selectivity (p_{RRDE}) is calculated as follows:

$$p_{\mathrm{RRDE}}\,(\%) = \frac{2 \times \frac{i_{\mathrm{ring}}}{N}}{i_{\mathrm{disk}} + \frac{i_{\mathrm{ring}}}{N}} \times 100\%$$

where i_{disk} and i_{ring} are the respective disk and ring current, and N is the collection efficiency. For the ease of visualizing the H_2O_2 selectivity from RRDE voltammograms (Figure 4.2a), both disk and ring current densities (j_{disk} and j_{ring}) are normalized to the geometric area of the disk electrode (A_{disk}), and the ring current density is further adjusted by the collection efficiency:

$$j_{\mathrm{disk}} = \frac{i_{\mathrm{disk}}}{A_{\mathrm{disk}}}$$

$$j_{\mathrm{ring}} = \frac{i_{\mathrm{ring}}}{A_{\mathrm{disk}} \times N} = j_{\mathrm{peroxide}}$$

where j_{peroxide} is the partial current density for H_2O_2 production.

The protocols for long-term RRDE stability tests were described in Figure A4.7. After these stability tests, the spent catalysts were recovered from the disk electrode by sonicating in water and ultracentrifuging at 13200 rpm for 1 min, followed by re-dispersing in minimal amount of water and drop-casting onto graphite substrates for XPS and Raman characterization (vide supra). To monitor the catalyst leaching during these stability tests, the spent electrolyte solutions were filtered with 0.22-µm syringe filters (Restek) and then analyzed with inductively coupled plasma mass spectrometry (ICP-MS) measurements on an Agilent 8900 Triple Quadrupole ICP-MS spectrometer. ICP-MS standard solutions were prepared by dissolving $NiSO_4 \cdot 6H_2O$ (≥98%), or $CoSO_4 \cdot 7H_2O$ (≥99%), or SeO_2 (≥99.9%) in a matrix solution of 0.05 M H_2SO_4 (pH ~1.2) or 0.1 M $NaHSO_4/Na_2SO_4$ (pH ~2.8).

4.5.6 Bulk Electrosynthesis of H_2O_2

$NiSe_2$/CFP cathode (vide supra) was used for constant-potential bulk electrosynthesis of H_2O_2 in O_2-saturated 0.05 M H_2SO_4 (pH ~1.2) or 0.1 M $NaHSO_4/Na_2SO_4$ (pH ~2.8) solution (4 mL, stirred at 1200 rpm) placed in the cathode compartment of a two-compartment three-electrode H-cell (see Figure A4.12). Nafion 117 membrane (Fuel Cell Store) was cleaned by successively immersing in 3 wt% H_2O_2, water, 1 M H_2SO_4, and water at 80 °C for 1 h for each cleaning step, and stored in 0.05 M H_2SO_4 at room temperature before use. $NiSe_2$/CFP cathode was first conditioned by running CV between − 0.025 V and 0.75 V vs. RHE at 100 mV s^{-1} for 5 cycles to reach the steady state. Chronoamperometry was then performed at $NiSe_2$/CFP cathode for H_2O_2 bulk electrosynthesis, and the optimum operating potential was found to be 0.60 V vs. RHE (see Figure 4.2d) to maximize the H_2O_2 accumulation and minimize the undesired H_2O_2 electroreduction. A small aliquot (25 µL) of catholyte was periodically sampled during chronoamperometry and mixed with 8 mL of $Ce(SO_4)_2$ stock solution (~0.4 mM Ce^{4+} in 0.5 M

H_2SO_4 matrix solution) to chemically detect the produced H_2O_2 by UV-Vis spectrophotometry at 318 nm ($2\ Ce^{4+} + H_2O_2 \rightarrow 2\ Ce^{3+} + O_2 + 2\ H^+$). The concentration of the produced H_2O_2 can be calculated as follows:

$$[H_2O_2] = \frac{8\ \text{mL} \times [Ce^{4+}]_{\text{before}} - 8.025\ \text{mL} \times [Ce^{4+}]_{\text{after}}}{2 \times 0.025\ \text{mL}}$$

where $[H_2O_2]$ is the cumulative H_2O_2 concentration, $[Ce^{4+}]_{\text{before}}$ and $[Ce^{4+}]_{\text{after}}$ are the $[Ce^{4+}]$ in the stock solution (determined by fitting to the standard curve) before and after mixing with the catholyte aliquot. The cumulative H_2O_2 yield ($n_{H_2O_2}$), H_2O_2 selectivity ($p_{H_2O_2}$), and Faradaic efficiency (FE) are calculated based on $[H_2O_2]$, the catholyte volume (taking into account the evaporation), and the total amount of charge passed (Q_{total}) (see detailed methodology for these calculations described in our previous report^{35}):

$$p_{H_2O_2}\ (\%) = \frac{n_{H_2O_2}\ (\text{mol})}{n_{H_2O_2}(\text{mol}) + \frac{Q_{\text{total}}\ (\text{C}) - 2 \times n_{H_2O_2}\ (\text{mol})\ \times F}{4 \times F}} \times 100\%$$

$$\text{FE}\ (\%) = \frac{2 \times n_{H_2O_2}\ (\text{mol}) \times F}{Q_{\text{total}}\ (\text{C})} \times 100\%$$

where F is the Faraday constant (96485 C mol^{-1}). To monitor the catalyst leaching during H_2O_2 bulk electrosynthesis, the spent catholytes were filtered with 0.22-μm syringe filters (Restek) and diluted by 15 times with a matrix solution of 0.05 M H_2SO_4 for ICP-MS analysis (vide supra).

4.5.7 Glycerol Valorization and Product Analysis

All experiments of glycerol valorization were performed in the two-compartment three-electrode H-cell (vide supra). Half-cell studies of glycerol valorization via the electro-Fenton process at $NiSe_2$ cathode were performed by chronoamperometry with controlled amounts of charge passed at 0.60 V vs. RHE in O_2-saturated 0.1 M $NaHSO_4/Na_2SO_4$ solution (pH ~2.8) containing glycerol (~50 mM) and Fe^{2+} (0.1, 0.5, 1.0, or 2.5 mM, prepared from $FeSO_4 \cdot 7H_2O$, ≥99.0%) (see detailed experimental conditions in Figure A4.19). Half-cell studies of direct oxidation of glycerol at Pt/C anode were performed by chronopotentiometry with controlled amounts of charge passed at 1.7 mA in Ar-saturated 0.05 M H_2SO_4 solution (pH ~1.2) containing glycerol (~50 mM) (see detailed experimental conditions in Figure A4.26). Linear paired glycerol valorization at the $NiSe_2$ cathode (in O_2-saturated 0.1 M or 0.5 M $NaHSO_4/Na_2SO_4$ solution containing ~50 mM glycerol and 0.5 mM Fe^{2+}, pH ~2.8) and Pt/C anode (in Ar-saturated H_2SO_4 solution containing ~50 mM glycerol) was performed by operating the cathode via chronoamperometry at 0.60 V vs. RHE while recording the applied potential of the anode (see detailed experimental conditions in Figure A4.27). The analysis of the products from glycerol valorization was performed by ^1H and ^{13}C NMR spectroscopy on a Bruker AVANCE III 600 MHz NMR spectrometer. Glycerol (≥99.0%), DL-glyceraldehyde (≥90%), dihydroxyacetone (Pharmaceutical Secondary Standard; Certified Reference Material), DL-glyceric acid (TCI America, 20% in water, ca. 2 mol/L), β-hydroxypyruvic acid (≥95.0%), tartronic acid (Alfa Aesar, 98%), sodium mesoxalate monohydrate (≥98.0%), glycolaldehyde dimer (crystalline, mixture of stereoisomers), glycolic acid (99%), glyoxylic acid monohydrate (98%), oxalic acid (99.999%), and formic acid (≥98%) were individually prepared into NMR standard samples (500 μL) in Norell® Sample Vault Series™ NMR tubes (diam. × L 5 mm × 178 mm) using D_2O (99.9 atom % D) as the solvent and maleic acid (Standard for quantitative NMR, TraceCERT®) as the internal standard[15] (detailed ratios among the different components in these NMR samples are described in Figure A4.20 and A4.21). To achieve quantitative ^1H NMR results, the relaxation delay was set to 20 seconds (longer than 5 times of the T1 relaxation times of all compounds of interest determined by inversion recovery experiments), and the zgcppr.UW pulse sequence was used for the solvent suppression, and 4 scans were collected. For ^{13}C NMR results, the relaxation delay was set to 2 seconds, and 256 scans were collected. After the half-cell or linear-paired glycerol valorization experiments, the catholytes and/or anolytes of interest were filtered with 0.22-μm syringe filters (Restek) and prepared into NMR samples accordingly (detailed ratios among the different components in these NMR samples are described in Figure A4.22, A4.23, A4.24). The quantifications of $[\text{glycerol}]_i$, $[\text{glycerol}]_f$, and $[\text{C}_n\ \text{product}]_f$ are based on the selected ^{1}H NMR peak integration ratios relative to the maleic acid internal standard (see peak assignments and peak selections in Figure A4.20). The glycerol conversion, C_n product selectivity (n = 1, 2, 3), and carbon balance of all detected liquid products are calculated as follows:

$$\text{glycerol conversion (\%)} = \frac{[\text{glycerol}]_i \times V_i - [\text{glycerol}]_f \times V_f}{[\text{glycerol}]_i \times V_i} \times 100\%$$

$$\text{C}_n\ \text{product selectivity (\%)} = \frac{n}{3} \times \frac{[\text{C}_n\ \text{product}]_f \times V_f}{[\text{glycerol}]_i \times V_i - [\text{glycerol}]_f \times V_f} \times 100\%$$

$$\text{carbon balance (\%)} = \frac{3 \times [\text{glycerol}]_f \times V_f + \sum_{n=1}^{3} \{n \times [\text{C}_n\ \text{product}]_f \times V_f\}}{3 \times [\text{glycerol}]_i \times V_i} \times 100\%$$

where V_i and V_f are the initial and final electrolyte volume, $[\text{glycerol}]_i$ and $[\text{glycerol}]_f$ are the initial and final concentration of glycerol, $[\text{C}_n\ \text{product}]_f$ is the final concentration of C_n product (n = 1, 2, 3) (listed in Table A4.2 and A4.3).

4.6 References

1. Luna, P. D.; Hahn, C.; Higgins, D.; Jaffer, S. A.; Jaramillo, T. F.; Sargent, E. H. What would it take for renewably powered electrosynthesis to displace petrochemical processes? *Science* ***364***, eaav3506 (2019).

2. Tang, C.; Zheng, Y.; Jaroniec, M.; Qiao, S.-Z. Electrocatalytic Refinery for Sustainable Production of Fuels and Chemicals. *Angew. Chem. Int. Ed.* ***60***, 19572-19590 (2021).

3. Lucas, F. W. S.; Grim, R. G.; Tacey, S. A.; Downes, C. A.; Hasse, J.; Roman, A. M.; Farberow, C. A.; Schaidle, J. A.; Holewinski, A. Electrochemical Routes for the Valorization of Biomass-Derived Feedstocks: From Chemistry to Application. *ACS Energy Lett.* ***6***, 1205-1270 (2021).

4. Werpy, T.; Petersen, G. *Top Value Added Chemicals from Biomass: Volume I -- Results of Screening for Potential Candidates from Sugars and Synthesis Gas*: United States, 2004.

5. Da Silva Ruy, A. D.; Ferreira, A. L. F.; Bresciani, A. É.; de Brito Alves, R. M.; Pontes, L. A. M.: Market Prospecting and Assessment of the Economic Potential of Glycerol from Biodiesel. In *Biotechnological Applications of Biomass*; IntechOpen, 2020.

6. Pagliaro, M.; Ciriminna, R.; Kimura, H.; Rossi, M.; Della Pina, C. From Glycerol to Value-Added Products. *Angew. Chem. Int. Ed.* ***46***, 4434-4440 (2007).

7. Katryniok, B.; Kimura, H.; Skrzyńska, E.; Girardon, J.-S.; Fongarland, P.; Capron, M.; Ducoulombier, R.; Mimura, N.; Paul, S.; Dumeignil, F. Selective catalytic oxidation of glycerol: perspectives for high value chemicals. *Green Chem.* ***13***, 1960-1979 (2011).

8. Dodekatos, G.; Schünemann, S.; Tüysüz, H. Recent Advances in Thermo-, Photo-, and Electrocatalytic Glycerol Oxidation. *ACS Catal.* ***8***, 6301-6333 (2018).

9. Simões, M.; Baranton, S.; Coutanceau, C. Electrochemical Valorisation of Glycerol. *ChemSusChem* **5**, 2106-2124 (2012).

10. Li, T.; Harrington, D. A. An Overview of Glycerol Electrooxidation Mechanisms on Pt, Pd and Au. *ChemSusChem* ***14***, 1472-1495 (2021).

11. Kwon, Y.; Schouten, K. J. P.; Koper, M. T. M. Mechanism of the Catalytic Oxidation of Glycerol on Polycrystalline Gold and Platinum Electrodes. *ChemCatChem* **3**, 1176-1185 (2011).

12. Kwon, Y.; Birdja, Y.; Spanos, I.; Rodriguez, P.; Koper, M. T. M. Highly Selective Electro-Oxidation of Glycerol to Dihydroxyacetone on Platinum in the Presence of Bismuth. *ACS Catal.* ***2***, 759-764 (2012).

13. Lee, S.; Kim, H. J.; Lim, E. J.; Kim, Y.; Noh, Y.; Huber, G. W.; Kim, W. B. Highly selective transformation of glycerol to dihydroxyacetone without using oxidants by a PtSb/C-catalyzed electrooxidation process. *Green Chem.* ***18***, 2877-2887 (2016).

14. Fan, L.; Liu, B.; Liu, X.; Senthilkumar, N.; Wang, G.; Wen, Z. Recent Progress in Electrocatalytic Glycerol Oxidation. *Energy Technol.* ***9***, 2000804 (2021).

15. Li, Y.; Wei, X.; Chen, L.; Shi, J.; He, M. Nickel-molybdenum nitride nanoplate electrocatalysts for concurrent electrolytic hydrogen and formate productions. *Nat. Commun.* ***10***, 5335 (2019).

16. Han, X.; Sheng, H.; Yu, C.; Walker, T. W.; Huber, G. W.; Qiu, J.; Jin, S. Electrocatalytic Oxidation of Glycerol to Formic Acid by CuCo2O4 Spinel Oxide Nanostructure Catalysts. *ACS Catal.* ***10***, 6741-6752 (2020).

17. Simões, M.; Baranton, S.; Coutanceau, C. Electro-oxidation of glycerol at Pd based nano-catalysts for an application in alkaline fuel cells for chemicals and energy cogeneration. *Appl. Catal. B: Environ.* ***93***, 354-362 (2010).

18. Chen, Y. X.; Lavacchi, A.; Miller, H. A.; Bevilacqua, M.; Filippi, J.; Innocenti, M.; Marchionni, A.; Oberhauser, W.; Wang, L.; Vizza, F. Nanotechnology makes biomass electrolysis more energy efficient than water electrolysis. *Nat. Commun.* ***5***, 4036 (2014).

19. Dagdougui, H.; Sacile, R.; Bersani, C.; Ouammi, A.: Chapter 2 - Hydrogen Production and Current Technologies. In *Hydrogen Infrastructure for Energy Applications*; Dagdougui, H., Sacile, R., Bersani, C., Ouammi, A., Eds.; Academic Press, 2018; pp 7-21.

20. Liu, D.; Liu, J.-C.; Cai, W.; Ma, J.; Yang, H. B.; Xiao, H.; Li, J.; Xiong, Y.; Huang, Y.; Liu, B. Selective photoelectrochemical oxidation of glycerol to high value-added dihydroxyacetone. *Nat. Commun.* ***10***, 1779 (2019).

21. Verma, S.; Lu, S.; Kenis, P. J. A. Co-electrolysis of CO2 and glycerol as a pathway to carbon chemicals with improved technoeconomics due to low electricity consumption. *Nat. Energy* ***4***, 466-474 (2019).

22. Yadegari, H.; Ozden, A.; Alkayyali, T.; Soni, V.; Thevenon, A.; Rosas-Hernández, A.; Agapie, T.; Peters, J. C.; Sargent, E. H.; Sinton, D. Glycerol Oxidation Pairs with Carbon Monoxide Reduction for Low-Voltage Generation of C2 and C3 Product Streams. *ACS Energy Lett.* ***6***, 3538-3544 (2021).

23. Li, R.; Xiang, K.; Peng, Z.; Zou, Y.; Wang, S. Recent Advances on Electrolysis for Simultaneous Generation of Valuable Chemicals at both Anode and Cathode. *Adv. Energy Mater.* ***n/a***, 2102292).

24. Aust, N.; Kirste, A.: Paired Electrosynthesis. In *Encyclopedia of Applied Electrochemistry*; Kreysa, G., Ota, K.-i., Savinell, R. F., Eds.; Springer New York: New York, NY, 2014; pp 1505-1510.

25. Ibanez, J. G.; Frontana-Uribe, B. A.; Vasquez-Medrano, R. Paired electrochemical processes: overview, systematization, selection criteria, design strategies, and projection. *J. Mex. Chem. Soc.* ***60***, 247-260 (2016).

26. Strehl, J.; Abraham, M. L.; Hilt, G. Linear Paired Electrolysis—Realising 200% Current Efficiency for Stoichiometric Transformations—The Electrochemical Bromination of Alkenes. *Angew. Chem. Int. Ed.* ***60***, 9996-10000 (2021).

27. Yang, S.; Verdaguer-Casadevall, A.; Arnarson, L.; Silvioli, L.; Čolić, V.; Frydendal, R.; Rossmeisl, J.; Chorkendorff, I.; Stephens, I. E. L. Toward the Decentralized Electrochemical Production of H2O2: A Focus on the Catalysis. *ACS Catal.* ***8***, 4064-4081 (2018).

28. Perry, S. C.; Pangotra, D.; Vieira, L.; Csepei, L.-I.; Sieber, V.; Wang, L.; Ponce de León, C.; Walsh, F. C. Electrochemical synthesis of hydrogen peroxide from water and oxygen. *Nat. Rev. Chem.* ***3***, 442-458 (2019).

29. Brillas, E.; Sirés, I.; Oturan, M. A. Electro-Fenton Process and Related Electrochemical Technologies Based on Fenton's Reaction Chemistry. *Chem. Rev.* ***109***, 6570-6631 (2009).

30. Teong, S. P.; Li, X.; Zhang, Y. Hydrogen peroxide as an oxidant in biomass-to-chemical processes of industrial interest. *Green Chem.* ***21***, 5753-5780 (2019).

31. Moody, G. J. The action of fenton's reagent on carbohydrates. *Tetrahedron* ***19***, 1705-1710 (1963).

32. Vitale, A. A.; Bernatene, E. A.; Vitale, M. G.; Pomilio, A. B. New Insights of the Fenton Reaction Using Glycerol as the Experimental Model. Effect of O2, Inhibition by Mg2+, and Oxidation State of Fe. *J. Phys. Chem. A* ***120***, 5435-5445 (2016).

33. Zeng, J.; Yoo, C. G.; Wang, F.; Pan, X.; Vermerris, W.; Tong, Z. Biomimetic Fenton-Catalyzed Lignin Depolymerization to High-Value Aromatics and Dicarboxylic Acids. *ChemSusChem* ***8***, 861-871 (2015).

34. Sheng, H.; Hermes, E. D.; Yang, X.; Ying, D.; Janes, A. N.; Li, W.; Schmidt, J. R.; Jin, S. Electrocatalytic Production of H2O2 by Selective Oxygen Reduction Using Earth-Abundant Cobalt Pyrite (CoS2). *ACS Catal.* ***9***, 8433-8442 (2019).

35. Sheng, H.; Janes, A. N.; Ross, R. D.; Kaiman, D.; Huang, J.; Song, B.; Schmidt, J. R.; Jin, S. Stable and selective electrosynthesis of hydrogen peroxide and the electro-Fenton process on CoSe2 polymorph catalysts. *Energy Environ. Sci.* ***13***, 4189-4203 (2020).

36. Siahrostami, S.; Verdaguer-Casadevall, A.; Karamad, M.; Deiana, D.; Malacrida, P.; Wickman, B.; Escudero-Escribano, M.; Paoli, E. A.; Frydendal, R.; Hansen, T. W.; Chorkendorff, I.; Stephens, I. E. L.; Rossmeisl, J. Enabling direct H2O2 production through rational electrocatalyst design. *Nat. Mater.* ***12***, 1137-1143 (2013).

37. Siahrostami, S.; Villegas, S. J.; Bagherzadeh Mostaghimi, A. H.; Back, S.; Farimani, A. B.; Wang, H.; Persson, K. A.; Montoya, J. A Review on Challenges and Successes in Atomic-Scale Design of Catalysts for Electrochemical Synthesis of Hydrogen Peroxide. *ACS Catal.* ***10***, 7495-7511 (2020).

38. The Materials Project. https://materialsproject.org/ (accessed Dec. 7, 2021).

39. Ryu, J.; Bregante, D. T.; Howland, W. C.; Bisbey, R. P.; Kaminsky, C. J.; Surendranath, Y. Thermochemical aerobic oxidation catalysis in water can be analysed as two coupled electrochemical half-reactions. *Nat. Catal.* ***4***, 742-752 (2021).

40. Kresse, G.; Hafner, J. Ab initio molecular dynamics for liquid metals. *Phys. Rev. B* ***47***, 558-561 (1993).

41. Kresse, G.; Hafner, J. Ab initio molecular-dynamics simulation of the liquid-metal--amorphous-semiconductor transition in germanium. *Phys. Rev. B* ***49***, 14251-14269 (1994).

42. Kresse, G.; Furthmüller, J. Efficiency of ab-initio total energy calculations for metals and semiconductors using a plane-wave basis set. *Comput. Mat. Sci.* ***6***, 15-50 (1996).

43. Kresse, G.; Furthmüller, J. Efficient iterative schemes for ab initio total-energy calculations using a plane-wave basis set. *Phys. Rev. B* ***54***, 11169-11186 (1996).

44. Bahn, S. R.; Jacobsen, K. W. An object-oriented scripting interface to a legacy electronic structure code. *Comput. Sci. Eng.* ***4***, 56-66 (2002).

45. Blöchl, P. E. Projector augmented-wave method. *Phys. Rev. B* ***50***, 17953-17979 (1994).

46. Kresse, G.; Joubert, D. From ultrasoft pseudopotentials to the projector augmented-wave method. *Phys. Rev. B* ***59***, 1758-1775 (1999).

47. Perdew, J. P.; Burke, K.; Ernzerhof, M. Generalized Gradient Approximation Made Simple. *Phys. Rev. Lett.* ***77***, 3865-3868 (1996).

48. Perdew, J. P.; Burke, K.; Ernzerhof, M. Generalized Gradient Approximation Made Simple [Phys. Rev. Lett. 77, 3865 (1996)]. *Phys. Rev. Lett.* ***78***, 1396-1396 (1997).

49. Grimme, S.; Antony, J.; Ehrlich, S.; Krieg, H. A consistent and accurate ab initio parametrization of density functional dispersion correction (DFT-D) for the 94 elements H-Pu. *J. Chem. Phys.* ***132***, 154104 (2010).

50. Anisimov, V. I.; Zaanen, J.; Andersen, O. K. Band theory and Mott insulators: Hubbard U instead of Stoner I. *Phys. Rev. B* ***44***, 943-954 (1991).

51. Wu, X.; Han, S.; He, D.; Yu, C.; Lei, C.; Liu, W.; Zheng, G.; Zhang, X.; Lei, L. Metal Organic Framework Derived Fe-Doped CoSe2 Incorporated in Nitrogen-Doped Carbon Hybrid for Efficient Hydrogen Evolution. *ACS Sustain. Chem. Eng.* ***6***, 8672-8678 (2018).

52. Mathew, K.; Sundararaman, R.; Letchworth-Weaver, K.; Arias, T. A.; Hennig, R. G. Implicit solvation model for density-functional study of nanocrystal surfaces and reaction pathways. *J. Chem. Phys.* ***140***, 084106 (2014).

53. Mathew, K.; Kolluru, V. S. C.; Mula, S.; Steinmann, S. N.; Hennig, R. G. Implicit self-consistent electrolyte model in plane-wave density-functional theory. *arXiv*, 1601.03346 (2019).

54. Monkhorst, H. J.; Pack, J. D. Special points for Brillouin-zone integrations. *Phys. Rev. B* ***13***, 5188-5192 (1976).

55. Alchagirov, A. B.; Perdew, J. P.; Boettger, J. C.; Albers, R. C.; Fiolhais, C. Energy and pressure versus volume: Equations of state motivated by the stabilized jellium model. *Phys. Rev. B* ***63***, 224115 (2001).

56. Henkelman, G.; Uberuaga, B. P.; Jónsson, H. A climbing image nudged elastic band method for finding saddle points and minimum energy paths. *J. Chem. Phys.* ***113***, 9901-9904 (2000).

57. Henkelman, G.; Jóhannesson, G.; Jónsson, H.: Methods for Finding Saddle Points and Minimum Energy Paths. In *Theoretical Methods in Condensed Phase Chemistry*; Schwartz, S. D., Ed.; Springer Netherlands: Dordrecht, 2002; pp 269-302.

58. Henkelman, G.; Jónsson, H. A dimer method for finding saddle points on high dimensional potential surfaces using only first derivatives. *J. Chem. Phys.* ***111***, 7010-7022 (1999).

59. Heyden, A.; Bell, A. T.; Keil, F. J. Efficient methods for finding transition states in chemical reactions: Comparison of improved dimer method and partitioned rational function optimization method. *J. Chem. Phys.* ***123***, 224101 (2005).

60. Kästner, J.; Sherwood, P. Superlinearly converging dimer method for transition state search. *J. Chem. Phys.* ***128***, 014106 (2008).

61. Nørskov, J. K.; Rossmeisl, J.; Logadottir, A.; Lindqvist, L.; Kitchin, J. R.; Bligaard, T.; Jónsson, H. Origin of the Overpotential for Oxygen Reduction at a Fuel-Cell Cathode. *J. Phys. Chem. B* ***108***, 17886-17892 (2004).

62. NIST Chemistry WebBook. https://webbook.nist.gov/cgi/cbook.cgi?ID=C7722841&Mask=10#Solubility (accessed Dec. 7, 2021).

63. Vinogradova, O.; Krishnamurthy, D.; Pande, V.; Viswanathan, V. Quantifying Confidence in DFT-Predicted Surface Pourbaix Diagrams of Transition-Metal Electrode–Electrolyte Interfaces. *Langmuir* ***34***, 12259-12269 (2018).

64. Hansen, H. A.; Rossmeisl, J.; Nørskov, J. K. Surface Pourbaix diagrams and oxygen reduction activity of Pt, Ag and Ni(111) surfaces studied by DFT. *Phys. Chem. Chem. Phys.* ***10***, 3722-3730 (2008).

65. Viswanathan, V.; Hansen, H. A.; Rossmeisl, J.; Nørskov, J. K. Unifying the 2e– and 4e– Reduction of Oxygen on Metal Surfaces. *J. Phys. Chem. Lett.* ***3***, 2948-2951 (2012).

66. Kulkarni, A.; Siahrostami, S.; Patel, A.; Nørskov, J. K. Understanding Catalytic Activity Trends in the Oxygen Reduction Reaction. *Chem. Rev.* ***118***, 2302-2312 (2018).

67. Ford, D. C.; Nilekar, A. U.; Xu, Y.; Mavrikakis, M. Partial and complete reduction of O2 by hydrogen on transition metal surfaces. *Surf. Sci.* ***604***, 1565-1575 (2010).

68. Bhat, K. S.; Barshilia, H. C.; Nagaraja, H. S. Porous nickel telluride nanostructures as bifunctional electrocatalyst towards hydrogen and oxygen evolution reaction. *Int. J. Hydrog. Energy* ***42***, 24645-24655 (2017).

69. Kolb, E. D.; Laudise, R. A. The solubility of trigonal Se in Na2S solutions and the hydrothermal growth of Se. *J. Cryst. Growth* ***8***, 191-196 (1971).

70. Ravel, B.; Newville, M. ATHENA, ARTEMIS, HEPHAESTUS: data analysis for X-ray absorption spectroscopy using IFEFFIT. *J. Synchrotron Radiat.* ***12***, 537-541 (2005).

71. Lu, Z.; Chen, G.; Siahrostami, S.; Chen, Z.; Liu, K.; Xie, J.; Liao, L.; Wu, T.; Lin, D.; Liu, Y.; Jaramillo, T. F.; Nørskov, J. K.; Cui, Y. High-efficiency oxygen reduction to hydrogen peroxide catalysed by oxidized carbon materials. *Nat. Catal.* ***1***, 156-162 (2018).

72. Jiang, K.; Back, S.; Akey, A. J.; Xia, C.; Hu, Y.; Liang, W.; Schaak, D.; Stavitski, E.; Nørskov, J. K.; Siahrostami, S.; Wang, H. Highly selective oxygen reduction to hydrogen peroxide on transition metal single atom coordination. *Nat. Commun.* ***10***, 3997 (2019).

CHAPTER 5

Electrocatalytic Oxidation of Glycerol to Formic Acid by $Cu_2Co_2O_4$ Spinel Oxide Nanostructure Catalysts[*]

5.1 Abstract

The electrochemical oxidation of abundantly available glycerol for the production of value-added chemicals, such as formic acid, could be a promising approach to utilize glycerol more effectively and to meet the future demand for formic acid as a fuel for direct or indirect formic acid fuel cells. Here we report a comparative study of a series of earth-abundant cobalt-based spinel oxide (MCo_2O_4, M = Mn, Fe, Co, Ni, Cu, and Zn) nanostructures as robust electrocatalysts for the glycerol oxidation to selectively produce formic acid. Their intrinsic catalytic activities in alkaline solution follow the sequence of $CuCo_2O_4 > NiCo_2O_4 > CoCo_2O_4 > FeCo_2O_4 > ZnCo_2O_4 > MnCo_2O_4$. Using the best-performing $CuCo_2O_4$ catalyst directly integrated onto carbon fiber paper electrodes for the bulk electrolysis reaction of glycerol oxidation (pH = 13) at the constant potential of 1.30 V vs. reversible hydrogen electrode (RHE), a high selectivity of 80.6% for formic acid production and an overall Faradaic efficiency of 89.1% toward all value-added products were achieved with a high glycerol conversion of 79.7%. Various structural characterization techniques confirm the stability of the $CuCo_2O_4$ catalyst after electrochemical testing. These results open up

---

[*] This chapter was originally published in *ACS Catal.* ***10***, 6741–6752 (2020), in collaboration with Xiaotong Han, Chang Yu, Theodore W. Walker, George W. Huber, Jieshan Qiu, and Song Jin.

opportunities for studying earth-abundant electrocatalysts for efficient and selective oxidation of glycerol to produce formic acid or other value-added chemicals.

5.2 Introduction

The rapid development of the biodiesel industry over the last decades has resulted in a large surplus of glycerol production (as a byproduct from biodiesel production) compared to its demand,[1] and has made glycerol an abundantly available chemical with a very low price (US \$0.11 per kg[2] or \$0.010 per mole for crude glycerin). In fact, glycerol was listed in the original report by the U.S. Department of Energy as one of the top ten biomass-derived platform molecules for the production of high-value chemicals.[3,4] Since then, significant research efforts have been focused on the catalytic oxidation of the inexpensive glycerol feedstock into value-added products, such as glyceraldehyde, dihydroxyacetone, glyceric acid, tartronic acid, glycolic acid, oxalic acid, and formic acid.[5] Among the various C_3 – C_1 products that can be derived from glycerol oxidation, formic acid (US \$0.40 per kg[6] or \$0.018 per mole) is an attractive value-added product for efficient and effective utilization of glycerol. Formic acid is the fuel for direct formic acid fuel cells (DFAFCs) that have attracted growing attention because of their high power densities, limited fuel crossover, and facile power system integration.[7,8] Moreover, the liquid nature and low toxicity of formic acid make it more convenient and less dangerous to store, transport, and handle compared with hydrogen gas; therefore, formic acid has been proposed to be an alternative hydrogen energy carrier with high volumetric capacity that finds its applications in indirect formic acid fuel cells.[8-10] The future demand for formic acid may rapidly increase with the development and deployment of applications such as direct or indirect FAFCs, and may not be satisfied by the present global capacity of formic acid (0.72 million tons per year in 2013[11]). Therefore, the selective production of three equivalence of formic acid from one equivalence of glycerol could be a promising approach to explore.

The catalytic conversion of glycerol to formic acid could be achieved through thermal oxidation processes.[12-16] Thermocatalytic glycerol oxidation reactions can proceed under aerobic conditions utilizing oxygen gas as the chemical oxidant but are typically performed at elevated oxygen pressures and high temperatures[12,13] that require specialized infrastructure. Otherwise, a large excess of other chemical oxidants (such as H_2O_2[14,15] and oxone[16]) are used to oxidize glycerol, however, these processes are poorly selective toward formic acid production and generate large amounts of undesired chemical wastes. In this context, the electrochemical oxidation of biomass-derived molecules is a promising alternative approach that offer several advantages over thermal oxidation methods.[17-23] Firstly, the electrochemical oxidation can be effectively performed at ambient pressure and temperature. Secondly, the electrochemically driven oxidation eliminates the need for chemical oxidants that often cause environmental problems. Thirdly, a valuable reduction reaction, such as the hydrogen evolution reaction (HER), can be easily coupled with the biomass oxidation reaction to simultaneously produce hydrogen gas on the cathode and value-added chemicals on the anode, which increases the economic value of the overall electrochemical process. Fourthly, the electrochemical oxidation can be conveniently performed in small-scale reactors at distributed locations near the sources of biomass. Finally, as the cost of electricity from renewable sources (such as solar and wind) continues to decline, the electrochemical approach will become increasingly cost competitive.[24,25] In this regard, the electrochemical oxidation strategy offers new opportunities for the production of formic acid from the electrocatalytic oxidation of glycerol, therefore effective and selective electrocatalysts are highly desired. However, the catalysts studied for the electrochemical oxidation of glycerol so far have been mostly limited to noble metals (such as Pd,[26] Pt,[27] Au[28]) and their alloys (such as PtRu,[29] PtRuSn,[30] PtSb,[31] Pt_xBi,[32] Pd_xBi[33]). Moreover, the reaction pathways of glycerol oxidation are quite complex: various C_3 – C_1 intermediates can interconvert into one another electrochemically, leading to many different possible oxidation products[20] and hence a poor selectivity of the desired product(s).

Earth-abundant transition metal-based electrocatalysts have been intensely studied as promising and cost-effective alternatives to noble metal catalysts for water splitting and hydrogen fuel cells,[34-37] yet they remain relatively underexplored for electrocatalytic biomass conversion. The electrochemical oxidation of biomass-derived 5-hydroxymethylfurfural (HMF) were studied on earth-abundant metal,[23,38] metal pnictide[39,40] and chalcogenide[19] catalysts; however, these catalysts are chemically unstable and are often oxidized into metal (oxyhydr)oxides under electrochemical operations.[41,42] This is also the case for the few transition metal-based electrocatalysts studied so far for the glycerol oxidation.[43-47] Another distinctive feature of the glycerol oxidation is that it can yield various C_3 – C_1 products because of the C-C bond cleavage,[20,48] which is usually not observed (or desired) in the electrochemical oxidation of HMF and other biomass-derived alcohol substrates.[19,23] Therefore, although comparative studies of structurally stable transition metal oxyhydroxides for the HMF oxidation have recently emerged,[17,49] such structure-activity relationships may not be directly translatable to glycerol oxidation, because of the complications in its reaction pathways and product selectivity.

In this work, we set out to systematically investigate, for the first time, a series of earth-abundant cobalt-based spinel oxide (MCo_2O_4, M = Mn, Fe, Co, Ni, Cu, and Zn) nanostructures as catalysts for the electrochemical oxidation of glycerol. Our results show that, among this series of spinel oxides, $CuCo_2O_4$ exhibits the highest *intrinsic* catalytic activity for the glycerol oxidation in alkaline solution (pH = 13) and selectively catalyzes this reaction toward formic acid production.

Using the best-performing $CuCo_2O_4$ catalyst directly integrated onto carbon fiber paper electrodes, we ran the bulk electrolysis reaction of glycerol oxidation (pH = 13) at the constant potential of 1.30 V vs. reversible hydrogen electrode (RHE), achieving a high selectivity of 80.6% for formic acid production and an overall Faradaic efficiency of 89.1% toward all value-added products with a high glycerol conversion of 79.7%. This work paves the way for future design and exploration of diverse earth-abundant catalysts to drive the electrochemical oxidation of glycerol with high efficiency and selectivity for the production of formic acid or other value-added chemicals.

5.3 Results and Discussion

5.3.1 Synthesis and Characterization of Cobalt-Based Spinel Oxide (MCo_2O_4) Nanostructure Catalysts

The series of MCo_2O_4 (M = Mn, Fe, Co, Ni, Cu, and Zn) nanostructures were directly grown on carbon fiber paper (CFP) substrates by a general hydrothermal method followed by calcination (see experimental details in the Experimental Section).[50] The prototypical $CoCo_2O_4$ (or Co_3O_4) spinel oxide exists in a cubic crystal structure (space group: Fd-$3m$) containing both Co^{2+} and Co^{3+} cations: the Co^{2+} cations sit at the tetrahedral coordination sites, whereas the Co^{3+} cations are octahedrally bonded to adjacent oxygen anions (Figure 5.1a).[51] Other first-row transition metal cations (M = Mn, Fe, Ni, Cu, and Zn) can also form the analogous crystal structures of MCo_2O_4 spinel oxides by stoichiometrically substituting one third of the Co cations in the $CoCo_2O_4$ crystal lattices. As-synthesized MCo_2O_4 samples were structurally characterized by powder X-ray diffraction (PXRD): all MCo_2O_4 samples display similar diffraction peaks (Figure 5.1b) that match with the standard pattern of $CoCo_2O_4$ (JCPDS No. 43-1003) with minor peak shifts as expected (Figure 5.1c), indicating the formation of spinel oxide structures.

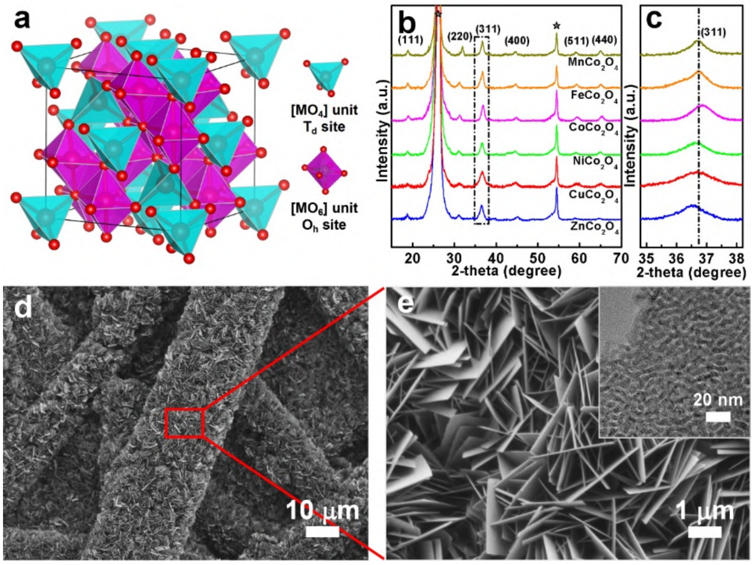

Figure 5.1. Synthesis and characterization of MCo_2O_4 (M = Mn, Fe, Co, Ni, Cu, and Zn) spinel oxide nanostructure catalysts.

(**a**) General crystal structure of MCo_2O_4 spinel oxides (M = Mn, Fe, Co, Ni, Cu, and Zn). (**b**) PXRD patterns and (**c**) magnified PXRD patterns of MCo_2O_4 nanoplate or nanowire arrays directly grown on carbon fiber paper substrates (the diffraction peaks from carbon fiber paper substrates are marked with asterisks). (**d**) Low-magnification and (**e**) high-magnification SEM images of the representative $CuCo_2O_4$ nanoplates grown on carbon fiber paper. The inset of (**e**) shows a high-magnification TEM image of the $CuCo_2O_4$ nanoplates.

The nanostructure morphology of as-synthesized MCo_2O_4 samples were further characterized by scanning electron microscopy (SEM), showing that MCo_2O_4 nanoplates (or nanowires) are vertically grown with high density and uniform distribution over the entire surface of CFP substrate (Figures 5.1d,e, and Figure A5.1 in the Appendix 5). Depending on the metal cations, the morphology of these MCo_2O_4 nanostructures could vary. The morphology of $CuCo_2O_4$ sample (Figure 5.1d) is similar to that of $CoCo_2O_4$ sample (Figures A5.1a,b), featuring vertical nanoplates densely interconnected with each other. The rest of these MCo_2O_4 samples (M = Mn, Fe, Ni, Zn) exhibit nanowire morphology (Figures A5.1c-j). The high-magnification SEM image of the representative $CuCo_2O_4$ sample (Figure 5.1e) reveals that the nanoplates have a thickness on the nanometer scale and a typical lateral size of 2-4 µm with smooth surfaces. The high-magnification TEM image (inset of Figure 5.1e) shows that the $CuCo_2O_4$ nanoplates consist of nanocrystalline domains because they are thermally converted from the corresponding metal hydroxide precursor (see details in the Experimental Section). The elemental mapping of $CuCo_2O_4$ nanoplates by energy dispersive X-ray spectroscopy (EDS) further confirms the uniform distribution of Co and Cu elements with an atomic ratio of Co to Cu close to 2 (Figure A5.2 and Table A5.1).

5.3.2 Electrochemical Characterization and Activity Trends of MCo_2O_4 Catalysts for Electrochemical Oxidation of Glycerol in Alkaline Solution

We then evaluated the electrocatalytic activities of this series of MCo_2O_4 nanostructure catalysts for the glycerol oxidation reaction (GOR) in a single-compartment three-electrode cell (Figure A5.3) under alkaline condition (0.1 M KOH) at room temperature. The carbon fiber paper substrates grown with MCo_2O_4 nanostructures were directly fabricated into integrated working anodes with a geometric area of ~1 cm^2 (Figure A5.4). A Pt wire counter electrode (for the cathodic hydrogen evolution reaction) and an Hg/HgO (1 M KOH) reference electrode were used for electrochemical measurements (see more experimental details in the Experimental Section). Note that the main competing anodic reaction is the oxygen evolution reaction (OER) from water oxidation,[17] which means the ideal GOR electrocatalyst should feature a high selectivity toward the glycerol oxidation and less catalytic activity toward the OER. Therefore, for comparison purposes, water oxidation on these MCo_2O_4 catalysts was also investigated in the absence of glycerol with all other conditions remain the same.

Figure 5.2a shows the linear sweep voltammetry (LSV) curves (based on geometric current densities, mA cm^{-2}) of the series of MCo_2O_4 catalysts in 0.1 M KOH solution (pH = 13) with and without the presence of 0.1 M glycerol. In the absence of glycerol (dash-dotted lines in Figure 5.2a), all these MCo_2O_4 catalyst anodes drive the OER with very similar overall electrode performances (within a narrow applied potential range of 1.55 to 1.60 V vs. RHE to deliver 10 mA cm^{-2}). After introducing 0.1 M glycerol into the electrolyte, the catalytic onset on all these MCo_2O_4 catalyst anodes significantly shift to less positive potentials (solid lines in Figure 5.2a), suggesting that glycerol oxidation is more kinetically favorable than water oxidation on these MCo_2O_4 catalysts. Importantly, in contrast to their comparable OER performances, these MCo_2O_4 catalyst anodes exhibit very different catalytic onset as well as overall electrode performances toward the glycerol oxidation: $CuCo_2O_4$ and $NiCo_2O_4$ (which only require an applied potential of 1.26 and 1.30 V vs. RHE, respectively, to deliver a catalytic current density of 10 mA cm^{-2} for glycerol oxidation) are the better-performing GOR catalyst anodes that show significant enhancements over than the prototypical $CoCo_2O_4$ (which requires 1.38 V vs. RHE at 10 mA cm^{-2}). On the other hand, the rest of the MCo_2O_4 catalyst anodes (M = Zn, Fe, and Mn) exhibit inferior GOR performances compared with $CoCo_2O_4$. The GOR performances of the MCo_2O_4 catalyst anodes originate from the catalysts themselves because the bare carbon fiber paper is catalytically inactive toward glycerol oxidation (Figure 5.2a).

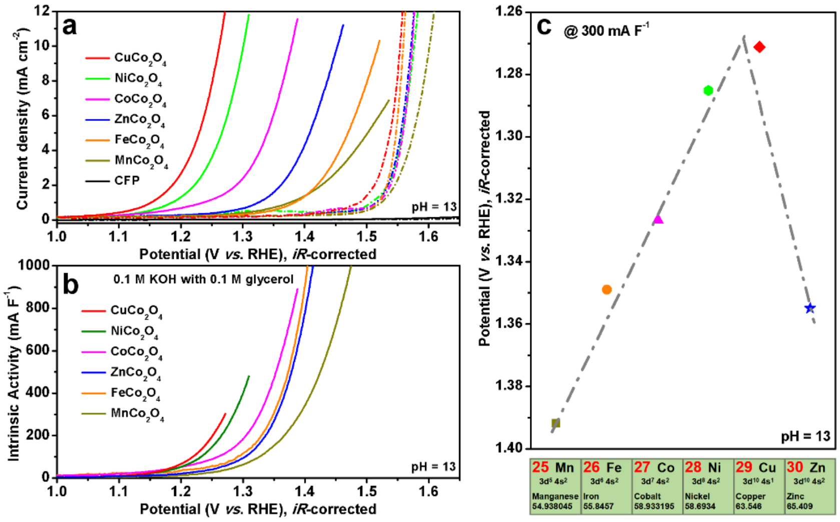

Figure 5.2. Electrochemical characterization and intrinsic catalytic activities of MCo_2O_4 (M = Mn, Fe, Co, Ni, Cu, and Zn) catalysts for electrochemical oxidation of glycerol in alkaline solution.

(**a**) LSV curves (based on geometric current densities, mA cm^{-2}) of the series of MCo_2O_4 (M = Mn, Fe, Co, Ni, Cu, Zn) nanostructures grown on carbon fiber paper in comparison with the bare carbon fiber paper at the scan rate of 1 mV s^{-1} in 0.1 M KOH solution with (solid lines) and without (dash-dotted lines) the presence of 0.1 M glycerol. (**b**) Intrinsic GOR catalytic activities of the series of MCo_2O_4 catalysts in 0.1 M KOH solution with 0.1 M glycerol after ECSA normalization (see Figures 5.2a, and Figure A5.6 and Table A5.3 in the Appendix 5 for reference). (**c**) The intrinsic GOR catalytic activity trend within the series of MCo_2O_4 catalysts (in the order of increasing atomic number of M from left to right).

Considering the slight variations in the catalyst mass loadings among the series of MCo_2O_4 catalyst electrodes (determined by the mass differences before and after the materials growth, see Table A5.2), we divided the geometric current densities (mA cm^{-2}) in the LSV curves shown in Figure 5.2a by the catalyst mass loadings (mg cm^{-2}) to calculate the mass activity (A g^{-1}) of each

MCo_2O_4 catalyst toward the glycerol oxidation. Figure A5.5 displays the LSV curves after this normalization of catalyst mass loadings, in which the $CuCo_2O_4$ and $NiCo_2O_4$ catalyst anodes, achieving a mass activity of 10 A g^{-1} at an applied potential of 1.27 and 1.29 V vs. RHE, respectively, still show enhanced GOR mass activity compared with the prototypical $CoCo_2O_4$.

To further develop a more rigorous understanding of the *intrinsic* catalytic activities of this series of MCo_2O_4 catalysts toward the glycerol oxidation, we systematically measured their cyclic voltammograms (CVs) in non-Faradaic regions to estimate their electrochemically active surface areas (ECSAs) based on double-layer capacitance (C_{dl}) values (Figure A5.6). The better-performing GOR catalyst anodes in 0.1 M KOH solution with 0.1 M glycerol (Figure 5.2a) exhibit higher C_{dl} values (Table A5.3). To better represent the intrinsic GOR catalytic activities, the geometric GOR catalytic current densities (mA cm^{-2}) of these MCo_2O_4 catalysts were divided by the respective estimated ECSAs (mF cm^{-2}). As shown in Figure 5.2b, even after ECSA normalization, the intrinsic GOR catalytic activity (mA F^{-1}) within the series of MCo_2O_4 catalysts still follows the same trend in their overall electrode performance: $CuCo_2O_4$ and $NiCo_2O_4$ catalysts are indeed *intrinsically* more active toward GOR than $CoCo_2O_4$. Interestingly, by arranging these MCo_2O_4 catalysts in the order of increasing atomic number of M, their intrinsic GOR catalytic activities show a pyramid-shaped trend, with $CuCo_2O_4$ catalyst sitting at the peak (Figure 5.2c). Therefore, we focus the rest of our studies of the GOR reaction pathways and product analyses on $CuCo_2O_4$ and $NiCo_2O_4$ catalysts, the two intrinsically most active ones among the series of MCo_2O_4 catalysts.

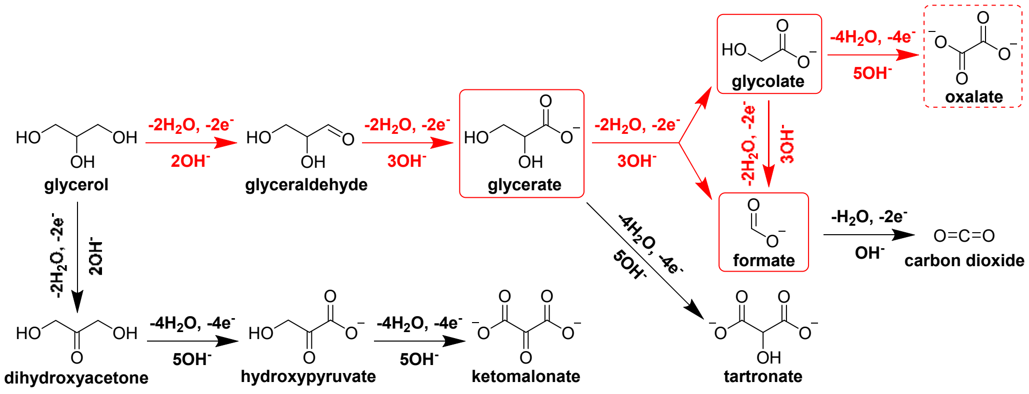

Scheme 5.1. Possible reaction pathways for electrochemical oxidation of glycerol to various value-added products in alkaline solution.

Possible reaction pathways for the electrochemical oxidation of glycerol to various value-added products in alkaline solution. Those reactions and products observed for the $CuCo_2O_4$ and $NiCo_2O_4$ electrocatalysts in this work are highlighted with red arrows and boxes, respectively.

Since the electrochemical oxidation of glycerol can proceed via multiple reaction pathways with various possible intermediate products involved (Scheme 5.1), we *individually* examined the electrochemical oxidation of those GOR intermediate products that are relevant to $CuCo_2O_4$ and $NiCo_2O_4$ catalysts (namely glyceraldehyde, glyceric acid, glycolic acid, oxalic acid, and formic acid) in 0.1 M KOH solution containing 0.1 M of the respective molecule (Figure A5.7). On both $CuCo_2O_4$ and $NiCo_2O_4$ catalysts, the catalytic onset of glyceraldehyde oxidation takes place at similar or lower potentials compared with glycerol oxidation, while the oxidation of glyceric acid and glycolic acid occur at slightly higher potentials but still partially overlap with glycerol oxidation. In contrast, the oxidation of formic acid and oxalic acid require substantially higher potentials, suggesting the electrochemical oxidation of glycerol could eventually stop at the reaction stage of formic acid (or oxalic acid) without appreciable CO_2 formation and water oxidation.

We also examined the cathodic reaction on the Pt wire counter electrode when these relevant GOR intermediate products are present in the electrolyte solution. In all cases, the hydrogen evolution reaction (HER) dominates on the Pt cathode without noticeable occurrence of the reduction of GOR intermediate products, as reflected by the similar catalytic onset potentials and current densities on the Pt cathode with and without the presence of the respective molecules (Figure A5.8). If side reactions of the reduction of GOR intermediate products could take place on the Pt cathode, they would generate additional reduction currents regardless of the opposite signs of diffusion currents and migration currents considering some of these intermediate products exist in the carboxylate forms in alkaline solution.[52] Instead, these intermediate products could potentially adsorb on the Pt cathode and slightly lower the cathodic HER current (Figure A5.8). Given this information, it is safe to perform the bulk electrolysis of glycerol oxidation in an undivided single-compartment cell (Figure A5.3) without being concerned about appreciable side reactions on the counter electrode.

5.3.3 Bulk Electrolysis and Product Analysis of Glycerol Oxidation Using the Active $CuCo_2O_4$ and $NiCo_2O_4$ Catalysts

Next, we carried out the bulk electrolysis of glycerol oxidation at the constant potential using the highly active $CuCo_2O_4$ and $NiCo_2O_4$ catalysts in 0.1 M KOH solution (2 mL) containing 0.1 M glycerol. Note that formic acid can be potentially oxidized to generate CO_2 at sufficiently high applied potentials[53] (beyond 1.30 V vs. RHE on our $CuCo_2O_4$ and $NiCo_2O_4$ catalysts, see Figure A5.7), which could lead to the loss of Faradaic efficiency toward value-added products. Therefore, we ran the chronoamperometry tests of $CuCo_2O_4$ and $NiCo_2O_4$ catalysts at the potentials below the formic acid oxidation threshold to study the product distributions and reaction pathways of glycerol oxidation. No appreciable water or formic acid oxidation could occur at these chosen potentials, and hence a high Faradaic efficiency of glycerol oxidation to value-added products is anticipated.

The first set of bulk electrolysis reactions on $CuCo_2O_4$ and $NiCo_2O_4$ catalysts was performed at different potentials (1.20, 1.23, 1.26, and 1.30 V vs. RHE) but with the same amount of total charge passed (60 C), aiming to investigate the effect of the applied oxidation potential on the product selectivity. Before and after the electrolysis reactions, the concentrations of glycerol and its oxidation products were monitored using high-performance liquid chromatography (HPLC) (see experimental details in the Experimental Section). For the reactions over the $CuCo_2O_4$ electrocatalyst, the resulting HPLC chromatograms (Figure A5.9a) show elution peaks at the retention time of 10.5, 12.0, 12.8, and 13.5 min, corresponding to glyceric acid, glycolic acid, glycerol, and formic acid, respectively (as determined individually from the standard samples, see Figure A5.10). The potential intermediate product of glyceraldehyde was not found in the chromatograms in this work. This is perhaps understandable because glyceraldehyde oxidation exhibits similar or less positive catalytic onset potential compared with glycerol oxidation on both $CuCo_2O_4$ and $NiCo_2O_4$ electrocatalysts (see Figure A5.7), which makes glyceraldehyde more readily oxidized than glycerol and hard to stabilize in the present reaction system. On the basis of these HPLC results, the glycerol conversion, product selectivity, and Faradaic efficiency over the $CuCo_2O_4$ catalyst at different applied potentials were calculated and summarized in Figure A5.9b and Table A5.4: the overall Faradaic efficiency toward all value-added products (glyceric acid, glycolic acid, and formic acid) remains as high as ~88% with a glycerol conversion of ~49% after a total charge of 60 C is passed at different oxidation potentials; the product selectivity turns out to be fairly insensitive to the chosen potentials, with formic acid being the major product of glycerol oxidation (~70% selectivity). The HPLC results for the electrolysis reactions over the

$NiCo_2O_4$ catalyst at different potentials (Figure A5.11a) are similar to those for the $CuCo_2O_4$ catalyst, except that a small elution peak at 6.8 min identified as oxalic acid was observed. There is also no significant difference in the product selectivity at different oxidation potentials for the $NiCo_2O_4$ catalyst (Figure A5.11b and Table A5.5).

Based on these results showing the insensitivity of product selectivity to the applied oxidation potential, we choose to apply the highest oxidation potential without appreciable water or formic acid oxidation (0.42 V vs. Hg/HgO, which is equivalent to 1.30 V vs. RHE at pH = 13) for long-term bulk electrolysis reactions (in 0.1 M KOH solution with 0.1 M glycerol) to achieve a higher glycerol conversion at a faster reaction rate by using our best $CuCo_2O_4$ electrocatalyst. As the reaction progressed with the increased amount of total charge passed, the glycerol concentration continuously decreased and the concentration of formic acid as the major product of the glycerol oxidation steadily increased, as revealed by the HPLC results (Figure 5.3a). It is interesting that the concentrations of the intermediate products of glyceric acid and glycolic acid were almost unchanged and remained at low concentrations. The concentrations of glycerol and its oxidation products as a function of the total charge passed throughout the entire electrolysis are presented in Figure 5.3b, with the corresponding product selectivity and Faradaic efficiency results summarized in Table 5.1. These results show a high selectivity of 80.6% toward formic acid formation after a total charge of 112 C is passed. The overall Faradaic efficiency toward all value-added products is 89.1%, which is slightly lower than the theoretical value and is likely due to the formation of CO_2 from the further oxidation of formic acid, since CO_2 is not detected by the HPLC analysis of the output carbon amount which only consider the aqueous phase organic carbon species (Table 5.1). Nevertheless, this plausible side reaction of CO_2 formation does not cause a significant loss of value-added products because the catalytic onset potential of formic acid oxidation on the $CuCo_2O_4$ catalyst is relatively high at pH = 13 (Figure A5.7) compared to the constant potential of 1.30 V vs. RHE applied for bulk electrolysis reactions.

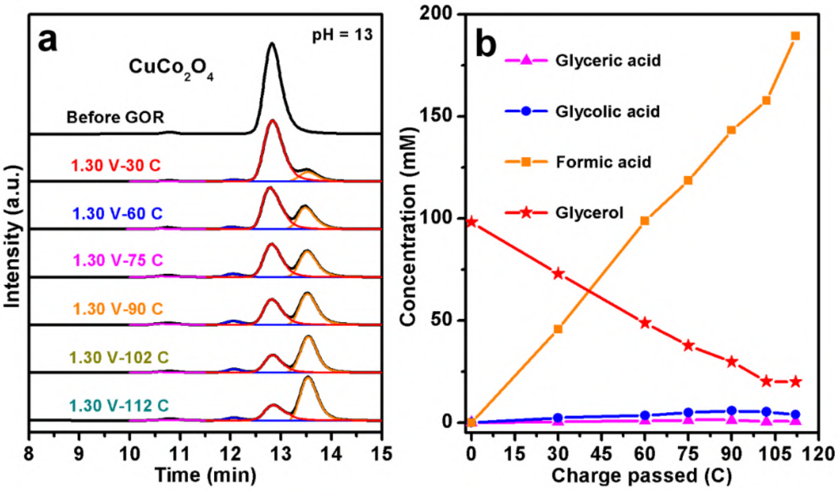

Figure 5.3. Product analysis and product selectivity of the bulk electrolysis of glycerol oxidation on $CuCo_2O_4$ catalyst at 1.3 V vs. RHE in 0.1 M KOH solution (pH = 13).

(**a**) HPLC chromatograms of the reaction products from the electrochemical oxidation of glycerol using $CuCo_2O_4$ as electrocatalyst at the constant potential of 0.42 V vs. Hg/HgO (1.30 V vs. RHE at pH = 13) in 0.1 M KOH solution containing 0.1 M glycerol with different amounts of total charge passed. (**b**) Concentrations of glycerol and its oxidation products as a function of the total charge passed after the glycerol oxidation using $CuCo_2O_4$ as electrocatalyst at 0.42 V vs. Hg/HgO (1.30 V vs. RHE at pH = 13) in 0.1 M KOH solution containing 0.1 M glycerol.

However, the glycerol conversion is still only 79.7% over 19 h, which is because the reaction rate is getting slower as more and more charge has been passed. Examination of the chronoamperometry data reveals that the catalytic current density for the glycerol oxidation declined continuously as the bulk electrolysis progressed (Figure A5.12), and the delivered current density was as low as 0.4 mA cm^{-2} after the electrolysis was run for 5 h (with ~105 C passed). The current density decrease and the incomplete glycerol conversion could be ascribed to the following reasons. First of all, as the concentration of glycerol is depleted due to its oxidation, the GOR reaction rate and the catalytic current density are expected to be reduced. Secondly, the various acid products (glyceric acid, glycolic acid, and formic acid) from the glycerol oxidation consume OH^- in the electrolyte solution and exist in the carboxylate forms (see Equations A5.1–A5.8 in the Appendix 5). As a result, the pH of the bulk solution kept decreasing during the electrolysis: the solution pH decreased to below 12 after 5 h reaction and was approaching 10 after even longer time (Table 5.1, also see inset of Figure A5.12). Last but not least, the applied potential versus reversible hydrogen electrode (RHE) also kept declining because of the continuous decrease in the solution pH (Table 5.1 and Figure A5.13), which further reduced the GOR reaction rate and hence led to the incomplete conversion of glycerol. We believe better pH-buffering would help to further drive the glycerol oxidation toward completion.

Table 5.1. Summary of the glycerol conversion, product selectivity, and Faradaic efficiency of the glycerol oxidation using $CuCo_2O_4$ as electrocatalyst at 0.42 V vs. Hg/HgO (1.30 V vs. RHE at pH = 13) in 0.1 M KOH solution containing 0.1 M glycerol with different amounts of total charge passed.

Potential (V vs. Hg/HgO)	Potential (V vs. RHE) [a]	Charge Passed (C)	Glycerol conversion (%)	Selectivity (%)			Faradaic efficiency (%)	Aqueous phase organic carbon amount (mM)		pH
				Glyceric acid	Glycolic acid	Formic acid		Input	Output [b]	
0.42	1.30	30	25.7	1.6	6.2	60.1	82.0	75.9	51.5	12.91
0.42	1.29	60	48.4	1.7	5.1	71.9	88.4	137.6	108.2	12.75
0.42	1.28	75	61.6	2.1	5.3	65.3	85.5	181.5	131.9	12.63
0.42	1.27	90	69.7	1.8	5.6	69.7	85.8	205.5	158.5	12.44
0.42	1.24	102	79.4	0.5	4.5	67.4	82.0	234.2	169.5	11.96
0.42	1.14	112	79.7	0.9	3.3	80.6	89.1	235.1	199.3	10.22

[a] The change in the applied potential versus reversible hydrogen electrode (RHE) is due to the decrease in the bulk solution pH, as the various acid products from the glycerol oxidation consume OH^- in the electrolyte solution and exist in the carboxylate forms.

[b] Output aqueous phase organic carbon amount does not include the CO_2 byproduct, which may be solubilized as CO_3^{2-} in alkaline solution.

In order to realize more complete conversion of glycerol, we carried out another set of bulk electrolysis reactions of glycerol oxidation at the constant potential (0.32 V vs. Hg/HgO, which is equivalent to 1.26 V vs. RHE at pH = 14) but at a higher pH value (in 1 M KOH solution with 0.1 M glycerol) using the $CuCo_2O_4$ electrocatalyst. The 10 times higher KOH concentration should better buffer the change in the solution pH caused by the conversion of glycerol. $CuCo_2O_4$ is also the best-performing GOR electrocatalyst in 1 M KOH solution (pH = 14) among this series of MCo_2O_4 catalysts (Figure A5.14), which is rooted in its highest *intrinsic* GOR catalytic activity (Figure 5.2c). However, because it is easier to further oxidize formic acid to the undesired CO_2 on the $CuCo_2O_4$ catalyst at pH = 14 (Figure A5.15) than at pH = 13 (Figure A5.7), we performed the bulk electrolysis reactions of glycerol oxidation at pH = 14 at a slightly less positive constant potential of 1.26 V vs. RHE. The chronoamperometry data in 1 M KOH solution (pH = 14) show that although the GOR catalytic current density still displayed a continuous decrease due to the depletion of glycerol, it did not decrease as quickly (Figure A5.16). Moreover, the pH of the bulk solution was considerably more stable and only decreased by less than 0.2 pH unit after a higher total charge of 145 C was passed over 30 h (Table A5.6, also see inset of Figure A5.16). These results further suggest the more rapid decrease in the GOR catalytic current density previously observed in 0.1 M KOH solution (pH = 13) is mainly due to the consumption of base as the conversion of glycerol proceeds. For 2 mL of electrolyte solution containing 0.1 M glycerol, a total charge of ~154 C is theoretically needed for the complete oxidation of glycerol to formic acid. After passing a total charge of 145 C through the $CuCo_2O_4$ electrocatalyst in 1 M KOH solution (pH = 14), the HPLC elution peak of glycerol almost completely disappeared (Figure A5.17a), and a near-unity glycerol conversion of 98.9% was eventually achieved (Table A5.6). Formic acid is still the major product of the glycerol oxidation, while glyceric acid and glycolic acid remain at low concentrations (Figure A5.17b and Table A5.6). However, as the reaction time went on toward complete glycerol conversion, the increase of formic acid concentration became slower and the overall Faradaic efficiency toward all value-added products (aqueous phase organic carbon species) decreased to 64.3%. We note that because the OER catalytic onset potential on the $CuCo_2O_4$ catalyst at pH = 14 (Figure A5.14) is substantially higher than the constant potential of 1.26 V vs. RHE applied for glycerol oxidation (Figure A5.16), O_2 formation from water oxidation is highly unlikely to take place during bulk electrolysis reactions. In fact, there is no OER catalyst that can produce O_2 at such a low overpotential of 30 mV (based on the standard equilibrium water oxidation potential of 1.23 V vs. RHE). Instead, we suspect that this larger Faradaic efficiency loss at pH = 14 is likely due to the production of CO_2 from the further oxidation of formic acid, which is easier at this higher pH condition (Figure A5.15 vs. A5.7). Better pH-buffering at lower pH value might enable higher glycerol conversion and higher overall Faradaic efficiency toward value-added products at the same time in the future.

5.3.4 Proposed Reaction Pathways of Glycerol Oxidation on the $CuCo_2O_4$ and $NiCo_2O_4$ Catalysts

On the basis of the general reaction scheme for glycerol oxidation[1] and our HPLC results, we propose the reaction pathways for the electrochemical oxidation of glycerol on the $CuCo_2O_4$ and $NiCo_2O_4$ electrocatalysts follow the red arrows shown in Scheme 5.1. The initial two-electron oxidation of glycerol takes place selectively on the terminal carbon (rather than the central carbon) of the glycerol molecule to form glyceraldehyde, which is more readily oxidized to glyceric acid in the subsequent two-electron transfer. Glyceric acid further undergoes C-C bond cleavage during the following two-electron oxidation to form equivalent amounts of glycolic acid and formic acid. Finally, glycolic acid undertakes two-electron oxidative cleavage into two equivalence of formic acid. In addition, only over the $NiCo_2O_4$ electrocatalyst, a fraction of glycolic acid could be further oxidized to oxalic acid via a four-electron transfer process. Note that due to the basic pH of the electrolyte solution, the products are always in the carboxylate forms (glycerate, glycolate, oxalate, and formate) instead of the acid forms. We could not observe the first intermediate of glyceraldehyde because it can be oxidized at even lower potentials than the oxidation of glycerol (as discussed earlier) and is also chemically unstable in alkaline solution.[54] The instability of glyceraldehyde under alkaline conditions could allow for its chemical oxidation by the dissolved oxygen into other oxidation products even in the absence of an electrocatalyst or applied potential, however, such homogeneous chemical transformation predominantly yields glycerate.[54] However, because the major product of glycerol oxidation on the $CuCo_2O_4$ catalyst we observe here is formate instead of glycerate (see Table 5.1), and all the collected electrolyte samples were immediately neutralized before the HPLC analysis (see details in the Experimental Section), we reason that the glycerol oxidation product distributions observed here is mainly governed by the electrocatalytic processes on the $CuCo_2O_4$ catalyst rather than by the chemical interconversion of the intermediates. Moreover, the presence of formate as the major product indicates the reaction pathway involving glyceraldehyde (instead of dihydroxyacetone) is more probable in strongly basic solutions, which is consistent with the previous reports of various Ni-based catalysts.[43-46] Although the C-C bond cleavage and formate formation were observed on these Ni-based catalysts,[43-46] their catalytic selectivity and activity toward the formate product was quite low, for example, 32.2%, 7.5%, 4.0%, and 34.1% at a higher potential of 1.6 V vs. RHE and pH = 13 for oxidized Ni, CoNi, FeNi, and FeCoNi catalyst, respectively.[45] Therefore, the $CuCo_2O_4$ catalyst presented here can more effectively cleave the C-C bonds in glycerol and more selectively produce formate with a significantly higher selectivity of ~70% at an even lower potential of 1.3 V vs. RHE at pH = 13 (Table 5.1). These comparisons, along with the presence vs. absence of the oxalate product on the $CuCo_2O_4$ vs. $NiCo_2O_4$ catalyst presented here (Tables A5.4 and A5.5), clearly show that the catalyst compositions can influence the degree of C-C bond cleavage and the glycerol oxidation product distributions. We further compare the C-C bond cleavage on the $CuCo_2O_4$ catalyst with those on noble metal catalysts such as Pt and Au.[43,54,55] The C-C bond cleavage on Pt takes place mostly in acidic solution at high overpotentials rather than in alkaline solution.[55] Under alkaline conditions, unlike Pt which mainly produces glycerate without cleaving the C-C bonds in glycerol, Au is more active toward C-C bond cleavage to form glycolate and formate at high overpotentials.[54] Therefore, we reason that the effective C-C bond cleavage and the high formate selectivity observed here on the $CuCo_2O_4$ catalyst cannot be solely attributed to the alkaline pH or the applied overpotential but indeed depend on the catalyst used.

5.3.5 Characterization of the Tested $CuCo_2O_4$ Catalyst After Bulk Electrolysis of Glycerol Oxidation

Finally, we confirmed the structural and morphological stability of the $CuCo_2O_4$ electrocatalyst after the bulk electrolysis reaction of glycerol oxidation using various structural characterization techniques. SEM image (Figure A5.18) shows that the nanoplate morphology of $CuCo_2O_4$ was well-maintained after the reaction. PXRD pattern (Figure 5.4a) displays no detectable diffraction peak of crystalline impurities after the electrolysis, indicative of the negligible change in the crystal structure. Raman spectra (Figure 5.4b) are in good agreement with the reported spectra of $CuCo_2O_4$ in the literature,[56] and suggest no obvious amorphization of the catalyst surfaces after electrochemical testing. We further carried out X-ray photoelectron spectroscopy (XPS) to probe the surface composition and chemical states of the catalyst. The Co $2p_{3/2}$ peak of as-synthesized $CuCo_2O_4$ catalyst (Figure 5.4c) suggests Co exists predominantly in the form of octahedral Co^{3+} (779.7 eV) with a minor portion of tetrahedral Co^{2+} (781.9 eV).[57] The Cu $2p_{3/2}$ peak of as-synthesized $CuCo_2O_4$ catalyst (Figure 5.4d) can be deconvoluted into two components attributed to the coexistence of tetrahedral Cu^{2+} (935.8 eV) and octahedral Cu^{2+} (933.9 eV).[57] After the bulk electrolysis of glycerol oxidation, both Co 2*p* and Cu 2*p* XPS spectra of the $CuCo_2O_4$ electrocatalyst are nearly identical to those of as-synthesized one, confirming the retention of its surface composition and oxidation states. These results unambiguously confirm the structural and morphological stability of the $CuCo_2O_4$ electrocatalyst under the GOR operating conditions and its promise as a robust catalyst for the electrochemical oxidation of glycerol.

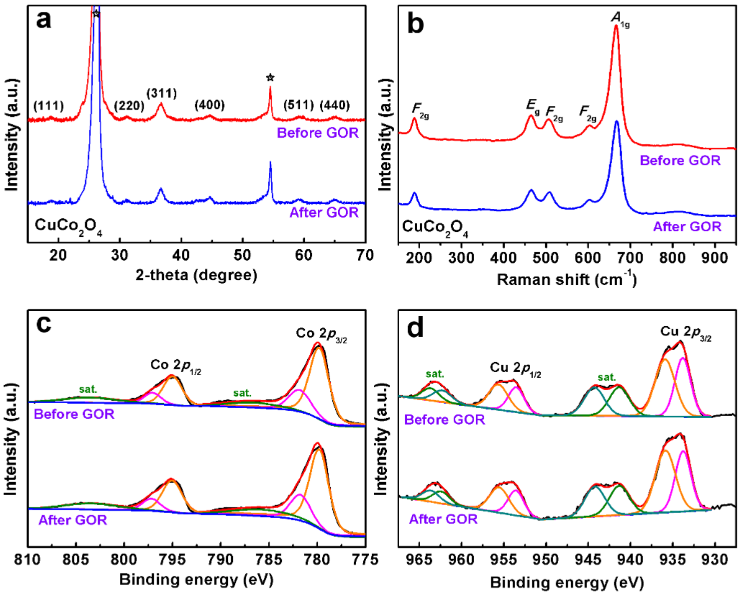

Figure 5.4. Structural and compositional characterization of the $CuCo_2O_4$ electrocatalyst before and after the bulk electrolysis reaction of glycerol oxidation (GOR).

(**a**) PXRD patterns, (**b**) Raman spectra, (**c**) Co 2*p* and (d) Cu 2*p* XPS spectra of the $CuCo_2O_4$ electrocatalyst before and after the bulk electrolysis reaction of glycerol oxidation (GOR).

To the best of our knowledge, this is the first reported comparative study of non-noble metal oxides as electrocatalysts to enable the electrochemical oxidation of glycerol. This study identifies spinel-type $CuCo_2O_4$ to exhibit a robust electrocatalytic performance and a high selectivity toward the production of formic acid from glycerol oxidation. The comparison of this series of six cobalt-based spinel oxides (MCo_2O_4, M = Mn, Fe, Co, Ni, Cu, Zn) for the GOR versus the OER catalysis clearly illustrates that these two oxidation reactions follow very different trends in the catalytic activities of these MCo_2O_4 electrocatalysts. Many spinel oxides (such as Co_3O_4,[58] $NiCo_2O_4$,[59] $Co_xMn_{3-x}O_4$,[60] $Ni_xFe_{3-x}O_4$,[61] $NiFeAlO_4$[62]) are active OER catalysts but $CuCo_2O_4$ is not known to be very active toward OER (which is confirmed herein). Intriguingly, among the series of six cobalt-based spinel oxides, the $CuCo_2O_4$ exhibits the highest GOR catalytic activity, suggesting that the Cu cation may feature the highly intrinsic ability to facilitate the glycerol oxidation. The current comparative study could not distinguish the contributions of the tetrahedral versus the octahedral coordination sites[51,59,63] to the intrinsic GOR catalytic activity and selectivity of the series of MCo_2O_4 catalysts. Therefore, theoretical[64] and *in-situ* and/or *operando* experimental studies[43,65-67] are particularly needed in the future to examine the GOR mechanisms (such as the C-C cleavage discussed above) and the catalytic active sites on these metal oxide surfaces to establish more rigorous structure-activity-selectivity relationships, and to propose qualitative or quantitative descriptors that can accelerate the search of more efficient and more selective GOR electrocatalysts for the production of formic acid or other value-added compounds. We hope this study will stimulate more research efforts in exploring various earth-abundant transition metal oxide electrocatalysts for glycerol oxidation. The major product of formic acid demonstrated here is useful, however, the various C_3 and C_2 products that can be derived from glycerol oxidation, such as dihydroxyacetone[64,68] and the minor products of glyceric acid and glycolic acid in this work, are even more valuable in general,[1] thus achieving such exquisite selectivity would be even more desirable. Exploring buffered neutral pH could be an interesting direction for future studies to possibly achieve a different product selectivity from glycerol oxidation on spinel oxide electrocatalysts (acidic pH is generally not possible for spinel oxides due to their chemical instability).

5.4 Conclusions

In summary, we systematically studied a series of cobalt-based spinel oxide (MCo_2O_4, M = Mn, Fe, Co, Ni, Cu, and Zn) nanostructures as catalyst anodes for the electrochemical oxidation of glycerol and, for the first time, identified $CuCo_2O_4$ as an efficient and stable catalyst that selectively produce formic acid from glycerol oxidation in alkaline solution. The *intrinsic* catalytic activities of this series of spinel oxide catalysts for the glycerol oxidation in 0.1 M or 1 M KOH solution are substantially distinct and follow the sequence of $CuCo_2O_4$ > $NiCo_2O_4$ > $CoCo_2O_4$ > $FeCo_2O_4$ > $ZnCo_2O_4$ > $MnCo_2O_4$. A high glycerol conversion of 79.7% and a high selectivity of 80.6% toward formic acid production were achieved from the bulk electrolysis reaction of glycerol oxidation in 0.1 M KOH solution (pH = 13) at the constant potential of 1.30 V vs. RHE using our most active $CuCo_2O_4$ catalyst with an overall Faradaic efficiency of 89.1% toward all value-added products of glyceric acid, glycolic acid, and formic acid. As the first comparative study of using earth-abundant transition metal oxides for the electrocatalytic oxidation of glycerol, this work opens up new paths for the design and exploration of different classes of earth-abundant catalysts for efficient and selective electrochemical oxidation of glycerol to produce formic acid or other value-added chemicals.

5.5 Experimental Section

5.5.1 Chemicals and Materials

Glycerol ($C_3H_8O_3$, ≥ 99.0%, CAS# 56-81-5), glyceraldehyde ($C_3H_6O_3$, ≥ 90.0%, CAS# 56-82-6), glyceric acid ($C_3H_6O_4$, ≥ 95.0%, CAS# 6000-40-4), glycolic acid ($C_2H_4O_3$, ≥ 99.0%, CAS# 79-14-1), oxalic acid ($C_2H_2O_4$, ≥ 99.0%, CAS# 144-62-7), formic acid (CH_2O_2, ≥ 98.0%, CAS# 64-18-6), potassium hydroxide (KOH, ≥ 85.0%, CAS# 1310-58-3), manganese (II) chloride tetrahydrate ($MnCl_2•4H_2O$, ≥ 98.0%, CAS# 13446-34-9), ferrous (II) chloride tetrahydrate ($FeCl_2•4H_2O$, ≥ 99.0%, CAS# 13478-10-9), cobalt (II) nitrate hexahydrate ($Co(NO_3)_2•6H_2O$, ≥ 98.0%, CAS# 10026-22-9), nickel (II) nitrate hexahydrate ($Ni(NO_3)_2•6H_2O$, ≥ 97.0%, CAS# 13478-00-7), copper (II) nitrate trihydrate ($Cu(NO_3)_2•3H_2O$, ≥ 98.0%, CAS# 10031-43-3), zinc (II) nitrate hexahydrate ($Zn(NO_3)_2•6H_2O$, ≥ 98.0%, CAS# 10196-18-6), ammonium fluoride (NH_4F, ≥ 98.0%, CAS# 12125-01-8), urea ($(NH_2)_2CO$, ≥ 99.5%, CAS# 57-13-6), and ethanol (C_2H_6O, ≥ 99.5%, CAS# 64-17-5) were purchased from Sigma-Aldrich and were used as received unless otherwise noted. Carbon fiber paper (TGP-H-060) was purchased from Fuel Cell Earth (Woburn, MA, USA) and was subjected to hydrophilic treatment (see descriptions below) to remove the surface Teflon coating before use.

5.5.2 Hydrophilic Treatment of Carbon Fiber Paper

The carbon fiber paper was treated with oxygen plasma at 150 W using a plasma cleaner system (LFE Corporation, PUC-502) for 5 min for each side. The surface Teflon coating of the carbon fiber paper is oxidized after the oxygen plasma treatment. Subsequently, the carbon fiber paper was transferred into a preheated oven and was annealed in air at 700 °C for 5 min to remove the oxidized surface coating, resulting in an enhanced hydrophilicity of the carbon surfaces. After being cooled naturally to room temperature, the as-treated carbon fiber paper was stored in a petri dish for further use.

5.5.3 Synthesis of MCo_2O_4 Nanostructures on Carbon Fiber Paper

The series of MCo_2O_4 (M = Mn, Fe, Co, Ni, Cu, and Zn) nanostructures were directly grown on carbon fiber paper using a general hydrothermal method followed by subsequent calcination. In a typical synthesis, 1 mmol of $Co(NO_3)_2$•$6H_2O$ along with 0.5 mmol of respective metal nitrate ($M(NO_3)_2$•xH_2O, M = Co, Ni, Cu, or Zn) or metal chloride (MCl_2•xH_2O, M = Mn or Fe) were dissolved in 40 mL of nanopure deionized water (18.2 MΩ•cm), followed by the addition of 3 mmol of NH_4F and 6 mmol of urea into the solution. After transferring the solution into a 50-mL Teflon-lined stainless steel autoclave and immersing a piece of as-treated carbon fiber paper (2 cm × 3 cm) into the solution, the autoclave was sealed and heated in a pre-heated oven at 120 °C for 6 h. After the hydrothermal reaction, the carbon fiber paper grown with respective metal hydroxide nanostructure precursor was rinsed with nanopure water and ethanol, and then dried under N_2 gas flow. Finally, the as-grown metal hydroxide nanostructure precursor on the carbon fiber paper was annealed in a quartz tube furnace at 300 °C for 3 h under air atmosphere to convert into the corresponding MCo_2O_4 nanostructure catalyst. The catalyst mass loadings of MCo_2O_4 catalysts on carbon fiber paper were determined by the mass differences before and after the materials growth.

5.5.4 Materials Characterization

The nanostructure morphology of the MCo_2O_4 samples was examined using a Leo Supra 55 VP field-emission scanning electron microscope (SEM) operating at an acceleration voltage of 1 kV. Energy-dispersive X-ray spectroscopy (EDS) was performed on the same instrument at 15 kV with a Thermo Fisher Scientific Noran System Seven energy dispersive X-ray spectroscopy detector. Transmission electron microscopy (TEM) was performed on a Hitachi HT7700 transmission electron microscope at an acceleration voltage of 100 kV. Crystal structure characterization was carried out using a Bruker D8 Advance powder X-ray diffractometer (PXRD) equipped with a Cu Kα X-ray source (λ = 1.5418 Å) and a Lynxeye detector. PXRD scans were collected within the 2θ range of 10° to 70° with a step size of 0.02° and an exposure time of 3 s per step. Raman measurement was carried out on a Thermo Fisher Scientific DXR Raman Microscope using a laser excitation at 532 nm. X-ray photoelectron spectroscopy (XPS) was conducted on a Thermo Fisher Scientific K-alpha XPS spectrometer with a microfocused monochromatic Al Kα X-ray source to study the surface compositions and chemical states of the MCo_2O_4 samples.

5.5.5 Electrochemical Characterization

The electrochemical measurements were carried out in an undivided single-compartment three-electrode cell (shown in Figure A5.3) with a BioLogic SP-200 potentiostat. The as-synthesized MCo_2O_4 nanostructures grown on carbon fiber paper substrates were directly fabricated into the working electrodes with the geometric electrode area of ~1 cm^2. A Pt wire counter electrode and an Hg/HgO (1 M KOH) reference electrode were used for all electrochemical measurements. The potential of the Hg/HgO reference electrode was calibrated against a standard Hg/Hg_2Cl_2 (saturated KCl) reference electrode ($E(Hg/Hg_2Cl_2) = 0.241$ V vs. SHE), and all the potentials reported in this work were displayed versus reversible hydrogen electrode (RHE) according to the following equations:

$$E(\mathrm{Hg/HgO})\ \mathrm{vs.\ SHE} = E(\mathrm{Hg/Hg_2Cl_2})\ \mathrm{vs.\ SHE} - 0.128\ \mathrm{V} = 0.113\ \mathrm{V\ vs.\ SHE}$$

$$E\ \mathrm{vs.\ RHE} = E\ \mathrm{vs.\ Hg/HgO} + E(\mathrm{Hg/HgO})\ \mathrm{vs.\ SHE} + 0.059 \times \mathrm{pH}$$

The electrochemical glycerol oxidation reaction (GOR) was conducted in 2 mL of 0.1 M or 1 M KOH solution (pH = 13 or 14, respectively) with the presence of 0.1 M glycerol. For some electrochemical tests examining the electrochemical oxidation of various GOR intermediate products, 0.1 M of the respective molecule (glyceraldehyde, glyceric acid, glycolic acid, oxalic acid, or formic acid) was added to the electrolyte solution. Linear sweep voltammetry (LSV) was conducted by positively sweeping the potential at a scan rate of 1 mV s^{-1} at room temperature under vigorous stirring. All the LSV curves in this work were reported after iR-correction, with uncompensated solution resistance determined by electrochemical impedance spectroscopy (EIS). Long-term bulk electrolysis reactions of glycerol oxidation were carried out at the constant potentials of 1.20, 1.23, 1.26, and 1.30 V vs. RHE at room temperature under vigorous stirring. The constant potentials applied in these long-term chronoamperometry tests were presented without iR-correction.

5.5.6 Product Analysis

The products from the electrochemical glycerol oxidation were determined and analyzed by high-performance liquid chromatography (HPLC, Shimadzu Prominence LC-20AD). For each HPLC measurement, 150 μL of the electrolyte solution was sampled from the electrochemical cell and was diluted to 1.5 mL with dilute sulfuric acid solution (to adjust the sample pH below 7.0), and then 10 μL of the diluted sample was directly injected into a BioRad Aminex 87H column. 5 mM H_2SO_4 solution was used as the mobile phase in the isocratic mode with a constant flow rate of 0.6 mL min^{-1}. The glycerol oxidation products were identified by comparing the retention times of the HPLC elution peaks with the individual standard sample solutions (Figure A5.10). The retention times at 6.8, 10.5, 12.0, 12.8, and 13.5 min correspond to oxalic acid, glyceric acid, glycolic acid, glycerol, and formic acid, respectively. The product concentrations were calculated from the calibration curves made by measuring standard solutions of known concentrations (Figure

A5.10). The glycerol conversion (η_{glycerol}) and product selectivity of C_3, C_2, and C_1 products ($S_{\text{C3 product}}$, $S_{\text{C2 product}}$, and $S_{\text{C1 product}}$, respectively) can be calculated using the following equations:

$$\eta_{\text{glycerol}} = \frac{C_{0,\text{glycerol}} - C_{\text{glycerol}}}{C_{0,\text{glycerol}}} \times 100\%$$

$$S_{\text{C3 product}} = \frac{C_{\text{C3 product}}}{C_{0,\text{glycerol}} - C_{\text{glycerol}}} \times 100\%$$

$$S_{\text{C2 product}} = \frac{C_{\text{C2 product}} \times (2/3)}{C_{0,\text{glycerol}} - C_{\text{glycerol}}} \times 100\%$$

$$S_{\text{C1 product}} = \frac{C_{\text{C1 product}} \times (1/3)}{C_{0,\text{glycerol}} - C_{\text{glycerol}}} \times 100\%$$

where $C_{0,\text{glycerol}}$ and C_{glycerol} are the initial and final concentration of glycerol, respectively; $C_{\text{C3 product}}$, $C_{\text{C2 product}}$, and $C_{\text{C1 product}}$ are the final concentrations of C_3 product (glyceric acid), C_2 products (glycolic acid, oxalic acid), and C_1 product (formic acid), respectively. Note that a factor of 2/3 or 1/3 is involved when calculating the product selectivity of C_2 or C_1 product, respectively, because only 2/3 or 1/3 equivalence of glycerol is consumed to produce one equivalence of C_2 or C_1 product, respectively. Detailed calculations of Faradaic efficiency and the input and output aqueous phase organic carbon amounts of the electrochemical glycerol oxidation are described in the Appendix 5.

5.6 References

1. Dodekatos, G.; Schunemann, S.; Tuysuz, H. Recent Advances in Thermo-, Photo-, and Electrocatalytic Glycerol Oxidation. *ACS Catal.* ***8***, 6301-6333 (2018).

2. Quispe, C. A. G.; Coronado, C. J. R.; Carvalho, J. A. Glycerol: Production, Consumption, Prices, Characterization and New Trends in Combustion. *Renew. Sust. Energ. Rev.* ***27***, 475-493 (2013).

3. Werpy, T.; Petersen, G. *Top Value Added Chemicals from Biomass: Volume I -- Results of Screening for Potential Candidates from Sugars and Synthesis Gas*: United States2004.

4. Bozell, J. J.; Petersen, G. R. Technology Development for the Production of Biobased Products from Biorefinery Carbohydrates-the US Department of Energy's "Top 10" Revisited. *Green Chem.* ***12***, 539-554 (2010).

5. Pagliaro, M.; Ciriminna, R.; Kimura, H.; Rossi, M.; Della Pina, C. From Glycerol to Value-Added Products. *Angew. Chem. Int. Ed.* ***46***, 4434-4440 (2007).

6. Zhang, Z. H.; Huber, G. W. Catalytic Oxidation of Carbohydrates into Organic Acids and Furan Chemicals. *Chem. Soc. Rev.* ***47***, 1351-1390 (2018).

7. Yu, X. W.; Pickup, P. G. Recent Advances in Direct Formic Acid Fuel Cells (DFAFC). *J. Power Sources* ***182***, 124-132 (2008).

8. Grasemann, M.; Laurenczy, G. Formic Acid as a Hydrogen Source - Recent Developments and Future Trends. *Energy Environ. Sci.* ***5***, 8171-8181 (2012).

9. Eppinger, J.; Huang, K. W. Formic Acid as a Hydrogen Energy Carrier. *ACS Energy Lett.* ***2***, 188-195 (2017).

10. van Putten, R.; Wissink, T.; Swinkels, T.; Pidko, E. A. Fuelling the Hydrogen Economy: Scale-Up of an Integrated Formic Acid-to-Power System. *Int. J. Hydrog. Energy* ***44***, 28533-28541 (2019).

11. Sordakis, K.; Tang, C.; Vogt, L. K.; Junge, H.; Dyson, P. J.; Beller, M.; Laurenczy, G. Homogeneous Catalysis for Sustainable Hydrogen Storage in Formic Acid and Alcohols. *Chem. Rev.* ***118***, 372-433 (2018).

12. Zhang, J. Z.; Sun, M.; Han, Y. Selective Oxidation of Glycerol to Formic Acid in Highly Concentrated Aqueous Solutions with Molecular Oxygen Using V-Substituted Phosphomolybdic Acids. *RSC Adv.* ***4***, 35463-35466 (2014).

13. Xu, J. L.; Zhao, Y. F.; Xu, H. J.; Zhang, H. Y.; Yu, B.; Hao, L. D.; Liu, Z. M. Selective Oxidation of Glycerol to Formic Acid Catalyzed by Ru(OH)(4)/r-GO in the Presence of FeCl3. *Appl. Catal. B: Environ.* ***154***, 267-273 (2014).

14. Farnetti, E.; Crotti, C. Selective Oxidation of Glycerol to Formic Acid Catalyzed by Iron Salts. *Catal. Commun.* ***84***, 1-4 (2016).

15. Crotti, C.; Farnetti, E. Selective Oxidation of Glycerol Catalyzed by Iron Complexes. *J. Mol. Catal. A: Chem.* ***396***, 353-359 (2015).

16. Pullanikat, P.; Lee, J. H.; Yoo, K. S.; Jung, K. W. Direct Conversion of Glycerol into Formic Acid via Water Stable Pd(II) Catalyzed Oxidative Carbon-Carbon Bond Cleavage. *Tetrahedron Lett.* ***54***, 4463-4466 (2013).

17. Liu, W. J.; Dang, L. N.; Xu, Z. R.; Yu, H. Q.; Jin, S.; Huber, G. W. Electrochemical Oxidation of 5-Hydroxymethylfurfural with NiFe Layered Double Hydroxide (LDH) Nanosheet Catalysts. *ACS Catal.* ***8***, 5533-5541 (2018).

18. Liu, W.-J.; Xu, Z.; Zhao, D.; Pan, X.-Q.; Li, H.-C.; Hu, X.; Fan, Z.-Y.; Wang, W.-K.; Zhao, G.-H.; Jin, S.; Huber, G. W.; Yu, H.-Q. Efficient Electrochemical Production of Glucaric Acid and H2 via Glucose Electrolysis. *Nat. Commun.* ***11***, 265 (2020).

19. You, B.; Liu, X.; Jiang, N.; Sun, Y. A General Strategy for Decoupled Hydrogen Production from Water Splitting by Integrating Oxidative Biomass Valorization. *J. Am. Chem. Soc.* ***138***, 13639-13646 (2016).

20. Simoes, M.; Baranton, S.; Coutanceau, C. Electrochemical Valorisation of Glycerol. *ChemSusChem* ***5***, 2106-2124 (2012).

21. Kim, H. J.; Lee, J.; Green, S. K.; Huber, G. W.; Kim, W. B. Selective Glycerol Oxidation by Electrocatalytic Dehydrogenation. *ChemSusChem* ***7***, 1051-1056 (2014).

22. Verma, S.; Lu, S.; Kenis, P. J. A. Co-Electrolysis of CO2 and Glycerol as a Pathway to Carbon Chemicals with Improved Technoeconomics Due to Low Electricity Consumption. *Nat. Energy* ***4***, 466-474 (2019).

23. You, B.; Liu, X.; Liu, X.; Sun, Y. Efficient H2 Evolution Coupled with Oxidative Refining of Alcohols via A Hierarchically Porous Nickel Bifunctional Electrocatalyst. *ACS Catal.* ***7***, 4564-4570 (2017).

24. Seh, Z. W.; Kibsgaard, J.; Dickens, C. F.; Chorkendorff, I. B.; Norskov, J. K.; Jaramillo, T. F. Combining Theory and Experiment in Electrocatalysis: Insights into Materials Design. *Science* ***355***, 1 (2017).

25. Chu, S.; Cui, Y.; Liu, N. The Path Towards Sustainable Energy. *Nat. Mater.* ***16***, 16-22 (2017).

26. Simoes, M.; Baranton, S.; Coutanceau, C. Electro-Oxidation of Glycerol at Pd Based Nano-Catalysts for an Application in Alkaline Fuel Cells for Chemicals and Energy Cogeneration. *Appl. Catal. B: Environ.* ***93***, 354-362 (2010).

27. Zhang, Z.; Xin, L.; Li, W. Electrocatalytic Oxidation of Glycerol on Pt/C in Anion-Exchange Membrane Fuel Cell: Cogeneration of Electricity and Valuable Chemicals. *Appl. Catal. B: Environ.* ***119***, 40-48 (2012).

28. Qi, J.; Xin, L.; Chadderdon, D. J.; Qiu, Y.; Jiang, Y. B.; Benipal, N.; Liang, C. H.; Li, W. Z. Electrocatalytic Selective Oxidation of Glycerol to Tartronate on Au/C Anode Catalysts in Anion Exchange Membrane Fuel Cells with Electricity Cogeneration. *Appl. Catal. B: Environ.* ***154***, 360-368 (2014).

29. Kim, H. J.; Choi, S. M.; Seo, M. H.; Green, S.; Huber, G. W.; Kim, W. B. Efficient Electrooxidation of Biomass-Derived Glycerol over a Graphene-Supported PtRu Electrocatalyst. *Electrochem. Commun.* ***13***, 890-893 (2011).

30. Kim, H. J.; Choi, S. M.; Green, S.; Tompsett, G. A.; Lee, S. H.; Huber, G. W.; Kim, W. B. Highly Active and Stable PtRuSn/C Catalyst for Electrooxidations of Ethylene Glycol and Glycerol. *Appl. Catal. B: Environ.* ***101***, 366-375 (2011).

31. Lee, S.; Kim, H. J.; Lim, E. J.; Kim, Y.; Noh, Y.; Huber, G. W.; Kim, W. B. Highly Selective Transformation of Glycerol to Dihydroxyacetone without Using Oxidants by a PtSb/C-Catalyzed Electrooxidation Process. *Green Chem.* ***18***, 2877-2887 (2016).

32. Simoes, M.; Baranton, S.; Coutanceau, C. Enhancement of Catalytic Properties for Glycerol Electrooxidation on Pt and Pd Nanoparticles Induced by Bi Surface Modification. *Appl. Catal. B: Environ.* ***110***, 40-49 (2011).

33. Zalineeva, A.; Serov, A.; Padilla, M.; Martinez, U.; Artyushkova, K.; Baranton, S.; Coutanceau, C.; Atanassov, P. B. Self-Supported PdxBi Catalysts for the Electrooxidation of Glycerol in Alkaline Media. *J. Am. Chem. Soc.* ***136***, 3937-3945 (2014).

34. Faber, M. S.; Jin, S. Earth-Abundant Inorganic Electrocatalysts and Their Nanostructures for Energy Conversion Applications. *Energy Environ. Sci.* ***7***, 3519-3542 (2014).

35. Roger, I.; Shipman, M. A.; Symes, M. D. Earth-Abundant Catalysts for Electrochemical and Photoelectrochemical Water Splitting. *Nat. Rev. Chem.* ***1***, 0003 (2017).

36. Suen, N.-T.; Hung, S.-F.; Quan, Q.; Zhang, N.; Xu, Y.-J.; Chen, H. M. Electrocatalysis for the Oxygen Evolution Reaction: Recent Development and Future Perspectives. *Chem. Soc. Rev.* ***46***, 337-365 (2017).

37. Xia, W.; Mahmood, A.; Liang, Z.; Zou, R.; Guo, S. Earth-Abundant Nanomaterials for Oxygen Reduction. *Angew. Chem. Int. Ed.* **55**, 2650-2676 (2016).

38. Nam, D.-H.; Taitt, B. J.; Choi, K.-S. Copper-Based Catalytic Anodes To Produce 2,5-Furandicarboxylic Acid, a Biomass-Derived Alternative to Terephthalic Acid. *ACS Catal.* ***8***, 1197-1206 (2018).

39. You, B.; Jiang, N.; Liu, X.; Sun, Y. Simultaneous H2 Generation and Biomass Upgrading in Water by an Efficient Noble-Metal-Free Bifunctional Electrocatalyst. *Angew. Chem. Int. Ed.* **55**, 9913-9917 (2016).

40. Jiang, N.; You, B.; Boonstra, R.; Terrero Rodriguez, I. M.; Sun, Y. Integrating Electrocatalytic 5-Hydroxymethylfurfural Oxidation and Hydrogen Production via Co–P-Derived Electrocatalysts. *ACS Energy Lett.* ***1***, 386-390 (2016).

41. Jin, S. Are Metal Chalcogenides, Nitrides, and Phosphides Oxygen Evolution Catalysts or Bifunctional Catalysts? *ACS Energy Lett.* ***2***, 1937-1938 (2017).

42. Zhu, Y.; Chen, H.-C.; Hsu, C.-S.; Lin, T.-S.; Chang, C.-J.; Chang, S.-C.; Tsai, L.-D.; Chen, H. M. Operando Unraveling of the Structural and Chemical Stability of P-Substituted CoSe2 Electrocatalysts toward Hydrogen and Oxygen Evolution Reactions in Alkaline Electrolyte. *ACS Energy Lett.* ***4***, 987-994 (2019).

43. Chang, S. C.; Ho, Y.; Weaver, M. J. Applications of Real-Time FTIR Spectroscopy to the Elucidation of Complex Electroorganic Pathways: Electrooxidation of Ethylene Glycol on Gold, Platinum, and Nickel in Alkaline Solution. *J. Am. Chem. Soc.* ***113***, 9506-9513 (1991).

44. Oliveira, V. L.; Morais, C.; Servat, K.; Napporn, T. W.; Tremiliosi-Filho, G.; Kokoh, K. B. Glycerol Oxidation on Nickel Based Nanocatalysts in Alkaline Medium – Identification of the Reaction Products. *J. Electroanal. Chem.* ***703***, 56-62 (2013).

45. Oliveira, V. L.; Morais, C.; Servat, K.; Napporn, T. W.; Tremiliosi-Filho, G.; Kokoh, K. B. Studies of the Reaction Products Resulted from Glycerol Electrooxidation on Ni-Based Materials in Alkaline Medium. *Electrochim. Acta* ***117***, 255-262 (2014).

46. Lam, C. H.; Bloomfield, A. J.; Anastas, P. T. A Switchable Route to Valuable Commodity Chemicals from Glycerol via Electrocatalytic Oxidation with an Earth Abundant Metal Oxidation Catalyst. *Green Chem.* ***19***, 1958-1968 (2017).

47. Li, Y.; Wei, X.; Chen, L.; Shi, J.; He, M. Nickel-Molybdenum Nitride Nanoplate Electrocatalysts for Concurrent Electrolytic Hydrogen and Formate Productions. *Nat. Commun.* ***10***, 5335 (2019).

48. Sun, S.; Sun, L.; Xi, S.; Du, Y.; Anu Prathap, M. U.; Wang, Z.; Zhang, Q.; Fisher, A.; Xu, Z. J. Electrochemical Oxidation of C3 Saturated Alcohols on Co3O4 in Alkaline. *Electrochim. Acta* ***228***, 183-194 (2017).

49. Taitt, B. J.; Nam, D.-H.; Choi, K.-S. A Comparative Study of Nickel, Cobalt, and Iron Oxyhydroxide Anodes for the Electrochemical Oxidation of 5-Hydroxymethylfurfural to 2,5-Furandicarboxylic Acid. *ACS Catal.* ***9***, 660-670 (2019).

50. Zheng, J.; Chen, X. L.; Zhong, X.; Li, S. Q.; Liu, T. Z.; Zhuang, G. L.; Li, X. N.; Deng, S. W.; Mei, D. H.; Wang, J. G. Hierarchical Porous NC@CuCo Nitride Nanosheet Networks: Highly Efficient Bifunctional Electrocatalyst for Overall Water Splitting and Selective Electrooxidation of Benzyl Alcohol. *Adv. Funct. Mater.* ***27***, 11 (2017).

51. Zhao, Q.; Yan, Z.; Chen, C.; Chen, J. Spinels: Controlled Preparation, Oxygen Reduction/Evolution Reaction Application, and Beyond. *Chem. Rev.* ***117***, 10121-10211 (2017).

52. Bard, A. J.; Faulkner, L. R.: *Electrochemical Methods: Fundamentals and Applications*; 2nd ed.; John Wiley & Sons, Inc., 2001. pp. 140-141.

53. Garcia, A. C.; Kolb, M. J.; van Nierop y Sanchez, C.; Vos, J.; Birdja, Y. Y.; Kwon, Y.; Tremiliosi-Filho, G.; Koper, M. T. M. Strong Impact of Platinum Surface Structure on Primary and Secondary Alcohol Oxidation during Electro-Oxidation of Glycerol. *ACS Catal.* ***6***, 4491-4500 (2016).

54. Kwon, Y.; Schouten, K. J. P.; Koper, M. T. M. Mechanism of the Catalytic Oxidation of Glycerol on Polycrystalline Gold and Platinum Electrodes. *ChemCatChem* ***3***, 1176-1185 (2011).

55. Roquet, L.; Belgsir, E. M.; Léger, J. M.; Lamy, C. Kinetics and Mechanisms of the Electrocatalytic Oxidation of Glycerol as Investigated by Chromatographic Analysis of the Reaction Products: Potential and pH Effects. *Electrochim. Acta* ***39***, 2387-2394 (1994).

56. Kaverlavani, S. K.; Moosavifard, S. E.; Bakouei, A. Designing Graphene-Wrapped Nanoporous CuCo2O4 Hollow Spheres Electrodes for High-Performance Asymmetric Supercapacitors. *J. Mater. Chem. A* **5**, 14301-14309 (2017).

57. Li, G. H.; Dai, L. Z.; Lu, D. S.; Peng, S. Y. Characterization of Copper Cobalt Mixed-Oxide. *J. Solid State Chem.* ***89***, 167-173 (1990).

58. Sun, S. N.; Sun, Y. M.; Zhou, Y.; Xi, S. B.; Ren, X.; Huang, B. C.; Liao, H. B.; Wang, L. Y. P.; Du, Y. H.; Xu, Z. C. Shifting Oxygen Charge Towards Octahedral Metal: A Way to Promote Water Oxidation on Cobalt Spinel Oxides. *Angew. Chem. Int. Ed.* ***58***, 6042-6047 (2019).

59. Wei, C.; Feng, Z. X.; Scherer, G. G.; Barber, J.; Shao-Horn, Y.; Xu, Z. C. J. Cations in Octahedral Sites: A Descriptor for Oxygen Electrocatalysis on Transition-Metal Spinels. *Adv. Mater.* ***29***, 8 (2017).

60. Cheng, F. Y.; Shen, J. A.; Peng, B.; Pan, Y. D.; Tao, Z. L.; Chen, J. Rapid Room-Temperature Synthesis of Nanocrystalline Spinels as Oxygen Reduction and Evolution Electrocatalysts. *Nat. Chem.* ***3***, 79-84 (2011).

61. Huang, J. Z.; Han, J. C.; Wang, R.; Zhang, Y. Y.; Wang, X. J.; Zhang, X. H.; Zhang, Z. H.; Zhang, Y. M.; Song, B.; Jin, S. Improving Electrocatalysts for Oxygen Evolution Using NixFe3-xO(4)/Ni Hybrid Nanostructures Formed by Solvothermal Synthesis. *ACS Energy Lett.* ***3***, 1698-1707 (2018).

62. Chen, J. Y. C.; Miller, J. T.; Gerken, J. B.; Stahl, S. S. Inverse Spinel NiFeAlO4 as a Highly Active Oxygen Evolution Electrocatalyst: Promotion of Activity by a Redox-Inert Metal Ion. *Energy Environ. Sci.* ***7***, 1382-1386 (2014).

63. Wang, H.-Y.; Hung, S.-F.; Chen, H.-Y.; Chan, T.-S.; Chen, H. M.; Liu, B. In Operando Identification of Geometrical-Site-Dependent Water Oxidation Activity of Spinel Co3O4. *J. Am. Chem. Soc.* ***138***, 36-39 (2016).

64. Liu, D.; Liu, J. C.; Cai, W. Z.; Ma, J.; Yang, H. B.; Xiao, H.; Li, J.; Xiong, Y. J.; Huang, Y. Q.; Liu, B. Selective Photoelectrochemical Oxidation of Glycerol to High Value-Added Dihydroxyacetone. *Nat. Commun.* ***10***, 8 (2019).

65. Holade, Y.; Morais, C.; Servat, K.; Napporn, T. W.; Kokoh, K. B. Toward the Electrochemical Valorization of Glycerol: Fourier Transform Infrared Spectroscopic and Chromatographic Studies. *ACS Catal.* ***3***, 2403-2411 (2013).

66. Huang, L.; Sun, J. Y.; Cao, S. H.; Zhan, M.; Ni, Z. R.; Sun, H. J.; Chen, Z.; Zhou, Z. Y.; Sorte, E. G.; Tong, Y. J.; Sun, S. G. Combined EC-NMR and In Situ FTIR Spectroscopic Studies of Glycerol Electrooxidation on Pt/C, PtRu/C, and PtRh/C. *ACS Catal.* ***6***, 7686-7695 (2016).

67. Zhu, Y.; Wang, J.; Chu, H.; Chu, Y.-C.; Chen, H. M. In Situ/Operando Studies for Designing Next-Generation Electrocatalysts. *ACS Energy Lett.*, 1281-1291 (2020).

68. Kwon, Y.; Birdja, Y.; Spanos, I.; Rodriguez, P.; Koper, M. T. M. Highly Selective Electro-Oxidation of Glycerol to Dihydroxyacetone on Platinum in the Presence of Bismuth. *ACS Catal.* ***2***, 759-764 (2012).

CHAPTER 6

Stable Tetrasubstituted Quinone Redox Reservoir for Enhancing Decoupled Hydrogen and Oxygen Evolution[*]

6.1 Abstract

Redox reservoirs (RRs) may be used to decouple the two half-reactions of water electrolysis, enabling spatial and temporal separation of hydrogen and oxygen evolution. Organic RRs are appealing candidates for this application; however, their instability limits their utility. Here, we show that a tetrathioether-substituted quinone, tetramercaptopropanesulfonate quinone (TMQ), exhibits significantly enhanced stability relative to anthraquinone-2,7-disulfonate (AQDS), the most effective organic RR reported previously. The enhanced stability, confirmed by symmetric flow battery experiments under relevant conditions, enables stable electrochemical production of H_2 and O_2 in a continuous flow electrolysis cell. The reduced RR, tetramercaptopropanesulfonate hydroquinone (TMHQ), is not susceptible to decomposition, while the oxidized state, TMQ, undergoes slow decomposition, evident only after sustained operation (>60 h). Analysis of the byproducts provides that basis for a decomposition mechanism, establishing a foundation for the design of new organic RRs with even better performance.

---

[*] This chapter was originally published in *ACS Energy Lett.* ***6***, 1533–1539 (2021), in collaboration with Fei Wang, Wenjie Li, James B. Gerken, Song Jin, and Shannon S. Stahl.

6.2 Introduction

Hydrogen is a sustainable energy carrier and a commodity chemical for industrial synthesis. As the vast majority of contemporary hydrogen production relies on the steam reforming of methane,[1] water electrolysis driven by renewable power sources represents an appealing alternative.[2–4] Conventional water electrolysis takes place in a two-electrode configuration, with the hydrogen evolution reaction (HER) taking place at the cathode, and the oxygen evolution reaction (OER) taking place at the anode. A membrane separator minimizes gas mixing; however, nontrivial gas crossover, which can occur when the system is operated at low current densities and/or elevated pressures, can create safety hazards, require gas purification, and/or cause electrolyzer degradation.[5–8] Decoupled water splitting circumvents this issue by pairing the individual HER and OER half reactions with electrochemical reactions of a "redox reservoir" (RR),[9] or redox mediator, or electron-coupled-proton buffer (Figure 6.1a).[10–13] Analogous to the water reservoir in pumped hydroelectric storage, the function of a RR is to store the electrons and ions temporarily so they can be used for different electrochemical half-reactions. Both solid-state[9,14–17] and molecular[18–26] redox mediators have been used for this purpose. Increasing attention has been focused on redox active organic molecules because they are composed of earth-abundant materials and have properties that may be tuned synthetically (e.g., redox potential, solubility, stability, electrochemical kinetics).[27,28] One configuration for decoupled water splitting, schematically depicted in Figure 6.1b, features two individual electrolytic flow cells in which protons are exchanged via the soluble RR. Specifically, hydrogen evolution in the HER cell is coupled to oxidation of RR, rather than water oxidation, and water oxidation in the OER cell is coupled to reduction of RR, rather than proton reduction. This approach enables spatial and temporal separation of hydrogen and oxygen evolution and also has other advantageous features. For example, the voltage of each individual cell is typically much less than that of a cell performing direct water splitting, potentially facilitating integration of the decoupled process with renewable power sources (e.g., solar and/or wind),[10,18] and the fast HER rate is not intrinsically constrained by the comparatively sluggish OER rate.[29]

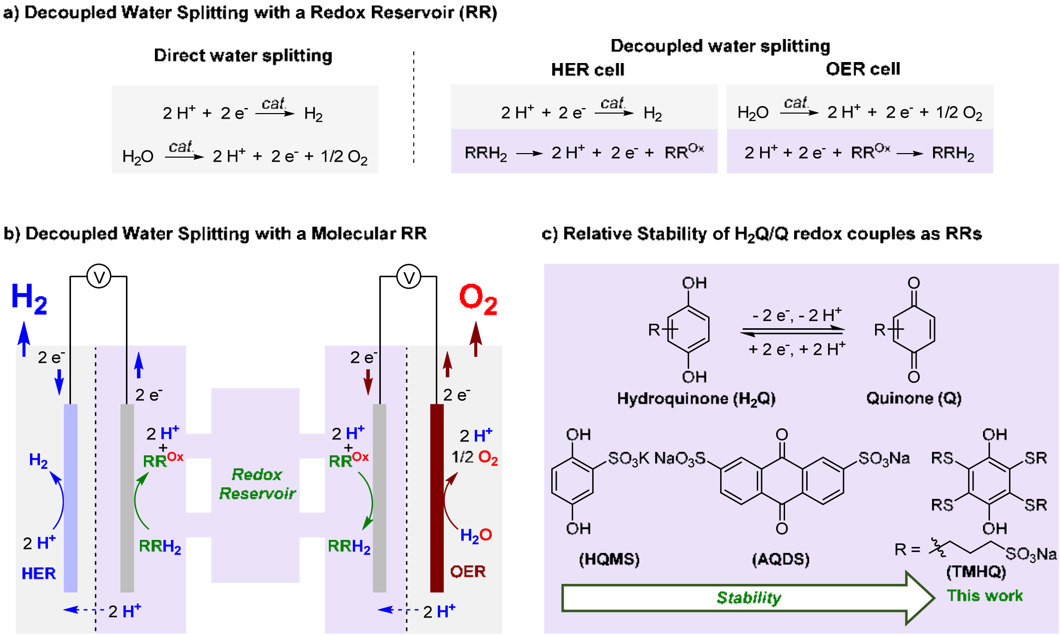

Figure 6.1. Schematic illustration of decoupled electrocatalytic water splitting enabled by a redox reservoir based on a hydroquinone/quinone (H_2Q/Q) redox couple.

(**a**) Decoupled electrolytic water splitting enabled by a redox reservoir (RR). (**b**) Schematic of decoupled hydrogen and oxygen evolution using a molecular RR in two flow cells, where RRH_2 and RR^{Ox} are the reduced and oxidized form of RR, respectively. (**c**) Stability comparison of hydroquinone/quinone (H_2Q/Q) redox couples as the RRs.

Decoupled redox processes are well-known in the photosynthetic electron transport chains of bacteria and green plants. Such processes generate O_2 gas and H_2 equivalents in the form of NADH (NAD = nicotinamide adenine dinucleotide) at separate sites, using quinone derivatives, such as plastoquinone and coenzyme Q10, and other mediators to shuttle electrons and protons.[30−32] In an abiotic analog of this process, Cronin and coworkers demonstrated hydroquinone monosulfonate (HQMS, Figure 6.1c) as a molecular RR for decoupled water splitting in 2013 (Figure 6.1c).[19] The oxidized form of this RR, quinone monosulfonate (QMS), is susceptible to nucleophilic attack by water,[33] decreasing its redox capacity and limiting its practical utility. The same group recently used anthraquinone-2,7-disulfonate (AQDS, Figure 6.1c) as a RR for decoupled water splitting in flow electrolysis cells.[24] AQDS is substantially more stable than QMS; however, its reduced form, anthrahydroquinone-2,7-disulfonate (AHQDS), is prone to disproportionation under acidic conditions to produce redox-inactive byproducts.[34–36] We recently reported the synthesis of a series of densely functionalized water soluble quinones with redox potentials of 440–750 mV vs. SHE.[37] Tetramercaptopropanesulfonate hydroquinone/quinone (TMHQ/TMQ, Figure 6.1c) are appealing because stability tests performed in the context of fuel cell[38] and flow battery[39] applications indicated that TMHQ/TMQ are much more stable than other quinones with similar redox potentials. Herein, we show the utility of TMHQ/TMQ as RRs for decoupled water splitting and demonstrate their improved stability relative to the previously reported AHQDS/AQDS RRs.[24]

Ideal molecular RRs for decoupled water splitting should meet several criteria:[10,11] exhibit a redox potential between the catalytic HER and the OER potentials; buffer the solution pH by accepting and releasing protons upon reduction and oxidation, respectively; be readily synthesized from low-cost materials; and have composition stability and high solubility in aqueous solutions.[40,41] The basic attributes of TMHQ/TMQ suggest that TMHQ/TMQ might be good RR candidates for decoupled water splitting.[37–39] Cyclic voltammetry (CV) data shows that the 2 H^+/2 e^- redox potential of TMHQ/TMQ (0.61 V vs. SHE) is approximately halfway between the standard potentials of the HER and the OER (see Figures A6.1 and A6.2 in Section 3 of the Appendix 6 for full CV and rotating-disk electrochemical analysis). TMHQ is readily prepared on >100 g quantities in a single step from inexpensive commercially available reagents.[37] The tetrasodium salt is readily soluble in aqueous solution with a saturation concentration of ~0.25 M at room temperature, and the facile ion exchange of Na^+ to proton using a resin column further increases the solubility to >1.0 M.[38]

6.3 Results and Discussion

6.3.1 Symmetric Redox Flow Battery Approach for Stability Evaluation of the TMHQ/TMQ vs. AHQDS/AQDS Redox Couple

Our initial efforts focused on comparing the stability of the TMHQ/TMQ and AHQDS/AQDS redox couples by using a symmetric redox flow battery approach reported by Goulet and Aziz.[35] This method uses the same redox electrolytes and identical concentrations on both sides of the cell to eliminate effects arising from crossover. Different electrolyte volumes are used, defined as the capacity-limiting side (CLS) and the non-capacity-limiting side (NCLS), respectively (Figure 6.2a). Preliminary ^{1}H NMR spectroscopic studies (see Figures A6.3–A6.8 in Section 4 of the Appendix 6 for details) revealed that each hydroquinone/quinone pair features a redox state that is comparatively less stable. Specifically, the oxidized TMQ state undergoes decomposition more rapidly than the reduced TMHQ state (see below for analysis of the decomposition mechanism). In contrast, decomposition of AHQDS/AQDS primarily occurs from the reduced state (AHQDS), as noted above in the introduction. Because effective RRs should be able to be stored in either the oxidized or reduced form, subsequent stability testing prioritized analysis of the less stable form of these redox couples (i.e., TMQ and AHQDS, respectively).

Symmetric redox flow battery tests started with the electrolytes in both the CLS and the NCLS having equal amounts of oxidized and reduced quinones/hydroquinones (i.e., at 50% state of charge, SOC). Redox cycling was paused periodically after every two charge/discharge cycles in order to hold the CLS electrolyte at the less stable redox state (i.e., when charged/discharged to 100% TMQ and AHQDS, respectively) (see Section 5 of the Appendix 6 for details).[35] The experiments employed 0.25 M concentration of the RRs in 1 M H_2SO_4 (aq) electrolyte solutions and the charge/discharge cycles were conducted at a constant current density of 50 mA/cm^2 (Figure A6.9 in Section 5 of the Appendix 6). An elevated temperature of 50 °C was used to accelerate the decomposition rate. The TMHQ/TMQ symmetric flow battery data show that these RRs retain their charge capacity, with a less than 1.5% decay after 9 days under such stringent conditions (Figures 6.2b, and 6.2d red curves). ^{1}H NMR analysis of CLS solution after testing showed negligible byproduct formation (see Figure A6.10 in Section 5 of the Appendix 6). An identical symmetric flow battery test was conducted with AHQDS/AQDS, and the data show a ~26% loss in charge capacity over the same time period (Figures 6.2c, and 6.2d blue curves).[42] ^{1}H NMR analysis of this CLS solution revealed significant unidentified byproducts derived from AHQDS decomposition (see Figure A6.11 in Section 5 of the Appendix 6). These results demonstrate the improved stability of the TMHQ/TMQ RR pair relative to AHQDS/AQDS.

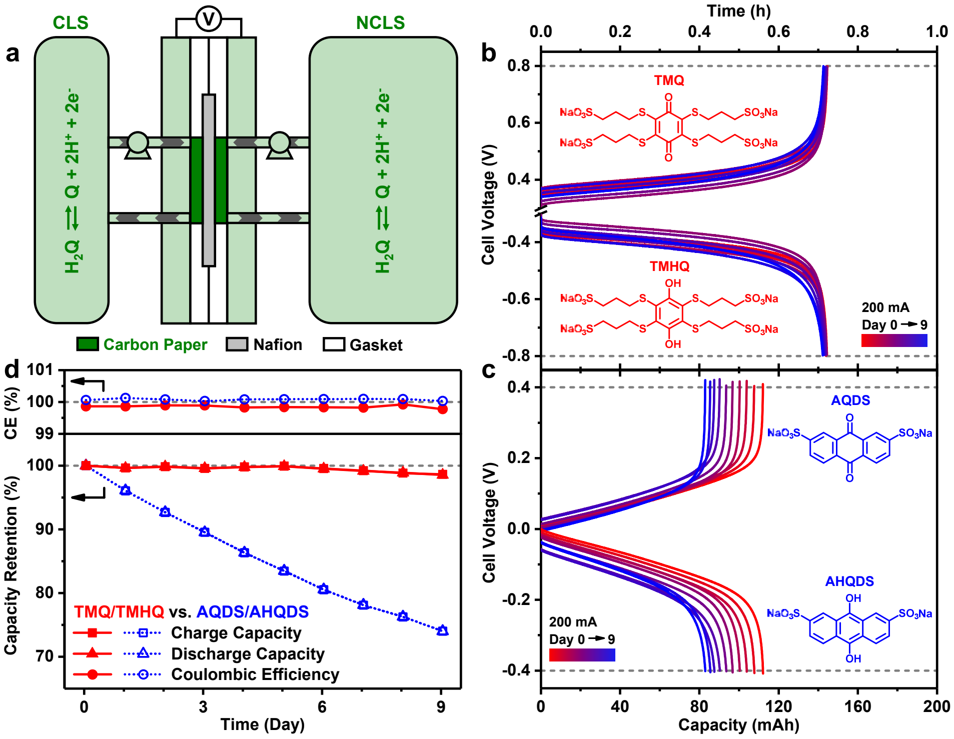

Figure 6.2. Stability comparisons of TMHQ/TMQ vs. AHQDS/AQDS using a symmetric redox flow battery approach.

(**a**) Schematic description of a symmetric flow battery with a capacity-limiting side (CLS) and a non-capacity-limiting side (NCLS). (**b,c**) Galvanostatic cycling curves of (**b**) TMHQ/TMQ and (**c**) AHQDS/AQDS symmetric flow batteries (electrolyte: 0.25 M redox mediator in 1 M H_2SO_4 solution; temperature: 50 °C; current density: 50 mA/cm^2; cut-off cell voltage: ±0.8 and ±0.4 V for TMHQ/TMQ and AHQDS/AQDS, respectively). (**d**) Coulombic efficiencies (CE) and capacity retention rates of TMHQ/TMQ (red curves) and AHQDS/AQDS (blue curves) symmetric flow batteries (the green vs. red color bars indicate the timespans of the charge/discharge cycles vs. the static aging of the CLS electrolyte, see Section 5 of the Appendix 6 for details).

6.3.2 Decay Byproducts Analysis and Plausible Decay Mechanism of TMQ

While the data in Figure 6.2 highlight the potential utility of TMHQ/TMQ for decoupled water splitting, the slow decomposition of TMQ evident at 50 °C merits further attention. To characterize the byproducts from TMQ decay and probe the decomposition mechanism, we stored a solution of TMQ (0.25 M in 1 M H_2SO_4) at 80 °C, an even higher temperature intended to expedite its decay (see Section 6 of the Appendix 6 for details). After two weeks, the ^{1}H NMR spectrum of the resulting reaction mixture revealed two byproducts after full consumption of TMQ: the hydroquinone TMHQ and a symmetrical disulfide, in a 2.2:1 molar ratio (Figure 6.3a). Although the precise pathway for generation of these byproducts is not certain, a plausible mechanism that accounts for the byproduct stoichiometry involves the stepwise nucleophilic substitution of the sulfonated thioether groups by water, followed by the redox reaction between TMQ and the displaced sulfonated thiols (Figure 6.3b).[43] These results indicate the "fully decomposed" TMQ will still retain ~80% of its capacity, because the major decomposition product is the reduced form of the quinone (i.e., TMHQ).

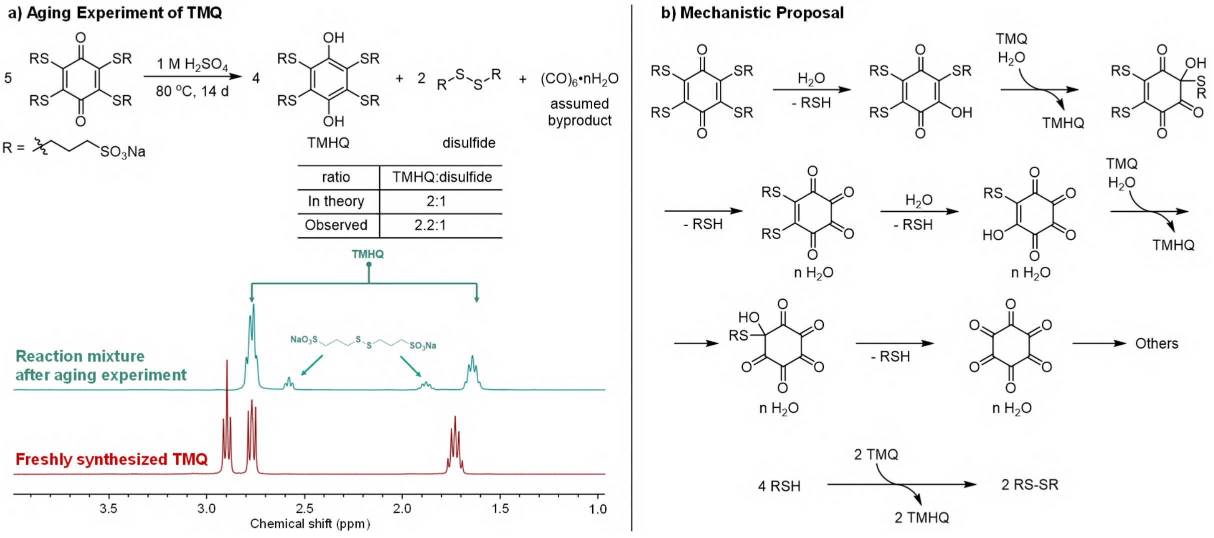

Figure 6.3. Accelerated aging experiment and plausible decay mechanism of TMQ revealed by NMR.

(**a**) Identification of byproducts from TMQ decay based on comparing the NMR spectra of the reaction mixture before and after accelerated aging experiment, and (**b**) a plausible mechanism that accounts for the ~2:1 stoichiometry of the byproducts.

6.3.3 Stable Operation Decoupled Water Splitting in a Flow Device Enabled by TMHQ/TMQ as a Redox Reservoir (RR)

The TMHQ/TMQ mixture was then tested as the RR for decoupled water splitting.[24] The experimental set-up includes two independent electrolyzer assemblies, one each for RR-coupled HER and OER, three electrolyte tanks, and peristaltic pumps to transport the RR solutions between the two electrolyzers (see Figure 6.4a for schematics and Figure A6.15a for a photograph of the system). The RR tank was filled with 0.25 M TMHQ/TMQ in 1 M H_2SO_4 solution at 50% SOC, while both the HER and the OER solutions consist of only 1 M H_2SO_4 solution. Carbon paper was used as the working electrode for the oxidation and reduction of the RR, while commercial Pt/C and $IrRuO_x$ electrocatalysts were employed for the HER and OER, respectively. Carbon paper and platinized titanium screen were used as the gas diffusion layers for the HER and OER, respectively. The decoupled water splitting experiments were conducted at 50 °C with an electrolyte flow rate of 200 mL/min (see Figures A6.15-A6.16 and Section 8 of the Appendix 6 for details). Control experiments investigating direct water splitting experiments using a single electrolyzer assembly under the same conditions were also performed (see Figures A6.13-A6.14 and Section 7 of the Appendix 6 for details).

Figure 6.4b shows the polarization curves obtained with the direct HER/OER water splitting cell and the RR-coupled HER and OER cells. The onset cell voltage of the direct water splitting cell (Figure 6.4b green curve) is ~1.50 V, while the onset potential with the RR-coupled HER (Figure 6.4b blue curve) and OER (Figure 6.4b red curve) cells is much lower, corresponding to approximately 0.60 V and 0.85 V, respectively. The practical device performance of the direct and decoupled water splitting configurations was compared by conducting chronopotentiometry experiments at a high current density of 250 mA/cm^2 (Figure 6.4c). The direct water-splitting cell exhibited a slow increase in the cell voltage, rising from 1.77 V to 1.88 V over 24 h (Figure 6.4c green curve). The small increase in voltage was traced to deactivation of the $IrRuO_x$ OER catalyst over the course of the experiment. In the decoupled water splitting tests, the HER cell maintained a steady 0.97 V cell voltage throughout the experiment (Figure 6.4c blue curve). The 62 h time period is significantly longer than the 24 h period used to assess the previous AHQDS/AQDS RR, thus providing a more stringent test of RR stability.[24] The stable HER performance during this experiment reflects the stability of both the TMHQ/TMQ RR and the Pt/C HER catalyst. Cell polarization curves recorded before and after the long-term chronopotentiometry experiment nearly overlap, providing further confirmation of the system stability (see Figure A6.15b blue curves and Table A6.1 in Section 8 of the Appendix 6). The decoupled OER cell exhibits a slight increase in the steady-state cell voltage, rising from 1.40 V to 1.60 V over the 62 h chronopotentiometry experiment (Figure 6.4c red curve). The stability of the RR electrolyte, evident in the HER cell, suggests the instability arises from slow deactivation of the $IrRuO_x$ OER catalyst during the experiment. This conclusion is supported by the similar deactivation observed in the direct water splitting experiment (Figure 6.4c green curve, also see Figure A6.13b in Section 7 of the Appendix 6), and non-overlapping polarization curves obtained before and after the long-term chronopotentiometry experiment provided further evidence of this deactivation (see Figure A6.15b red curves in Section 8 of the

Appendix 6). Furthermore, volumetric measurement of the H_2 and O_2 gases produced from the decoupled HER and OER cells indicate ~100% Faradaic efficiency based on the total charge passed during the extended experiment (Figure 6.4d, also see Table A6.2 in Section 8 of the Appendix 6). Further calculations showed that the energy efficiency of the decoupled water splitting process enabled by the TMHQ/TMQ RR was 62.4% when the decoupled HER and OER cells were operated at 250 mA/cm^2 in 1 M H_2SO_4 at 50 °C, comparable to the reported value achieved using the AHQDS/AQDS RR in a similar two-electrode flow cell setup under similar operating conditions[24] and higher than those achieved using other molecular RRs in three-electrode stirred cells[18,19] (see Table A6.3 and Section 8 of the Appendix 6 for details).

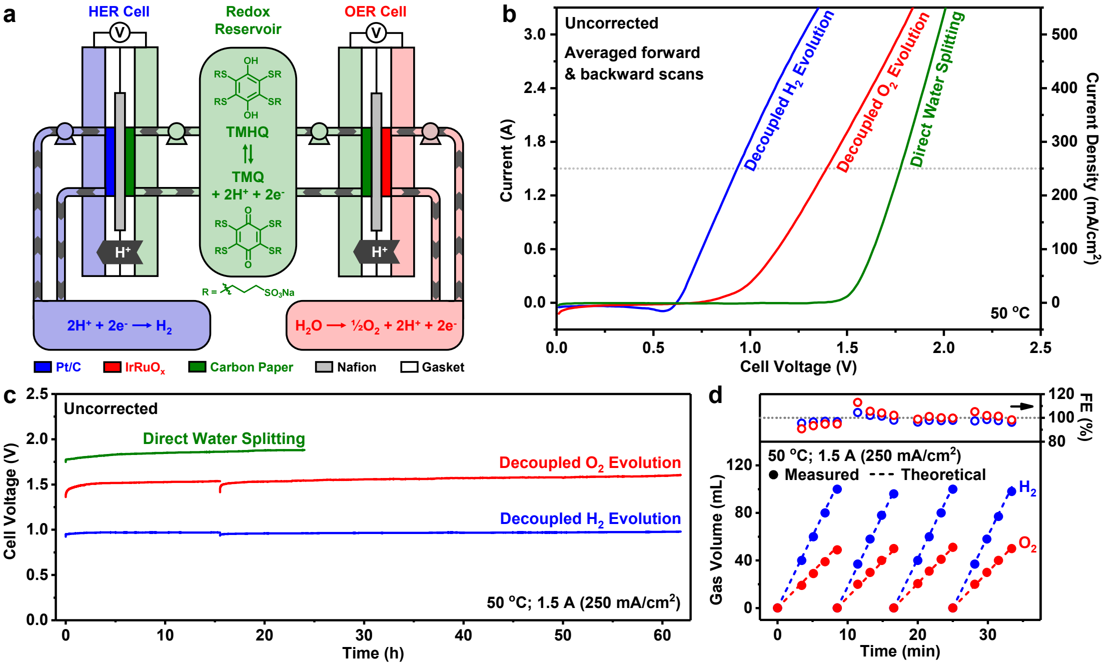

Figure 6.4. Long-term stable operation of decoupled water splitting in a flow device using TMHQ/TMQ as a RR.

(**a**) Schematic depiction of the decoupled water splitting flow cell using TMHQ/TMQ as a RR (electrolyte: 0.25 M TMHQ/TMQ with a 50% SOC in 1 M H_2SO_4 solution for RR tank, 1 M

H_2SO_4 solution for both HER and OER tanks; temperature: 50 °C; flow rate: 200 mL/min). (**b**) Polarization curves of decoupled HER cell (blue trace) and decoupled OER cell (red trace) vs. direct water splitting cell (green trace) without *iR*-correction. (**c**) Chronopotentiometry curves of decoupled HER cell (blue trace) and decoupled OER cell (red trace) vs. direct water splitting cell (green trace) operated at a constant current density of 250 mA/cm^2 without *iR*-correction at 50 °C. (**d**) Quantification of the H_2 and O_2 gas yields and Faradaic efficiencies (FE) from decoupled water splitting during four ~10 min periods of the chronoamperometry test operated at 250 mA/cm^2 and 50 °C.

6.4 Conclusions

The results presented above demonstrate that TMHQ/TMQ is a compelling molecular redox reservoir system for decoupled water splitting, demonstrating stable performance in the flow electrolysis cells for >60 h. The appealing features TMHQ/TMQ as a RR reflect its facile synthetic accessibility from inexpensive precursors, positioning of its redox potential between the catalytic HER/OER potentials, its high aqueous solubility capable of supporting high current densities, and enhanced stability. This quinone/hydroquinone pair is found to be substantially more stable than AHQDS/AQDS, which has been used previously for decoupled water splitting and flow battery applications. Characterization of decomposition byproducts suggest that TMQ decays via nucleophilic cleavage of the thioether linkage, displacing thiols that undergo oxidative coupling to disulfides in the presence of TMQ. This insight into the mechanism of the TMQ decay provides an important starting point for the future studies focused on designing even more stable redox couples capable of achieving even more robust performance for redox reservoirs or flow batteries.

6.5 References

(1) Stamenkovic, V. R.; Strmcnik, D.; Lopes, P. P.; Markovic, N. M. Energy and fuels from electrochemical interfaces. *Nat. Mater.* ***16***, 57-69 (2017).

(2) Lewis, N. S.; Nocera, D. G. Powering the Planet: Chemical Challenges in Solar Energy Utilization. *Proc. Natl. Acad. Sci. U.S.A.* ***103***, 15729-15735 (2006).

(3) Walter, M. G.; Warren, E. L.; McKone, J. R.; Boettcher, S. W.; Mi, Q.; Santori, E. A.; Lewis, N. S. Solar Water Splitting Cells. *Chem. Rev.* ***110***, 6446-6473 (2010).

(4) Niu, F.; Wang, D.; Li, F.; Liu, Y.; Shen, S.; Meyer, T. J. Hybrid Photoelectrochemical Water Splitting Systems: From Interface Design to System Assembly. *Adv. Energy Mater.* 1900399 (2019).

(5) Carmo, M.; Fritz, D. L.; Mergel, J.; Stolten, D. A Comprehensive Review on PEM Water Electrolysis. *Int. J. Hydrogen Energy* ***38***, 4901-4934 (2013).

(6) Paidar, M.; Fateev, V.; Bouzek, K. Membrane electrolysis—History, current status and perspective. *Electrochim. Acta* ***209***, 737-756 (2016).

(7) Chandesris, M.; Medeau, V.; Guillet, N.; Chelghoum, S.; Thoby, D.; Fouda-Onana, F. Membrane Degradation in PEM Water Electrolyzer: Numerical Modeling and Experimental Evidence of the Influence of Temperature and Current Density. *Int. J. Hydrogen Energy* ***40***, 1353-1366 (2015).

(8) Kusoglu, A.; Weber, A. Z. New Insights into Perfluorinated Sulfonic-Acid Ionomers. *Chem. Rev.* ***117***, 987-1104 (2017).

(9) Wang, F.; Li, W.; Wang, R.; Guo, T.; Sheng, H.; Fu, H.-C.; Stahl, S. S.; Jin, S. Modular Electrochemical Synthesis Using a Redox Reservoir Paired with Independent Half-Reactions. *Joule* ***5***, 149-165 (2021).

(10) Wallace, A. G.; Symes, M. D. Decoupling Strategies in Electrochemical Water Splitting and Beyond. *Joule* ***2***, 1390-1395 (2018).

(11) Liu, X.; Chi, J.; Dong, B.; Sun, Y. Recent Progress in Decoupled H2 and O2 Production from Electrolytic Water Splitting. *ChemElectroChem* ***6***, 2157-2166 (2019).

(12) You, B.; Sun, Y. Innovative Strategies for Electrocatalytic Water Splitting. *Acc. Chem. Res.* ***51***, 1571−1580 (2018).

(13) Lagadec, M. F.; Grimaud, A. Water Electrolysers with Closed and Open Electrochemical Systems. *Nat. Mater.* ***19***, 1140-1150 (2020).

(14) Chen, L.; Dong, X.; Wang, Y.; Xia, Y. Separating Hydrogen and Oxygen Evolution in Alkaline Water Electrolysis Using Nickel Hydroxide. *Nat. Commun.* ***7***, 11741 (2016).

(15) Landman, A.; Dotan, H.; Shter, G. E.; Wullenkord, M.; Houaijia, A.; Maljusch, A.; Grader, G. S.; Rothschild, A. Photoelectrochemical Water Splitting in Separate Oxygen and Hydrogen Cells. *Nat. Mater.* ***16***, 646-651 (2017).

(16) Dotan, H.; Landman, A.; Sheehan, S. W.; Malviya, K. D.; Shter, G. E.; Grave, D. A.; Arzi, Z.; Yehudai, N.; Halabi, M.; Gal, N.; Hadari, N.; Cohen, C.; Rothschild, A.; Grader, G. S. Decoupled Hydrogen and Oxygen Evolution by a Two-Step Electrochemical–Chemical Cycle for Efficient Overall Water Splitting. *Nat. Energy* ***4***, 786-795 (2019).

(17) Ma, Y.; Dong, X.; Wang, Y.; Xia, Y. Decoupling Hydrogen and Oxygen Production in Acidic Water Electrolysis Using a Polytriphenylamine-Based Battery Electrode. *Angew. Chem. Int. Ed.* ***57***, 2904-2908 (2018).

(18) Symes, M. D.; Cronin, L. Decoupling Hydrogen and Oxygen Evolution During Electrolytic Water Splitting Using an Electron-Coupled-Proton Buffer. *Nat. Chem.* ***5***, 403-409 (2013).

(19) Rausch, B.; Symes, M. D.; Cronin, L. A Bio-Inspired, Small Molecule Electron-Coupled-Proton Buffer for Decoupling the Half-Reactions of Electrolytic Water Splitting. *J. Am. Chem. Soc.* ***135***, 13656-13659 (2013).

(20) Rausch, B.; Symes, M. D.; Chisholm, G.; Cronin, L. Decoupled Catalytic Hydrogen Evolution from a Molecular Metal Oxide Redox Mediator in Water Splitting. *Science* ***345***, 1326-1330 (2014).

(21) Bloor, L.G.; Solarska, R.; Bienkowski, K.; Kulesza, P.J.; Augustynski, J.; Symes, M. D.; Cronin, L. Solar-Driven Water Oxidation and Decoupled Hydrogen Production Mediated by an Electron-Coupled-Proton Buffer. *J. Am. Chem. Soc.* ***138***, 6707-6710 (2016).

(22) Goodwin, S.; Walsh, D. A. Closed Bipolar Electrodes for Spatial Separation of H2 and O2 Evolution during Water Electrolysis and the Development of High-Voltage Fuel Cells. *ACS Appl. Mater. Interfaces* ***9***, 23654-23661 (2017).

(23) Amstutz, V.; Toghill, K. E.; Powlesland, F.; Vrubel, H.; Comninellis, C.; Hu, X.; Girault, H. H. Renewable Hydrogen Generation from a Dual-Circuit Redox Flow Battery. *Energy Environ. Sci.* ***7***, 2350-2358 (2018).

(24) Kirkaldy, N.; Chisholm, G.; Chen, J.-J.; Cronin, L. A Practical, Organic-Mediated, Hybrid Electrolyser That Decouples Hydrogen Production at High Current Densities. *Chem. Sci.* ***9***, 1621-1626 (2018).

(25) Chen, J.-J.; Symes, M. D.; Cronin, L. Highly reduced and protonated aqueous solutions of [P2W18O62]6− for on-demand hydrogen generation and energy storage. *Nat. Chem.* ***10***, 1042-1047 (2018).

(26) Zhang, F.; Zhang, H.; Salla, M.; Qin, N.; Gao, M.; Ji, Y.; Huang, S.; Wu, S.; Zhang, R.; Lu, Z.; Wang, Q. Decoupled Redox Catalytic Hydrogen Production with a Robust Electrolyte-Borne Electron and Proton Carrier. *J. Am. Chem. Soc.* ***143***, 223-231 (2021).

(27) Han, C.; Li, H.; Shi, R.; Zhang, T.; Tong, J.; Li, J.; Li, B. Organic Quinones Towards Advanced Electrochemical Energy Storage: Recent Advances and Challenges. *J. Mater. Chem. A* ***7***, 23378-233415 (2019).

(28) Luo, J.; Hu, B.; Hu, M.; Zhao, Y.; Liu, T. L. Status and Prospects of Organic Redox Flow Batteries toward Sustainable Energy Storage. *ACS Energy Lett.* ***4***, 2220-2240 (2019).

(29) Fabbri, E.; Schmidt, T. J. Oxygen Evolution Reaction − the Enigma in Water Electrolysis. *ACS Catal.* ***8***, 9765-9774 (2018).

(30) Dau, H.; Zaharieva, I.; Haumann, M. Recent Developments in Research on Water Oxidation by Photosystem II. *Curr. Opinion Chem. Biol.* ***16***, 3-10 (2012).

(31) Saito, K.; Rutherford, A. W.; Ishikita, H. Mechanism of Proton-Coupled Quinone Reduction in Photosystem II. *Proc. Natl. Acad. Sci. U.S.A.* ***110***, 954-959 (2013).

(32) Crane, F. L. Discovery of Ubiquinone (Coenzyme Q) and an Overview of Function. *Mitochondrion* ***7***, S2-S7 (2007).

(33) Erdtman, H.; Högberg, H.-E. The Acid-Catalysed Oligomerisation of p-Benzoquinone. *Tetrahedron* ***35***, 535-540 (1979).

(34) Matthews, M. A. XXXV.—Reaction of the meso-Hydroxyanthrones. *J. Chem. Soc.* ***129***, 236-245 (1926).

(35) Goulet, M. A.; Aziz, M. J. Flow Battery Molecular Reactant Stability Determined by Symmetric Cell Cycling Methods. *J. Electrochem. Soc.* ***165***, A1466-A1477 (2018).

(36) Wermeckes, B.; Beck, F. Acid Catalyzed Disproportionation of Anthrahydroquinone to Anthraquinone and Anthrone. *Denki Kagaku* ***62***, 1202−1205 (1994).

(37) Gerken, J. B.; Stamoulis, A. G.; Suh, S.-E.; Fischer, N. D.; Kim, Y.-J.; Guzei, I. A.; Stahl, S. S. Efficient Electrochemical Synthesis of Robust, Densely Functionalized Water Soluble Quinones. *Chem. Commun.* ***56***, 1199-1202 (2020).

(38) Preger, Y.; Gerken, J. B.; Biswas, S.; Anson, C. W.; Johnson, M. R.; Root, T. W.; Stahl, S. S. Quinone-Mediated Electrochemical O2 Reduction Accessing High Power Density with an Off-Electrode Co-N/C Catalyst. *Joule* ***2***, 2722-2731 (2018).

(39) Gerken, J. B.; Anson, C. W.; Preger, Y.; Symons, P. G.; Genders, J. D.; Qiu, Y.; Li, W.; Root, T. W.; Stahl, S. S. Comparison of Quinone-Based Catholytes for Aqueous Redox Flow Batteries and Demonstration of Long-Term Stability with Tetrasubstituted Quinones. *Adv. Energy Mater.* 2000340 (2020).

(40) Kwabi, D. G.; Ji, Y.; Aziz, M. J. Electrolyte Lifetime in Aqueous Organic Redox Flow Batteries: A Critical Review. *Chem. Rev.* ***120***, 16467-6489 (2020).

(41) Brushett, F. R.; Aziz, M. J.; Rodby, K. E. On Lifetime and Cost of Redox-Active Organics for Aqueous Flow Batteries. *ACS Energy Lett.* ***5***, 879-884 (2020).

(42) Compared to the AHQDS/AQDS cell, the TMHQ/TMQ cell exhibits a larger charge/discharge overpotential due to the slower electrochemical kinetics of the redox couple (see Figure A6.2 in Section 2 of the Appendix 6 for details).

(43) The fully oxidized hexaketone product has characterized previously as a hexahydrate: Klapotke, T. M.; Polborn, K.; Weigand, J. J. Dodecahydroxycyclohexane Dihydrate. *Acta Cryst. E* ***61***, o1393-o1395 (2005).

APPENDIX 1

Supplementary Information for CHAPTER 1: Metal Compound-Based Electrocatalysts for Electrochemical Synthesis of Hydrogen Peroxide and the Electro-Fenton Process[*]

---

[*] This appendix will be submitted for future publication as the Supporting Information for the Chapter 1, in collaboration with R. Dominic Ross, J. R. Schmidt, and Song Jin.

Supplementary Figures and Tables

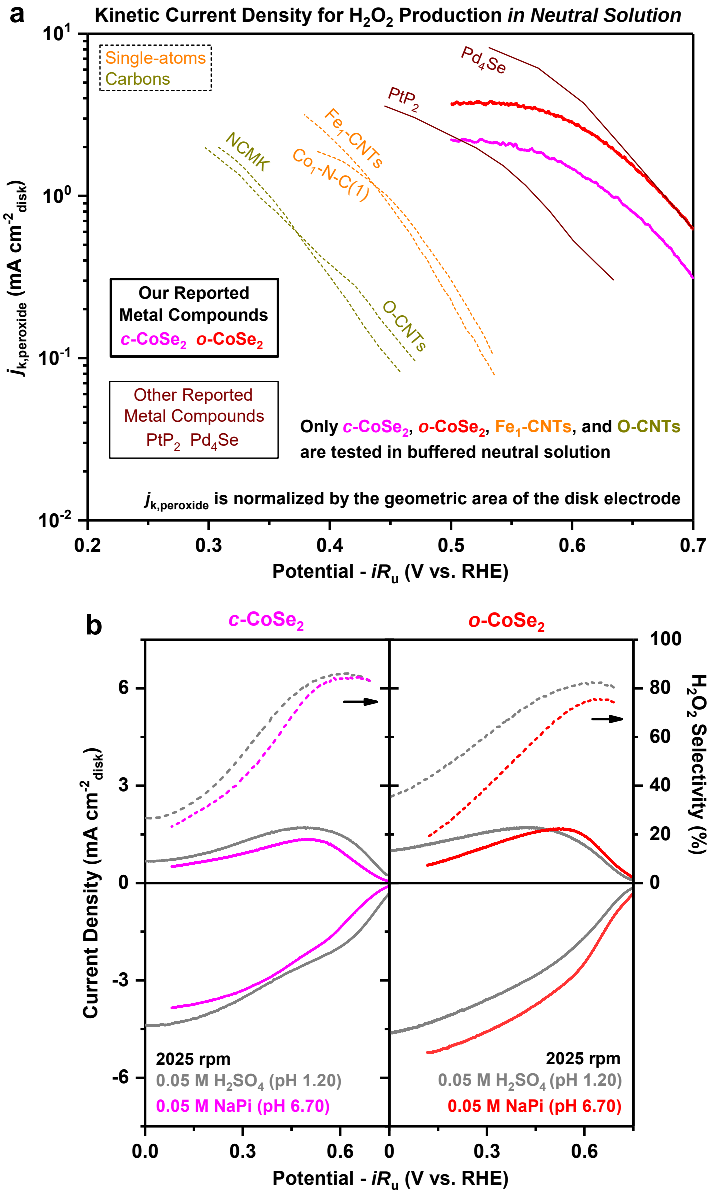

Figure A1.1. Comparisons of kinetic current density for H_2O_2 production in neutral solution. (a) Comparisons of kinetic current densities for H_2O_2 production ($j_{\mathrm{k,peroxide}}$) on metal compound-based 2e$^-$ ORR catalysts (vs. other classes of 2e$^-$ ORR catalysts) based on RRDE experiments at 1600 rpm in neutral solution. (b) RRDE voltammograms and the corresponding H_2O_2 selectivity of *c*-$CoSe_2$ and *o*-$CoSe_2$ at 2025 rpm in O_2-saturated 0.05 M H_2SO_4 (the same traces as shown in Figure 1.3a$_1$ in Chapter 1) vs. 0.05 M NaH_2PO_4/Na_2HPO_4 neutral buffer (denoted as NaPi). Detailed catalyst and electrode information are described in Table A1.2.

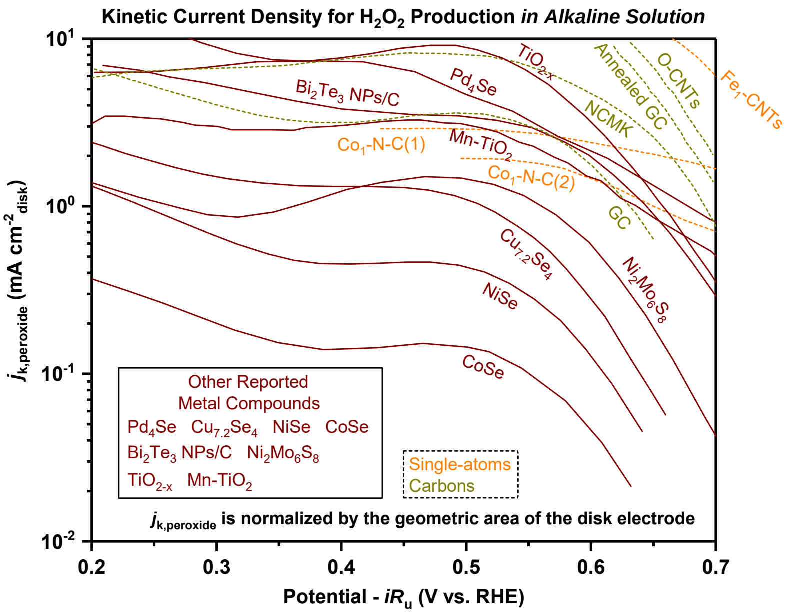

Figure A1.2. Comparisons of kinetic current density for H_2O_2 production in alkaline solution. Comparisons of kinetic current densities for H_2O_2 production ($j_{\mathrm{k,peroxide}}$) on metal compound-based 2e$^-$ ORR catalysts (vs. other classes of 2e$^-$ ORR catalysts) based on RRDE experiments at 1600 rpm in alkaline solution. Detailed catalyst and electrode information are described in Table A1.3.

Table A1.1. Summary of detailed catalyst and electrode information of various reported 2e$^-$ ORR catalysts in acidic solutions.

Classification	Catalyst	Acidic Electrolyte	Catalyst Loading	Reference
Metal compounds	c-CoS$_2$ (Figure 1.3a$_1$, 1.3b)	0.05 M H_2SO_4	305 μg$_{Co}$ cm$^{-2}_{disk}$ (C_{dl} at 0.35 V vs. RHE = 226 μF cm$^{-2}_{disk}$)	ref [1]
	c-CoSe$_2$ (Figure 1.3a$_1$, 1.3b)	0.05 M H_2SO_4	305 μg$_{Co}$ cm$^{-2}_{disk}$ (C_{dl} at 0.35 V vs. RHE = 325 μF cm$^{-2}_{disk}$)	ref [1]
	o-CoSe$_2$ (Figure 1.3a$_1$, 1.3b)	0.05 M H_2SO_4	152 μg$_{Co}$ cm$^{-2}_{disk}$ (C_{dl} at 0.35 V vs. RHE = 661 μF cm$^{-2}_{disk}$)	ref [1]
	c-NiSe$_2$ (Figure 1.3a$_1$, 1.3b)	0.05 M H_2SO_4	458 μg$_{Ni}$ cm$^{-2}_{disk}$ (C_{dl} at 0.35 V vs. RHE = 431 μF cm$^{-2}_{disk}$)	ref [2]
	$CuCo_2S_4$ (Figure 1.3a$_2$)	0.05 M H_2SO_4	159 μg$_{catalyst}$ cm$^{-2}_{disk}$ (C_{dl} = 253 μF cm$^{-2}_{disk}$)	ref [3]
	$CuCo_{1.6}Ni_{0.4}S_4$ (Figure 1.3a$_2$)	0.05 M H_2SO_4	159 μg$_{catalyst}$ cm$^{-2}_{disk}$ (C_{dl} = 391 μF cm$^{-2}_{disk}$)	ref [3]
	$CuCo_{1.2}Ni_{0.8}S_4$ (Figure 1.3a$_2$)	0.05 M H_2SO_4	159 μg$_{catalyst}$ cm$^{-2}_{disk}$ (C_{dl} = 387 μF cm$^{-2}_{disk}$)	ref [3]
	$CuCo_{0.8}Ni_{1.2}S_4$ (Figure 1.3a$_2$, 1.3b)	0.05 M H_2SO_4	159 μg$_{catalyst}$ cm$^{-2}_{disk}$ (C_{dl} = 326 μF cm$^{-2}_{disk}$)	ref [3]
	PtP_2 (Figure 1.3b)	0.1 M $HClO_4$	200 μg$_{catalyst}$ cm$^{-2}_{disk}$	ref [4]
	Pd_4Se (Figure 1.3b)	0.1 M $HClO_4$	N.A.	ref [5]
	NiS_2 (Figure 1.3b)	0.05 M H_2SO_4	158 μg$_{catalyst}$ cm$^{-2}_{disk}$ (C_{dl} = 203 μF cm$^{-2}_{disk}$)	ref [6]
	sc-CoSe$_2$ (Figure 1.3b)	0.5 M H_2SO_4	200 μg$_{catalyst}$ cm$^{-2}_{disk}$	ref [7]
	CoTe@NC (Figure 1.3b)	0.1 M $HClO_4$	40 μg$_{catalyst}$ cm$^{-2}_{disk}$ (C_{dl} at 0.806 V vs. RHE = 420 μF cm$^{-2}_{disk}$)	ref [8]
	$MoTe_2$ (Figure 1.3b)	0.5 M H_2SO_4	10 μg$_{catalyst}$ cm$^{-2}_{disk}$	ref [9]
	Co_3O_4-400 (Figure 1.3b)	0.5 M H_2SO_4	50 μg$_{catalyst}$ cm$^{-2}_{disk}$	ref [10]
Noble metal nanoparticles	Pt-Hg NPs/C (Figure 1.3b)	0.1 M $HClO_4$	14 μg$_{Pt}$/cm$^2_{disk}$	ref [11]
	Pd-Hg NPs/C (Figure 1.3b)	0.1 M $HClO_4$	10 μg$_{Pd}$/cm$^2_{disk}$	ref [12]
Single-atom catalysts	Pt$_1$/SC (Figure 1.3b)	0.1 M $HClO_4$	50 μg$_{catalyst}$/cm$^2_{disk}$ (5.0 wt% Pt)	ref [13]
	h-Pt$_1$-CuS$_x$ (Figure 1.3b)	0.1 M $HClO_4$	101 μg$_{catalyst}$/cm$^2_{disk}$ (24.8 at% Pt)	ref [14]
	Co$_1$-N-C(1) (Figure 1.3b)	0.5 M H_2SO_4	100 μg$_{catalyst}$/cm$^2_{disk}$ (0.4 at% Co)	ref [15]
	Co$_1$-N-C(2) (Figure 1.3b)	0.1 M $HClO_4$	25 μg$_{catalyst}$/cm$^2_{disk}$ (1.4 wt% Co)	ref [16]
	Co$_1$-NG(O) (Figure 1.3b)	0.1 M $HClO_4$	10 μg$_{catalyst}$/cm$^2_{disk}$ (1.4 wt% Co)	ref [17]
	Mo$_1$-OSG-H (Figure 1.3b)	0.05 M H_2SO_4	101 μg$_{catalyst}$/cm$^2_{disk}$ (13.47 wt% Mo)	ref [18]
Carbon materials	O-CNTs (Figure 1.3b)	0.1 M $HClO_4$	101 μg$_{catalyst}$/cm$^2_{disk}$	ref [19]
	NCMK (Figure 1.3b)	0.5 M H_2SO_4	50 μg$_{catalyst}$/cm$^2_{disk}$	ref [20]

Table A1.2. Summary of detailed catalyst and electrode information of various reported 2e$^-$ ORR catalysts in neutral solutions.

Classification	Catalyst	Neutral Electrolyte	Catalyst Loading	Reference
Metal compounds	*c*-$CoSe_2$ (Figure A1.1a, A1.1b)	0.05 M NaPi (pH 6.70)	305 μg_{Co} cm^{-2}_{disk} (C_{dl} at 0.35 V vs. RHE = 282 μF cm^{-2}_{disk})	Unpublished results from ref [1]
	o-$CoSe_2$ (Figure A1.1a, A1.1b)	0.05 M NaPi (pH 6.70)	152 μg_{Co} cm^{-2}_{disk} (C_{dl} at 0.35 V vs. RHE = 456 μF cm^{-2}_{disk})	Unpublished results from ref [1]
	PtP_2 (Figure A1.1a)	0.5 M K_2SO_4 (pH 7)	200 $\mu g_{catalyst}$ cm^{-2}_{disk}	ref [4]
	Pd_4Se (Figure A1.1a)	0.1 M KCl	N.A.	ref [5]
Single-atom catalysts	Co_1-N-C(1) (Figure A1.1a)	0.1 M K_2SO_4 (pH 7)	100 $\mu g_{catalyst}/cm^2_{disk}$ (0.4 at% Co)	ref [15]
	Fe_1-CNTs (Figure A1.1a)	0.1 M PBS (pH 7.2)	100 $\mu g_{catalyst}/cm^2_{disk}$ (0.1 at% Fe)	ref [21]
Carbon materials	O-CNTs (Figure A1.1a)	0.1 M PBS (pH ~7)	101 $\mu g_{catalyst}/cm^2_{disk}$	ref [19]
	NCMK (Figure A1.1a)	0.1 M K_2SO_4 (pH 7)	50 $\mu g_{catalyst}/cm^2_{disk}$	ref [20]

Table A1.3. Summary of detailed catalyst and electrode information of various reported 2e$^-$ ORR catalysts in alkaline solutions.

Classification	Catalyst	Alkaline Electrolyte	Catalyst Loading	Reference
Metal compounds	Pd_4Se (Figure A1.2)	0.1 M KOH	N.A.	ref [5]
	$Cu_{7.2}Se_4$ (Figure A1.2)	0.1 M KOH	100 $\mu g_{catalyst}/cm^2_{disk}$	ref [22]
	NiSe (Figure A1.2)	0.1 M KOH	100 $\mu g_{catalyst}/cm^2_{disk}$	ref [22]
	CoSe (Figure A1.2)	0.1 M KOH	100 $\mu g_{catalyst}/cm^2_{disk}$	ref [22]
	Activated Bi_2Te_3 NPs/C (Figure A1.2)	0.1 M KOH	405 $\mu g_{catalyst}/cm^2_{disk}$ (50 wt% Bi_2Te_3)	ref [23]
	$Ni_2Mo_6S_8$ (Figure A1.2)	0.1 M KOH	220 $\mu g_{catalyst}/cm^2_{disk}$	ref [24]
	TiO_{2-x} (Figure A1.2)	0.1 M KOH	81 $\mu g_{catalyst}$ cm^{-2}_{disk} (C_{dl} = 44 μF cm^{-2}_{disk})	ref [25]
	Mn-TiO_2 (Figure A1.2)	0.1 M KOH	162 $\mu g_{catalyst}$ cm^{-2}_{disk} (C_{dl} = 142 μF cm^{-2}_{disk})	ref [26]
Single-atom catalysts	Co_1-N-C(1) (Figure A1.2)	0.1 M KOH	100 $\mu g_{catalyst}/cm^2_{disk}$ (0.4 at% Co)	ref [15]
	Co_1-N-C(2) (Figure A1.2)	0.1 M KOH	25 $\mu g_{catalyst}/cm^2_{disk}$ (1.4 wt% Co)	ref [16]
	Fe_1-CNTs (Figure A1.2)	0.1 M KOH	100 $\mu g_{catalyst}/cm^2_{disk}$ (0.1 at% Fe)	ref [21]
Carbon materials	GC (Figure A1.2)	0.1 M KOH	N.A.	ref [27]
	Annealed GC (Figure A1.2)	0.1 M KOH	N.A.	ref [27]
	O-CNTs (Figure A1.2)	0.1 M KOH	101 $\mu g_{catalyst}/cm^2_{disk}$	ref [19]
	NCMK (Figure A1.2)	0.1 M KOH	50 $\mu g_{catalyst}/cm^2_{disk}$	ref [20]

References Cited in the Appendix 1

1. Sheng, H.; Janes, A. N.; Ross, R. D.; Kaiman, D.; Huang, J.; Song, B.; Schmidt, J. R.; Jin, S. Stable and selective electrosynthesis of hydrogen peroxide and the electro-Fenton process on CoSe2 polymorph catalysts. *Energy Environ. Sci.* ***13***, 4189-4203 (2020).

2. Sheng, H.; Janes, A. N.; Ross, R. D.; Hofstetter, H.; Schmidt, J. R.; Jin, S. Linear Paired Electrochemical Valorization of Glycerol Enabled by the Electro-Fenton Process Using a Stable NiSe2 Cathode. *To be submitted for future publication (see Chapter 4)* (2022).

3. Ross, R. D.; Sheng, H.; Parihar, A.; Huang, J.; Jin, S. Compositionally Tuned Trimetallic Thiospinel Catalysts for Enhanced Electrosynthesis of Hydrogen Peroxide and Built-In Hydroxyl Radical Generation. *ACS Catal.* ***11***, 12643-12650 (2021).

4. Li, H.; Wen, P.; Itanze, D. S.; Hood, Z. D.; Adhikari, S.; Lu, C.; Ma, X.; Dun, C.; Jiang, L.; Carroll, D. L.; Qiu, Y.; Geyer, S. M. Scalable neutral H2O2 electrosynthesis by platinum diphosphide nanocrystals by regulating oxygen reduction reaction pathways. *Nat. Commun.* ***11***, 3928 (2020).

5. Yang, C.; Bai, S.; Yu, Z.; Feng, Y.; Huang, B.; Lu, Q.; Wu, T.; Sun, M.; Zhu, T.; Cheng, C.; Zhang, L.; Shao, Q.; Huang, X. A newly-explored Pd-based nanocrystal for the pH-universal electrosynthesis of H2O2. *Nano Energy* ***89***, 106480 (2021).

6. Liang, J.; Wang, Y.; Liu, Q.; Luo, Y.; Li, T.; Zhao, H.; Lu, S.; Zhang, F.; Asiri, A. M.; Liu, F.; Ma, D.; Sun, X. Electrocatalytic hydrogen peroxide production in acidic media enabled by NiS2 nanosheets. *J. Mater. Chem. A* **9**, 6117-6122 (2021).

7. Zhang, X.-L.; Su, X.; Zheng, Y.-R.; Hu, S.-J.; Shi, L.; Gao, F.-Y.; Yang, P.-P.; Niu, Z.-Z.; Wu, Z.-Z.; Qin, S.; Wu, R.; Duan, Y.; Gu, C.; Zheng, X.-S.; Zhu, J.-F.; Gao, M.-R. Strongly Coupled Cobalt Diselenide Monolayers for Selective Electrocatalytic Oxygen Reduction to H2O2 under Acidic Conditions. *Angew. Chem. Int. Ed.* ***60***, 26922-26931 (2021).

8. Zhang, L.; Liang, J.; Yue, L.; Dong, K.; Xu, Z.; Li, T.; Liu, Q.; Luo, Y.; Liu, Y.; Gao, S.; Asiri, A. M.; Kong, Q.; Guo, X.; Sun, X. CoTe nanoparticle-embedded N-doped hollow carbon polyhedron: an efficient catalyst for H2O2 electrosynthesis in acidic media. *J. Mater. Chem. A* **9**, 21703-21707 (2021).

9. Zhao, X.; Wang, Y.; Da, Y.; Wang, X.; Wang, T.; Xu, M.; He, X.; Zhou, W.; Li, Y.; Coleman, J. N.; Li, Y. Selective electrochemical production of hydrogen peroxide at zigzag edges of exfoliated molybdenum telluride nanoflakes. *Natl. Sci. Rev.* ***7***, 1360-1366 (2020).

10. Yan, L.; Cheng, X.; Wang, Y.; Wang, Z.; Zheng, L.; Yan, Y.; Lu, Y.; Sun, S.; Qiu, W.; Chen, G. Exsolved Co3O4 with tunable oxygen vacancies for electrocatalytic H2O2 production. *Mater. Today Energy* ***24***, 100931 (2022).

11. Siahrostami, S.; Verdaguer-Casadevall, A.; Karamad, M.; Deiana, D.; Malacrida, P.; Wickman, B.; Escudero-Escribano, M.; Paoli, E. A.; Frydendal, R.; Hansen, T. W.; Chorkendorff, I.; Stephens, I. E. L.; Rossmeisl, J. Enabling direct H_2O_2 production through rational electrocatalyst design. *Nat. Mater.* ***12***, 1137-1143 (2013).

12. Verdaguer-Casadevall, A.; Deiana, D.; Karamad, M.; Siahrostami, S.; Malacrida, P.; Hansen, T. W.; Rossmeisl, J.; Chorkendorff, I.; Stephens, I. E. L. Trends in the Electrochemical Synthesis of H2O2: Enhancing Activity and Selectivity by Electrocatalytic Site Engineering. *Nano Lett.* ***14***, 1603-1608 (2014).

13. Choi, C. H.; Kim, M.; Kwon, H. C.; Cho, S. J.; Yun, S.; Kim, H.-T.; Mayrhofer, K. J. J.; Kim, H.; Choi, M. Tuning selectivity of electrochemical reactions by atomically dispersed platinum catalyst. *Nat. Commun.* ***7***, 10922 (2016).

14. Shen, R.; Chen, W.; Peng, Q.; Lu, S.; Zheng, L.; Cao, X.; Wang, Y.; Zhu, W.; Zhang, J.; Zhuang, Z.; Chen, C.; Wang, D.; Li, Y. High-Concentration Single Atomic Pt Sites on Hollow CuSx for Selective O2 Reduction to H2O2 in Acid Solution. *Chem* **5**, 2099-2110 (2019).

15. Sun, Y.; Silvioli, L.; Sahraie, N. R.; Ju, W.; Li, J.; Zitolo, A.; Li, S.; Bagger, A.; Arnarson, L.; Wang, X.; Moeller, T.; Bernsmeier, D.; Rossmeisl, J.; Jaouen, F.; Strasser, P. Activity–Selectivity Trends in the Electrochemical Production of Hydrogen Peroxide over Single-Site Metal–Nitrogen–Carbon Catalysts. *J. Am. Chem. Soc.* ***141***, 12372-12381 (2019).

16. Gao, J.; Yang, H. b.; Huang, X.; Hung, S.-F.; Cai, W.; Jia, C.; Miao, S.; Chen, H. M.; Yang, X.; Huang, Y.; Zhang, T.; Liu, B. Enabling Direct H2O2 Production in Acidic Media through Rational Design of Transition Metal Single Atom Catalyst. *Chem* **6**, 658-674 (2020).

17. Jung, E.; Shin, H.; Lee, B.-H.; Efremov, V.; Lee, S.; Lee, H. S.; Kim, J.; Hooch Antink, W.; Park, S.; Lee, K.-S.; Cho, S.-P.; Yoo, J. S.; Sung, Y.-E.; Hyeon, T. Atomic-level tuning of Co–

N–C catalyst for high-performance electrochemical H2O2 production. *Nat. Mater.* ***19***, 436-442 (2020).

18. Tang, C.; Jiao, Y.; Shi, B.; Liu, J.-N.; Xie, Z.; Chen, X.; Zhang, Q.; Qiao, S.-Z. Coordination Tunes Selectivity: Two-Electron Oxygen Reduction on High-Loading Molybdenum Single-Atom Catalysts. *Angew. Chem. Int. Ed.* ***59***, 2-8).

19. Lu, Z.; Chen, G.; Siahrostami, S.; Chen, Z.; Liu, K.; Xie, J.; Liao, L.; Wu, T.; Lin, D.; Liu, Y.; Jaramillo, T. F.; Nørskov, J. K.; Cui, Y. High-efficiency oxygen reduction to hydrogen peroxide catalysed by oxidized carbon materials. *Nat. Catal.* ***1***, 156-162 (2018).

20. Sun, Y.; Sinev, I.; Ju, W.; Bergmann, A.; Dresp, S.; Kühl, S.; Spöri, C.; Schmies, H.; Wang, H.; Bernsmeier, D.; Paul, B.; Schmack, R.; Kraehnert, R.; Roldan Cuenya, B.; Strasser, P. Efficient Electrochemical Hydrogen Peroxide Production from Molecular Oxygen on Nitrogen-Doped Mesoporous Carbon Catalysts. *ACS Catal.* ***8***, 2844-2856 (2018).

21. Jiang, K.; Back, S.; Akey, A. J.; Xia, C.; Hu, Y.; Liang, W.; Schaak, D.; Stavitski, E.; Nørskov, J. K.; Siahrostami, S.; Wang, H. Highly selective oxygen reduction to hydrogen peroxide on transition metal single atom coordination. *Nat. Commun.* ***10***, 3997 (2019).

22. Yuan, Q.; Zhao, J.; Mok, D. H.; Zheng, Z.; Ye, Y.; Liang, C.; Zhou, L.; Back, S.; Jiang, K. Electrochemical Hydrogen Peroxide Synthesis from Selective Oxygen Reduction over Metal Selenide Catalysts. *Nano Lett.* (2021).

23. Zhang, N.; Zheng, F.; Huang, B.; Ji, Y.; Shao, Q.; Li, Y.; Xiao, X.; Huang, X. Exploring Bi2Te3 Nanoplates as Versatile Catalysts for Electrochemical Reduction of Small Molecules. *Adv. Mater.* ***32***, 1906477 (2020).

24. Xia, F.; Li, B.; Liu, Y.; Liu, Y.; Gao, S.; Lu, K.; Kaelin, J.; Wang, R.; Marks, T. J.; Cheng, Y. Carbon Free and Noble Metal Free Ni2Mo6S8 Electrocatalyst for Selective Electrosynthesis of H2O2. *Adv. Funct. Mater.* ***31***, 2104716 (2021).

25. Dong, K.; Liang, J.; Wang, Y.; Ren, Y.; Xu, Z.; Zhou, H.; Li, L.; Liu, Q.; Luo, Y.; Li, T.; Asiri, A. M.; Li, Q.; Ma, D.; Sun, X. Plasma-induced defective TiO2-x with oxygen vacancies: A high-active and robust bifunctional catalyst toward H2O2 electrosynthesis. *Chem Catal.* ***1***, 1437-1448 (2021).

26. Chen, Q.; Ma, C.; Yan, S.; Liang, J.; Dong, K.; Luo, Y.; Liu, Q.; Li, T.; Wang, Y.; Yue, L.; Zheng, B.; Liu, Y.; Gao, S.; Jiang, Z.; Li, W.; Sun, X. Greatly Facilitated Two-Electron Electroreduction of Oxygen into Hydrogen Peroxide over TiO2 by Mn Doping. *ACS Appl. Mater. Interfaces* ***13***, 46659-46664 (2021).

27. Yang, S.; Verdaguer-Casadevall, A.; Arnarson, L.; Silvioli, L.; Čolić, V.; Frydendal, R.; Rossmeisl, J.; Chorkendorff, I.; Stephens, I. E. L. Toward the Decentralized Electrochemical Production of H2O2: A Focus on the Catalysis. *ACS Catal.* ***8***, 4064-4081 (2018).

APPENDIX 2

Supplementary Information for CHAPTER 2:

Electrocatalytic Production of H_2O_2 by Selective Oxygen Reduction Using Earth-Abundant Cobalt Pyrite (CoS_2)[*]

---

[*] This appendix was originally made available online as the Supporting Information for *ACS Catal.* **9**, 8433-8442 (2019), in collaboration with Eric D. Hermes, Xiaohua Yang, Diwen Ying, Aurora N. Janes, Wenjie Li, J. R. Schmidt, and Song Jin.

Supplementary Experimental Methods

Details for Materials Synthesis. The synthesis of CoS_2 nanomaterials and the direct growth of CoS_2 nanowires onto carbon fiber paper substrate (CoS_2/CFP) follow a published procedure with minor modifications.[1] In a typical synthesis, 1.275 mmol of cobalt(II) chloride hexahydrate ($CoCl_2 \cdot 6H_2O$, Sigma-Aldrich, 98.0%) and 3 mmol of urea [$CO(NH_2)_2$, Riedel-de Haën, 99.5–100.5%] were dissolved in 75 mL of nanopure water, transferred into a 100-mL PTFE-lined stainless steel autoclave, sealed and heated at 120 °C for 5 h. Upon cooling to room temperature, the pink precipitates [cobalt hydroxide carbonate hydrate, $Co(OH)(CO_3)_{0.5} \cdot xH_2O$, CHCH] were washed with nanopure water and ethanol, collected by centrifuge and dried in a vacuum desiccator at room temperature. To convert CHCH nanomaterials into CoS_2 nanomaterials via thermal sulfidation, an alumina boat (CoorsTek) containing 50 mg of CHCH powders was placed in the center of a fused silica tube within a tube furnace (Lindberg/Blue M, TF55035A-1) with both pressure and gas flow controller, another alumina boat containing 2 g of sulfur (Sigma-Aldrich, 99.5–100.5%) was placed in the tube at the farthest upstream position within the tube furnace. The pressure in the tube was maintained at 780 Torr under a steady flow of Ar carrier gas (99.999%) at 25 sccm. The furnace temperature was quickly ramped from room temperature to 500 °C at a rate of approximately 80 °C/min and then held at 500 °C for 1 h, while the temperature of the sulfur boat was around 400 °C during thermal sulfidation. The tube furnace was then opened to allow natural cooling to room temperature under Ar flow, and the as-sulfidized CoS_2 nanomaterial product was stored in an Ar-filled glove box to minimize the exposure to air.

In a typical synthesis of CoS_2/CFP, Teflon-treated carbon fiber paper (Fuel Cell Earth, TGP-H-060) was first cleaned with oxygen plasma at 150 W power for 5 min (×2 for both sides) and further annealed in air at 700 °C for 5 min, resulting in improved surface wettability. 2.1 mmol of cobalt(II) nitrate hexahydrate [$Co(NO_3)_2 \cdot 6H_2O$, Sigma-Aldrich, ≥98.0%), 4.2 mmol of ammonium fluoride (NH_4F, Sigma-Aldrich, ≥98.0%), and 10.5 mmol of urea were dissolved in 80 mL of nanopure water, transferred into a 100-mL autoclave with a piece of annealed carbon fiber paper (3 cm × 6 cm) placed inside, and the sealed autoclave was heated at 110 °C for 5 h. Upon cooling to room temperature, the carbon fiber paper substrate covered with CHCH nanowires was sonicated in nanopure water (to remove loosely-bound CHCH powders), rinsed with nanopure water and ethanol, and dried under N_2 flow. The subsequent thermal sulfidation was the same as mentioned above, except for replacing CHCH powders with the carbon fiber paper substrate covered with CHCH nanowires (which was cut into 1.5 cm × 6 cm for sulfidation). The as-sulfidized CoS_2/CFP was immersed in CS_2 to remove the excess sulfur and was then stored in an Ar-filled glove box to minimize the exposure to air. The catalyst loading of CoS_2/CFP was estimated by the mass difference of the CFP substrate before and after the growth of CoS_2 nanowires.

Sample Preparation for Materials Characterization. SEM samples of CoS_2 nanomaterials were prepared by drop-casting suspension of CoS_2 powders in ethanol onto Si wafer and drying under ambient condition. Graphite disk substrates were used for preparing the XPS samples of CoS_2 powders before and after ORR stability tests. Graphite disk substrate was made by cutting thin slices of graphite rod (Ultra Carbon Corp., Ultra “F” Purity), abrading both sides with 600-grit silicon carbide paper (Allied High Tech Products, Inc.), and sonicating in nanopure water and ethanol until clean. To prepare the XPS samples, the as-synthesized CoS_2 powders were dispersed in nanopure water and drop-casted on graphite disk substrates, while the CoS_2 powders after ORR stability tests were first recovered from the electrodes by sonicating in nanopure water and ultracentrifuging at 13.2K rpm for 1 min, followed by re-dispersing in minimal amount of nanopure water and drop-casting on graphite disk substrates. The XPS samples were used for Raman experiments without modification.

Detailed Protocols for Calibrating the Collection Efficiency of RRDE. Calibration of the collection efficiency was performed on the bare RRDE. The electrolyte was prepared by dissolving 4 mM of potassium ferricyanide(III) ($K_3[Fe(CN)_6]$, Sigma-Aldrich, 99%) in 0.05 M Na_2SO_4. The electrolyte was purged with Ar gas for at least 15 min prior to the measurements in order to eliminate dissolved O_2 gas. A blanket of Ar gas was maintained over the surface of the electrolyte during the measurements.

(a) Cyclic voltammetry (CV) was performed separately on the disk and the ring between 0 V and 1.23 V vs. RHE at 100 mV/s and 0 rpm (Figure A2.4a shows the CV voltammogram of the disk).

(b) Linear sweep voltammetry (LSV) was performed on the disk from 1.23 V to 0 V vs. RHE at 50 mV/s and 1600 rpm, meanwhile the ring was held at 1.20 V vs. RHE. Ferricyanide reduction on the bare GC disk was found to be diffusion-limited at 0 V vs. RHE.

(c) LSV was performed on the ring from 0 V to 1.23 V vs. RHE at 50 mV/s and 1600 rpm, meanwhile the disk was held at 0 V vs. RHE. Ferrocyanide oxidation on the Pt ring was found to be diffusion-limited at 1.20 V vs. RHE (Figure A2.4b).

(d) RRDE voltammograms were recorded by performing LSV on the disk from 1.23 V to 0 V vs. RHE at 50 mV/s and different rotation rates (400, 625, 900, 1225, 1600, and 2025 rpm), meanwhile the ring was held at 1.20 V vs. RHE (Figure A2.4c). The collection efficiency (*N*) of RRDE is calculated using the equation:

$$N = \frac{i_{\text{ring}}}{i_{\text{disk}}}$$

where i_{ring} and i_{disk} are the ring and the disk current, respectively. When both ferricyanide reduction on the bare GC disk and ferrocyanide oxidation on the Pt ring became diffusion-limited, the collection efficiency was found to be 0.43 and was independent of the RRDE rotation rate (Figure A2.4d).

Detailed Protocols for ORR Measurements of Pt/C and Vulcan Carbon Black. The electrolyte (0.05 M H_2SO_4 or 0.05 M Na_2SO_4) was purged with Ar gas for at least 15 min prior to the measurements in order to eliminate dissolved O_2 gas. A blanket of Ar gas was maintained over the surface of the electrolyte during the measurements.

(a) 5 mg of 20 wt% Pt/C (Sigma-Aldrich) or Vulcan XC72R carbon black (Cabot Corp.) was suspended in 250 μL of Nafion solution (Sigma-Aldrich, 5 wt% in lower aliphatic alcohols and water) and 2250 μL of nanopure water by sonicating for 1 h, then 10 μL of the suspension was drop-casted onto the disk of RRDE and dried under ambient condition at a rotation rate of 700 rpm to achieve a uniform catalyst film.

(b) The Pt/C- or Vulcan-casted disk was first conditioned in Ar-saturated electrolyte by performing CV between 0.05 V and 1.20 V vs. RHE (without *iR*-correction) at 100 mV/s and 1600 rpm for 50 cycles, meanwhile the Pt ring was held at 0.70 V vs. RHE.

(c) The Pt ring was conditioned in Ar-saturated electrolyte by performing CV between 0.05 V and 1.20 V vs. RHE (without *iR*-correction) at 100 mV/s and 1600 rpm for 50 cycles, meanwhile the Pt/C- or Vulcan-casted disk was held at 0.70 V vs. RHE.

(d) For background current measurements, LSV of the Pt/C-casted disk was swept in positive direction from 0 to 1.2 V vs. RHE (without *iR*-correction) at 50 mV/s and 400 rpm, LSV of the Vulcan-casted disk was swept in negative direction from 1.2 to 0 V vs. RHE (without *iR*-correction) at 50 mV/s and 400 rpm.

(e) The electrolyte was then saturated with O_2 gas for ORR measurements. The Pt/C- or Vulcan-casted disk was conditioned in O_2-saturated electrolyte by performing CV between 0.05 V and 1.20 V vs. RHE (without *iR*-correction) at 100 mV/s and 1600 rpm for 10 cycles, meanwhile the Pt ring was held at 1.3 V vs. RHE.

(f) The Pt ring was conditioned in O_2-saturated electrolyte by performing CV between 0.05 V and 1.20 V vs. RHE (without *iR*-correction) at 100 mV/s and 1600 rpm for 10 cycles, meanwhile the Pt/C- or Vulcan-casted disk was held at 1.2 V vs. RHE.

(g) To record RRDE voltammograms in O_2-saturated electrolyte, LSV of the Pt/C-casted disk was swept in positive direction from 0 to 1.2 V vs. RHE (without *iR*-correction) at 50 mV/s and different rotation rates, LSV of the Vulcan-casted disk was swept in negative direction from 1.2 to 0 V vs. RHE (without *iR*-correction) at 50 mV/s and different rotation rates, meanwhile the Pt ring was held at 1.3 V vs. RHE. The H_2O_2 selectivity (p) and the electron transfer number (n) is calculated using the following equations:

$$p = 2 \times \frac{\frac{i_{\text{ring}}}{N}}{i_{\text{disk}} + \frac{i_{\text{ring}}}{N}}$$

$$n = 4 \times \frac{i_{\text{disk}}}{i_{\text{disk}} + \frac{i_{\text{ring}}}{N}}$$

where i_{disk} and i_{ring} are the disk and the ring current, respectively, and N is the collection efficiency determined above (0.43). We note that, for the ease of directly visualizing the H_2O_2 selectivity from the RRDE voltammograms (Figure A2.5a, A2.5c, A2.6a, A2.6c), both the disk and the ring current densities are presented based on the geometric area of the disk electrode (0.126 cm^2), and the ring current density is further adjusted by collection efficiency:

$$j_{\text{disk}} = \frac{i_{\text{disk}}}{A_{\text{disk}}}$$

$$j_{\text{ring}} = \frac{i_{\text{ring}}}{A_{\text{disk}} \times N} = j_{\text{peroxide}}$$

where j_{peroxide} is the partial disk current density that produces hydrogen peroxide (i.e., the hydrogen peroxide current density). Besides the RRDE method described above, the electron transfer number (n) can also be calculated based on the Koutecky-Levich (K-L) method that describes the behavior of the disk current density:

$$\frac{1}{j_{\text{disk}}} = \frac{1}{j_{\text{k}}} + \frac{1}{j_{\text{L}}}$$

$$j_{\text{L}} = 0.62 \times n \times F \times D^{2/3} \times v^{-1/6} \times C^{*} \times \omega^{1/2}$$

$$\frac{1}{j_{\text{disk}}} = \frac{1}{j_{\text{k}}} + \frac{1}{0.62 \times n \times F \times D^{2/3} \times v^{-1/6} \times C^{*}} \times \omega^{-1/2}$$

where j_{k} and j_{L} are the kinetic and diffusion-limited current density, respectively, F is the Faraday constant, D is the diffusion coefficient of O_2, v is the kinematic viscosity of the electrolyte, C^{*} is the concentration of O_2 in the bulk electrolyte, and ω is the angular velocity (in rad/s) of the disk electrode. Thus, n can be deduced from and should be inversely proportional to the slope of the linear plot of $\frac{1}{j_{\text{disk}}}$ vs. $\omega^{-1/2}$.

(f) The uncompensated resistance (R_u) was finally measured using electrochemical impedance spectroscopy (EIS). EIS measurement was performed on the CoS_2-casted disk (held at open circuit potential) over the frequency range from 100 kHz to 100 mHz. R_u could be estimated at the high-frequency region of the EIS spectrum where the phase angle is closest to 0°.[2] The magnitude of R_u was dependent of the electrolyte (around 50 Ω in 0.05 M H_2SO_4 and around 130 Ω in 0.05 M Na_2SO_4). For all the RRDE voltammograms of Pt/C and Vulcan carbon black recorded in O_2-saturated electrolyte (Figure A2.5, A2.6), iR-correction was manually performed after subtracting background current.

Detailed Protocols for ORR Measurements of Drop-Casted CoS_2. The electrolyte (0.05 M H_2SO_4 or 0.05 M Na_2SO_4) was purged with O_2 gas for at least 15 min prior to the measurements in order to reach a saturated concentration of dissolved O_2 gas. During the measurements, a blanket of O_2 gas was maintained over the surface of the electrolyte to ensure that the concentration of dissolved O_2 gas remained stable.

(a) The CoS_2-casted disk was conditioned in O_2-saturated electrolyte by performing CV between -0.025 V and 0.80 V vs. RHE (without *iR*-correction) at 100 mV/s and 1600 rpm for 10 cycles, meanwhile the Pt ring was held at 1.3 V vs. RHE.

(b) The Pt ring was conditioned in O_2-saturated electrolyte by performing CV between 0.05 V and 1.20 V vs. RHE (without *iR*-correction) at 100 mV/s and 1600 rpm for 10 cycles, meanwhile the CoS_2-casted disk was held at 0.80 V vs. RHE.

(c) To record RRDE voltammograms in O_2-saturated electrolyte, LSV of the CoS_2-casted disk was performed from 0.80 V to -0.025 V vs. RHE (without *iR*-correction) at 50 mV/s and different rotation rates, meanwhile the Pt ring was held at 1.3 V vs. RHE.

(d) The electrolyte was then saturated with Ar gas for background current measurements. LSV was performed on the CoS_2-casted disk from 0.80 V to -0.025 V vs. RHE (without *iR*-correction) at 50 mV/s and 400 rpm.

(e) The electrochemically active surface area (ECSA) of the CoS_2-casted disk was determined by performing CV at different scan rates between -0.025 V and 0.80 V vs. RHE (without *iR*-correction) in Ar-saturated electrolyte.

(f) The uncompensated resistance (R_u) was finally measured using electrochemical impedance spectroscopy (EIS) For all the RRDE voltammograms of CoS_2 recorded in O_2- and Ar-saturated electrolyte (Figure 2.2 in the Chapter 2, A2.7, A2.8, A2.10 to A2.12, A2.14 to A2.16), *iR*-correction was manually performed after subtracting background current.

Detailed Protocols for Bulk ORR Electrolysis on Integrated CoS_2/CFP Electrode and Chemical Quantification of H_2O_2 Product. For bulk ORR electrolysis, CoS_2 nanowires directly grown on carbon fiber paper (CoS_2/CFP) was used as the working electrode to achieve a larger catalytic current and therefore a higher H_2O_2 yield. To prepare working electrodes of CoS_2/CFP, 5-minute epoxy (Devcon) was used to define the geometric area of the working electrodes to about 1 cm × 1 cm (Figure A2.19a). A three-electrode H-cell setup was used to avoid the oxidation of H_2O_2 product on the counter electrode, and a minimal volume (3 mL) of electrolyte was filled into the working electrode compartment to obtain higher concentrations of H_2O_2 (Figure A2.19b).

(a) To prepare for ORR electrolysis in a three-electrode H-cell, Nafion 117 membrane (Sigma-Aldrich) was cut into circular pieces (with appropriate diameter to cover the junction of H-cell), cleaned by immersing into 3 wt% H_2O_2, nanopure water, 1 M H_2SO_4, and nanopure water (at 80 °C for 1 h for each step), and stored in 0.05 M H_2SO_4 at room temperature before use. The graphite rod counter electrode was separated from the CoS_2/CFP working electrode and the Hg/Hg_2SO_4 (saturated K_2SO_4) reference electrode by Nafion membrane. The electrolyte (0.05 M H_2SO_4) was purged with O_2 gas for at least 15 min prior to the measurements in order to reach a saturated concentration of dissolved O_2 gas, a blanket of O_2 gas was maintained over the electrolyte during the measurements to ensure that the concentration of dissolved O_2 gas remained stable.

(b) To figure out the operating conditions of ORR electrolysis, we performed CV on CoS_2/CFP between -0.025 V and 0.80 V vs. RHE (without *iR*-correction) at 100 mV/s in O_2-saturated 0.05 M H_2SO_4 and found that vigorous stirring the electrolyte enhanced the catalytic current by facilitating the mass transport of O_2 (Figure A2.20a, A2.20b). Therefore, we performed ORR electrolysis at the maximum stir rate (1200 rpm) of the stir plate used. We also performed control experiments to confirm that plain CFP was inert towards ORR in 0.05 M H_2SO_4 (Figure A2.20c, A2.20d). We chose 0.5 V vs. RHE as the working electrode potential for ORR electrolysis because the RRDE results suggested the H_2O_2 production at high catalyst loadings peaked around 0.5 V vs. RHE (Figure 2.3b in the Chapter 2). Note that R_u became much smaller in the H-cell (1 to 3 Ω for 0.05 M H_2SO_4) compared with that in the RRDE cell since the reference electrode can be much closer to the surface of the working electrode in the H-cell setup.

(c) The ceric sulfate titration of H_2O_2 follows the reaction: $2\ Ce^{4+} + H_2O_2 \rightarrow 2\ Ce^{3+} + 2\ H^+ + O_2$; Ce^{4+} has a peak absorbance at 319 nm while Ce^{3+} is colorless, the reduction of Ce^{4+} to Ce^{3+} by H_2O_2 results in a decrease in the absorbance. Note that Ce^{4+} is only soluble in highly acidic solution due to its strong tendency to hydrolyze. Therefore, anhydrous $Ce(SO_4)_2$ (Sigma-Aldrich) was dissolved in 0.5 M H_2SO_4 to prepare a series of standard Ce^{4+} solutions (up to 0.5 mM). Absorption spectroscopy of standard Ce^{4+} solutions was performed on a JASCO V-570 UV/Vis/NIR spectrophotometer at 319 nm, and a calibration curve was generated (Figure A2.22a and inset).

$$Abs = \varepsilon \times l \times [Ce^{4+}]$$

where *Abs* is the absorbance at 319 nm, $[Ce^{4+}]$ is the Ce^{4+} concentration (mM), ε is the molar absorptivity of Ce^{4+} ($mM^{-1}\ cm^{-1}$), and l is the path length (1 cm).

(d) Before performing ORR electrolysis on CoS_2/CFP in 0.05 M H_2SO_4, CV was first performed on CoS_2/CFP between -0.025 V and 0.80 V vs. RHE (without *iR*-correction) at 100 mV/s to condition the working electrode (10 cycles each at the stir rate of 0 rpm and 1200 rpm). A 50-μL aliquot of the working electrode compartment electrolyte was sampled and injected into 4 mL of 0.422 mM Ce^{4+} stock solution in 0.5 M H_2SO_4, which allows for calculating the initial H_2O_2 concentration in the electrolyte before the ORR electrolysis started:

$$[Ce^{4+}]_{\text{before}} = \frac{Abs_{\text{before}}}{\varepsilon \times l}$$

$$[Ce^{4+}]_{\text{after}} = \frac{Abs_{\text{after}}}{\varepsilon \times l}$$

$$H_2O_2 \text{ concentration (mM) in the 50-μL aliquot} = \frac{4 \times [Ce^{4+}]_{\text{before}} - 4.05 \times [Ce^{4+}]_{\text{after}}}{2 \times 0.05}$$

where Abs_{before} and Abs_{after} are the absorbances of Ce^{4+} stock solution at 319 nm before and after injecting H_2O_2-containing aliquot. Note that (1) the initial concentration of Ce^{4+} stock solution, $[Ce^{4+}]_{\text{before}}$, does not need to be exact and can always be found using the calibration curve; (2) H_2O_2 always need to be the limiting reagent when reacting with Ce^{4+} stock solution so that $[Ce^{4+}]_{\text{after}} > 0$; (3) Ce^{4+} stock solution should remain almost the same acidic pH after aliquot injection to avoid cerium hydroxides precipitate out at higher pH.[3]

(e) We then carried out ORR electrolysis on CoS_2/CFP in 0.05 M H_2SO_4 at 0.5 V vs. RHE and 1200 rpm stir rate for 60 min, with eight 50-μL aliquots of the working electrode compartment electrolyte sampled at 5, 10, 15, 20, 30, 40, 50, and 60 min after electrolysis started. The volume of the electrolyte left in the working electrode compartment at the end of electrolysis was 2.55 mL. The relationships among cumulative H_2O_2 yield, H_2O_2 selectivity, and Faradaic efficiency can be described by the following equations:

$$\text{Cumulative Faradaic efficiency (\%)} = 100 \times \frac{2 \times 96485 \times \text{Cumulative } H_2O_2 \text{ yield (mol)}}{\int_0^t I\, dt}$$

$$\text{Cumulative } H_2O_2 \text{ selectivity (\%)} = \frac{200}{1 + \dfrac{\int_0^t I\, dt}{2 \times 96485 \times \text{Cumulative } H_2O_2 \text{ yield (mol)}}}$$

$$\text{Cumulative } H_2O_2 \text{ selectivity (\%)} = \frac{200}{1 + \dfrac{100}{\text{Cumulative Faradaic efficiency (\%)}}}$$

where $\int_0^t I\, dt$ stands for the cumulative charge passed (C) during electrolysis.

Detailed Protocols for Examining the Chemical Stability of Nonstabilized H_2O_2 Under Different pH Conditions. 0.03 wt% H_2O_2 aqueous solutions in 0.5 M H_2SO_4 (pH 0.5), in 0.5 M Na_2SO_4 with 1.6 mM H_2SO_4 (pH 3.3), in 0.5 M Na_2SO_4 with 1.6 mM NaOH (9.3), and in 0.1 M NaOH (pH 12.7) were prepared from the following chemicals: 30 wt% H_2O_2 (Acros Organics, nonstabilized in water), H_2SO_4 (Sigma-Aldrich, 95.0-98.0%), Na_2SO_4 (Sigma-Aldrich, ⩾99.0%), NaOH (Sigma-Aldrich, semiconductor grade, 99.99% trace metals basis), and nanopure water. These 0.03 wt% H_2O_2 aqueous solutions were kept at room temperature and ambient pressure in sealed polypropylene centrifuge tubes (VWR Superclear Ultra High Performance). The concentration of H_2O_2 in these 0.03 wt% H_2O_2 aqueous solutions were periodically quantified on a daily basis over the time period of one week using the ceric sulfate titration method described above.

Supplementary Figures and Tables

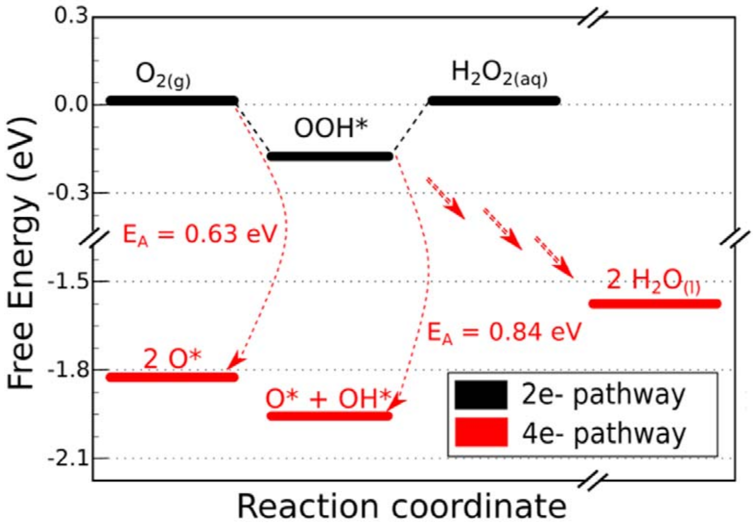

Figure A2.1. Free energy diagram for ORR pathways on CoS_2 (100) surface with the PBE-D3(ABC) dispersion-corrected density functional method.

Free energy diagram for both two-electron ($2e^-$) and four-electron ($4e^-$) ORR on the CoS_2 (100) surface at the calculated standard equilibrium reduction potential of $2e^-$ ORR with the PBE-D3(ABC) dispersion-corrected density functional method.

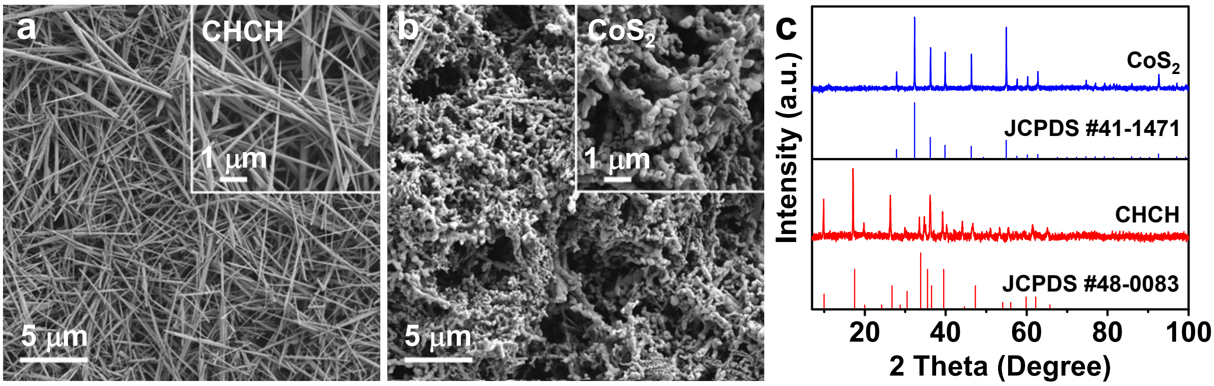

Figure A2.2. Materials characterization of CoS_2 nanomaterial powders.

SEM images of (a) CHCH and (b) CoS_2 nanomaterial powders. (c) PXRD patterns of CHCH and CoS_2 powders in comparison with the standard PXRD patterns of CHCH (JCPDS #48-0083) and CoS_2 (JCPDS #41-1471).

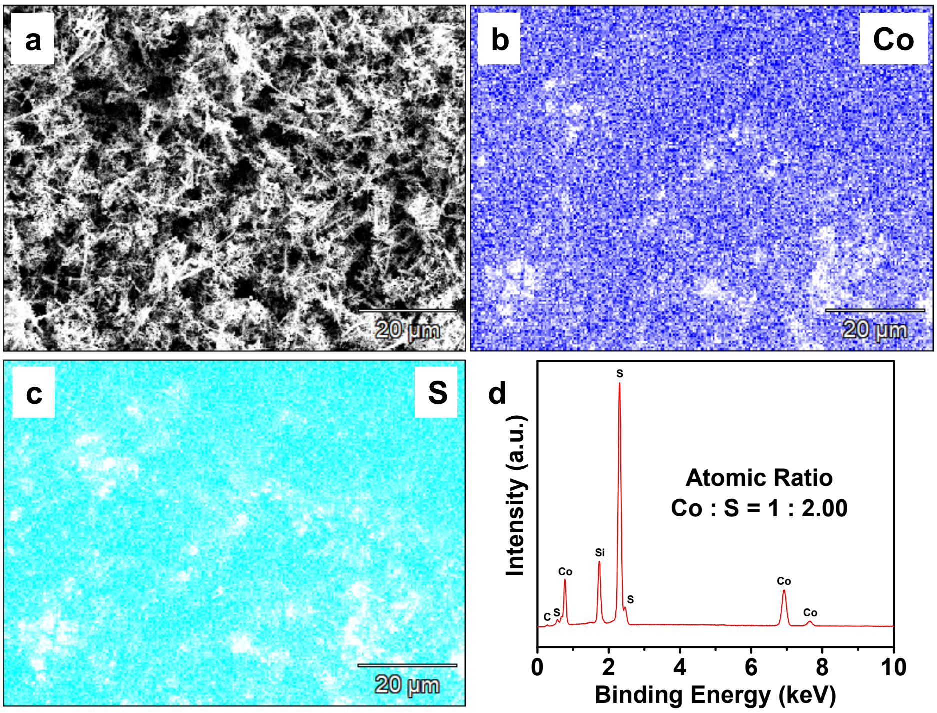

Figure A2.3. SEM characterization of CoS_2 powders.

(a) SEM image, (b,c) EDS elemental maps, and (d) EDS spectrum of CoS_2 powders.

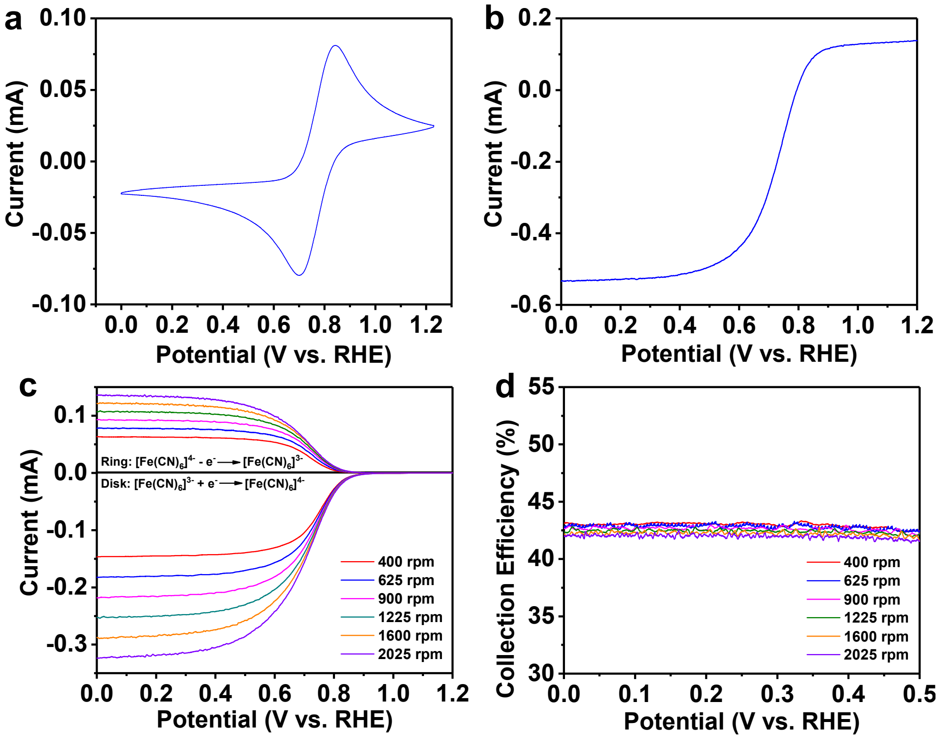

Figure A2.4. Calibration of the collection efficiency of the bare RRDE.

Calibration of the collection efficiency of the bare RRDE in Ar-saturated 0.05 M Na_2SO_4 dissolved with 4 mM of $K_3[Fe(CN)_6]$. (a) CV voltammogram of the bare GC disk of RRDE at 100 mV/s and 0 rpm, (b) LSV voltammogram of the Pt ring from 0 V to 1.23 V vs. RHE at 50 mV/s and 1600 rpm while holding the GC disk at 0 V vs. RHE, (c) RRDE voltammograms recorded at different rotation rates by performing LSV on the disk from 1.23 V to 0 V vs. RHE at 50 mV/s while holding the ring at 1.20 V vs. RHE, (d) the corresponding collection efficiency of RRDE voltammograms as a function of the potential. All potentials in this figure are presented without *iR*-correction (R_u for the bare GC disk is 130.2 Ω in this experiment).

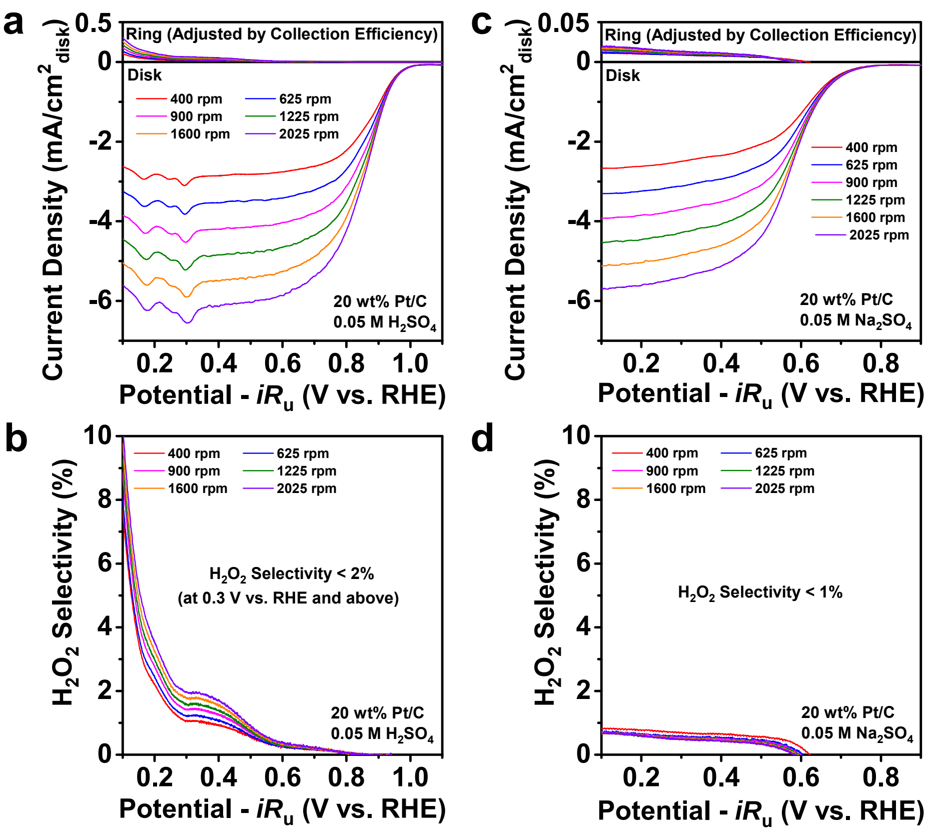

Figure A2.5. RRDE measurements of drop-casted Pt/C.

RRDE measurements and the corresponding H_2O_2 selectivity of drop-casted Pt/C in O_2-saturated (a,b) 0.05 M H_2SO_4 and (c,d) 0.05 M Na_2SO_4. Very low H_2O_2 selectivity was observed in both acidic and neutral solution (Pt/C is a known 4e$^-$ ORR catalyst), showing that 1.3 V vs. RHE is an appropriate ring potential (without triggering water oxidation) for RRDE measurements in both acidic and neutral solutions**.**

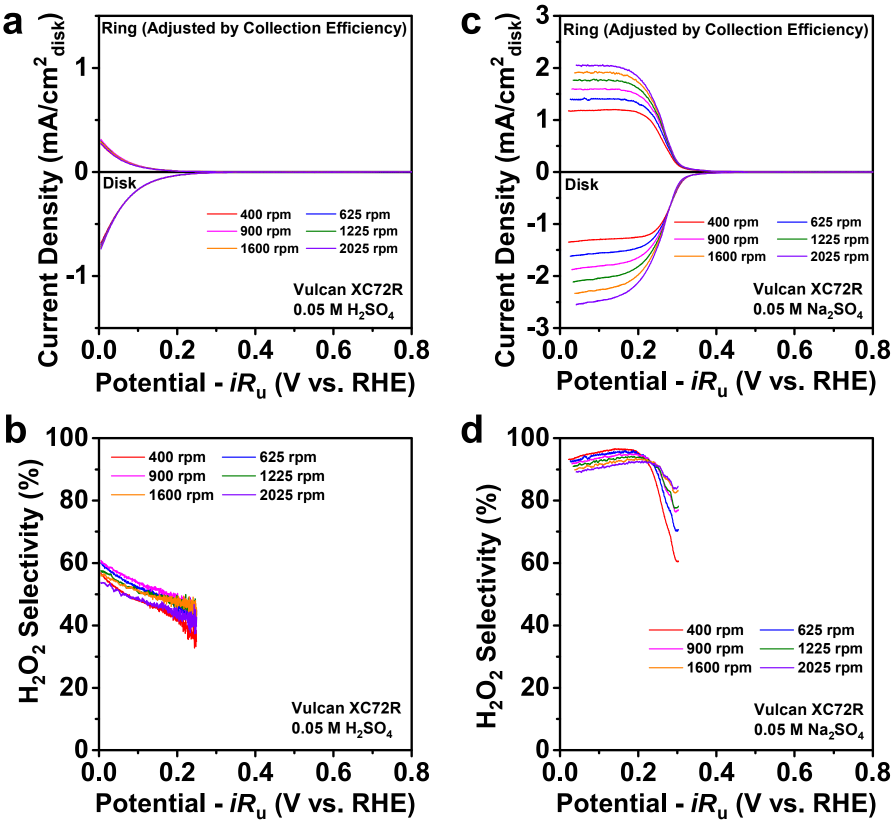

Figure A2.6. RRDE measurements of drop-casted Vulcan carbon black.

RRDE measurements and the corresponding H_2O_2 selectivity of drop-casted Vulcan carbon black in O_2-saturated (a,b) 0.05 M H_2SO_4 and (c,d) 0.05 M Na_2SO_4. Considerable H_2O_2 selectivity was observed in both acidic and neutral solution (Vulcan carbon black is moderately selective towards $2e^-$ ORR but has a poor catalytic activity), showing that 1.3 V vs. RHE is an appropriate ring potential (driving fast H_2O_2 oxidation) for RRDE measurements in both acidic and neutral solutions.

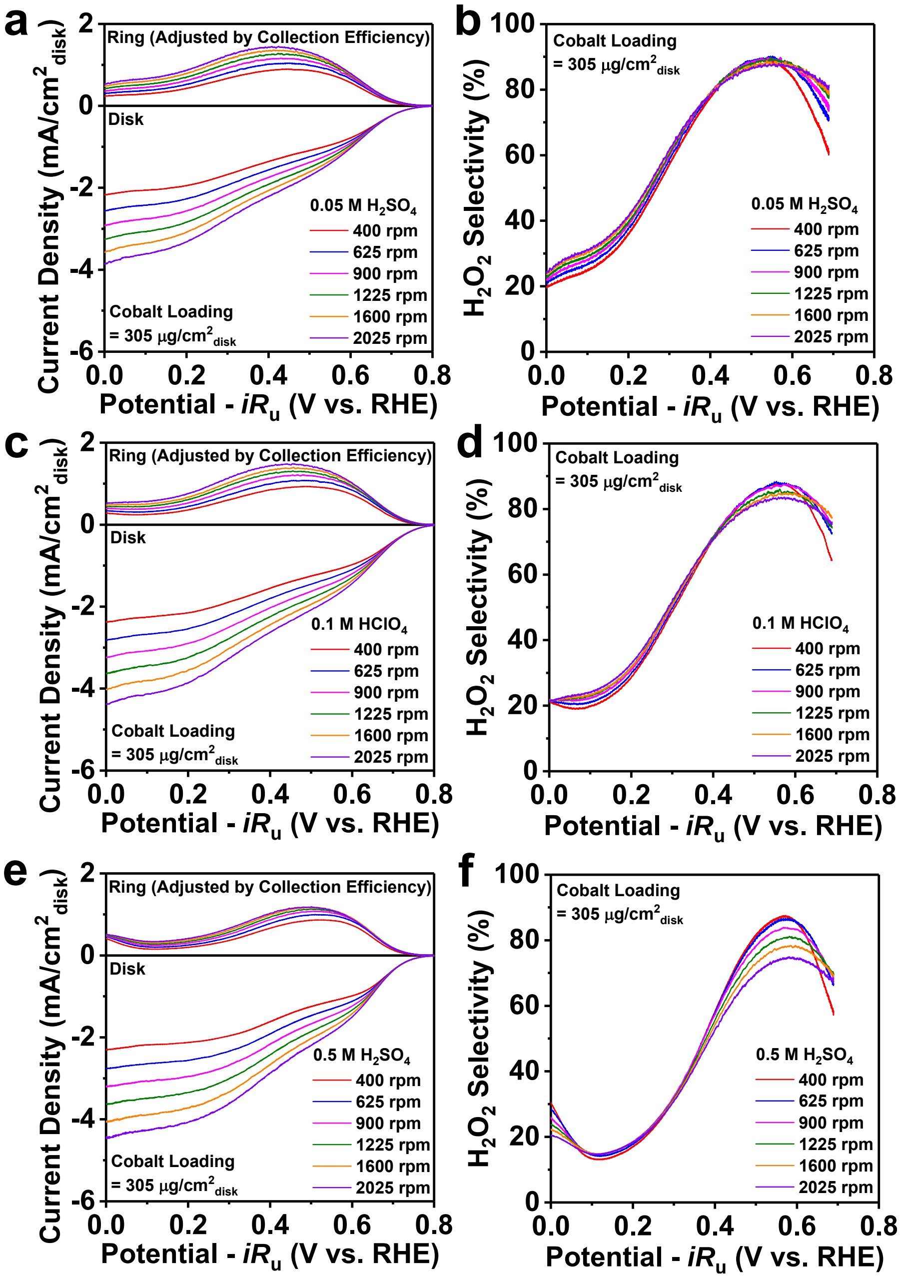

Figure A2.7. RRDE measurements of drop-casted CoS_2 in different acidic electrolyte solutions.

RRDE measurements and the corresponding H_2O_2 selectivity of drop-casted CoS_2 (cobalt loading = 305 μg/cm$^2_{disk}$) in O_2-saturated (a,b) 0.05 M H_2SO_4 (pH 1.21), (c,d) 0.1 M $HClO_4$ (pH 1.02), and (e,f) 0.5 M H_2SO_4 (pH 0.35).

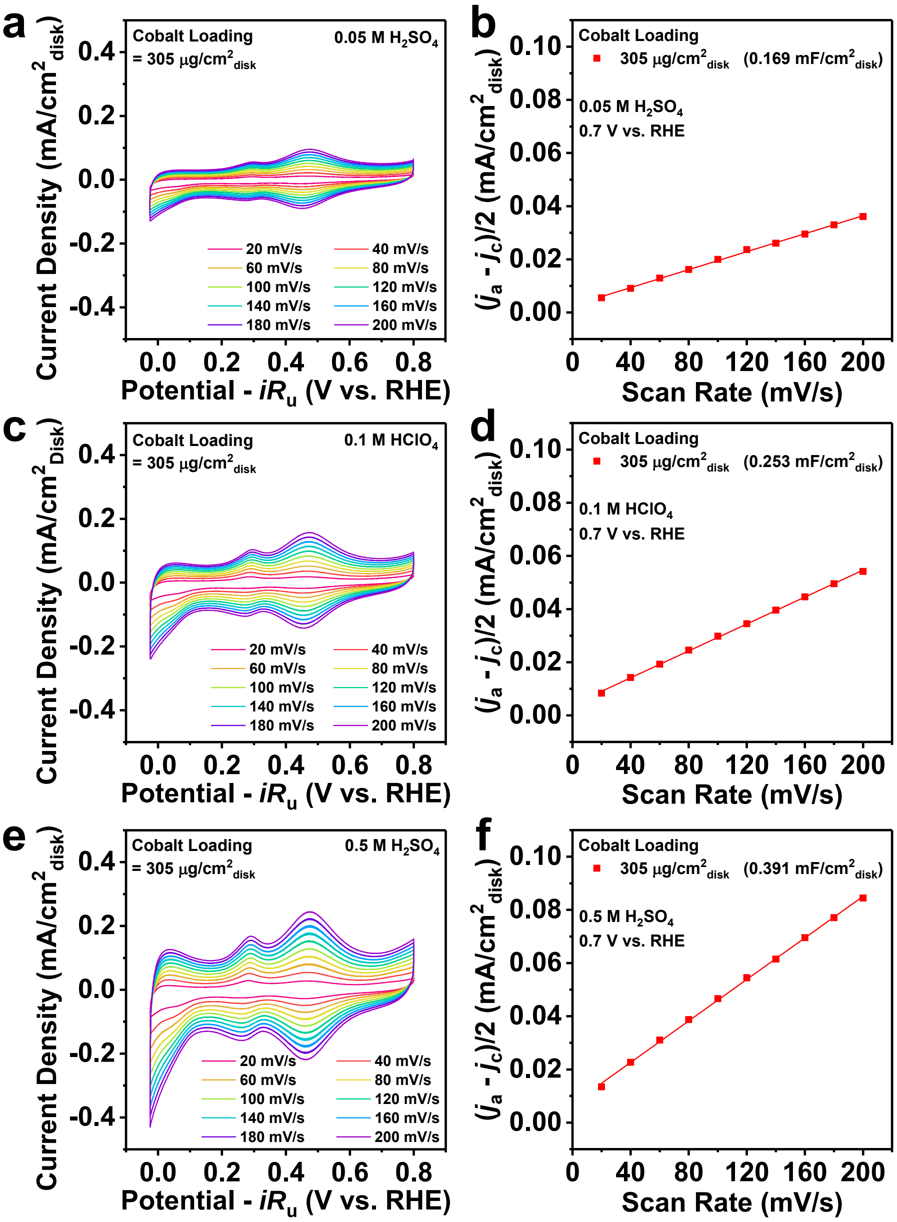

Figure A2.8. Electrochemically active surface area measurements of drop-casted CoS_2 in different acidic electrolyte solutions.

Electrochemically active surface area (ECSA) measurements of drop-casted CoS_2 (cobalt loading = 305 μg/cm$^2_{disk}$) in Ar-saturated (a,b) 0.05 M H_2SO_4, (c,d) 0.1 M $HClO_4$, and (e,f) 0.5 M H_2SO_4. RRDE measurements were shown in Figure A2.7. Double-layer capacitances (C_{dl}) were determined at 0.7 V vs. RHE in all cases to avoid the interference of Faradaic currents.

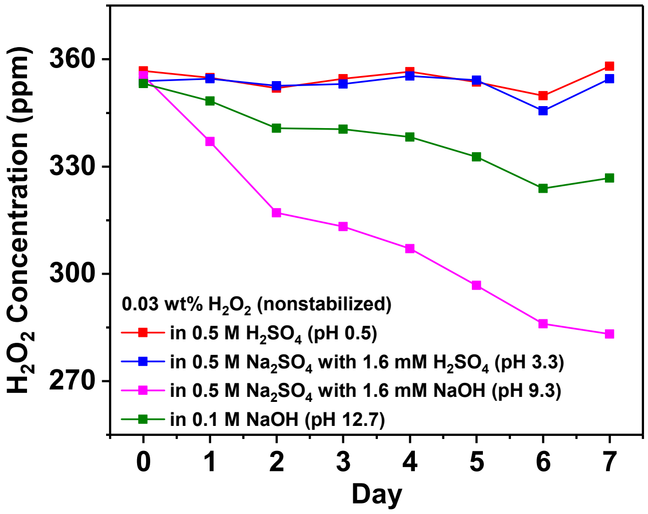

Figure A2.9. Chemical stability of nonstabilized H_2O_2 under different pH conditions.

Chemical stability of nonstabilized H_2O_2 under different pH conditions, showing a higher decomposition rate of H_2O_2 in alkaline solution compared with that in acidic solution which is negligible over the time period of one week.

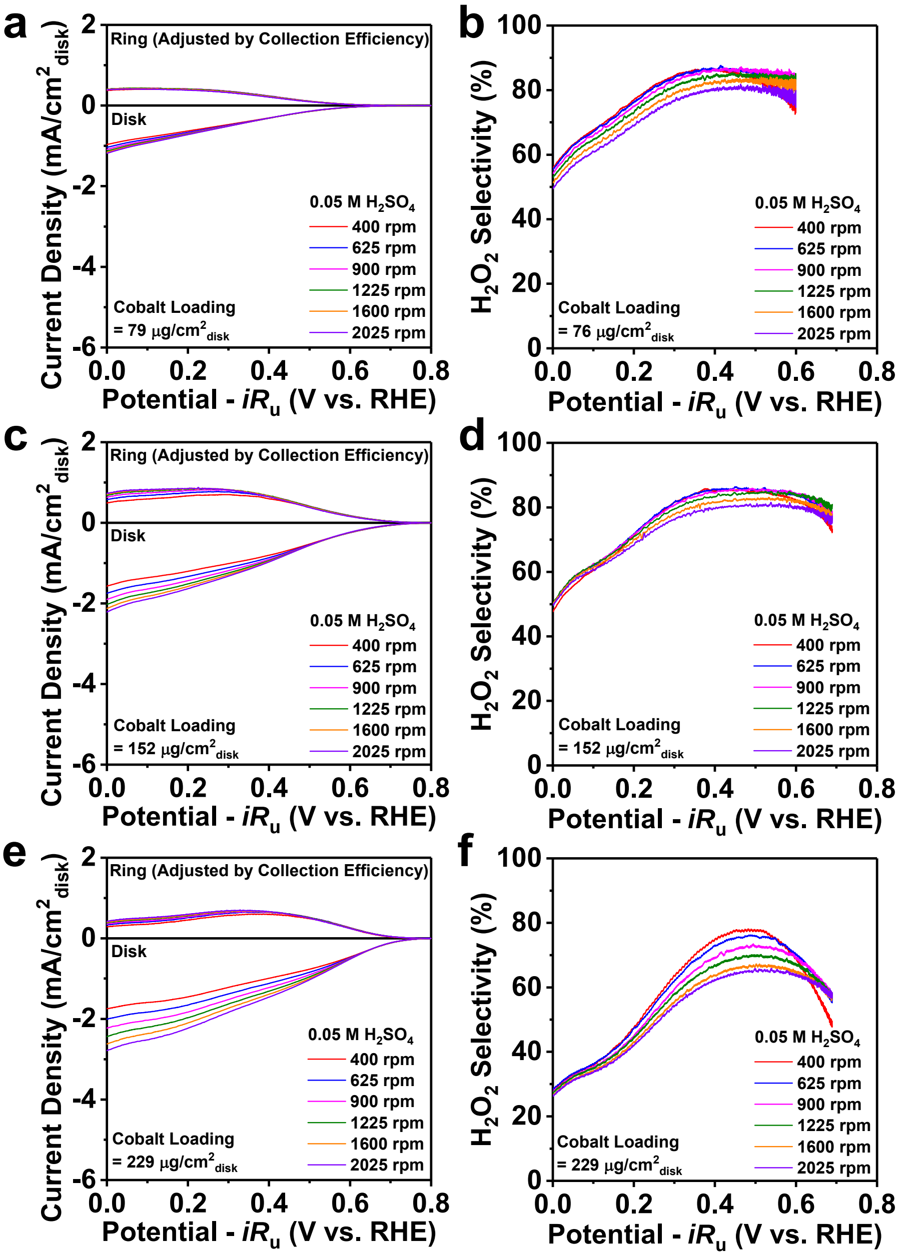

Figure A2.10. RRDE measurements of drop-casted CoS_2 in O_2-saturated 0.05 M H_2SO_4 with various cobalt loadings.

RRDE measurements and the corresponding H_2O_2 selectivity of drop-casted CoS_2 in O_2-saturated 0.05 M H_2SO_4 with various cobalt loadings: (a,b) 76 µg/cm$^2_{disk}$, (c,d) 152 µg/cm$^2_{disk}$, and (e,f) 229 µg/cm$^2_{disk}$.

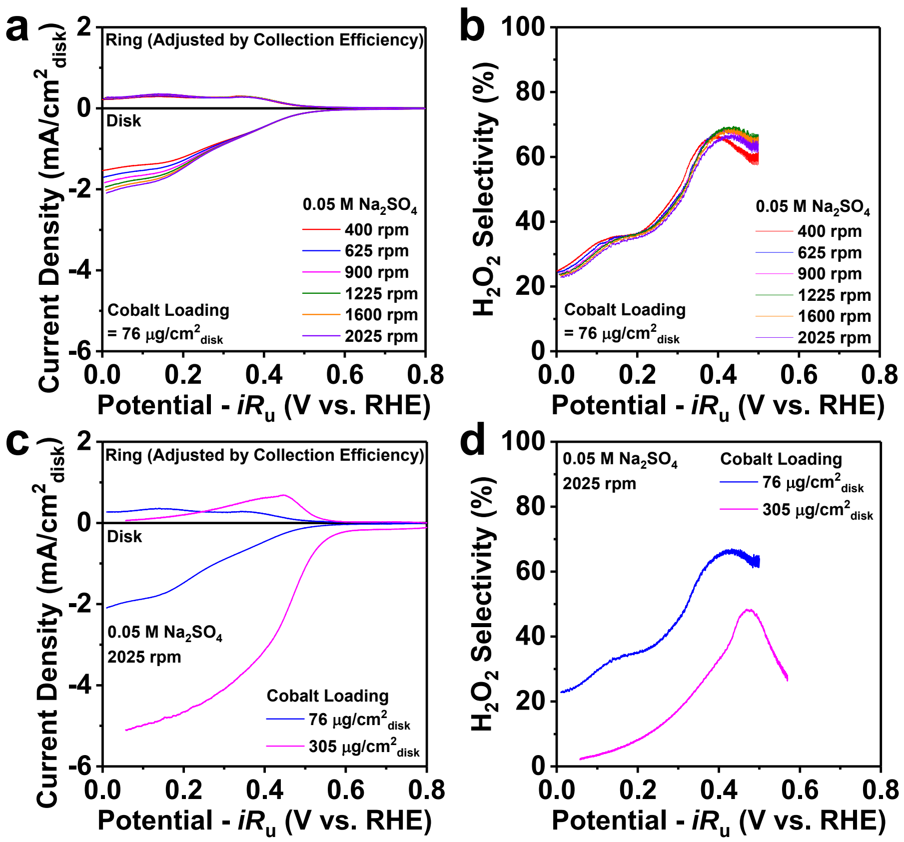

Figure A2.11. RRDE measurements of drop-casted CoS_2 in O_2-saturated 0.05 M Na_2SO_4 with various cobalt loadings.

(a) RRDE measurements and (b) the corresponding H_2O_2 selectivity of drop-casted CoS_2 (cobalt loading = 76 μg/cm$^2_{disk}$) in O_2-saturated 0.05 M Na_2SO_4. Comparisons of (c) RRDE voltammograms at 2025 rpm and (d) H_2O_2 selectivity at different cobalt loadings.

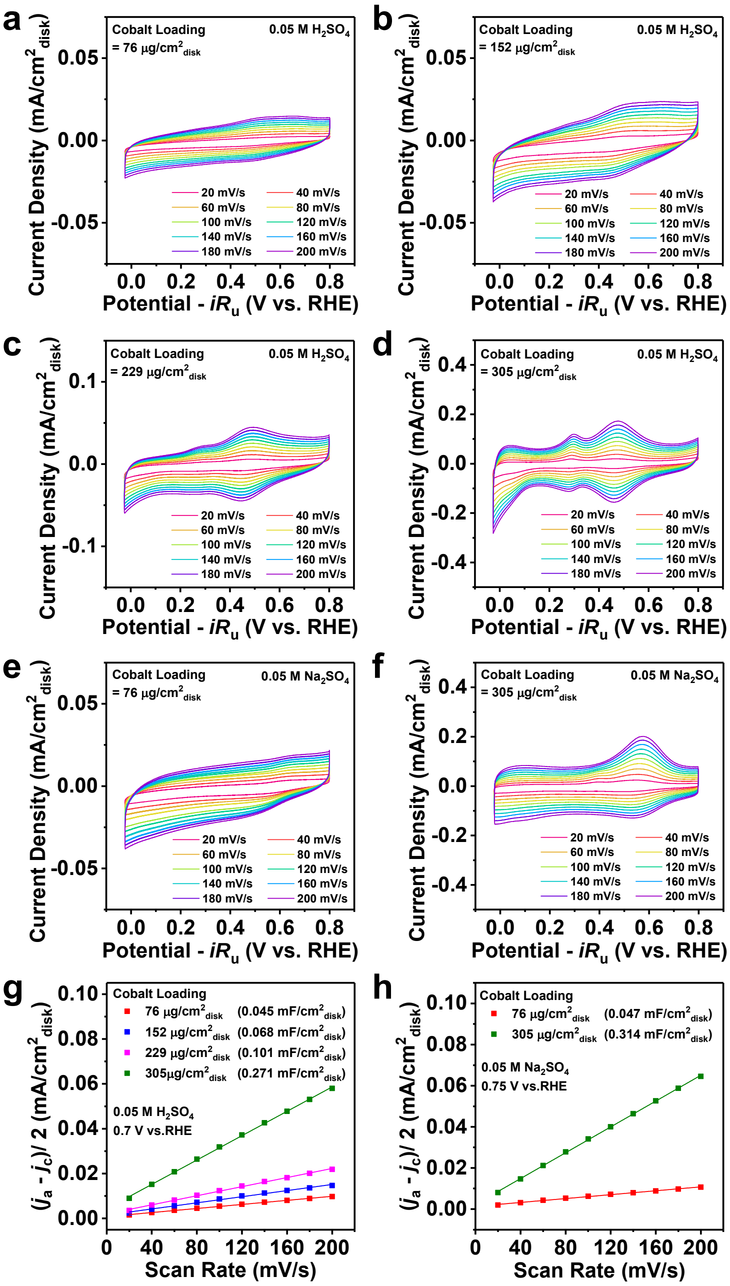

Figure A2.12. Electrochemically active surface area measurements of drop-casted CoS_2 with various cobalt loadings.

Electrochemically active surface area (ECSA) measurements of drop-casted CoS_2 at different cobalt loadings in Ar-saturated (a-d) 0.05 M H_2SO_4 and (e,f) 0.05 M Na_2SO_4. RRDE measurements were shown in Figure 2.2 in the Chapter 2, A2.10, A2.11. Double-layer capacitances (C_{dl}) were determined at (g) 0.7 V vs. RHE in 0.05 M H_2SO_4 and (h) 0.75 V vs. RHE in 0.05 M Na_2SO_4, respectively, to avoid the interference of Faradaic currents.

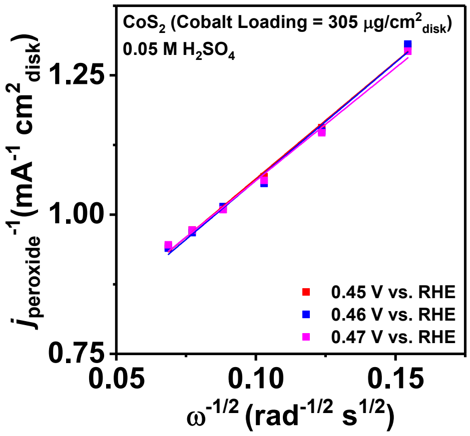

Figure A2.13. Koutecky-Levich analysis of the hydrogen peroxide current density of drop-casted CoS$_2$.

Koutecky-Levich (K-L) analysis of the hydrogen peroxide current density ($j_{peroxide}$) of drop-casted CoS$_2$ (cobalt loading = 305 μg/cm$^2_{disk}$) in O$_2$-saturated 0.05 M H$_2$SO$_4$ (RRDE voltammograms shown in Figure 2.2a in the Chapter 2). The K-L analysis was performed around 0.46 V vs. RHE where the maximum $j_{peroxide}$ was reached (see Table A2.2 for detailed analysis).

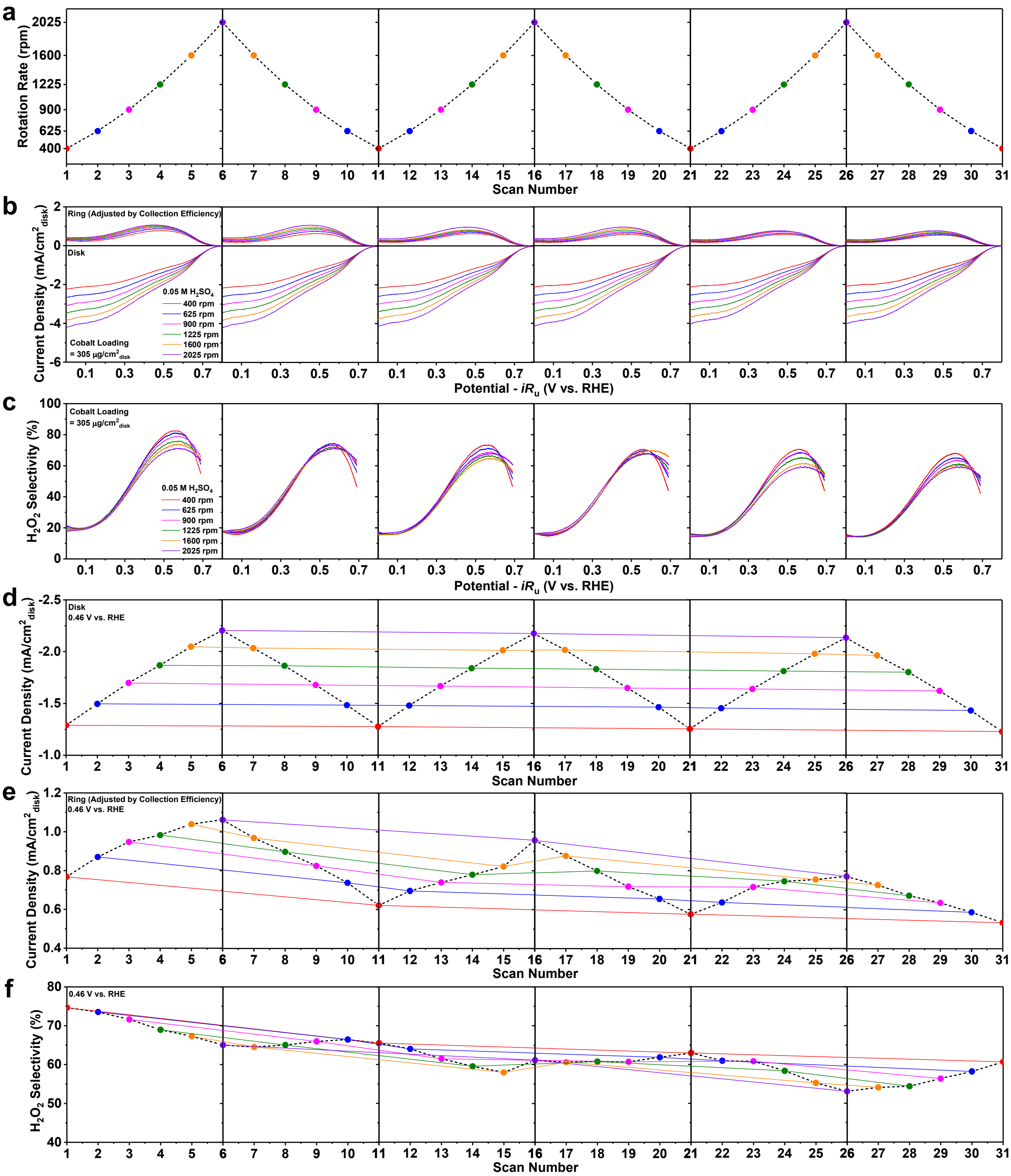

Figure A2.14. ORR operational stability test of drop-casted CoS_2 in O_2-saturated 0.05 M H_2SO_4.

(a) RRDE scan profile, (b) RRDE voltammograms, and (c) the corresponding H_2O_2 selectivity. Time evolution of (d) the disk current density, (e) the ring current density, and (f) the corresponding H_2O_2 selectivity at the disk potential of 0.46 V vs. RHE (after *iR*-correction).

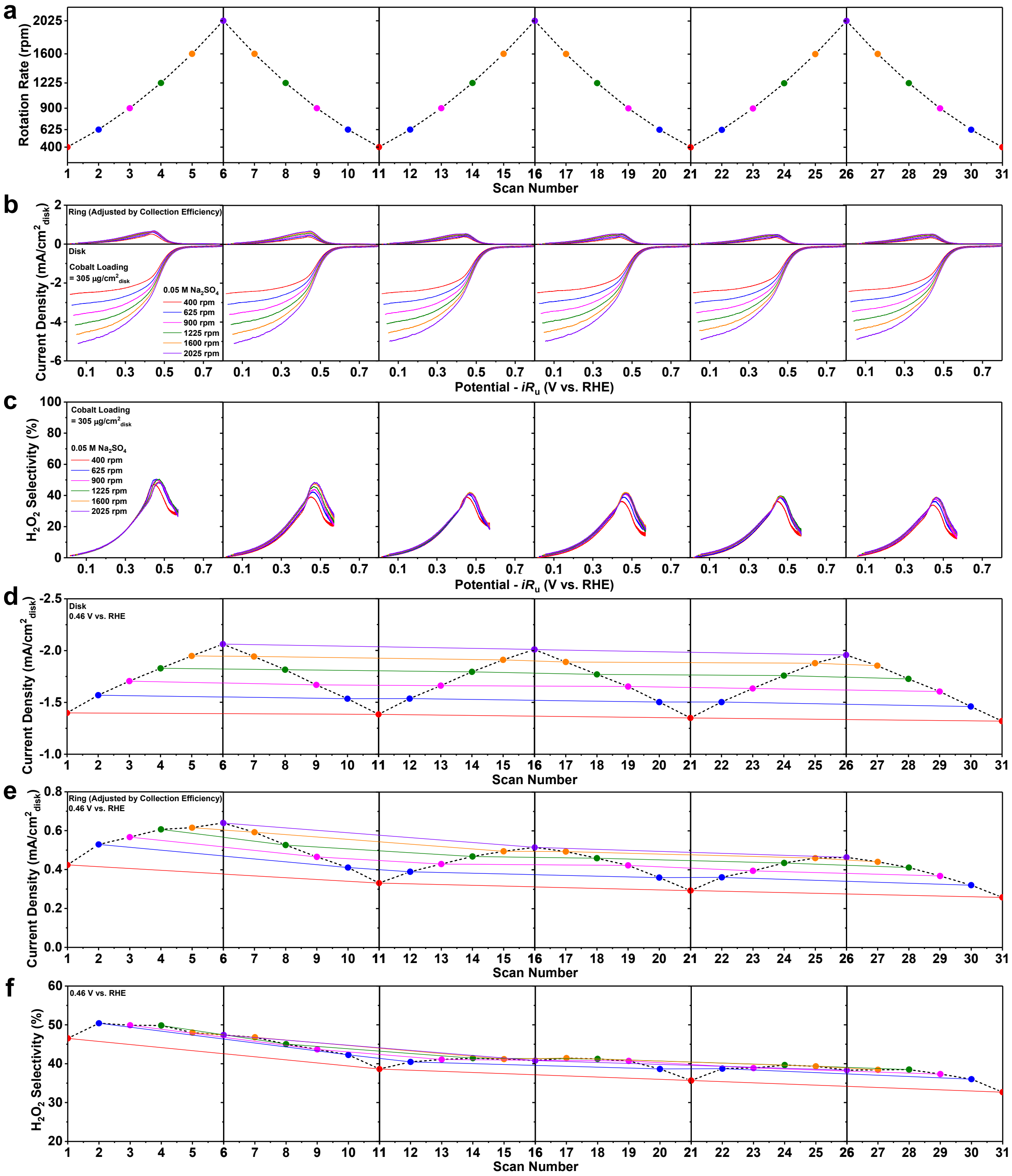

Figure A2.15. ORR operational stability tests of drop-casted CoS_2 in O_2-saturated 0.05 M Na_2SO_4.

(a) RRDE scan profile, (b) RRDE voltammograms, and (c) the corresponding H_2O_2 selectivity. Time evolution of (d) the disk current density, (e) the ring current density, and (f) the corresponding H_2O_2 selectivity at the disk potential of 0.46 V vs. RHE (after *iR*-correction).

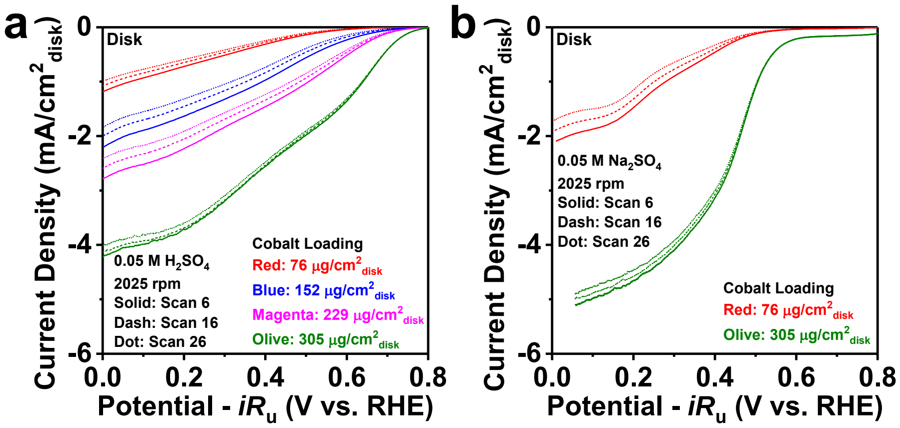

Figure A2.16. Time evolution of the disk current density during ORR operational stability tests of drop-casted CoS_2.

Time evolution of the disk current density at 2025 rpm during ORR operational stability tests of drop-casted CoS_2 with various cobalt loadings in O_2-saturated (a) 0.05 M H_2SO_4 and (b) 0.05 M Na_2SO_4.

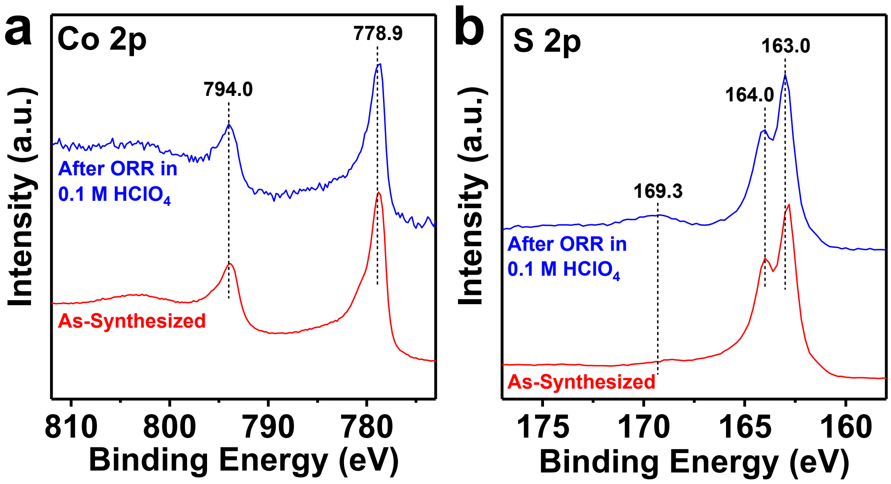

Figure A2.17. XPS characterization of drop-casted CoS_2 before and after operational stability tests in O_2-saturated 0.1 M $HClO_4$.

(a) Co 2p and (b) S 2p XPS spectra of drop-casted CoS_2 before and after operational stability tests in O_2-saturated 0.1 M $HClO_4$.

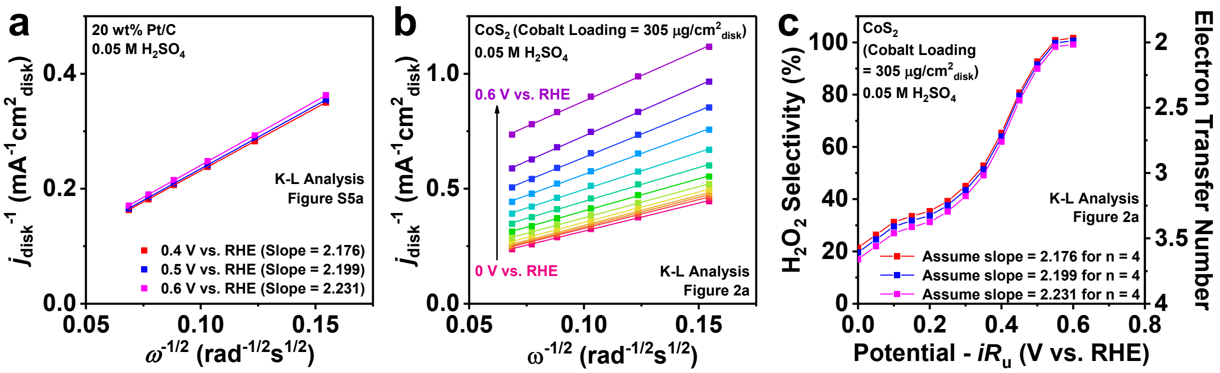

Figure A2.18. Koutecky-Levich analysis of drop-casted Pt/C in O_2-saturated 0.05 M H_2SO_4. (a) Koutecky-Levich (K-L) analysis of drop-casted Pt/C in O_2-saturated 0.05 M H_2SO_4, where the limiting current for the $4e^-$ ORR (~6 mA/cm^2_{disk} at 1600 rpm) was achieved. (b) K-L analysis and (c) the corresponding H_2O_2 selectivity and electron transfer number (*n*) of drop-casted CoS_2 (cobalt loading = 305 $\mu g/cm^2_{disk}$) in O_2-saturated 0.05 M H_2SO_4. RRDE voltammograms of Pt/C and CoS_2 were shown in Figure A2.5a and 2.2a (in the Chapter 2), respectively. The K-L slopes of Pt/C at different potentials were used as internal standards of the $4e^-$ ORR ($n = 4$) for the K-L analysis of CoS_2 (see Table A2.4 for details).

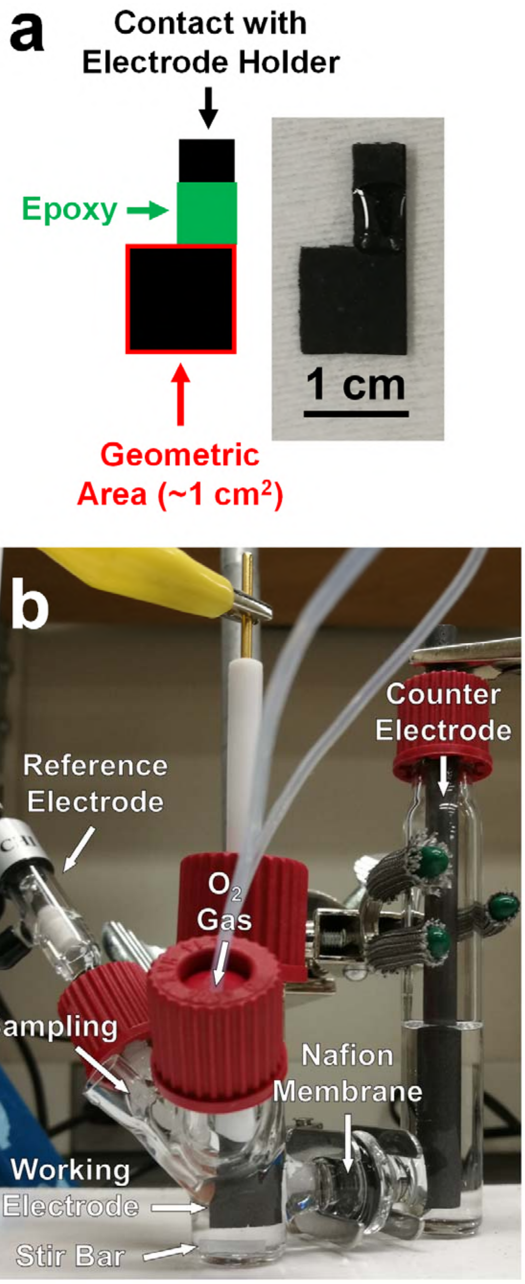

Figure A2.19. Schematics and digital photographs of CoS_2/CFP working electrodes and the three-electrode H-cell setup.

(a) Schematic and digital photograph of CoS_2/CFP working electrodes. (b) Digital photograph of the three-electrode H-cell setup (with key components labeled) for the bulk electrocatalytic production of H_2O_2.

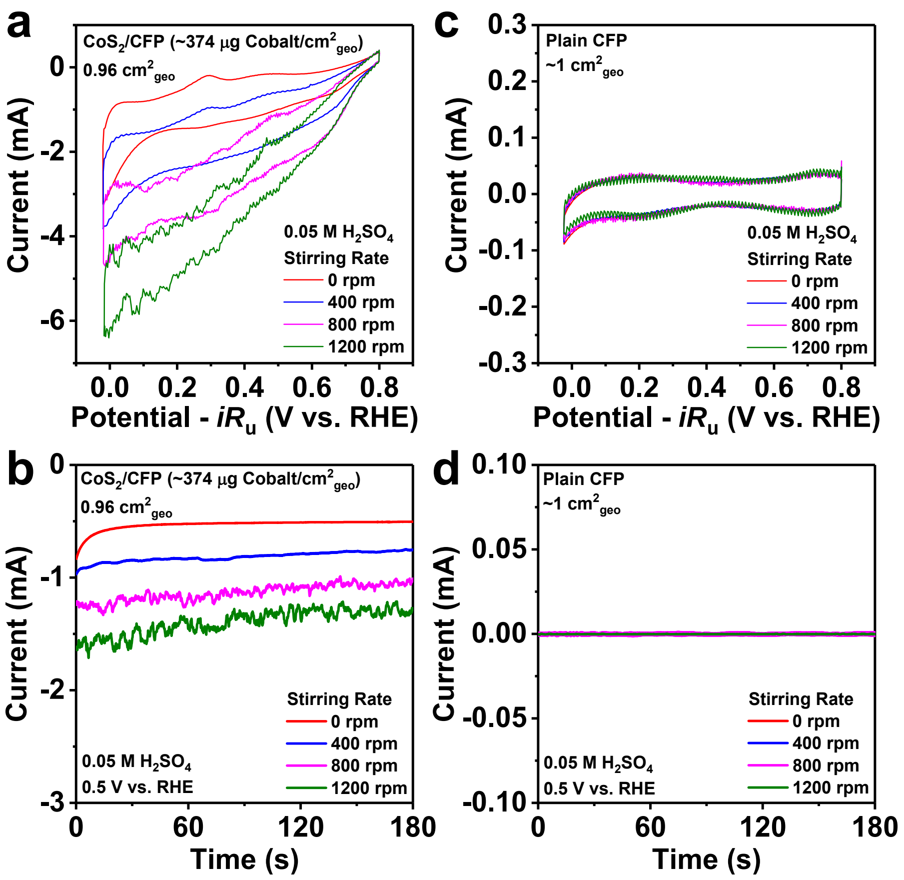

Figure A2.20. Cyclic voltammetry and chronoamperometry tests of CoS_2/CFP.

CV voltammograms (at 100 mV/s) and chronoamperometry tests (at 0.5 V vs. RHE) of (a,b) CoS_2/CFP and (c,d) plain CFP in O_2-saturated 0.05 M H_2SO_4 at different stir rates using the three-electrode H-cell setup.

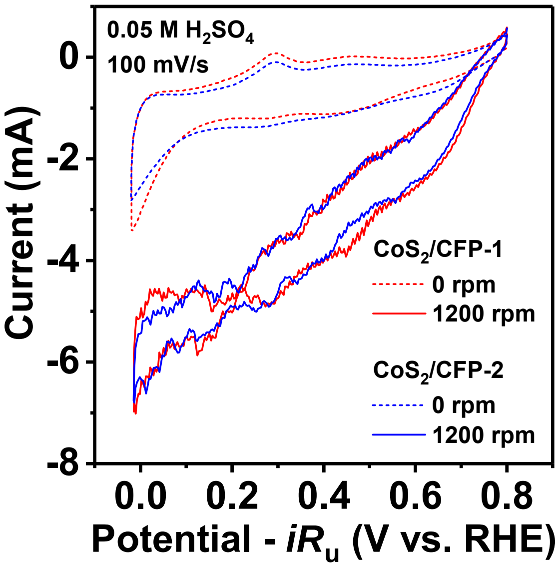

Figure A2.21. Cyclic voltammetry and chronoamperometry tests of two CoS_2/CFP working electrodes.

CV voltammograms (at 100 mV/s) of two CoS_2/CFP working electrodes (shown in Figure 2.6 in the Chapter 2) in O_2-saturated 0.05 M H_2SO_4 at 0 and 1200 rpm stir rates using the three-electrode H-cell setup.

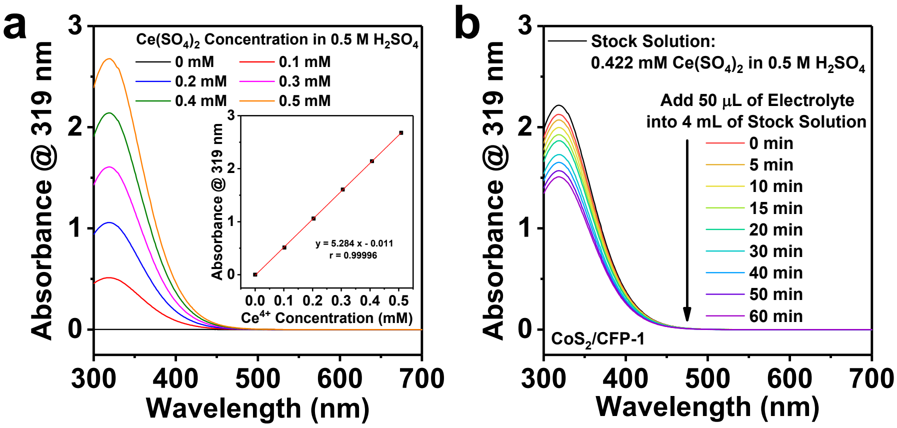

Figure A2.22. UV-Vis spectrophotometric detection of the produced H_2O_2.

(a) Absorbance spectra of standard $Ce(SO_4)_2$ solutions (up to 0.5 mM) in 0.5 M H_2SO_4, generating a linear calibration curve (shown as an inset) at the peak wavelength (319 nm). (b) Absorbance spectra of $Ce(SO_4)_2$ stock solution (0.422 mM, determined from calibration curve) in 0.5 M H_2SO_4 before and after injecting aliquot of electrolyte taken out of the working electrode compartment at specific time intervals during electrolysis.

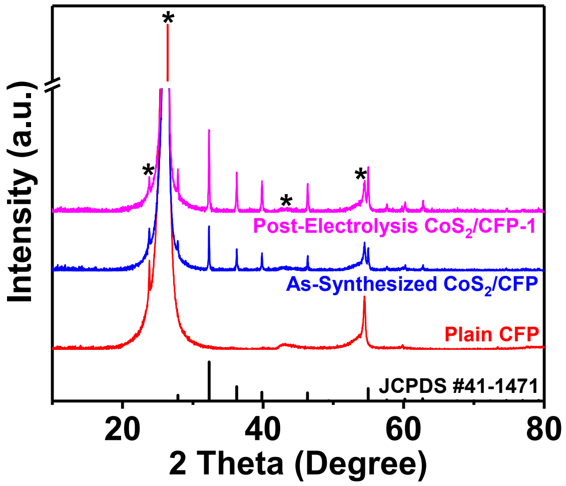

Figure A2.23. PXRD pattern of CoS_2/CFP before and after bulk ORR electrolysis.

PXRD pattern of the as-synthesized CoS_2/CFP and the post-electrolysis CoS_2/CFP-1 electrode (shown in Figure 2.6 in the Chapter 2) in comparison with the standard PXRD pattern of CoS_2 (JCPDS #41-1471). The peaks marked with asterisks come from carbon fiber paper.

Table A2.1. Preparation and electrochemically active surface area (ECSA) of drop-casted CoS_2 on RRDE.

Electrolyte	CoS_2 Mass	5 wt% Nafion Volume	Water Volume	Drop-Cast Volume	Cobalt Loading	Nafion Loading	Double-Layer Capacitance[a]
0.05 M H_2SO_4	5.2 mg	2340 µL	260 µL	10 µL	76 $\mu g/cm^2_{disk}$	191 $\mu g/cm^2_{disk}$	0.045 mF/cm^2_{disk}
	5.0 mg	1125 µL	125 µL	10 µL	152 $\mu g/cm^2_{disk}$	191 $\mu g/cm^2_{disk}$	0.068 mF/cm^2_{disk}
	5.2 mg	780 µL	87 µL	10 µL	229 $\mu g/cm^2_{disk}$	191 $\mu g/cm^2_{disk}$	0.101 mF/cm^2_{disk}
	5.1 mg	574 µL	64 µL	10 µL	305 $\mu g/cm^2_{disk}$	191 $\mu g/cm^2_{disk}$	0.271 mF/cm^2_{disk}
0.05 M Na_2SO_4	5.3 mg	2385 µL	265 µL	10 µL	76 $\mu g/cm^2_{disk}$	191 $\mu g/cm^2_{disk}$	0.047 mF/cm^2_{disk}
	5.0 mg	562 µL	63 µL	10 µL	305 $\mu g/cm^2_{disk}$	192 $\mu g/cm^2_{disk}$	0.314 mF/cm^2_{disk}

[a] Double-layer capacitances were determined at 0.7 V vs. RHE in 0.05 M H_2SO_4 and 0.75 V vs. RHE in 0.05 M Na_2SO_4, respectively, to avoid the interference of Faradaic currents (see Figure A2.12).

Table A2.2. Koutecky-Levich analysis of the hydrogen peroxide current density of drop-casted CoS_2.

Koutecky-Levich (K-L) analysis of the hydrogen peroxide current density (j_{peroxide}) of drop-casted CoS_2 (cobalt loading = 305 $\mu g/cm^2_{\text{disk}}$) in O_2-saturated 0.05 M H_2SO_4 (RRDE voltammograms shown in Figure 2.2a in the Chapter 2). The K-L analysis was performed around 0.46 V vs. RHE where the maximum j_{peroxide} was reached.

Catalyst	Potential (V vs. RHE)	Slope of j_{peroxide}^{-1} vs. $\omega^{-1/2}$ ($\text{mA}^{-1}\,\text{cm}^2_{\text{disk}}\,\text{rad}^{1/2}\,\text{s}^{-1/2}$)	$j_{\text{k peroxide}}$ ($\text{mA cm}^{-2}_{\text{disk}}$)	$j_{\text{L peroxide}}$ at 1600 rpm ($\text{mA cm}^{-2}_{\text{disk}}$)	r^2
CoS_2 (cobalt loading = 305 $\mu g/cm^2_{\text{disk}}$) (Figure 2.2a)	0.45	4.191	1.550	3.089	0.995
	0.46	4.232	1.567	3.059	0.989
	0.47	4.047	1.523	3.198	0.992

Equations:

$$j_{\text{disk}} = \frac{i_{\text{disk}}}{A_{\text{disk}}}$$

$$j_{\text{ring}} = \frac{i_{\text{ring}}}{A_{\text{disk}} \times N} = j_{\text{peroxide}}$$

$$\frac{1}{j_{\text{peroxide}}} = \frac{1}{j_{\text{k peroxide}}} + \frac{1}{j_{\text{L peroxide}}}$$

$$\frac{1}{j_{\text{peroxide}}} = \frac{1}{j_{\text{k peroxide}}} + B \times \omega^{-1/2}$$

$$j_{\text{L peroxide}} = \frac{1}{B} \times \omega^{1/2}$$

where j_{peroxide} is the hydrogen peroxide current density, $j_{\text{k peroxide}}$ is the kinetic current density for H_2O_2 production, $j_{\text{L peroxide}}$ is the diffusion-limited current density for H_2O_2 production, B is the slope of j_{peroxide}^{-1} vs. $\omega^{-1/2}$.

Explanations:

1. We confirmed that the Koutecky-Levich equation is applicable to the hydrogen peroxide current density given the good linearity of j_{peroxide}^{-1} vs. $\omega^{-1/2}$ (Figure A2.13).

2. We calculated $j_{\text{L peroxide}}$ at 1600 rpm ($j_{\text{L peroxide}} = \frac{1}{B} \times \omega^{1/2}$) and found it in good agreement with the theoretical limiting current density for $2e^-$ ORR (~3 $\text{mA/cm}^2_{\text{disk}}$ at 1600 rpm, see Table A2.2). Therefore, we used $j_{\text{L peroxide}} = 3$ $\text{mA/cm}^2_{\text{disk}}$ to correct for mass-transport loss.

3. We used the equation $j_{\text{k peroxide}} = \frac{j_{\text{peroxide}} \times j_{\text{L peroxide}}}{j_{\text{L peroxide}} - j_{\text{peroxide}}} = \frac{j_{\text{peroxide}} \times 3\ \text{mA/cm}^2_{\text{disk}}}{3\ \text{mA/cm}^2_{\text{disk}} - j_{\text{peroxide}}}$ to correct for mass-transport loss in the hydrogen peroxide current density of drop-casted CoS_2 (cobalt loading = 305 $\mu g/cm^2_{\text{disk}}$) in 0.05 M H_2SO_4 at the rotation rate of 1600 rpm (RRDE voltammograms shown in Figure 2.2a in the Chapter 2), yielding a plot of $j_{\text{k peroxide}}$ vs. potential (shown in Figure 2.4 in the Chapter 2).

Table A2.3. Summary of RRDE electrode information of CoS_2 and other reported ORR electrocatalysts for H_2O_2 production in acidic solution.

Classification	Catalyst	Electrolyte; Scan Rate; Rotation Rate; Ring Potential	Electrode Preparation	Geometric Area of GC Disk	Surface Area of Catalyst	Catalyst Loading	Reference
Earth-abundant transition metal compounds	CoS_2 nanomaterials	0.05 M H_2SO_4; 50 mV/s; 1600 rpm; 1.3 V vs. RHE	CoS_2 drop-casted on RRDE (GC disk-Pt-ring)	0.126 cm^2_{disk}	Not mentioned	305 ug Co/cm^2_{disk}	This work
Noble metal nanoparticles (NPs)	Pd-Au NPs (Au_3Pd)	0.1 M $HClO_4$; 50 mV/s; 900 rpm; 1.28 V vs. RHE	Pd-Au NPs drop-casted on RRDE (GC disk-Pt-ring)	0.196 cm^2_{disk}	surface area of Pd-Au NPs 1.93 cm^2	10 ug total metal/cm^2_{disk} (7.7 ug Au/cm^2_{disk}) (2.3 ug Pd/cm^2_{disk})	Ref. [4]
	Pt-Hg NPs/C (Pt core, $PtHg_4$ shell)	0.1 M $HClO_4$; 50 mV/s; 1600 rpm; 1.2 V vs. RHE	60 wt% Pt NPs/C drop-casted on RRDE (GC disk-Pt-ring); Hg electrodeposition into Pt NPs	0.196 cm^2_{disk}	surface area of Pt NPs 1.07 ± 0.06 cm^2	14 ug Pt/cm^2_{disk}	Ref. [5]
	Pd-Hg NPs/C (Pd core, Pd_2Hg_5 shell)	0.1 M $HClO_4$; 50 mV/s; 1600 rpm; 1.2 V vs. RHE	60 wt% Pd NPs/C drop-casted on RRDE (GC disk-Pt-ring); Hg electrodeposition into Pd NPs	0.196 cm^2_{disk}	surface area of Pd NPs 1.11 ± 0.04 cm^2	10 ug Pd/cm^2_{disk}	Ref. [6]
Noble metal polycrystalline extended surfaces (pc)	Pt-Hg (pc) ($PtHg_4$ surface)	0.1 M $HClO_4$; 50 mV/s; 1600 rpm; 1.2 V vs. RHE	Pt disk-Pt ring RRDE; Hg electrodeposition into Pt disk	0.196 cm^2_{disk}	surface area of Pt disk 0.196 cm^2	Not applicable	Ref. [5]
	Pd-Hg (pc) (Pd_2Hg_5 surface)	0.1 M $HClO_4$; 50 mV/s; 1600 rpm; 1.2 V vs. RHE	Pd disk-Pt ring RRDE; Hg electrodeposition into Pd disk	0.196 cm^2_{disk}	surface area of Pd disk 0.196 cm^2	Not applicable	Ref. [6]
	Ag (pc)	0.1 M $HClO_4$; 50 mV/s; 1600 rpm; 1.2 V vs. RHE	Ag disk-Pt ring RRDE	0.196 cm^2_{disk}	surface area of Ag disk 0.196 cm^2	Not applicable	Ref. [6]
	Ag-Hg (pc)	0.1 M $HClO_4$; 50 mV/s; 1600 rpm; 1.2 V vs. RHE	Ag disk-Pt ring RRDE; Hg electrodeposition into Ag disk	0.196 cm^2_{disk}	surface area of Ag disk 0.196 cm^2	Not applicable	Ref. [6]
	Cu-Hg (pc) (Cu_2Hg_5 surface)	0.1 M $HClO_4$; 50 mV/s; 1600 rpm; 1.2 V vs. RHE	Cu disk-Pt ring RRDE; Hg electrodeposition into Cu disk	0.196 cm^2_{disk}	surface area of Cu disk 0.196 cm^2	Not applicable	Ref. [6]
Carbon materials	Nitrogen-doped carbon (N/C)	0.1 M $HClO_4$; 5 mV/s; 1600 rpm; 1.2 V vs. RHE	N/C drop-casted on RRDE (GC disk-Pt ring)	0.196 cm^2_{disk}	Not mentioned	310 ug catalyst/cm^2_{disk}	Ref. [7]
Single-atom noble metal catalysts	5 wt% single-atom Pt on sulfur-doped carbon (Pt_1/SC)	0.1 M $HClO_4$; 10 mV/s; 900 rpm; 1.2 V vs. RHE	Pt_1/SC drop-casted on RRDE (GC disk-Pt ring)	0.126 cm^2_{disk}	Not mentioned	50 ug catalyst/cm^2_{disk} (2.5 ug Pt/cm^2_{disk})	Ref. [8]
	0.35 wt% single-atom Pt on TiN (Pt_1/TiN)	0.1 M $HClO_4$; 10 mV/s; 1600 rpm; 1.2 V vs. RHE	Pt_1/TiN and carbon black drop-casted on RRDE (GC disk-Pt ring)	Not mentioned	Not mentioned	15 ug catalyst (0.052 ug Pt)	Ref. [9]
	24.8 at% single-atom Pt on hollow CuS_x (h-Pt_1-CuS_x)	0.1 M $HClO_4$; Not mentioned; 1600 rpm; 1.1 V vs. RHE	h-Pt_1-CuS_x supported on carbon black (Pt loading ~15 wt%) drop-casted on RRDE (GC disk-Pt ring)	0.2475 cm^2_{disk}	Not mentioned	101 ug catalyst/cm^2_{disk} (15.2 ug Pt/cm^2_{disk})	Ref. [10]
Porphyrin-like structures	Heat-treated 0.3 wt% Co-porphyrin on carbon black (Co-N/C)	0.6 M H_2SO_4; 20 mV/s; 1600 rpm; ~1.3 V vs. RHE	Co-N/C drop-casted on RRDE (GC disk-Pt ring)	0.071 cm^2_{disk}	Not mentioned	1 mg catalyst/cm^2_{disk} (3 ug Co/cm^2_{disk})	Ref. [11]

Table A2.4. Koutecky-Levich analysis of drop-casted Pt/C and CoS_2.

Koutecky-Levich analysis of drop-casted Pt/C and CoS_2 (cobalt loading = 305 μg/cm$^2_{disk}$) in O_2-saturated 0.05 M H_2SO_4. RRDE voltammograms of Pt/C and CoS_2 (cobalt loading = 305 μg/cm$^2_{disk}$) were presented in Figure A2.5a and Figure 2.2a (in the Chapter 2), respectively.

Catalyst	Potential (V vs. RHE)	Slope of j_{disk}^{-1} vs. $\omega^{-1/2}$ (mA^{-1} cm$^2_{disk}$ rad$^{1/2}$ s$^{-1/2}$)	r^2
Pt/C (Figure A2.5a)	0.40	2.176	0.99997
	0.50	2.199	0.99987
	0.60	2.231	0.99994
CoS_2 (cobalt loading = 305 μg/cm$^2_{disk}$) (Figure 2.2a)	0	2.438	0.9988
	0.05	2.507	0.9992
	0.10	2.579	0.9995
	0.15	2.614	0.9994
	0.20	2.644	0.9996
	0.25	2.708	0.9994
	0.30	2.809	0.9988
	0.35	2.958	0.9979
	0.40	3.234	0.9983
	0.45	3.651	0.9985
	0.50	4.055	0.9989
	0.55	4.389	0.9993
	0.60	4.426	0.9984

Table A2.5. Comparisons of the bulk electrocatalytic H_2O_2 production performance of CoS_2/CFP with the benchmark Pt-Hg alloy catalyst.

Catalyst	Electrolyte	Electrolysis Potential	Electrolysis Time	Cumulative Charge	Cumulative H_2O_2 Yield	Cumulative H_2O_2 Concentration	Cumulative H_2O_2 Selectivity	Cumulative Faradaic Efficiency
CoS_2/CFP[a]	0.05 M H_2SO_4 (3 mL)	0.5 V vs. RHE	5 min	0.563 C	1.23 μmol	0.41 mM	59.3%	42.1%
			10 min	1.046 C	2.88 μmol	0.96 mM	69.4%	53.1%
			15 min	1.532 C	4.44 μmol	1.48 mM	71.7%	55.9%
			20 min	***2.021 C***	***5.72 μmol***	***1.91 mM***	***70.6%***	***54.6%***
			30 min	2.994 C	8.60 μmol	2.87 mM	71.3%	55.4%
			40 min	3.968 C	10.20 μmol	3.40 mM	66.3%	49.6%
			50 min	5.006 C	11.87 μmol	3.96 mM	62.8%	45.8%
			60 min	***6.125 C***	***13.08 μmol***	***4.36 mM***	***58.4%***	***41.2%***
Pt-Hg Alloy[b]	0.1 M $HClO_4$ (15 mL)	0.4 V vs. RHE	4.2 min	0.500 C	2.49 μmol	0.17 mM	98.0%	96.1%
			7.1 min	0.836 C	3.01 μmol	0.20 mM	82.1%	69.5%
			9.2 min	1.056 C	4.50 μmol	0.30 mM	90.3%	82.3%
			18.3 min	***2.034 C***	***7.00 μmol***	***0.47 mM***	***79.8%***	***66.4%***

[a] All numerical data for the electrocatalytic H_2O_2 production performance of CoS_2/CFP are based on the CoS_2/CFP-1 electrode (shown in Figure 2.6 in the Chapter 2).

[b] All numerical data for the electrocatalytic H_2O_2 production performance of the Pt-Hg alloy catalyst were estimated from the published figures (Figure A2.24 in ref. [5]).

References Cited in the Appendix 2

1. Faber, M. S.; Dziedzic, R.; Lukowski, M. A.; Kaiser, N. S.; Ding, Q.; Jin, S. High-Performance Electrocatalysis Using Metallic Cobalt Pyrite (CoS_2) Micro- and Nanostructures. *J. Am. Chem. Soc.* ***136***, 10053-10061 (2014).

2. Stevens, M. B.; Enman, L. J.; Batchellor, A. S.; Cosby, M. R.; Vise, A. E.; Trang, C. D. M.; Boettcher, S. W. Measurement Techniques for the Study of Thin Film Heterogeneous Water Oxidation Electrocatalysts. *Chem. Mater.* ***29***, 120-140 (2017).

3. Bouchaud, B.; Balmain, J.; Bonnet, G.; Pedraza, F. pH-distribution of cerium species in aqueous systems. *J. Rare Earth.* ***30***, 559-562 (2012).

4. Pizzutilo, E.; Kasian, O.; Choi, C. H.; Cherevko, S.; Hutchings, G. J.; Mayrhofer, K. J. J.; Freakley, S. J. Electrocatalytic synthesis of hydrogen peroxide on Au-Pd nanoparticles: From fundamentals to continuous production. *Chem. Phys. Lett.* ***683***, 436-442 (2017).

5. Siahrostami, S.; Verdaguer-Casadevall, A.; Karamad, M.; Deiana, D.; Malacrida, P.; Wickman, B.; Escudero-Escribano, M.; Paoli, E. A.; Frydendal, R.; Hansen, T. W.; Chorkendorff, I.; Stephens, I. E. L.; Rossmeisl, J. Enabling direct H_2O_2 production through rational electrocatalyst design. *Nat. Mater.* ***12***, 1137-1143 (2013).

6. Verdaguer-Casadevall, A.; Deiana, D.; Karamad, M.; Siahrostami, S.; Malacrida, P.; Hansen, T. W.; Rossmeisl, J.; Chorkendorff, I.; Stephens, I. E. L. Trends in the electrochemical synthesis of H2O2: Enhancing activity and selectivity by electrocatalytic site engineering. *Nano Lett.* ***14***, 1603-1608 (2014).

7. Hasché, F.; Oezaslan, M.; Strasser, P.; Fellinger, T.-P. Electrocatalytic hydrogen peroxide formation on mesoporous non-metal nitrogen-doped carbon catalyst. *J. Energy Chem.* ***25***, 251-257 (2016).

8. Choi, C. H.; Kim, M.; Kwon, H. C.; Cho, S. J.; Yun, S.; Kim, H.-T.; Mayrhofer, K. J. J.; Kim, H.; Choi, M. Tuning selectivity of electrochemical reactions by atomically dispersed platinum catalyst. *Nat. Commun.* ***7***, 10922 (2016).

9. Yang, S.; Kim, J.; Tak, Y. J.; Soon, A.; Lee, H. Single-atom catalyst of platinum supported on titanium nitride for selective electrochemical reactions. *Angew. Chem. Int. Ed.* ***55***, 2058-2062 (2016).

10. Shen, R.; Chen, W.; Peng, Q.; Lu, S.; Zheng, L.; Cao, X.; Wang, Y.; Zhu, W.; Zhang, J.; Zhuang, Z.; Chen, C.; Wang, D.; Li, Y. High-Concentration Single Atomic Pt Sites on Hollow CuS_x for Selective O_2 Reduction to H_2O_2 in Acid Solution. *Chem* (2019).

11. Yamanaka, I.; Ichihashi, R.; Iwasaki, T.; Nishimura, N.; Murayama, T.; Ueda, W.; Takenaka, S. Electrocatalysis of heat-treated cobalt-porphyrin/carbon for hydrogen peroxide formation. *Electrochim. Acta* ***108***, 321-329 (2013).

APPENDIX 3

Supplementary Information for CHAPTER 3: Stable and Selective Electrosynthesis of Hydrogen Peroxide and the Electro-Fenton Process on $CoSe_2$ Polymorph Catalysts[*]

---

[*] This appendix was originally made available online as the Electronic Supplementary Information for *Energy Environ. Sci.* ***13***, 4189-4203 (2020), in collaboration with Aurora N. Janes, R. Dominic Ross, Dave Kaiman, Jinzhen Huang, Bo Song, J. R. Schmidt, and Song Jin.

Supplementary Experimental Section

Detailed Methods for Materials Synthesis. To synthesize cobalt hydroxide carbonate hydrate (CHCH) precursor, 1.275 mmol of $CoCl_2·6H_2O$ (Sigma-Aldrich, 98.0%) and 3 mmol of urea (Riedel-de Haën, 99.5–100.5%) were dissolved in 75 mL of nanopure water and was heated at 120 °C for 5 h in a sealed 100-mL Teflon-lined stainless steel autoclave. The CHCH precursor was washed with water and ethanol and dried in vacuum at room temperature. The hydrothermal selenization of CHCH precursor was performed as follows: 4.29 g of NaOH (Sigma-Aldrich, ≥97.0%) and 571 mg of Se powder (Sigma-Aldrich, ≥99.5%) was mixed in 50 mL of nanopure water via sonication and was heated at 220 °C for 24 h in a sealed 80-mL autoclave; upon cooling to room temperature, 50 mg of CHCH precursor was suspended in 10 mL of nanopure water and added dropwise into the Se-containing solution under vigorous stirring, and then heated at 220 °C for another 24 h in the same autoclave. The as-converted $CoSe_2$ sample was washed with water and ethanol and dried in vacuum at room temperature. To control the polymorphism while removing the elemental Se impurity, an alumina boat containing 60 mg of as-converted $CoSe_2$ sample was placed in the center of a fused silica tube within a tube furnace (Thermo Scientific, TF55035A-1) and was annealed under a steady flow of Ar gas (99.999%) at 790 torr and 25 sccm. The *o*-$CoSe_2$ catalyst was obtained by annealing at 300 °C for 3 h, while the *c*-$CoSe_2$ catalyst was obtained by annealing at 500 °C for 1 h, both of which are polymorphic pure and free of elemental Se impurity. The *c*-CoS_2 catalyst was prepared via vapor-phase sulfidation: 50 mg of CHCH precursor was placed in an alumina boat at the center of the tube furnace, 2 g of sulfur (Sigma-Aldrich, 99.5–100.5%) was placed in another alumina boat at the farthest upstream position within the tube furnace, the sulfidation took place at 500 °C for 1 h. To synthesize CHCH nanowires on CFP substrate (CHCH/CFP), Teflon-coated carbon fiber paper (Fuel Cell Earth, TGP-H-060) was first treated with oxygen plasma at 150 W power for 5 min for each side and annealed in air at 700 °C for 5 min. A 3 cm × 6 cm piece of annealed CFP substrate was placed in the solution made of 2.1 mmol of $Co(NO_3)_2·6H_2O$ (Sigma-Aldrich, ≥98.0%), 4.2 mmol of NH_4F (Sigma-Aldrich, ≥98.0%), and 10.5 mmol of urea in 80 mL of nanopure water and was heated in a sealed 100-mL autoclave at 110 °C for 5 h. The CHCH/CFP was sonicated in nanopure water to remove loosely-bound CHCH particles and dried under N_2 gas flow. *o*-$CoSe_2$/CFP and *c*-CoS_2/CFP were prepared via the same selenization or sulfidation method mentioned above, except for replacing CHCH precursor with 1.5 cm × 6 cm pieces of CHCH/CFP. The as-converted *c*-CoS_2/CFP was immersed in CS_2 to remove any excess sulfur. All catalyst samples were stored in an Ar-filled glove box to minimize the exposure to air.

Detailed Sample Preparation for Materials Characterization. Scanning electron microscopy (SEM) samples were prepared by drop-casting catalysts in ethanol suspensions onto silicon wafers. Graphite substrates were used for X-ray photoelectron spectroscopy (XPS) experiments, which were made by cutting thin slices of graphite rod (Graphite Store, low wear EDM rod), abrading with 600 grit silicon carbide paper (Allied High Tech Products), and sonicating in nanopure water and ethanol until clean. The tested catalysts after rotating ring-disk electrode (RRDE) measurements were recovered from the disk electrode by sonicating in nanopure water and ultracentrifuging at 13.2K rpm for 1 min, followed by re-dispersing in minimal amount of nanopure water and drop-casting onto graphite substrates. XPS samples were used for Raman experiments without modification. X-ray absorption spectroscopy (XAS) samples were prepared by spreading a uniform layer of catalyst powders onto scotch tape, followed by folding into four layers to achieve a proper absorption length.

Supplementary Figures and Tables

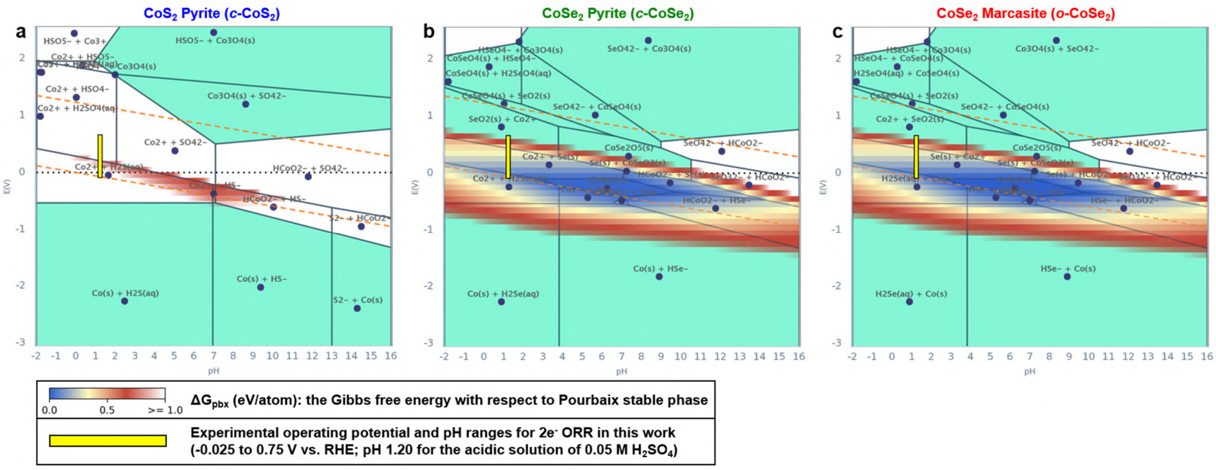

Figure A3.1. Calculated bulk Pourbaix diagrams of *c*-CoS_2, *c*-$CoSe_2$, and *o*-$CoSe_2$. Calculated bulk Pourbaix diagrams of (a) *c*-CoS_2, (b) *c*-$CoSe_2$, and (c) *o*-$CoSe_2$ assuming an ionic concentration of 10^{-6} mol/kg for each element of interest (59 ppb Co, 32 ppb S, and 79 ppb Se, which are reasonably low concentrations that can fairly reflect the acidic electrolyte solution of 0.05 M H_2SO_4 used in our experiments). These diagrams are adapted from the Materials Project.[1] The diagram of *c*-CoS_2 is in agreement with that in a previous report.[2] The multicolor gradient indicates the Gibbs free energy of the compound at a given set of potential and pH conditions with respect to its Pourbaix stable phase (ΔG_{pbx}), reflecting the electrochemical stability window of the compound. It was surmised in a previous report that materials with ΔG_{pbx} up to high values as much as 0.5 eV/atom can persist in electrochemical environments because of the energy barriers for the dissociation reactions.[3] The electrochemical stability windows of both *c*-$CoSe_2$ (Figure A3.1b) and *o*-$CoSe_2$ (Figure A3.1c) are clearly much wider than that of *c*-CoS_2 (Figure A3.1a) and, more importantly, cover the entire potential range of interest for 2e$^-$ ORR in acidic solution (indicated by the yellow color bars).

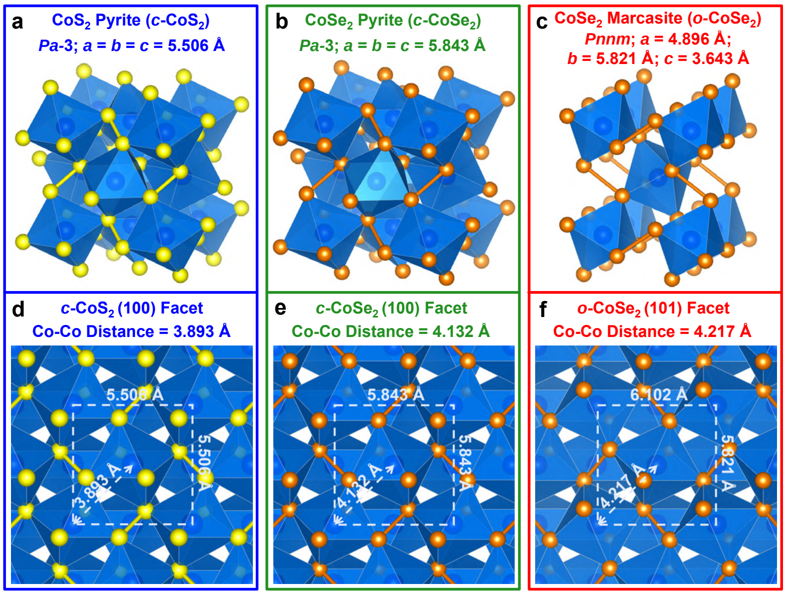

Figure A3.2. Crystal structures and Co-Co interatomic distances of c-CoS_2, c-$CoSe_2$, and o-$CoSe_2$.

Crystal structures, space groups, and lattice parameters of (a) c-CoS_2, (b) c-$CoSe_2$, and (c) o-$CoSe_2$. The Co, S, and Se atoms are displayed in blue, yellow, and orange, respectively. Top views and Co-Co interatomic distances of (d) c-CoS_2 (100), (e) c-$CoSe_2$ (100), and (f) o-$CoSe_2$ (101) surfaces. The o-$CoSe_2$ (101) surface mostly resembles the (100) surface of c-$CoSe_2$.

Table A3.1. Surface energies of the most thermodynamically stable facets.

(a) Cubic c-CoS_2 and c-$CoSe_2$, and (b) orthorhombic o-$CoSe_2$.

(a)

Facet	Surface Energy (eV/Å^2)	
	c-CoS_2 [a]	c-$CoSe_2$ [b]
(100)	0.032	0.044
(110)	0.060	0.064
(111)	0.057	0.069

(b)

Facet	Surface Energy (eV/Å^2)
	o-$CoSe_2$ [b]
(101)	0.044
(001)	0.060
(111)	0.060
(100)	0.070

[a] Data of c-CoS_2 are taken from ref. 4 and are calculated without a dispersion correction.

[b] Data of c-$CoSe_2$ and o-$CoSe_2$ are calculated with a dispersion correction using Grimme's D3(ABC) method.5

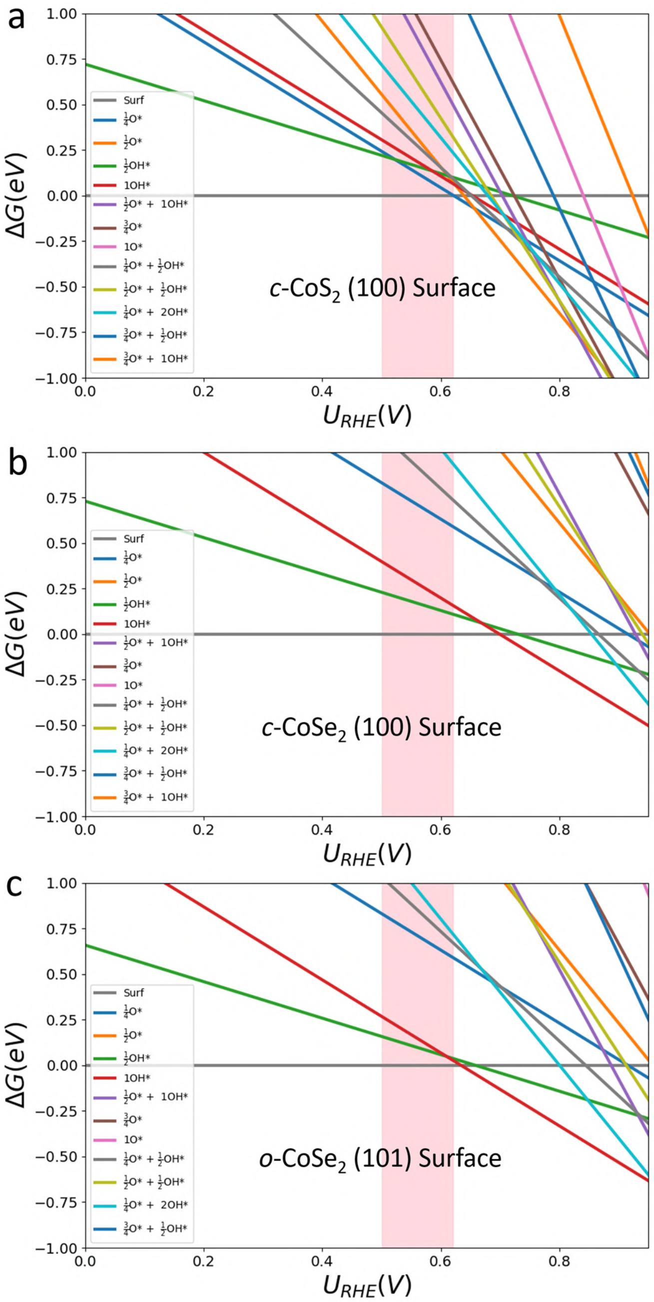

Figure A3.3. Surface Pourbaix diagrams showing all the modeled surface coverages. Surface Pourbaix diagrams (ΔG vs. U_{RHE}) of (a) *c*-CoS_2 (100), (b) *c*-$CoSe_2$ (100), and (c) *o*-$CoSe_2$ (101) surfaces showing all the modeled surface coverages (from clean surface to ¾ ML O* + 1 ML OH*). The highlight regions in light red represent the experimental relevant potential range where the optimal H_2O_2 production performances are achieved. In comparison, Figure 3.1 in the Chapter 3 shows only the most stable surface coverages in the potential range of 0 to 1 V.

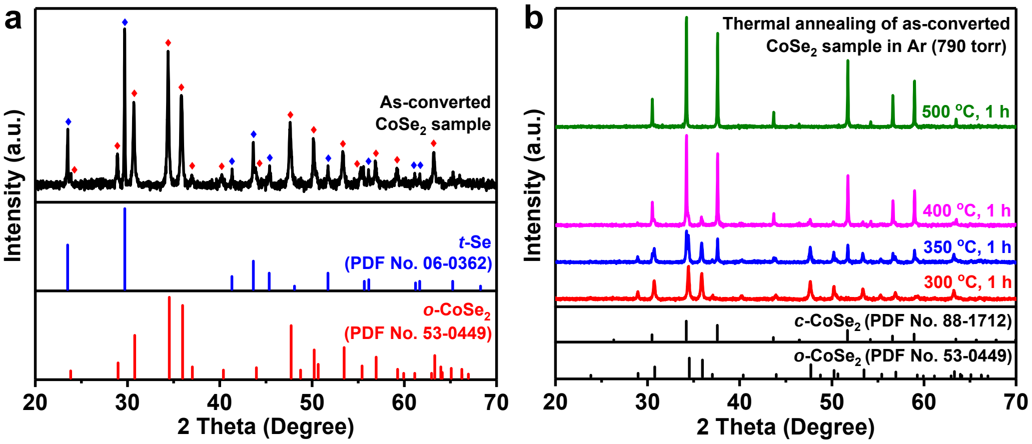

Figure A3.4. PXRD characterization of *c*-CoSe$_2$ and o-CoSe$_2$ samples.

(a) PXRD pattern of as-converted CoSe$_2$ sample, showing the coexistence of CoSe$_2$ marcasite with the orthorhombic phase (denoted as *o*-CoSe$_2$) and crystalline elemental Se impurity with the trigonal crystal structure (denoted as *t*-Se). (b) PXRD patterns of as-converted CoSe$_2$ sample annealed in Ar atmosphere (790 torr) at 300, 350, 400, and 500 °C for 1 h. Standard PXRD patterns of *o*-CoSe$_2$ (PDF No. 53-0449), *c*-CoSe$_2$ (PDF No. 88-1712), and *t*-Se (PDF No. 06-0362) are adapted from the International Centre for Diffraction Data (ICDD) database.

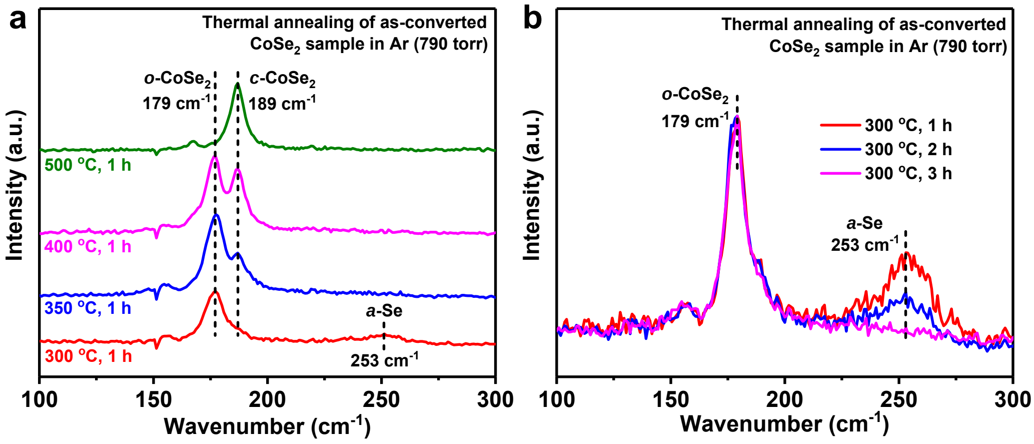

Figure A3.5. Raman characterization of *c*-CoSe$_2$ and o-CoSe$_2$ samples.

(a) Raman spectra of as-converted CoSe$_2$ sample annealed in Ar atmosphere (790 torr) at 300, 350, 400, and 500 °C for 1 h, confirming the polymorphic transformation from *o*-CoSe$_2$ to *c*-CoSe$_2$. The weak signal at 253 cm^{-1}, only present in the *o*-CoSe$_2$ sample annealed at 300 °C for 1 h, corresponds to the residual amorphous elemental Se impurity (denoted as *a*-Se) due to the relatively low annealing temperature and short annealing time. (b) Raman spectra of as-converted CoSe$_2$ sample annealed in Ar atmosphere (790 torr) at 300 °C for 1, 2, and 3 h, showing that the residual *a*-Se impurity in the *o*-CoSe$_2$ sample can be completely removed by extending the annealing time without affecting the marcasite structure.

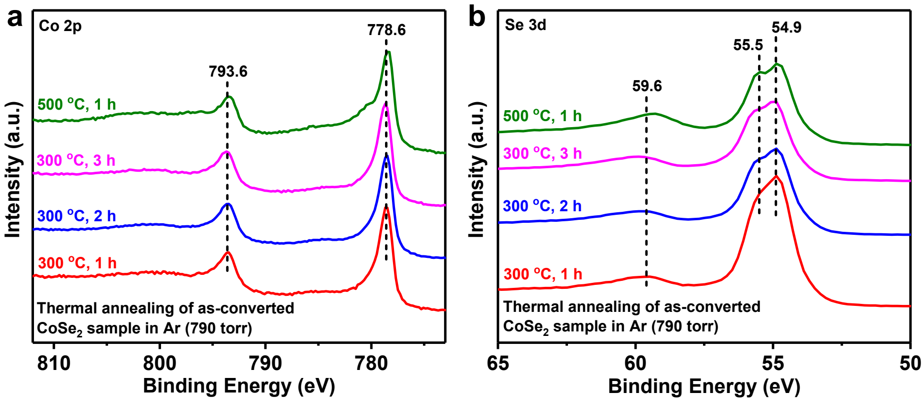

c

Annealing Condition	*Surface* Atomic Ratio of Co : Se
300 °C, 1 h	0.16
300 °C, 2 h	0.22
300 °C, 3 h	0.30
500 °C, 1 h	0.32

Figure A3.6. XPS characterization of *c*-CoSe$_2$ and o-CoSe$_2$ samples.

(a) Co 2p and (b) Se 3d XPS spectra of as-converted CoSe$_2$ sample annealed in Ar atmosphere (790 torr) under different conditions (at 300 °C for 1, 2, and 3 h; at 500 °C for 1 h). The Co 2p signals (778.6 and 793.6 eV) suggest the +2 oxidation state of Co, meanwhile the weak Se 3d signals (59.6 eV) indicate the presence of small amounts of surface SeO$_x$. (c) Surface atomic ratio of Co : Se in as-converted CoSe$_2$ sample annealed under different conditions. The *o*-CoSe$_2$ sample annealed at 300 °C for 3 h exhibit almost the same surface atomic ratio as the *c*-CoSe$_2$ sample annealed at 500 °C for 1 h, showing that the amorphous elemental Se impurity in the *o*-CoSe$_2$ sample can be completely removed by extending the annealing time.

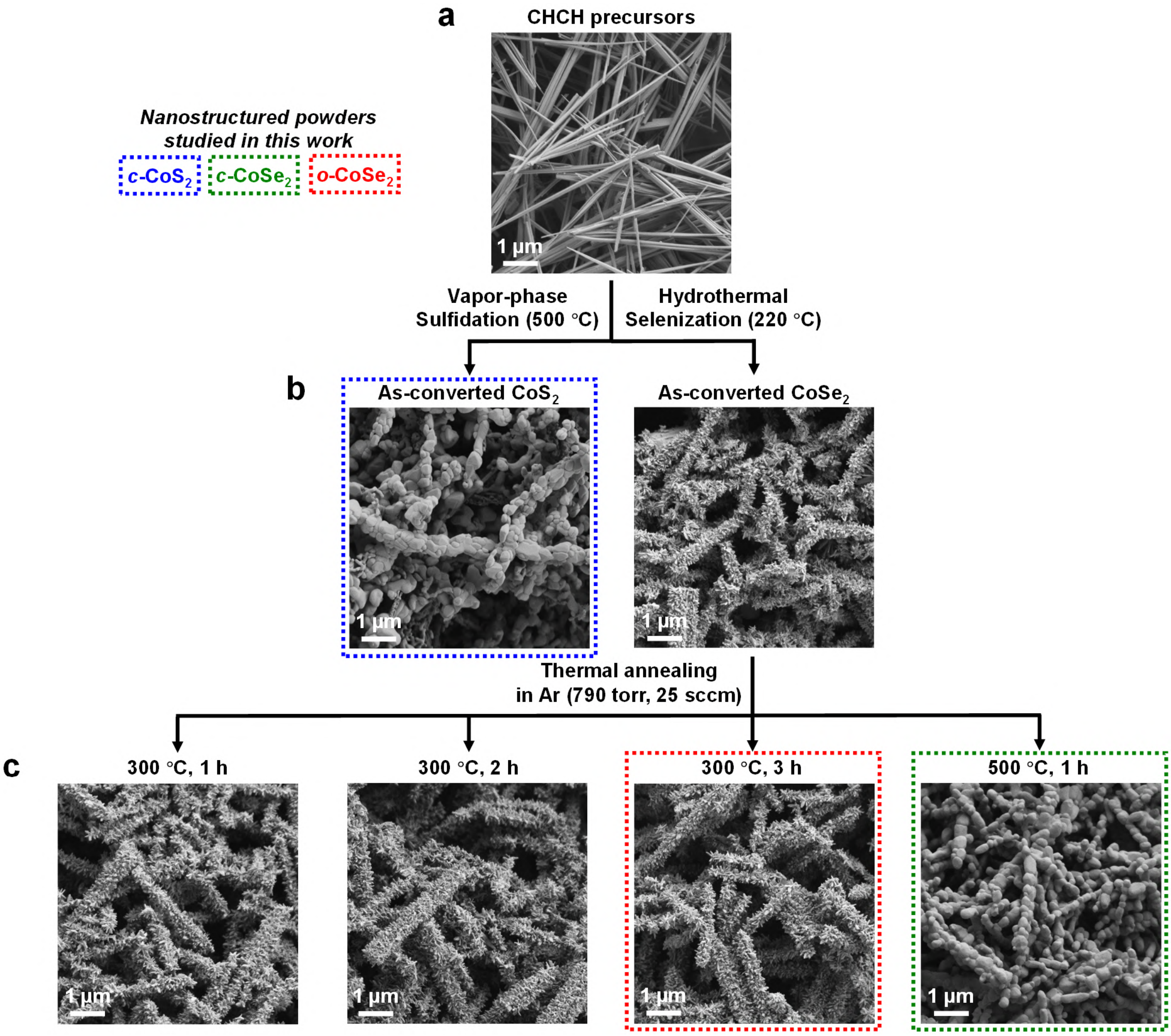

Figure A3.7. SEM characterization of *c*-$CoSe_2$ and o-$CoSe_2$ samples.

SEM images of (a) CHCH precursor, (b) as-converted CoS_2 and $CoSe_2$ samples, and (c) as-converted $CoSe_2$ samples annealed in Ar atmosphere (790 torr) under different conditions (at 300 °C for 1, 2, and 3 h; at 500 °C for 1 h). Dashed color boxes specify the catalyst samples studied in this work: "*c*-CoS_2 catalyst" refers to as-converted CoS_2 sample; "*c*-$CoSe_2$ catalyst" refers to the *c*-$CoSe_2$ sample annealed at 500 °C for 1 h; "*o*-$CoSe_2$ catalyst" refers to the *o*-$CoSe_2$ sample annealed at 300 °C for 3 h.

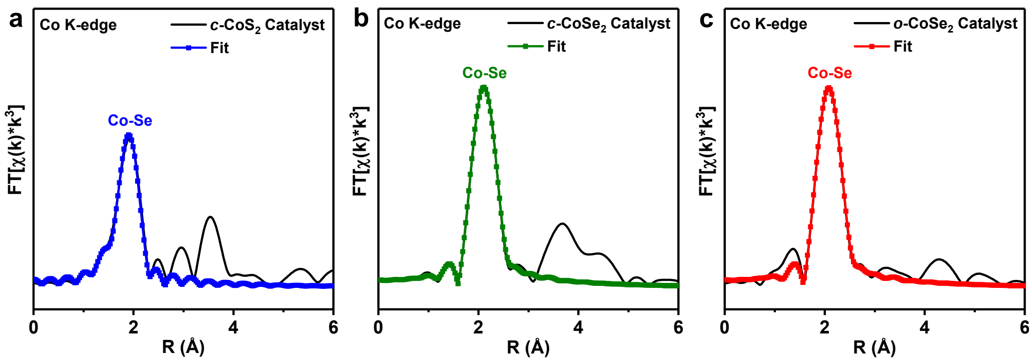

Figure A3.8. The first shell fittings of Co K-edge EXAFS spectra.

The first shell fittings of Co K-edge EXAFS spectra of (a) *c*-CoS_2, (b) *c*-$CoSe_2$, and (c) *o*-$CoSe_2$ catalysts. The Fourier transform parameters and fitting results are summarized in Table A3.2.

Table A3.2. The first shell fitting results of Co K-edge EXAFS spectra of *c*-CoS_2, *c*-$CoSe_2$, and *o*-$CoSe_2$ catalysts.

Sample	Shell	N [c]	R (Å) [c]	σ^2 (10^{-3} Å^2) [c]	ΔE_0 (eV) [c]	Reduced χ^2 [c]	R-factor [c]
c-CoS_2 catalyst [a]	Co-S	5.8 ± 1.0	2.322 ± 0.005	5.8 ± 0.6	4.1 ± 0.9	73.8604902	0.0038897
c-$CoSe_2$ catalyst [b]	Co-Se	5.9 ± 0.9	2.425 ± 0.002	5.6 ± 0.3	1.3 ± 0.6	19.2082886	0.0016189
o-$CoSe_2$ catalyst [b]	Co-Se	5.9 ± 1.1	2.404 ± 0.005	5.7 ± 0.6	0.6 ± 1.4	62.3247933	0.0082318

[a] For *c*-CoS_2 catalyst, the Fourier transform parameters are: Hanning window, $k_{min} = 3$, $k_{max} = 12$, dk = 1, no phase correction; the fitting parameters are: $r_{min} = 1$, $r_{max} = 2.3$, dr = 0, fitting k-weight = 3.

[b] For *c*-$CoSe_2$ and *o*-$CoSe_2$ catalysts, the Fourier transform parameters are: Hanning window, $k_{min} = 3$, $k_{max} = 12$, dk = 1, no phase correction; the fitting parameters are: $r_{min} = 1$, $r_{max} = 3$, dr = 0, fitting k-weight = 3.

[c] N is the coordination number of the absorbing Co atom. R is the interatomic distance between the absorbing Co atom and the backscattering S/Se atom. σ^2 is the mean square relative displacement (i.e., the Debye-Waller factor). ΔE_0 is the energy shift parameter used to align the theoretical calculated spectrum to the energy grid of the measured spectrum. For all the first shell fittings, the amplitude reduction factor (S_0^2) is constrained to 0.90 as a reasonable estimation, and the added uncertainty in the coordination number (N) due to the estimation of S_0^2 has already been considered.[6] Reduced χ^2 and R-factor are goodness-of-fit parameters.

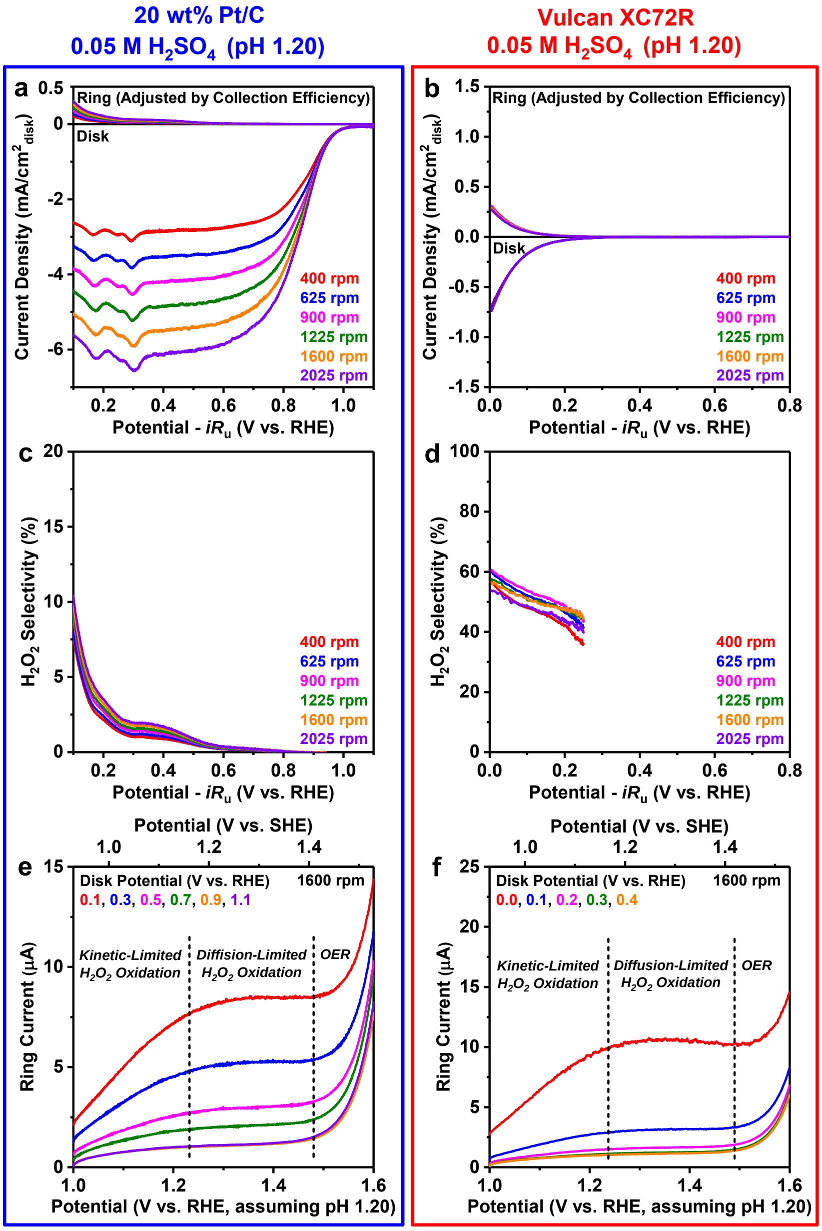

Figure A3.9. RRDE measurements of Pt/C and carbon black in acidic solution.

RRDE voltammograms recorded at various rotation rates and the corresponding H_2O_2 selectivity of commercial (a,c) Pt/C and (b,d) carbon black catalysts in O_2-saturated 0.05 M H_2SO_4 solution (pH 1.20). The ring potential is set at 1.3 V vs. RHE, assuming the local pH near the electrode is equal to the pH of the bulk solution. (e,f) Linear sweep voltammograms of the ring electrode from 1.0 to 1.6 V vs. RHE recorded at the time when the catalyst-coated disk electrode is held at various constant potentials (either ORR-active or -inactive) at 1600 rpm in O_2-saturated 0.05 M H_2SO_4 solution (pH 1.20). *See additional discussion on the next page.*

Additional Discussion of Figure A3.9. We reason that oxygen evolution reaction (OER) on the Pt ring electrode can serve as a probe reaction to monitor the local pH change, as the OER catalytic onset potential should not shift on the standard hydrogen electrode (SHE) scale if the local pH stays constant. We held the catalyst-coated disk electrode at various constant potentials (either ORR-active or -inactive), and performed linear sweep voltammetry (LSV) on the ring electrode to drive the kinetic- and diffusion-limited H_2O_2 oxidation (if any) and then OER as the ring potential was increased. As a result, the OER catalytic onset potential on the ring electrode remained the same whether or not ORR took place on these benchmark catalysts (Figure A3.9e,f), confirming that the local pH was unaffected during electrochemical operations.

Table A3.3. Preparation of drop-casted *c*-$CoSe_2$, *o*-$CoSe_2$, and *c*-CoS_2 catalysts with various catalyst loadings for RRDE measurements in O_2-saturated 0.05 M H_2SO_4 solution (pH 1.20).

Catalyst	Catalyst Mass (mg)	5 wt% Nafion Volume (μL)	Water Volume (μL)	Drop-casted Volume (μL)	Catalyst loading ($\mu g_{Co}/cm^2_{disk}$)	Nafion Loading ($\mu g/cm^2_{disk}$)
c-CoS_2 catalyst	2.5	125	1125	10	76	348
	2.6	65	585	10	152	348
	2.7	45	405	10	229	348
	4.0	50	450	10	305	348
c-$CoSe_2$ catalyst	4.7	134	1202	10	76	348
	4.8	68	614	10	152	348
	4.5	42	383	10	229	348
	4.5	32	288	10	305	348
o-$CoSe_2$ catalyst	4.6	523	4704	10	19	348
	4.1	233	2096	10	38	348
	4.1	116	1048	10	76	348
	4.3	61	549	10	152	348

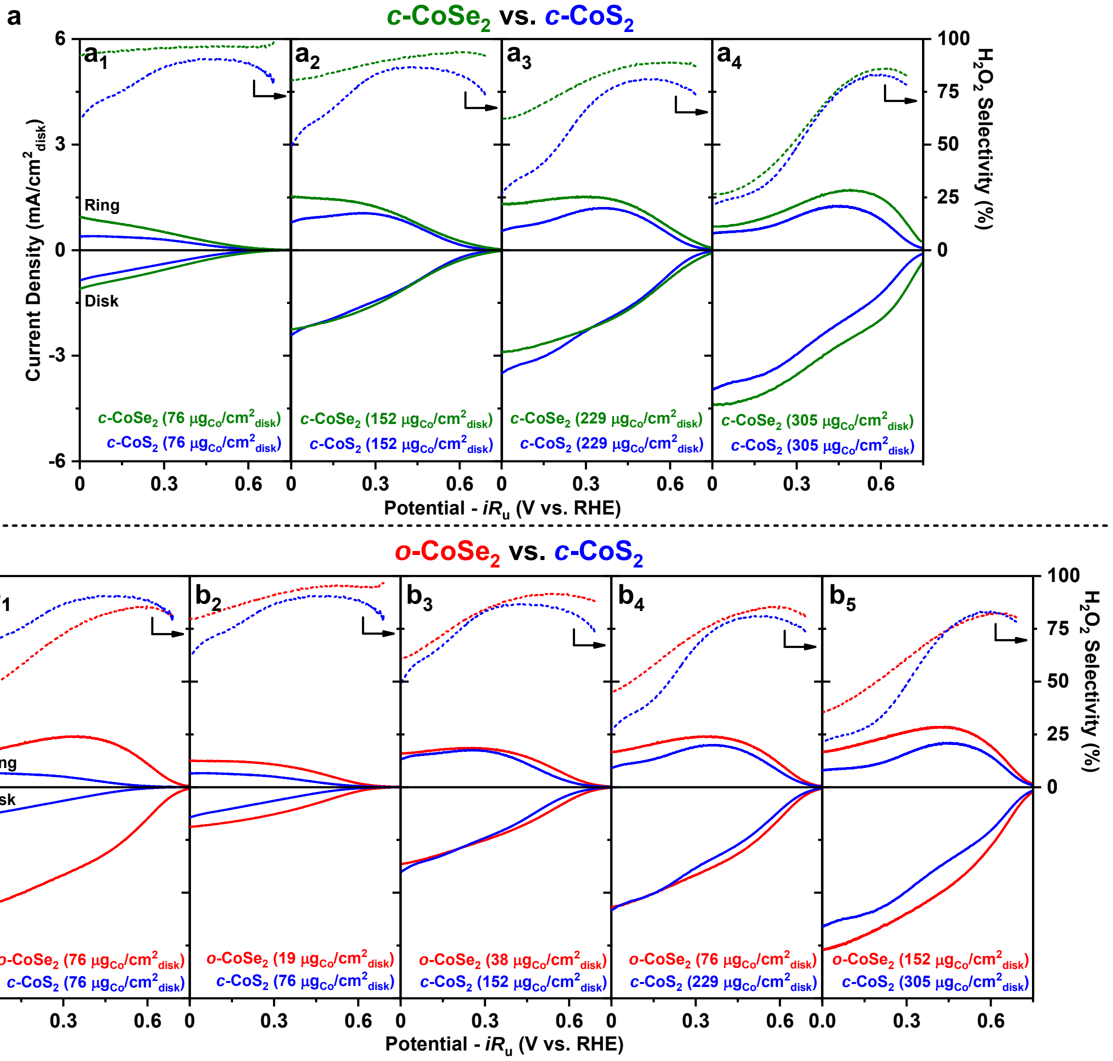

Figure A3.10. Comparisons of RRDE voltammograms and the H_2O_2 selectivity of *c*-$CoSe_2$ and *c*-$CoSe_2$ catalysts vs. *c*-CoS_2 catalyst.

(a) Comparisons of RRDE voltammograms recorded at 2025 rpm and the corresponding H_2O_2 selectivity of *c*-$CoSe_2$ and *c*-CoS_2 catalysts with the same catalyst loading (76, 152, 229, or 305 $\mu g_{Co}/cm^2_{disk}$) in O_2-saturated 0.05 M H_2SO_4 solution (pH 1.20). (b) Comparisons of RRDE voltammograms recorded at 2025 rpm and the corresponding H_2O_2 selectivity of *o*-$CoSe_2$ and *c*-CoS_2 catalysts (b_1) with the same catalyst loading (76 $\mu g_{Co}/cm^2_{disk}$) or (b_2–b_5) with different catalyst loadings that deliver similar overall ORR current densities (19, 38, 76, or 152 $\mu g_{Co}/cm^2_{disk}$ for *o*-$CoSe_2$; 76, 152, 229, or 305 $\mu g_{Co}/cm^2_{disk}$ for *c*-CoS_2) in O_2-saturated 0.05 M H_2SO_4 solution (pH 1.20).

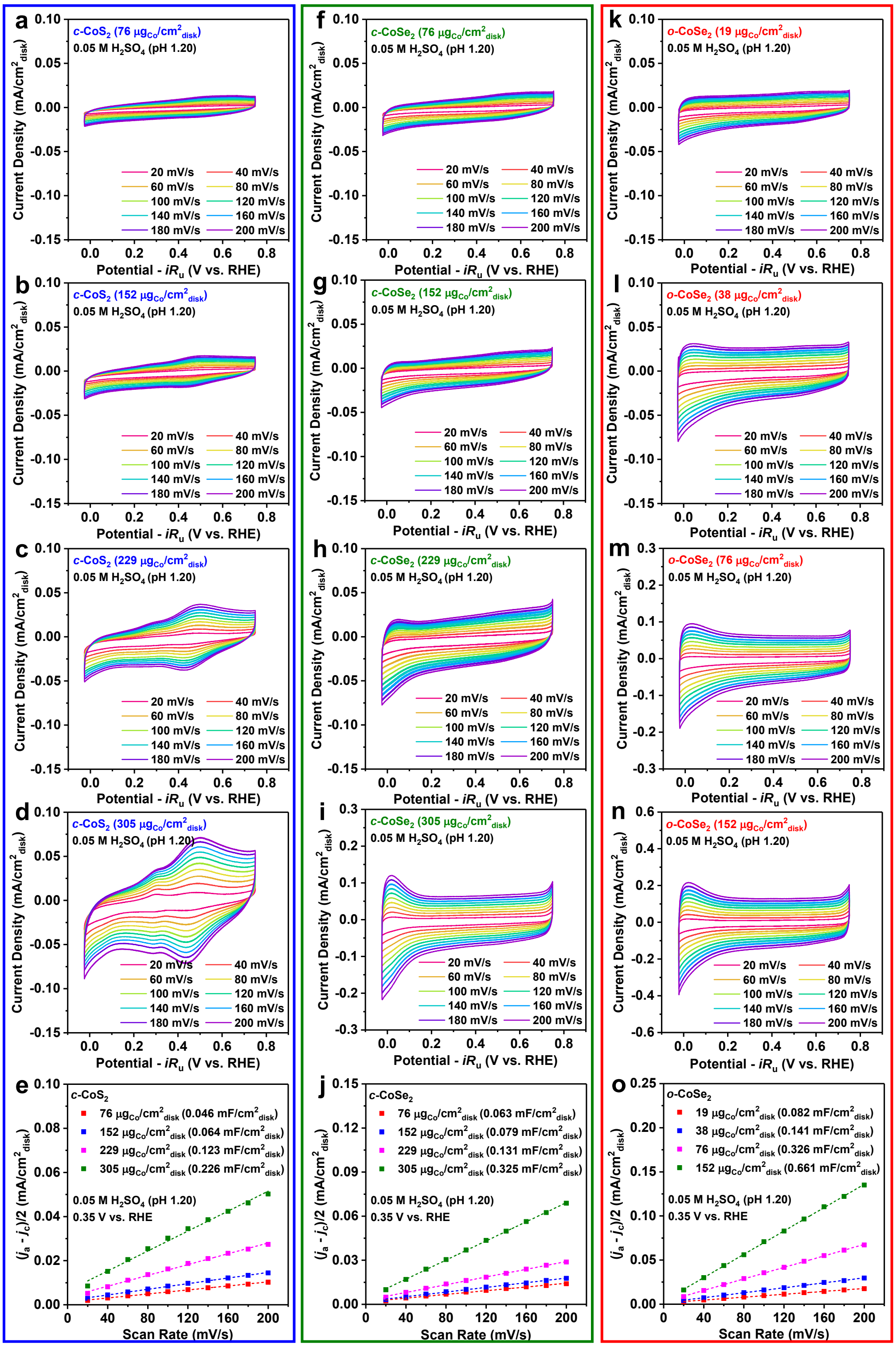

Figure A3.11. C_{dl} measurements of *c*-CoS_2, *c*-$CoSe_2$, and *o*-$CoSe_2$ catalysts.

C_{dl} measurements of (a–e) *c*-CoS_2, (f–j) *c*-$CoSe_2$, and (k–o) *o*-$CoSe_2$ catalysts with various catalyst loadings in the Ar-saturated 0.05 M H_2SO_4 solution (pH 1.20). *c*-CoS_2 displays redox features centered around 0.45 V vs. RHE, whereas both *c*-$CoSe_2$ and *o*-$CoSe_2$ polymorphs are free of redox features over a wide potential window. Therefore, to minimize the interference from the redox features of *c*-CoS_2, we chose the fixed potential of 0.35 V vs. RHE to extract the C_{dl} values of all three catalysts from linear fittings, which are summarized in Table A3.4.

Table A3.4. Summary of the C_{dl} values of *c*-CoS_2, *c*-$CoSe_2$, and *o*-$CoSe_2$ catalysts.

Summary of the C_{dl} values (extracted from linear fittings at 0.35 V vs. RHE) of *c*-CoS_2, *c*-$CoSe_2$, and *o*-$CoSe_2$ catalysts with various catalyst loadings in the Ar-saturated 0.05 M H_2SO_4 solution (pH 1.20).

Catalyst	Catalyst loading ($\mu g_{Co}/cm^2_{disk}$)	C_{dl} at 0.35 V vs. RHE (mF/cm^2_{disk})
c-CoS_2 catalyst	76	0.046
	152	0.064
	229	0.123
	305	0.226
c-$CoSe_2$ catalyst	76	0.063
	152	0.079
	229	0.131
	305	0.325
o-$CoSe_2$ catalyst	19	0.082
	38	0.141
	76	0.326
	152	0.661

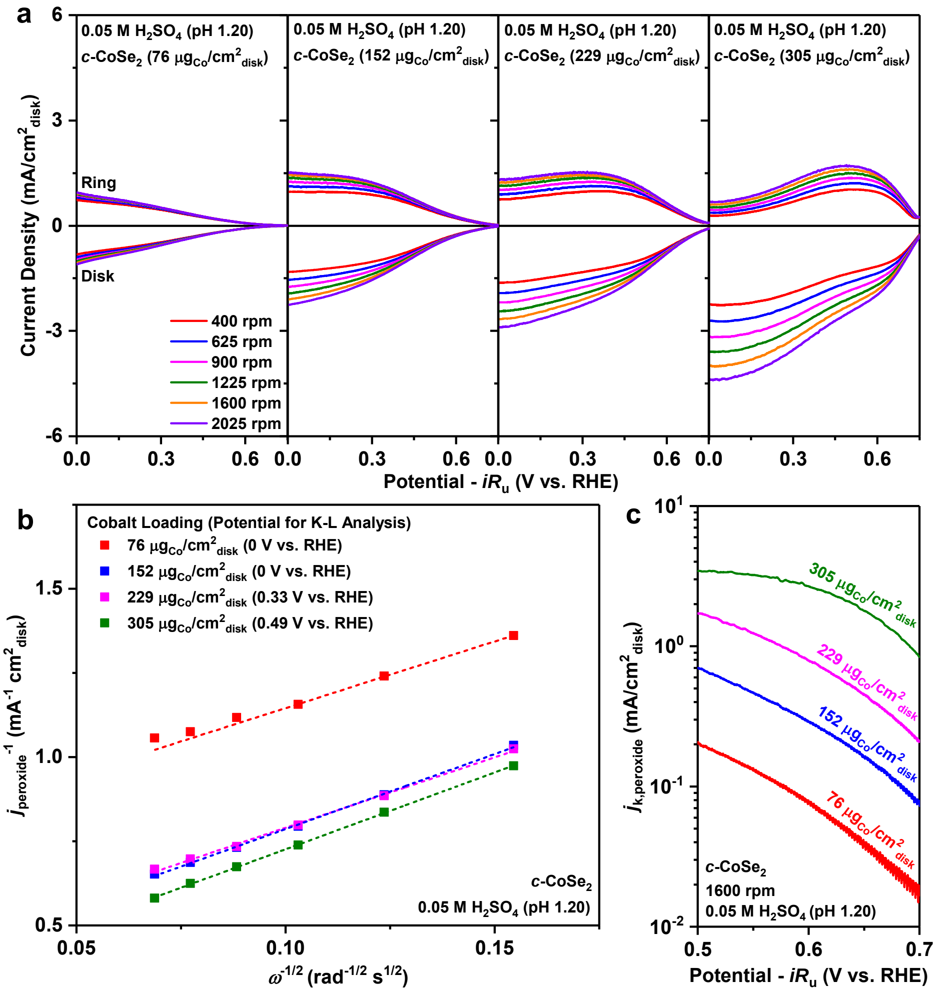

Figure A3.12. Koutecky-Levich analysis of *c*-CoSe$_2$ catalyst.

(a) RRDE voltammograms of *c*-CoSe$_2$ catalyst with various catalyst loadings in O$_2$-saturated 0.05 M H$_2$SO$_4$ solution (pH 1.20) recorded at various rotation rates. (b) K-L analysis (j_{peroxide}^{-1} vs. $\omega^{-1/2}$) based on RRDE measurements. (c) Kinetic current density for H$_2$O$_2$ production normalized to the geometric area of the disk electrode ($j_{\text{k,peroxide}}$) at 1600 rpm.

Table A3.5. Koutecky-Levich analysis of *c*-$CoSe_2$ catalyst.

K-L analysis (j_{peroxide}^{-1} vs. $\omega^{-1/2}$) based on RRDE voltammograms of *c*-$CoSe_2$ catalyst with various catalyst loadings in O_2-saturated 0.05 M H_2SO_4 solution (pH 1.20) recorded at various rotation rates.

Catalyst loading ($\mu g_{Co}/cm^2_{\text{disk}}$)	Potential for K-L Analysis (V vs. RHE) [a]	Slope of j_{peroxide}^{-1} vs. $\omega^{-1/2}$ (mA^{-1} cm^2_{disk} $rad^{1/2}$ $s^{-1/2}$) [b]	$j_{\text{L,peroxide}}$ at 1600 rpm (mA/cm^2_{disk}) [c]
76	0	3.97	3.26
152	0	4.46	2.90
229	0.32	4.19	3.09
305	0.49	4.57	2.83

[a] For each catalyst loading, K-L analysis was performed at the potential where the approximate maximum of j_{peroxide} was achieved.

[b] $j_{\text{peroxide}}^{-1} = j_{\text{k,peroxide}}^{-1} + j_{\text{L,peroxide}}^{-1} = j_{\text{k,peroxide}}^{-1} + B \times \omega^{-1/2}$, where j_{peroxide} is the partial current density for H_2O_2 production (mA/cm^2_{disk}), $j_{\text{k,peroxide}}$ is the kinetic current density for H_2O_2 production (mA/cm^2_{disk}), $j_{\text{k,peroxide}}$ is the diffusion-limited current density for H_2O_2 production (mA/cm^2_{disk}), B is the slope (mA^{-1} cm^2_{disk} $rad^{1/2}$ $s^{-1/2}$) of the linear fit of j_{peroxide}^{-1} vs. $\omega^{-1/2}$ (see Figure A3.12b).

[c] $j_{\text{L,peroxide}}$ at 1600 rpm $= B^{-1} \times \omega^{1/2} = B^{-1}$ ($mA\ cm^{-2}_{\text{disk}}$ $rad^{-1/2}$ $s^{1/2}$) $\times$ $(1600 \times \pi / 30)^{1/2}$. The calculated $j_{\text{L,peroxide}}$ at 1600 rpm were in good agreement with the theoretical limiting current density for $2e^-$ ORR (~3 mA/cm^2_{disk} at 1600 rpm under O_2 saturation). Therefore, we used $j_{\text{L,peroxide}}$ = 3 mA/cm^2_{disk} in the equation $j_{\text{k,peroxide}} = \frac{j_{\text{peroxide}} \times j_{\text{L,peroxide}}}{j_{\text{L,peroxide}} - j_{\text{peroxide}}} = \frac{j_{\text{peroxide}} \times 3\ mA/cm^2_{\text{disk}}}{3\ mA/cm^2_{\text{disk}} - j_{\text{peroxide}}}$ to correct for mass-transport loss in j_{peroxide}.

Table A3.6. Summary of RRDE electrode information of *c*-$CoSe_2$ and *o*-$CoSe_2$ catalysts compared with *c*-CoS_2 and other reported $2e^-$ ORR electrocatalysts in *acidic* solution.

Classification	Catalyst	*Acidic* Electrolyte	Catalyst Loading	Reference
Earth-abundant transition metal compounds	*c*-$CoSe_2$	0.05 M H_2SO_4	305 $\mu g_{Co}/cm^2_{disk}$	this work
	o-$CoSe_2$	0.05 M H_2SO_4	152 $\mu g_{Co}/cm^2_{disk}$	this work
	c-CoS_2	0.05 M H_2SO_4	305 $\mu g_{Co}/cm^2_{disk}$	this work
Noble metal nanoparticles (NPs)	Pt-Hg NPs/C	0.1 M $HClO_4$	14 $\mu g_{Pt}/cm^2_{disk}$	ref. [7]
	Pd-Hg NPs/C	0.1 M $HClO_4$	10 $\mu g_{Pd}/cm^2_{disk}$	ref. [8]
	Pd-Au NPs	0.1 M $HClO_4$	10 $\mu g_{metal}/cm^2_{disk}$	ref. [9]
Noble metal polycrystalline surfaces (pc)	Pt-Hg (pc)	0.1 M $HClO_4$	N/A	ref. [7]
	Pd-Hg (pc)	0.1 M $HClO_4$	N/A	ref. [8]
	Ag (pc)	0.1 M $HClO_4$	N/A	ref. [8]
	Ag-Hg (pc)	0.1 M $HClO_4$	N/A	ref. [8]
	Cu-Hg (pc)	0.1 M $HClO_4$	N/A	ref. [8]
Noble metal single-atom catalysts	Pt_1/SC	0.1 M $HClO_4$	50 $\mu g_{catalyst}/cm^2_{disk}$ (5.0 wt% Pt)	ref. [10]
	Pt_1/TiN	0.1 M $HClO_4$	15 $\mu g_{catalyst}$ (0.35 wt% Pt)	ref. [11]
	h-Pt_1-CuS_x	0.1 M $HClO_4$	101 $\mu g_{catalyst}/cm^2_{disk}$ (24.8 at% Pt)	ref. [12]
Transition metal single-atom catalysts	Co_1-N-C(1)	0.5 M H_2SO_4	100 $\mu g_{catalyst}/cm^2_{disk}$ (0.4 at% Co)	ref. [13]
	Co_1-N-C(2)	0.1 M $HClO_4$	25 $\mu g_{catalyst}/cm^2_{disk}$ (1.4 wt% Co)	ref. [14]
	Co_1-NG(O)	0.1 M $HClO_4$	10 $\mu g_{catalyst}/cm^2_{disk}$ (1.4 wt% Co)	ref. [15]
	Mo_1-OSG-H	0.05 M H_2SO_4	101 $\mu g_{catalyst}/cm^2_{disk}$ (13.47 wt% Mo)	ref. [16]
Carbon materials	O-CNTs	0.1 M $HClO_4$	101 $\mu g_{catalyst}/cm^2_{disk}$	ref. [17]
	meso-BMP	0.1 M $HClO_4$	306 $\mu g_{catalyst}/cm^2_{disk}$	ref. [18]
	NCMK	0.5 M H_2SO_4	50 $\mu g_{catalyst}/cm^2_{disk}$	ref. [19]

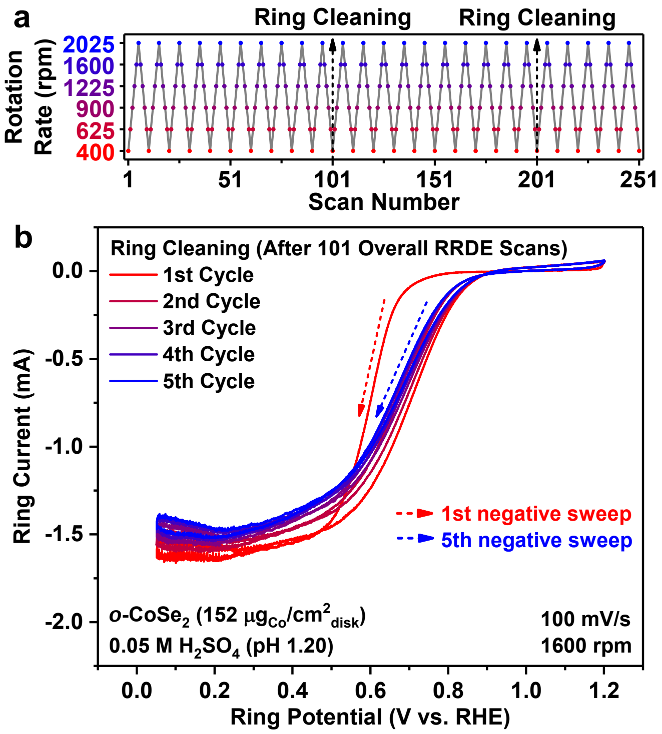

Figure A3.13. Rotation rate profile and ring cleaning protocol for catalyst stability tests from RRDE measurements.

(a) Rotation rate profile of catalyst stability tests from RRDE measurements in O_2-saturated 0.05 M H_2SO_4 solution (pH 1.20). (b) Electrochemical cleaning of the Pt ring electrode by running cyclic voltammetry at low overpotentials until observing typical ORR polarization curves for fresh Pt. The example shown here was performed during catalyst stability test of *o*-$CoSe_2$ (152 $\mu g_{Co}/cm^2_{disk}$) after 101 overall RRDE scans. In the first negative sweep, the ORR catalytic onset on the Pt ring electrode took place at a high overpotential. Starting the second negative sweep, the surface PtO_x was reduced and the ORR catalytic activity of the Pt ring electrode was recovered.

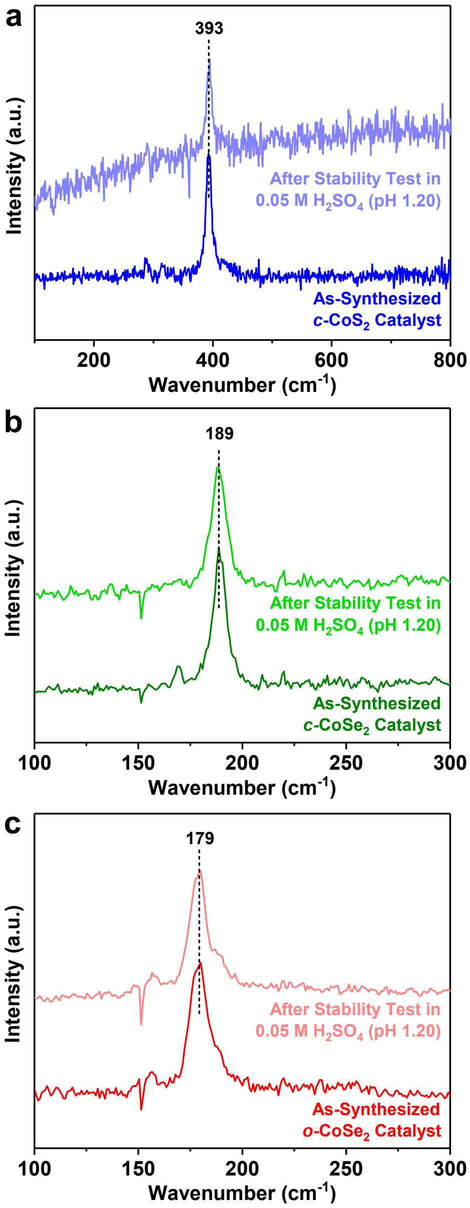

Figure A3.14. Raman characterization of *c*-CoS_2, *c*-$CoSe_2$, and *o*-$CoSe_2$ catalysts before and after catalyst stability tests from RRDE measurements.

Raman spectra of (a) *c*-CoS_2, (b) *c*-$CoSe_2$, and (c) *o*-$CoSe_2$ catalysts before and after catalyst stability tests from RRDE measurements in 0.05 M H_2SO_4 solution (pH 1.20). Background Raman spectra of bare graphite disk substrate were subtracted from as-measured Raman spectra of *c*-CoS_2, *c*-$CoSe_2$, and *o*-$CoSe_2$ catalysts.

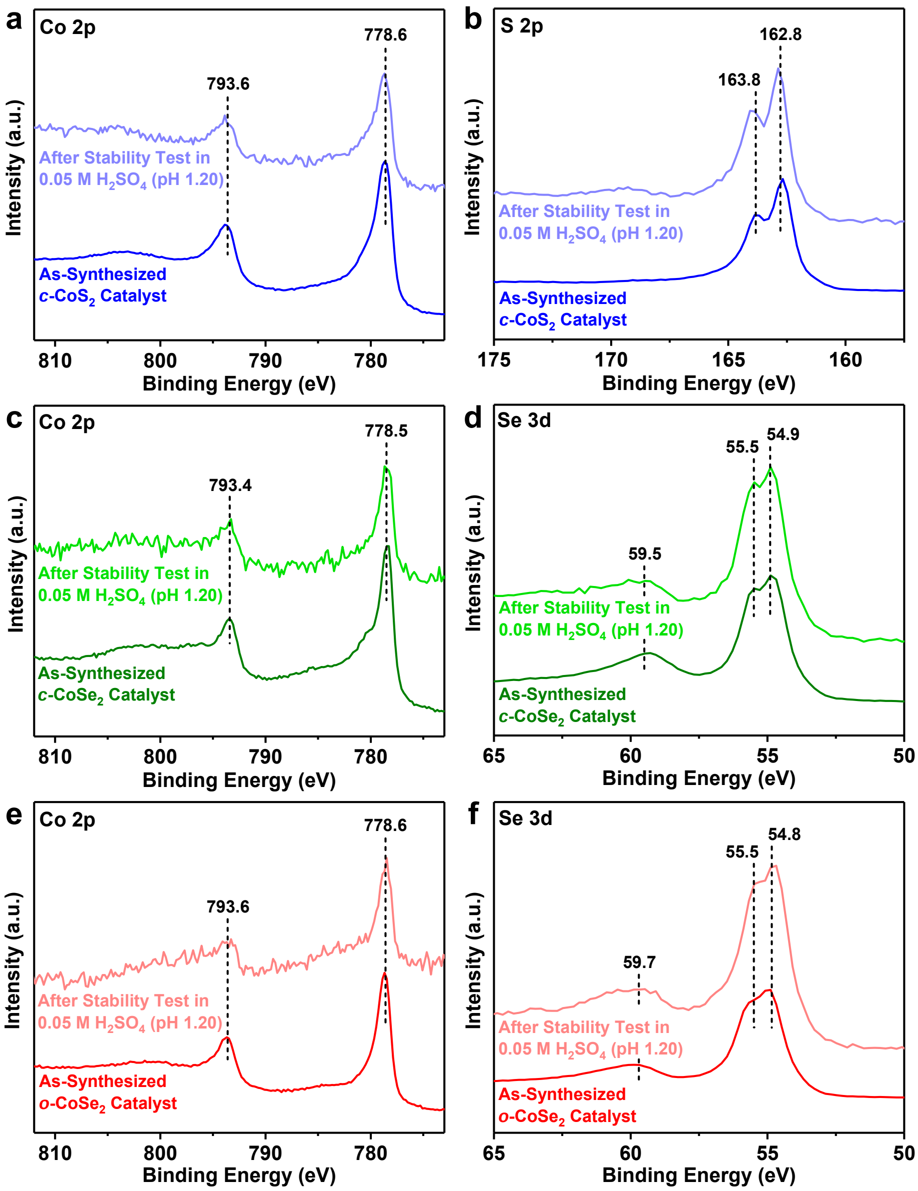

Figure A3.15. XPS characterization of *c*-CoS_2, *c*-$CoSe_2$, and *o*-$CoSe_2$ catalysts before and after catalyst stability tests from RRDE measurements.

XPS spectra of (a,b) *c*-CoS_2, (c,d) *c*-$CoSe_2$, and (e,f) *o*-$CoSe_2$ catalysts before and after catalyst stability tests from RRDE measurements in 0.05 M H_2SO_4 solution (pH 1.20). The strong Co 2p signals of all three catalysts (~778.6 and ~793.6 eV, see Figure A3.15a,c,e) suggest the +2 oxidation state of Co. The strong S 2p signals of *c*-CoS_2 catalyst (162.8 and 163.8 eV, see Figure A3.15b) correspond to the S_2^{2-} anions. The strong Se 3d signals of both $CoSe_2$ polymorphs (~54.9 and ~55.5 eV, see Figure A3.15d,f) correspond to the Se_2^{2-} anions, whereas the weak Se 3d signals (~59.6 eV) indicate the presence of small amounts of surface SeO_x.

Table A3.7. Surface compositions of *c*-CoS_2, *c*-$CoSe_2$, and *o*-$CoSe_2$ catalysts before and after catalyst stability tests from RRDE measurements.

Surface atomic ratios of Co : S/Se in *c*-CoS_2, *c*-$CoSe_2$, and *o*-$CoSe_2$ catalysts before and after catalyst stability tests from RRDE measurements (see XPS spectra in Figure A3.15) and those of Co : Se in the *o*-$CoSe_2$/CFP electrode #3 before and after the bulk electrolysis at 0.5 V vs. RHE in 0.05 M H_2SO_4 for 5 h (see XPS spectra in Figure A3.23).

Sample	Surface Atomic Ratio of Co : S/Se	
	Before	After
c-CoS_2	0.378 ± 0.004 [a]	0.25 ± 0.03 [b]
c-$CoSe_2$	0.325 ± 0.001 [a]	0.25 ± 0.03 [b]
o-$CoSe_2$	0.29 ± 0.02 [a]	0.26 ± 0.04 [b]
o-$CoSe_2$/CFP #3	0.32 [c]	0.26 [c]

[a] The averages and standard deviations for the as-synthesized catalysts come from two samples made from two replicate synthesis. See representative XPS spectra in Figure A3.15.

[b] The averages and standard deviations for the used catalysts come from four samples recovered from four replicate RRDE measurements. See representative XPS spectra in Figure A3.15.

[c] See XPS spectra in Figure A3.23.

Table A3.8. ICP-MS analysis of the tested electrolyte solutions after catalyst stability tests. ICP-MS analysis of the tested electrolyte solutions after catalyst stability tests of *c*-CoS_2 (305 µg$_{Co}$/cm$^2_{disk}$), *c*-$CoSe_2$ (305 µg$_{Co}$/cm$^2_{disk}$), and *o*-$CoSe_2$ (152 µg$_{Co}$/cm$^2_{disk}$) from RRDE measurements in 0.05 M H_2SO_4 solution.

ICP-MS Sample		Intensity	Standard Curve	[Co]	Average Cobalt Leaching Rate
Standard solution of $CoSO_4$ in 0.05 M H_2SO_4	[Co] = 0 ug$_{Co}$/L	0.7	y = 42.9 x + 3.4 (r^2 = 0.99995)	-	-
	[Co] = 5.0 ug$_{Co}$/L	214.2		-	-
	[Co] = 20.0 ug$_{Co}$/L	872.3		-	-
	[Co] = 50.0 ug$_{Co}$/L	2146.6		-	-
Tested electrolyte solution of 0.05 M H_2SO_4 (45 mL)	*c*-CoS_2 (305 µg$_{Co}$/cm$^2_{disk}$) [a] 2.5 h (151 RRDE scans)	1576.0	-	36.6 ug$_{Co}$/L	0.66 ug$_{Co}$/h
	c-$CoSe_2$ (305 µg$_{Co}$/cm$^2_{disk}$) [a] 2.5 h (151 RRDE scans)	941.6	-	21.8 ug$_{Co}$/L	0.39 ug$_{Co}$/h
	o-$CoSe_2$ (152 µg$_{Co}$/cm$^2_{disk}$) [a] 4.2 h (251 RRDE scans)	1228.7	-	28.5 ug$_{Co}$/L	0.31 ug$_{Co}$/h

[a] Geometric area of the disk electrode is 0.126 cm$^2_{disk}$.

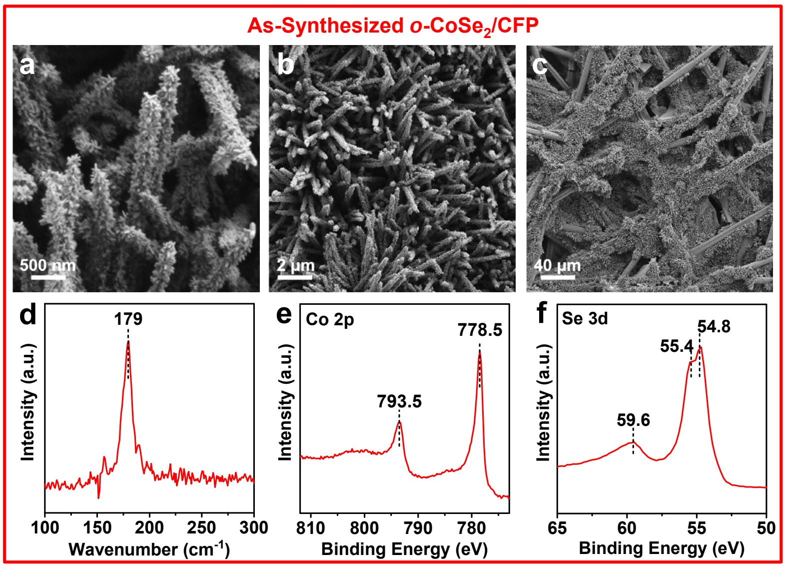

Figure A3.16. Materials characterization of *o*-$CoSe_2$/CFP.

(a–c) SEM images at different magnifications, (d) Raman spectra, (e) Co 2p and (f) Se 3d XPS spectra of as-synthesized *o*-$CoSe_2$/CFP. Background Raman spectra of bare carbon fiber paper substrate were subtracted from as-measured Raman spectra of *o*-$CoSe_2$/CFP.

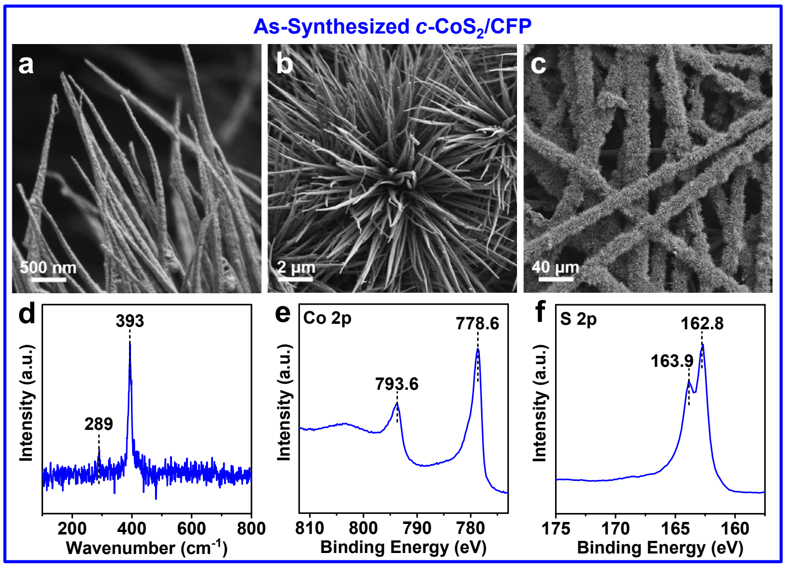

Figure A3.17. Materials characterization of *c*-CoS_2/CFP.

(a–c) SEM images at different magnifications, (d) Raman spectra, (e) Co 2p and (f) S 2p XPS spectra of as-synthesized *c*-CoS_2/CFP. Background Raman spectra of bare carbon fiber paper substrate were subtracted from as-measured Raman spectra of *c*-CoS_2/CFP.

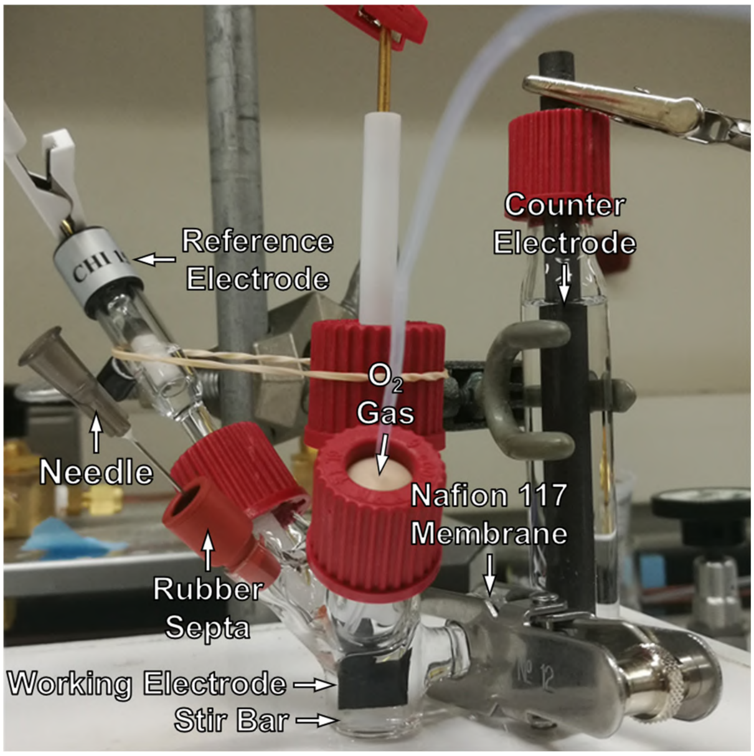

Figure A3.18. Digital photograph of the two-compartment three-electrode H-cell setup used for bulk electrosynthesis of H_2O_2.

Nafion 117 membrane was used to separate the two compartments to avoid the oxidation of H_2O_2 product on the counter electrode. A minimal volume (3–4 mL) of electrolyte solution was used and vigorously stirred at 1200 rpm in the working electrode compartment to achieve higher H_2O_2 concentrations under facilitated mass transfer of O_2 gas. A blanket of O_2 gas was maintained over the surface of O_2-saturated electrolyte solution during bulk electrosynthesis. A rubber septum punctured with a syringe needle served as the gas outlet, which was removed when a small aliquot of electrolyte solution was sampled from the working electrode compartment for chemical detection of H_2O_2 product and was capped for the rest of the time to minimize the evaporation of electrolyte solution during bulk electrosynthesis.

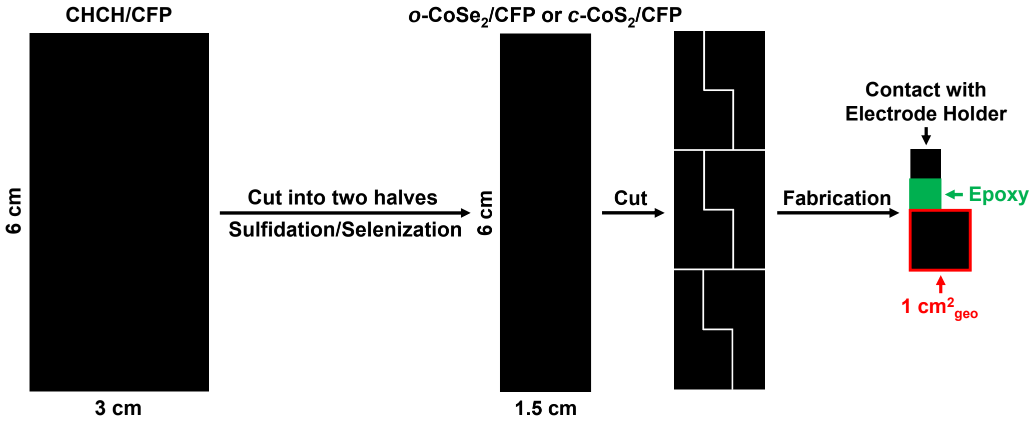

Figure A3.19. Fabrication of *o*-$CoSe_2$/CFP and *c*-CoS_2/CFP working electrodes. Fabrication of *o*-$CoSe_2$/CFP and *c*-CoS_2/CFP working electrodes with the same geometric area of ~1 cm^2_{geo} for bulk electrosynthesis of H_2O_2.

Table A3.9. Summary of the catalyst loadings of *o*-$CoSe_2$/CFP and *c*-CoS_2/CFP working electrodes.

Sample	Mass (mg)	Catalyst loading ($\mu g_{Co}/cm^2_{geo}$)
Bare CFP (3 × 6 cm^2_{geo})	142.8	-
CHCH/CFP (3 × 6 cm^2_{geo})	155.4	~376 [a]
CHCH/CFP (1st half; 1.5 × 6 cm^2_{geo}) [b]	78.1	~376 [a]
o-$CoSe_2$/CFP (1st half; 1.5 × 6 cm^2_{geo}) [b]	84.5	~384
CHCH/CFP (2nd half; 1.5 × 6 cm^2_{geo}) [b]	76.7	~376 [a]
c-CoS_2/CFP (2nd half; 1.5 × 6 cm^2_{geo}) [b]	77.3	~363

[a] The chemical formula of CHCH is $Co(CO_3)_{0.5}(OH)\cdot 0.11H_2O$ (MW = 107.93 g/mol).

[b] The geometric area is illustrated in Figure A3.19.

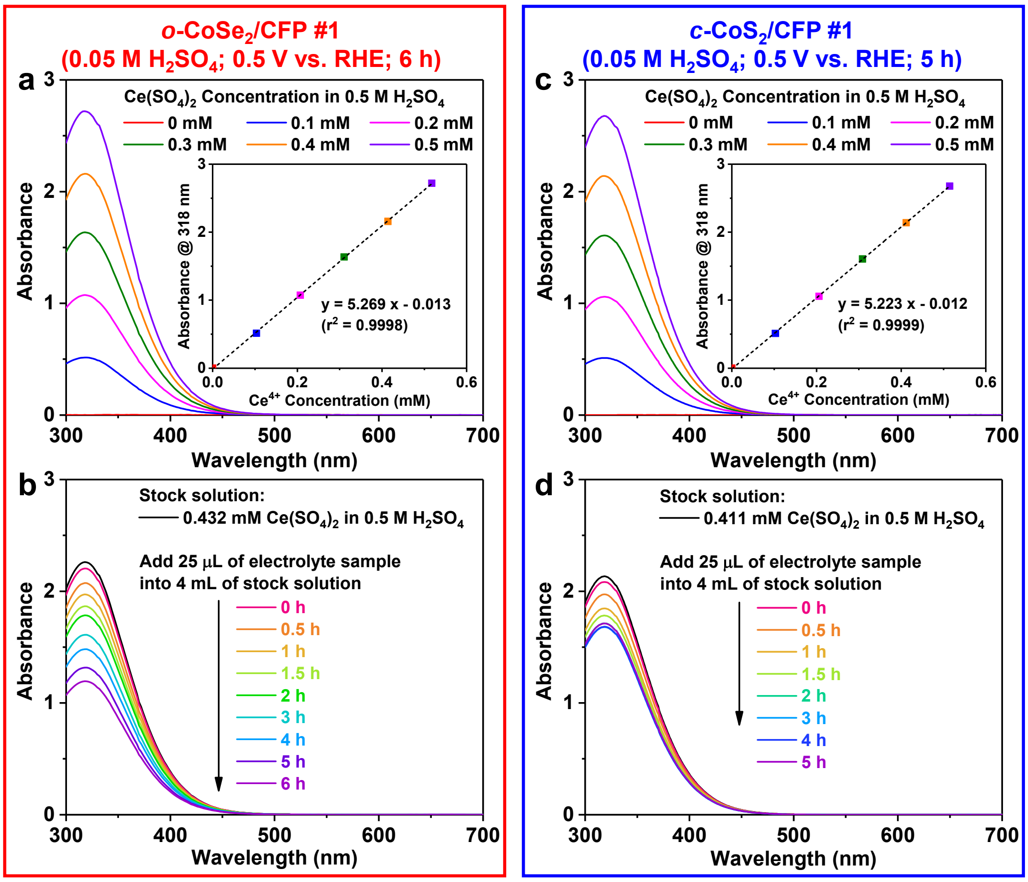

Figure A3.20. UV-Vis spectrophotometric detection of the produced H_2O_2 on *o*-$CoSe_2$/CFP vs. *c*-CoS_2/CFP.

(a,c) Absorption spectra of standard solutions of $Ce(SO_4)_2$ (up to 0.5 mM) in 0.5 M H_2SO_4 and the resultant calibration curve at the peak wavelength of 318 nm (shown as an inset) measured for each run of bulk electrolysis: (a) *o*-$CoSe_2$/CFP electrode #1 and (c) *c*-CoS_2/CFP electrode #1 (see Figure 3.6 in the Chapter 3). (b,d) Absorption spectra of stock solution of $Ce(SO_4)_2$ (~0.4 mM, exact concentration was determined from the respective calibration curve) in 0.5 M H_2SO_4 with and without being titrated with a small aliquot of electrolyte solution sampled from the working electrode compartment at various time points during each run of bulk electrolysis: (b) *o*-$CoSe_2$/CFP electrode #1 and (d) *c*-CoS_2/CFP electrode #1 (see Figure 3.6 in the Chapter 3).

Table A3.10. Summary of cumulative H_2O_2 concentration and cumulative H_2O_2 yield. Summary of cumulative H_2O_2 concentration and cumulative H_2O_2 yield during the bulk electrolysis runs of *o*-$CoSe_2$/CFP electrode #1 and *c*-CoS_2/CFP electrode #1 at 0.5 V vs. RHE in 0.05 M H_2SO_4 solution (continuously operated for 5–6 h, see Figure 3.6 in the Chapter 3).

Electrolyte Evaporation Rate During Bulk Electrolysis Run	Time Point for Aliquot Sampling	Electrolyte Volume Before (and After) Aliquot Sampling [b]	Absorbance at 318 nm Before (and After) Adding Aliquot into Ce^{4+} Stock Solution [c]	Ce^{4+} Concentration Before (and After) Adding Aliquot into Ce^{4+} Stock Solution	Cumulative H_2O_2 Concentration [f]	Cumulative H_2O_2 Yield (and H_2O_2 Produced Between Two Nearest Aliquot Samplings [g])
o-$CoSe_2$/CFP #1 (0.05 M H_2SO_4; 0.5 V vs. RHE; 6 h) Initial Volume = 4 mL Final Volume = 2.15 mL [a] Aliquot Volume = 25 μL × 9 Electrolyte Evaporation Rate $= \frac{(4\text{ mL} - 25\mu\text{L} \times 9) - 2.15\text{ mL}}{6\text{ h}}$ **= 0.271 mL/h**	0 h	4 mL (3.975 mL)	2.262 (2.204)	0.432 (0.421) [d]	0.67 mM	0 μmol (0 μmol)
	0.5 h	3.840 mL (3.815 mL)	2.262 (2.074)	0.432 (0.396)	2.65 mM	7.53 μmol (7.53 μmol)
	1 h	3.679 mL (3.654 mL)	2.262 (1.972)	0.432 (0.377)	4.21 mM	12.91 μmol (5.38 μmol)
	1.5 h	3.519 mL (3.494 mL)	2.262 (1.866)	0.432 (0.357)	5.83 mM	18.04 μmol (5.13 μmol)
	2 h	3.358 mL (3.333 mL)	2.262 (1.785)	0.432 (0.341)	7.04 mM	21.31 μmol (3.27 μmol)
	3 h	3.062 mL (3.037 mL)	2.262 (1.610)	0.432 (0.308)	9.71 mM	27.57 μmol (6.27 μmol)
	4 h	2.767 mL (2.742 mL)	2.262 (1.481)	0.432 (0.284)	11.68 mM	30.39 μmol (2.82 μmol)
	5 h	2.471 mL (2.446 mL)	2.262 (1.317)	0.432 (0.252)	14.19 mM	33.44 μmol (3.05 μmol)
	6 h	2.175 mL (2.15 mL)	2.262 (1.195)	0.432 (0.229)	16.08 mM	33.69 μmol (0.25 μmol)
c-CoS_2/CFP #1 (0.05 M H_2SO_4; 0.5 V vs. RHE; 5 h) Initial Volume = 4 mL Final Volume = 2.59 mL [a] Aliquot Volume = 25 μL × 8 Electrolyte Evaporation Rate $= \frac{(4\text{ mL} - 25\mu\text{L} \times 8) - 2.59\text{ mL}}{5\text{ h}}$ **= 0.242 mL/h**	0 h	4 mL (3.975 mL)	2.133 (2.083)	0.411 (0.401) [e]	0.57 mM	0 μmol (0 μmol)
	0.5 h	3.854 mL (3.829 mL)	2.133 (1.972)	0.411 (0.380)	2.28 mM	6.51 μmol (6.51 μmol)
	1 h	3.707 mL (3.682 mL)	2.133 (1.846)	0.411 (0.356)	4.22 mM	13.42 μmol (6.91 μmol)
	1.5 h	3.562 mL (3.537 mL)	2.133 (1.783)	0.411 (0.344)	5.20 mM	16.39 μmol (2.97 μmol)
	2 h	3.416 mL (3.391 mL)	2.133 (1.713)	0.411 (0.330)	6.28 mM	19.45 μmol (3.06 μmol)
	3 h	3.149 mL (3.124 mL)	2.133 (1.678)	0.411 (0.324)	6.81 mM	19.61 μmol (0.16 μmol)
	4 h	2.882 mL (2.857 mL)	2.133 (1.683)	0.411 (0.325)	6.74 mM	17.77 μmol (-1.84 μmol)
	5 h	2.615 mL (2.59 mL)	2.133 (1.712)	0.411 (0.330)	6.28 mM	14.94 μmol (-2.83 μmol)

[a] Final volume of electrolyte solution at the end of bulk electrolysis was determined by transferring all the remaining electrolyte solution out of the working compartment using an Eppendorf pipette.

[b] The volume of electrolyte solution before and after each aliquot sampling was calculated under the assumption that the electrolyte evaporation rate was constant throughout the bulk electrolysis.

[c] For chemical detection of H_2O_2 product, 25-μL aliquot of electrolyte solution was quantitatively added into 4 mL of Ce^{4+} stock solution (see Figure A3.20b,d).

[d] For the bulk electrolysis run of *o*-$CoSe_2$/CFP #1, the calibration curve of absorbance at 318 nm vs. Ce^{4+} concentration (mM) was y = 5.269 x - 0.013 (see Figure A3.20a).

[e] For the bulk electrolysis run of *o*-$CoSe_2$/CFP #1, the calibration curve of absorbance at 318 nm vs. Ce^{4+} concentration (mM) was y = 5.223 x - 0.012 (see Figure A3.20c).

[f] Cumulative H_2O_2 Concentration (mM) = (4 mL × $[Ce^{4+}]_{before}$ – 4.025 mL × $[Ce^{4+}]_{after}$) / (2 × 0.025 mL) , where $[Ce^{4+}]_{before}$ and $[Ce^{4+}]_{after}$ are the Ce^{4+} concentration (mM) before and after adding 25-μL aliquot of electrolyte solution into 4 mL of Ce^{4+} stock solution, respectively. For example, for the bulk electrolysis run of *o*-$CoSe_2$/CFP #1, cumulative H_2O_2 concentration at 0.5 h = (4 mL × 0.432 mM – 4.025 mL × 0.396 mM) / (2 × 0.025 mL) = 2.65 mM.

[g] H_2O_2 produced between two nearest aliquot samplings (μmol) = $[H_2O_2]_{later} \times V_{later} - [H_2O_2]_{earlier} \times V_{earlier}$, where $[H_2O_2]_{later}$ and $[H_2O_2]_{earlier}$ are the cumulative H_2O_2 concentration (mM) at the later time point and at the earlier time point, respectively; V_{later} (mL) is the electrolyte volume at the later time point *before* aliquot sampling; $V_{earlier}$ (mL) is the electrolyte volume at the earlier time point *after* aliquot sampling. For example, for the bulk electrolysis run of *o*-$CoSe_2$/CFP #1, H_2O_2 produced between 0 h and 0.5 h = 2.65 mM × 3.840 mL – 0.67 mM × 3.975 mL = 7.53 μmol, H_2O_2 produced between 0.5 h and 1 h = 4.21 mM × 3.679 mL – 2.65 mM × 3.815 mL = 5.38 μmol.

Table A3.11. Summary of cumulative H_2O_2 selectivity and cumulative Faradaic efficiency. Summary of cumulative H_2O_2 selectivity and cumulative Faradaic efficiency during the bulk electrolysis runs of *o*-$CoSe_2$/CFP electrode #1 and *c*-CoS_2/CFP electrode #1 at 0.5 V vs. RHE in 0.05 M H_2SO_4 solution (continuously operated for 5–6 h, see Figure 3.6 in the Chapter 3).

Bulk Electrolysis Run	Time Point for Aliquot Sampling	Cumulative H_2O_2 Yield (and H_2O_2 Produced Between Two Nearest Aliquot Samplings [a])	Cumulative Charge Passed	Theoretical H_2O_2 Yield [b]	Cumulative H_2O_2 Selectivity [c]	Cumulative Faradaic Efficiency [d]
***o*-$CoSe_2$/CFP #1 (0.05 M H_2SO_4; 0.5 V vs. RHE; 6 h)**	0 h	0 μmol (0 μmol)	0 C	0 μmol	-	-
	0.5 h	7.53 μmol (7.53 μmol)	2.013 C	10.43 μmol	83.8%	72.2%
	1 h	12.91 μmol (5.38 μmol)	3.520 C	18.24 μmol	82.9%	70.8%
	1.5 h	18.04 μmol (5.13 μmol)	4.875 C	25.26 μmol	83.3%	71.4%
	2 h	21.31 μmol (3.27 μmol)	6.053 C	31.37 μmol	80.9%	67.9%
	3 h	27.57 μmol (6.27 μmol)	8.045 C	41.69 μmol	79.6%	66.1%
	4 h	30.39 μmol (2.82 μmol)	9.642 C	49.96 μmol	75.6%	60.8%
	5 h	33.44 μmol (3.05 μmol)	10.98 C	56.87 μmol	74.1%	58.8%
	6 h	33.69 μmol (0.25 μmol)	12.15 C	62.95 μmol	69.7%	53.5%
***c*-CoS_2/CFP #1 (0.05 M H_2SO_4; 0.5 V vs. RHE; 5 h)**	0 h	0 μmol (0 μmol)	0 C	0 μmol	-	-
	0.5 h	6.51 μmol (6.51 μmol)	2.905 C	15.05 μmol	60.4%	43.3%
	1 h	13.42 μmol (6.91 μmol)	6.144 C	31.84 μmol	59.3%	42.2%
	1.5 h	16.39 μmol (2.97 μmol)	9.729 C	50.42 μmol	49.1%	32.5%
	2 h	19.45 μmol (3.06 μmol)	13.71 C	71.03 μmol	43.0%	27.4%
	3 h	19.61 μmol (0.16 μmol)	22.28 C	115.44 μmol	29.0%	17.0%
	4 h	17.77 μmol (-1.84 μmol)	31.26 C	161.97 μmol	19.8%	11.0%
	5 h	14.94 μmol (-2.83 μmol)	40.60 C	210.40 μmol	13.3%	7.1%

[a] See Table A3.10.

[b] $\text{Theoretical } H_2O_2 \text{ Yield } (\mu\text{mol}) = \text{Cumulative Charge Passed (C)} \times \frac{1 \text{ mol e}^-}{96485 \text{ C}} \times \frac{1 \text{ mol } H_2O_2}{2 \text{ mol e}^-} \times \frac{10^6\ \mu\text{mol } H_2O_2}{1 \text{ mol } H_2O_2}$

[c] $\text{Cumulative } H_2O_2 \text{ Selectivity (\%)} = \frac{\text{Cumulative } O_2 \text{ Consumption that Yields } H_2O_2\ (\mu\text{mol})}{\text{Cumulative } O_2 \text{ Consumption } (\mu\text{mol})} \times 100\%$

$$= \frac{\text{Cumulative } H_2O_2 \text{ Yield } (\mu\text{mol})}{\text{Cumulative } H_2O_2 \text{ Yield } (\mu\text{mol}) + \text{Cumulative } O_2 \text{ Consumption that Yields } H_2O\ (\mu\text{mol})} \times 100\%$$

$$= \frac{\text{Cumulative } H_2O_2 \text{ Yield } (\mu\text{mol})}{\text{Cumulative } H_2O_2 \text{ Yield } (\mu\text{mol}) + [\ \text{Cumulative Charge Passed (C)} - \text{Cumulative } H_2O_2 \text{ Yield } (\mu\text{mol}) \times \frac{1 \text{ mol } H_2O_2}{10^6\ \mu\text{mol } H_2O_2} \times \frac{1 \text{ mol } O_2}{1 \text{ mol } H_2O_2} \times \frac{2 \text{ mol e}^-}{1 \text{ mol } O_2} \times \frac{96485 \text{ C}}{1 \text{ mol e}^-}\ ] \times \frac{1 \text{ mol e}^-}{96485 \text{ C}} \times \frac{2 \text{ mol } H_2O}{4 \text{ mol e}^-} \times \frac{1 \text{ mol } O_2}{2 \text{ mol } H_2O} \times \frac{10^6\ \mu\text{mol } O_2}{1 \text{ mol } O_2}} \times 100\%$$

[d] $\text{Cumulative Faradaic Efficiency (\%)} = \frac{\text{Cumulative Charge Passed that Yields } H_2O_2 \text{ (C)}}{\text{Cumulative Charge Passed (C)}} \times 100\%$

$$= \frac{\text{Cumulative } H_2O_2 \text{ Yield } (\mu\text{mol}) \times \frac{1 \text{ mol } H_2O_2}{10^6\ \mu\text{mol } H_2O_2} \times \frac{2 \text{ mol e}^-}{1 \text{ mol } H_2O_2} \times \frac{96485 \text{ C}}{1 \text{ mol e}^-}}{\text{Cumulative Charge Passed (C)}} \times 100\%$$

Table A3.12. ICP-MS analysis of the tested electrolyte solutions after the bulk electrolysis runs of *o*-$CoSe_2$/CFP and *c*-CoS_2/CFP.

ICP-MS analysis of the tested electrolyte solutions of 0.05 M H_2SO_4 after the bulk electrolysis runs of *o*-$CoSe_2$/CFP electrode #1 and *c*-CoS_2/CFP electrode #1 (continuously operated for 5 h, see Figure 3.6 in the Chapter 3) as well as *o*-$CoSe_2$/CFP electrode #2 and *c*-CoS_2/CFP electrode #2 (first operated for 1.5 h, and then operated for another 2.5 h after the H_2O_2-free electrolyte solution was reintroduced, see Figure A3.21).

ICP-MS Sample		Intensity	Standard Curve	[Co] in Diluted ICP-MS Sample	Final Electrolyte Volume After Bulk Electrolysis	Average Cobalt Leaching Rate [b]
Standard solution of $CoSO_4$ in 0.05 M H_2SO_4	[Co] = 0 ug_{Co}/L	1.0	$y = 45.5\,x - 114.7$ ($r^2 = 0.99996$)	-	-	-
	[Co] = 52.3 ug_{Co}/L	2058.4		-	-	-
	[Co] = 104.5 ug_{Co}/L	4715.2		-	-	-
	[Co] = 209.1 ug_{Co}/L	9469.0		-	-	-
	[Co] = 522.7 ug_{Co}/L	23605.7		-	-	-
	[Co] = 1045.5 ug_{Co}/L	47499.7		-	-	-
1:15 Dilution of tested electrolyte solution with 0.05 M H_2SO_4 [a]	***o*-$CoSe_2$/CFP #1** (4 mL of 0.05 M H_2SO_4; 0.5 V vs. RHE; **6 h**)	5720.2	-	128.2 ug_{Co}/L	2.15 mL	0.69 ug_{Co}/h
	***o*-$CoSe_2$/CFP #2** (3 mL of 0.05 M H_2SO_4; 0.5 V vs. RHE; **1.5 h**)	2724.3	-	62.4 ug_{Co}/L	2.00 mL	1.25 ug_{Co}/h
	***o*-$CoSe_2$/CFP #2 (Reused)** (3 mL of 0.05 M H_2SO_4; 0.5 V vs. RHE; **2.5 h**)	256.9	-	8.16 ug_{Co}/L	1.99 mL	0.10 ug_{Co}/h
	***c*-CoS_2/CFP #1** (4 mL of 0.05 M H_2SO_4; 0.5 V vs. RHE; **5 h**)	16299.7	-	360.6 ug_{Co}/L	2.59 mL	2.80 ug_{Co}/h
	***c*-CoS_2/CFP #2** (3 mL of 0.05 M H_2SO_4; 0.5 V vs. RHE; **1.5 h**)	4201.4	-	94.8 ug_{Co}/L	2.06 mL	1.97 ug_{Co}/h
	***c*-CoS_2/CFP #2 (Reused)** (3 mL of 0.05 M H_2SO_4; 0.5 V vs. RHE; **2.5 h**)	8400.3	-	187.1 ug_{Co}/L	2.08 mL	2.31 ug_{Co}/h

[a] To prepare ICP-MS sample, 1 part of tested electrolyte solution was diluted with 14 part of 0.05 M H_2SO_4.

[b] Average Cobalt Leaching Rate (μg_{Co}/h) = $\dfrac{\text{[Co] in Diluted ICP-MS Sample } (ug_{Co}/L) \times 15 \times \text{Final Electrolyte Volume After Bulk Electrolysis (mL)} \times \frac{1\ L}{10^3\ mL}}{\text{Bulk Electrolysis Time (h)}}$

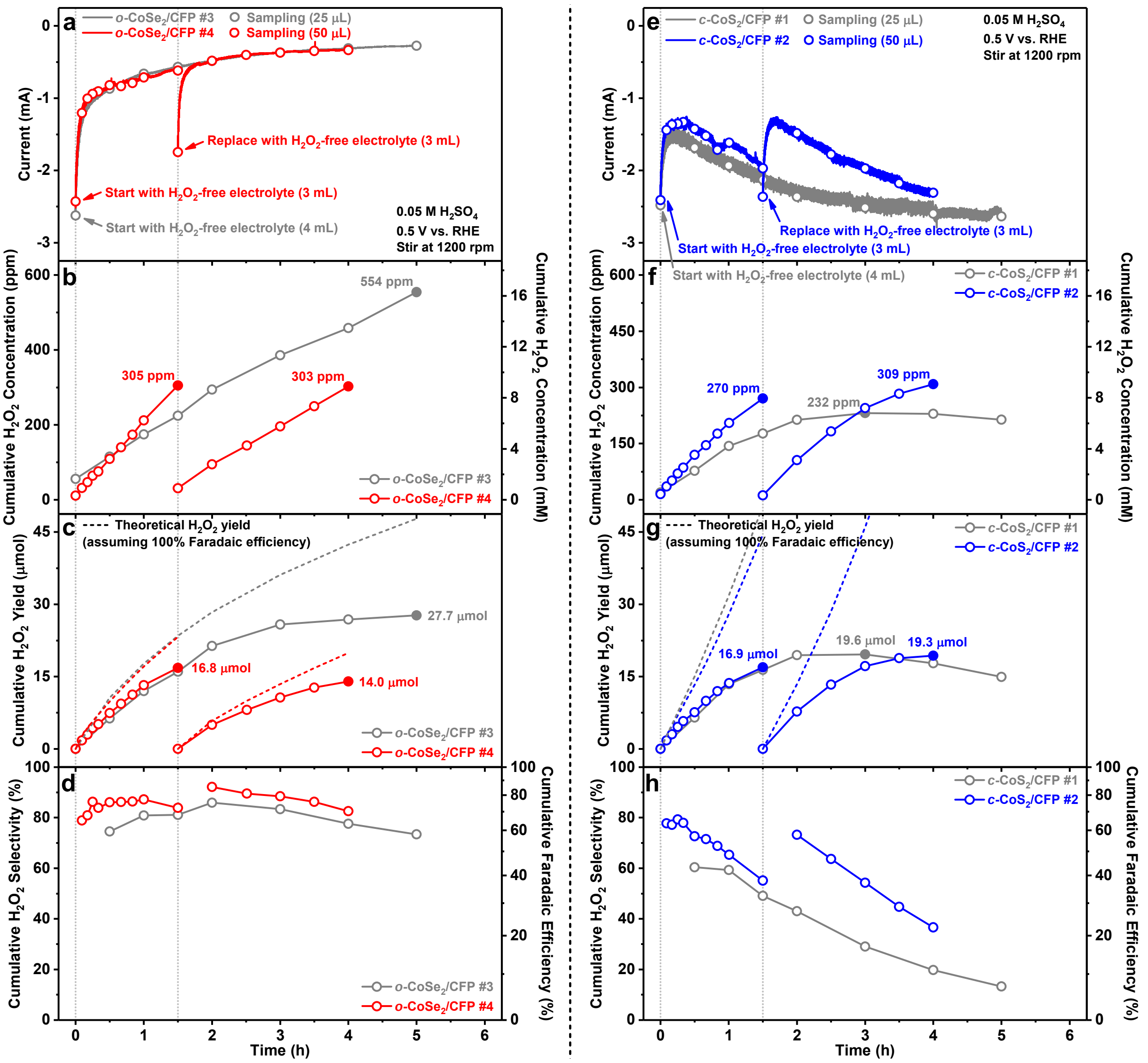

Figure A3.21. Comparisons of bulk electrolysis runs of *o*-$CoSe_2$/CFP vs. *c*-CoS_2/CFP.

(a) Chronoamperometry curves of *o*-$CoSe_2$/CFP electrode #3 (continuously operated for 5 h) and #4 (first operated for 1.5 h, and then operated for another 2.5 h after the H_2O_2-free electrolyte solution was reintroduced) at 0.5 V vs. RHE in O_2-saturated 0.05 M H_2SO_4 solution (pH 1.20) under vigorous stirring (1200 rpm). (b) Cumulative H_2O_2 concentration, (c) cumulative H_2O_2 yield, and (d) cumulative H_2O_2 selectivity and Faradaic efficiency during the bulk electrolysis runs of *o*-$CoSe_2$/CFP electrode #3 and #4. (e–h) Similar bulk experiments were performed on *c*-CoS_2/CFP electrode #1 (continuously operated for 5 h) and #2 (first operated for 1.5 h, and then operated for another 2.5 h after the H_2O_2-free electrolyte solution was reintroduced).

Table A3.13. Additional ICP-MS analysis of the tested electrolyte solutions after the bulk electrolysis runs of *o*-$CoSe_2$/CFP.

ICP-MS analysis of the tested electrolyte solutions of 0.05 M H_2SO_4 after the bulk electrolysis runs of *o*-$CoSe_2$/CFP electrode #3 (continuously operated for 5 h, see Figure A3.21) and #4 (first operated for 1.5 h, and then operated for another 2.5 h after the H_2O_2-free electrolyte solution was reintroduced, see Figure A3.21).

ICP-MS Sample		Intensity	Standard Curve	[Co] in Diluted ICP-MS Sample	Final Electrolyte Volume After Bulk Electrolysis	Average Cobalt Leaching Rate [b]
Standard solution of $CoSO_4$ in 0.05 M H_2SO_4	[Co] = 0 ug_{Co}/L	0.9	y = 47.2 x + 25.6 (r^2 = 0.99996)	-	-	-
	[Co] = 100.0 ug_{Co}/L	4791.0		-	-	-
	[Co] = 200.0 ug_{Co}/L	9331.4		-	-	-
	[Co] = 500.0 ug_{Co}/L	23832.4		-	-	-
	[Co] = 1000.0 ug_{Co}/L	47176.3		-	-	-
1:15 Dilution of tested electrolyte solution with 0.05 M H_2SO_4 [a]	***o*-$CoSe_2$/CFP #3** (4 mL of 0.05 M H_2SO_4; 0.5 V vs. RHE; **5 h**)	2041.4	-	42.7 ug_{Co}/L	2.00 mL	0.26 ug_{Co}/h
	***o*-$CoSe_2$/CFP #4** (3 mL of 0.05 M H_2SO_4; 0.5 V vs. RHE; **1.5 h**)	4873.8	-	102.7 ug_{Co}/L	1.79 mL	1.84 ug_{Co}/h
	***o*-$CoSe_2$/CFP #4 (Reused)** (3 mL of 0.05 M H_2SO_4; 0.5 V vs. RHE; **2.5 h**)	830.7	-	17.1 ug_{Co}/L	1.71 mL	0.18 ug_{Co}/h

[a] To prepare ICP-MS sample, 1 part of tested electrolyte solution was diluted with 14 part of 0.05 M H_2SO_4.

[b] Average Cobalt Leaching Rate (μg_{Co}/h) = $\frac{\text{[Co] in Diluted ICP-MS Sample } (ug_{Co}/L) \times 15 \times \text{Final Electrolyte Volume After Bulk Electrolysis (mL)} \times \frac{1\ L}{10^3\ mL}}{\text{Bulk Electrolysis Time (h)}}$

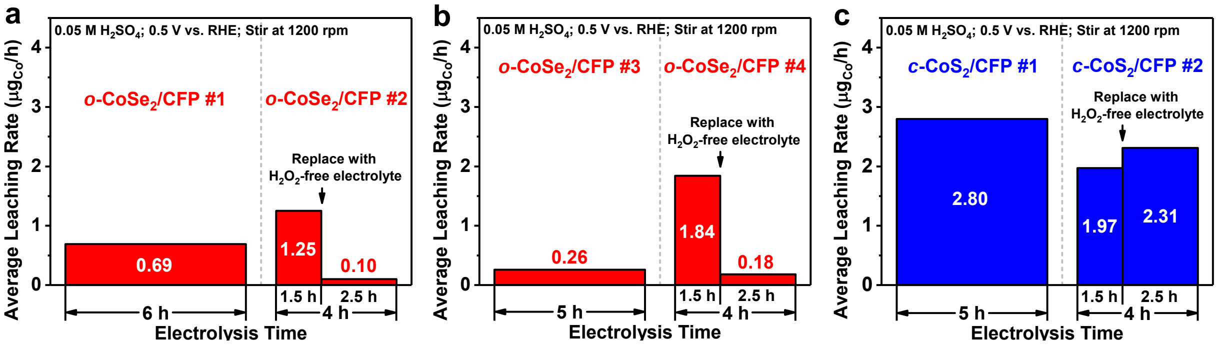

Figure A3.22. ICP-MS analysis of the tested electrolyte solutions after the bulk electrolysis runs of *o*-$CoSe_2$/CFP and *c*-CoS_2/CFP.

ICP-MS analysis of the tested electrolyte solutions of 0.05 M H_2SO_4 after the bulk electrolysis runs of (a) *o*-$CoSe_2$/CFP electrode #1 and #2, (b) *o*-$CoSe_2$/CFP electrode #3 and #4, and (c) *c*-CoS_2/CFP electrode #1 and #2. The transient catalyst leaching of *o*-$CoSe_2$ took place mostly at the beginning of bulk electrolysis and was minimal afterwards (see Figure A3.22a,b for two replicate experiments), whereas *c*-CoS_2 continuously leached into electrolyte solution throughout the entire bulk electrolysis (see Figure A3.22c). *See additional discussion below.*

Additional Discussion of Figure A3.22. Based on the low steady state cobalt leaching rate of the *o*-$CoSe_2$ catalyst (0.10 and 0.18 μg$_{Co}$/h in two replicate experiments, see Figure A3.22a,b) and the catalyst mass loading of the *o*-$CoSe_2$/CFP electrode (~370 μg$_{Co}$ on each electrode with ~1 cm$^2_{geo}$, see Table A3.9), a back-of-the-envelope estimate suggests the *o*-$CoSe_2$ catalyst, in theory, could last for several months under the operating conditions of the bulk electrosynthesis of H_2O_2. An example calculation is shown below.

$$370\ \mu g_{Co}/cm^2_{geo} \times 1\ cm^2_{geo} \times \frac{1\ h}{0.10\ \mu g_{Co}} \times \frac{1\ day}{24\ h} \times \frac{1\ month}{30\ day} = 5.1\ months$$

Table A3.14. Comparisons of the leaching results of *o*-$CoSe_2$/CFP under operating conditions of the bulk electrosynthesis of H_2O_2 to those of other cobalt-based electrocatalysts reported for water splitting reactions.

This is due to the fact that there has been no rigorous analysis of metal leaching in the recently reported earth-abundant $2e^-$ ORR catalysts.

Reaction [1]	Electrolyte	Catalyst (Substrate)	Catalyst Loading	Catalyst Mass	Cobalt Mass	Electrochemical Operation	Average Cobalt Leaching Percentage	Average Cobalt Leaching Rate	Reference
HER	1 M KOH	CoS_2 (Ti plate)	~2.1 mg/cm^2_{geo}	~4.2 mg	~1.9 mg_{Co}	-20 mA/cm^2_{geo}; 250 h	~59.4% (after 250 h) [2]	~0.24%/h (after 250 h)	ref. [20]
HER	1 M KOH	Ce-doped CoS_2 (Ti plate)	~2.1 mg/cm^2_{geo}	~4.1 mg	~1.8 mg_{Co}	-20 mA/cm^2_{geo}; 250 h	~3.2% (after 250 h) [3]	~0.013%/h (after 250 h)	ref. [20]
HER	0.5 M H_2SO_4	CoS_2/CNT (carbon fiber paper)	~0.8 mg/cm^2_{geo}	~0.4 mg	N/A	-0.077 V vs. RHE; 20 h	~17.5% (the initial 0.5 h) [2]	~35.0%/h (the initial 0.5 h)	ref. [21]
							~6.7% (from 0.5 h to 20 h) [3]	~0.45%/h (from 0.5 h to 20 h)	
HER	0.5 M H_2SO_4	CoS|P/CNT (carbon fiber paper)	~0.8 mg/cm^2_{geo}	~0.4 mg	N/A	-0.077 V vs. RHE; 20 h	~5.0% (after 12 h) [3]	~0.42%/h (after 12 h)	ref. [21]
OER	0.5 M H_2SO_4	300 nm Co_3O_4 film (FTO)	~0.36 mg/cm^2_{geo} [3]	~0.36 mg [3]	~0.27 mg_{Co} [3]	10 mA/cm^2_{geo}; ~10 h	~25% (after ~10 h) [3]	~2.5%/h (after ~10 h)	ref. [22]
						1 mA/cm^2_{geo}; ~72 h	~34% (after ~72 h) [3]	~0.47%/h (after ~72 h)	
$2e^-$ ORR	0.05 M H_2SO_4	*o*-$CoSe_2$/CFP #2 (carbon fiber paper)	~1.4 mg/cm^2_{geo}	~1.4 mg	~0.37 mg_{Co}	0.5 V vs. RHE; 1.5 h + 2.5 h	~0.51% (the initial 1.5 h) [4]	~0.34%/h (the initial 1.5 h)	This work
							~0.07% (reused for 2.5 h) [4]	**~0.027%/h** (reused for 2.5 h)	

[1] "HER" stands for hydrogen evolution reaction, "OER" stands for oxygen evolution reaction.

[2] These values were present in the original literature.

[3] These values were calculated based on the information present in the original literature.

[4] These values were calculated based on the data of the *o*-$CoSe_2$/CFP #2 electrode presented in Figure A3.22a.

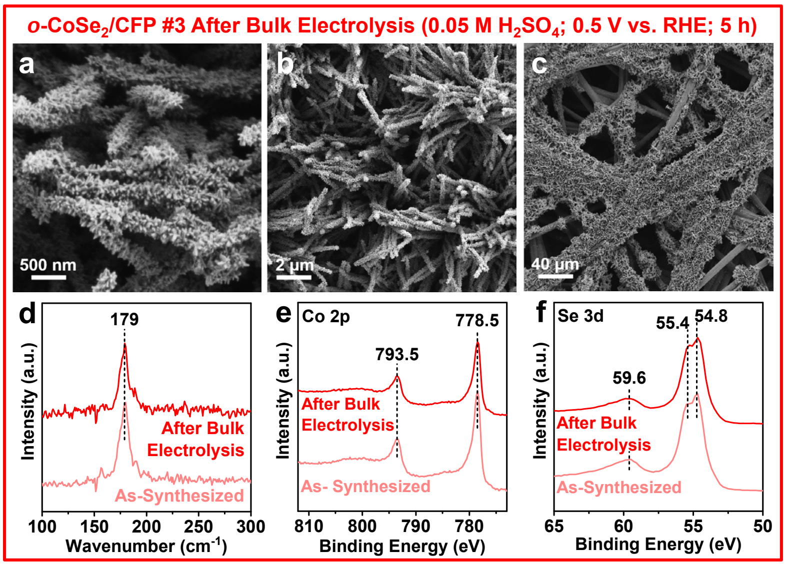

Figure A3.23. Materials characterization of *o*-CoSe$_2$/CFP before and after the bulk electrolysis.

(a–c) SEM images at different magnifications, (d) Raman spectra, (e) Co 2p and (f) Se 3d XPS spectra of the *o*-CoSe$_2$/CFP electrode #3 after the bulk electrolysis at 0.5 V vs. RHE in 0.05 M H_2SO_4 for 5 h (see Figure A3.21). Background Raman spectra of bare carbon fiber paper substrate were subtracted from all as-measured Raman spectra of *o*-CoSe$_2$/CFP.

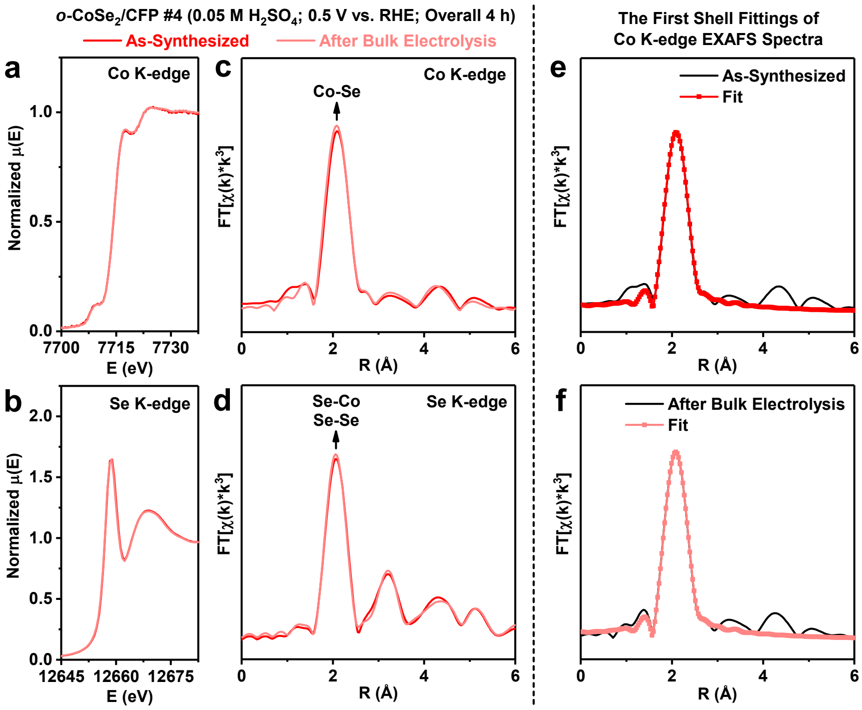

Figure A3.24. Co K-edge and Se K-edge XANES and EXAFS spectra of *o*-CoSe$_2$/CFP before and after the bulk electrolysis.

(a) Co K-edge and (b) Se K-edge XANES spectra, Fourier transforms of (c) Co K-edge and (d) Se K-edge EXAFS spectra, and the first shell fittings of Co K-edge EXAFS spectra of the *o*-CoSe$_2$/CFP electrode #4 (e) before and (f) after the bulk electrolysis at 0.5 V vs. RHE in 0.05 M H_2SO_4 for overall 4 h (see Figure A3.21). The Fourier transform parameters and fitting results are summarized in Table A3.15.

Table A3.15. The first shell fitting results of Co K-edge EXAFS spectra of *o*-$CoSe_2$/CFP before and after the bulk electrolysis.

The first shell fitting results of Co K-edge EXAFS spectra of the *o*-$CoSe_2$/CFP electrode #4 before and after bulk electrolysis at 0.5 V vs. RHE in 0.05 M H_2SO_4 for overall 4 h.

Sample	Shell	N [b]	R (Å) [b]	σ^2 (10^{-3} Å^2) [b]	ΔE_0 (eV) [b]	Reduced χ^2 [b]	R-factor [b]
As-Synthesized	Co-Se	5.9 ± 1.1	2.411 ± 0.007	5.7 ± 0.7	1.9 ± 1.7	43.7445612	0.0120876
After Bulk Electrolysis	Co-Se	5.7 ± 1.0	2.405 ± 0.004	5.4 ± 0.4	0.9 ± 1.0	50.1007662	0.0042312

[a] For both samples, the Fourier transform parameters are: Hanning window, $k_{min} = 3$, $k_{max} = 12$, dk = 1, no phase correction; the fitting parameters are: $r_{min} = 1$, $r_{max} = 3$, dr = 0, fitting k-weight = 3.

[b] N is the coordination number of the absorbing Co atom. R is the interatomic distance between the absorbing Co atom and the backscattering S/Se atom. σ^2 is the mean square relative displacement (i.e., the Debye-Waller factor). ΔE_0 is the energy shift parameter used to align the theoretical calculated spectrum to the energy grid of the measured spectrum. For all the first shell fittings, the amplitude reduction factor (S_0^2) is constrained to 0.90 as a reasonable estimation, and the added uncertainty in the coordination number (N) due to the estimation of S_0^2 has already been considered.[6] Reduced χ^2 and R-factor are goodness-of-fit parameters.

Table A3.16. Comparisons of the cumulative H_2O_2 concentrations achieved from bulk electrosynthesis of H_2O_2 in *acidic* solution using *o*-$CoSe_2$/CFP and other reported 2e$^-$ ORR electrocatalysts in a similar H-cell setup. *See additional discussion on the next page.*

Classification	Catalyst	Catalyst Loading (Geometric Area)	*Acidic* Electrolyte (Volume)	Potential	Time	H_2O_2 Production Rate (mmol $g_{catalyst}^{-1}$ h^{-1})	Cumulative H_2O_2 Concentration	Cumulative H_2O_2 Selectivity	Catalyst Leaching Rate Monitored?	Reference
Earth-abundant transition metal compounds	*o*-$CoSe_2$/CFP	~370 $\mu g_{Co}/cm^2_{geo}$ ~1.42 $mg_{catalyst}/cm^2_{geo}$ (1 cm^2_{geo})	0.05 M H_2SO_4 (4 mL)	0.5 V vs. RHE	6 h	4.0	**547 ppm**	~70%	**Yes**	this work
Noble metal catalysts	Pt-Hg foil	N/A (0.98 cm^2_{geo})	0.1 M $HClO_4$ (15 mL)	0.4 V vs. RHE	~1 h	N/A	21 ppm	~80% [a]	No	ref. 7
Single-atom catalysts	Co_1-N-C(1)	100 $\mu g_{catalyst}/cm^2_{geo}$ (1 cm^2_{geo}) [b]	0.5 M H_2SO_4 (42 mL) [b]	0.5 V vs. RHE	4 h	9.7	3.1 ppm	~47% [a]	No	ref. 13
	Co_1-N-C(2)	100 $\mu g_{catalyst}/cm^2_{geo}$ (1 cm^2_{geo})	0.1 M $HClO_4$ (100 mL) [b]	0.5 V vs. RHE	10 h	80	27.2 ppm	~81%	No	ref. 14
	h-Pt_1-CuS_x	250 $\mu g_{catalyst}$ (3 cm^2_{geo})	0.5 M $HClO_4$ (110 mL) [b]	0.05 V vs. HOR [c]	1 h	546	~58 ppm	>90%	No	ref. 12
Carbon materials	meso-BMP	~307 $\mu g_{catalyst}/cm^2_{geo}$ (0.196 cm^2_{geo})	0.1 M $HClO_4$ (N/A)	0.1 V vs. RHE	4 h	N/A	13 ppm	N/A	No	ref. 18
	NCMK	50 $\mu g_{catalyst}/cm^2_{geo}$ (1 cm^2_{geo}) [b]	0.5 M H_2SO_4 (145 mL)	0.3 V vs. RHE	6 h	~35	~1.6 ppm	~87% [a]	No	ref. 19

[a] Cumulative H_2O_2 selectivity is calculated from the literature value of cumulative Faradaic efficiency using the following equation:

$$\text{Cumulative } H_2O_2 \text{ Selectivity } (\%) = 200 \times \frac{1}{1 + \frac{100}{\text{Cumulative Faradaic Efficiency } (\%)}}$$

[b] These information was not present in the original literature but was provided by the authors upon request.

[c] In this previous report,[12] the authors operated the H-cell setup as a fuel cell, where the h-Pt_1-CuS_x catalyst was loaded on the cathode for H_2O_2 production and a Pt mesh was used as the anode for hydrogen oxidation reaction (HOR). The cell output was controlled at 0.05 V without any energy input. This operation mode was different from the rest of the previous reports in this Table A3.16, where the anode was used to drive water oxidation and the H-cell setup was operated as an electrolyzer.[7, 13-14, 18-19]

Additional Discussion of Table A3.16. For on-site water treatment applications, it is essential to accumulate a practically useful H_2O_2 concentration up to 1000 ppm from bulk electrosynthesis.[23] We demonstrated that *o*-$CoSe_2$/CFP successfully accumulated 547 ppm H_2O_2 over 6 h from the steady bulk electrosynthesis at 0.5 V vs. RHE in 0.05 M H_2SO_4 using a two-compartment three-electrode H-cell setup (Figure 3.6 in the Chapter 3). We compare this cumulative H_2O_2 concentration achieved by *o*-$CoSe_2$/CFP with the few previous reports where the bulk electrosynthesis of H_2O_2 in *acidic* solution was conducted on other $2e^-$ ORR electrocatalysts in a similar H-cell setup (Table A3.16). We found that these reported catalysts were operated in larger volumes of electrolyte solution, and the cumulative H_2O_2 concentrations were one or two order(s) of magnitude lower than 547 ppm (Table A3.16). Therefore, they were evaluated under much less stringent operating conditions because the catalyst stability was less challenged and the electrochemical side reactions of H_2O_2 reduction and/or decomposition were less probable to take place without a significant buildup of H_2O_2 concentration. Although the H_2O_2 production rate of *o*-$CoSe_2$/CFP (4.0 mmol $g_{catalyst}^{-1}$ h^{-1}, see Table A3.16) could be further improved by nanostructuring the catalyst and engineering the oxygen gas diffusion, *o*-$CoSe_2$/CFP shows enhanced catalyst stability and is highly resistant to electrochemical side reactions under stringent operating conditions, and the cumulative H_2O_2 concentration of 547 ppm is the highest among all the reported $2e^-$ ORR catalysts evaluated in *acidic* solution in a similar H-cell setup.

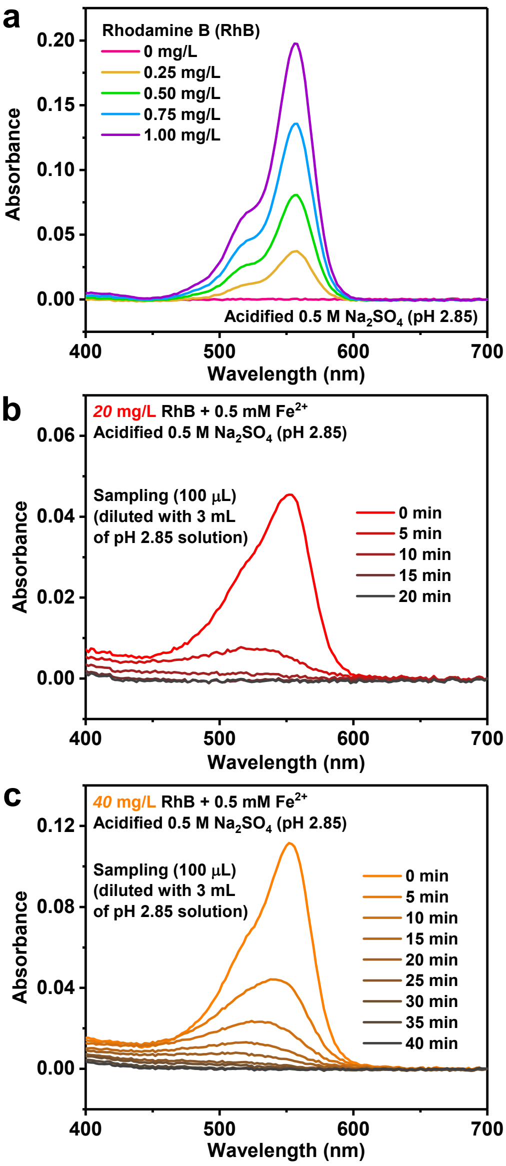

Figure A3.25. UV-Vis spectrophotometric monitoring of RhB degradation by the electro-Fenton process at *o*-$CoSe_2$/CFP.

(a) Absorption spectra of standard solutions of RhB (up to 1.00 mg/L) in acidified 0.5 M Na_2SO_4 solution (pH 2.85). (b,c) Absorption spectra of the quantitatively diluted small aliquot of electrolyte solution sampled from the working electrode compartment at various time points during each electro-Fenton degradation test shown in Figure 3.7 in the Chapter 3: (b) 20 mg/L or (c) 40 mg/L RhB in O_2-saturated acidified 0.5 M Na_2SO_4 solution (pH 2.85) with the presence of 0.5 mM Fe^{2+}.

References Cited in the Appendix 3

1. The Materials Project. https://materialsproject.org/ (accessed April 14, 2020).

2. Zhao, W.-W.; Bothra, P.; Lu, Z.; Li, Y.; Mei, L.-P.; Liu, K.; Zhao, Z.; Chen, G.; Back, S.; Siahrostami, S.; Kulkarni, A.; Nørskov, J. K.; Bajdich, M.; Cui, Y. Improved oxygen reduction reaction activity of nanostructured CoS2 through electrochemical tuning. *ACS Appl. Energy Mater.* ***2***, 8605-8614 (2019).

3. Singh, A. K.; Zhou, L.; Shinde, A.; Suram, S. K.; Montoya, J. H.; Winston, D.; Gregoire, J. M.; Persson, K. A. Electrochemical Stability of Metastable Materials. *Chem. Mater.* ***29***, 10159-10167 (2017).

4. Sheng, H.; Hermes, E. D.; Yang, X.; Ying, D.; Janes, A. N.; Li, W.; Schmidt, J. R.; Jin, S. Electrocatalytic production of H2O2 by selective oxygen reduction using earth-abundant cobalt pyrite (CoS2). *ACS Catal.* ***9***, 8433-8442 (2019).

5. Grimme, S.; Antony, J.; Ehrlich, S.; Krieg, H. A consistent and accurate ab initio parametrization of density functional dispersion correction (DFT-D) for the 94 elements H-Pu. *J. Chem. Phys.* ***132***, 154104 (2010).

6. Calvin, S.: XAFS for Everyone. CRC Press, 2013; pp 353-354.

7. Siahrostami, S.; Verdaguer-Casadevall, A.; Karamad, M.; Deiana, D.; Malacrida, P.; Wickman, B.; Escudero-Escribano, M.; Paoli, E. A.; Frydendal, R.; Hansen, T. W.; Chorkendorff, I.; Stephens, I. E. L.; Rossmeisl, J. Enabling direct H_2O_2 production through rational electrocatalyst design. *Nat. Mater.* ***12***, 1137-1143 (2013).

8. Verdaguer-Casadevall, A.; Deiana, D.; Karamad, M.; Siahrostami, S.; Malacrida, P.; Hansen, T. W.; Rossmeisl, J.; Chorkendorff, I.; Stephens, I. E. L. Trends in the electrochemical synthesis of H2O2: Enhancing activity and selectivity by electrocatalytic site engineering. *Nano Lett.* ***14***, 1603-1608 (2014).

9. Pizzutilo, E.; Kasian, O.; Choi, C. H.; Cherevko, S.; Hutchings, G. J.; Mayrhofer, K. J. J.; Freakley, S. J. Electrocatalytic synthesis of hydrogen peroxide on Au-Pd nanoparticles: From fundamentals to continuous production. *Chem. Phys. Lett.* ***683***, 436-442 (2017).

10. Choi, C. H.; Kim, M.; Kwon, H. C.; Cho, S. J.; Yun, S.; Kim, H.-T.; Mayrhofer, K. J. J.; Kim, H.; Choi, M. Tuning selectivity of electrochemical reactions by atomically dispersed platinum catalyst. *Nat. Commun.* ***7***, 10922 (2016).

11. Yang, S.; Kim, J.; Tak, Y. J.; Soon, A.; Lee, H. Single-atom catalyst of platinum supported on titanium nitride for selective electrochemical reactions. *Angew. Chem. Int. Ed.* ***55***, 2058-2062 (2016).

12. Shen, R.; Chen, W.; Peng, Q.; Lu, S.; Zheng, L.; Cao, X.; Wang, Y.; Zhu, W.; Zhang, J.; Zhuang, Z.; Chen, C.; Wang, D.; Li, Y. High-Concentration Single Atomic Pt Sites on Hollow CuS_x for Selective O_2 Reduction to H_2O_2 in Acid Solution. *Chem* ***5***, 2099-2110 (2019).

13. Sun, Y.; Silvioli, L.; Sahraie, N. R.; Ju, W.; Li, J.; Zitolo, A.; Li, S.; Bagger, A.; Arnarson, L.; Wang, X.; Moeller, T.; Bernsmeier, D.; Rossmeisl, J.; Jaouen, F.; Strasser, P. Activity–selectivity trends in the electrochemical production of hydrogen peroxide over single-site metal–nitrogen–carbon catalysts. *J. Am. Chem. Soc.* ***141***, 12372-12381 (2019).

14. Gao, J.; Yang, H. b.; Huang, X.; Hung, S.-F.; Cai, W.; Jia, C.; Miao, S.; Chen, H. M.; Yang, X.; Huang, Y.; Zhang, T.; Liu, B. Enabling direct H2O2 production in acidic media through rational design of transition metal single atom catalyst. *Chem* ***6***, 658-674 (2020).

15. Jung, E.; Shin, H.; Lee, B.-H.; Efremov, V.; Lee, S.; Lee, H. S.; Kim, J.; Hooch Antink, W.; Park, S.; Lee, K.-S.; Cho, S.-P.; Yoo, J. S.; Sung, Y.-E.; Hyeon, T. Atomic-level tuning of Co–N–C catalyst for high-performance electrochemical H2O2 production. *Nat. Mater.* ***19***, 436-442 (2020).

16. Tang, C.; Jiao, Y.; Shi, B.; Liu, J.-N.; Xie, Z.; Chen, X.; Zhang, Q.; Qiao, S.-Z. Coordination Tunes Selectivity: Two-Electron Oxygen Reduction on High-Loading Molybdenum Single-Atom Catalysts. *Angew. Chem. Int. Ed.* ***59***, 2-8).

17. Lu, Z.; Chen, G.; Siahrostami, S.; Chen, Z.; Liu, K.; Xie, J.; Liao, L.; Wu, T.; Lin, D.; Liu, Y.; Jaramillo, T. F.; Nørskov, J. K.; Cui, Y. High-efficiency oxygen reduction to hydrogen peroxide catalysed by oxidized carbon materials. *Nat. Catal.* ***1***, 156-162 (2018).

18. Hasché, F.; Oezaslan, M.; Strasser, P.; Fellinger, T.-P. Electrocatalytic hydrogen peroxide formation on mesoporous non-metal nitrogen-doped carbon catalyst. *J. Energy Chem.* ***25***, 251-257 (2016).

19. Sun, Y.; Sinev, I.; Ju, W.; Bergmann, A.; Dresp, S.; Kühl, S.; Spöri, C.; Schmies, H.; Wang, H.; Bernsmeier, D.; Paul, B.; Schmack, R.; Kraehnert, R.; Roldan Cuenya, B.; Strasser, P. Efficient electrochemical hydrogen peroxide production from molecular oxygen on nitrogen-doped mesoporous carbon catalysts. *ACS Catal.* ***8***, 2844-2856 (2018).

20. Li, J.; Xia, Z.; Zhang, M.; Zhang, S.; Li, J.; Ma, Y.; Qu, Y. Ce-doped CoS2 pyrite with weakened O2 adsorption suppresses catalyst leaching and stabilizes electrocatalytic H2 evolution. *J. Mater. Chem. A* ***7***, 17775-17781 (2019).

21. Liu, W.; Hu, E.; Jiang, H.; Xiang, Y.; Weng, Z.; Li, M.; Fan, Q.; Yu, X.; Altman, E. I.; Wang, H. A highly active and stable hydrogen evolution catalyst based on pyrite-structured cobalt phosphosulfide. *Nat. Commun.* ***7***, 10771 (2016).

22. Mondschein, J. S.; Callejas, J. F.; Read, C. G.; Chen, J. Y. C.; Holder, C. F.; Badding, C. K.; Schaak, R. E. Crystalline Cobalt Oxide Films for Sustained Electrocatalytic Oxygen Evolution under Strongly Acidic Conditions. *Chem. Mater.* ***29***, 950-957 (2017).

23. Yang, S.; Verdaguer-Casadevall, A.; Arnarson, L.; Silvioli, L.; Čolić, V.; Frydendal, R.; Rossmeisl, J.; Chorkendorff, I.; Stephens, I. E. L. Toward the decentralized electrochemical production of H2O2: A focus on the catalysis. *ACS Catal.* ***8***, 4064-4081 (2018).

APPENDIX 4

Supplementary Information for CHAPTER 4:

Linear Paired Electrochemical Valorization of Glycerol Enabled by the Electro-Fenton Process Using a Stable Cathode[*]

---

[*] This appendix will be submitted for future publication as the Supplementary Information for the Chapter 4, in collaboration with Aurora N. Janes, R. Dominic Ross, Heike Hofstetter, J. R. Schmidt, and Song Jin.

Supplementary Figures and Tables

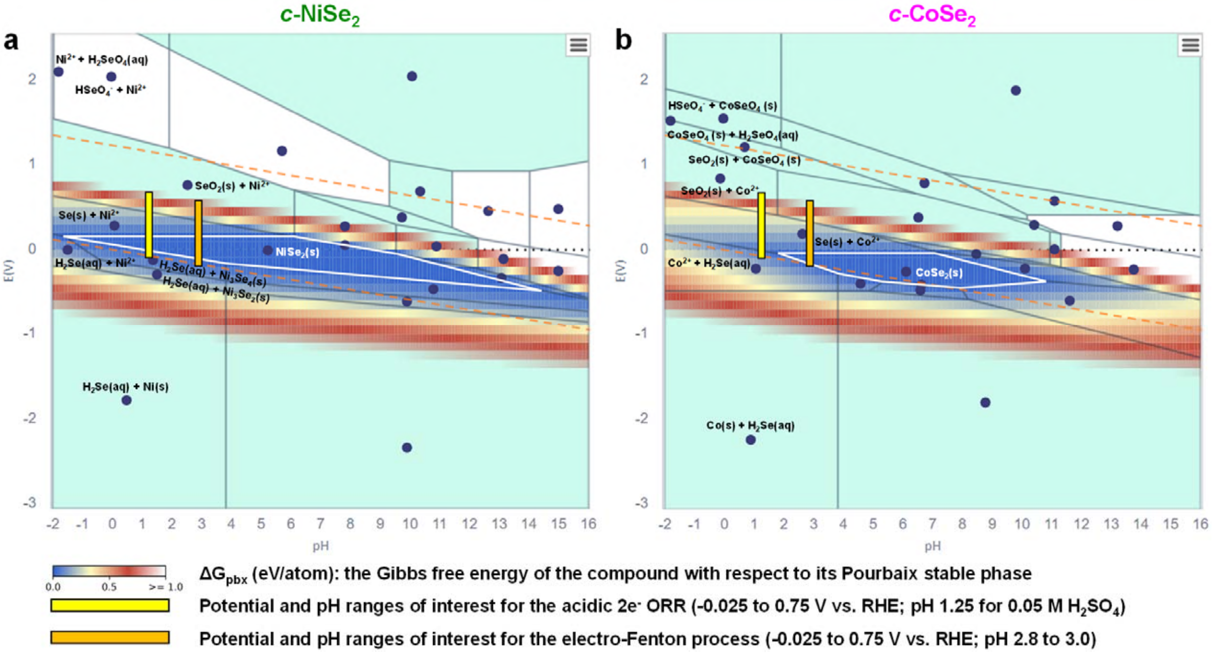

Figure A4.1. Calculated bulk Pourbaix diagrams of *c*-NiSe$_2$ and *c*-CoSe$_2$.

Calculated bulk Pourbaix diagrams of (a) *c*-NiSe$_2$ and (b) *c*-CoSe$_2$ assuming an ionic concentration of 10^{-6} mol/kg for each element of interest (59 ppb Ni, 59 ppb Co, and 79 ppb Se, which are reasonably low concentrations that can fairly reflect the acidic electrolyte solutions used in our experiments). These diagrams are adapted from the Materials Project. The multicolor gradient indicates the Gibbs free energy of the compound at a given set of potential and pH conditions with respect to its Pourbaix stable phase (ΔG_{pbx}), reflecting the electrochemical stability window of the compound. It was surmised in a previous report that materials with ΔG_{pbx} up to high values as much as 0.5 eV/atom can persist in electrochemical environments because of the energy barriers for the dissociation reactions. The solid white frame defines the thermodynamic equilibrium stability window of the compound without considering the kinetics of the dissociation reactions. The yellow and orange color bars indicate the potential and pH ranges of interest for the acidic 2e$^-$ ORR (in 0.05 M H_2SO_4) and for the Fe^{2+}-mediated electro-Fenton process (at the optimum pH of 2.8 to 3.0), respectively.

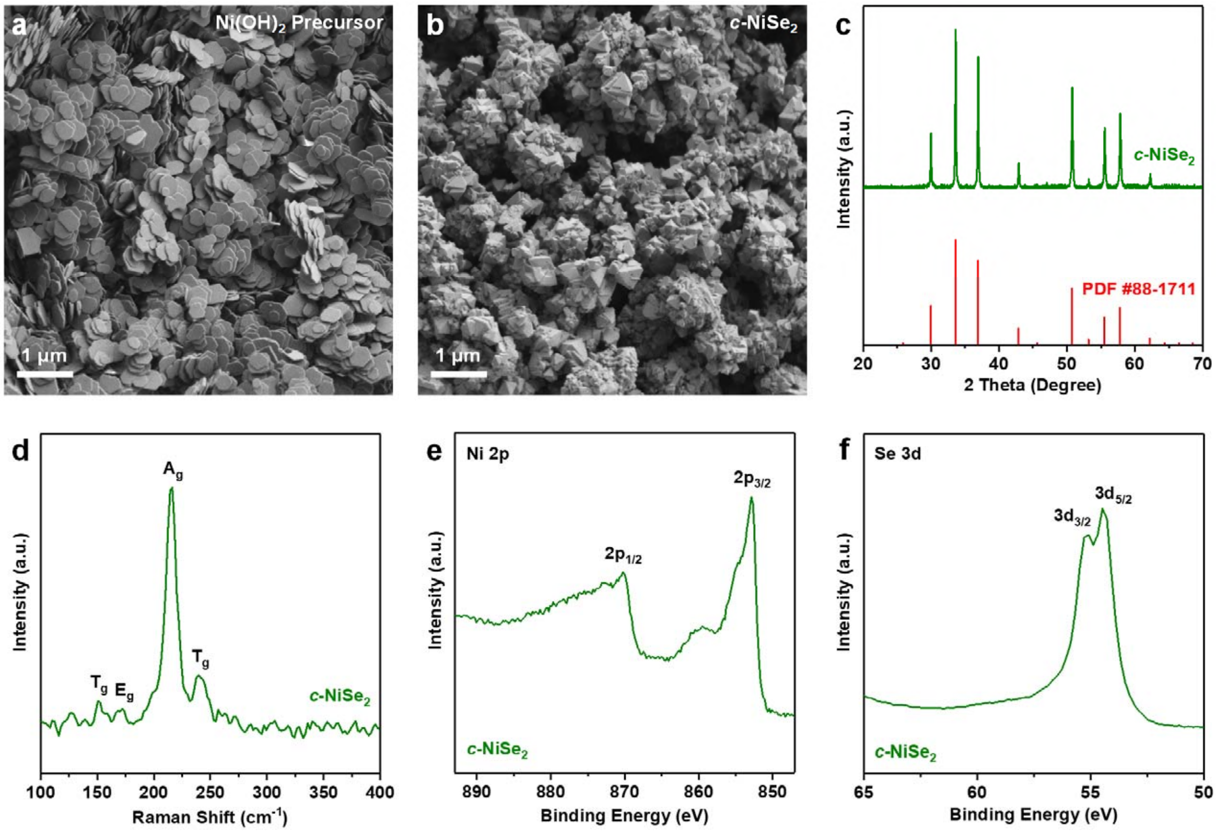

Figure A4.2. Materials characterization of *c*-NiSe$_2$ powder sample.

(a) SEM image of Ni(OH)$_2$ precursor. (b) SEM image, (c) PXRD pattern, (c) Raman spectrum, (d) Ni 2p and (e) Se 3d XPS spectra of as-synthesized *c*-NiSe$_2$ sample. The standard PXRD pattern of *c*-NiSe$_2$ (PDF #88-1711) is adapted from the International Centre for Diffraction Data (ICDD) database. From the structural characterization results, as-synthesized *c*-NiSe$_2$ sample is phase-pure and exhibits unoxidized surface.

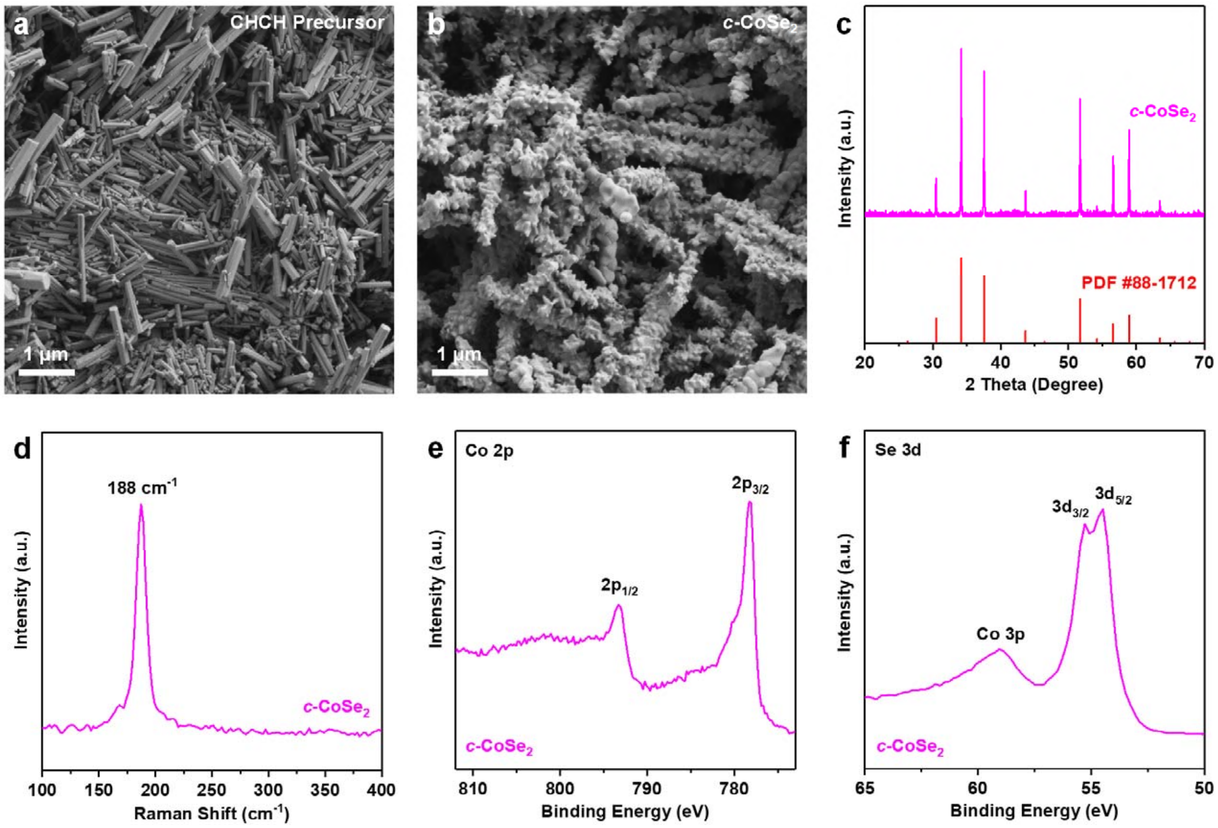

Figure A4.3. Materials characterization of *c*-CoSe$_2$ powder sample.

(a) SEM image of CHCH precursor. (b) SEM image, (c) PXRD pattern, (c) Raman spectrum, (d) Co 2p and (e) Se 3d XPS spectra of as-synthesized *c*-CoSe$_2$ sample. The standard PXRD pattern of *c*-CoSe$_2$ (PDF #88-1712) is adapted from the International Centre for Diffraction Data (ICDD) database. From the structural characterization results, as-synthesized *c*-CoSe$_2$ sample is phase-pure and exhibits unoxidized surface.

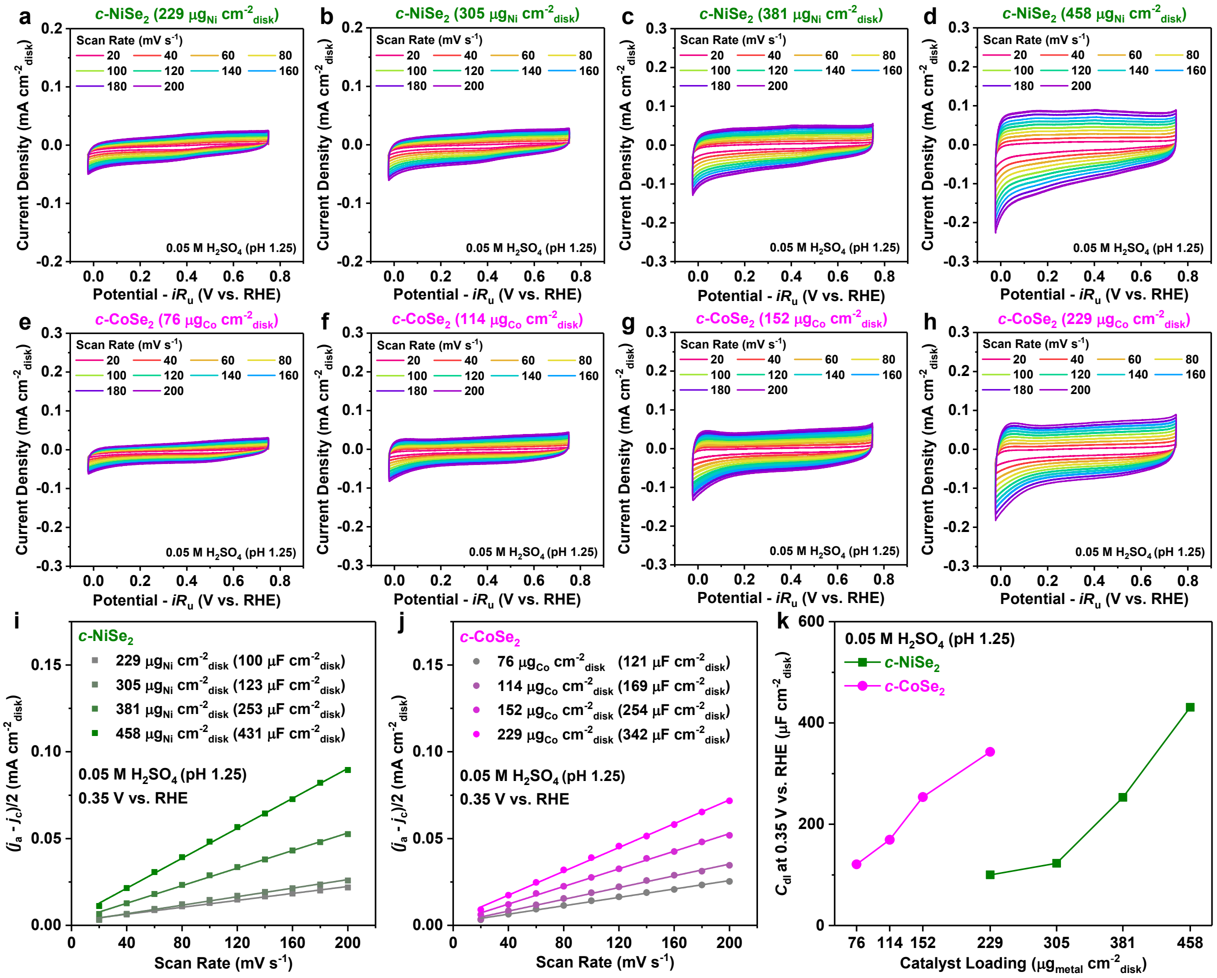

Figure A4.4. C_{dl} measurements of *c*-$NiSe_2$ and *c*-$CoSe_2$ catalysts in 0.05 M H_2SO_4 solution. Cyclic voltammograms of (a–d) *c*-$NiSe_2$ and (e–h) *c*-$CoSe_2$ catalysts with various catalyst loadings recorded in Ar-saturated 0.05 M H_2SO_4 solution (pH 1.25) at various scan rates. The corresponding C_{dl} values of (i) *c*-$NiSe_2$ and (j) *c*-$CoSe_2$ catalysts with various catalyst loadings at 0.35 V vs. RHE in Ar-saturated 0.05 M H_2SO_4 solution (pH 1.25). (k) Various catalyst loadings of *c*-$NiSe_2$ and *c*-$CoSe_2$ catalysts result in similar ranges of C_{dl} values between these two catalysts at 0.35 V vs. RHE in Ar-saturated 0.05 M H_2SO_4 solution (pH 1.25).

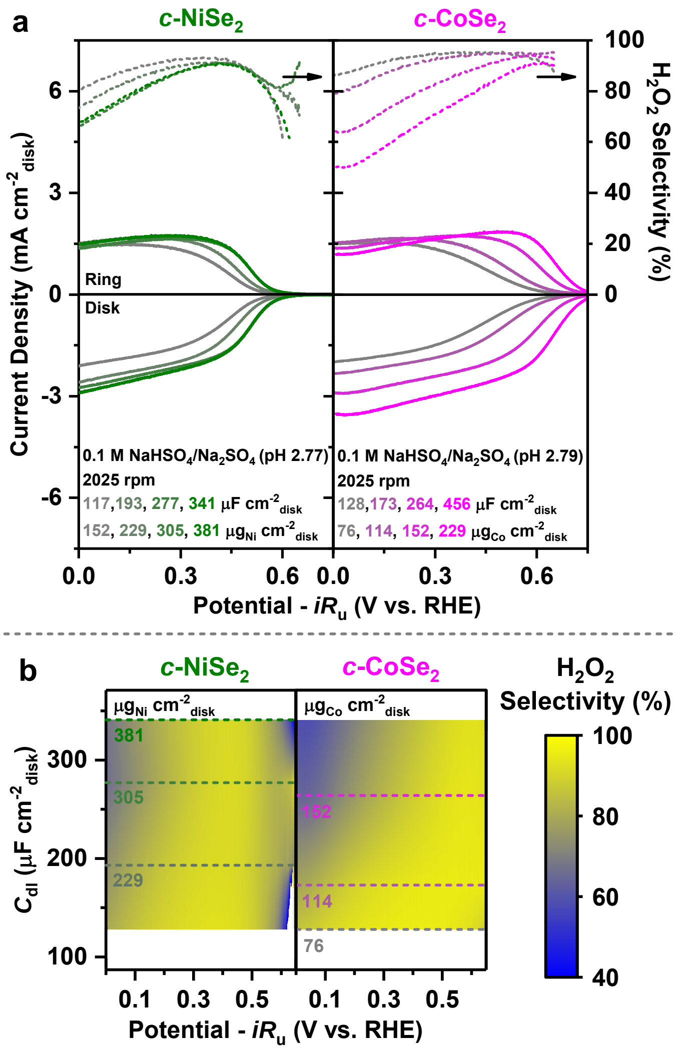

Figure A4.5. Comparisons of the H_2O_2 selectivity as a function of potential and catalyst loading for *c*-$NiSe_2$ vs. *c*-$CoSe_2$ in 0.1 M $NaHSO_4$/Na_2SO_4 buffer solution.

(a) RRDE voltammograms recorded at 2025 rpm and (b) the corresponding H_2O_2 selectivity of the *c*-$NiSe_2$ (left) and *c*-$CoSe_2$ (right) catalyst with various catalyst loadings in O_2-saturated 0.1 M $NaHSO_4$/Na_2SO_4 buffer solution (pH ~2.8, relevant to the electro-Fenton process).

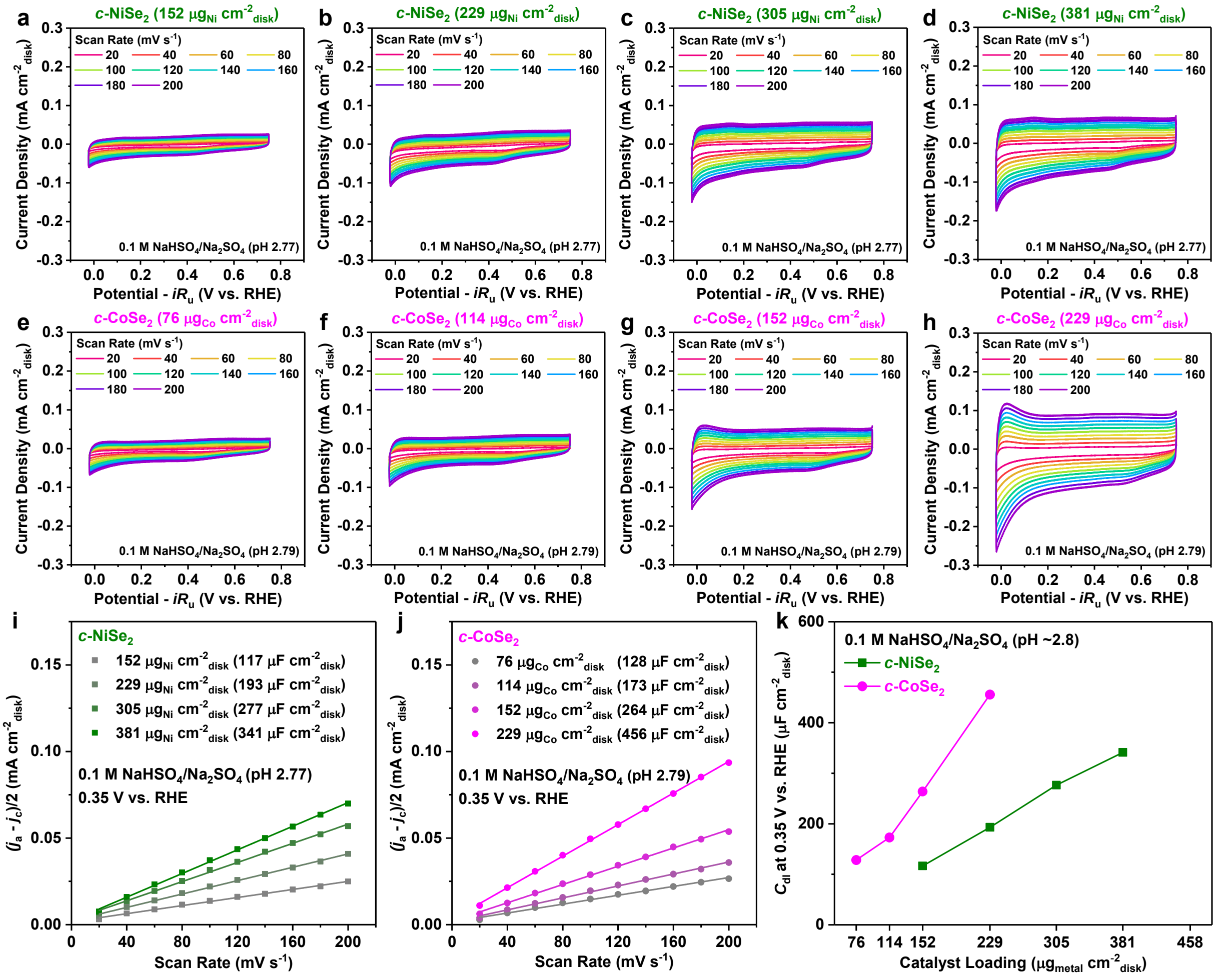

Figure A4.6. C_{dl} measurements of *c*-$NiSe_2$ and *c*-$CoSe_2$ catalysts in 0.1 M $NaHSO_4/Na_2SO_4$ buffer solution.

Cyclic voltammograms of (a–d) *c*-$NiSe_2$ and (e–h) *c*-$CoSe_2$ catalysts with various catalyst loadings recorded in Ar-saturated 0.1 M $NaHSO_4/Na_2SO_4$ buffer solution (pH ~2.8) at various scan rates. The corresponding C_{dl} values of (i) *c*-$NiSe_2$ and (j) *c*-$CoSe_2$ catalysts with various catalyst loadings at 0.35 V vs. RHE in Ar-saturated 0.1 M $NaHSO_4/Na_2SO_4$ buffer solution (pH ~2.8). (k) Various catalyst loadings of *c*-$NiSe_2$ and *c*-$CoSe_2$ catalysts result in similar ranges of C_{dl} values between these two catalysts at 0.35 V vs. RHE in Ar-saturated 0.1 M $NaHSO_4/Na_2SO_4$ buffer solution (pH ~2.8).

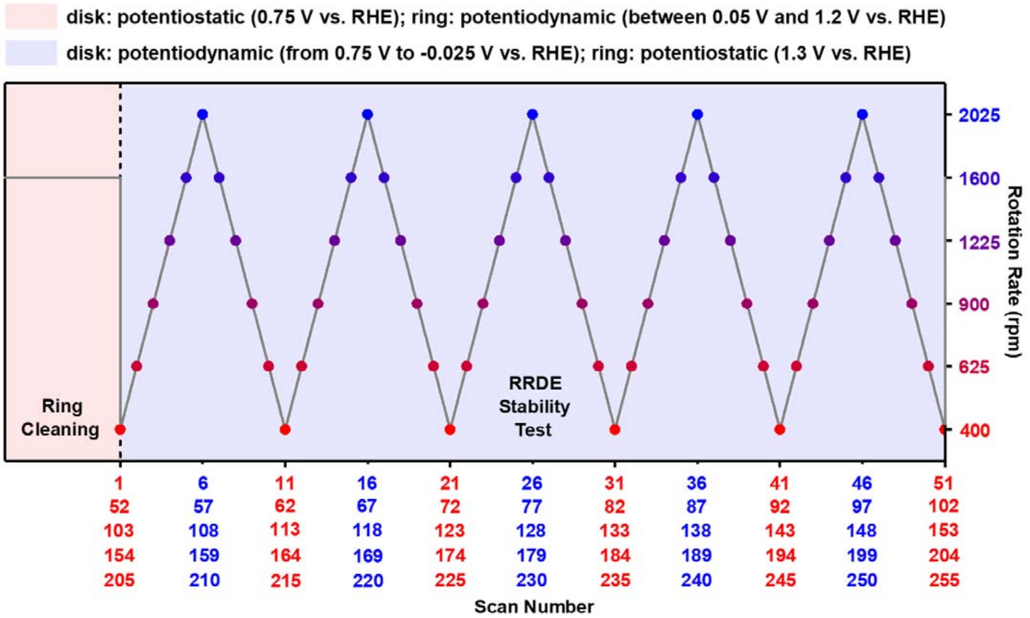

Figure A4.7. Protocols for the RRDE stability tests of *c*-$NiSe_2$ and *c*-$CoSe_2$ catalysts.

Step 1 (red shaded region): In O_2-saturated electrolyte solution, the Pt ring electrode was electrochemically cleaned by running cyclic voltammetry between 0.05 V and 1.2 V vs. RHE (without *iR*-correction) at the scan rate of 100 mV s^{-1} and the rotation rate of 1600 rpm for 10 cycles, meanwhile holding the catalyst-coated disk electrode at 0.75 V vs. RHE. The purpose of this step is to remove PtO_x from the Pt ring electrode surface.[1,2]

Step 2 (blue shaded region): In O_2-saturated electrolyte solution, the catalyst-coated disk electrode was linearly swept from 0.75 V to -0.025 vs. RHE (without *iR*-correction) at the scan rate of 50 mV s^{-1} and a constant rotation rate (400, 625, 900, 1225, 1600, or 2025 rpm) to drive the acidic $2e^-$ ORR, meanwhile holding the Pt ring electrode at 1.3 V vs. RHE to detect the H_2O_2 production. The rotation rate was sequentially changed between scans.

Overall procedure: Since holding the Pt ring electrode at 1.3 V vs. RHE for an extended period of time in *Step 2* would result in the formation of the surface PtO_x,[1,2] the Pt ring electrode was periodically cleaned during the RRDE stability tests using the protocol described in *Step 1*. Thus, the RRDE stability tests were performed by alternating between *Step 1* and *Step 2*, leading to overall 255 linear sweep voltammetry scans on the disk electrode over the entire course of ~4.0 h. The catalyst stability was described by the disk potential required to deliver a disk current density (j_{disk}) or peroxide current density (j_{peroxide}) of 0.5 mA $cm^{-2}{}_{\text{disk}}$ at 2025 rpm (Figures A4.8 and A4.9).

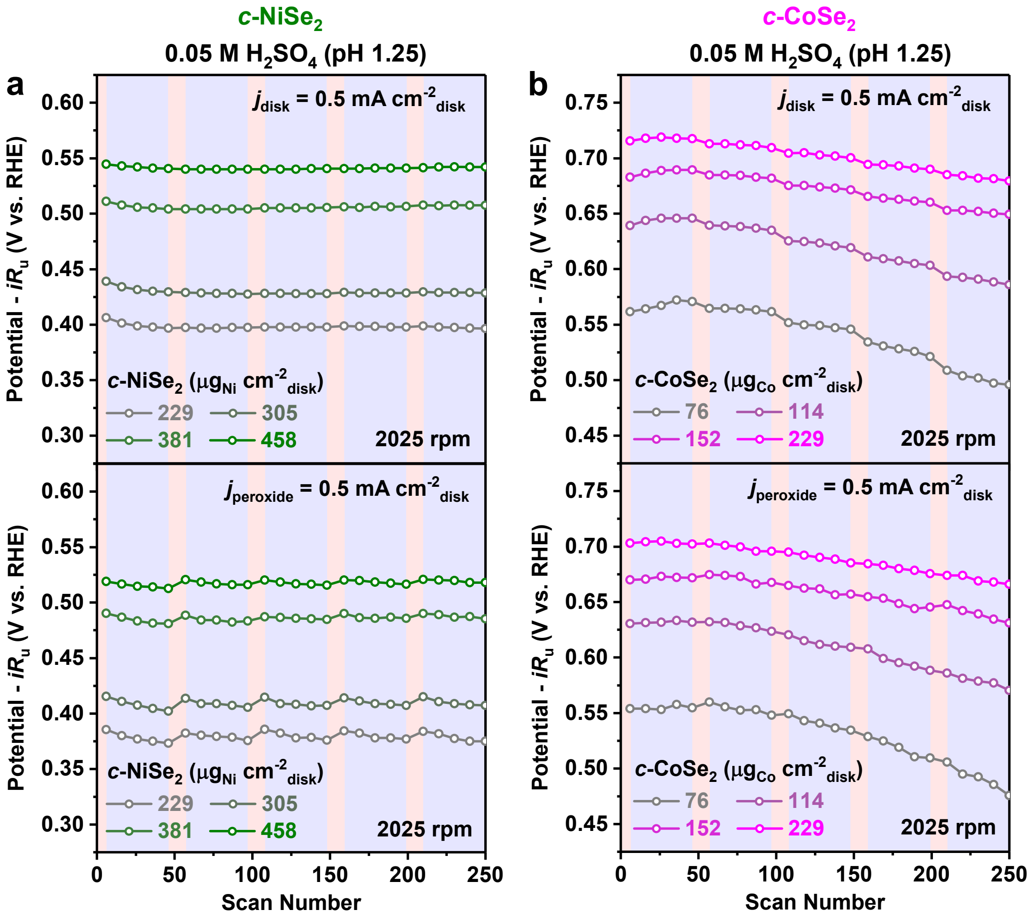

Figure A4.8. The catalyst stability of *c*-NiSe₂ and *c*-CoSe₂ during the RRDE stability tests in 0.05 M H_2SO_4 solution.

The catalyst stability of (a) *c*-$NiSe_2$ and (b) *c*-$CoSe_2$ with various catalyst loadings described by the disk potential required to deliver a disk current density (j_{disk}, top) or peroxide current density ($j_{peroxide}$, bottom) of 0.5 mA cm^{-2}_{disk} at 2025 rpm during the RRDE stability tests in O_2-saturated 0.05 M H_2SO_4 solution (pH 1.25). The red shaded regions refer to the electrochemical cleaning of the Pt ring electrode, and the blue shaded regions refer to the linear sweep voltammetry of the catalyst-coated disk electrode (Figure A4.7). The disk potential of *c*-$NiSe_2$ remained stable to reach the same magnitude of j_{disk} or $j_{peroxide}$ throughout the tests (panel a), whereas that of *c*-$CoSe_2$ cathodically shifted over the scans (panel b).

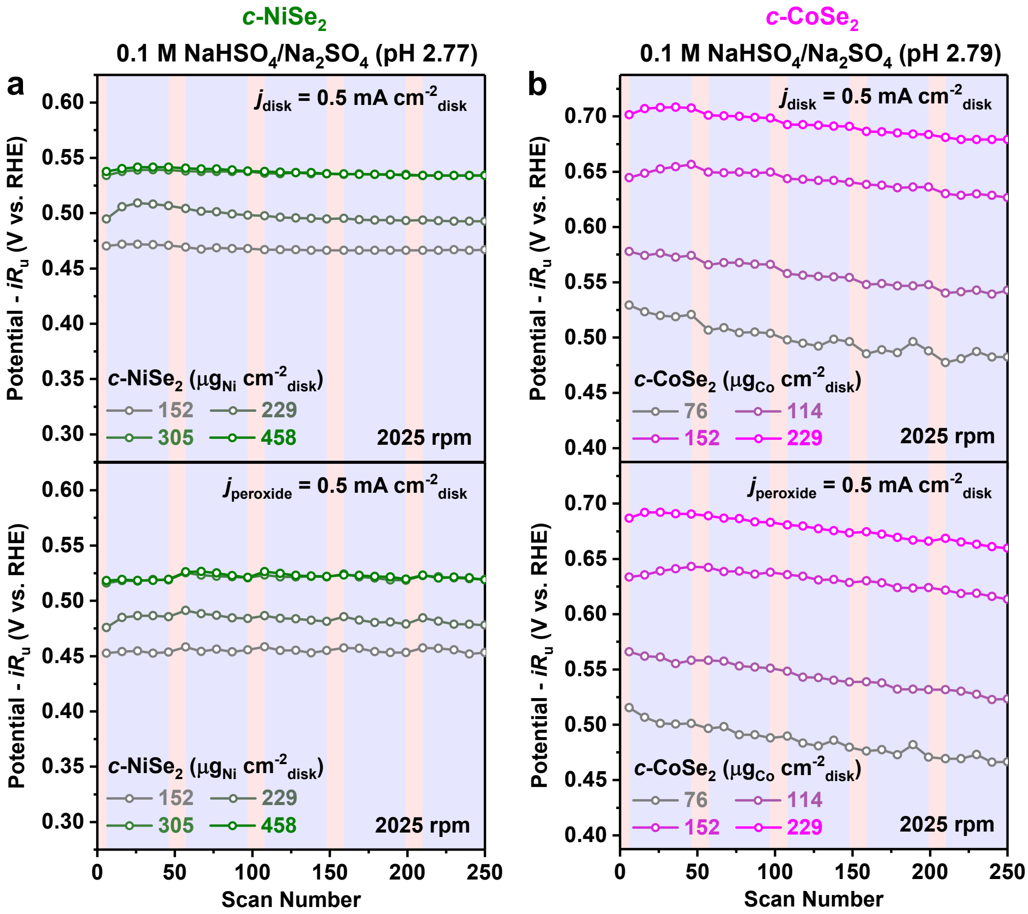

Figure A4.9. The catalyst stability of *c*-NiSe$_2$ and *c*-CoSe$_2$ during the RRDE stability tests in 0.1 M NaHSO$_4$/Na$_2$SO$_4$ buffer solution.

The catalyst stability of (a) *c*-NiSe$_2$ and (b) *c*-CoSe$_2$ with various catalyst loadings described by the disk potential required to deliver a disk current density (j_{disk}, top) or peroxide current density ($j_{peroxide}$, bottom) of 0.5 mA cm$^{-2}_{disk}$ at 2025 rpm during the RRDE stability tests in O$_2$-saturated 0.1 M NaHSO$_4$/Na$_2$SO$_4$ buffer solution (pH ~2.8, relevant to the electro-Fenton process). The red shaded regions refer to the electrochemical cleaning of the Pt ring electrode, and the blue shaded regions refer to the linear sweep voltammetry of the catalyst-coated disk electrode (Figure A4.7). The disk potential of *c*-NiSe$_2$ remained stable to reach the same magnitude of j_{disk} or $j_{peroxide}$ throughout the tests (panel a), whereas that of *c*-CoSe$_2$ cathodically shifted over the scans (panel b).

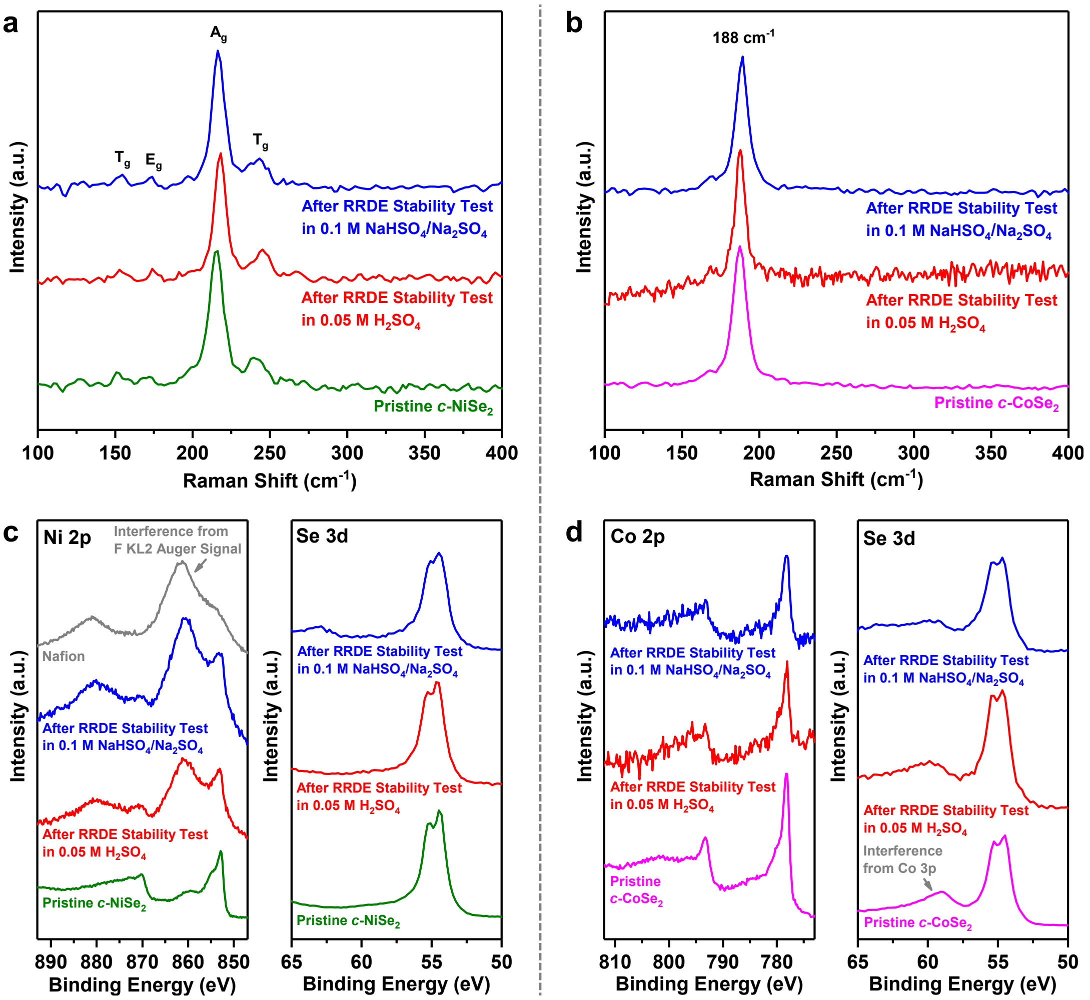

Figure A4.10. Raman and XPS characterizations of *c*-$NiSe_2$ and *c*-$CoSe_2$ before and after the RRDE stability tests.

(a,b) Raman spectra of (a) *c*-$NiSe_2$ and (b) *c*-$CoSe_2$ catalysts before and after RRDE stability tests in O_2-saturated 0.05 M H_2SO_4 (pH 1.25) or 0.1 M $NaHSO_4$/Na_2SO_4 (pH ~2.8), showing no change after electrochemical testing. (c,d) X-ray photoelectron spectra of (c) *c*-$NiSe_2$ and (d) *c*-$CoSe_2$ catalysts before and after RRDE stability tests in O_2-saturated 0.05 M H_2SO_4 (pH 1.25) or 0.1 M $NaHSO_4$/Na_2SO_4 (pH ~2.8). The Ni 2p spectra of the spent *c*-$NiSe_2$ catalyst were interfered by the F KL2 Auger signal because of the presence of Nafion in the recovered catalyst (panel c, left). Since the Se 3d spectra of the spent *c*-$NiSe_2$ catalyst (panel c, right) and the Co 2p and Se 3d spectra of the spent *c*-$CoSe_2$ catalyst (panel d) showed no change after electrochemical testing, it can be concluded that the surface chemical states of the spent *c*-$NiSe_2$ and *c*-$CoSe_2$ catalysts remained the same as those of the pristine samples.

Table A4.1. ICP-MS analyses of the spent electrolytes after the RRDE stability tests of *c*-$NiSe_2$ and *c*-$CoSe_2$ catalysts.

ICP-MS analyses of the spent electrolytes after the RRDE stability tests of *c*-$NiSe_2$ and *c*-$CoSe_2$ catalysts at various catalyst loadings in 0.05 M H_2SO_4 (pH 1.25) and 0.1 M $NaHSO_4/Na_2SO_4$ (pH ~2.8) solutions.

Electrolyte	Catalyst	Catalyst Loading (μg_{metal} cm^{-2}_{disk})	Electrolyte Volume (mL)	Time (h)	[Metal] (ppb)	[Se] (ppb)	Normalized Metal Leaching Rate (μmol_{metal} $g_{catalyst}^{-1}$ h^{-1})	Normalized Se Leaching Rate (μmol_{Se} $g_{catalyst}^{-1}$ h^{-1})
O_2-saturated 0.05 M H_2SO_4 (pH 1.25)	*c*-$NiSe_2$	229	41.0	4.0	7.75	2.75	12.8	3.38
		305	42.5	3.9	10.6	3.74	13.8	3.62
		381	41.0	4.0	17.2	9.02	17.0	6.63
		458	41.5	4.0	30.5	15.4	25.2	9.45
		-	-	-	-	-	Avg. ± Std. Dev. = **17.2 ± 5.6**	Avg. ± Std. Dev. = **5.77 ± 2.86**
	c-$CoSe_2$	76	45.0	4.1	2.93	5.31	15.5	21.0
		114	42.0	4.0	5.69	11.0	19.0	27.6
		152	43.0	4.2	8.91	19.6	21.9	35.9
		229	44.5	4.1	13.6	27.8	23.5	35.9
		-	-	-	-	-	Avg. ± Std. Dev. = **20.0 ± 3.5**	Avg. ± Std. Dev. = **30.1 ± 7.2**
O_2-saturated 0.1 M $NaHSO_4/Na_2SO_4$ (pH ~2.8)	*c*-$NiSe_2$	152	42.5	4.1	2.44	2.15	6.15	4.03
		229	41.5	4.0	3.62	3.06	6.06	3.82
		305	41.0	4.0	6.15	6.07	7.54	5.53
		381	43.0	4.0	6.55	6.22	6.79	4.79
		-	-	-	-	-	Avg. ± Std. Dev. = **6.64 ± 0.68**	Avg. ± Std. Dev. = **4.54 ± 0.78**
	c-$CoSe_2$	76	41.5	4.0	3.37	6.32	17.0	23.9
		114	40.0	4.0	4.98	8.42	16.1	20.4
		152	41.5	4.0	9.62	19.2	24.1	36.0
		229	41.5	4.0	22.8	53.6	38.5	67.6
		-	-	-	-	-	Avg. ± Std. Dev. = **23.9 ± 10.3**	Avg. ± Std. Dev. = **37.0 ± 21.5**

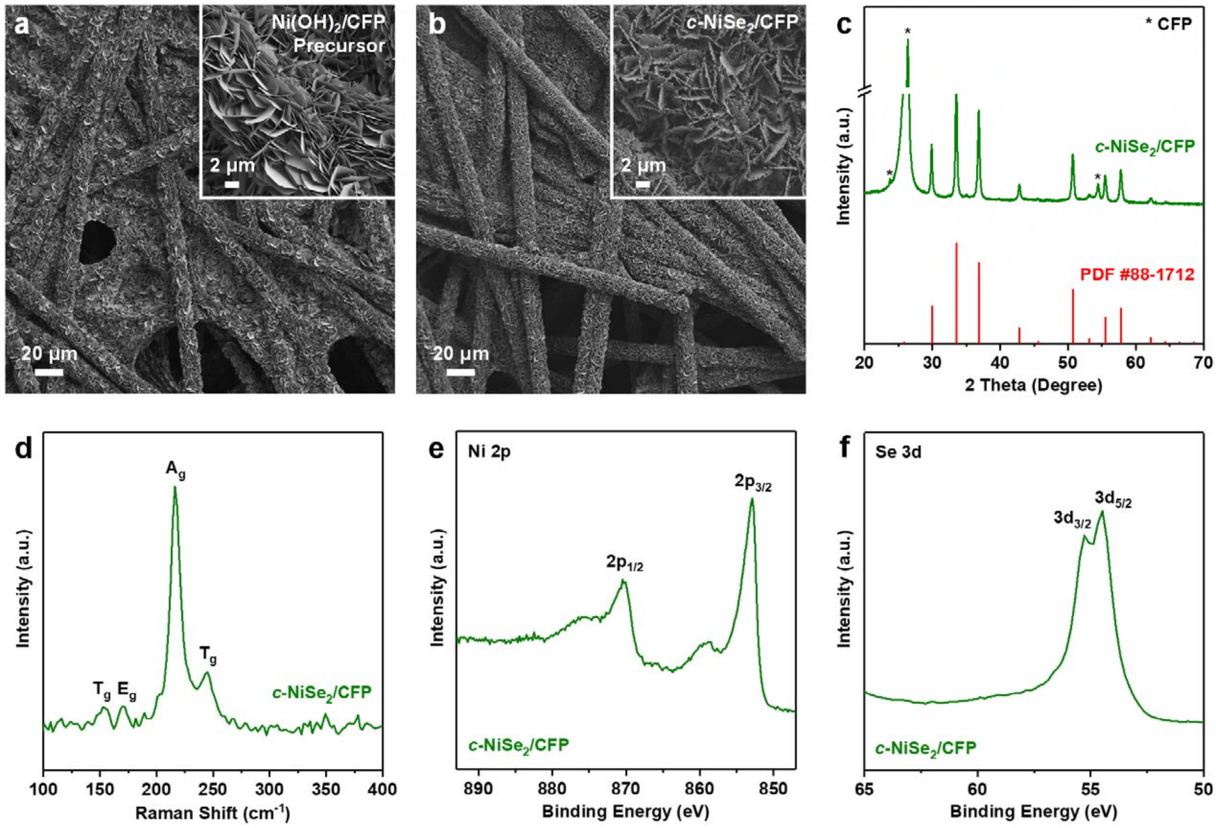

Figure A4.11. Materials Characterization of *c*-NiSe$_2$/CFP.

(a) SEM image of Ni(OH)$_2$/CFP precursor. (b) SEM image, (c) PXRD pattern, (c) Raman spectrum, (d) Ni 2p and (e) Se 3d XPS spectra of as-synthesized *c*-NiSe$_2$/CFP sample. The asterisks in (c) indicate the PXRD peaks of the CFP substrate. The standard PXRD pattern of *c*-NiSe$_2$ (PDF #88-1711) is adapted from the International Centre for Diffraction Data (ICDD) database. From the structural characterization results, as-synthesized *c*-NiSe$_2$/CFP sample is phase-pure and exhibits unoxidized surface.

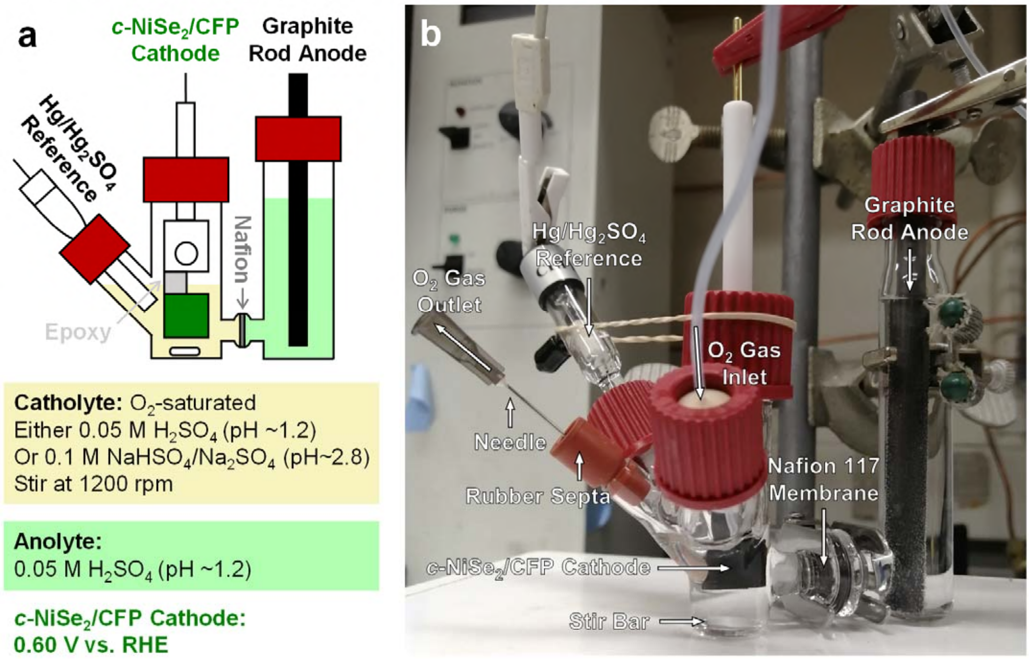

Two-Compartment Three-Electrode H-Cell for Bulk Electrosynthesis of H_2O_2 in Acidic Solution

Figure A4.12. Schematic and digital photograph of the two-compartment three-electrode setup for bulk electrosynthesis of H_2O_2 in acidic solution.

(a) Schematic and (b) digital photograph of the two-compartment three-electrode setup for bulk electrosynthesis of H_2O_2 in acidic solution. Nafion 117 membrane was used to separate the two compartments to avoid the oxidation of H_2O_2 product on the anode. A minimal volume (4 mL) of catholyte was used and vigorously stirred at 1200 rpm to achieve higher H_2O_2 concentrations under facilitated mass transfer of O_2 gas. A blanket of O_2 gas was maintained over the surface of O_2-saturated catholyte during H_2O_2 bulk electrosynthesis. A rubber septum punctured with a syringe needle served as the gas outlet, which was only removed when a small aliquot of catholyte was sampled for chemical detection of H_2O_2 product and was otherwise capped to minimize the evaporation of catholyte during H_2O_2 bulk electrosynthesis.

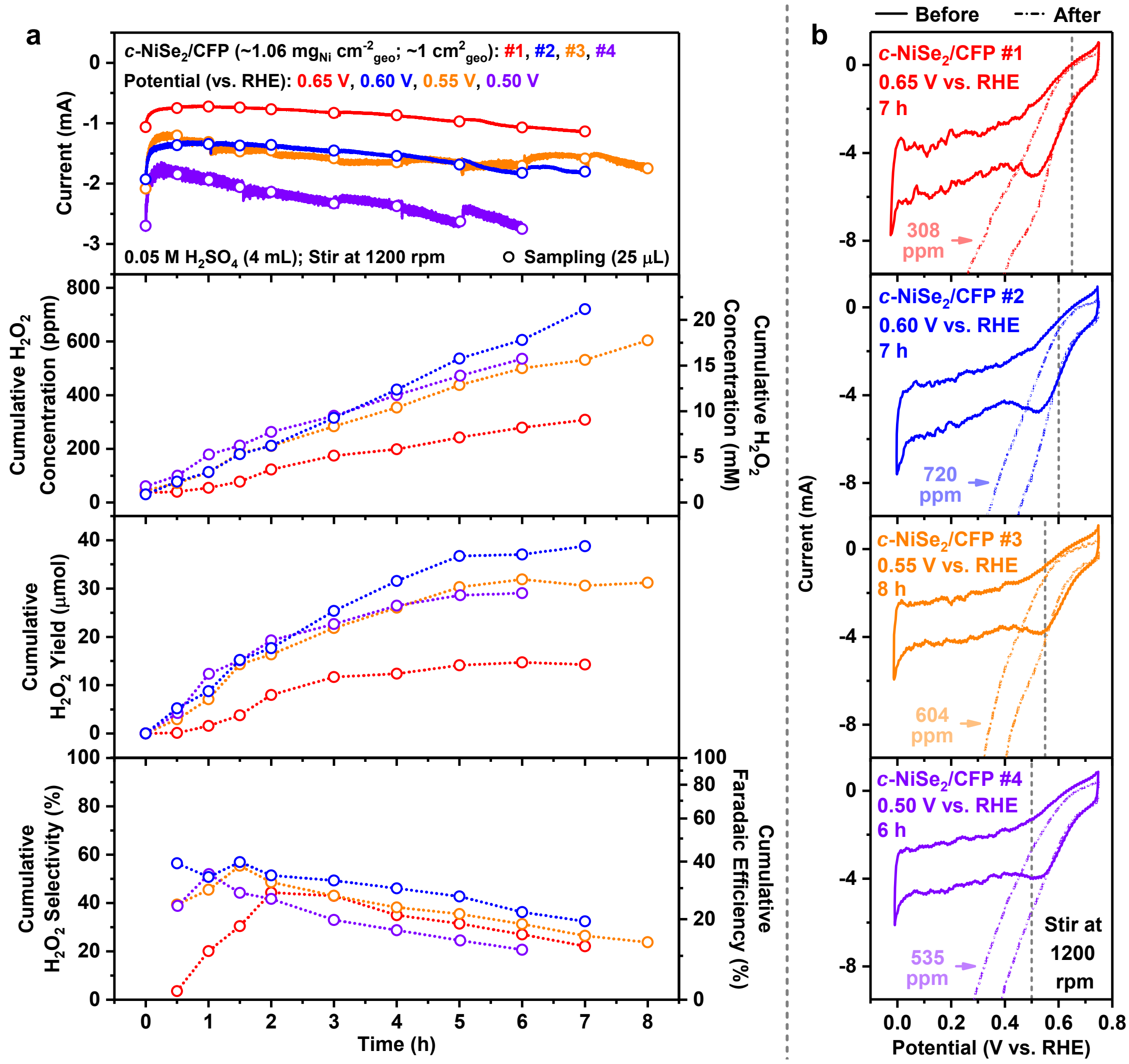

Figure A4.13. Bulk electrosynthesis of H_2O_2 in 0.05 M H_2SO_4 using *c*-$NiSe_2$/CFP electrodes operated at different applied potentials.

Bulk electrosynthesis of H_2O_2 in O_2-saturated 0.05 M H_2SO_4 solution (pH 1.23, 4 mL, stirred at 1200 rpm) using four *c*-$NiSe_2$/CFP electrodes (~1.06 mg_{Ni} cm^{-2}_{geo}, ~1 cm^2_{geo}) operated at four different fixed applied potentials (0.65 V, 0.60 V, 0.55 V, 0.50 V vs. RHE). (a) Chronoamperometry curves, cumulative H_2O_2 concentration, cumulative H_2O_2 yield, cumulative H_2O_2 selectivity and Faradaic efficiency as a function of time. Comparisons of the cumulative H_2O_2 yield and H_2O_2 selectivity at the 6-hour mark of each trial are shown in Figure 4.2d in the Chapter 4. (b) Cyclic voltammograms of the *c*-$NiSe_2$/CFP electrodes recorded before and after each trial of the H_2O_2 bulk electrosynthesis in O_2-saturated 0.05 M H_2SO_4 solution (stirred at 1200 rpm).

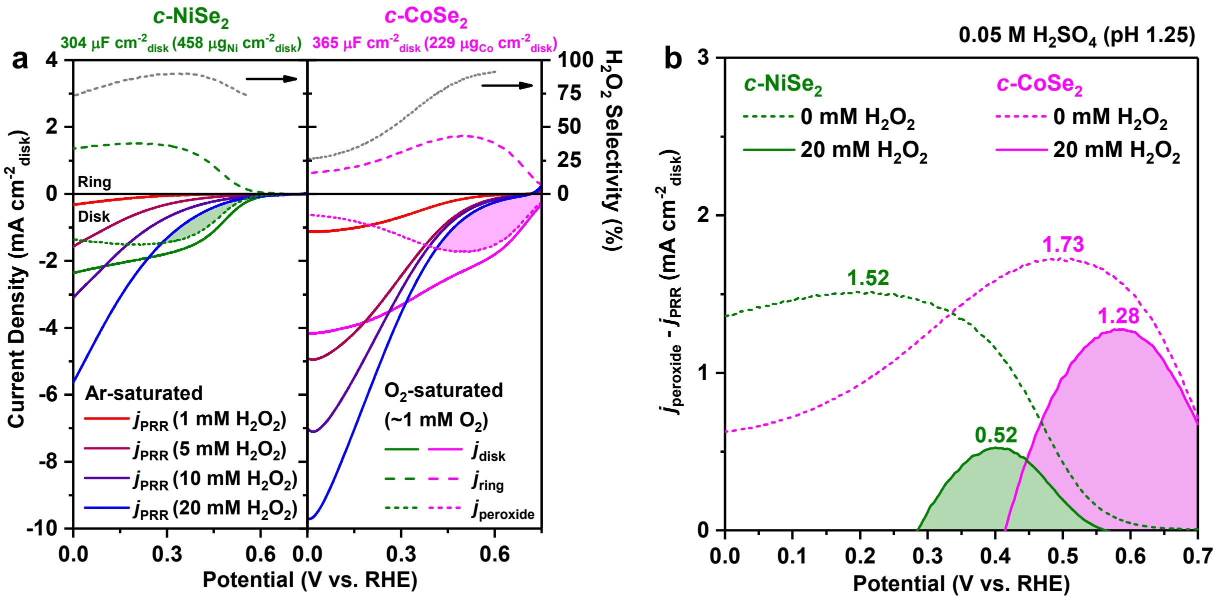

Figure A4.14. RRDE studies of H_2O_2 electroreduction on *c*-$NiSe_2$ and *c*-$CoSe_2$ catalysts in 0.05 M H_2SO_4 solution.

(a) RRDE voltammograms of *c*-$NiSe_2$ (left, 458 μg_{Ni} $cm^{-2}{}_{disk}$) and *c*-$CoSe_2$ (right, 229 μg_{Co} $cm^{-2}{}_{disk}$) catalysts recorded at 1600 rpm in O_2-saturated 0.05 M H_2SO_4 solution (pH 1.25) were performed to study the 2e$^-$ ORR (j_{disk}: disk current density; j_{ring}: ring current density; $j_{peroxide}$: peroxide current density). C_{dl} values of *c*-$NiSe_2$ (304 μF $cm^{-2}{}_{disk}$) and *c*-$CoSe_2$ (365 μF $cm^{-2}{}_{disk}$) was evaluated at 0.35 V vs. RHE in Ar-saturated 0.05 M H_2SO_4 solution (pH 1.25). Linear sweep voltammograms of the catalyst-coated disk electrode recorded at 1600 rpm in Ar-saturated 0.05 M H_2SO_4 solution (pH 1.25) containing 1 mM, 5 mM, 10 mM, or 20 mM H_2O_2 were performed to study the electroreduction of H_2O_2 (j_{PRR}: current density of the hydrogen peroxide reduction reaction). The shaded regions (green: *c*-$NiSe_2$; magenta: *c*-$CoSe_2$) defined the potential range where the magnitude of $j_{peroxide}$ under O_2 saturation (~1 mM O_2) was greater than that of j_{PRR} under 20 mM H_2O_2. (b) $j_{peroxide} - j_{PRR}$ plotted against potential under 0 mM H_2O_2 (where j_{PRR} = 0) or 20 mM H_2O_2. The shaded regions in (b) had the same physical meanings as those in (a). Compared to *c*-$CoSe_2$, the H_2O_2 production on *c*-$NiSe_2$ was more affected by the H_2O_2 electroreduction, as reflected by the greater decrease in the peak value of $j_{peroxide} - j_{PRR}$ when the H_2O_2 concentration increased from 0 mM to 20 mM.

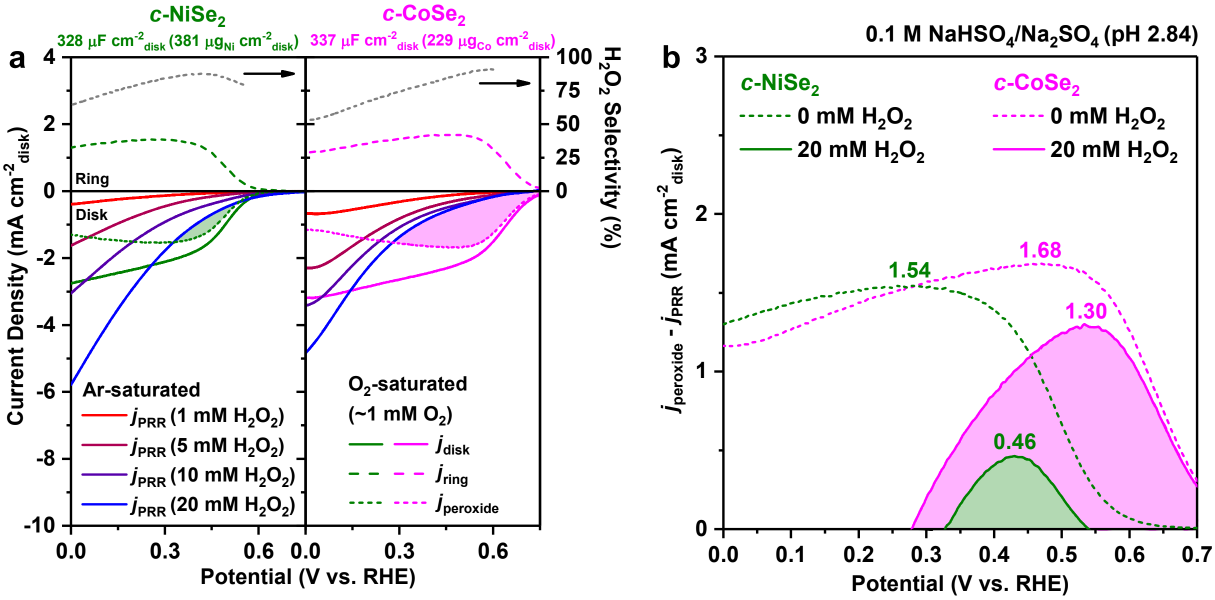

Figure A4.15. RRDE studies of H_2O_2 electroreduction on *c*-$NiSe_2$ and *c*-$CoSe_2$ catalysts in 0.1 M $NaHSO_4$/Na_2SO_4 buffer solution.

(a) RRDE voltammograms of *c*-$NiSe_2$ (left, 381 μg_{Ni} cm^{-2}_{disk}) and *c*-$CoSe_2$ (right, 229 μg_{Co} cm^{-2}_{disk}) catalysts recorded at 1600 rpm in O_2-saturated 0.1 M $NaHSO_4$/ Na_2SO_4 solution (pH 2.84) were performed to study the $2e^-$ ORR (j_{disk}: disk current density; j_{ring}: ring current density; $j_{peroxide}$: peroxide current density). C_{dl} values of *c*-$NiSe_2$ (328 µF cm^{-2}_{disk}) and *c*-$CoSe_2$ (337 µF cm^{-2}_{disk}) was evaluated at 0.35 V vs. RHE in Ar-saturated 0.1 M $NaHSO_4$/ Na_2SO_4 solution (pH 2.84). Linear sweep voltammograms of the catalyst-coated disk electrode recorded at 1600 rpm in Ar-saturated 0.1 M $NaHSO_4$/Na_2SO_4 solution (pH 2.84) containing 1 mM, 5 mM, 10 mM, or 20 mM H_2O_2 were performed to study the electroreduction of H_2O_2 (j_{PRR}: current density of the hydrogen peroxide reduction reaction). The shaded regions (green: *c*-$NiSe_2$; magenta: *c*-$CoSe_2$) defined the potential range where the magnitude of $j_{peroxide}$ under O_2 saturation (~1 mM O_2) was greater than that of j_{PRR} under 20 mM H_2O_2. (b) $j_{peroxide} - j_{PRR}$ plotted against potential under 0 mM H_2O_2 (where $j_{PRR} = 0$) or 20 mM H_2O_2. The shaded regions in (b) had the same physical meanings as those in (a). Compared to *c*-$CoSe_2$, the H_2O_2 production on *c*-$NiSe_2$ was more affected by the H_2O_2 electroreduction, as reflected by the greater decrease in the peak value of $j_{peroxide} - j_{PRR}$ when the H_2O_2 concentration increased from 0 mM to 20 mM.

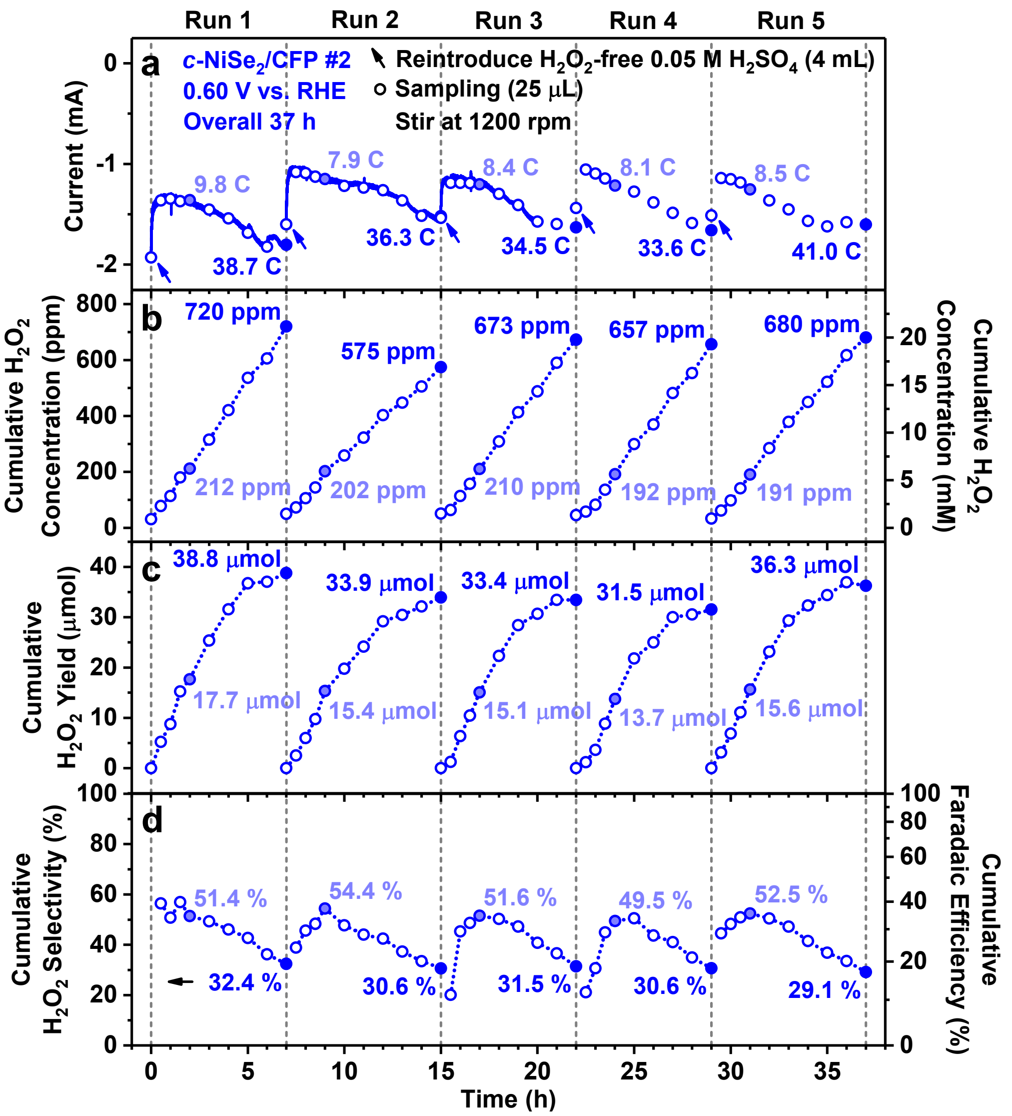

Figure A4.16. Bulk electrosynthesis of H_2O_2 in 0.05 M H_2SO_4 using *c*-NiSe$_2$/CFP operated at the optimum potential of 0.60 V vs. RHE.

Bulk electrosynthesis of H_2O_2 in O_2-saturated 0.05 M H_2SO_4 solution (pH 1.23, 4 mL, stirred at 1200 rpm) at the optimum potential of 0.60 V vs. RHE using one *c*-NiSe$_2$/CFP electrode (~1.06 mg$_{Ni}$ cm$^{-2}_{geo}$, ~1 cm$^{2}_{geo}$) repeatedly for five consecutive runs and overall 37 hours. (a) Chronoamperometry curve. (b) Cumulative H_2O_2 concentration, (c) cumulative H_2O_2 yield, (d) cumulative H_2O_2 selectivity and Faradaic efficiency as a function of time. Fresh H_2O_2-free electrolyte solution was replaced into the cathode compartment between runs. Comparisons of the cumulative H_2O_2 yield and H_2O_2 selectivity at the 2-hour mark and the end of each run are shown in Figure 4.2e in the Chapter 4.

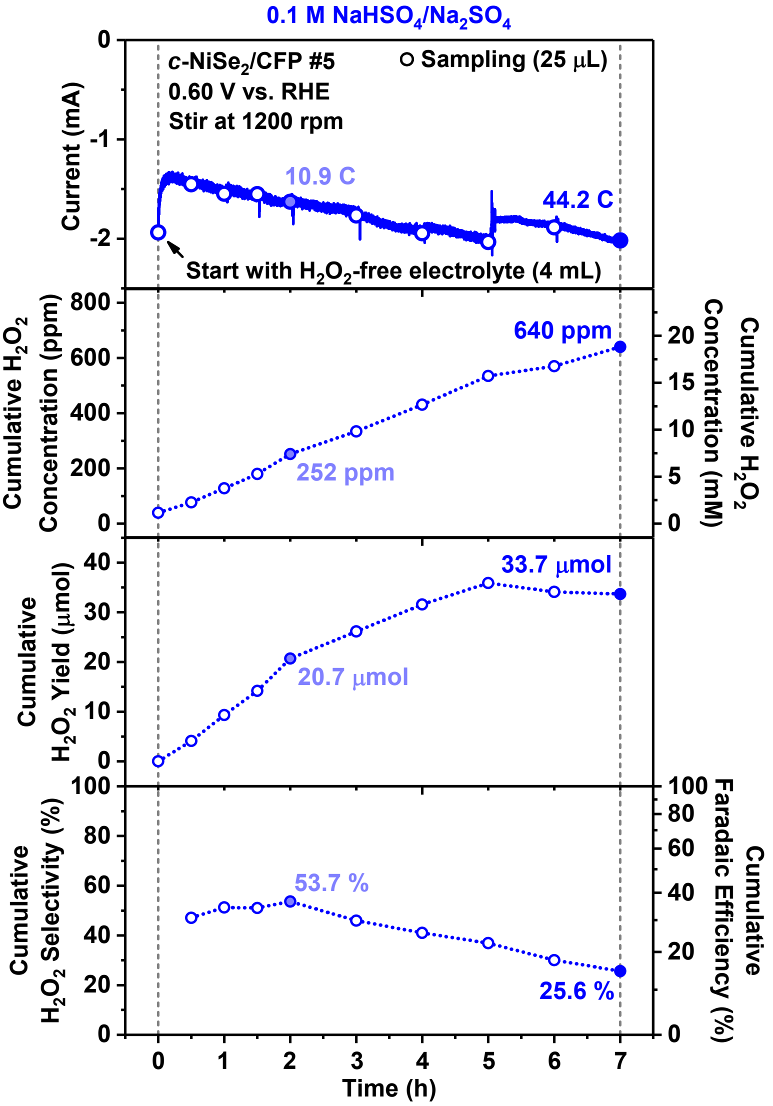

Figure A4.17. Bulk electrosynthesis of H_2O_2 in 0.1 M $NaHSO_4/Na_2SO_4$ using *c*-$NiSe_2$/CFP operated at 0.60 V vs. RHE.

Bulk electrosynthesis of H_2O_2 in O_2-saturated 0.1 M $NaHSO_4/Na_2SO_4$ solution (pH 2.84, 4 mL, stirred at 1200 rpm) using *c*-$NiSe_2$/CFP electrode (~1.06 mg_{Ni} cm^{-2}_{geo}, ~1 cm^2_{geo}) operated at 0.60 vs. RHE. (a) Chronoamperometry curve. (b) Cumulative H_2O_2 concentration, (c) cumulative H_2O_2 yield, (d) cumulative H_2O_2 selectivity and Faradaic efficiency as a function of time.

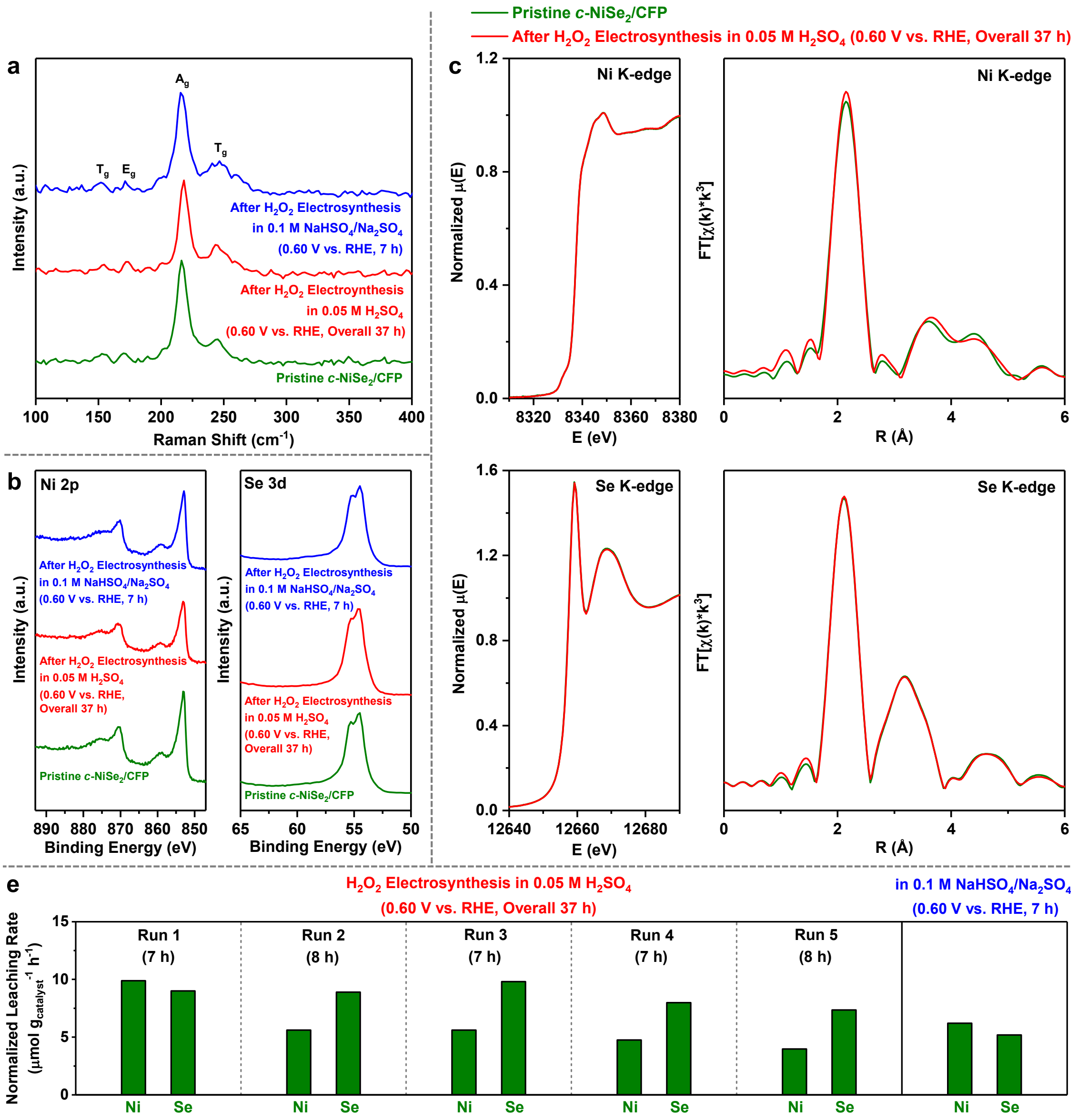

Figure A4.18. Characterization of the tested c-$NiSe_2$/CFP after H_2O_2 bulk electrosynthesis. (a) Raman spectra and (b) X-ray photoelectron spectra of c-$NiSe_2$/CFP before and after H_2O_2 bulk electrosynthesis at 0.60 V vs. RHE in O_2-saturated 0.05 M H_2SO_4 (pH 1.23) or 0.1 M $NaHSO_4/Na_2SO_4$ (pH 2.84). (c) Ni K-edge and Se K-edge X-ray absorption near edge structure (XANES, left) and extended X-ray absorption fine structure (EXAFS, right) spectra of c-$NiSe_2$/CFP before and after H_2O_2 bulk electrosynthesis at 0.60 V vs. RHE in O_2-saturated 0.05 M H_2SO_4, which almost overlapped. (e) Normalized nickel and selenium leaching rates of c-$NiSe_2$/CFP (~1.06 μg_{Ni} cm^{-2}_{geo}, ~1 cm^2_{geo}) during H_2O_2 bulk electrosynthesis at 0.60 V vs. RHE in O_2-saturated 0.05 M H_2SO_4 or 0.1 M $NaHSO_4/Na_2SO_4$.

Half-Cell Studies of the Electro-Fenton Process for Glycerol Valorization at *c*-$NiSe_2$ Cathode

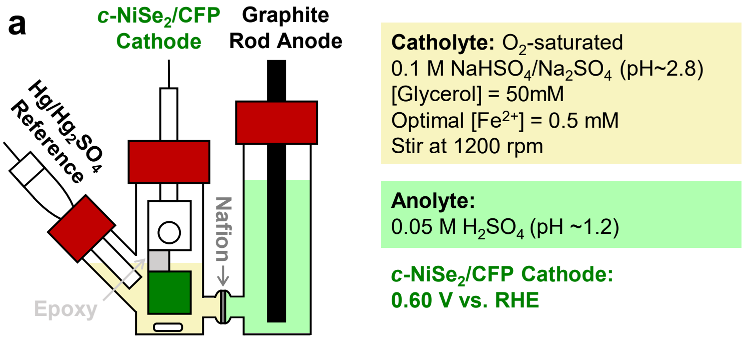

---

b

① **Electro-Fenton Process (Electrochemical)**

- Acidic 2e⁻ ORR: $O_2 + (2\,H^+ + 2\,e^-) \longrightarrow H_2O_2$
- ·OH Formation: $Fe^{2+} + H_2O_2 + H^+ \longrightarrow Fe^{3+} + H_2O + \cdot OH$
- Fe^{2+} Regeneration: $Fe^{3+} + e^- \longrightarrow Fe^{2+}$

② **Glycerol Oxidized by ·OH (Chemical)**

- ·OH is a one-electron oxidant: $n\,\cdot OH + (n\,H^+ + n\,e^-) \longrightarrow n\,H_2O$
- Glycerol - $(n\,H^+ + n\,e^-) + m\,H_2O \longrightarrow$ Oxidation Products

①+② **Cathodic Half-Cell Rxn** Glycerol + $n\,O_2 + (3n\,H^+ + 3n\,e^-) \longrightarrow$ Oxidation Products + $(2n-m)\,H_2O$

Since the cathodic half-cell reaction consumes protons, it is critical to place 0.05 M H_2SO_4 solution in the anode compartment to solely transport protons through the Nafion membrane to stabilize the acidic pH of the cathode compartment.

Figure A4.19. Schematic of the two-compartment three-electrode setup for half-cell studies of the electro-Fenton process for glycerol valorization, and derivation of balanced equation of the cathodic half-cell reaction.

(a) Schematic of the two-compartment three-electrode setup for half-cell studies of the electro-Fenton process for glycerol valorization at *c*-$NiSe_2$ cathode. (b) Derivation of balanced equation of the cathodic half-cell reaction, and the necessity of solely transporting protons through the Nafion 117 membrane to stabilize the acidic pH of the cathode compartment.

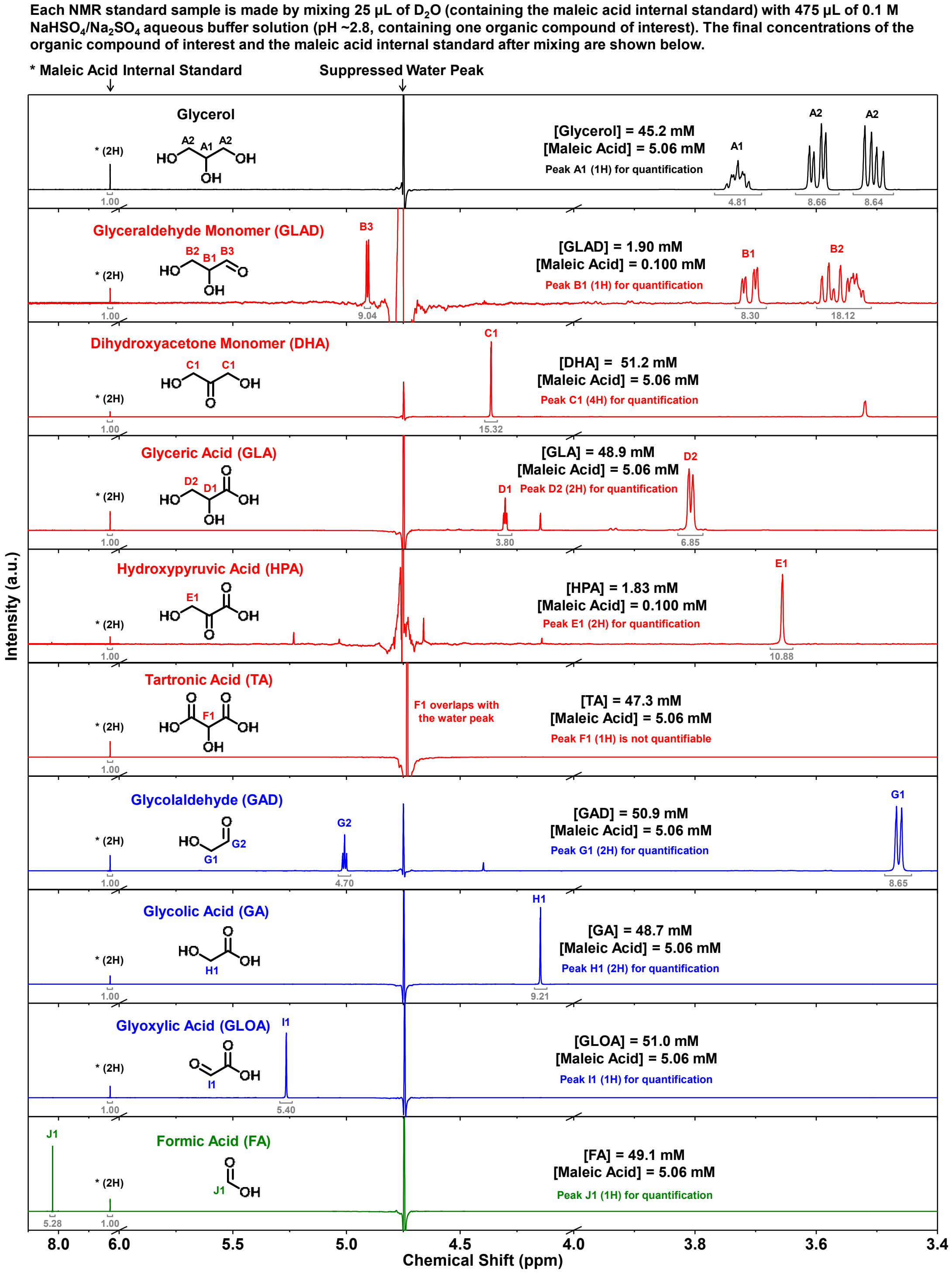

Figure A4.20. ^{1}H NMR standard spectra of the organic compounds of interest for the glycerol valorization. Detailed NMR sample preparation is described on the top. These ^{1}H NMR spectra are quantitative because the relaxation delay (20 sec) is longer than at least 5 times the T1 relaxation times of all these compounds (determined by inversion recovery experiments).

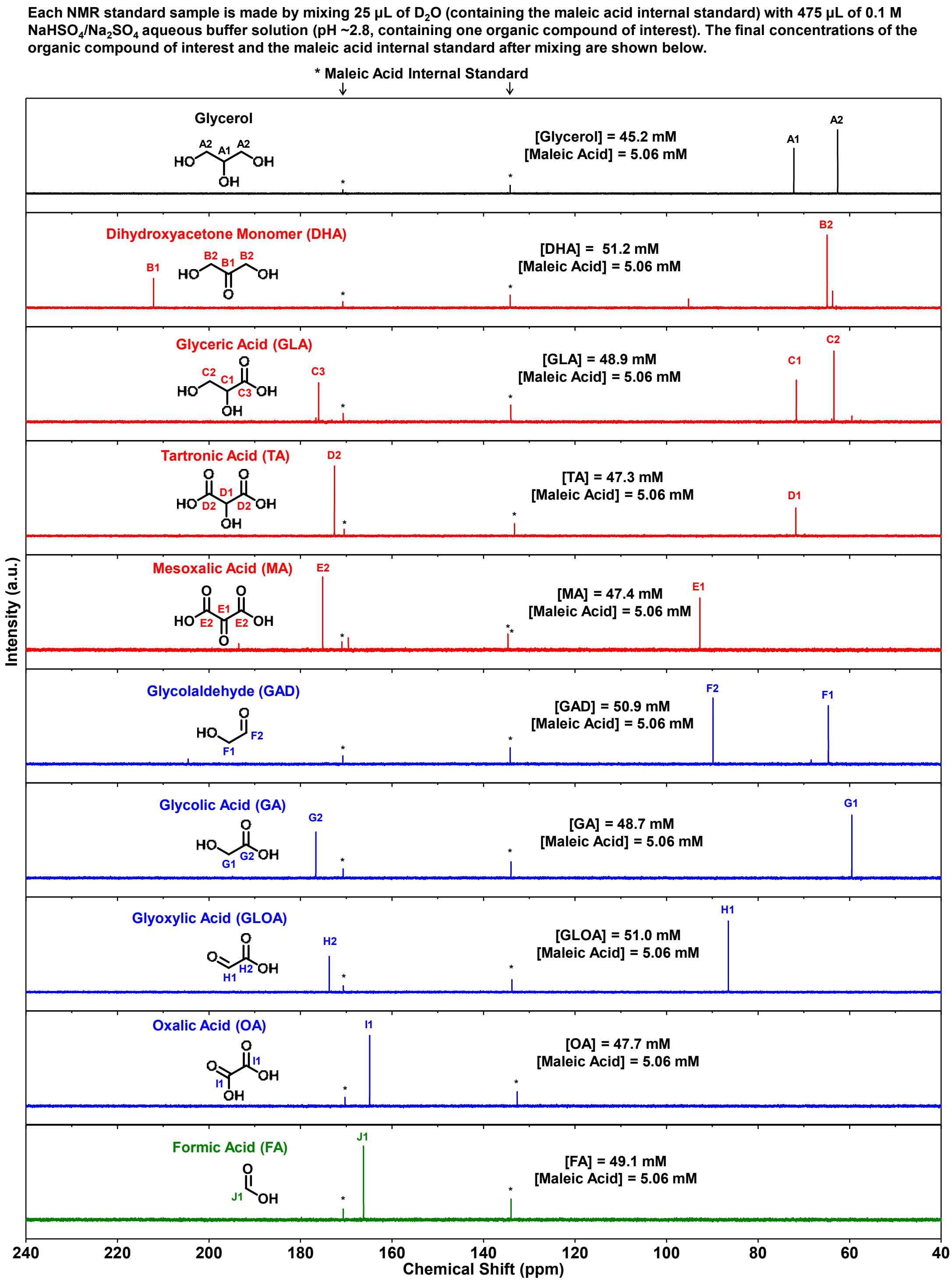

Each NMR standard sample is made by mixing 25 μL of D_2O (containing the maleic acid internal standard) with 475 μL of 0.1 M $NaHSO_4/Na_2SO_4$ aqueous buffer solution (pH ~2.8, containing one organic compound of interest). The final concentrations of the organic compound of interest and the maleic acid internal standard after mixing are shown below.

Figure A4.21. ^{13}C NMR standard spectra of the organic compounds of interest for the glycerol valorization. Detailed NMR sample preparation is described on the top. These ^{13}C NMR spectra are not quantitative because the relaxation delay (2 sec) is not long enough. The ^{13}C NMR peak assignments were partially referred to ref. 3.

a Each NMR sample in (a) is made by mixing 25 μL of D_2O (containing the maleic acid internal standard) with 475 μL of aqueous catholyte (5.18 mM glycerol + 0 mM Fe^{2+} in 0.1 M $NaHSO_4/Na_2SO_4$ before or after passing charge). The final concentration of the maleic acid internal standard after mixing is ~0.5 mM in (a).

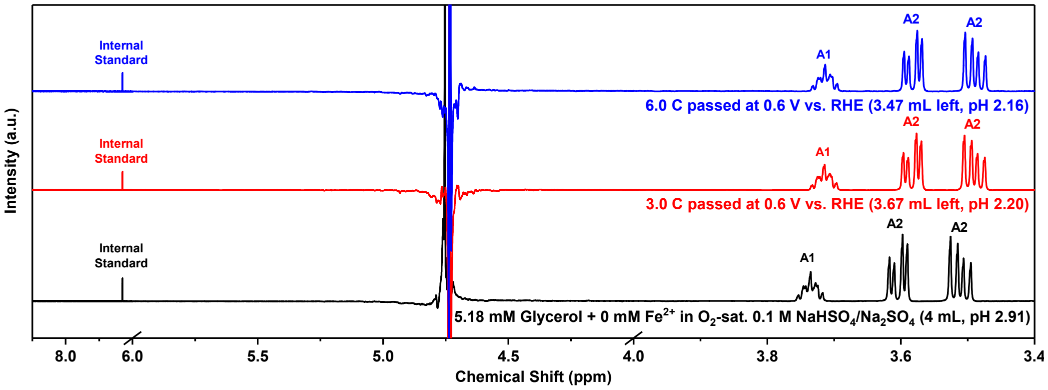

b Each NMR sample in (b) is made by mixing 25 μL of D_2O (containing the maleic acid internal standard) with 475 μL of aqueous catholyte (5.11 mM glycerol + 0.5 mM Fe^{2+} in 0.1 M $NaHSO_4/Na_2SO_4$ before or after passing charge). The final concentration of the maleic acid internal standard after mixing is ~0.1 mM in (b).

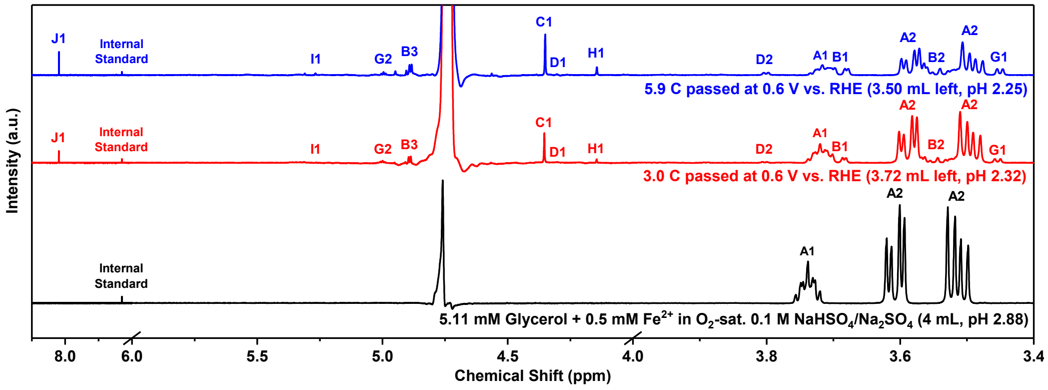

Figure A4.22. ^{1}H NMR spectra for the cathodic electro-Fenton half-cell studies with and without the presence of Fe^{2+}.

(a) ^{1}H NMR spectra showed no conversion of glycerol after passing a charge of 3.0 C or 6.0 C through *c*-$NiSe_2$/CFP cathode (~1.06 mg_{Ni} cm^{-2}_{geo}, ~1 cm^2_{geo}) at 0.60 V vs. RHE in 4 mL of O_2-saturated 0.1 M $NaHSO_4/Na_2SO_4$ solution (pH ~2.8, stirred at 1200 rpm) containing ~5 mM glycerol but no Fe^{2+}. (b) ^{1}H NMR spectra showed the emergence of oxidation products after passing a charge of 3.0 C or 5.9 C through *c*-$NiSe_2$/CFP cathode (~1.06 mg_{Ni} cm^{-2}_{geo}, ~1 cm^2_{geo}) at 0.60 V vs. RHE in 4 mL of O_2-saturated 0.1 M $NaHSO_4/Na_2SO_4$ solution (pH ~2.8, stirred at 1200 rpm) containing ~5 mM glycerol and 0.5 mM Fe^{2+}. Detailed NMR sample preparation is described on the top of each panel. The ^{1}H NMR peaks were assigned with labels according to the standard spectra presented in Figure A4.20. As the amount of charge passed increased, the solution volume in the cathode compartment decreased due to evaporation under the O_2 gas flow, the solution pH in the cathode compartment decreased due to proton permeation from the more acidic 0.05 M H_2SO_4 solution in the anode compartment (see Figure A4.19).

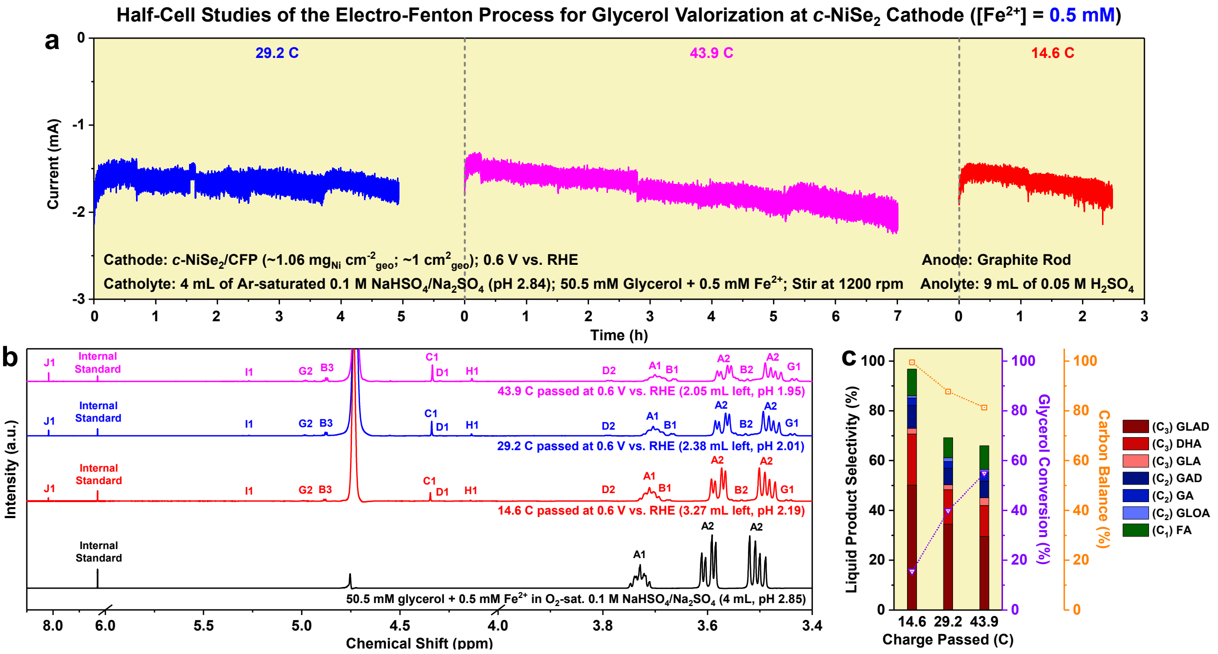

Figure A4.23. Chronoamperometry curves, ^{1}H NMR spectra, and glycerol conversion percentage and liquid product selectivity for the cathodic electro-Fenton half-cell studies at the Fe^{2+} concentration of 0.5 mM.

(a) Chronoamperometry curves when passing a controlled amount of charge (14.6 C, 29.2 C, or 43.9 C) through the c-NiSe$_2$ cathode (~1.06 mg$_{Ni}$ cm$^{-2}_{geo}$, ~1 cm$^2_{geo}$) at 0.60 V vs. RHE in 4 mL of O$_2$-saturated 0.1 M NaHSO$_4$/Na$_2$SO$_4$ solution (pH ~2.8, stirred at 1200 rpm) containing ~50 mM glycerol and 0.5 mM Fe^{2+}. (b) ^{1}H NMR spectra before and after passing a controlled amount of charge through the c-NiSe$_2$ cathode. Each NMR sample in (b) was made by mixing 25 μL of D$_2$O (containing the maleic acid internal standard) with 475 μL of aqueous catholyte, and the final concentration of the maleic acid internal standard after mixing is ~5 mM in (b). The ^{1}H NMR peaks were assigned with labels according to the standard spectra presented in Figure A4.20. As the amount of charge passed increased, the solution volume in the cathode compartment decreased due to evaporation under the O$_2$ gas flow, the solution pH in the cathode compartment decreased due to proton permeation from the more acidic 0.05 M H$_2$SO$_4$ solution in the anode compartment (see Figure A4.19). (c) Liquid product selectivity, glycerol conversion percentage, and carbon balance determined by ^{1}H NMR results after passing a controlled amount of charge through the c-NiSe$_2$ cathode.

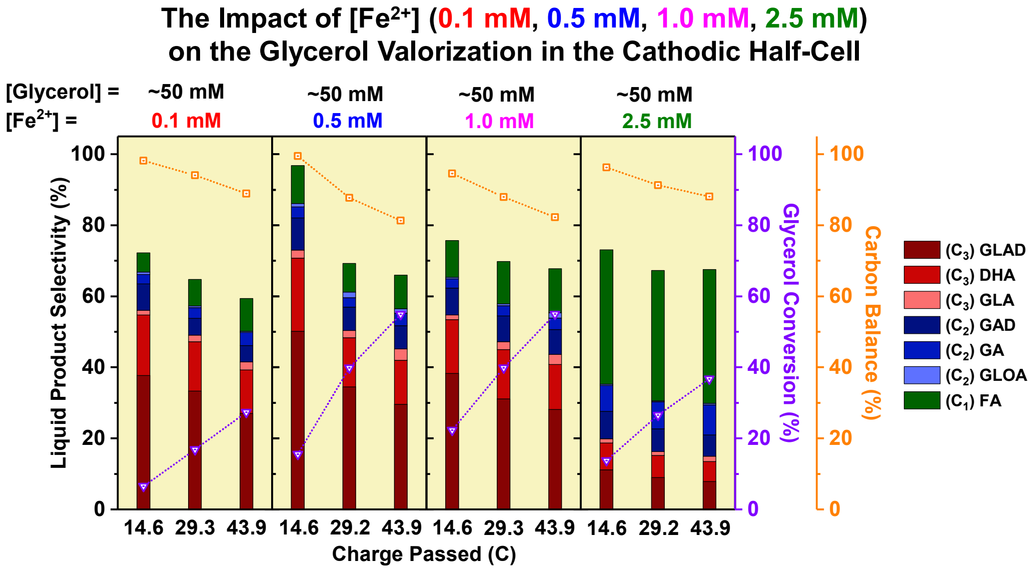

Figure A4.24. Comparisons of glycerol conversion percentage and liquid product selectivity for the cathodic electro-Fenton half-cell studies at different Fe^{2+} concentrations.

The impact of Fe^{2+} concentration on the glycerol valorization in the cathodic half-cell after passing a controlled amount of charge (14.6 C, 29.2 C, or 43.9 C) through the *c*-NiSe$_2$ cathode (~1.06 mg$_{Ni}$ cm$^{-2}_{geo}$, ~1 cm$^2_{geo}$) at 0.60 V vs. RHE in 4 mL of O$_2$-saturated 0.1 M NaHSO$_4$/Na$_2$SO$_4$ solution (pH ~2.8, stirred at 1200 rpm) containing ~50 mM glycerol and a certain concentration of Fe^{2+} (0.1, 0.5, 1.0, or 2.5 mM). Liquid product selectivity, glycerol conversion percentage, and carbon balance were determined by ^{1}H NMR analyses. As high concentrations of paramagnetic metal ions would cause ^{1}H NMR peak broadening, the NMR samples were prepared differently depending on the [Fe^{2+}] in the aqueous catholyte. When [Fe^{2+}] was in the low concentration regime (0.1 mM or 0.5 mM), the NMR sample was made by mixing 25 µL of D$_2$O (containing the maleic acid internal standard) with 475 µL of aqueous catholyte, and the final concentration of the maleic acid internal standard after mixing was ~5 mM. When [Fe^{2+}] was in the high concentration regime (1.0 mM or 2.5 mM), the NMR sample was made by mixing 450 µL of D$_2$O (containing the maleic acid internal standard) with 50 µL of aqueous catholyte, and the final concentration of the maleic acid internal standard after mixing is ~0.5 mM.

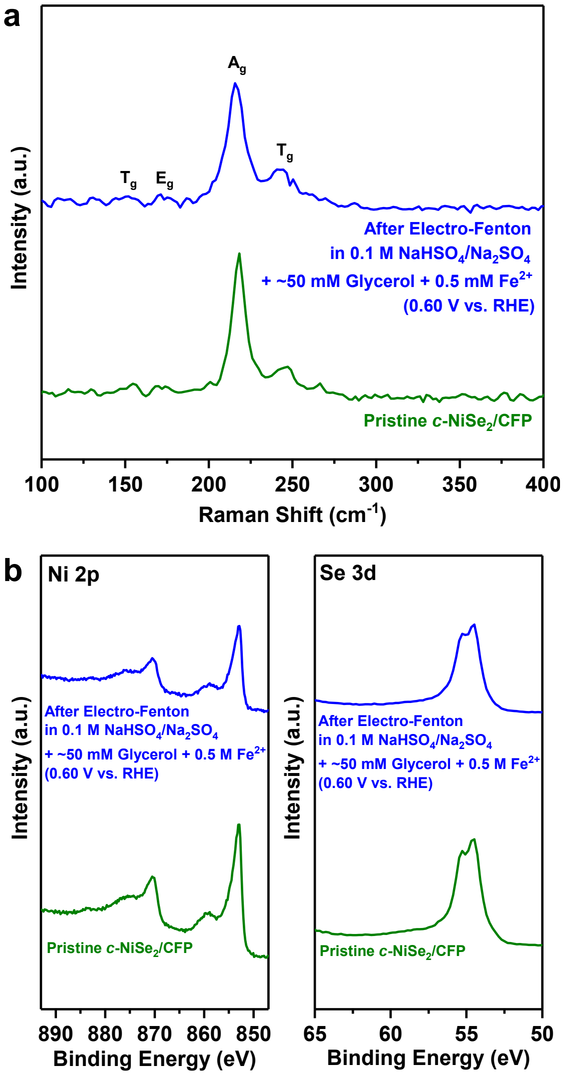

Figure A4.25. Raman and XPS of the tested *c*-NiSe$_2$/CFP after the electro-Fenton process for glycerol valorization.

(a) Raman spectra and (b) X-ray photoelectron spectra of *c*-NiSe$_2$/CFP before and after half-cell studies of the cathodic valorization of glycerol via the electro-Fenton process at 0.60 V vs. RHE in O_2-saturated 0.1 M $NaHSO_4/Na_2SO_4$ (pH ~2.8) containing ~50 mM glycerol and 0.5 mM Fe^{2+}.

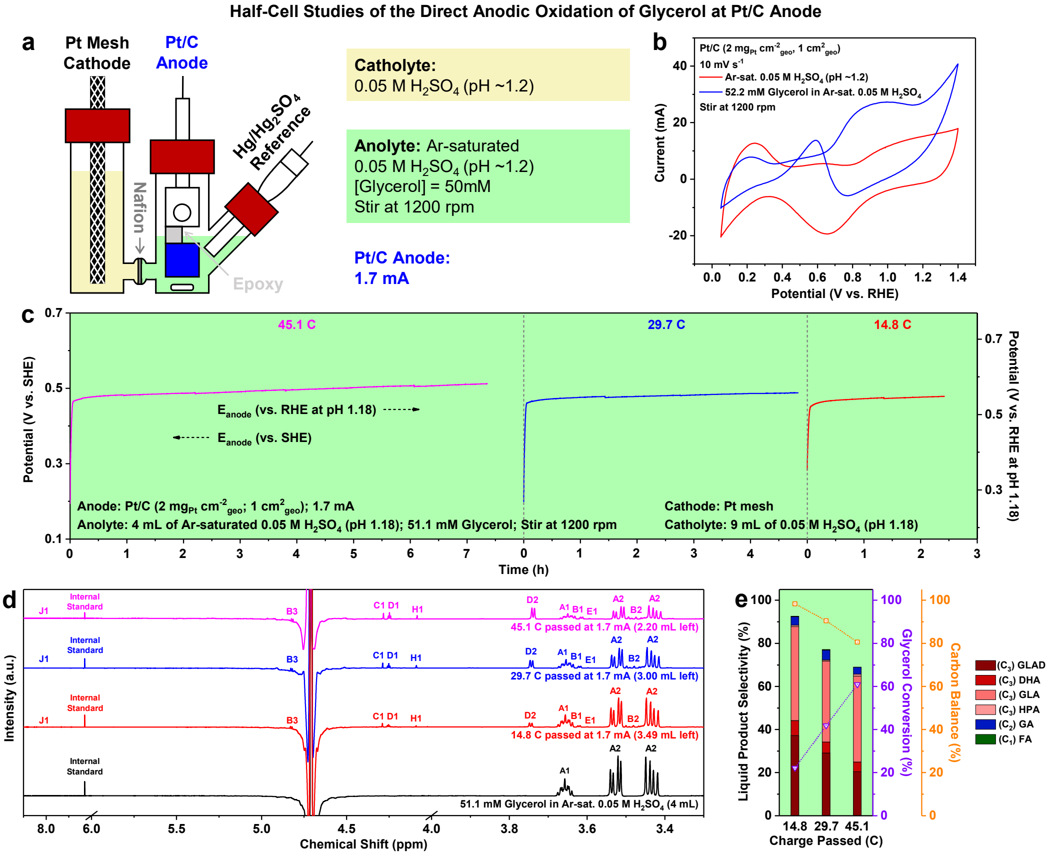

Figure A4.26. Half-cell studies of the direct anodic oxidation of glycerol at Pt/C anode.

(a) Schematic of the two-compartment three-electrode setup for half-cell studies of the direct anodic oxidation of glycerol at Pt/C anode. (b) Cyclic voltammograms of Pt/C anode (2 mg$_{Pt}$ cm^{-2}$_{geo}$, 1 cm^2$_{geo}$) for glycerol oxidation. (c) Chronopotentiometry curves when passing a controlled amount of charge (14.8 C, 29.7 C, or 45.1 C) through the Pt/C anode at 1.7 mA in 4 mL of Ar-saturated 0.05 M H_2SO_4 solution (pH ~1.2, stirred at 1200 rpm) containing ~50 mM glycerol. (d) ^{1}H NMR spectra before and after passing a controlled amount of charge through the Pt/C anode. Each NMR sample in (d) was made by mixing 25 μL of D_2O (containing the maleic acid internal standard) with 475 μL of aqueous anolyte, and the final concentration of the maleic acid internal standard after mixing was ~5 mM in (d). The ^{1}H NMR peaks were assigned with labels according to the standard spectra presented in Figure A4.20. As the amount of charge passed increased, the solution volume in the anode compartment decreased due to evaporation under the Ar gas flow. (e) Liquid product selectivity, glycerol conversion percentage, and carbon balance determined by ^{1}H NMR results after passing a controlled amount of charge through the Pt/C anode.

Table A4.2. Summary of the liquid product selectivity, glycerol conversion percentage, and carbon balance of the glycerol valorization from the cathodic and anodic half-cell studies.

Summary of the liquid product selectivity, glycerol conversion percentage, and carbon balance of the glycerol valorization in the cathodic half-cell via the electro-Fenton process at *c*-$NiSe_2$/CFP cathode (see Figure 4.3 in the Chapter 4, and Figures A4.23 and A4.24) and the direct anodic oxidation at Pt/C anode (see Figure A4.26).

Half-Cell Studies	Starting Volume (mL)	Starting [Glycerol] (mM)	Starting [Fe^{2+}] (mM)	Starting pH	Charge Passed (C)	Final Volume (mL)	Final [Glycerol] (mM)	Final pH	Glycerol Conversion (%)	Liquid Product Selectivity (%)								Carbon Balance (%)
										C_3				C_2			C_1	
										GLAD	DHA	GLA	HPA	GAD	GA	GLOA	FA	
Electro-Fenton Process at *c*-$NiSe_2$ Cathode	4	50.6	0.1	2.79	14.6	3.23	58.5	2.11	6.6	37.7	17.1	1.3	-	7.4	2.7	0.7	5.4	98.2
	4	50.6	0.1	2.79	29.3	2.66	63.3	2.06	16.9	33.3	13.9	1.9	-	4.7	3.0	0.4	7.5	94.1
	4	50.6	0.1	2.79	43.9	2.39	61.5	1.96	27.4	27.0	12.3	2.3	-	4.6	3.7	0.3	9.3	88.9
	4	50.5	0.5	2.85	14.6	3.27	52.2	2.19	15.6	50.2	20.6	2.3	-	9.1	3.0	1.0	10.7	99.5
	4	50.5	0.5	2.83	29.2	2.38	51.1	2.01	39.8	34.5	13.8	2.0	-	6.6	2.6	1.6	8.0	87.7
	4	50.5	0.5	2.85	43.9	2.05	44.4	1.95	54.9	29.6	12.4	3.2	-	6.6	3.5	1.3	9.5	81.3
	4	50.6	1.0	2.80	14.6	3.42	45.0	2.20	22.3	38.3	15.1	1.3	-	7.5	2.6	0.4	10.4	94.6
	4	50.6	1.0	2.80	29.3	2.87	41.6	2.08	39.8	31.1	13.9	2.2	-	7.2	2.9	0.5	11.9	88.0
	4	50.6	1.0	2.81	43.9	2.61	34.2	2.03	55.0	28.1	12.7	2.9	-	7.0	3.2	1.5	12.4	82.3
	4	50.5	2.5	2.84	14.6	3.14	53.7	2.16	13.8	11.2	7.5	1.2	-	7.8	7.3	0.4	37.8	96.3
	4	50.5	2.5	2.86	29.2	2.62	54.8	2.08	26.6	9.0	6.3	1.1	-	6.4	7.6	0.3	36.7	91.3
	4	50.5	2.5	2.85	43.9	2.08	59.5	1.94	36.8	7.9	5.6	1.5	-	6.0	8.5	0.4	37.6	88.0
Direct Anodic Oxidation at Pt/C Anode	4	51.1	-	1.21	14.8	3.49	45.6	1.15	22.2	37.2	7.0	43.6	0.7	-	3.9	-	0.2	98.4
	4	51.1	-	1.21	29.7	3.00	39.7	1.09	41.8	29.1	5.1	37.6	0.6	-	4.5	-	0.3	90.4
	4	51.9	-	1.21	45.1	2.20	36.9	0.95	60.9	20.4	4.5	39.9	0.9	-	3.2	-	0.1	80.6

Note A4.1. Glycerol valorization in the cathodic half-cell via the electro-Fenton process was studied by applying a fixed potential of 0.60 V vs. RHE to *c*-$NiSe_2$/CFP cathode (~1.06 mg_{Ni} cm^{-2}_{geo}, ~1 cm^2_{geo}) in O_2-saturated 0.1 M $NaHSO_4$/Na_2SO_4 (pH ~2.8) containing ~50 mM glycerol and 0.5 mM Fe^{2+}, and the cathode current was ~1.7 mA (Figure A4.23a). Direct oxidation of glycerol in the anodic half-cell was studied by applying a fixed current of 1.7 mA to Pt/C anode (2 mg_{Pt} cm^{-2}_{geo}, 1 cm^2_{geo}) in Ar-saturated 0.05 M H_2SO_4 (pH ~1.2) containing ~50 mM glycerol, and the anode potential was ~0.55 V vs. RHE at pH ~1.2 (Figure A4.26c). If *c*-$NiSe_2$/CFP cathode (in O_2-saturated 0.1 M $NaHSO_4$/Na_2SO_4 containing ~50 mM glycerol and 0.5 mM Fe^{2+}, pH ~2.8) and Pt/C anode (in Ar-saturated 0.05 M H_2SO_4 containing ~50 mM glycerol, pH ~1.2) were coupled together and both operated at 1.7 mA for glycerol valorization in a linear paired electrochemical system (as shown in Figure A4.27), the cell voltage (E_{cell}) in principle could be estimated by the cathode potential ($E_{cathode}$) and the anode potential (E_{anode}) from the respective half-cell studies.

From the cathodic half-cell study:

$$E_{cathode} \text{ (at ~1.7 mA)} = 0.60 \text{ V vs. RHE (at pH ~2.8)} = \text{~}0.435 \text{ V vs. SHE}$$

From the anodic half-cell study:

$$E_{anode} \text{ (at 1.7 mA)} = \text{~}0.55 \text{ V vs. RHE (at pH ~1.2)} = \text{~}0.479 \text{ V vs. SHE}$$

Under the *ideal* assumption of no internal resistance (i.e., no ohmic overpotential) in the linear paired electrochemical system:

$$\begin{aligned} E_{cell} \text{ (at ~1.7 mA)} &= E_{anode} \text{ vs. SHE} - E_{cathode} \text{ vs. SHE} \\ &= \text{~}0.479 \text{ V vs. SHE} - \text{~}0.435 \text{ V vs. SHE} \\ &= \text{~}44 \text{ mV} \end{aligned}$$

This *ideal* estimation suggested that, to deliver a current of ~1.7 mA for glycerol valorization at both *c*-$NiSe_2$/CFP cathode and Pt/C anode, the linear paired electrochemical system ideally could operate at a cell voltage as low as <50 mV with almost no external energy input needed if the internal resistance was negligible.

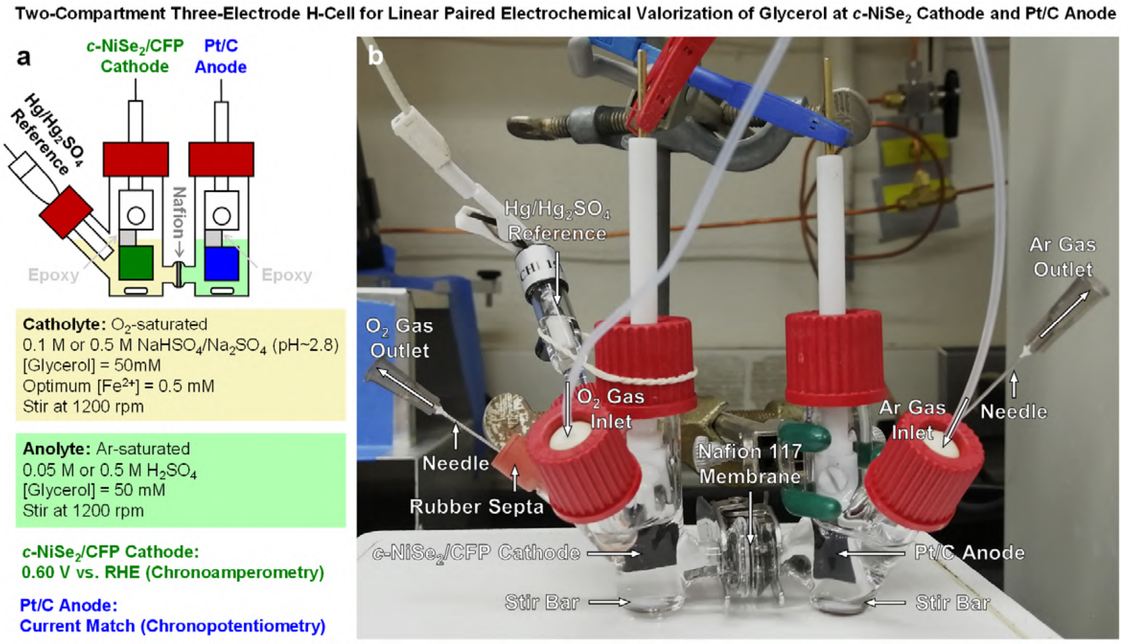

Figure A4.27. Schematic and digital photograph of the two-compartment three-electrode setup for linear paired electrochemical valorization of glycerol at *c*-NiSe$_2$ cathode and Pt/C anode.

(a) Schematic and (b) digital photograph of the two-compartment three-electrode setup for linear paired electrochemical valorization of glycerol at *c*-NiSe$_2$ cathode and Pt/C anode. The electro-Fenton process for glycerol valorization took place in the cathode compartment at the *c*-NiSe$_2$ cathode in O$_2$-saturated NaHSO$_4$/Na$_2$SO$_4$ buffer solution (pH ~2.8) containing ~50 mM glycerol and 0.5 mM Fe^{2+}. The direct anodic oxidation of glycerol took place in the anode compartment at the Pt/C anode in Ar-saturated H$_2$SO$_4$ solution containing ~50 mM glycerol, which solely transported protons through the Nafion 117 membrane to stabilize the acidic pH of the cathode compartment (see Figure 4.4a in the Chapter 4).

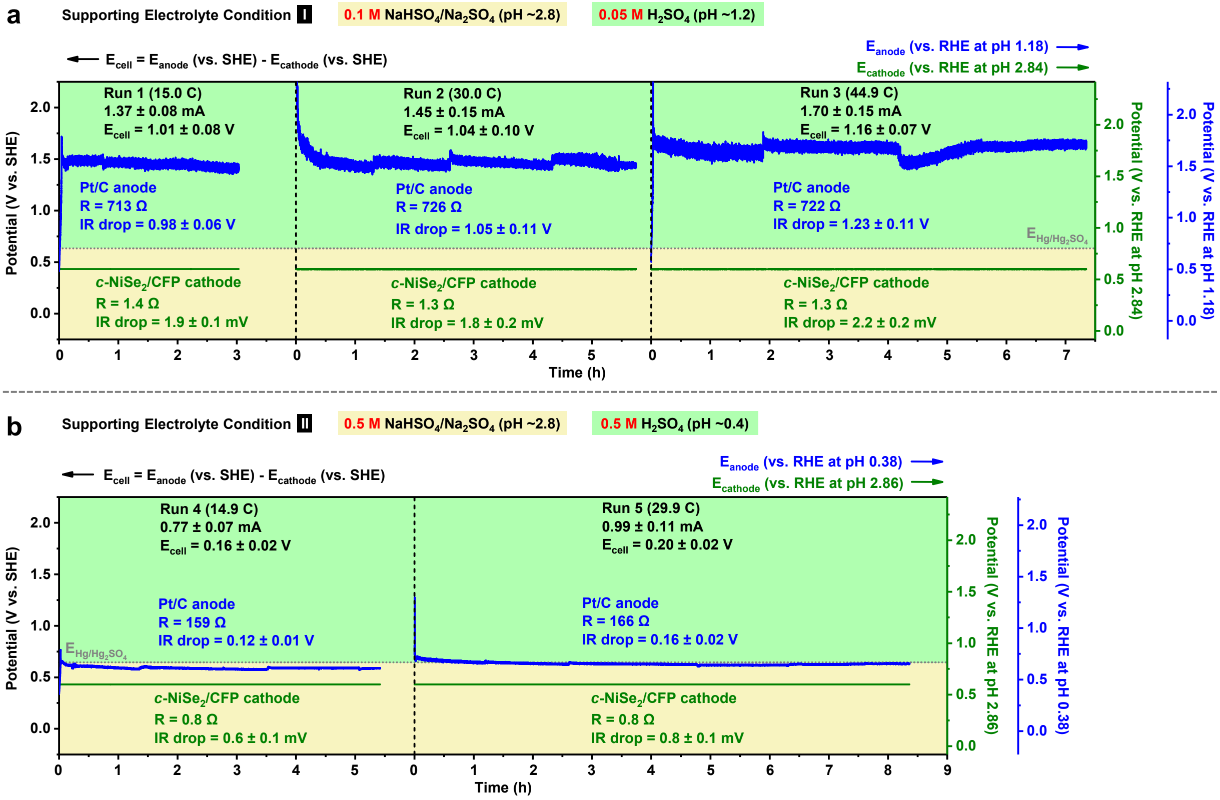

Figure A4.28. The *c*-$NiSe_2$ cathode potential and the Pt/C anode potential during the linear paired electrochemical valorization of glycerol.

The *c*-$NiSe_2$ cathode potential and the Pt/C anode potential during the linear paired electrochemical valorization of glycerol (catholyte: O_2-saturated $NaHSO_4/Na_2SO_4$ solution containing ~50 mM glycerol and 0.5 mM Fe^{2+}, pH ~2.8; anolyte: Ar-saturated H_2SO_4 solution containing ~50 mM glycerol) under supporting electrolyte condition I (panel a: 0.1 M $NaHSO_4/Na_2SO_4$ for catholyte, 0.05 M H_2SO_4 for anolyte) or condition II (panel b: 0.5 M $NaHSO_4/Na_2SO_4$ for catholyte, 0.5 M H_2SO_4 for anolyte). Additional discussion of the results shown in this figure is presented in Note A4.2 on the next page.

Note A4.2. As estimated in Note A4.1, this linear paired system ideally could operate at a cell voltage (E_{cell}) as low as <50 mV if there was no internal resistance. In Figure A4.28a, the measured E_{cell} was higher than the ideally estimated value, mostly caused by the large solution IR drop at the anode as it situated on the opposite side of the Hg/Hg_2SO_4 reference electrode across the Nafion 117 membrane. The magnitude of the ohmic overpotential (solution IR drop) at the anode was almost identical to the measured E_{cell}, meaning the ideal estimation in Note A4.1 was still valid. The large solution IR drop at the anode was mostly caused by the solution resistance rather than the membrane resistance, because it was almost unaffected by the membrane thickness when the catholyte and anolyte compositions remained the same (see comparisons between the 183 μm-thick Nafion 117 membrane and the 89 μm-thick Nafion NE1035 membrane in the table below). As shown in Figure A4.28b, by increasing the supporting electrolyte concentrations of both catholyte and anolyte, the measured E_{cell} was lowered because of the decrease in the solution IR drop at the anode. To operate this linear paired system at an even lower (or zero) cell voltage in the future, the ohmic overpotential needs to be further decreased, and one possible optimization pathway is to employ zero-gap cell designs involving membrane electrode assemblies.

Membrane	Thickness	Catholyte	Anolyte	R at Cathode	R at Anode
Nafion 117	183 μm	0.1 M $NaHSO_4/Na_2SO_4$ (pH ~2.8) + ~50 mM Glycerol + 0.5 mM Fe^{2+}	0.05 M H_2SO_4 + ~50 mM Glycerol	1.4 Ω (Run 1) [1] 1.3 Ω (Run 2) [1] 1.3 Ω (Run 3) [1]	713 Ω (Run 1) [1] 726 Ω (Run 1) [1] 722 Ω (Run 1) [1]
		0.5 M $NaHSO_4/Na_2SO_4$ (pH ~2.8) + ~50 mM Glycerol + 0.5 mM Fe^{2+}	0.5 M H_2SO_4 + ~50 mM Glycerol	0.8 Ω (Run 4) [2] 0.8 Ω (Run 5) [2]	159 Ω (Run 4) [2] 166 Ω (Run 5) [2]
Nafion NE1035	89 μm	0.1 M $NaHSO_4/Na_2SO_4$ (pH ~2.8)	0.05 M H_2SO_4	2.2 Ω	685 Ω
		0.5 M $NaHSO_4/Na_2SO_4$ (pH ~2.8)	0.5 M H_2SO_4	1.8 Ω	173 Ω

[1] See Figure A4.28a.

[2] See Figure A4.28b.

Table A4.3. Summary of the liquid product selectivity, glycerol conversion percentage, and carbon balance of linear paired electrochemical valorization of glycerol.

Summary of the liquid product selectivity, glycerol conversion percentage, and carbon balance of linear paired electrochemical valorization of glycerol at *c*-$NiSe_2$/CFP cathode and Pt/C anode (see Figure 4.4 in the Chapter 4).

Supporting Electrolyte Condition (I or II)			Starting Volume (mL)	Starting [Glycerol] (mM)	Starting [Fe^{2+}] (mM)	Starting pH	Charge Passed (C)	Final Volume (mL)	Final [Glycerol] (mM)	Final pH	Glycerol Conversion (%)	Liquid Product Selectivity (%)								Carbon Balance (%)
												C_3				C_2			C_1	
												GLAD	DHA	GLA	HPA	GAD	GA	GLOA	FA	
I	Run 1	Catholyte	4	50.4	0.5	2.91	15.0	3.24	50.6	1.95	18.8	47.8	19.1	2.6	-	10.1	3.7	0.5	12.0	99.2
		Anolyte	4	53.1	-	1.21	15.0	3.58	48.1	1.29	18.9	43.1	6.6	37.9	0.7	-	3.6	-	0.3	98.5
	Run 2	Catholyte	4	50.4	0.5	2.89	30.0	2.80	44.7	1.85	38.0	37.1	15.9	4.0	-	7.9	4.1	0.7	11.9	93.0
		Anolyte	4	53.1	-	1.21	30.0	3.33	39.6	1.29	37.8	32.3	5.2	35.4	1.0	-	3.7	-	0.4	91.7
	Run 3	Catholyte	4	50.4	0.5	2.89	44.9	2.35	40.1	1.66	53.3	29.5	13.9	4.7	-	8.4	5.9	2.1	15.9	89.5
		Anolyte	4	53.1	-	1.21	44.9	3.20	32.1	1.34	51.6	29.4	5.8	40.9	1.4	-	4.7	-	0.4	91.0
II	Run 4	Catholyte	4	50.4	0.5	2.91	14.9	2.65	58.4	1.13	23.2	33.2	10.3	1.8	0.3	7.5	2.5	1.0	9.1	92.0
		Anolyte	4	52.9	-	0.38	14.9	3.41	50.8	0.43	18.1	44.3	8.3	38.1	0.4	-	3.9	-	0.3	99.2
	Run 5	Catholyte	4	50.4	0.5	2.88	29.9	2.20	55.6	0.97	39.3	25.4	9.4	2.9	1.4	7.2	4.3	1.5	14.1	86.7
		Anolyte	4	52.9	-	0.38	29.9	3.12	43.4	0.43	35.9	32.7	5.7	40.0	0.5	-	5.0	-	0.3	94.3

Note A4.3. In the linear paired electrochemical system for glycerol valorization, when the supporting electrolyte concentration for the catholyte ($NaHSO_4/Na_2SO_4$, pH ~2.8) was increased from 0.1 M (Condition I) to 0.5 M (Condition II), the detected liquid products in the catholyte decreased in quantities after a controlled amount of charge was passed (Figure 4.4c in the Chapter 4). This could be because the O_2 solubility in aqueous electrolyte solution decreases with increasing electrolyte concentration in general[4], which influenced the H_2O_2 bulk electrosynthesis and the electro-Fenton process at *c*-$NiSe_2$ cathode. H_2O_2 bulk electrosynthesis at pH ~2.8 using the same *c*-$NiSe_2$ cathode operated at the same applied potential of 0.60 V vs. RHE resulted in a smaller cathodic current in 0.5 M $NaHSO_4/Na_2SO_4$ as compared to in 0.1 M $NaHSO_4/Na_2SO_4$ (see the figure below, also refer to Figure A4.17).

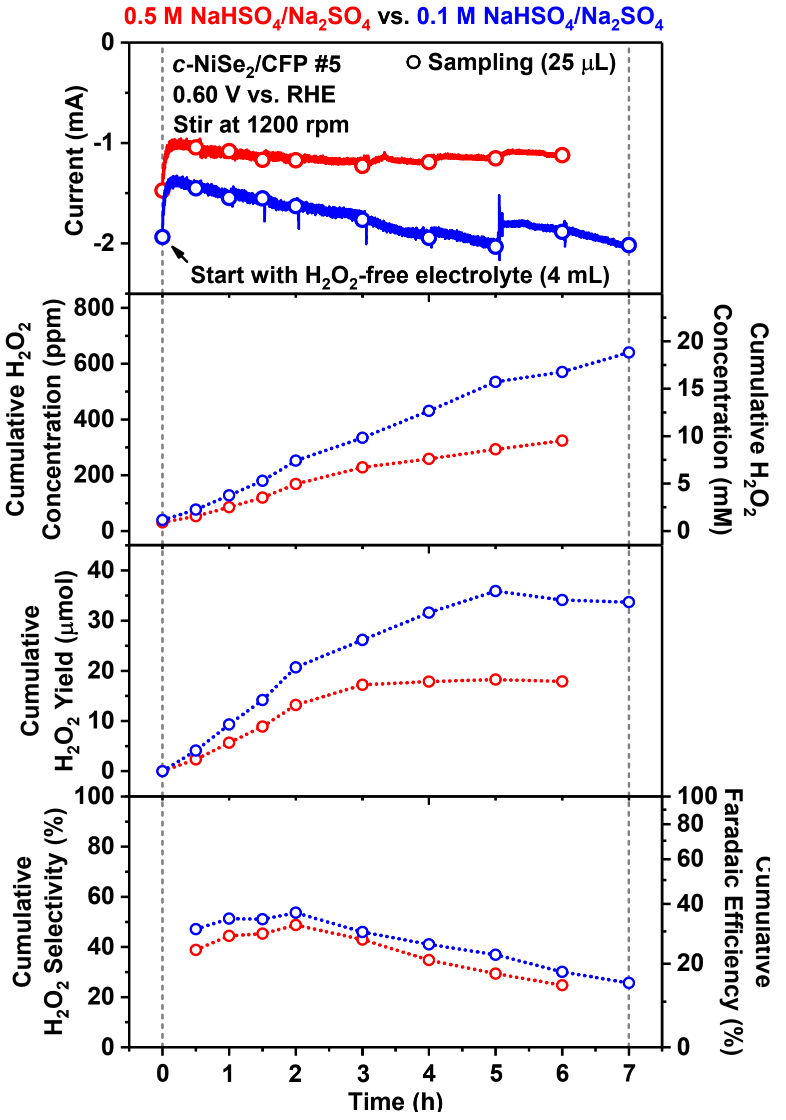

Similarly, the cathodic current on *c*-$NiSe_2$ cathode during the cathodic valorization of glycerol at pH ~2.8 via the electro-Fenton process at the same applied potential of 0.60 V vs. RHE was also smaller in 0.5 M $NaHSO_4$/Na_2SO_4 compared to in 0.1 M $NaHSO_4$/Na_2SO_4, and thus required a longer time to reach the controlled amount of charge passed in 0.5 M $NaHSO_4$/Na_2SO_4 (see Figure 4.4b in the Chapter 4). As a result, when the supporting electrolyte concentration increased, glycerol in the catholyte was in contact with the continuously generated ·OH for a longer period of time with the same amount of charge passed, and the glycerol oxidation in the half-cell was driven to later stages with decreased quantities of the detected liquid products in the catholyte (see Figure 4.4c in the Chapter 4).

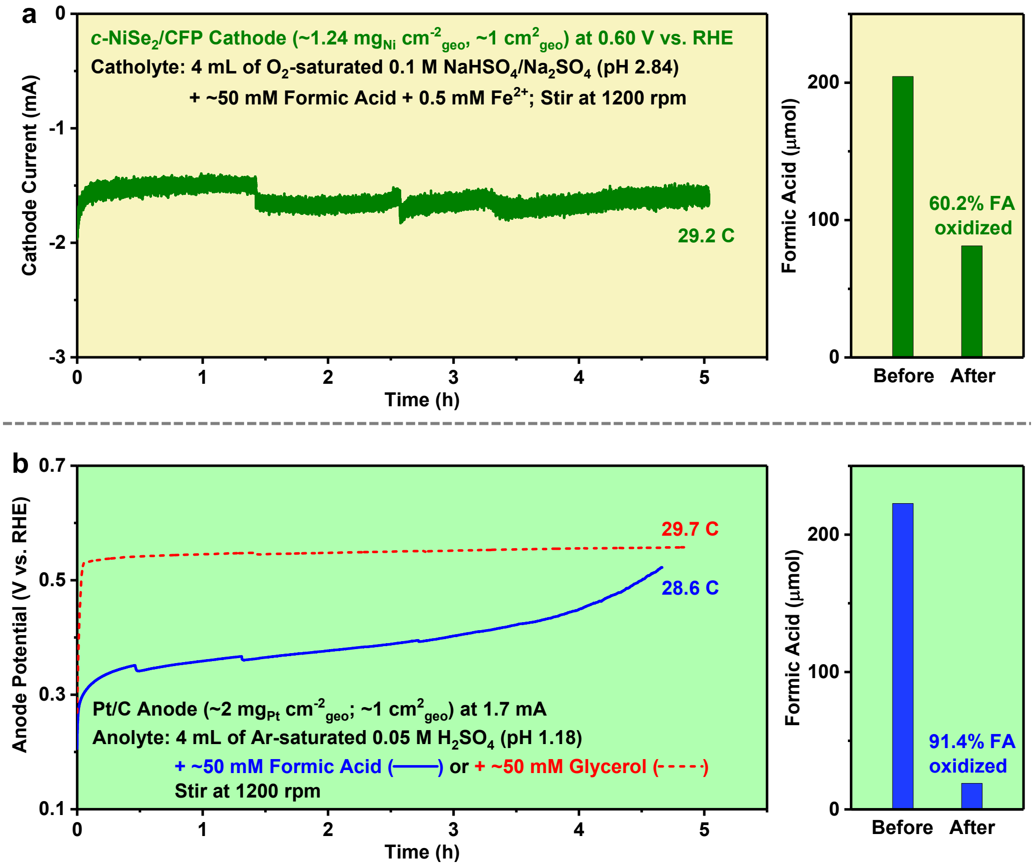

Figure A4.29. The oxidation of formic acid by the electro-Fenton process at *c*-NiSe$_2$/CFP cathode and by direct oxidation at Pt/C anode.

(a) Chronoamperometry curve of the *c*-NiSe$_2$/CFP cathode (~1.24 mg$_{Ni}$ cm$^{-2}_{geo}$, ~1cm$^2_{geo}$) at 0.60 V vs. RHE in 4 mL of O$_2$-saturated 0.1 M NaHSO$_4$/Na$_2$SO$_4$ solution (pH ~2.8, stirred at 1200 rpm) containing ~50 mM formic acid and 0.5 mM Fe^{2+}. After passing 29.2 C of charge through the *c*-NiSe$_2$/CFP cathode, 60.2% of the formic acid (FA) starting material was oxidized (into gaseous CO$_2$) based on ^{1}H NMR analyses. (b) Chronopotentiometry curve of the Pt/C anode (~2 mg$_{Pt}$ cm$^{-2}_{geo}$, ~1cm$^2_{geo}$) at 1.7 mA in 4 mL of O$_2$-saturated 0.05 M H$_2$SO$_4$ solution (pH ~1.2, stirred at 1200 rpm) containing ~50 mM formic acid. After passing 28.6 C of charge through the Pt/C anode, 91.4% of the formic acid (FA) starting material was oxidized (into gaseous CO$_2$) based on ^{1}H NMR analyses. Formic acid oxidation on Pt/C anode required a less positive applied potential as compared to glycerol oxidation (panel b, left, solid blue trace vs. dashed red trace). An earlier literature also showed the formation of CO$_2$ from glycerol oxidation at Pt anode under similar applied potential and pH conditions.[5]

Note A4.4. Control experiments in Figure A4.29 suggested that both the electro-Fenton process at *c*-NiSe2 cathode and the anodic oxidation at Pt/C anode could further oxidize formic acid (FA) into gaseous CO_2, which may account for the loss in the carbon balance of all detected liquid products in both catholyte and anolyte during linear paired electrochemical valorization of glycerol (Figure 4.4c in the Chapter 4). We would like to note that the loss in carbon balance of all detected liquid products may also be caused by the limitations of the ^1H NMR product analysis methodology: tartronic acid (TA) was not quantifiable by ^1H NMR because its signal overlaps with the water peak (Figure A4.20), mesoxalic acid (MA) and oxalic acid (OA) were also not quantifiable by ^1H NMR because they lack ^1H NMR signal. Therefore, the detection of these three compounds (TA, MA, and OA) could only rely on ^{13}C NMR which is less sensitive and quantitative. In the respective cathodic and anodic half-cell studies of glycerol valorization, we applied ^{13}C NMR (in addition to ^1H NMR) to analyze the respective catholyte and anolyte (see the ^{13}C NMR spectra below). In comparison with the ^{13}C NMR standard spectra (Figure A4.21), there were no obvious ^{13}C NMR signal corresponding to TA, MA, or OA, indicating these three compounds were not likely formed during either the electro-Fenton process or the anodic oxidation as their quantities were below the detection limit of ^{13}C NMR. Therefore, we considered the formic acid oxidation into gaseous CO_2 as a more probable cause of the loss in carbon loss of all detected liquid products.

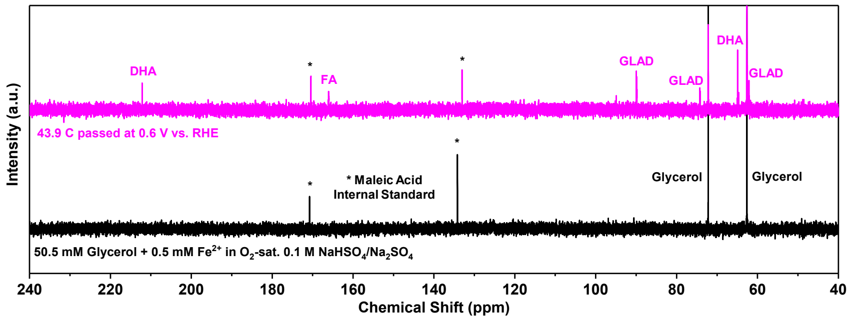
Cathodic Half-Cell Study of *c*-NiSe$_2$/CFP Cathode (See Supplementary Fig. 23)

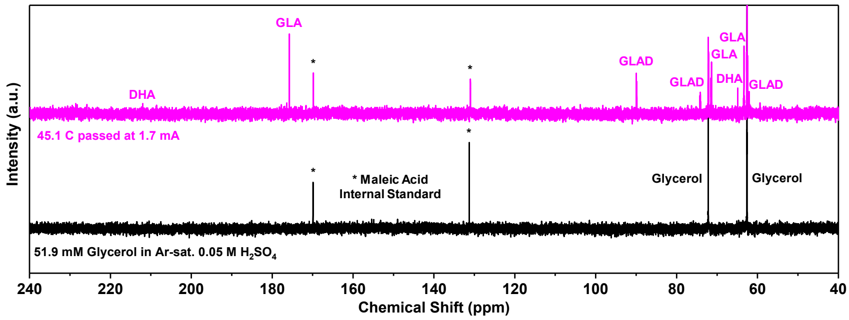
Anodic Half-Cell Study of Pt/C Anode (See Supplementary Fig. 26)

References Cited in the Appendix 4

1. Lu, Z.; Chen, G.; Siahrostami, S.; Chen, Z.; Liu, K.; Xie, J.; Liao, L.; Wu, T.; Lin, D.; Liu, Y.; Jaramillo, T. F.; Nørskov, J. K.; Cui, Y. High-efficiency oxygen reduction to hydrogen peroxide catalysed by oxidized carbon materials. *Nat. Catal.* ***1***, 156-162 (2018).

2. Jiang, K.; Back, S.; Akey, A. J.; Xia, C.; Hu, Y.; Liang, W.; Schaak, D.; Stavitski, E.; Nørskov, J. K.; Siahrostami, S.; Wang, H. Highly selective oxygen reduction to hydrogen peroxide on transition metal single atom coordination. *Nat. Commun.* ***10***, 3997 (2019).

3. Nguyen, R.; Amouroux, M.; Duda, A.; Mouloungui, Z. Quantification of Mixtures of C2 and C3 Hydroxy Acids and Products of Glycerol Oxidation by High-Performance Liquid Chromatography and Quantitative 13C NMR. *J. Am. Oil Chem. Soc.* ***97***, 679-689 (2020).

4. Xing, W.; Yin, M.; Lv, Q.; Hu, Y.; Liu, C.; Zhang, J.: 1 - Oxygen Solubility, Diffusion Coefficient, and Solution Viscosity. In *Rotating Electrode Methods and Oxygen Reduction Electrocatalysts*; Xing, W., Yin, G., Zhang, J., Eds.; Elsevier: Amsterdam, 2014; pp 1-31.

5. Kwon, Y.; Schouten, K. J. P.; Koper, M. T. M. Mechanism of the Catalytic Oxidation of Glycerol on Polycrystalline Gold and Platinum Electrodes. *ChemCatChem* ***3***, 1176-1185 (2011).

APPENDIX 5

Supplementary Information for CHAPTER 5:

Electrocatalytic Oxidation of Glycerol to Formic Acid by $CuCo_2O_4$ Spinel Oxide Nanostructure Catalysts[*]

---

[*] This appendix was originally made available online as the Supporting Information for *ACS Catal.* ***10***, 6741–6752 (2020), in collaboration with Xiaotong Han, Chang Yu, Theodore W. Walker, George W. Huber, Jieshan Qiu, and Song Jin.

Supporting Experimental Section

Product Analysis. Calculations of Faradaic efficiency of the electrochemical glycerol oxidation are based on the following balanced half-reactions corresponding to the conversion of glycerol into *individual* GOR product in alkaline solution:

$$C_3H_8O_3 \text{ (glycerol)} + 2\ OH^- \rightarrow C_3H_6O_3 \text{ (glyceraldehyde)} + 2\ H_2O + 2\ e^- \quad \text{(A5.1)}$$

$$C_3H_8O_3 \text{ (glycerol)} + 5\ OH^- \rightarrow C_3H_5O_4^- \text{ (glycerate)} + 4\ H_2O + 4\ e^- \quad \text{(A5.2)}$$

$$C_3H_8O_3 \text{ (glycerol)} + 13/2\ OH^- \rightarrow 3/2\ C_2H_3O_3^- \text{ (glycolate)} + 5\ H_2O + 5\ e^- \quad \text{(A5.3)}$$

$$C_3H_8O_3 \text{ (glycerol)} + 11\ OH^- \rightarrow 3\ HCOO^- \text{ (formate)} + 8\ H_2O + 8\ e^- \quad \text{(A5.4)}$$

$$C_3H_8O_3 \text{ (glycerol)} + 14\ OH^- \rightarrow 3/2\ C_2O_4^{2-} \text{ (oxalate)} + 11\ H_2O + 11\ e^- \quad \text{(A5.5)}$$

where reactions A5.3-A5.5 are derived from reactions A5.6-A5.8 below:

$$C_3H_8O_3 \text{ (glycerol)} + 8\ OH^- \rightarrow C_2H_3O_3^- \text{ (glycolate)} + HCOO^- \text{ (formate)} + 6\ H_2O + 6\ e^- \text{ (A5.6)}$$

$$C_2H_3O_3^- \text{ (glycolate)} + 3\ OH^- \rightarrow 2\ HCOO^- \text{ (formate)} + 2\ H_2O + 2\ e^- \quad \text{(A5.7)}$$

$$C_2H_3O_3^- \text{ (glycolate)} + 5\ OH^- \rightarrow C_2O_4^{2-} \text{ (oxalate)} + 4\ H_2O + 4\ e^- \quad \text{(A5.8)}$$

The overall Faradaic efficiency (FE) toward all value-added products (glycerate, glycolate, and formate for the $CuCo_2O_4$ catalyst; glycerate, glycolate, oxalate, and formate for the $NiCo_2O_4$ catalyst) is calculated based on the following equations:

$$\text{FE (for } CuCo_2O_4) = \frac{C_{\text{glycerate}} \times 4 + C_{\text{glycolate}} \times (2/3) \times 5 + C_{\text{formate}} \times (1/3) \times 8}{Q_{\text{total}}} \times V \times F \times 100\%$$

$$\text{FE (for } NiCo_2O_4) = \frac{C_{\text{glycerate}} \times 4 + C_{\text{glycolate}} \times (2/3) \times 5 + C_{\text{formate}} \times (1/3) \times 8 + C_{\text{oxalate}} \times (2/3) \times 11}{Q_{\text{total}}} \times V \times F \times 100\%$$

where $C_{\text{glycerate}}$, $C_{\text{glycolate}}$, C_{oxalate}, and C_{formate} are the concentrations (mol L^{-1}) of respective GOR product; V is the volume of the electrolyte solution (2×10^{-3} L); F is Faraday's constant (96485 C mol^{-1}); Q_{total} is the total charge (C) passed during the electrolysis reaction. The input and output aqueous phase organic carbon amounts are calculated based on the following equations:

$$\text{Input aqueous phase organic carbon amount} = (C_{0,\text{glycerol}} - C_{\text{glycerol}}) \times 3$$

$$\text{Output aqueous phase organic carbon amount} = \Sigma(C_{\text{C3 product}} \times 3 + C_{\text{C2 product}} \times 2 + C_{\text{C1 product}} \times 1)$$

where $C_{0,\mathrm{glycerol}}$ and C_{glycerol} are the initial and final concentration of glycerol, respectively; $C_{\mathrm{C3\ product}}$, $C_{\mathrm{C2\ product}}$, and $C_{\mathrm{C1\ product}}$ are the final concentrations of C_3 product (glyceric acid), C_2 products (glycolic acid, oxalic acid), and C_1 product (formic acid), respectively.

Supporting Figures and Tables

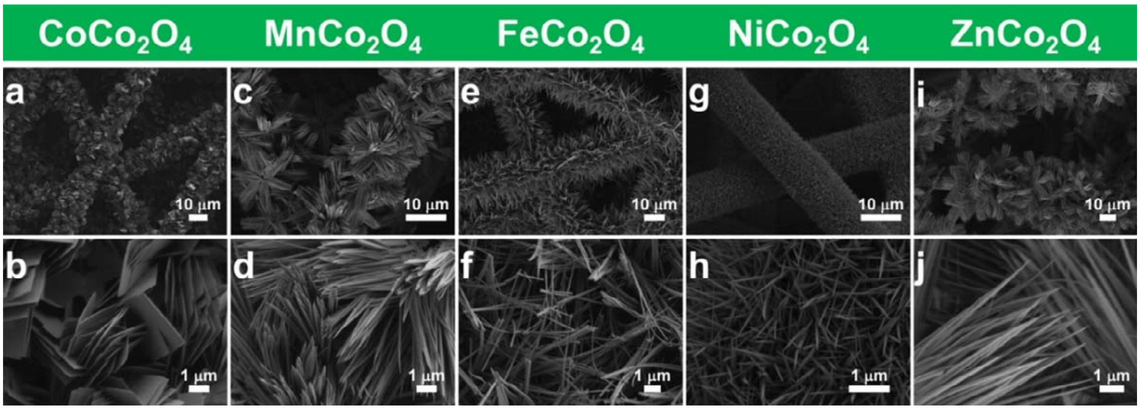

Figure A5.1. SEM characterization of MCo_2O_4 catalysts. Low- and high-magnification SEM images of the (a,b) $CoCo_2O_4$, (c,d) $MnCo_2O_4$, (e,f) $FeCo_2O_4$, (g,h) $NiCo_2O_4$, and (i,j) $ZnCo_2O_4$ nanoplate or nanowire arrays directly grown on carbon fiber paper.

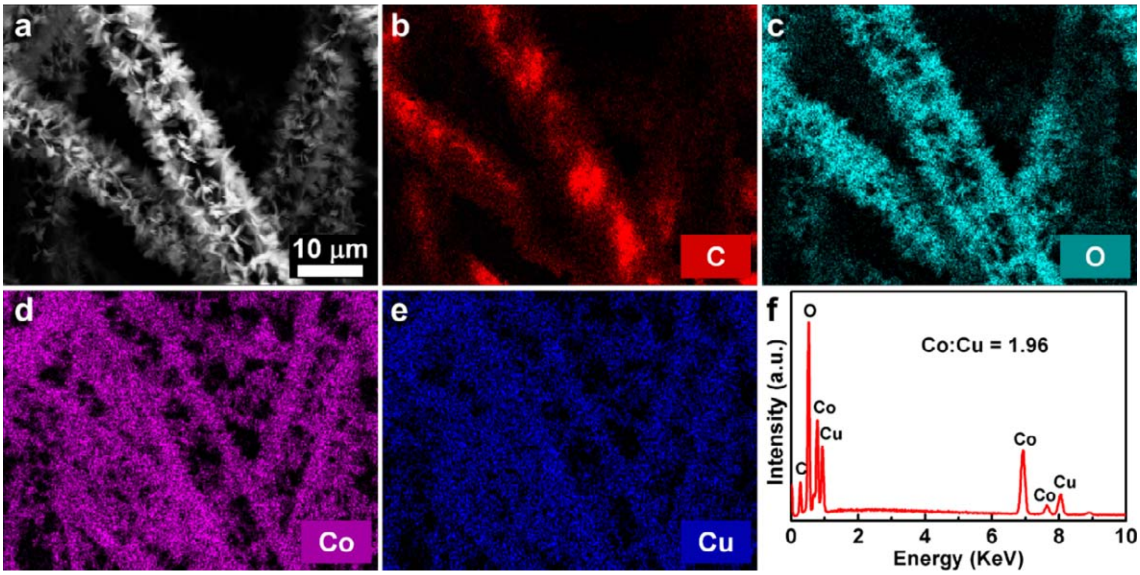

Figure A5.2. EDS elemental mapping of $CuCo_2O_4$ catalyst. (a) SEM image, (b-e) EDS elemental mapping images and (f) EDS spectrum of the representative $CuCo_2O_4$ nanoplates grown on carbon fiber paper.

Table A5.1. SEM-EDS results of the atomic ratio of Co to M (M = Mn, Fe, Ni, Cu, and Zn) in the MCo_2O_4 nanostructures grown on carbon fiber paper.

$MnCo_2O_4$	$FeCo_2O_4$	$NiCo_2O_4$	$CuCo_2O_4$	$ZnCo_2O_4$
Co/Mn	Co/Fe	Co/Ni	Co/Cu	Co/Zn
2.20	2.14	2.05	1.96	2.09

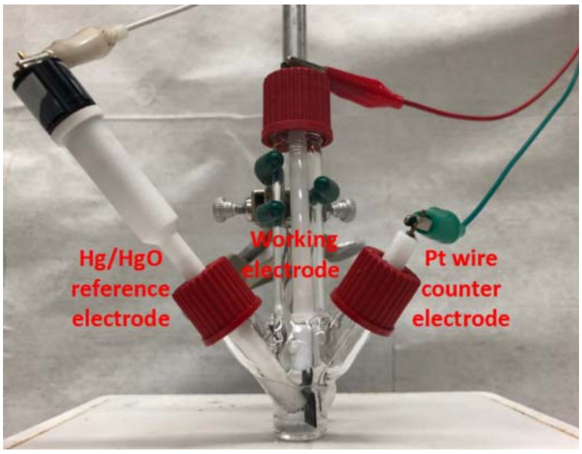

Figure A5.3. Digital photograph of the single-compartment three-electrode cell designed for running electrochemical glycerol oxidation reaction in a small volume of electrolyte.

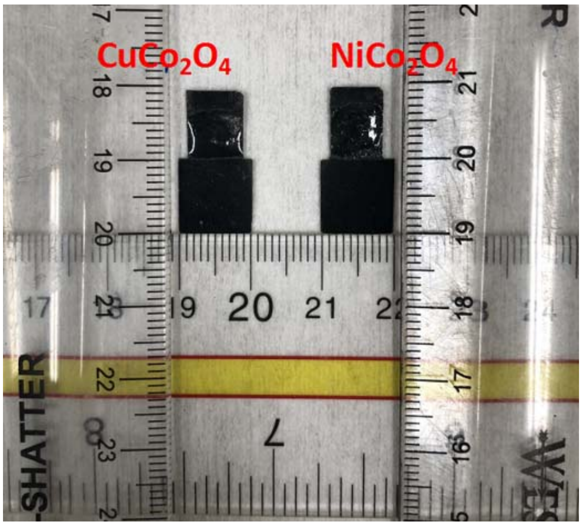

Figure A5.4. Digital photograph of the working electrodes fabricated from the carbon fiber paper substrates grown with $CuCo_2O_4$ and $NiCo_2O_4$ nanostructures. Epoxy resins are applied to define the geometric area of the working electrodes (~1 cm^2).

Table A5.2. The catalyst mass loadings of MCo_2O_4 nanostructures grown on carbon fiber paper.

	$MnCo_2O_4$	$FeCo_2O_4$	$CoCo_2O_4$	$NiCo_2O_4$	$CuCo_2O_4$	$ZnCo_2O_4$
Mass Loading ($mg_{catalyst}\ cm^{-2}$)	1.31	0.70	1.29	0.86	1.13	1.35

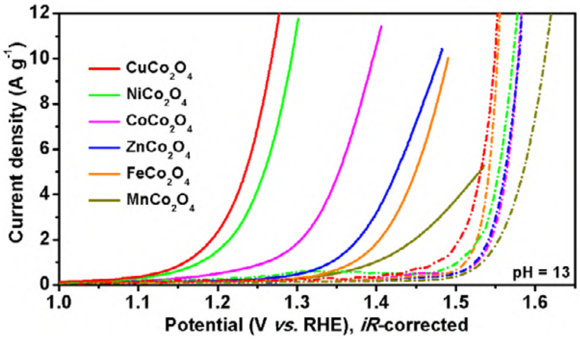

Figure A5.5. Glycerol oxidation current normalized by mass loading of MCo_2O_4 catalysts. The same sets of LSV curves shown in Figure 5.2a (Chapter 5) but normalized by the mass loadings of MCo_2O_4 catalysts on carbon fiber paper, still displaying the same trend of electrode performances in 0.1 M KOH solution (pH = 13) containing 0.1 M glycerol.

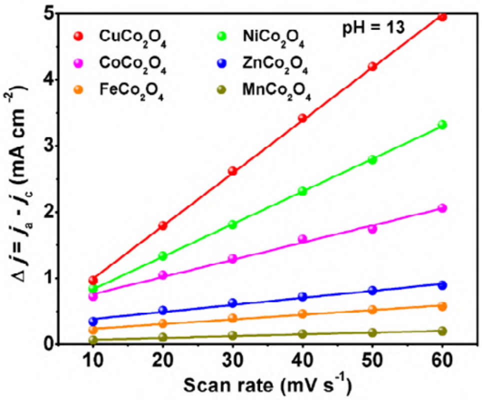

Figure A5.6. C_{dl} measurements of MCo_2O_4 catalysts. Estimation of electrochemically active surface areas (ECSAs) of the series of MCo_2O_4 nanostructure catalysts grown on carbon paper based on double-layer capacitance (C_{dl}) values extracted from cyclic voltammetry (CV) measurements in non-Faradaic regions. The CV measurements are performed in 0.1 M KOH solution (pH = 13) with 0.1 M glycerol.

Table A5.3. C_{dl} values of MCo_2O_4 catalysts. C_{dl} values (mF cm^{-2}, normalized to the geometric area of the electrode) of MCo_2O_4 nanostructure catalysts grown on carbon fiber paper based on CV measurements in non-Faradaic regions (see Figure A5.6).

	$MnCo_2O_4$	$FeCo_2O_4$	$CoCo_2O_4$	$NiCo_2O_4$	$CuCo_2O_4$	$ZnCo_2O_4$
C_{dl} (mF cm^{-2})	1.3	3.5	13.0	24.7	39.9	5.3

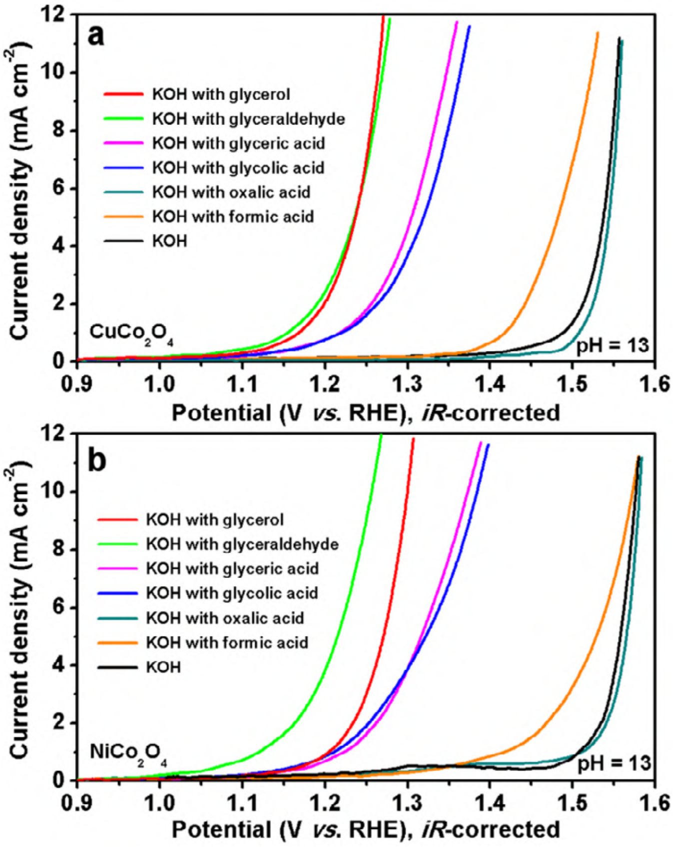

Figure A5.7. Evaluation of electrochemical oxidation of glycerol-derived intermediate products on $CuCo_2O_4$ and $NiCo_2O_4$ catalysts at pH = 13. LSV curves of (a) $CuCo_2O_4$ and (b) $NiCo_2O_4$ catalysts at a scan rate of 1 mV s^{-1} in 0.1 M KOH solution with and without the presence of 0.1 M glycerol or various possible intermediate products of the glycerol oxidation (glyceraldehyde, glyceric acid, glycolic acid, oxalic acid, and formic acid).

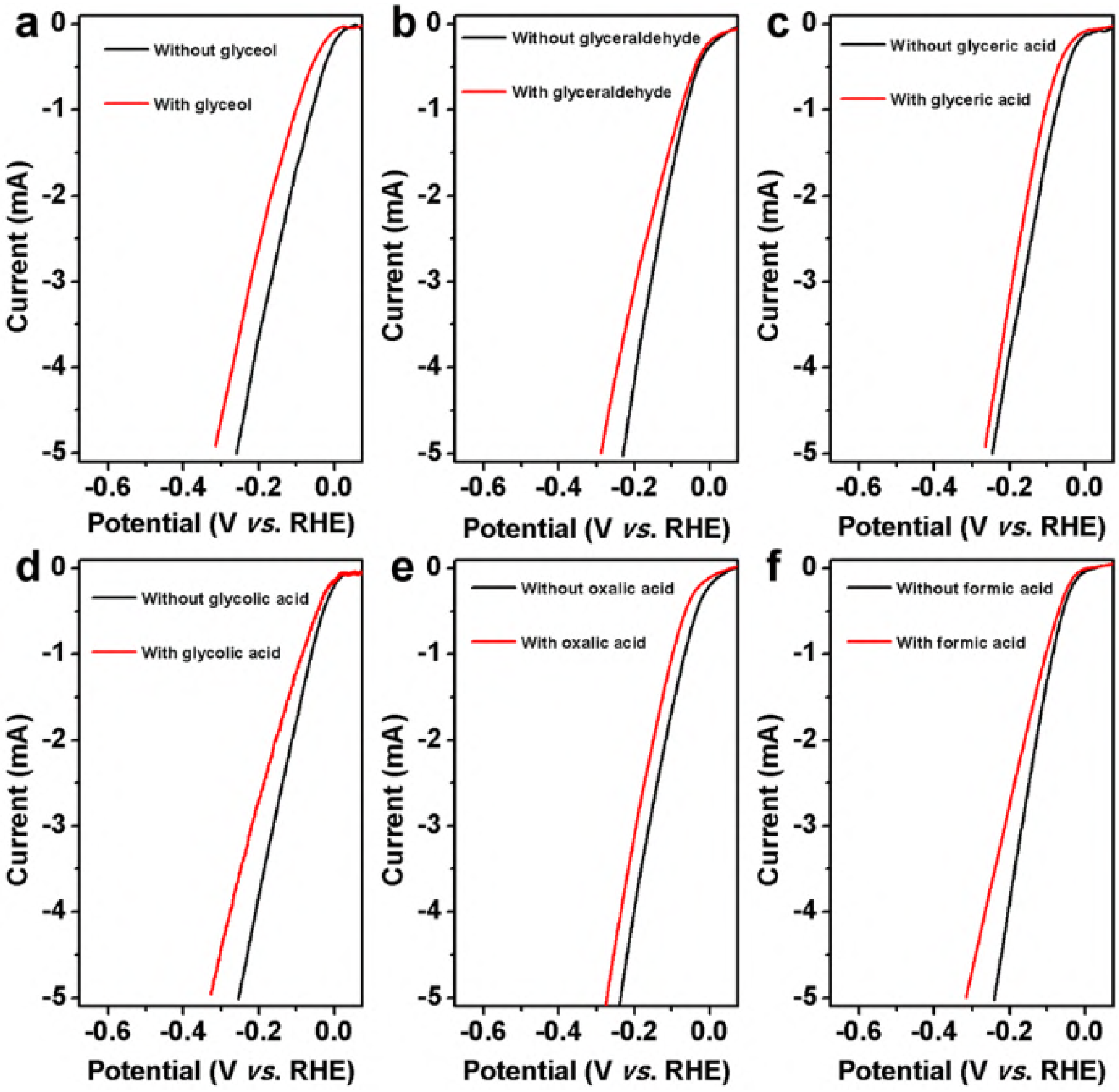

Figure A5.8. Evaluation of hydrogen evolution reaction on the Pt counter electrode with and without the presence of glycerol-derived intermediate products. LSV curves of the Pt wire counter electrode in 0.1 M KOH solution with and without the presence of of 0.1 M (a) glycerol or (b–f) various possible intermediate products of the glycerol oxidation including (b) glyceraldehyde, (c) glyceric acid, (d) glycolic acid, (e) oxalic acid, and (f) formic acid. It should be noted that the pH values of the electrolyte solutions with and without the addition of the respective molecules were measured separately, and the slight differences in these pH values have been taken into account when displaying all the potentials versus reversible hydrogen electrode (RHE) based on the following equation: E vs. RHE = E vs. Hg/HgO + E(Hg/HgO) vs. SHE + 0.059 × pH.

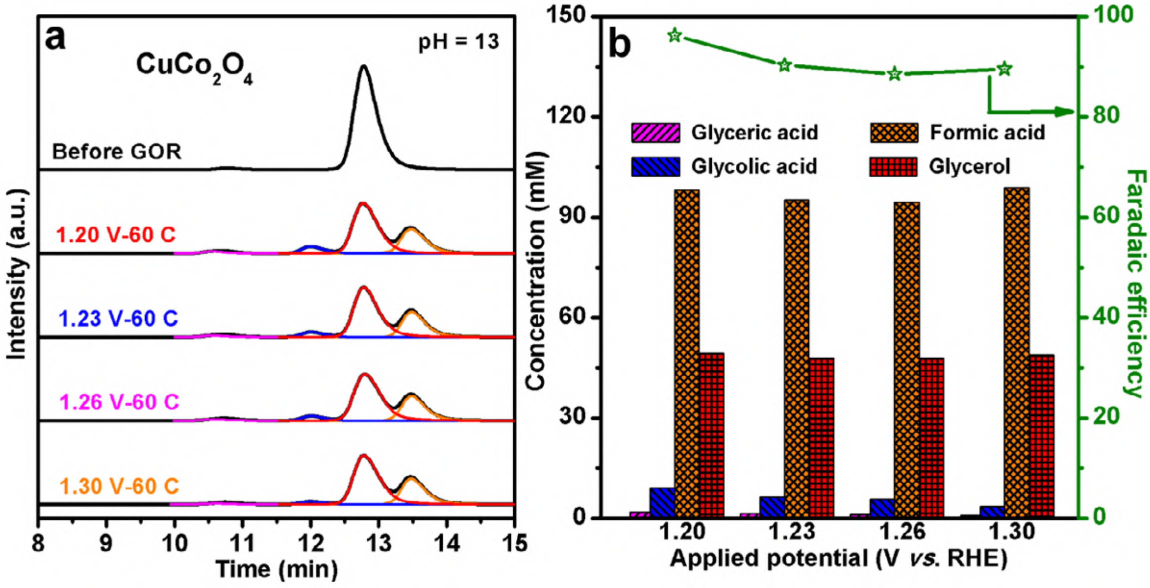

Figure A5.9. Product analysis of the glycerol oxidation on $CuCo_2O_4$ catalyst at different applied potentials at pH = 13. (a) HPLC chromatograms of the reaction products from the electrochemical oxidation of glycerol at different applied potentials using $CuCo_2O_4$ as electrocatalyst in 0.1 M KOH solution containing 0.1 M glycerol (pH = 13) with a total charge of 60 C passed. (b) Concentration distributions of glycerol and the various products and the corresponding overall Faradaic efficiency toward value-added products (glyceric acid, glycolic acid, and formic acid) after the glycerol oxidation at different applied potentials using $CuCo_2O_4$ as electrocatalyst in 0.1 M KOH solution containing 0.1 M glycerol (pH = 13) with a total charge of 60 C passed.

Table A5.4. Summary of the glycerol oxidation at different applied potentials using $CuCo_2O_4$ as electrocatalyst in 0.1 M KOH solution containing 0.1 M glycerol (pH = 13) with a total charge of 60 C passed.

Potential (V vs. RHE)	Charge passed (C)	Glycerol conversion (%)	Selectivity (%)			Faradaic efficiency (%)	Aqueous phase organic carbon amount (mM)	
			Glyceric acid	Glycolic acid	Formic acid		Input	Output [a]
1.20	60	47.9	4.3	13.3	72.1	93.3	136.0	121.9
1.23	60	49.4	3.2	8.9	67.9	88.3	140.3	112.2
1.26	60	49.4	2.4	8.1	67.3	86.7	140.4	109.2
1.30	60	48.4	1.7	5.1	71.9	88.4	137.6	108.3

[a] Output aqueous phase organic carbon amount does not include the CO_2 byproduct, which may be solubilized as CO_3^{2-} in alkaline solution.

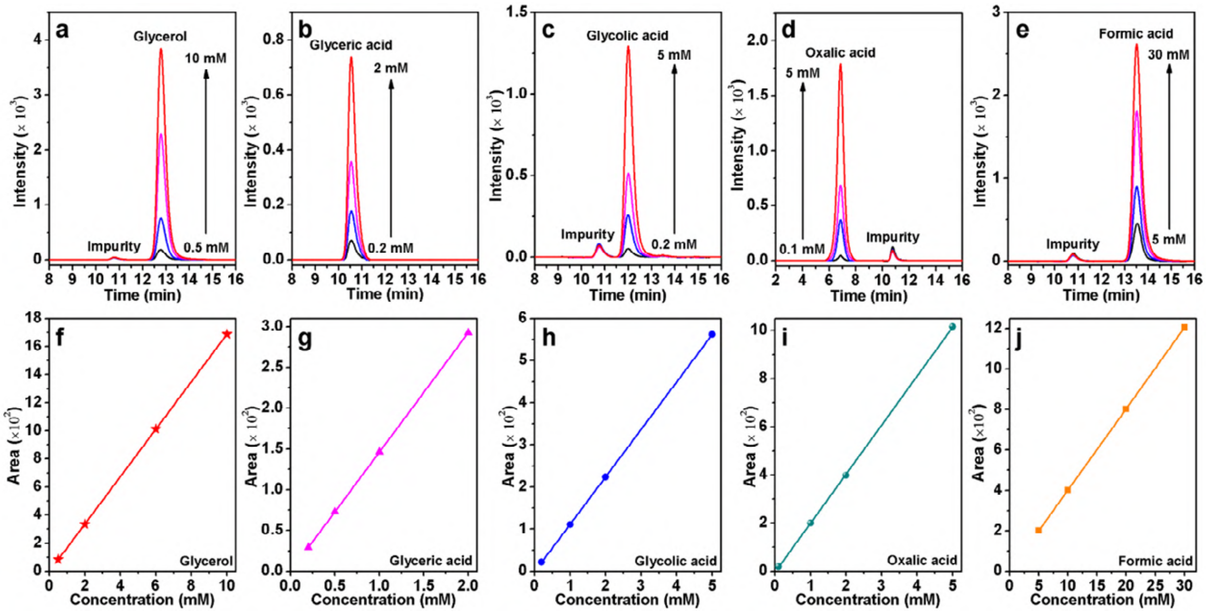

Figure A5.10. Standard HPLC chromatograms and calibration curves of glycerol and various potential products derived from the glycerol oxidation. (a–e) Standard HPLC chromatograms of glycerol and various potential products derived from the glycerol oxidation, including glyceric acid, glycolic acid, oxalic acid, and formic acid, in various concentrations. (f–j) The corresponding calibriation curves used to quantify the concentrations of the respective molecules from the chromatograms. It should be noted that an unknown impurity peak at the retention time of 10.8 min was always present in the chromatogram with roughly the same intensity even when we ran the blank sample (either nanopure water or KOH solution) under the same condition. For the quantification of glyceric acid whose retention time (10.5 min) is close to that of the unknown impurity, the area of the unknown impurity peak was subtracted for the sake of accuracy.

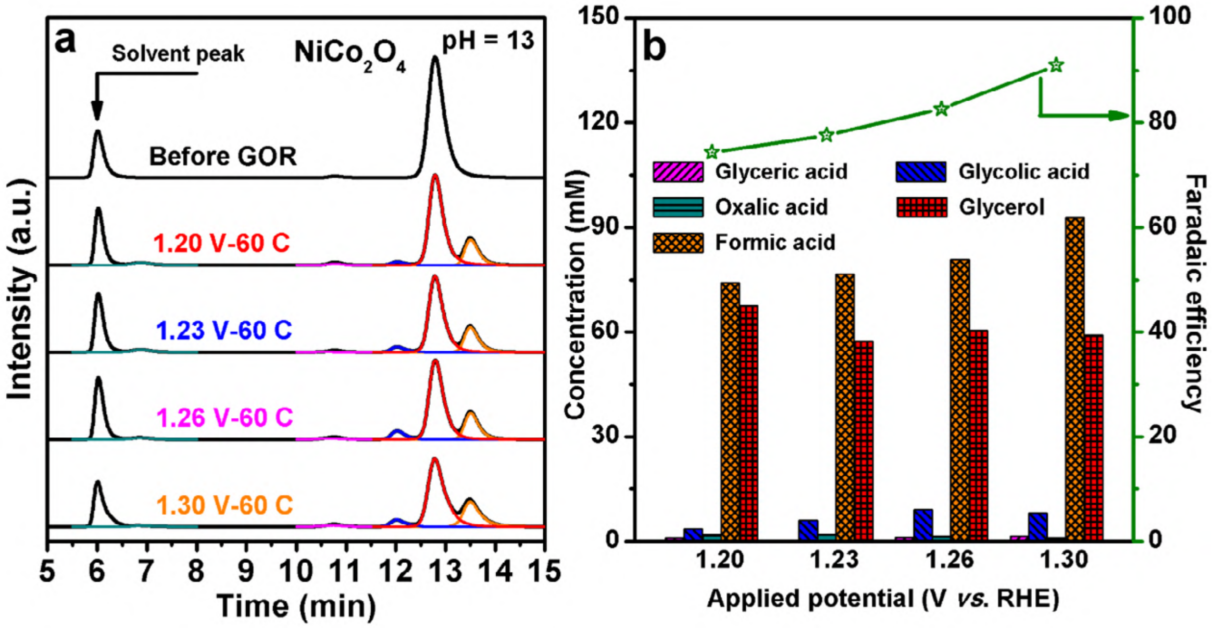

Figure A5.11. Product analysis of the glycerol oxidation on NiCo$_2$O$_4$ catalyst at different applied potentials at pH = 13. (a) HPLC chromatograms of the reaction products from the electrochemical oxidation of glycerol at different applied potentials using NiCo$_2$O$_4$ as electrocatalyst in 0.1 M KOH solution containing 0.1 M glycerol (pH = 13) with a total charge of 60 C passed. (b) Concentration distributions of glycerol and the various products and the corresponding overall Faradaic efficiency toward value-added products (glyceric acid, glycolic acid, glycolic acid, oxalic acid, and formic acid) after the glycerol oxidation at different applied potentials using NiCo$_2$O$_4$ as electrocatalyst in 0.1 M KOH solution containing 0.1 M glycerol (pH = 13) with a total charge of 60 C passed. Note that an additional minor product of oxalic acid (HPLC elution peak around 6.8 min) was observed for the glycerol oxidation using NiCo$_2$O$_4$ as electrocatalyst. The HPLC elusion peak around 6.0 min was the solvent peak, which was present in all the analyzed HPLC samples.

Table A5.5. Summary of the glycerol oxidation at different applied potentials using $NiCo_2O_4$ as electrocatalyst in 0.1 M KOH solution containing 0.1 M glycerol (pH = 13) with a total charge of 60 C passed.

Potential (V vs. RHE)	Charge passed (C)	Glycerol conversion (%)	Selectivity (%)				Faradaic efficiency (%)	Aqueous phase organic carbon amount (mM)	
			Glyceric acid	Glycolic acid	Oxalic Acid	Formic acid		Input	Output [a]
1.20	60	33.3	3.0	6.9	3.7	73.3	74.1	101.1	87.9
1.23	60	39.6	0.6	10.5	3.6	67.6	77.6	113.3	93.3
1.26	60	39.6	3.0	15.3	2.4	67.8	82.6	119.0	105.2
1.30	60	41.2	3.4	13.2	1.6	74.6	91.0	124.4	115.3

[a] Output aqueous phase organic carbon amount does not include the CO_2 byproduct, which may be solubilized as CO_3^{2-} in alkaline solution.

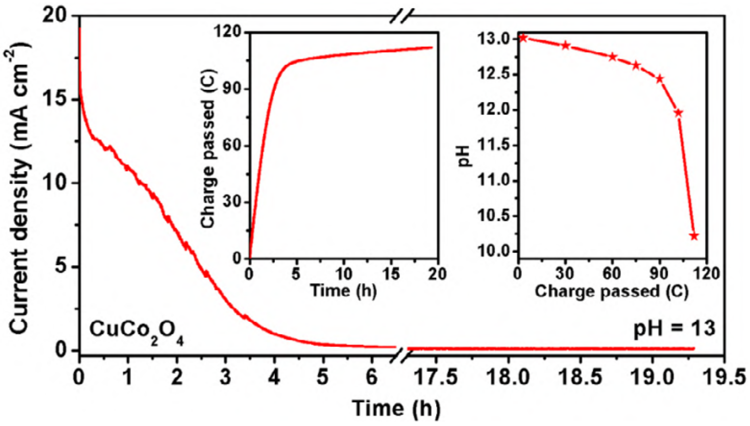

Figure A5.12. The changes in oxidation current density and bulk solution pH with increasing amount of charge passed during bulk electrolysis of glycerol oxidation on $CuCo_2O_4$ catalyst at pH = 13. The evolution of oxidation current density with time during the electrochemical oxidation of glycerol using $CuCo_2O_4$ as electrocatalyst at the constant potential of 0.42 V vs. Hg/HgO (1.30 V vs. RHE at pH = 13) in 0.1 M KOH solution containing 0.1 M glycerol. Insets are the corresponding curve of the total charge passed as a function of reaction time, and the change in the bulk solution pH as a function of the total charge passed during the electrochemical oxidation of glycerol.

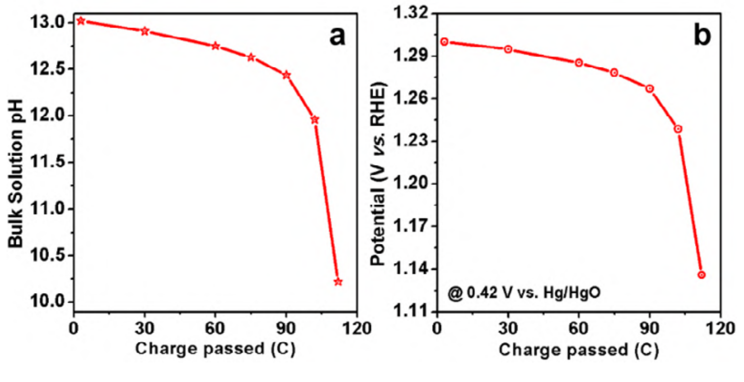

Figure A5.13. The changes in the bulk solution pH and the applied potential versus reversible hydrogen electrode (RHE). The changes in (a) the bulk solution pH and (b) the applied potential versus reversible hydrogen electrode (RHE) as a function of the total charge passed during the electrochemical oxidation of glycerol using $CuCo_2O_4$ as electrocatalyst at the constant potential of 0.42 V vs. Hg/HgO (1.30 V vs. RHE at pH = 13) in 0.1 M KOH solution containing 0.1 M glycerol (see Figure A5.12).

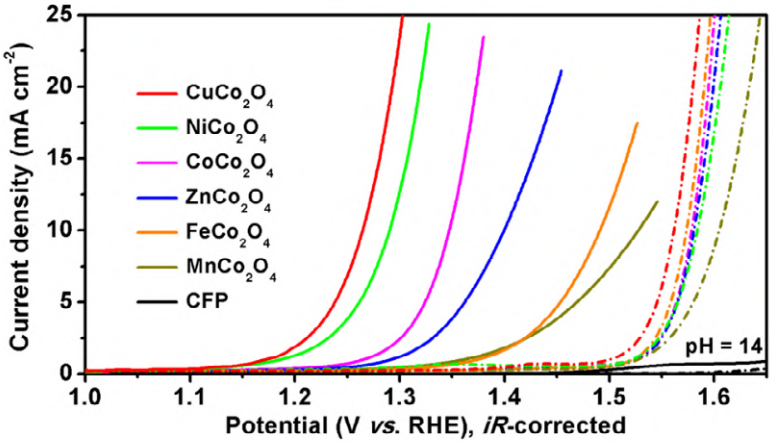

Figure A5.14. Electrochemical oxidation of glycerol on MCo_2O_4 catalysts at pH = 14. LSV curves (based on geometric current densities, mA cm^{-2}) of the series of MCo_2O_4 (M = Mn, Fe, Co, Ni, Cu, Zn) nanostructures grown on carbon fiber paper in comparison with the bare carbon fiber paper at the scan rate of 1 mV s^{-1} in 1 M KOH solution with (solid lines) and without (dash-dotted lines) the presence of 0.1 M glycerol.

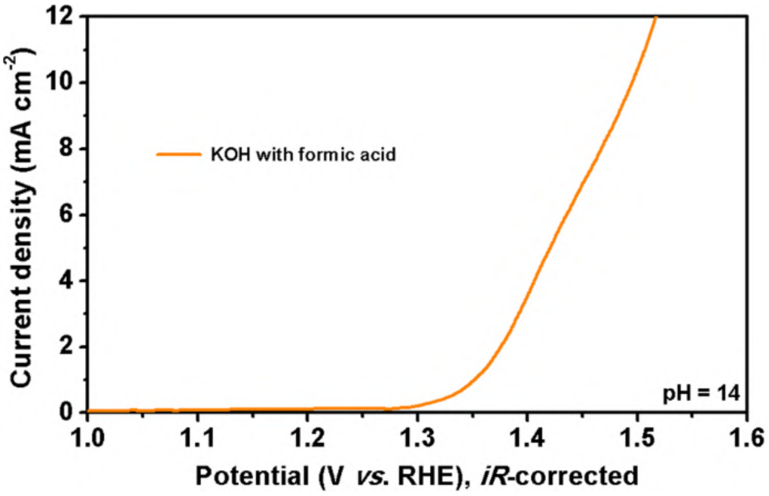

Figure A5.15. Evaluation of electrochemical oxidation of formic acid on $CuCo_2O_4$ catalyst at pH = 14. LSV curve of $CuCo_2O_4$ catalyst at a scan rate of 1 mV s^{-1} in 1 M KOH with the presence of 0.1 M formic acid.

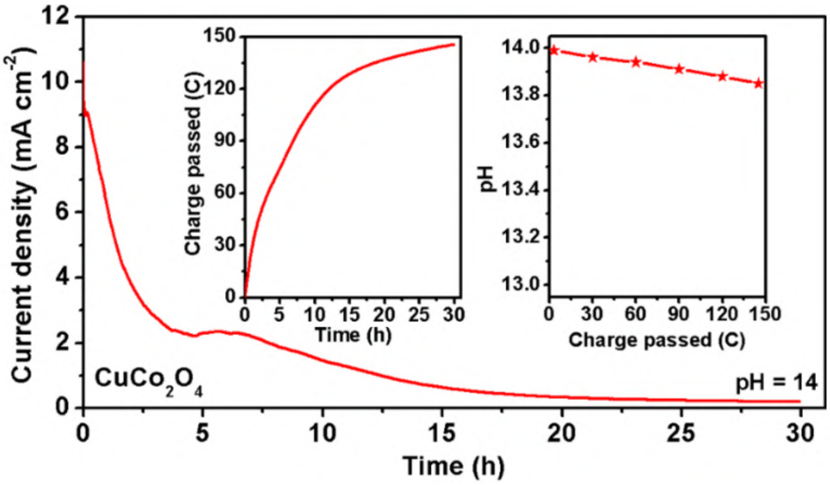

Figure A5.16. The evolution of oxidation current density and the less change in bulk solution pH with increasing amount of charge passed during bulk electrolysis of glycerol oxidation on $CuCo_2O_4$ catalyst at pH = 14. The evolution of oxidation current density with time during the electrochemical oxidation of glycerol using $CuCo_2O_4$ as electrocatalyst at 0.32 V vs. Hg/HgO (1.26 V vs. RHE at pH = 14) in 1 M KOH solution containing 0.1 M glycerol. Insets are the corresponding curve of the total charge passed as a function of reaction time, and the change of the bulk solution pH as a function of the total charge passed during the electrochemical oxidation of glycerol. Due to the better pH-buffering of 1 M KOH solution, the changes in the oxidation current density and the solution pH here are less drastic than the case of 0.1 M KOH solution presented in Figure A5.12.

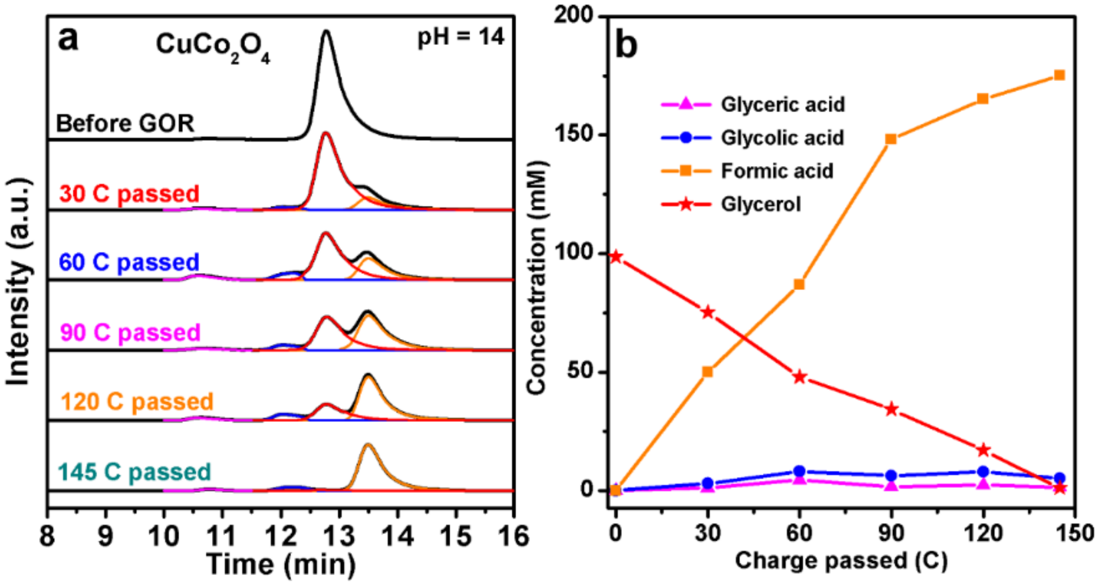

Figure A5.17. Product analysis of the glycerol oxidation on $CuCo_2O_4$ catalyst at pH = 14. (a) HPLC chromatograms of the reaction products from the electrochemical oxidation of glycerol using $CuCo_2O_4$ as electrocatalyst at 0.32 V vs. Hg/HgO (1.26 V vs. RHE at pH = 14) in 1 M KOH solution containing 0.1 M glycerol with different amounts of total charge passed. (b) Concentrations of glycerol and its oxidation products as a function of the total charge passed after the glycerol oxidation using $CuCo_2O_4$ as electrocatalyst at 0.32 V vs. Hg/HgO (1.26 V vs. RHE at pH = 14) in 1 M KOH solution containing 0.1 M glycerol.

Table A5.6. Summary of the glycerol conversion, product selectivity, and Faradaic efficiency of the glycerol oxidation using $CuCo_2O_4$ as electrocatalyst at 0.32 V vs. Hg/HgO (1.26 V vs. RHE at pH = 14) in 1 M KOH solution containing 0.1 M glycerol with different amounts of total charge passed.

Potential (V vs. Hg/HgO)	Potential (V vs. RHE) [a]	Charge passed (C)	Glycerol conversion (%)	Selectivity (%)			Faradaic efficiency (%)	Aqueous phase organic carbon amount (mM)		pH
				Glyceric acid	Glycolic acid	Formic acid		Input	Output [b]	
0.32	1.26	30	23.8	4.3	8.5	70.9	92.8	70.4	59.0	13.96
0.32	1.26	60	51.4	8.8	10.7	57.0	86.3	152.3	116.6	13.94
0.32	1.25	90	65.2	2.5	6.5	76.7	89.3	193.2	165.7	13.91
0.32	1.25	120	82.7	2.9	6.4	67.4	75.1	245.0	188.0	13.88
0.32	1.25	145	98.9	1.4	3.5	58.8	64.3	298.2	189.8	13.85

[a] The change in the applied potential versus reversible hydrogen electrode (RHE) is due to the decrease in the bulk solution pH, as the various acid products from the glycerol oxidation consume OH^- in the electrolyte solution and exist in the carboxylate forms.

[b] Output aqueous phase organic carbon amount does not include the CO_2 byproduct, which may be solubilized as CO_3^{2-} in alkaline solution.

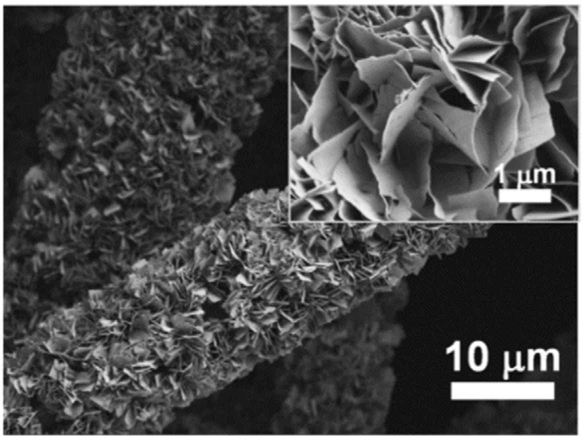

Figure A5.18. SEM image of the $CuCo_2O_4$ electrocatalyst after the bulk electrolysis reaction of glycerol oxidation.

APPENDIX 6

Supplementary Information for CHAPTER 6:

Stable Tetrasubstituted Quinone Redox Reservoir for Enhancing Decoupled Hydrogen and Oxygen Evolution[*]

---

[*] This appendix was originally made available online as the Supporting Information for *ACS Energy Lett.* ***6***, 1533–1539 (2021), in collaboration with Fei Wang, Wenjie Li, James B. Gerken, Song Jin, and Shannon S. Stahl.

1. General Experimental Considerations

All commercially available chemicals and materials were used as received unless otherwise noted. Deionized water or D_2O was used for all the experiments. Cyclic voltammetry (CV) measurements were performed in 1 M H_2SO_4 using either a glassy carbon disk electrode (BASi, 3 mm diameter, polished with 0.05 μm alumina suspension before each experiment) or an as-received carbon paper electrode (GDL 39 AA, SIGRACET®) as the working electrode, along with an Ag/AgCl (saturated KCl) reference electrode and a Pt wire counter electrode. Prior to CV experiments, the electrolyte solution was purged with nitrogen gas. CV experiments were performed with the cell headspace under a nitrogen blanket. ^{1}H NMR spectra were recorded on a Bruker Avance III 400 spectrometer. ^{1}H NMR stability tests were performed in 1 M H_2SO_4 in the D_2O solvent. ^{1}H NMR spectra were acquired at a proton frequency of 400 MHz with frequency lock to the D_2O solvent.

2. Synthesis of TMHQ

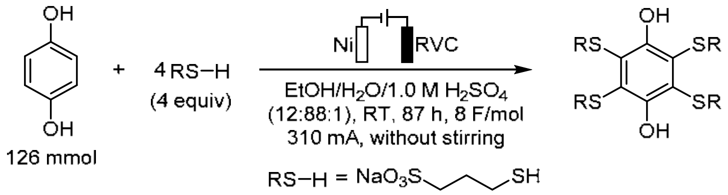

TMHQ used in this work was synthesized using the previously reported procedure on the same scale.[1] In a 1 L beaker, hydroquinone (13.9 g, 126mmol) was wetted with 60 mL of ethanol and then 440 mL of water. Sodium mercaptopropanesulfonate (MPSNa, 90% technical grade, 100 g, 505 mmol) was added into the mixture and stirred until all solids dissolve, followed by the addition of 5 mL of 1 M H_2SO_4 aqueous solution, resulting in a final pH of ~2. A reticulated vitreous carbon (RVC) anode and a nickel wire cathode were placed in the solution for the bulk electrosynthesis reaction. A current of 310 mA was passed without stirring for 87 h (8 F/mol). After the reaction completed, each electrode was withdrawn and rinsed with 10 mL of water into the reaction beaker, and the reaction mixture was divided into two portions for isolation of the product. Each reaction mixture portion was transferred to a 3 L plastic beaker and diluted with four 300 mL portions and then two 250 mL portions of ethanol: the first two 300 mL portions of ethanol were added slowly with agitation until precipitation commenced, and the subsequent portions of ethanol were added with vigorous agitation until the suspension became less viscous. The suspension was allowed to stand for 0.5 h and was then filtered and rinsed with two 100 mL portions of ethanol. The combined solids from both reaction mixture portions were dried overnight in a vacuum oven at 40 °C to yield 93.5 g (115 mmol) of the product with a 91% yield, with spectroscopic properties identical to those reported previously.[1] The solid product of TMHQ deposited on carbon tape was also characterized by energy dispersive X-ray spectroscopy (EDS) under a Zeiss SUPRA 55VP field emission scanning electron microscope (SEM) at the acceleration voltage of 16 keV, showing that it is a tetrasodium salt (atomic ratio of Na : S = 0.55 : 1) without nickel contamination.

3. Cyclic Voltammetry Studies of TMHQ

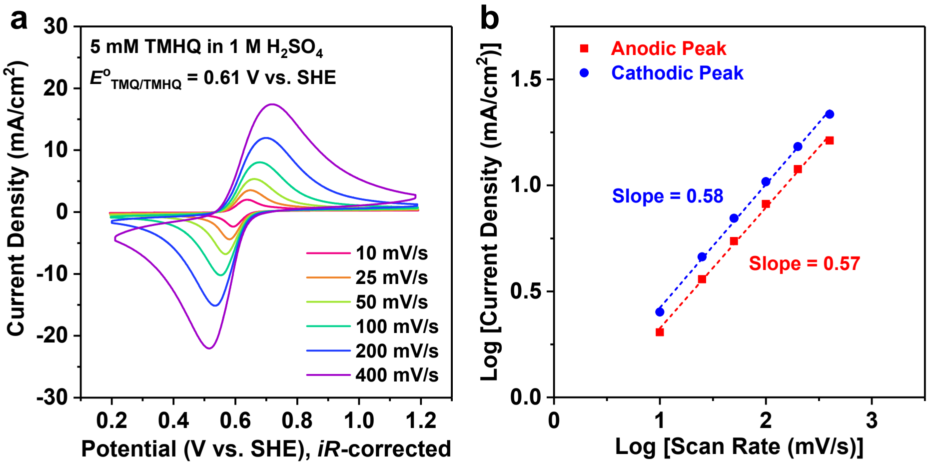

Figure A6.1. Cyclic voltammetry studies of TMHQ.

Cyclic voltammetry of 5 mM TMHQ in 1 M H_2SO_4 using carbon paper as the working electrode. (a) Cyclic voltammograms recorded at different scan rates. (b) Anodic and cathodic peak current densities as a function of scan rate. According to the slopes of the linear fittings of the log–log plots are close to 0.5, the peak current densities can be considered to increase linearly with almost the square root of scan rate, indicating a diffusion-controlled redox process rather than a surface-adsorbed redox process.

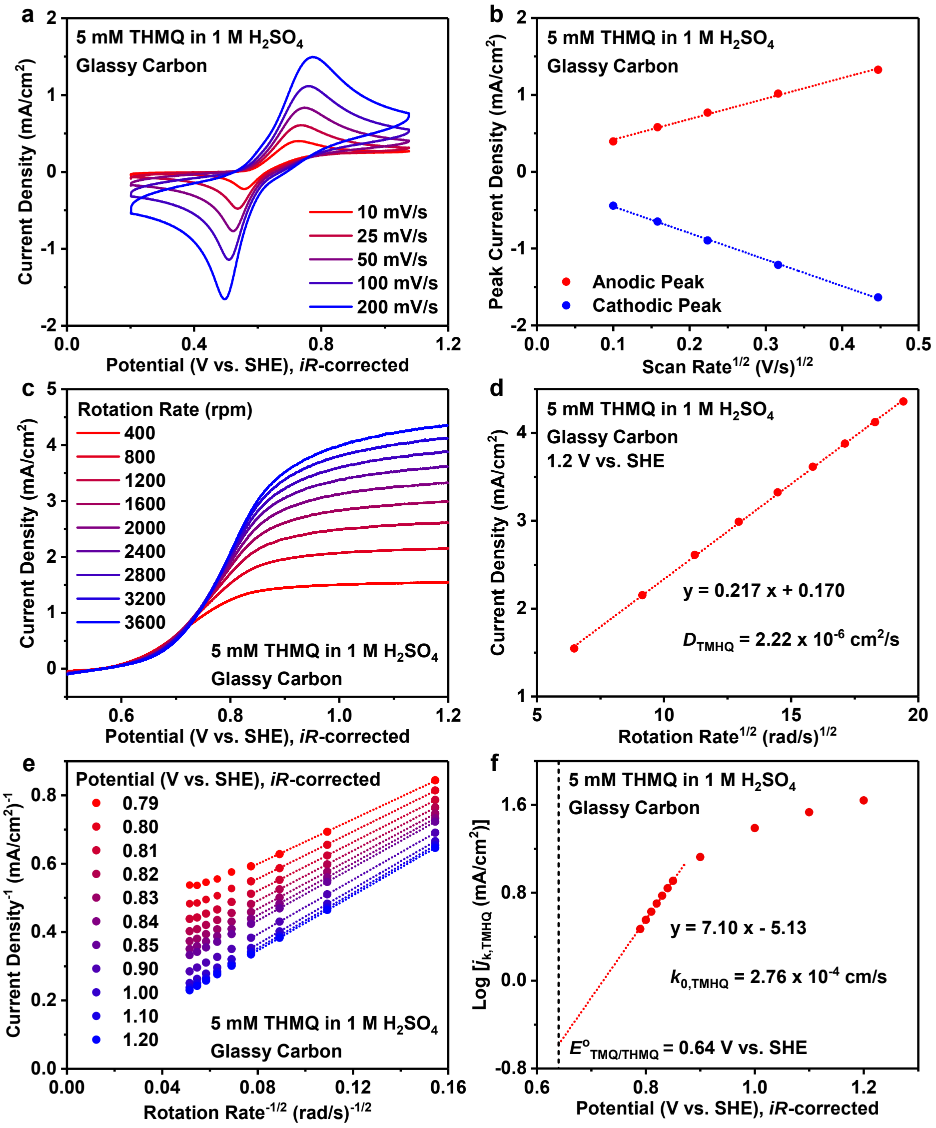

Figure A6.2. Diffusion constant and standard rate constant of TMHQ extracted from cyclic voltammetry studies.

Cyclic voltammetry of 5 mM TMHQ in 1 M H_2SO_4 using glassy carbon rotating disk electrode as the working electrode. (a) Cyclic voltammograms recorded at different scan rates. (b) Anodic and cathodic peak current densities as a function of the square root of scan rate. (c) Linear sweep voltammograms recorded at 25 mV/s under different rotation rates. (d) Levich analysis of anodic diffusion-limited current density as a function of the square root of rotation rate at 1.2 V vs. SHE. (e) Koutecky-Levich analysis of the reciprocal of anodic current density as a function of the reciprocal square root of rotation rate at various potentials. (f) Logarithm of kinetic anodic current density ($j_{k,TMHQ}$) as a function of potential.

The diffusion coefficient (D) and the standard kinetic constant (k_0) of TMHQ in 1 M H_2SO_4 was evaluated using a glassy carbon rotating disk electrode (RDE) (Figure A6.2). The glassy carbon RDE electrode was first activated by performing CV in 1 M Na_2SO_4 solution between -0.55 V and 1.95 V vs. SHE at 100 mV/s and 0 rpm for 30 cycles. The fast electron transfer kinetics of the activated glassy carbon RDE was verified by performing CV in 5 mM $K_3[Fe(CN)_6]$ in 1 M Na_2SO_4 solution at 10 mV/s and 0 rpm, where the experimental peak separation of 61 mV was almost the same as the ideal peak separation of 59 mV for a reversible one-electron redox couple.

Figure A6.2a shows the CV curves of 5 mM TMHQ in 1 M H_2SO_4 solution recorded on the activated glassy carbon RDE at 0 rpm and different scan rates, where the anodic and cathodic peak current densities increase linearly with the square root of scan rate (Figure A6.2b). The experimental peak separation of the TMHQ/TMQ redox couple at 10 mV is 172 mV (Figure A6.2a), which is greater than the ideal peak separation of 30 mV for a reversible two-electron redox couple.

To extract the diffusion coefficient of TMHQ, linear sweep voltammetry (LSV) was carried out from 0.5 V to 1.2 V vs. SHE at 25 mV/s and different rotation rates (Figure A6.2c). Levich analysis was performed at the potential of 1.2 V vs. SHE where the anodic current density was diffusion-limited (Figure A6.2d). The Levich equation is shown below:

$$j_L = 0.62\, n\, F\, D^{2/3}\ \omega^{1/2}\, v^{-1/6}\, C$$

where j_L is the diffusion-limited current density (A/cm^2), n is the electron transfer number (2), F is the Faraday constant (96485 C/mol), D is the diffusion coefficient (cm^2/s), ω is the angular rotation rate (rad/s), v is the kinematic viscosity of 1 M H_2SO_4 solution (1.05×10^{-2} cm^2/s), C is the analyte concentration (5×10^{-6} mol/cm^3). Since the slope of j_L vs. $\omega^{1/2}$ plot was 2.17×10^{-4} A·s$^{1/2}$/cm^2, the diffusion coefficient of TMHQ was calculated to be 2.22×10^{-6} cm^2/s (Figure A6.2d).

$$D_{\mathrm{TMHQ}} = \left[\frac{(2.17\times10^{-4}\ \mathrm{A\cdot s^{1/2}/cm^2})}{0.62\times2\times(96485\ \mathrm{A\cdot s/mol})\times(1.05\times10^{-2}\ \mathrm{cm^2/s})^{-1/6}\times(5\times10^{-6}\ \mathrm{mol/cm^3})}\right]^{3/2} = 2.22\times10^{-6}\ \mathrm{cm^2/s}$$

To extract the standard kinetic constant of TMHQ, Koutecky-Levich analysis was performed at various potentials spanning from 0.79 V to 1.20 V vs. SHE (Figure A6.2e). The Koutecky-Levich equation is shown below:

$$j^{-1} = j_k^{-1} + j_L^{-1} = j_k^{-1} + (0.62\, n\, F\, D^{2/3}\, v^{-1/6}\, C)^{-1}\ \omega^{-1/2}$$

where j is the total current density (A/cm^2), and j_k is the kinetic current density (A/cm^2). After obtaining j_k at various potentials from the vertical intercept of the linear fitting of j^{-1} vs. $\omega^{-1/2}$ plots

(Figure A6.2e), mass-transport-corrected Tafel plot was made by plotting logarithm of j_k as a function of potential (Figure A6.2f):

$$\log(j_k) = \log(j_0) + b \times \eta$$

where b is the mass-transport-corrected Tafel slope, η is the overpotential with respect to the formal potential of the TMHQ/TMQ redox couple ($E^o_{\text{TMQ/TMHQ}} = 0.64$ V vs. SHE, see Figure A6.2a), and j_0 is the exchange current density at $E^o_{\text{TMQ/TMHQ}}$. After obtaining j_0 by extrapolating the linear region (0.79 V to 0.85 V vs. SHE) of $\log(j_k)$ vs. potential plot to $E^o_{\text{TMQ/TMHQ}}$, the standard rate constant of TMHQ was calculated to be 2.76×10^{-4} cm/s (Figure A6.2f)。

$$j_{0,\text{TMHQ}} = 10^{(7.10\times0.64\ -\ 5.13)}\ \text{mA/cm}^2 = 0.260\ \text{mA/cm}^2$$

$$k_{0,\text{TMHQ}} = \frac{j_{0,\text{TMHQ}}}{n\,F\,C} = \frac{2.60\times10^{-4}\ \text{A/cm}^2}{2 \times (96485\ \text{A}\cdot\text{s/mol}) \times (5\times10^{-6}\ \text{mol/cm}^3)} = 2.76\times10^{-4}\ \text{cm/s}$$

According to a previous report, the diffusion coefficient (D) of AQDS is $3.8(1)\times10^{-6}$ cm^2/s, and the standard rate constant (k_0) of AQDS is $7.2(5)\times10^{-3}$ cm/s.[2] Therefore, our results suggest that the D of TMHQ is on the same order of magnitude as that of AQDS, but the k_0 of TMHQ is one order of magnitude smaller than that of AQDS.

4. NMR Analysis of TMHQ/TMQ vs. AHQDS/AQDS

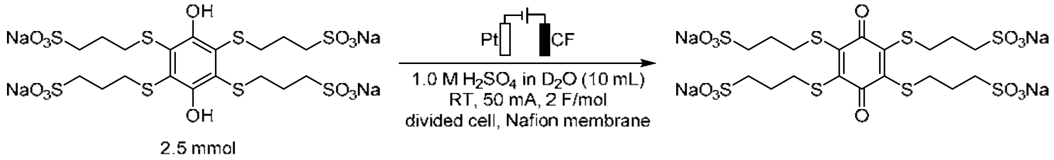

TMQ used for the NMR analysis was obtained by electrochemical oxidation of TMHQ in a divided H-cell. TMHQ (2.5 mmol, 2.04 g) was added into the anodic compartment containing 10 mL of 1 M H_2SO_4 in D_2O solution as the supporting electrolyte and carbon felt (CF) as the working electrode. In the cathodic compartment were placed 10 mL of 1 M H_2SO_4 in D_2O solution and a platinum mesh. The two compartments were separated with a Nafion 117 membrane. A current of 50 mA was passed with stirring for 2 h 40 min (2 F/mol). After the bulk electrolysis reaction, the CF electrode was withdrawn, and 2.5 mmol of *p*-toluenesulfonic acid was added into the anodic compartment as internal standard for the NMR analysis. Then, ~1 mL of the anodic compartment solution was sampled into an NMR tube, degassed with nitrogen gas for 1 min, capped and sealed with Teflon tape as the NMR sample of TMQ with a concentration of ca. 0.25 M in the D_2O solvent.

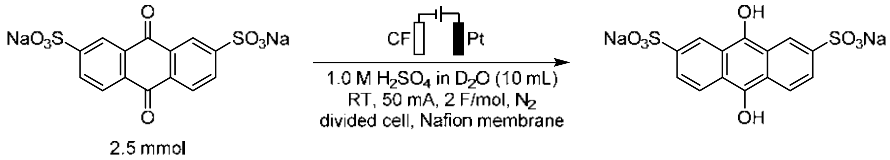

AHQDS used for the NMR analysis was obtained by electrochemical reduction of AQDS in a divided H-cell, analogous to the procedure above except for (1) placing AQDS into the cathodic compartment under nitrogen gas protection, and (2) using CF as the cathode and platinum mesh as the anode, respectively. Similarly, the NMR sample of AHQDS was degassed with nitrogen gas and had a concentration of ca. 0.25 M in the D_2O solvent with *p*-toluenesulfonic acid as internal standard.

The NMR samples of TMHQ and AQDS were directly prepared by dissolving 0.25 M each species in 1 M H_2SO_4 in D_2O solution with *p*-toluenesulfonic acid as internal standard, followed by degassing with nitrogen gas and sealing into NMR tubes.

All the four NMR samples were stored in a 50 °C oven and were periodically subjected to ^{1}H NMR analysis every 2-3 days. Figure A6.3 demonstrated that TMHQ was very stable with no obvious decomposition over 20 days. Figure A6.4 showed that its oxidized form, TMQ, underwent slow decay with an 81% retention after 17 days. In fact, the decay product from TMQ was mainly TMHQ (which accounted for ~14% of the overall starting material of TMQ). Since TMHQ is still redox active, the slow decay of TMQ is not expected to cause appreciable capacity loss as a RR. On the other hand, Figures A6.5 and A6.6 suggested that AQDS exhibited a high stability, whereas AHQDS decayed substantially with only 43% retention after 17 days. The temporal retention of ^{1}H NMR signals of TMHQ, TMQ, AHQDS, and AQDS are summarized in Figure A6.7.

CV tests (see Figure A6.8) were further carried out on the aged NMR samples. The electrolyte solution for each CV test was prepared by adding 200 μL of each aged NMR sample into 4.8 mL of 1 M H_2SO_4 aqueous solution and purging with nitrogen gas for 2 min prior to each CV test. CV experiments were performed using a freshly-polished glassy carbon working electrode (0.07 cm^2, see Section 1 of the Appendix 6 for details), an Ag/AgCl reference electrode, and a platinum wire counter electrode (~1 cm). A nitrogen blanket was maintained in the cell headspace during CV experiments. Figure A6.8a showed that the peak currents of the aged AHQDS sample were substantially lower than those of the aged AQDS sample, indicating at least part of the decayed product from AHQDS is redox inactive. In contrast, there was little difference in the peak currents of the aged TMQ vs. TMHQ samples (Figure A6.8b), indicating most of the decayed products (mainly TMHQ) from TMQ is still redox active.

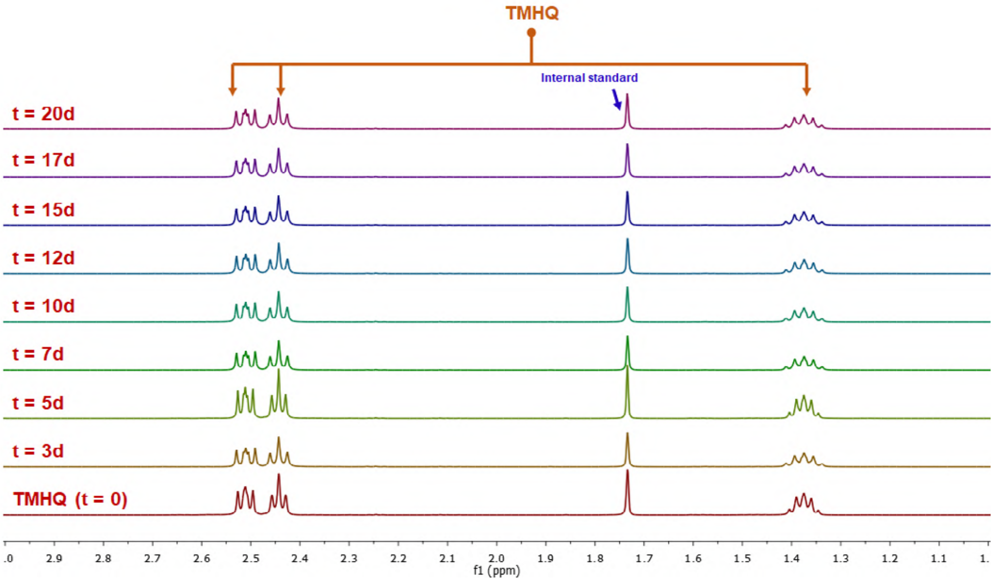

Figure A6.3. ^{1}H NMR analysis of the TMHQ sample (0.25 M in 1 M H_2SO_4 in D_2O solution) stored at 50 °C for 20 days.

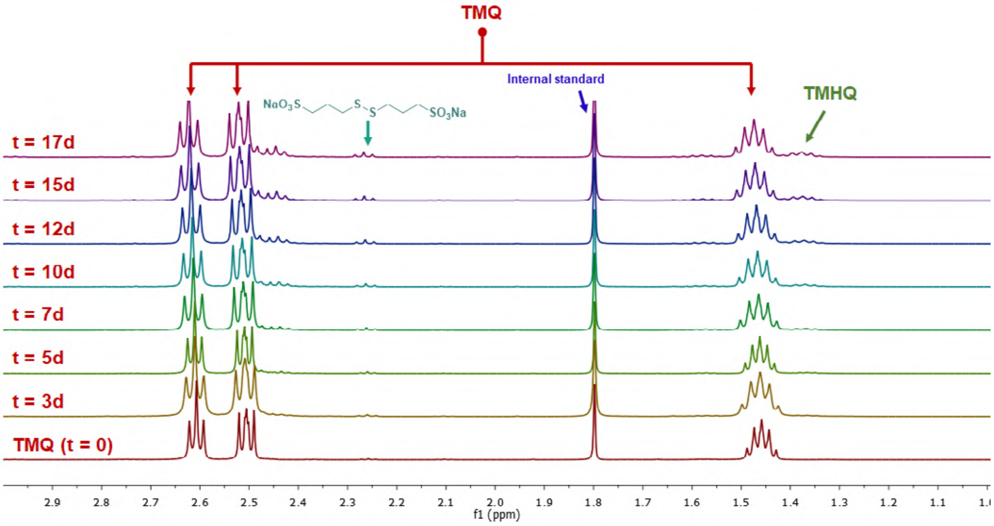

Figure A6.4. ^{1}H NMR analysis of the TMQ sample (0.25 M in 1 M H_2SO_4 in D_2O solution) stored at 50 °C for 17 days.

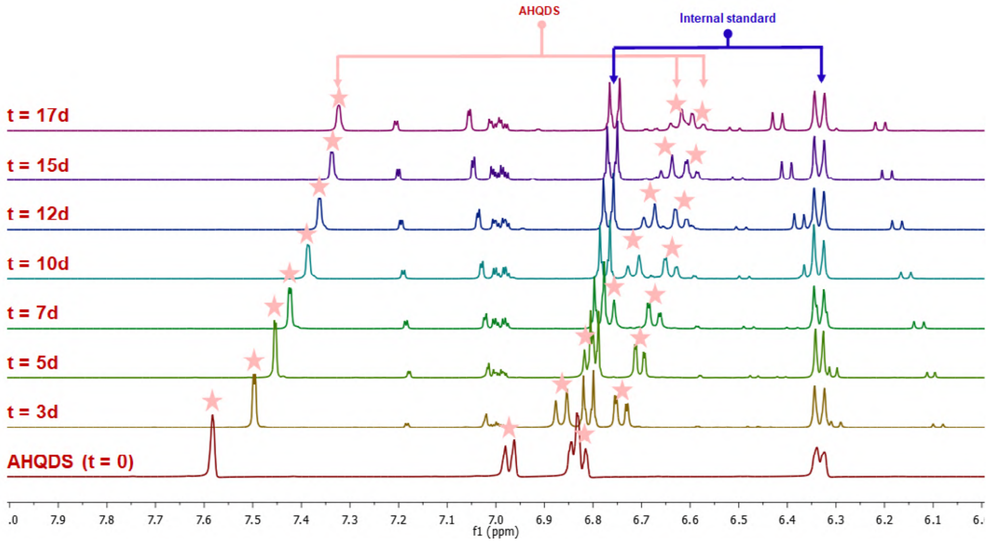

Figure A6.5. **^{1}H NMR analysis of the AHQDS sample (0.25 M in 1 M H_2SO_4 in D_2O solution) stored at 50 °C for 17 days.**

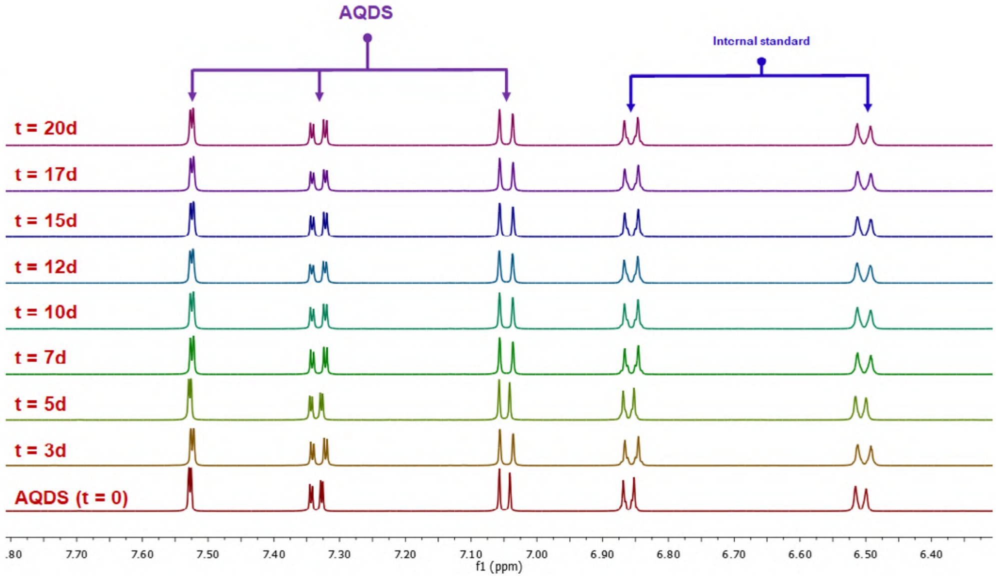

Figure A6.6. **^{1}H NMR analysis of the AQDS sample (0.25 M in 1 M H_2SO_4 in D_2O solution) stored at 50 °C for 20 days.**

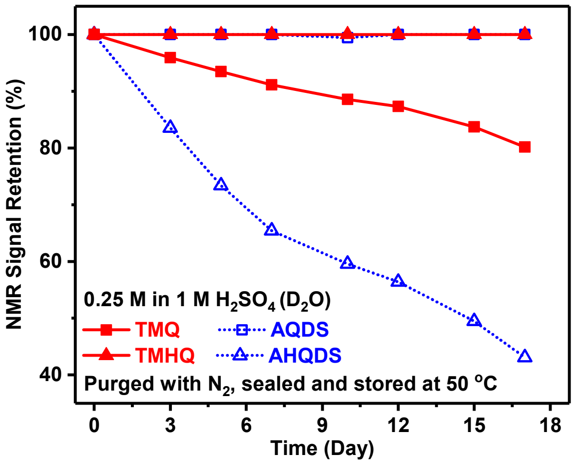

Figure A6.7. Temporal retention rates of ^{1}H NMR signals of the TMHQ, TMQ, AHQDS, and AQDS samples over time.

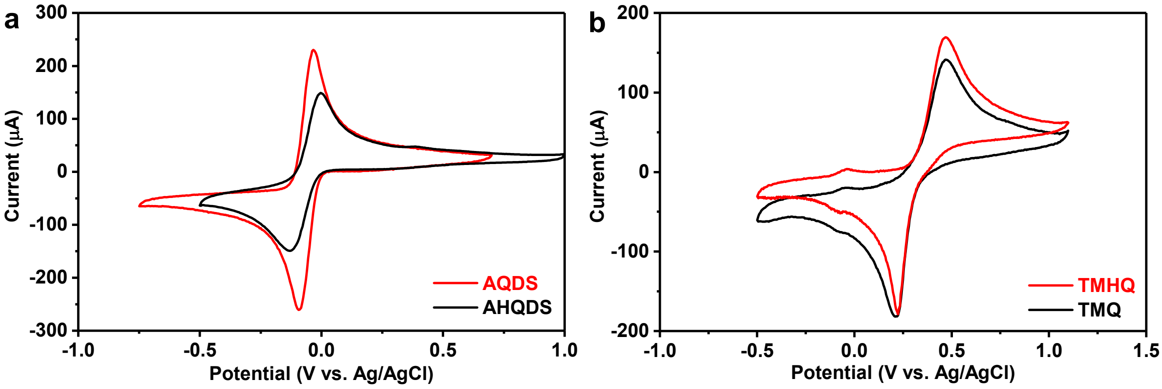

Figure A6.8. CV studies of the aged NMR samples diluted with 1 M H_2SO_4 aqueous solution, resulting in a concentration of ~10 mM of redox mediator. (a) AHQDS and AQDS. (b) TMHQ and TMQ.

5. Symmetric Redox Flow Battery of TMHQ/TMQ vs. AHQDS/AQDS

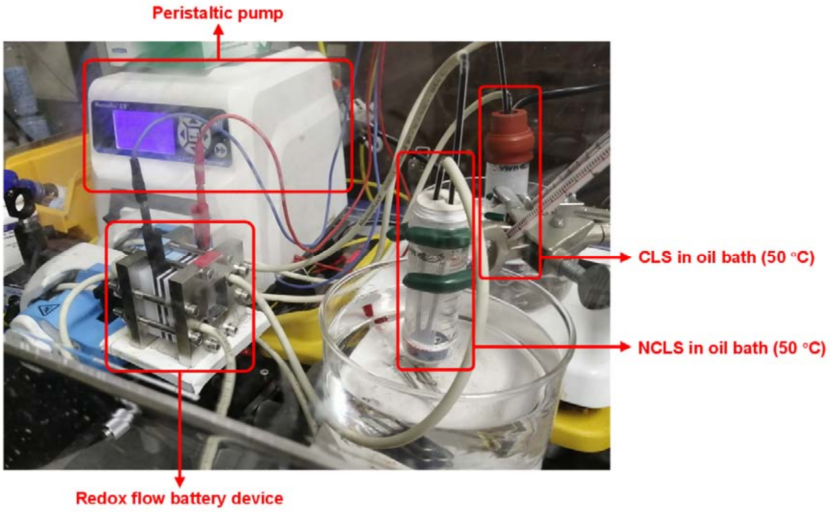

Figure A6.9. Experimental setup of the symmetric redox flow battery. CLS = capacity-limiting side; NCLS = non-capacity limiting side.

Symmetric redox flow battery (RFB) tests provide a practical approach to rigorously evaluate the stability of redox couple.[3] Aziz and coworkers have assessed the possibility of chemical vs. electrochemical decomposition mechanisms by introducing cycling pauses to hold the capacity-limiting side (CLS) electrolyte at different state of charges (SOCs) in a symmetric RFB test. The experiments were carried out using a custom-made zero-gap RFB device (Figure A6.9), matching the design used in a previous report.[4] Two pieces of graphite plate (1/8-inch thickness, Tokai Carbon) with a machined pocket (2 cm × 2 cm × 1.2 mm) were used as current collectors for the RFB device. Graphite felt electrodes (2 cm × 2 cm, GFD 3 EA, SIGRACELL®) were pre-treated in air at 400 °C for 24 h before used as the electrodes that sit in the graphite plate pockets. Nafion 212 membrane was treated with 3 wt% H_2O_2 at 80 °C for 1 h and immersed in 1 M H_2SO_4 before used as the proton-exchange membrane. The RFB device was assembled using four pieces of Teflon sheets (0.04-inch thickness) as the gaskets and was tightened with eight #10-24 bolts torqued to 4.0 N·m. The electrolyte solutions were stored in polypropylene centrifuge tubes (VWR), heated at 50 °C in oil baths, and circulated through the graphite plate pockets via PharMed BPT #14 tubing using a Cole-Parmer Masterflex L/S peristaltic pump operated at the flow rate of 60 mL/min. All symmetric RFB measurements were carried out in a custom-modified flush box (Terra Universal) with continuous nitrogen gas flushing.

Given that TMHQ and AQDS were incredibly stable in 1 M H_2SO_4 solution at 50 °C based on the ^1H NMR analysis presented earlier (see Section 4 of the Appendix 6), the symmetric RFB experiments prioritized comparison of the relative stability of TMQ and AHQDS under similar electrochemical conditions by periodically holding the CLS electrolyte of the RFB at the oxidized TMQ state and at the reduced AHQDS state, respectively. The detailed procedure is as follows:

a. To prepare 50% SOC (AHQDS/AQDS = 1:1) electrolyte solution for the AHQDS/AQDS symmetric flow battery test, the cathodic bulk electrolysis of the as-made 0.25 M AQDS in 1 M H_2SO_4 solution (30 mL) was first performed in a commercial electrolyzer assembly (same as the OER cell described in Section 8 of the Appendix 6). Prior to the cathodic bulk electrolysis, the 0.25 M AQDS in 1 M H_2SO_4 solution (30 mL) was purged with nitrogen gas for 5 min and sealed. The cathodic bulk electrolysis was conducted at 1.5 A for 8 min to pass the theoretical amount of charge needed to reach 50% SOC (assuming a Faradaic efficiency of unity for the reduction of AQDS to AHQDS).

b. The as-prepared 50% SOC electrolyte solution was then transferred into a nitrogen purged box and divided into two parts, 10 mL for the CLS and 20 mL for the non-capacity-limiting side (NCLS), for the AHQDS/AQDS symmetric RFB test. Both the CLS and NCLS electrolyte tanks were heated at 50 °C in oil baths. Figure A6.9 shows a photograph of the experimental setup.

c. The charge/discharge cycles of the AHQDS/AQDS symmetric RFB were conducted at 200 mA (50 mA/cm^2) with cutoff cell voltages of ±0.4 V (Figure 6.2c in the Chapter 6). The CLS electrolyte was first fully reduced to the AHQDS state (0% SOC), two charge-discharge cycles were then conducted to measure the charge capacity of the CLS electrolyte: charging to 100% SOC → discharging to 0% SOC → charging to 100% SOC → discharging to 0% SOC. The two charge-discharge cycles took ~3 h in total, and the CLS electrolyte was held at the reduced AHQDS state (0% SOC) after these cycles.

d. Both the CLS and NCLS electrolytes were pumped back into the tank and kept static at 50 °C for ~21 h. Therefore, the two charge-discharge cycles (step c) and the static aging of the CLS electrolyte (step d) took 24 h in total.

e. The two charge-discharge cycles (step c) and the static aging of the CLS electrolyte (step d) were repeated every 24 h for 9 consecutive days.

The TMHQ/TMQ symmetric RFB test followed a similar procedure with minor modification: (1) the TMHQ/TMQ symmetric RFB was tested at 50 °C but in ambient atmosphere because neither TMHQ nor TMQ is sensitive to air (unlike AHQDS can be easily oxidized when exposed to air); (2) the CLS and the NCLS electrolyte volumes are 10 mL and 40 mL, respectively; (3) the cutoff cell voltages were set as ±0.8 V (Figure 6.2b in the Chapter 6) due to the inferior redox kinetics of the TMHQ/TMQ redox couple; (4) The CLS electrolyte was first fully oxidized to the TMQ state (100% SOC), and two charge-discharge cycles were then conducted (discharging to 0% SOC → charging to 100% SOC → discharging to 0% SOC → charging to 100% SOC); (5) The CLS electrolyte was held at the oxidized TMQ state for static aging.

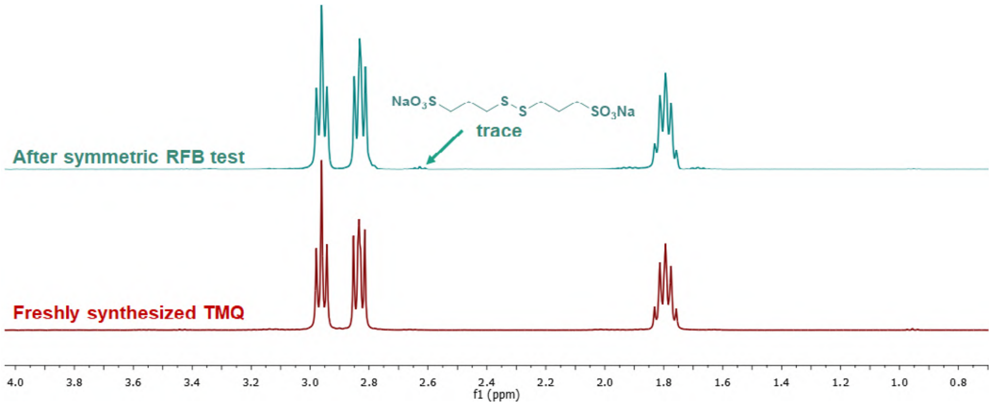

Figure A6.10. ^{1}H NMR spectra of the freshly synthesized TMQ (brown curve) and the CLS electrolyte after the TMHQ/TMQ symmetric RFB test for 9 days (cyan curve).

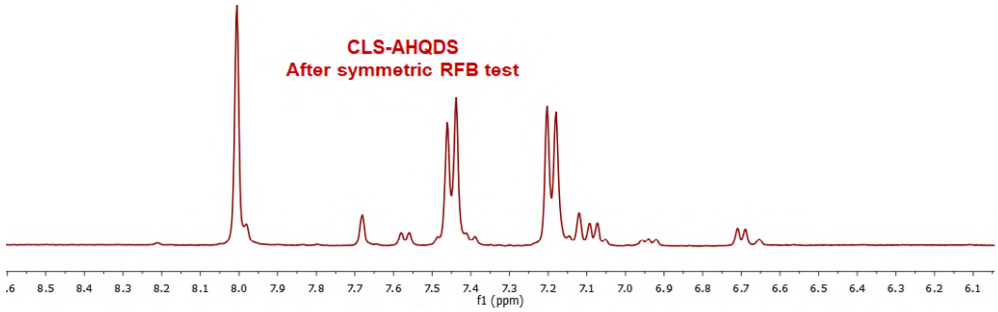

Figure A6.11. ^{1}H NMR spectrum of the CLS electrolyte after the AHQDS/AQDS symmetric RFB test for 9 days.

6. Decay Byproducts Analysis and Mechanistic Hypothesis

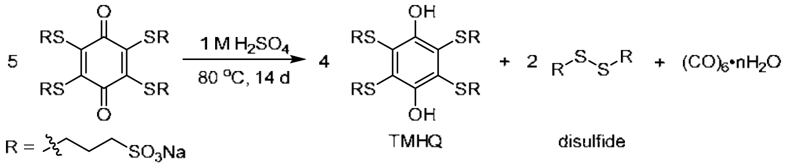

ratio	TMHQ:disulfide
In theory	2:1
Observed	2.2:1

TMQ was obtained by electrochemical oxidation of TMHQ in a divided H-cell as shown earlier, yielding ~0.25 M TMQ in 1 M H_2SO_4 in D_2O solution (see Section 4 of the Appendix 6). This solution was sealed in a 25 mL glass vial and heated at 80 °C in an oil bath under stirring for 2 weeks (to completely decay the TMQ) before subjected to the NMR analysis. The ^1H NMR result demonstrated that there were only two distinct byproducts in the solution, which were assigned to TMHQ and disulfide with the molar ratio of 2.2:1 (Figure A6.12). The mechanistic hypothesis based on this ^1H NMR result is provided in Figure 6.3 in the Chapter 6.

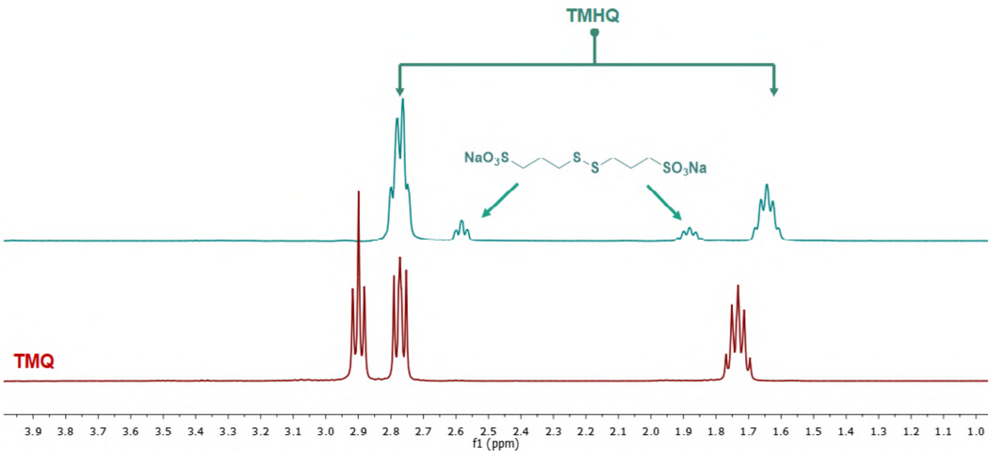

Figure A6.12. ^1H NMR spectra of the freshly synthesized TMQ (brown curve) vs. the completely decayed TMQ sample (cyan curve).

7. Direct Water Splitting without a RR

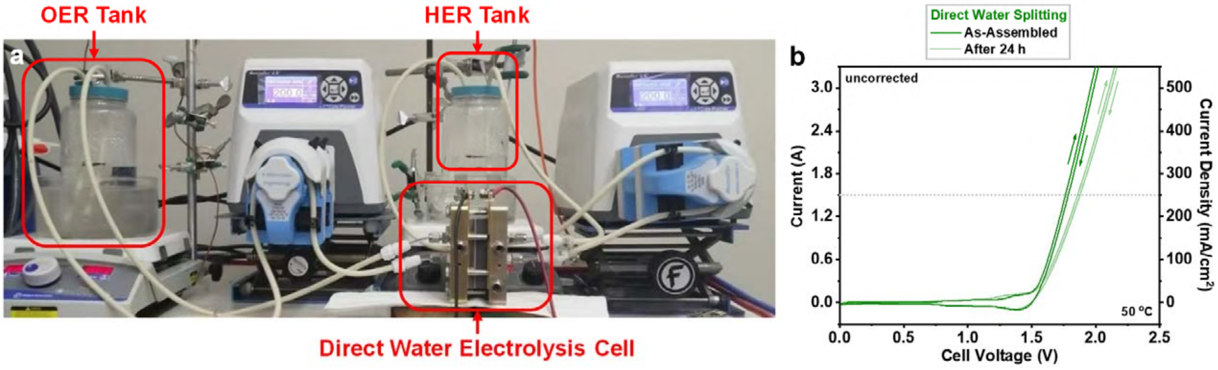

Figure A6.13. Experimental setup and polarization curves of the direct water splitting cell. (a) Experimental setup for the direct water splitting. (b) Polarization curves of direct water splitting (electrolyte: 1 M H_2SO_4 solution for both HER and OER tanks; temperature: 50 °C) before and after the long-term chronopotentiometry test at a constant current density of 250 mA/cm^2 for 24 h (see Figure 6.4b,c in the Chapter 6).

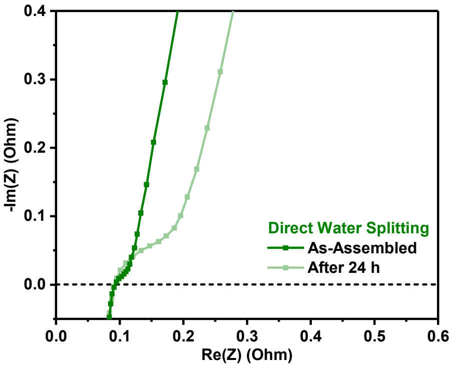

Figure A6.14. PEIS measurement of the direct water splitting cell. Potentiostatic electrochemical impedance spectroscopy (PEIS) measurement of the direct water splitting cell at the cell voltage of 0 V (electrode area:6 cm^2; electrolyte: 1 M H_2SO_4 solution for both HER and OER tanks; temperature: 50 °C) before and after the long-term chronopotentiometry test at a constant current density of 250 mA/cm^2 for 24 h (see Figure 6.4b,c in the Chapter 6).

Water electrolysis measurements were carried out using a commercial electrolyzer assembly (Fuel Cell Technologies), the same as a previous report.[5] The membrane electrode assembly (MEA, purchased from Fuel Cell Etc.) consists of a Nafion 115 membrane (4 cm × 4 cm), a hydrogen evolution reaction (HER) catalyst layer of 0.5 mg/cm^2 60% Pt/C (2.4 cm × 2.4 cm) and/or an oxygen evolution reaction (OER) catalyst layer of 3 mg/cm^2 $IrRuO_x$ (2.4 cm × 2.4 cm). Direct water splitting experiment was performed using a three-layer MEA (membrane + Pt/C layer + $IrRuO_x$ layer) in one electrolyzer assembly: four pieces of as-received carbon paper (GDL 39 AA, SIGRACET®, ~0.01-inch thickness) were attached to the Pt/C layer to serve as the gas diffusion layer for the HER half-cell, while three pieces of platinized titanium screen (0.004-inch thickness, purchased from Fuel Cell Store) were attached to the $IrRuO_x$ layer and served as the gas diffusion layer for the OER half-cell; the MEA and gas diffusion layers was enclosed by two pieces of Teflon gaskets (0.03-inch thickness for the HER side and 0.01-inch thickness for the OER side), flow plates (graphite for the HER half-cell and titanium for the OER half-cell) and gold-plated copper current collectors. The electrolytes (500 mL of 1 M H_2SO_4 solution) were stored in sealed glass jars with a needle punched through the cap for gas release, heated 50 °C in an oil bath, and circulated through the flow plates via PharMed BPT #16 tubing using a Cole-Palmer peristaltic pump Masterflex L/S operated at the flow rate of 200 mL/min. The actual temperature of the electrolyte in the device was measured to be 44 °C when the heated electrolyte was circulated at 200 mL/min. The polarization curves were collected by running CV at a scan rate of 100 mV/s while flowing the electrolytes (Figure 6.4b in the Chapter 6, and Figure A6.13b). Long-term chronopotentiometry test of direct water splitting was performed at a constant current density of 250 mA/cm^2 for 24 h (Figure 6.4c in the Chapter 6).

8. Decoupled Water Splitting Using TMHQ/TMQ as a RR

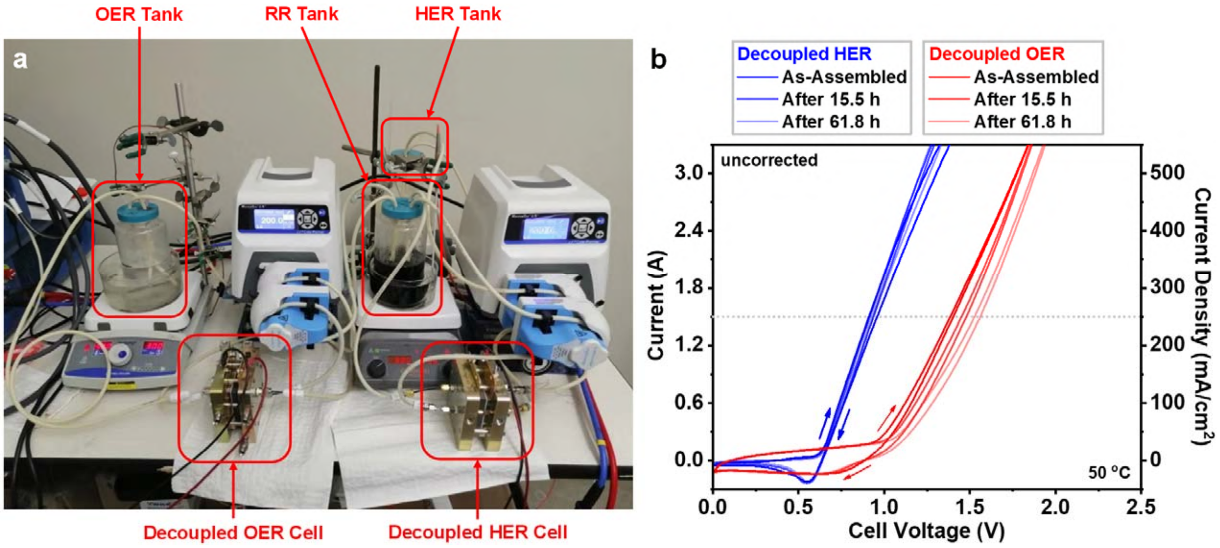

Figure A6.15. Experimental setup and polarization curves of the decoupled water splitting devices. (a) Experimental setup of the decoupled water splitting devices comprised of two individual cells, the HER cell and the OER cell. (b) Polarization curves of the decoupled HER (blue curves) and OER (red curves) cells (electrolyte: 0.25 M TMHQ/TMQ at 50% SOC in 1 M H_2SO_4 solution for RR tank, 1 M H_2SO_4 solution for both HER and OER tanks; temperature: 50 °C) before and after the long-term chronopotentiometry test at a constant current density of 250 mA/cm^2 for 61.8 h (see Figure 6.4b,c in the Chapter 6).

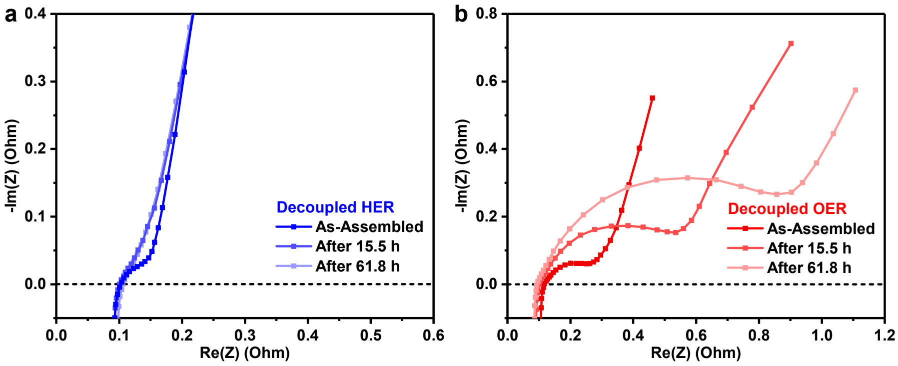

Figure A6.16. PEIS measurement of the decoupled water splitting devices. Potentiostatic electrochemical impedance spectroscopy (PEIS) measurement of the decoupled (a) HER and (b) OER cells at the cell voltage of 0 V (electrode area: 6 cm^2; electrolyte: 0.25 M TMHQ/TMQ at 50% SOC in 1 M H_2SO_4 solution for RR tank, 1 M H_2SO_4 solution for both HER and OER tanks;

temperature: 50 °C) before and after the long-term chronopotentiometry test at a constant current density of 250 mA/cm^2 for 24 h (see Figure 6.4b,c in the Chapter 6).

Decoupled water splitting experiment was performed using a pair of two-layer MEAs (membrane + Pt/C layer for HER cell; membrane + $IrRuO_x$ layer for OER cell) in two electrolyzer assemblies (Figure A6.15a) with the configuration similar to the report by Cronin and coworkers:[6] four pieces of as-received carbon paper (2.4 cm × 2.5 cm, GDL 39 AA, SIGRACET®) were used as electrode for the RR oxidation and reduction half-cells; graphite flow plates were used for the RR oxidation and reduction half-cells; the rest of the device configurations were the same as the direct water splitting experiment (see Section 7 of the Appendix 6). The RR tank held 500 mL of 0.25 M TMHQ/TMQ with a 50% SOC in 1 M H_2SO_4 solution, which was prepared by the anodic bulk electrolysis of 500 mL of 0.25 M TMHQ in 1 M H_2SO_4 solution at a constant current of 3 A for 67 min to pass the theoretical amount of charge needed to reach 50% SOC (assuming a Faradaic efficiency of unity for the oxidation of TMHQ to TMQ). Both the HER and the OER tanks held 500 mL of 1 M H_2SO_4 solution. All the electrolytes were stored in sealed glass jars with a needle punched through the cap of the HER and OER tanks for gas yield quantification (Figure 6.4d in the Chapter 6), heated at 50 °C in oil baths, and circulated through the flow plates via PharMed BPT #16 tubing using a Cole-Palmer peristaltic pump Masterflex L/S operated at the flow rate of 200 mL/min. The actual temperature of the electrolyte in the device was measured to be 44 °C when the heated electrolyte was circulated at 200 mL/min. The polarization curves were collected by running CV at a scan rate of 100 mV/s while flowing the electrolytes (Figure 6.4b in the Chapter 6, and Figure A6.15b). Long-term chronopotentiometry test of decoupled water splitting was performed at a constant current density of 250 mA/cm^2 for 61.8 h (Figure 6.4c in the Chapter 6).

The operational stability of the decoupled water splitting devices were evaluated by both the chronopotentiometry traces and the polarization curves. During the chronopotentiometry test, the cell voltage of the decoupled HER cell stayed extremely stable over the entire test period of 61.8 h (Figure 6.4c blue trace in the Chapter 6), suggesting both the RR and the Pt/C HER catalyst were stable. The extraordinary stability of the decoupled HER cell was further confirmed by the fact that the polarization curves collected before and after the chronopotentiometry test were almost overlapping (Figure A6.15b blue traces and Table A6.1), and the high-frequency resistance (based on the horizontal intercept) and the charge-transfer resistance (based on the semi-circle) in the

Nyquist plot were almost unchanged after the chronopotentiometry test (Figure A6.16a). A slight increase in the cell voltage of the decoupled OER cell was observed during the chronopotentiometry test (Figure 6.4c red trace in the Chapter 6), which was due to the slight deactivation of the $IrRuO_x$ OER catalyst over time (because the RR was stable according to the decoupled HER cell) and was evidenced by the non-overlapping polarization curves before and after the chronopotentiometry test (Figure A6.15b red traces and Table A6.1) and the increased charge-transfer resistance in the Nyquist plot after the chronopotentiometry test (Figure A6.16b). It should be noted that the slight deactivation of the $IrRuO_x$ OER catalyst was also observed in the direct water splitting cell after the chronopotentiometry test (Figure 6.4c green trace in the Chapter 6), evidenced by the non-overlapping polarization curves before and after the chronopotentiometry test (Figure A6.13b and Table A6.1) and the increased charge-transfer resistance in the Nyquist plot after the chronopotentiometry test (Figure A6.14).

Table A6.1. Cell voltage comparisons of the decoupled water splitting devices and the direct water splitting cell. Cell voltage comparisons of the decoupled HER and OER cells (Figure A6.15b) and the direct water splitting cell (Figure A6.13b) at 250 mA/cm^2 from the polarization curves collected before and after the long-term chronoamperometry tests (Figure 6.4c in the Chapter 6).

Time (h)	Cell Voltage (V) at 250 mA/cm^2 from Polarization Curves		
	Decoupled HER	Decoupled OER	Direct Water Splitting
0.0	0.94	1.39	1.78
15.5	0.93	1.47	-
24.0	-	-	1.87
61.8	0.93	1.55	-

Table A6.2. Quantification of the H_2 and O_2 gas yields from decoupled water splitting. Quantification of the H_2 and O_2 gas yields from decoupled water splitting enabled by the TMHQ/TMQ RR during four ~10 min periods of the chronoamperometry test operated at 250 mA/cm^2 and 50 °C (see Figure 6.4d in the Chapter 6).

Cumulative Time (min)	Time During Each Period (min)	Measured Volume of H_2 Gas (mL) [a]	Measured Volume of O_2 Gas (mL) [a]	Theoretical Volume of H_2 Gas (mL) [b]	Theoretical Volume of O_2 Gas (mL) [b]	Faradaic Efficiency of Decoupled HER (%) [c]	Faradaic Efficiency of Decoupled OER (%) [c]
0	0	0.0	0.0	0.0	0.0	-	-
3.45	3’27” = 3.45	40.0	19.0	41.9	20.9	95.5	90.8
5.12	5’07” = 5.12	60.0	29.0	62.1	31.0	96.6	93.4
6.78	6’47” = 6.78	80.0	39.0	82.3	41.2	97.2	94.7
8.52	8’31” = 8.52	100.0	49.0	103.4	51.7	96.7	94.8
8.52	0	0.0	0.0	0.0	0.0	-	-
11.43	2’55” = 2.92	37.0	20.0	35.4	17.7	104.5	113.0
13.20	4’41” = 4.68	58.0	30.0	56.8	28.4	102.0	105.6
14.85	6’20” = 6.33	78.0	40.0	76.9	38.4	101.5	104.1
16.58	8’04” = 8.07	96.0	50.0	97.9	49.0	98.1	102.1
16.58	0	0.0	0.0	0.0	0.0	-	-
20.00	3’25” = 3.42	40.0	20.5	41.5	20.7	96.5	98.9
21.63	5’03” = 5.05	60.0	31.0	61.3	30.6	97.9	101.2
23.33	6’45” = 6.75	80.0	41.0	81.9	41.0	97.7	100.1
25.00	8’25” = 8.42	100.0	51.0	102.1	51.1	97.9	99.9
25.00	0	0.0	0.0	0.0	0.0	-	-
28.13	3’08” = 3.13	37.0	20.0	38.0	19.0	97.3	105.2
29.85	4’51” = 4.85	58.0	30.0	58.9	29.4	98.5	101.9
31.50	6’30” = 6.50	77.0	40.0	78.9	39.4	97.6	101.4
33.38	8’23” = 8.38	98.0	50.0	101.7	50.9	96.3	98.3
						Average = 98.2	Average = 100.3

[a] Volumes of H_2 and O_2 gases were measured by collecting gases over water in two separate 100-mL graduated cylinders.

[b] Theoretical Volume of H_2 Gas (mL) = $\frac{1.5\text{ (A)} \times \text{Time During Each Period (min)} \times 60\text{ s/min}}{96485\text{ (C/mol e}^-) \times 2\text{ (mol e}^-\text{/mol H}_2)} \times \frac{8.3145\text{ [J/(mol·K)]} \times (273.15 + 44)\text{ (K)} \times 10^6\text{ (mL/m}^3)}{101325\text{ Pa}}$

Theoretical Volume of O_2 Gas (mL) = $\frac{1.5\text{ (A)} \times \text{Time During Each Period (min)} \times 60\text{ s/min}}{96485\text{ (C/mol e}^-) \times 4\text{ (mol e}^-\text{/mol O}_2)} \times \frac{8.3145\text{ [J/(mol·K)]} \times (273.15 + 44)\text{ (K)} \times 10^6\text{ (mL/m}^3)}{101325\text{ Pa}}$

The actual temperature of the electrolyte in the device was measured to be 44 °C.

[c] Faradaic Efficiency of Decoupled HER (%) = Measured Volume of H_2 Gas (mL) / Theoretical Volume of H_2 Gas (mL) × 100%

Faradaic Efficiency of Decoupled OER (%) = Measured Volume of O_2 Gas (mL) / Theoretical Volume of O_2 Gas (mL) × 100%

Energy efficiency calculations for the decoupled water splitting process were conducted by comparing the energy consumed to evolve a certain volume of H_2 gas from the decoupled water electrolyzers (E_{consumed}) vs. the energy theoretically contained in the evolved H_2 gas that can be released through its combustion (E_{H_2}). Only the energy consumed in the electrochemical processes of the electrolyzers but not that of the entire setup (including pumps, heating apparatus, etc.) was considered in the calculation of E_{consumed}. The higher heating value of H_2 gas (HHV_{H_2} = 285.60 kJ/mol) was used in the calculation of E_{H_2}.

$$E_{\text{consumed}} = (V_{\text{HER}} \times I_{\text{HER}} \times t_{\text{HER}}) + (V_{\text{OER}} \times I_{\text{OER}} \times t_{\text{OER}})$$

$$\text{In our case: } E_{\text{consumed}} = (V_{\text{HER}} + V_{\text{OER}}) \times I_{\text{HER}} \times t_{\text{HER}}$$

$$E_{H_2} = n_{H_2} \times HHV_{H_2} = \frac{I_{\text{HER}} \times t_{\text{HER}}}{2 \times F} \times HHV_{H_2}$$

where V_{HER}, I_{HER}, and t_{HER} are the cell voltage, applied current, and operation time of the decoupled HER cell; V_{OER}, I_{OER}, and t_{OER} are the cell voltage, applied current, and operation time of the decoupled OER cell; n_{H_2} is the number of mole of the evolved H_2 gas, F is the Faraday constant. Energy efficiency of the decoupled water splitting process ($EE_{\text{decoupled}}$) was calculated by dividing E_{H_2} by E_{consumed}.

$$EE_{\text{decoupled}} = \frac{E_{H_2}}{E_{\text{consumed}}} \times 100\%$$

$$\text{In our case: } EE_{\text{decoupled}} = \frac{HHV_{H_2}}{2 \times F \times (V_{\text{HER}} + V_{\text{OER}})} \times 100\%$$

Energy efficiency of the direct water splitting process (EE_{direct}) was calculated in a similar manner.

$$\text{In our case: } EE_{\text{direct}} = \frac{HHV_{H_2}}{2 \times F \times V_{\text{direct}}} \times 100\%$$

where V_{direct} is the cell voltage of the direct water splitting cell.

Table A6.3. Energy efficiency of the decoupled water splitting process. Energy efficiency of the decoupled water splitting process enabled by the TMHQ/TMQ RR, and its comparison with the direct water splitting process and other decoupled water splitting systems enabled by molecular RRs.

System	Molecular RR	Experimental Conditions of Water Splitting				Temperature (°C)	Current Density (mA/cm^2)	Cell voltage (V)			Energy Efficiency (%)	Reference
		Setup	Electrolyte	HER Catalyst	OER Catalyst			Direct Water Splitting	Decoupled HER	Decoupled OER		
Direct water splitting	-	Two-electrode flow cell	1 M H_2SO_4 (circulated at 200 mL/min)	60% Pt/C (0.5 mg/cm^2)	$IrRuO_x$ (3 mg/cm^2)	50	250	1.77	-	-	83.6	This work
Decoupled water splitting	TMHQ/TMQ (0.25 M in 1 M H_2SO_4)	Two-electrode flow cell	1 M H_2SO_4 (circulated at 200 mL/min)	60% Pt/C (0.5 mg/cm^2)	$IrRuO_x$ (3 mg/cm^2)	50	250	-	0.97	1.40	62.4	This work
	AHQDS/AQDS (0.5 M in 1 M H_2SO_4)	Two-electrode flow cell	1 M H_2SO_4 (circulated at 250 mL/min)	Pt (0.3 mg/cm^2)	IrO_2 (1 mg/cm^2)	50	500	-	0.585	1.778	62.6	*Chem. Sci.* **2018**, *9*, 1621-1626.
	HQMS/QMS (0.5 M in 1.8 M H_3PO_4)	Three-electrode stirred cell	1.8 M H_3PO_4	Pt mesh	Pt mesh	Room temperature	50	-	1.29	2.00	45.0	*J. Am. Chem. Soc.* **2013**, *135*, 13656-13659.
	$[H_4PMo_{12}O_{40}]^-$/ $[H_2PMo_{12}O_{40}]^-$ (0.5 M in 1 M H_3PO_4)	Three-electrode stirred cell	1 M H_3PO_4	Pt mesh	Pt mesh	Room temperature	100	-	1.23	1.71	50.3	*Nat. Chem.* **2013**, *5*, 403-409.

The energy efficiency of the decoupled water splitting process enabled by the TMHQ/TMQ RR is comparable to the reported value achieved using the AHQDS/AQDS RR in a similar two-electrode flow cell setup under similar operating conditions and is higher than those achieved using other molecular RRs in three-electrode stirred cells. On the other hand, it is lower compared to the direct water splitting process because of the use of an additional piece of membrane and the electrochemical kinetics of the RR, both of which result in an increase in the DC polarization resistance. Therefore, the energy efficiency of decoupled water splitting could be further improved by lowering the ohmic resistances of the cell components as well as improving the electrochemical kinetics of the molecular RRs.

9. References Cited in the Appendix 6

1. Gerken, J. B.; Stamoulis, A. G.; Suh, S.-E.; Fischer, N. D.; Kim, Y.-J.; Guzei, I. A.; Stahl, S. S. Efficient Electrochemical Synthesis of Robust, Densely Functionalized Water Soluble Quinones. *Chem. Commun.* ***56***, 1199-1202 (2020).

2. Huskinson, B.; Marshak, M. P.; Suh, C.; Er, S.; Gerhardt, M. R.; Galvin, C. J.; Chen, X.; Aspuru-Guzik, A.; Gordon, R. G.; Aziz, M. J. A Metal-Free Organic-Inorganic Aqueous Flow Battery. *Nature* ***505***, 195-198 (2014).

3. Goulet, M. A.; Aziz, M. J. Flow Battery Molecular Reactant Stability Determined by Symmetric Cell Cycling Methods. *J. Electrochem. Soc.* ***165***, A1466-A1477 (2018).

4. Li, W.; Fu, H.-C.; Zhao, Y.; He, J.-H.; Jin, S. 14.1% Efficient Monolithically Integrated Solar Flow Battery. *Chem* ***4***, 2644-2657 (2018).

5. Preger, Y.; Gerken, J. B.; Biswas, S.; Anson, C. W.; Johnson, M. R.; Root, T. W.; Stahl, S. S. Quinone-Mediated Electrochemical O_2 Reduction Accessing High Power Density with an Off-Electrode Co-N/C Catalyst. *Joule* ***2***, 2722-2731 (2018).

6. Kirkaldy, N.; Chisholm, G.; Chen, J.-J.; Cronin, L. A Practical, Organic-Mediated, Hybrid Electrolyser That Decouples Hydrogen Production at High Current Densities. *Chem. Sci.* ***9***, 1621-1626 (2018).